ARO 34596.2-EL-CF

PROCEEDINGS

1995 INTERNATIONAL SEMICONDUCTOR DEVICE RESEARCH SYMPOSIUM

December 5 - 8, 1995 • Omni Charlottesville Hotel



19960828 106

IEEE MTT

URSI

The Russian Physical Society

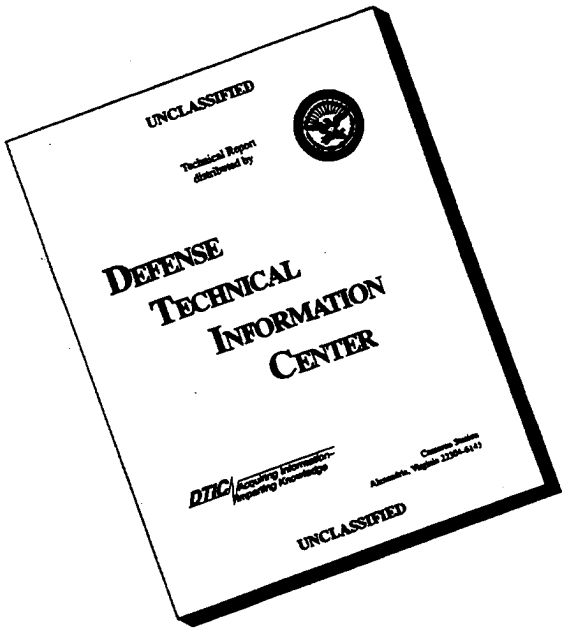
VOLUME II of II

SCHOOL OF ENGINEERING & APPLIED SCIENCE
Academic Outreach

EPS

DTIC QUALITY INSPECTED 1

DISCLAIMER NOTICE



THIS DOCUMENT IS BEST QUALITY AVAILABLE. THE COPY FURNISHED TO DTIC CONTAINED A SIGNIFICANT NUMBER OF PAGES WHICH DO NOT REPRODUCE LEGIBLY.

SF 298 MASTER COPY KEEP THIS COPY FOR REPRODUCTION PURPOSES

REPORT DOCUMENTATION PAGE

Form Approved
OMB NO. 0704-0188

Public reporting burden for this collection of information is estimated to average 1 hour per response, including the time for reviewing instructions, searching existing data sources, gathering and maintaining the data needed, and completing and reviewing the collection of information. Send comment regarding this burden estimates or any other aspect of this collection of information, including suggestions for reducing this burden, to Washington Headquarters Services, Directorate for information Operations and Reports, 1215 Jefferson Davis Highway, Suite 1204, Arlington, VA 22202-4302, and to the Office of Management and Budget, Paperwork Reduction Project (0704-0188), Washington, DC 20503.

1. AGENCY USE ONLY *(Leave blank)*	2. REPORT DATE	3. REPORT TYPE AND DATES COVERED
	Aug 96	Final 1 Sep 95 - 31 Aug 96

4. TITLE AND SUBTITLE

1995 International Semiconductor Device Research Symposium, Volume II

5. FUNDING NUMBERS

DAAH04-95-1-0502

6. AUTHOR(S)

E. Towe (principal investigator)

7. PERFORMING ORGANIZATION NAMES(S) AND ADDRESS(ES)

University of Virginia
Charlottesville, VA 22904

8. PERFORMING ORGANIZATION REPORT NUMBER

9. SPONSORING / MONITORING AGENCY NAME(S) AND ADDRESS(ES)

U.S. Army Research Office
P.O. Box 12211
Research Triangle Park, NC 27709-2211

10. SPONSORING / MONITORING AGENCY REPORT NUMBER

ARO 34596.2-EL-CF

11. SUPPLEMENTARY NOTES

The views, opinions and/or findings contained in this report are those of the author(s) and should not be construed as an official Department of the Army position, policy or decision, unless so designated by other documentation.

12a. DISTRIBUTION / AVAILABILITY STATEMENT

Approved for public release; distribution unlimited.

12 b. DISTRIBUTION CODE

13. ABSTRACT *(Maximum 200 words)*

This volume contains the Proceedings of the third International Semiconductor Device Research Symposium (ISDRS-95, Charlottesville,Virginia, December 5-8, 1995).

The goal of this international meeting is to provide a congenial forum for the exchange of information and new ideas for researchers from university, industry and government laboratories in the field

14. SUBJECT TERMS

15. NUMBER IF PAGES

16. PRICE CODE

17. SECURITY CLASSIFICATION OR REPORT	18. SECURITY CLASSIFICATION OF THIS PAGE	19. SECURITY CLASSIFICATION OF ABSTRACT	20. LIMITATION OF ABSTRACT
UNCLASSIFIED	UNCLASSIFIED	UNCLASSIFIED	UL

Papers have been printed without editing as received from the authors.

All opinions expressed in the Proceedings are those of the authors and are not binding on the sponsors of this Symposium.

The views, opinions and/or findings contained in this report are those of the authors(s) and should not be construed as an official position, policy, or decision of the U.S. Government unless so designated by other documentation.

Publication of a paper in this Proceedings is in no way intended to preclude publication of a fuller account of the paper elsewhere.

This work relates to Department of Navy Grant N00001-95-1-0972 issued by the Office of Naval Research and the U.S. Army Research Office Grant No. DAAH04-95-1-0502. The United States Government has a royalty-free license throughout the world in all copyrightable material contained herein.

Additional copies of this publication are available from

Engineering Academic Outreach
University of Virginia
Thornton Hall
Charlottesville, Virginia 22903-2442
(804) 924-3744

UVA/EAO Catalog Number: 95-CI086-3-004
ISBN Number: 1-880920-03-4

Organizing Committee

W. Anderson, *NRL*
Y. Arakawa, *University of Tokyo, Co-Chair, Japan*
J. Baek, *Semicon Technology Laboratory, Co-Chair, Asia*
I. Bahl, *ITT*
A. Ballato, *ARL*
G. Borsuk, *NRL*
R. Bradley, *NRAO*
F. Capasso, *AT&T Bell Labs, Symposium Co-Chair*
J. Comas, *NIST*
D. Crawford, *NSF*
M. Dutta, *ARL*
R. Dutton, *Stanford University*
L. Eastman, *Cornell University*
T. Fjeldly, *Norwegian Institute of Technology, Co-Chair, Europe*
B. Gelmont, *University of Virginia*
W. Gelnovatch, *ARL*
T. Giallorenzi, *NRL*
T. Globus, *University of Virginia*
E. Hu, *University of California Santa Barbara*
B. Jesser, *University of Virginia*
S. Jones, *University of Virginia, Program Chair*
T. J. King, *Xerox PARC*
K.-M. Lau, *University of Massachusetts*
J.-P. Leburton, *University of Illinois*
K. Lee, KAIST
M. Levinshtein, *Ioffe Institute, Russia, Co-Chair, CIS*
N. Lifshitz, *AT&T Bell Labs*
K. Likharev, *SUNY, Stony Brook*
M. Littlejohn, *ARO/NCSU*
S. Luryi, *SUNY, Stony Brook*
R. Mattauch, *University of Virginia, Past Senior Symposium Chair*
S. McAlister, *National Research Council, Canada*
J. Mink, *ARO*
J. Pankove, *University of Colorado*
Y. S. Park, *ONR*
T. Pearsall, *University of Washington*
W. Peatman, *University of Virginia, Local Arrangement Chair*
G. Pomrenke, *AFOSR*
Z. Popovic, *University of Colorado*
M. Pospieszalski, *NRAO*
H. Rupprecht, *Fraunhofer Institute, Germany*
M. Shur, *University of Virginia, Past Junior Symposium Chair*
P. Siegel, *JPL*
H. Slade, *University of Virginia, Symposium Secretary*
D. Slobodin, *ARPA*
M. Spencer, *Howard University, Publicity Chair*
M. Stroscio, *ARO*
E. Towe, *University of Virginia, Symposium Co-Chair*
R. Weikle, *University of Virginia, Symposium Treasurer*
D. Wu, *Chinese Academy of Science*
M. Yoder, *ONR*



Professor Aldert van der Ziel

(December 12, 1910 - January 20, 1991)

The van der Ziel Award, sponsored by Westinghouse Electric Company, was established in honor of Professor Aldert van der Ziel for his long, distinguished and illustrious career as an educator and a research scientist.



LESTER F. EASTMAN

Lester F. Eastman was born in Utica, NY, and obtained B.S. (1953), M.S. (1955), and Ph.D. (1957) degrees at Cornell University. He joined the faculty of Electrical Engineering at Cornell in 1957, and also serves as a member of the graduate fields of Applied Physics and Materials Science. Since 1965 he has been doing research on compound semiconductor materials, high speed devices, and circuits, and has been active in organizing workshops and conferences on these subjects elsewhere since 1965 and at Cornell from 1967. In 1977 he joined other Cornell faculty members in obtaining funding and founding the National Research and Resource Facility for Submicron Structures at Cornell (now Cornell Nanofabrication Facility). Also in 1977 he founded the Joint Services Electronics Program and directed it until 1987. He has recently joined with others at Cornell to develop a large effort in high frequency/high speed optoelectronics. He has supervised over 97 PhD theses, over 50 MS theses, and over 50 post-doctoral studies. In his research group effort is underway on molecular beam epitaxy, microwave transistors, high speed semiconductor lasers, high frequency photo-receivers and fundamental phenomena in compound semiconductor quantum electron and optical devices. During the 1978-1979 year he was on leave at MIT's Lincoln Laboratory, and during the 1985-86 year he was at IBM Watson Research Laboratory. During 1983 he was the IEEE Electron Device Society National Lecturer. He was a member of the U.S. Government Advisory Group on Electron Devices from 1978-1988, and has served as a consultant for several industries. From 1987-1993 he served as a member of the Kuratorium (Visiting Senior Advisory Board) of the Fraunhofer Applied Physics Institute in Freiburg, Germany. He is the Chairman of the Advisory Committee for the Materials Science Research Center of Excellence at Howard University. He is a founder in 1985 and has served as chairman of the board of directors of Northeast Semiconductors, Inc. from 1985-1993. He has been a Fellow of IEEE since 1969, a member of the National Academy of Engineering since 1986, and has been appointed the John L. Given Foundation Chair Professor of Engineering at Cornell in January 1985. In September 1991 he was awarded the GaAs Symposium Award, and the Heinrich Welker medal, for his "contributions to the development of ballistic electron devices, planar doping, buffer layers, and AlInAs/GaInAs/InP heterostructures". He was awarded the Alexander von Humboldt Senior Fellowship in 1994.

1995 INTERNATIONAL SEMICONDUCTOR DEVICE RESEARCH SYMPOSIUM

HISTORY OF SYMPOSIUM OFFICERS

YEAR	SYMPOSIUM CHAIR	PROGRAM CHAIR	LOCAL ARRANGEMENTS
1995	Elias Towe Federico Capasso	Stephen Jones	William Peatman
1993	Michael Shur	Elias Towe	Stephen Jones
1991	Robert Mattauch	Michael Shur	Stephen Jones

YEAR	TREASURER	SECRETARY	PUBLICITY
1995	Robert Weikle	Holly Slade	Michael Spencer
1993	William Peatman	—	—
1991	—	—	—

ALDERT VAN DER ZIEL AWARD

YEAR	RECIPIENT	AFFILIATION
1995	Lester F. Eastman	Cornell University
1993	Arthur G. Milnes	Carnegie Mellon University

BEST STUDENT PAPER AWARD

YEAR	RECIPIENT	AFFILIATION
1993	Edgar Martinez	Wright Laboratory
	Kaushik Bhaumik	Cornell University
1991	R. Mickevičius	Wayne State University

Introduction

This volume contains the Proceedings of the third International Semiconductor Device Research Symposium (ISDRS-95, Charlottesville,Virginia, December 5-8, 1995).

The goal of this international meeting is to provide a congenial forum for the exchange of information and new ideas for researchers from university, industry and government laboratories in the field of semiconductor devices and device physics. Our other goal is to make this conference truly international. To achieve this, the symposium has sub-committees in Asia, Europe, Japan and the former Soviet Union. This conference is organized in cooperation with the IEEE MTT Society, the European Physical Society, the United States National Committee of URSI and the Russian Physical Society.

The program committee received submissions from 22 countries, representing three (3) continents. Of the submitted papers, 150 have been selected for oral presentations and about 75 for poster presentations. These papers cover a broad range of topics, including novel and ultra-small devices, photonics and optoelectronics, heterostructure and cryogenic devices, wide band gap semiconductors, thin film transistors, MEMs, MOSFET technology and devices, carrier transport phenomena, materials and device characterization, simulation and modeling. It is hoped that such a broad range of topics will foster a cross-fertilization of the different fields related to semiconductor materials and devices.

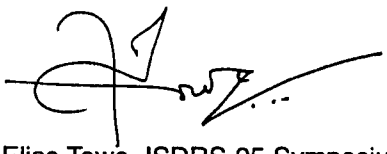
Three special symposia are also included this year: Mid-to-Far Infrared Semiconductor Lasers, Laser Modeling, and MEMs.

The first ISDRS symposium in 1991 was dedicated to the memory of Professor Aldert van der Ziel who made seminal contribution to the theory of semiconductor devices, especially to the theory of noise, and who educated literally hundreds of graduate students. At the second symposium in 1993, ISDRS established a van der Ziel Award sponsored by the Westinghouse Electric Corporation. We are pleased to announce that the 1995 award goes to Lester F. Eastman, Professor of Electrical Engineering, Cornell University.

Every year a Best Student Paper Award is chosen by the Organizing Committee at the close of the symposium from evaluations received from the participants. Two papers won the 1993 Best Student Paper Award. Recipients were Edgar Martinez, Solid State Electronics Directorate, Wright Laboratory, Wright-Patterson Air Force Base, *Factors Determining the Gate Leakage Current in Different Heterostructure Field Effect Transistor Technologies,* and Kaushik Bhaumik, Cornell University, *23 GHzf_T Room Temperature SiGe Quantum Well p-MOSFETs.*

ISDRS-95 was made possible by the generous support of the Office of Naval Research and Army Research Office.

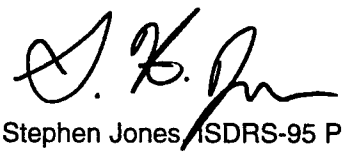
We hope that you find the symposium fruitful and that you will look forward to ISDRS-97.



Elias Towe, ISDRS-95 Symposium Co-Chair



Federico Capasso, ISDRS-95 Symposium Co-Chair



Stephen Jones, ISDRS-95 Program Committee Chair

TABLE OF CONTENTS

Session: W1A Plenary

W1A-3 **Deep Submicron III-V Based Electronics** 1
L.D. Nguyen
Hughes Research Laboratories

W1A-4 **Optoelectronics with Crystalline Organic Semiconductors** 5
S.R. Forrest
Princeton University

W1A-5 **Blue-Green Semiconductor Lasers** 7
A.V. Nurmikko
Brown University

Session: W1P Materials and Device Characterization

Co-Chairs R. Hull
University of Virginia
N. Anderson
University of Massachusetts-Amherst

W1P-1 *Invited* **Trends in ULSI Semiconductor Characterization** 9
T.J. Shaffner
Texas Instruments, Inc.

W1P-2 Effects of Gate Doping Species, Concentration and Microstructure on the Electrical and Reliability Characteristics of Ultrathin Oxides and N_2O-oxynitrides 13
K. Lai, A. Chou, K. Kumar, M. Gardner, J. Fulford, J.C. Lee
The University of Texas at Austin

W1P-3 *Invited* **Device Characterization with Focused Ion Beams** 17
J.F. Walker
FEI Europe Ltd., U.K.

W1P-4 **Structural, Electrical and Optical Characterization of Single Crystal Dysprosium Phosphide (DyP) Grown on GaAs by MBE** 19
R.J. Hwu, P.P. Lee, M. Patel, M. Nikols, J.E. Shield, L.P. Sadwick, D.C. Streit, D. Brehmer, K. McCormick, S.J. Allen, R.W. Gedridge, Jr.
University of Utah

W1P-5 *Invited* **Optical Methods for the Room Temperature, Nondestructive Characterization of Wafer-Sized Compound Semiconductor Device Structures** 23
F.H. Pollak, W. Krystek, M. Leibovitch, L. Malikova
Brooklyn College of the City University of New York

W1P-6 **Interference Technique for a-Si:H Films Optical Measurements** 27
T. Globus
University of Virginia

W1P-7 **Characterization of Pseudomorphic Heterostructure FETs by the Photoconduction Technique** 31
F. Schuermeyer, C. Cerny, J.P. Loehr, R.E. Sherriff
Wright-Patterson Air Force Base

W1P-8 **Near-Field Photoelectronic Studies of Nanometer-Scale Defects in Relaxed GeSi Films** 35
J.W.P. Hsu, E.A. Fitzgerald, Y.H. Xie, P.J. Silverman
University of Virginia

Session: W2P Simulation and Modeling I

Co-Chairs G. Tait
United States Military Academy
M. Stroscio
U.S. Army Research Office

W2P-1 *Invited* **Phonon Kinetics and Heat Removal from Low Dimensional Nanostructures** 39
V. Mitin, G. Paulavicius, N. Bannov, M.A. Stroscio, G.J. Iafrate
Wayne State University

W2P-2 *Invited* **Computation of Semiconductor Noise for Semiclassical Transport** 43
C.E. Korman, I.D. Mayergoyz
The George Washington University

W2P-3 **The Influence of Hydrodynamic Transport Models on the Prediction of Submicron Semiconductor Device Characteristics** 47
M.-K. Ieong, T.-W. Tang
University of Massachusetts-Amherst

W2P-4 **Electrothermal Effects in Semiconductor Power Devices Analyzed by Numerical Simulation and Internal Laser Deflection Measurement** 51
R. Thalhammer, G. Deboy, W. Keilitz, U. Müller, G. Wachutka
Technical University of Munich, Germany

W2P-5 **Temperature Dependence of Early Voltage in HBTs: Theory, Simulations, and Experiment** 55
C.M. Krowne, K. Ikossi-Anastasiou, E. Kougianos
Naval Research Laboratory

W2P-6 **Optimization of Light Emitting Diodes Based on Bipolar Double-Barrier Resonant-Tunneling Structures** 59
K.A. Chao
University of Trondheim, Norway

W2P-7 **Modulated S-Parameter Measurements, for Active Microwave Device Characterization, Using Pulsed-Bias Operation** 61
G. Metze, M. Calcatera, C. Eppers, B. Neidhard, J. Whalen
University of North Carolina at Charlotte

W2P-8 **Model of Backgating and Light Sensitivity in GaAs and LT MBE GaAs MESFETs** 67
D.-X Wu, R.-G. Li, Z.-G. Wong, J.-B. Liang, L.-Y. Lin
Chinese Academy of Sciences, P.R. China

W2P-9 **Analysis of the Charge Injection in MOS Analog Switches Using Physical Models** 71
E. Robilliart, E. Dubois
IEMN/ISEN, France

W2P-10 **Analytical Investigation of Electrical Performance of III-V Semiconductor Metal-Insulator-Semiconductor Field-Effect Transistors** 75
F. Stengel, S.N. Mohammad, H. Morkoç
University of Illinois at Urbana-Champaign

Session: W3P Novel Devices & Concepts

Co-Chairs G. Metze
University of North Carolina-Charlotte

W3P-1 *Student* **Comparison of 2-D and 3-D Side-gated FETs** 79
M.J. Hurt, W.C.B. Peatman, R. Tsai, B.J. Moon, T. Ytterdal, M. Shur
Advanced Device Technologies, Inc.

W3P-2 *Invited* **Coplanar-Strip Geometry Multiple-Quantum-Well Heterostructure Devices** 83
S.W. Kirchoefer
Naval Research Laboratory

W3P-3 **Corrugated Quantum Well Infrared Photodetector Structures for Normal Incidence Light Coupling** 87
C.J. Chen, K.K. Choi, M.Z. Tidrow, D.C. Tsui
Princeton University

W3P-4 **The Silicon Hot Avalanche Injection Transistor (HAIT)** 91
G. Müller, G.A.M. Hurkx, W.B. de Boer, R. Dekker, W.T.A. van den Einden, M.J.J. Theunissen
Philips Research Laboratories, The Netherlands

W3P-5 **The Design and Performance of the Uniphase CMCCD and Its Possible Application as an Analog Memory** 95
L. Chen, H.L. Kwok
University of Victoria, Canada

W3P-6 *Invited* **Effect of Pulsed Fir Laser Radiation on Tunnel and Channel Resistance of δ-Doped GaAs** 99
I.N. Kotel'nikov, A.Y. Shul'man, N.A. Mordovets, N.A. Varvanin, S.D. Ganichev, B. Mayerhofer, W. Prettl
Institute of Radioengineering and Electronics of Russian Academy of Science, Russia

W3P-7 **Harmonic Generation in Bloch Miniband Transport Across a Quantum Wire Superlattice Subject to a Strong AC Signal** 103
X.L. Lei, N.J.M. Horing, H.L. Cui, K.K. Thornber
State Key Laboratory of Functional Materials for Informatics, Shanghai Institute of Metallurgy, Chinese Academy of Sciences, China

W3P-8 **A New Concept for Low-Power All-Optical Switching in MQW Structures** 107
C. Knorr, U. Wilhelm, V. Härle, F. Scholz, A. Hangleiter
Universität Stuttgart, Germany

W3P-9 **Photonic Control of DC and Microwave Characteristics in AlGaAs/GaAs/InGaAs Double Heterostructure Pseudomorphic HEMT's** 111
H.J. Kim, S.J. Kim, D.J. Kim, H. Chung, D.H. Woo, I.K. Han, W.J. Choi, S.H. Kim, J.I. Lee, K.N. Kang, K. Cho
KIST, Korea

W3P-10 **Si/SiGe Heterojunction Phototransistors** 115
K.D. Hobart, F.J. Kub, N. Papanicolaou, P.E. Thompson
Naval Research Laboratory

W3P-11 *Invited* **Device Physics of Modulation Doped Type I and Type II GaAs/AlAs and AlGaAs/AlAs Quantum Well Structures** 119
M. Dutta, A. Petrou
Army Research Laboratory

Session:PW1.1P Device & Materials Characterization

PW1.1P-1 **Study of I-V Characteristics of Asymmetric Double Barrier Resonant Tunneling Diodes with Superlattice Emitters** 123
K. Banoo, T. Daniels-Race
Duke University

PW1.1P-2 **Correlation Between Charge-to-Breakdown (Qbd) and the Endurance (Program/Erase cycling) of Thin Tunnel Oxide** 127
S.-H. Soh, C.-P. Liu, R. Peterson, B. Baker, L. Sadwick
National Semiconductor Corp.

PW1.1P-3 **A Novell MOSFET Series Resistance Measurement Technique Using One Single MOSFET** 131
J.A.M Otten, F.M. Klaassen
Eindhoven University of Technology, The Netherlands

PW1.1P-4 *In situ* Doping of Epitaxial Silicon at Low Temperature and Very Low Pressure 135
X.D. Huang, P. Han, Y.D. Zheng, L.Q. Hu, R.H. Wang, S.M. Zhu
Nanjing University, P.R. China

PW1.1P-5 **Formation and Optical Properties of Ge-Si-Fe Alloys** 139
H. Chen, P. Han, L.Q. Hu, Y. Shi, Y.D. Zheng
Nanjing University, P.R. China

PW1.1P-6 **Evaluation of Silicon Ion Implant Damage in Epitaxial MBE-Grown GaAs from Room and High Temperature Capacitance-Voltage Measurements** 143
E. Russell, R.J. Hwu, L.P. Sadwick, N.A. Papanicolaou
University of Utah

PW1.1P-7 **Nanometer-Scale Mapping of Doped Layers in InP Structures and Devices** 147
M.V. Moore, R. Hull, R.F. Karlicek, Jr., M. Geva, P.D. Carleson, J.F. Walker
University of Virginia

PW1.1P-8 **Effects of Emitter Set-Back Layer Thickness on the Performance of GaInP/GaAs Heterostructure-Emitter Bipolar Transistors** 151
Y.F. Yang, C.C. Hsu, E.S. Yang
Columbia University

PW1.1P-9 **Optical Techniques for the Nondestructive Characterization of 3-580μm Thick Si Substrates** 155
C.S. DeMain, S.H. Jones, T. Globus
University of Virginia

PW1.1P-10 **Phonon Oscillations in a Spectrum of Reversible Bleaching of Gallium Arsenide Under Interband Absorption of a High-Power Picosecond Light Pulse** 157
I.L. Bronevoi
Institute of Radioengineering and Electronics, Russia

Session:PW1.2P Simulation and Modeling I

PW1.2P-1 **A Monte-Carlo Study of Diffusion Phenomena in III-V Heterostructures** 159
A. Sleiman, J.L. Thobel, F. Dessenne, P. Bourel, R. Fauquembergue
Institut d'Electronique et de Microélectronique du Nord, France

PW1.2P-2 **Simple Hydrodynamic Transport Model** 163
J.O. Bark, G. Gildenblat
Penn State University

PW1.2P-3 *Student* **A Large Signal HBT Model for Two-Tone Intermodulation Analysis** 167
B. Li, T.L. Fu, S. Prasad
Northeastern University

PW1.2P-4 **Airy's Function Implementation of the Transfer Matrix Method for Resonant Tunneling** 171
S. Vatannia, G. Gildenblat, B. Gelmont
The Pennsylvania State University

PW1.2P-5 **Simulation of the GaAs MESFET Electrical Burnout** 175
V.A. Vaschenko, J.B. Martynov, V.F. Sinkevitch, A.S. Tager
Science & Research Institute "Pulsar", Russia

Session:PW1.3P Novel Devices & Concepts

PW1.3P-1 **Intrinsic Oscillations in Modified Heterojunction Bipolar Transistors** 179
V. Posse, B. Jalali
University of California, Los Angeles

PW1.3P-2 **Electron System Properties in Semiconductor Structures Based on PbS and ZnCdHgTe Thin Layers** 183
G. Khylap, A. Andrukhiv, L.V. Bochkariova
I. Franko Pedagogical Institute, Ukraine

PW1.3P-3 **Phonon Wall as a Mean of Enhancing Electron Mobility in 2D Structures** 187
J. Pozela, V. Juciene, K. Pozela
Semiconductor Physics Institute, Lithuania

PW1.3P-4 **Identification of a Coulomb Correlation Gap and its Influence on Carrier Transport in Non-Metallic Si:B** 189
M. Lee, J.G. Massey
University of Virginia

PW1.3P-5 **Hot-Electron Fluctuations in n-type GaAs at Extremely High Electric Fields** 193
V. Aninkevicius, V. Bareikis, R. Katilius, J. Liberis, I. Matulioniene, A. Matulionis, P. Sakalas, R. Saltis
Semiconductor Physics Institute, Lithuania

PW1.3P-6 **Concept of the Realization of the Ultimate Possible Photogain in Intrinsic Photoresistors under Given Concentration of the Impurity Recombination Centres** 197
A.A. Drugova, V.A. Kholodnov
Research, Development and Production Centre, "Orion", Russia

PW1.3P-7 **Study of the Effects of High Temperature and Substrate Biasing on the D.C./High Frequency Characteristics of GaAs-Based Devices** 201
R.P. Rozario, R. Narasimhan, L.P. Sadwick, R.J. Hwu
The University of Utah

PW1.3P-8 **Bipolar-Mode Programming Method of EPROM/Flash EEPROM for Low Voltage Applications** 205
Y.-S. Kim, K.-Y. Na
Chungbuk National University, Korea

PW1.3P-9 **New Heterostructures PbS-HgCdTe and their Main Properties** 209
G. Khylap
Drogobych Pedagogical Institute, Ukraine

PW1.3P-10 **Fast Impact Ionization Fronts in Large Area Diode Structures: An Analytical Approach to the Stability and 3D Dynamics** 213
A.M. Minarsky, P.B. Rodin
Ioffe Physical Technical Institute, Russia

PW1.3P-11 Spin-Polarized Electron Photocathodes Based on $In_xGa_{1-x}P$ - GaAs Superlattices 217
A. Subashiev
State Technical University, Russia

PW1.3P-12 **Chaotic Oscillations Emission by NDC Semiconductor Devices** 221
G.S. Simin, A.L. Fradkov, S.A. Shadchin
GIRICOND Sci.-Res. Institute, Russia

PW1.3P-13 **Extrinsic Hopping Photoconductivity in Diamond-Like Semiconductors** 225
O.I. Smirnova, Y.E. Pokrovskii, N.A. Khvalkovskii
Institute of Radioengineering & Electronics, Russia

PW1.3P-14 **Theory of Schottky-Barrier Tunnel Junction Response to Radiation Pressure** 229
A.Y. Shul'man
Institute of Radioengineering and Electronics of the Russian Academy of Sciences, Russia

Session:PW2.1P Millimeter Wave & Microwave Devices

PW2.1P-1 *Invited* **Physical Limitation for Drain Voltage of Power pHEMTs** 233
V.A. Vaschenko, V.F. Sinkevitch
Sci. & Research Institute "Pulsar", Russia

PW2.1P-2 **Comparitive Study on Resonant Tunneling Diode (RTD) and Traditional Tunnel Diode (TD) and Their Co-Integration with Heterojunction Bipolar Transistors (HBTs)** 237
X. Wang, W.L. Chen, G.O. Munns, J.R. East, G.I. Haddad
The University of Michigan

PW2.1P-3 **Microwave Characteristics of High Electron Mobilitly Transistors** 239
H. Ahn, K. Varakorn, M. El Nokali
University of Pittsburgh

PW2.1P-4 **Quasi-Optical Power Combining Techniques for Dielectric Substrates** 243
H. Hwang, T.W. Nuteson, M.B. Steer, J.W. Mink, J. Harvey, A. Paolella
North Carolina State University

PW2.1P-5 **GaInP/InGaAs MODFETs on GaAs Grown by OMPVE for High Frequency and Power Applications** 247
B. Pereiaslavets, K. Bachem, J. Braunstein, L.F. Eastman
Cornell University

PW2.1P-6 **Low Frequency Triggering of Oscillators with a Series Connection of Tunneling Diodes** 251
O. Boric-Lubecke, D.-S. Pan, T. Itoh
University of California-Los Angeles

PW2.1P-7 **Semi-Classical Effects of Ballistic Electrons in Schottky Diodes** 255
D.W. van der Weide
University of Delaware

PW2.1P-8 **Numerical Device/Harmonic-Balance Circuit Analysis of Schottky Barrier Varactors** 259
L.F. Horvath, J.R. Jones, S.H. Jones, G.B. Tait
University of Virginia

PW2.1P-9 **Monte Carlo Simulation of Terahertz Frequency Schottky Diodes** 263
U.V. Bhapkar, R.J. Mattauch
University of Virginia

PW2.1P-10 **Planar Schottky Varactor Diode Arrays for Millimeter-Wave Frequency Multipliers** 267
P.J. Koh, W.C.B. Peatman, T.W. Crowe, N.R. Erickson
University of Virginia

PW2.1P-11 **The Design, Construction and Evaluation of a 585 GHz Planar Schottky Mixer** 271
J.L. Hesler, T.W. Crowe, R.M. Weikle, R.F. Bradley, S.-K. Pan
University of Virginia

Session:PW2.2P Mid-to-Far Infrared Semiconductor Lasers (Special Symposium)

PW2.2P-1 **Generation and Modulation of Infrared Light by Hot Carriers in Ge and GaAs/(Al,Ga)As Structures** 273
L.E. Vorobjev, S.N. Danilov, D.V. Donetsky, Y.V. Kochegarov, D.A. Firsov, V.A. Shalygin
Saint Petersburg State Technical University, Russia

Session:PW2.3P Wide Band Gap Materials and Devices

PW2.3P-1 **Optical Pumping of Lattice-Matched ZnCdMgSe Quaternaries and ZnCdMgSe/ZnCdSe Quantum Wells on InP Substrates** 275
N. Bambha, F. Semendy, M. Tamargo, A. Cavus, L. Zeng, N. Dai
Army Research Laboratory

Session:PW2.4P Photonics & Optoelectronic Devices

PW2.4P-1 **Theory of Dark Resistance in Photodiodes for Arbitrary Diode Geometry** 277
B.L. Gelmont, M.S. Shur, R.J. Mattauch
University of Virginia

PW2.4P-2 **Laser Beam Interference Effects on the Photovoltage of a GaAs p-n Junction** 281
K. Weiser, F. Dahan, S.E. Schacham, E. Towe, H. Park
Technion-Israel Institute of Technology, Israel

PW2.4P-3 **High Speed Turn-Off of a GaAs Optoelectronic Thyristor** 283
V. Korobov, V. Mitin
Wayne State University

PW2.4P-4 **Optimizing p-i-n HBT Receivers for Bit-rate and Sensitivity Using SPICE** 287
M.-J. Kim, D.-K. Kim, S.-J. Kim, M.B. Das
Seoul National University, Korea

PW2.4P-5 *Invited* **Deep Cooling 2x128 Elements Hybrid Photoresistor Device for Spectral Range 6-20μ based on Epitaxial PbSnTe<In> Films Prepared by MBE Technique** 291
V.N. Shumsky, G.N. Feofanov, A.A. Frantsuzov, A.G. Klimenko, A.E. Klimov, N.I. Petikov, T.U. Shafirova, S.N. Shalapaev, V.V. Soldatenkova
Institute of Semiconductor Physics, Russia

PW2.4P-6 **High-Precision Description of Memory Effects in Low-Background IR Detectors** 295
B.I. Fouks
Institute of Radioeng. and Electronics, Russia

Session:PW3.1P Ultra Small Devices

PW3.1P-1 **GaSb/AlSb HBT-LED-RTD Optoelectronic Structures for Complex Nanoelectronic Signal Processing and Computation** 299
H.L. Hartnagel, L.J. Micheel
Technische Hochschule Darmstadt, Germany

PW3.1P-2 **Periodic Conductance Oscillations at Room Temperature in Novel Metal-Nano-Tip/Insulator/Semiconductor Anti-Dot Arrays** 303
J. Haruyama, D. Routkevitch, A.A. Tager, G.L. Tan, M. Moskovits, J.M. Xu
University of Toronto, Canada

PW3.1P-3 **Photoeffect as a Possible Explanation for Conductance Quantization in Nanostructured GaAs Schottky Diodes** 307
H.-W. Hübers, E. Bründermann, H.P. Röser
DLR, Institute for Space Sensor Technology, Germany

PW3.1P-4 **Switching Behavior of Quantum Cellular Automata** 309
P.D. Tougaw, C.S. Lent
University of Notre Dame

PW3.1P-5 *Student* **A Percolation Model for Rapid Vacancy Diffusion During Initial Void Growth in Minimum-Size VLSI Conductors** 313
B.A. Oakley, H.S. Abdel-Aty-Zohdy
Oakland University

PW3.1P-6 **3D Self-Consistent Simulation of Grid-gate Quantum Dot Devices** 319
V.Y.A. Thean, S.H. Nagaraja, P. Matagne, J.P. Leburton
University of Illinois at Urbana-Champaign

PW3.1P-7 **Multi-Phonon Processes in Optical Transitions in Quantum Nanostructures** 323
I.P. Ipatova, A.Y. Maslov, O.V. Proshina
A.F. Ioffe Physical Technical Institute, Russia

Session:PW3.2P Microelectromechanical Devices Special Symposium

PW3.2P-1 **Nonlinear Electrothermomechanical Equations of Deformable Ferroelectric Semiconductors** 327
N. Daher
LPNO-CNRS, France

Session: T1A Ultra Small Devices
Co-Chairs W.C.B. Peatman
University of Virginia
E. Martinez
Wright-Patterson Air Force Base

T1A-1 *Invited* **Ultra Electronics: Overview of ARPA's Nanoelectronics Program** 333
G. Pomrenke
ARPA

T1A-2 *Invited* **Device and Circuit Applications of Tunneling Phenomena** 335
G.I. Haddad
University of Michigan

T1A-3 *Invited* **High-Frequency (f~1 THz) Studies of Quantum-Effect Devices** 337
Q. Hu, S. Verghese, R.A. Wyss, T. Schäpers, J. del Alamo, S. Feng, K. Yakubo, M.J. Rooks, M.R. Melloch, A. Förster
Massachusetts Institute of Technology

T1A-4 *Invited* **Low Frequency Noise in Two-Dimensional Metal-Semiconductor Field Effect Transistor** 343
M. Levinshtein, H. Park, W.C.B Peatman, S.L. Rumyantsev, G.S. Simin, M.S. Shur
Ioffe Institute of Russian Academy of Science, Russia

T1A-5 Transport of Many Electrons in Nanostructured GaAs Schottky Diodes at 300 K Governed by h/e^2 347
H.P. Röser, E. Bründermann, H.-W. Hübers
DLR, Institute for Space Sensor Technology, Germany

T1A-6 A Fully Implanted Heavy Ion 0.10 μm Gate Length NMOS Transistor with Gallium Channel Implantation and Indium Pocket Doping 351
F. Benistant, G. Guegan, M. Lerme, S. Tedesco, F. Martin, M. Heitzmann
LETI (CEA), France

T1A-7 **Ultradense Hybrid SET/FET Dynamic RAM: Feasibility of Background-Charge-Independent Room-Temperature Single-Electron Digital Circuits** 355
K.K. Likharev, A.N. Korotkov
State University of New York at Stony Brook

T1A-8 **Tailoring Acoustic Modes in Mesoscopic Devices** 359
M.A. Stroscio, G.J. Iafrate, J. Zavada, K.W. Kim, Y. Sirenko, S.G. Yu, V. Mitin, N. Bannov, V. Mickevicius, M. Dutta, A. Ballato
U.S. Army Research Office

T1A-9 *Student* **2-D MESFET/RTD Logic Element for Compact, Ultra Low-Power Electronics** 365
J. Robertson, T. Ytterdal, W.C.B. Peatman, R. Tsai, E. Brown, M. Shur
University of Virginia

T1A-10 **Independent Control of Electron Density and Spatial Electron Distribution of Wire Gate Quantum Wire** 369
R. Yang, P.P. Ruden
University of Minnesota

T1A-11 **Self-Consistent Simulation of Vertical Quantum Dot Structures with Residual Coulombic Impurities** 373
P. Matagne, S. Nagaraja, V.Y. Thean, J.P. Leburton, J. Destine, G. Cantraine
University of Illinois at Urbana-Champaign

Session: T2A Microelectromechanical Devices Special Symposium

Co-Chairs D. Koester
Microelectronics Center of North Carolina
T. Kenny
Stanford University

T2A-1 **Piezoresistive Silicon Accelorometer Using Porous Silicon Etching Method and Bump Bonding Technique** 377
J.-H. Sim, S.-H. Lee, J.-S. Kim, J.-H. Lee, J.-H. Lee
Kyungpook National University, South Korea

T2A-2 *Invited* **Polysilicon-Micromachined Optical Devices** 381
N.C. Tien, M.J. Daneman, M.-H. Kiang, O. Solgaard, K.Y. Lau, R.S. Muller
University of California, Berkeley

T2A-3 *Invited* **Thermally Based Systems in CMOS Technology** 385
E.H. Klaassen, R.J. Reay, G.T.A. Kovacs
Stanford University

T2A-4 *Invited* **A μ-Magnetometer Based on Electron Tunneling** 389
L.M Miller, J.A. Podosek, E. Kruglick, T.W. Kenny, J.A. Kovacich, W.J. Kaiser
Jet Propulsion Laboratory

T2A-5 **Design and Fabrication of a Thermally Actuated Silicon Micropump** 393
C.-Q. Zhan, T.-C. Lo, L.-T. Liu, P.-H. Tsien
The Hong Kong University of Science and Technology, Hong Kong

T2A-6 *Invited* **Deep X-Ray Lithography Based Processing for Micromechanics** 397
T.R. Christenson
Sandia National Laboratories

T2A-7 *Invited* **Biomedical Microdevices: A Micromachining Approach** 401
B. Ziaie, K. Najafi
University of Michigan

T2A-8 *Invited* **Large-Area Imaging with Amorphous Silicon Photodiode Arrays** 405
R.B. Apte, P. Mei, R. Weisfield, R. Lujan, X.D. Wu, S.E. Ready, R.A. Street, P. Nylen
Xerox PARC

T2A-9 *Invited* **MEMS Infrastructure: The Multi-User MEMS Process (MUMPs)** 409
K.W. Markus, D.A. Koester, A. Cowen, R. Mahadevan, V.R. Dhuler, D. Roberson, L. Smith
MCNC MEMS Technology Application Center

Session: T3A Photonics & Optoelectronic Devices

Chair Y. Park
Office of Naval Research

T3A-1 *Invited* **Electrically Pumped Quantum Disk Lasers** 413
J. Temmyo, E. Kuramochi, M. Sugo, T. Nishiya, R. Nötzel, T. Tamamura
NTT Opto-Electronics Laboratories, Japan

T3A-2 **High Performance AlAs Native Oxide Confined Narrow Stripe InGaAs/GaAs Quantum Well Lasers for Application to OEIC's** 417
Y. Cheng, P.D. Dapkus, M.H. MacDougal, G.M. Yang, V. Pudikov, D. Tishinin
University of Southern California

T3A-3 *Invited* **Tunnel-Injection Laser Based on Type II Broken-Gap p-GaInAsSb/p-InAs Single Heterojunction** 421
M.P. Mikhailova, K.D. Moiseev, O.G. Ershov, G.G. Zegrya, Y.P. Yakovlev
Ioffe Institute of Russian Academy of Science, Russia

T3A-4 *Invited* **Blue Lasers Using Frequency Doubling in Optical Waveguides** 425
J.D. Bierlein
Du Pont Central Research & Development

T3A-5 **Polarization Sensitive Photodetector Arrays** 429
M.S. Ünlü, B. Onat, H.P. Zengingönül, R. Henderson, E. Towe
Boston University

T3A-6 **Correlation of Optical Pulses with a Low-Temperature-Grown GaAs Photoconductor** 433
S. Verghese, N. Zamdmer, E.R. Brown, A. Förster, Q. Hu
Massachusetts Institute of Technology

T3A-7 **Direct Broadband (130 MHz to 20 GHz) Amplitude Modulation-Frequency Response Measurements of InGaAsP Optical Amplifiers at a Wavelength of 1.55μm** 437
T.U. Horton, G.E. Stillman
University of Illinois at Urbana-Champaign

T3A-8 *Invited* **Surface-Normal Optical Pixels for Optical Interconnects** 441
Y. Sugimoto, K. Kasahara
NEC Corporation, Japan

T3A-9 **Intersubband Absorption in OMVPE Grown Delta-Doped GaAs/AlGAs Quantum Wells** 445
C.R. Lutz, J. Kanaley, K.M. Lau
University of Massachusetts-Amherst

Session: T1P Millimeter Wave & Microwave Devices
Co-Chairs R. Bradley
National Radio Astronomy Observatory
E. Kollberg
Chalmers University of Technology, Sweden

T1P-1 *Invited* **Ballistic Generatior of Terahertz Oscillations** 451
Z.S. Gribnikov, A.N. Korshak, N.Z. Vagidov, V. Mitin
Institute of Semiconductor Physics, Ukraine

T1P-2 *Invited* **Terahertz Devices using Two Dimensional Electron Fluid: Sources, Detectors, Multipliers, and Mixers** 455
M.I. Dyakonov, M.S. Shur
A.F. Ioffe Physico-Technical Institute, Russia

T1P-3 *Invited* **Room-Temperature Operating Hot-Electron Multiquantum Well Microwave Detector** 459
F. Beltram, S. Barbieri, M. Lazzarino, L. Sorba
Scuola Normale Superiore Pisa, Italy

T1P-4 **Micromachined Room-Temperature Microbolometers for Millimeter-Wave Detection** 463
A. Rahman, G. de Lange, Q. Hu
Massachusetts Institute of Technology

T1P-5 **InGaAs/InP PIN Diodes for Microwave and Millimeter-Wave Switching and Limiting Applications** 467
E. Alekseev, K. Hong, D. Pavlidis, D. Sawdai, A. Samelis
The University of Michigan

T1P-6 **Microwave Pulse Power Measurement Employing Semiconductor's Resistance Change in a Strong Electric Field** 471
M. Dagys, Z. Kancleris, V. Orsevskij, R. Simniskis
Microwave Laboratory Semicondictor Physics Institute, Lithuania

T1P-7 *Invited* **Resistive Mixers Based on the Heterostructure Field Effect Transistor** 475
H. Zirath
Chalmers University of Technology, Sweden

T1P-8 **Micromechanical Sliding Planar Backshorts** 477
V.M. Lubecke, W.R. McGrath, D.B. Rutledge
Jet Propulstion Laboratory

T1P-9 **A Tri-Layer Filter Structure for Individual Device Biasing of Subharmonically-Pumped Mixers Employing Antiparallel-Pair Diodes** 481
T.H. Lee, I. Mehdi, R.J. Dengler, A. Pease, P.H. Siegel
Jet Propulsion Laboratory

T1P-10 **Waveguide Augmented Integrated Circuit** 485
X.J. Lu, D.L. Rhodes, D.L. Woolard
U.S. Army Research Laboratory-PSD

Session: T2P Mid-to-Far Infrared Semiconductor Lasers Special Symposium
Chair F. Capasso
AT&T Bell Labs

T2P-1 *Invited* **Quantum Cascade Lasers for the 3-5μm and 8-12μm Atmospheric Windows** 489
J. Faist
AT&T Bell Laboratories

T2P-2 *Invited* **GaSb-Based Mid-Infrared Quantum-Well Diode Lasers** 491
H.K. Choi, G.W. Turner
Massachusetts Institute of Technology

T2P-3 *Invited* **Far-Infrared Germanium Cyclotron Resonance Lasers** 495
E. Gornik, W. Heiss, K. Unterrainer
Technische Universität Wien, Austria

T2P-4 *Invited* **Applications of Lead-Salt Semiconductor Lasers to Pollution Monitoring and Industrial Process Control** 499
E.A. Whittaker
Stevens Institute of Technology

T2P-5 **Progress Towards a Continuous Wave Intervalence Band Germanium-Laser** 503
A.M. Linhart, E. Bründermann, H.P. Röser, O.D. Dubon, W.L. Hansen, E.E. Haller
D.I.R., Institute for Space Sensor Technology, Germany

T2P-6 **Growth and Characterization of PbSeTe/PbSnSeTe/PbSeTe Double Heterostructures** 505
I.-N. Chao, S. Yuan, P.J. McCann
University of Oklahoma

Session: T3P Wide Band Gap Materials and Devices
Co-Chairs M. Yoder
Office of Naval Research
M. Spencer
Howard University

T3P-1 *Invited* **Carrier Recombination in 6H-SiC pn Structures Fabricated by Different Technological Techniques: Phenomena, Parameters and Centers** 509
A.M. Strel'chuk
Ioffe Institute of Russian Academy of Science, Russia

T3P-2 *Invited* **Low Frequency Noise in 4H-SiC JFETs** 513
J.W. Palmour, M.E. Levinshtein, S.L. Rumyantsev, G.S. Simin
Cree Research, Inc.

T3P-3 **A Highly Resistive Layer in Silicon-Carbide Obtained by Vanadium Ion Implantation** 517
M.P. Lam, K.T. Kornegay, J.A. Cooper, Jr.
Purdue University

T3P-4 **Modeling of Excitonic Gain in Ultra-Low Threshold Tensile-Strained ZnCdSe-ZnMgSSe Quantum Wire Lasers** 521
W. Huang, F. Jain
University of Connecticut

T3P-5 **Optical Properties of GaN Films on Sapphire Substrate** 525
R. Zhang, K. Yang, B. Shen, L.H. Qin, S.L. Gu, Y. Shi, Y.D. Zheng, Z.C. Huang, J.C. Chen
Nanjing University, P.R. China

T3P-6 **GaN and AlGaN p-i-n Structures** 529
N.I. Kuznetsov, V.A. Dmitriev
A.F. Ioffe Institute, Russia

T3P-7 **Electrical Conduction in Platinum-Gallium Nitride Schottky Diodes** 531
K. Suzue, S.N. Mohammad, Z.F. Fan, W. Kim, O. Aktas, A.E. Botchkarev, H. Morkoç
University of Illinois at Urbana-Champaign

T3P-8 *Invited* **Processing and Characterization of GaN-AlGaN Based Electronic and Optoelectronic Devices** 535
M.A. Khan, Q. Chen, J.W. Yang, C.J. Sun, I. Adesida, A.T. Ping, M.S. Shur
APA Optics, Inc.

T3P-9 **Elastic Strain Relaxation in GaN-AlN Superlattices** 541
A.D. Bykhovski, B.L. Gelmont, M.S. Shur
University of Virginia

Session: PT1.1P Millimeter Wave & Microwave Devices

PT1.1P-10 **The Design, Construction and Evaluation of a 585 GHz Planar Schottky Mixer**
J.L. Hesler, T.W. Crowe, R.M. Weikle, R.F. Bradley, S.-K. Pan
University of Virginia

Session: PT2.1P Amorphous and Poly Silicon Materials & Devices

PT2.1P-1 **The Interface Density States Asymmetry Influence on the Characteristicsof a-Si:H Thin Film Transistors** 545
D. Bilenko, Y. Galishnikova, A. Jarkova, O. Coldobanova, E. Khasina
Saratov State University, Russia

Session: PT2.2P Simulation & Modeling II

PT2.2P-1 **Microscopic Determination of Noise in Semiconductor Devices and its Application to Sub-μ Gate-Length Hetero-FETs** 549
A. Abou-Elnour, K. Schünemann
Technische Universität Hamburg-Harburg, Germany

PT2.2P-2 **Electron-Phonon Coupling in Multiply-Connected Quantum Wires via Tight-Binding Green's Functions** 553
W.R. Grisé
Morehead State University

PT2.2P-3 **Nonlinear Evolution of the Dyakonov-Shur Instability** 559
B. Gelmont
University of Virginia

PT2.2P-4 **Second and Third Order One-Dimensional Non-Quasi-State Bipolar Transistor Models** 563
E. Robilliart, E. Dubois
IEMN/ISEN, France

Session: PT2.4P Novel Fabrication

PT2.4P-1 Directed Vapor Deposition of Electronic Materials: Nonhydrogenated *a*-Si and Cu 567
J.F. Groves, P.L. Ratnaparkhi, H.N.G Wadley, T. Globus, S.H. Jones
University of Virginia

PT2.4P-2 **Reduced Lateral Diffusion of AuGe/Au and AuGe/Au/Ni Source-Drain Contacts in AlInAs/InGaAs/InP MODFET's** 571
J.K. Zahurak, A.A. Iliadis, S. Rishton, W.T. Masselink, T. Neil
University of Maryland

PT2.4P-3 **Very Low Resistance Multi-layer Ohmic Contact to n-GaN** 575
Z. Fan, S.N. Mohammad, A.E. Botchkarev, W. Kim, Ö. Aktas, H. Morkoç
University of Illinois at Urbana-Champaign

PT2.4P-4 **Modeling of Dielectric Film Deposition by Laser CVD** 577
J.-H. Ryoo, J.-K. Kim, Y.-K. Sung
Korea University, Korea

PT2.4P-5 **Spontaneous Formation of Ordered Arrays of Quantum Dots** 581
V.A. Shchukin, N.N. Ledentsov, P.S. Kop'ev, D. Bimberg
A.F. Ioffe Physical Technical Institute, Russia

PT2.4P-6 **On New Mechanism of Lateral Superlattice Formation at Vicinal Interface** 585
B.K. Medvedev, V.A. Petrov, N.V. Peskov
Institute for Radio Engineering and Electronics the RAS, Russia

PT2.4P-7 **Fabrication and RF Performance of GaAs MESFETs** 589
T. Abbott, T. Brock, J. East, G. Haddad
The University of Michigan

Session: PT2.6P MOSFETs

PT2.6P-1 *Student* **Unified Substrate Current Model for MOSFETs** 591
B. Iñíguez, F. Pedersen, T.A. Fjeldly
U.I.B., Spain

PT2.6P-2 **Differential Conductance Field-Effect Transistor Model** 595
A. Phillips Jr., C.S. Appel, S. Jordan
Cornell University

PT2.6P-3 **Simulations of the HOle and Current Distributions in Si-Ge p-Channel FETs with Graded Ge Profiles** 599
S.P. McAlister, W.R. McKinnon
National Research Council Canada, Canada

PT2.6P-4 **A Unified BSIM I-V Model for Circuit Simulation** 603
Y. Cheng, C. Hu, K. Chen, M. Chan, M.-C. Jeng, Z. Liu, J. Huang, P.K. Ko
University of California at Berkeley

PT2.6P-5 *Student* Universal MOSFET Carrier Mobility Model Explicitly Based on V_{t9}, V_g and T_{ox} and Its Application in Device Modeling and Optimization 607
K. Chen, J. Duster, H.C. Wann, T. Tanaka, M. Yoshida, P.K. Ko, C. Hu
University of California-Berkeley

Session: F1A Cryogenic Devices

Co-Chairs A. Lichtenberger
University of Virginia
S. Yngvesson
University of Massachusetts-Amherst

F1A-1 **Conversion Gain and Noise in the NbN Hot-Electron Submillimeter Mixer** 611
H. Ekström, B. Karasik, E. Kollberg
Chalmers University of Technology, Sweden

F1A-2 *Invited* **Microwave Detection Using the Photon-Activated Switch Behavior of the Single-Electron Transistor** 615
J.M. Hergenrother, J.G. Lu, M. Tinkham
Harvard University

F1A-3 **Hot Electron Mixing in NbN at 119 Micrometer Wavelength** 619
E. Gerecht, C.F. Musante, C.R. Lutz, Jr., Z. Wang, J. Bergendahl, K.S. Yngvesson, E.R. Mueller, J. Waldman, G.N. Gol'tsman, B.M. Voronov, E.M. Gershenzon
University of Massachusetts-Amherst

F1A-4 **THz Parametric Oscillators Using Coupled Double Quantum Wells** 623
Il Lyubomirsky, B. Xu, Q. Hu
Massachusetts Institute of Technology

F1A-5 *Invited* *Student* **Microwave Devices Based on S-N Transition in High-Tc Superconducting Films** 627
V. Osadchiy, A. Swishchev, V. Sherman, M. Gaidukov, I. Vendik
St. Petersburg Electrotechnical University, Russia

F1A-6 *Invited* **Cryogenic Optoelectronic Measurements of Single Flux Quantum Pulses in Superconducting Circuits** 631
C.-C. Wang, M. Currie, D. Jacobs-Perkins, R. Sobolewski, T.Y. Hsiang, M.J. Feldman
University of Rochester

F1A-7 The Spatial Distribution of the Critical Current Density in $YBa_2Cu_3O_7/YBa_2(Co_{0.01}Cu_{0.99})_3O_7/YBa_2Cu_3O_7$ Edge Junctions 635
S.C. Gausepohl, M. Lee, K. Char
University of Virginia

F1A-8 **Hot Electron Bolometric High-Tc Mixer: Next Step** 639
G.N. Gol'tsman
Moscow State Pedagogical University, Russia

F1A-9 *Invited* **A Novel Method for Producing the HTSC Planar Structures on Si** 643
O.V. Smolski, M.E. Gaevski, D.V. Denisov, V.P. Chalyi
Ioffe Institute of Russian Academy of Science, Russia

Session: F2A Simulation & Modeling II

Co-Chairs J.-P. Leburton
University of Illinois at Urbana-Champaign
C. Krowne
Naval Research Laboratory

F2A-1 *Invited* **Modeling of Low Dimensional Structures** 645
D. Lippens
Institut d'Electronique et de Microélectronique du Nord, France

F2A-2 **Quantum Effects and the Semiconductor Law of Mass Action** 649
H.L. Grubin, T.R. Govindan
Scientific Research Associates, Inc.

F2A-3 **Quasi-1D Coulomb Potential in Quantum Wires** 653
W.R. Grisé
Morehead State University

F2A-4 Solution of the Boltzmann Transport Equation in One-Dimensional Submicron n^+-n-n^+ Structures Based on Relaxation Scales of the Moments 657
M.-C. Cheng, L. Guo
University of New Orleans

F2A-5 *Student* **Drain Current Enhancement due to Velocity Overshoot Effects and Its Analytic Modeling** 661
J.-H. Song, W.-S. Choi, Y.-J. Park, H.-S. Min
Seoul National University, Korea

F2A-6 *Invited* **Effect of Tunneling Times on the Dynamic Response of Semiconductor Resonant Tunnel Diodes** 665
S.A. Mikhailov, D.V. Posvyanskii, V.A. Volkov
Institute of Radioengineering and Electronics of Russian Academy of Science, Russia

F2A-7 **Resonant Tunneling Diode I(V) Lineshapes: Analytical Formula** 669
J.N. Schulman, H.J. De Los Santos
Hughes Research Laboratories

F2A-8 *Student* **A Systematic Extraction Method for Noise Sources and Correlation Coefficient in MESFET** 673
J.-H. Han, K. Lee
Korea Advanced Institute of Science and Technology, Korea

F2A-9 An Efficient Current-Voltage Model of the SRH Generation-Recombination for $Al_xGa_{1-x}As$/GaAs N-p Heterojunction Diode 677
J.H. Choi, H.R. Kim, S.D. Yoo, B.G. Song, N.H. Jo, K.D. Kwack
Hanyang University, Korea

F2A-10 **Two-dimensional Modeling of Carrier Transport and Optimization of Graded-base Heterojunction Bipolar Transistors** 681
S.A. Tabatabaei, A.A. Iliadis, C.E.C. Wood, D.R. Stone
University of Maryland

F2A-11 *Invited* **Modeling of Bloch Oscillations** 683
J. Luscombe
Naval Postgraduate School

Session: F3A Amorphous and Poly Silicon Materials & Devices

Co-Chairs T. Globus
University of Virginia
T.-J. King
Xerox Parc

F3A-1 *Invited* **Modeling and Simulation of Thin Film Transistors for Active-Matrix Liquid Crystal Displays** 685
M. Hack
Xerox PARC

F3A-2 *Invited* **High Through-put Processing for Poly-Si TFT** 689
S.J. Fonash
The Pennsylvania State University

F3A-3 **Self-Aligned Offset Gated Poly-Si TFTs by Employing a Photo Resist Reflow Process** 695
C.-M. Park, B.-H. Min, M.-K. Han
Seoul National University, Korea

F3A-4 **High Performance Polycrystalline Silicon Thin Film Transistors Fabricated by Ultrahigh Vacuum Chemical Vapor Deposition and Chemical Mechanical Polishing with Plasma Treatment** 699
C.-Y. Chang, H.-Y. Lin, T.F. Lei, J.-Y. Cheng, L.-P. Chen, B.-T. Dai
National Chiao Tung University and National Nano Device Laboratory, Republic of China

F3A-5 Characteristics of Off Current in Amorphous Silicon Thin Film Transistors with SiO_2 Gate Insulator 703
J.H. Kim, W.S. Choi, C.H. Hong
LG Electronics Inc., Korea

F3A-6 **Doping and Geometric Effects on the Transient Drain Current in Amorphous Silicon Thin-film Transistor** 707
M.H. Chu, C.H. Wu
University of Missouri-Rolla

F3A-7 **Defect Density-of-States in a-Si:H TFTs Determined by the Field Effect Method** 711
T. Globus, B. Gelmont, L.Q. Sun, R.J. Mattauch
University of Virginia

F3A-8 **Advanced Polysilicon Bipolar Transistors: Noise and Gain Performance Evaluation for Microwave Low-Noise Applications** 715
A. Caddemi, P. Livreri, M. Sannino
Universita di Palermo, Italy

F3A-9 **On the Performance of the Noise Parameters of Advanced Polysilicon Bipolar Transistors vs Frequency and Bias** 719
A. Caddemi, M. Sannno
Universita di Palermo, Italy

Session: F1P Novel Fabrication

Co-Chairs S. Jones
University of Virginia
N. Papanicolaou
Naval Research Laboratory

F1P-1 **A Neural Network Based Qualitative Analysis of Semiconductor Device Manufacturing** 725
M. Vai
Northeastern University

F1P-2 *Invited* **Direct Wafer Bonding Technology for Multi-Material Integration** 729
T. Kamijoh, H. Wada
Optoelectronics Oki Laboratory, Real World Computing Partnership (RWCP), Japan

F1P-3 **A Novel Method of InAs Dot Array Formation for Nanostructure Devices** 731
K. Yoh, T. Saitoh, A. Tanimura
Hokkaido University, Japan

F1P-4 *Invited* **Novel Compound Semiconductor Devices Based on III-V Nitrides** 735
S.J. Pearton, C.R. Abernathy, J.W. Lee, F. Ren, R.J. Shul, J.C. Zolper
University of Florida

F1P-5 **Side-Gated Resonant Tunneling Transistors** 739
V. Kolagunta, D.B. Janes, G. Chen, K.J. Webb, M.R. Melloch
Purdue University

F1P-6 **Realization of Silicon Quantum Wires Based on SiGe/Si Heterostructure** 743
Y. Shi, J.L. Liu, F. Wang, Y. Lu, R. Zhang, P. Han, S.L. Gu, S.M. Zhu, Y.D. Zheng
Nanjing University, P.R. China

F1P-7 **Advanced Contact Technology for a Self Aligned 70GHz Double Mesa Si/SiGe Heterojunction Bipolar Transistor** 747
K. Wieczorek, H.-U. Schreiber
Ruhr-Universität Bochum, Germany

F1P-8 **Impact of LDD Structure on Channel-Hot-Electron Programming of Single-Poly EEPROM** 751
K.-Y. Na, J.-C. Han, S.-C. Lee, H.-J. Cho, Y.-S. Kim
Chungbuk National University, Korea

F1P-9 **Low Work Function Microminiature Thermionic Vacuum (MTV) Diodes** 755
L.P. Sadwick, Y.J. Zhang, B. Baker, R. Petersen, S. Johnson, D.G. Petelenz, R.J. Hwu
The University of Utah

Session: F2P Laser Modeling Special Symposium

F2P-6 **Studies and of the Effect of Electron Emission from the Active Region on Performance of InGaAsP/InP Lasers, Experiment and Modeling** 759
G.L. Belenky, R.F. Kazarinov, C.L. Reynolds, Jr., V. Swaminathan, S.L. Luryi
AT&T Bell Laboratories

F2P-2 *Invited* **Experiments and Models Probing Carrier Dynamics in Multiquantum Well Lasers** 763
N. Tessler
Technion, Israel

F2P-3 *Invited* **Application of Fast Time-Resolved Spectroscopy to Semiconductor Lasers** 767
J. Mørk, A. Mecozzi
Teledanmark Research, Denmark

F2P-4 *Invited* **Gain in InGaAsP Based Lasers: Comparison of Models to Experiment** 771
M.S. Hybertsen, D.A. Ackerman, G.E. Shtengel, P.A. Morton, R.F. Kazarinov, G.A. Baraff, T. Tanbun-Ek, R.A. Logan
AT&T Bell Laboratories

F2P-5 *Invited* **Role of Carrier Transport and Spectral Hole Burning in the Modulation Response of Semiconductor Quantum-Well Lasers** 775
K. Hess, M. Grupen
University of Illinois at Urbana-Champaign

F2P-1 *Invited* **Comprehensive Model of Vertical Cavity Surface Emitting Laser Performance** 779
G.R. Hadley, K.D. Choquette
Sandia National Laboratories

Session: F3P MOSFETs

Co-Chairs R. Dutton
Stanford University
S. McAlister
National Research Council of Canada

F3P-1 *Student* **Propagation of Defects in Hot-Carrier Degradation of LDD NMOSFETs-From the Early Mode to the Late Mode** 781
A. Raychaudhuri, W.S. Kwan, M.J. Deen, M.I.H. King
Simon Fraser University, Canada

F3P-2 *Student* **Technology-CAD Applied to the Development of DMOS Devices** 785
D. Wojciechowski, A. Van Calster, J.S. Witters
University of Gent, Belgium

F3P-3 **β-MOS FET: a Novel High Performance Transistor** 789
K. Yoh, R. Koizumi, N. Hashimoto, S. Ikeda
Hokkaido University, Japan

F3P-4 *Invited* **Self-Consistent Model for Fully Depleted SOI/MOSFETs Including Self-Heating** 793
Y. Cheng, T.A. Fjeldly
University of California at Berkeley

F3P-5 **Top-Gate Threshold Voltage Shifts Using an Individually Isolated Back Gate Bias in Dual-Gated P&N Channel Thin-Film SOI MOSFETs** 797
J.P. Denton, G.W. Neudeck
Purdue University

F3P-6 **Future Trend of Scaled LSI Devices and Single Electronics** 801
T. Hiramoto
University of Tokyo, Japan

F3P-7 **Suitability of Sub 0.10μm NMOSFET For Low & High Intetration Circuits** 803
F. Benistant, G. Guegan, S. Tedesco, F. Martin, M. Heitzmann
LETI (CEA), France

F3P-8 **Reliable Gate-Voltage-Dependent Channel-Length and Series Resistance Extraction Technique Taking into Account Threshold Voltage Reductionin MOSFETs** 807
S. Biesemans, S. Kubicek, K. De Meyer
IMEC, Belgium

F3P-9 *Student* **Thermionic Emission Model for Electron Gate Current in Submicron NMOSFETs** 811
K. Hasnat, C.-F. Yeap, S. Jallepalli, W.-K. Shih, S.A. Hareland, V.M. Agostinelli, Jr., A.F. Tasch, C.M. Maziar
University of Texas at Austin

F3P-10 **Better Understanding of the Hydrodynamic and Energy Transport Models for the Terminal Current and Reliability Predictions of Deep Submicron MOSFETs** 815
W.-S. Choi, Y.-J. Park, H.-S. Min
Seoul National University, Korea

Session Notation

W	Wednesday
T	Thursday
F	Friday
a	Morning
p	Afternoon

1,2,3 refer to the tracks

Papers appear in the Table of Contents under the country of the first author. Please refer to the papers for countries of co-authors.

MEMS Infrastructure: The Multi-User MEMS Processes (MUMPs)

K. W. Markus, D. A Koester, A. Cowen, R. Mahadevan, V. R. Dhuler, D. Roberson, L. Smith

Over the last decade silicon process technology, synonymous with integrated circuit processing, has been increasingly applied to the field of micromechanics, leading to the emerging field of MEMS (microelectromechanical systems). MEMS is an enabling technology, which partially accounts for the projections of 10 - 20% annual growth and the potential of a greater than $8 billion market by the year 2000 [1]. Current market estimates of approximately $800 million (1992/3) are possibly low since MEMS are already being incorporated into much more complex systems. Due to the enabling nature of MEMS and because of the significant impact they can play on both the commercial and defense markets, the federal government has taken special interest in nurturing growth in this field. One of the many ways this is being accomplished is through the MCNC MEMS Infrastructure program, supported by the Advanced Research Projects Agency (ARPA).

The MEMS Infrastructure program was established in 1993 to provide low-cost, easy access to advanced MEMS technologies. By lowering the barriers to accessing the technology, it is hoped that the cost (both time and dollars) of developing and incorporating MEMS into new applications will be significantly reduced. There are three key components to the Infrastructure program; the Multi-User MEMS processes (MUMPs), a publicly-accessible standard element MEMS library and the generation of Smart MEMS through the use of flip chip technology. These activities are described below. More information on this program can be found at the following URL: http://www.mcnc.org/HTML/ETD/MEMS/memshome.html

MULTI-USER MEMS PROCESSES (MUMPS)

While the cost of MEMS devices benefits from the leveraging of batch fabrication, the cost of micron-scale silicon processing is prohibitive. Building, maintaining and operating a cleanroom with knowledgeable workers can out price most universities and even small and medium-sized companies with interest in developing and/or commercializing MEMS technology. As is often the case, MEMS fabrication is too costly for individuals interested in experimenting with this technology. The result–broad dissemination of MEMS is inhibited, limiting the pool of creativity contributing to new and potentially lucrative products. MUMPs was established to mitigate the effects of these barriers by providing cost effective proof-of-concept fabrication. MUMPs also serves as an excellent, low-cost, educational tool. Many universities around the country are developing programs in MEMS. MUMPs allows the university to offer a course in

---

This work is supported by the Advanced Research Projects Agency (ARPA) under contract DABT63-93-C-0051.

All authors are with the MCNC MEMS Technology Applications Center, Research Triangle Park, NC 27709-2889.

MEMS without the financial burden of running a cleanroom facility. Small companies and government agencies benefit in this manner as well.

The MUMPs program currently offers access to two distinct MEMS technologies in a multi-user environment: polysilicon surface micromachining and LIGA (hereafter referred to as LIGAMUMPs), which is provided in conjunction with the University of Wisconsin.

MUMPs Description

Polysilicon surface micromachining encompasses many of the same fabrication techniques as traditional silicon IC fabrication–layers of CVD films are deposited and subsequently patterned using photolithography and plasma etch techniques. Alternating layers of silicon dioxide and polysilicon are deposited so when all the layers have been patterned, the silicon dioxide can be etched away with hydrofluoric acid leaving only the polysilicon structures behind. The chief benefit to this process is the ability to fabricate moving parts on a silicon substrate.

The MUMPs process provides seven different films (layers) with which to build structures. These films are silicon nitride, poly 0, first oxide, poly 1, second oxide, poly 2 and metal (fig. 1). The purpose of the oxide and polysilicon films has been described above. The silicon nitride film is a blanket layer that serves to isolate all structures electrically from the substrate. The metal layer serves two purposes, it provides electrical contact to the polysilicon simplifying wire bonding and a reflective surface for optical applications.

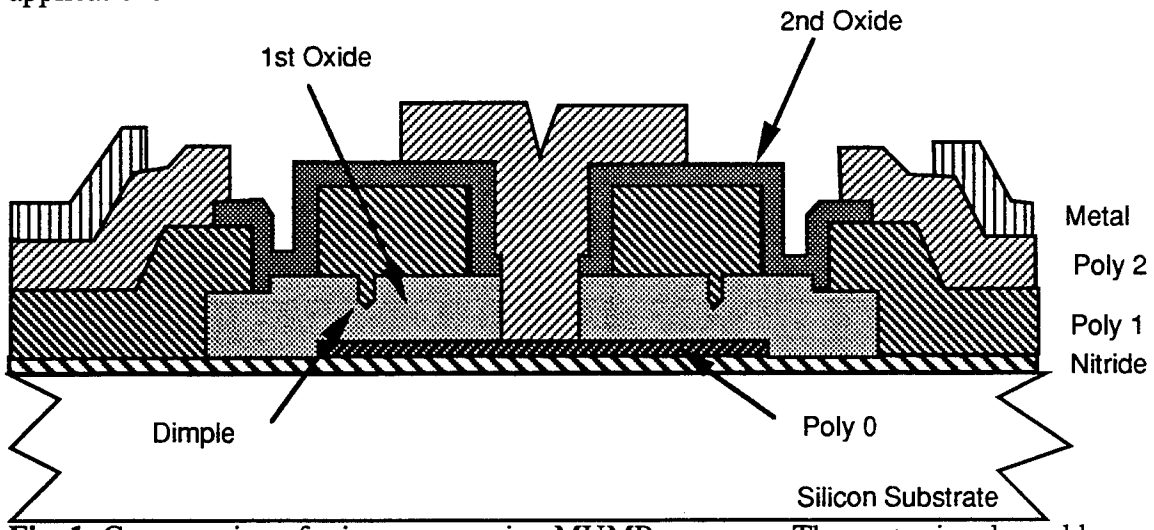


Fig. 1 Cross section of micromotor using MUMPs process. The motor is released by immersing it in hydrofluoric acid to remove the first and second oxide layers.

LIGAMUMPs Description

LIGA, a German acronym which translates to Lithography, Electroforming and Injection Molding, was developed in Germany in the 1980's and has slowly gained wide-spread interest. There are two key factors to LIGA's attractiveness - the ability to mass-replicate high aspect ratio structures out of metals, polymers and ceramics, and the ability to fabricate structures which can be assembled with a high degree of precision. LIGA requires the use of an extremely energetic, highly collimated photon source, which restricts its practice to those facilities with access to x-ray synchrotrons. This further exacerbates the access and cost issues mentioned above. The processes offered include

releasable single level metal and plastic structures. As our experience with the technology increases, so too will the complexity of the processes available as part of the MUMPs. Figure 2 shows an example of parts made using the University of Wisconsin LIGA process.

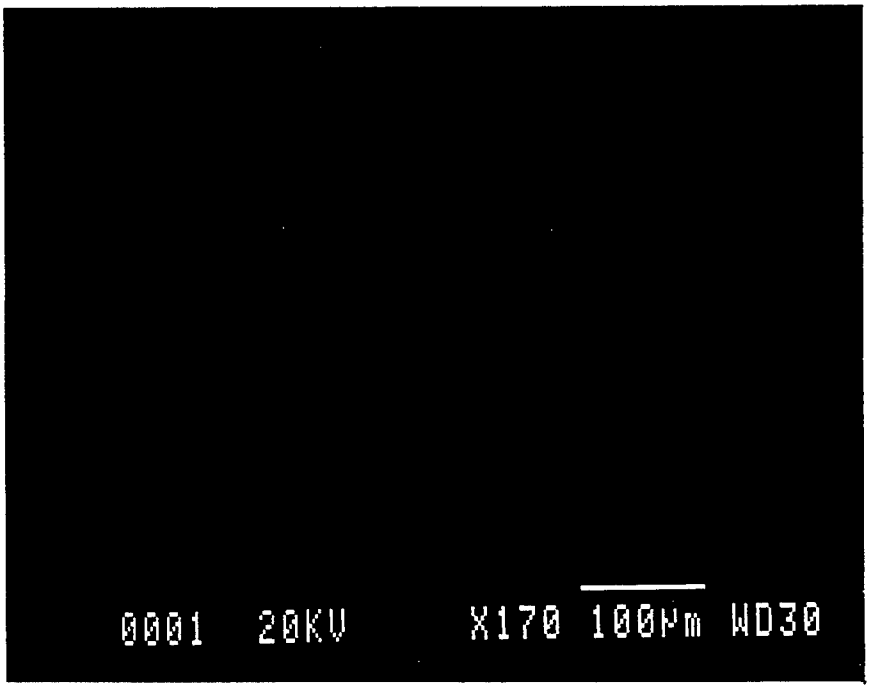


Fig. 2 Scanning electron micrograph of 150 µm tall nickel gears made using LIGA process.

CONSOLIDATED MICROMECHANICAL ELEMENT LIBRARY

The Consolidated Micromechanical Element Library (CaMEL) is a library of MEMS cells similar to standard cell libraries that proliferate in VLSI design. The CaMEL library consists of two independent parts; the nonparameterized cell database and the parameterized micromechanical element library. The aim is to provide MEMS cell libraries that are useful for novice MEMS designers, as well as experienced ones.

The nonparameterized cell library is a database of MEMS designs in various process technologies contributed by different sources. It is a resource of working MEMS devices and structures. A library browser permits the user to peruse brief descriptions of the cells and select desired ones. Selected cells can then be retrieved from the database. A companion program allows designers to submit MEMS designs for inclusion in the database along with the accompanying process information. Cells currently available in the library include designs for MUMPs and LIGAMUMPs processes.

The parameterized micromechanical element (PME) library is a set of generators that allow users to create customized versions of commonly used elements in a quick and easy manner. The PME library also provides a framework for writing cell generators. It enables the generators to be relatively process independent and allows limited cell hierarchy. Designs can be generated in CIF, GDS II, or PostScript output formats. Technology dependent design rules are read in from an environment specified technology

file. The library provides various geometric primitives and a set of available generators. Various types of elements are available, including active micromechanical elements, passive micromechanical elements, test mechanical structures, and electrical elements.

SMART MEMS: ELECTRONICS INTEGRATION FOR MEMS

There has been a growing interest in placing electronics closer to sensors and actuators to improve their performance. The hybrid approach, long the industry standard, is flexible but can suffer from system performance degradation due to stray or large capacitance[2]. A recent approach [3] has been to build MEMS on top of underlying electronics. This embedded approach results in significant improvement in performance but suffers from reduced yield and flexibility due to the processing complexity.

Flip chip MEMS combines the advantages of the hybrid and embedded approach. The electronics and the MEMS are fabricated on different substrates, reducing process complexity, and are then connected using solder bumping. Flip chip has been successfully used to connect IC chips to printed circuits or substrate carriers for almost 20 years. This approach has been modified to facilitate the connection of the MEMS chip to the electronics chip, taking into account the mechanical or 'released' nature of MEMS chips.

Electromechanical Control System

The Electromechanical Control System (ECOSYS) is a program to facilitate the fabrication of MEMS systems including the electronics. A standardized IC controller with various functional blocks is currently under production. The aim is to allow users to connect blocks and attach them to a MEMS device via flip-chip attachment to implement a system incorporating sensing, feedback, and control. A limited degree of user programmability will be provided via external RC components to tailor the response of the blocks for the application. Interconnections to the MEMS elements will be via solder bumps and the parasitics introduced by the solder bump and pad will be accounted for in the design of the blocks.

REFERENCES

[1] "Micro-machines Hold Promise for Aerospace", Aviations Weekly & Space Technology, 3-1-93.

[2] N. Najafi, K. D. Wise, R. Merchant, and J. W. Schwank, "An Integrated Multi-Element Ultra-Thin-Film Gas Analyzer", Technical digest, IEEE Solid-State Sensor and Actuator Workshop, (Hilton Head, SC 1992), pp. 19-22.

[3] T. Core, R. S. Pyne, D. Quinn, S. Sherman, and W. K. Wong, "Integrated, Complete, Affordable Accelerometer for Air-Bag Applications", Proceedings of Sensors Expo, Chicago IL, pp. 204B-1 (1991).

Electrically Pumped Quantum Disk Lasers

Jiro Temmyo, Eiichi Kuramochi, Mitsuru Sugo,
Teruhiko Nishiya, Richard Nötzel*, and Toshiaki Tamamura

NTT Opto-electronics Laboratories,
3-1 Morinosato-Wakamiya, Atsugi, Kanagawa 243-01, Japan.
*(* Present address: Paul-Drude-Institut, D-10117 Berlin, Germany)*
Phone: +81(462)40-2855 , Fax.: +81(462)40-4305
e-mail: temmyo@aecl.ntt.jp

Introduction: Progress in the research of low-dimensional nanostructures during the past decade has mainly been in the fabrication and characterization areas, mostly due to difficulties in producing nanometer-scale, device-quality structures[1].

However, we have recently found a new self-organization phenomenon in a strained InGaAs/AlGaAs system on a (311)B GaAs substrate grown by metalorganic vapor phase epitaxy[2] that results in the formation of nano-scale confined structures, i.e., strained InGaAs quantum disks. We describe and discuss the performance of electrically pumped strained InGaAs quantum disk lasers with nano-scale active regions fabricated by self-organization phenomenon[3].

Self-organization Phenomenon: The self-organization process is as follows: During a short period of growth interruption, after a thin InGaAs film is grown on an AlGaAs layer, the strained InGaAs film redistributes and separates into well-ordered and high-density nano-scale quantum disks. These disks are directly covered by AlGaAs layers due to mass transport to form the microcrystals (Fig. 1 & Fig. 2). This self-organization phenomenon seems to result from the barrier height for adatom migration being lower than that of the (100) surface. The size of the disks can be controlled in the range of 30-150 nm by adjusting the indium composition and the density can be varied by varying the nominal thickness. The buried InGaAs quantum disks exhibit strong and narrow photoluminescence emission at a wavelength between 850-950 nm at room temperature. Moreover, we found that the self-organization in strained InGaAs system also occurs on InP (311) substrates[4], indicating that this phenomenon on Miller high-index planes might be common to compound semiconductors.

Quantum Disk Laser: We fabricated laser structures containing 6 nm double-stacked $In_{0.25}Ga_{0.75}As$ quantum disks (DQDs) on a GaAs (311)B substrate and double quantum wells (DQWs) on a conventional (100) substrate, simultaneously. The vertical structure consisted of the separate confinement heterostructure (SCH) with guiding layers. After the deposition of each InGaAs layer, growth was interrupted under an arsine atmosphere for 3 minutes to promote self-organization at a substrate temperature of 750°C. The diameter of the InGaAs quantum disk inside microcrystals was estimated to be about 60 nm. The filling factor was calculated as about 6% on the plane. The transverse-mode stabilized ridge waveguide lasers were fabricated using the electron cyclotron resonance (ECR) dry-etching technique and the conventional fabrication process (Fig. 3). The ridge was 2 μm wide and the cavity was 900 μm long.

The threshold current of the DQD laser was 20-23 mA, which is considerably lower than that (27 mA) of the (100) DQW laser (Fig. 4). The FWHM for the vertical divergence angle of the emission was 25 degrees and that for the horizontal one was 10 degrees for both (311)B quantum disk lasers and (100) quantum well lasers, whereas the optical confinement factors for active volume were quite different for the two lasers. The characteristic temperature T_0 around room temperature is about 200K. Considering the filling factor of 6% , the low threshold current of quantum disk lasers appears to be related to better optical quality of the disks and might be attributed to the so-called volume effect. Moreover, other possible reasons are some gain enhancement effect, less guiding loss inside the active region, and a cooperative phenomenon in disk systems, whereas the estimated lateral size of the disk is not small enough to expect a lateral

confinement effect. The quantum efficiency of the DQD lasers was slightly worse than that of the DQW lasers on (100) substrates and tended to saturate, probably because of the reduced active volume. The lasing wavelength of the quantum disk lasers, about 940 nm, was blue-shifted from that of the (100) DQW lasers. This is consistent with the PL data, and indicates that lasing occurs inside the disks.

Conclusion: The results suggest the possibility of further using this self-organized nanostructure in optical device applications.

References:

[1] C. Weisbuch, *Proceedings of 22nd International Conference on the Physics of Semiconductors,* Vancouver, Aug. 15-19, pp. 1839-1846, 1994. [2] R. Nötzel, J. Temmyo, and T. Tamamura, *Nature*, **369**, pp. 131-133, 1994. [3] J. Temmyo, E. Kuramochi, T. Nishiya, M. Sugo, R. Nötzel, and T. Tamamura, *Electron. Lett.* **31**, pp. 209-211, 1995. [4] J. Temmyo, A. Kozen, T. Tamamura, R. Nötzel, T. Fukui, and H. Hasegawa, *J. Electronic Mat.* Dec. 1995 (to be published).

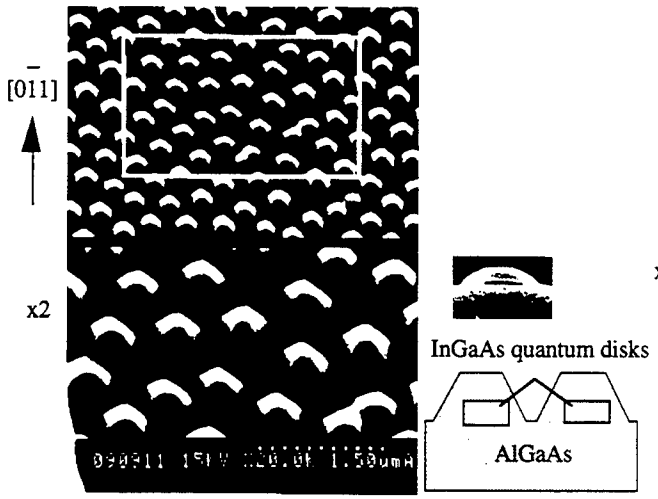


Fig. 1. SEM images with a schematic cross-sectional view of as-grown InGaAs on a GaAs (311)B substrate. The layer beneath is an AlGaAs film. The self-organization seems to result from the barrier height for adatom migration being lower than that of the (100) surface.

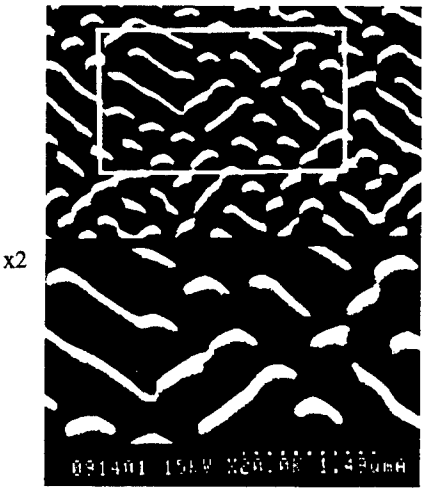


Fig. 2. SEM surface image of strained InGaAs on a (311)B substrate. The reconstruction process is on the way to complete self-organization. The self-organization strongly depends on the growth conditions such as the substrate temperature and the indium composition.

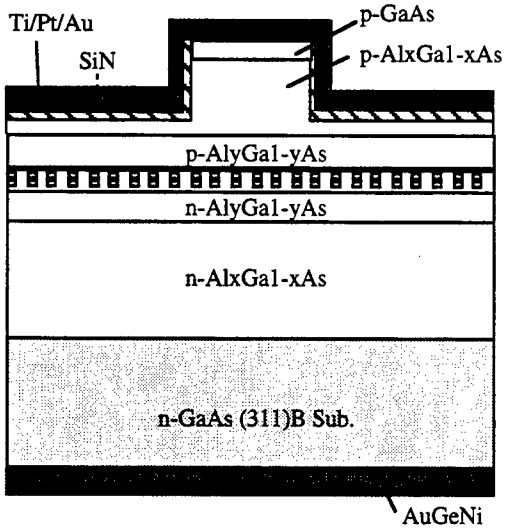


Fig. 3. Schematic cross-sectional view of a ridge waveguide quantum disk laser. Active region consists of doubly-stacked 6nm quantum disks.

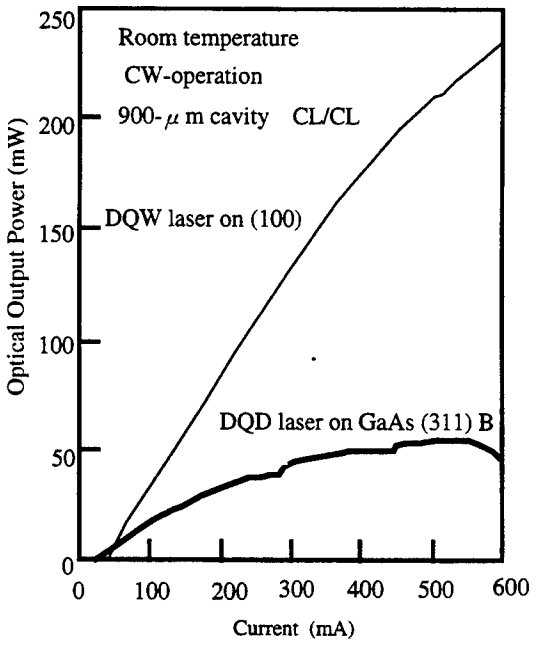


Fig. 4. Typical light output characteristics

Intentionally Left Blank

Intentionally Left Blank

High Performance AlAs Native-Oxide Confined Narrow-Stripe InGaAs/GaAs Quantum Well Lasers for Application to OEIC's

Yong Cheng, P.Daniel Dapkus, Michael H. MacDougal, Gye Mo Yang, Vasily Pudikov, and Dennis Tishinin

National Center for Integrated Photonic Technology

Department of Electrical Engineering/ Electrophysics

University of Southern California, Los Angeles, CA 90089-0483

Low threshold, high performance edge- and surface-emitting lasers are required for application to optoelectronic integrated circuits. The technology for such lasers must be compatible with the fabrication of high speed circuits on the same chip without sacrificing performance. In this paper we present the characterisitcs of edge-emitting lasers and folded-cavity-surface-emitting lasers fabricated using a novel quasi-planar buried oxide stripe geometry laser. There has recently been great progress achieved in the application of buried layers of a native oxide to optoelectronic devices. The native-oxide of AlGaAs is particualrly attractive because it provides both electronic and optical confinement making it possible to fabricate low threshold, high efficiency quantum well lasers in both the edge[1-2]- and vertical cavity surface-emitting[3-5] geometries. This paper explores further the design and properties of buried oxide stripe lasers with the goal of optimizing their performance for application to OEIC's, and implementing surface emitting lasers that are compatible with incorporation into OEIC's.

The basic device design is schematically shown in Fig.1. AlAs layers above and below the waveguide region are partially oxidized from the edge of an etched mesa or groove to form a narrow-stripe structure. Since the native-oxide AlAs is an insulator with a small refractive index, both electronic and optical confinement are achieved. The oxidation rate of AlGaAs depends strongly on Al composition.[6] AlAs is chosen in our devices to minimize effect of composition nonuniformity and to increase reproducibility. The laser structure is an InGaAs/GaAs SQW-GRINSCH structure grown by MOCVD. 1000Å n- and p-type AlAs layers are placed below and above the InGaAs/GaAs active region,

respectively. The top AlAs layer is about 2500Å above the active region. The mesas to expose the edge of the AlAs layers for oxidation are formed by wet chemical etching using an $H_2O/H_2O_2/H_2SO_4$ (160:8:1) solution. The oxidation is performed at 400°C in H_2O-vapor-saturated N_2. The aperture defined by top AlAs oxide layer is about 1.8μm after 8.5min oxidation. The lower oxide aperture is wider owing to the doping dependence of the oxidation process.[7]

Edge emitting and folded cavity surface emitting lasers based on this design have been fabricated and tested. An edge-emitting device with 1.8μm-wide aperture, 400μm-long cavity demonstrates a threshold current of 3.5mA (J_{th}~490A/cm^2) and external quantum efficiency of 82%. Devices with high-reflection (HR) dielectric (SiO_2/Si) coating on one facet exhibit a threshold current of 2.6mA. The threshold current is 1.7mA with both facets HR coated. The spectra for uncoated devices exhibit sigle mode behavior when I>5mA. This suggests that good current and optical confinement exist in these narrow-stripe structures. The near-field pattern measured at 6mA indicates an oval shape with the full width at half power (FWHP) of ~2μm due to the narrow active region. These characterisitics agree well with detailed simulations of the device performed to date. The far-field patterns are stable over a wide range of currents with a full width at half maximum (FWHM) perpendicular and parallel to the junction plane of 35° and 15°, respectively. CW threshold currents vary from 3mA to 4.7mA in the temperature range of 0°C-50°C with a characteristic temperature of 133K.

To optimize the performance of the devices we have stuidied the dependence of the laser threshold and efficiency on device length and stripe width. Fig.2 shows the cavity length dependence of the threshold current and the reciprocal external quantum efficiency (η_d^{-1}). Low threshold currents can be expected for laser cavity lengths in the range of 300-500μm. From the cavity length dependence of η_d^{-1}, the internal quantum efficiency and the internal losses for such narrow-stripe lasers are estimated as 90.2% and 4.1cm^{-1}, respectively. In Fig.3, the threshold currents for the devices with different current aperture widths are plotted. Compared with the previously reported devices of a similar design[4], the lasers in this work have lower threshold and higher efficiency. The data reported by H. Zhao *et al* [8] for buried-heterostructure lasers grown on the non-planar substrates are also shown in Fig.3 for comparison. Those devices exhibit lower threshold current at comparable width, presumably due to better lateral confinement of the carriers and the optical fields.

A similar stripe geometry technology has been used to fabricate folded cavity surface emitting lasers that incorporate one or two 45° mirrors in the cavity to deflect the light from the cavity toward the surface. Record low thresholds of 4.5 mA and high surface emission efficiencies of 59% have been achieved in such devices. We will describe the characteristics of these devices and the application of them to OEIC's in this talk.

ACKNOWLEDGEMENT: this work is supported by ARPA through the Ultra program and by the Office of Naval Research.

Fig. 1

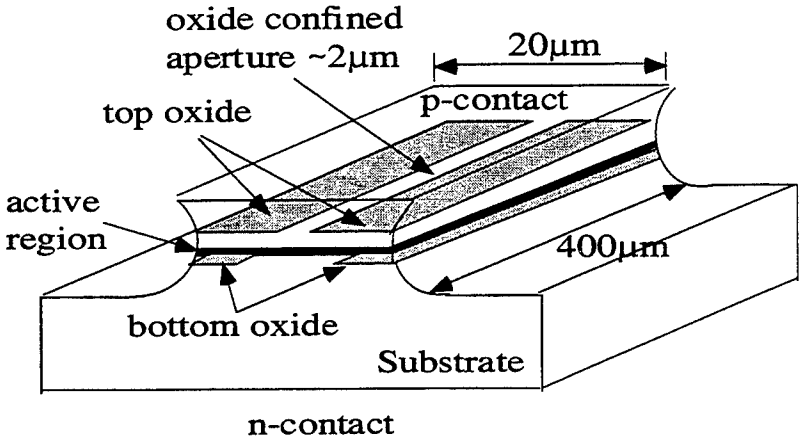


Fig. 2

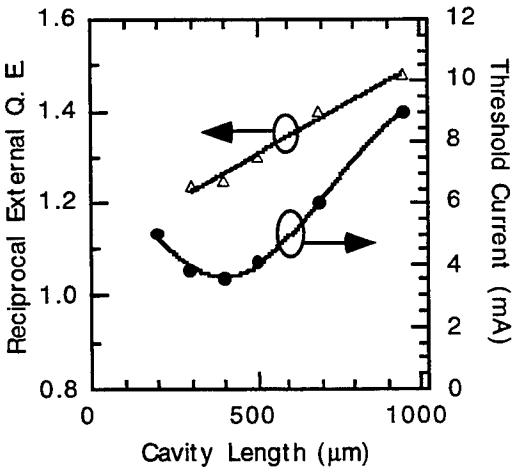
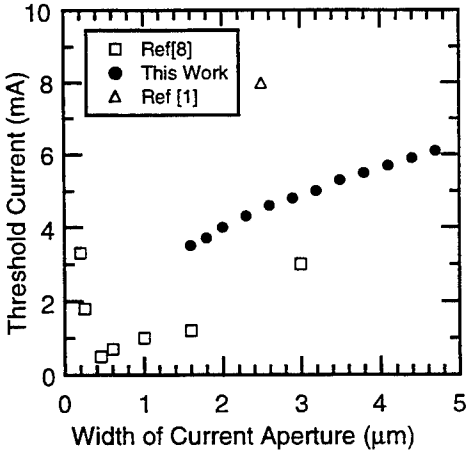


Fig. 3



REFERENCES

1. S.A.Maranowski, A.R.Sugg, E.I.Chen, and N.Holonyak,Jr., "Native oxide top- and bottom-confined narrow stripe p-n $Al_yGa_{1-y}As$-GaAs-$In_xGa_{1-x}As$ quantum well heterostructure laser", *Appl. Phys. Lett.*, 63, pp1660-1662(1993).

2. S.J.Caracci, F.A.Kish, N.Holonyak,Jr., S.A.Maranowski, S.C.Smith, and R.D.Burnham, "High-performance planar native-oxide buried-mesa index-guided AlGaAs-GaAs quantum well heterostructure lasers", *Appl. Phys. Lett.*, 61, pp321-323(1992).

3. M.H.MacDougal, P.D.Dapkus, V.Pudikov, H.Zhao, and G.M. Yang, "Ultralow threshold current vertical-cavity surface-emitting lasers with AlAs oxide-GaAs distributed Bragg reflectors", *IEEE, Photon. Technol. Lett.*, 7, 229(1995).

4. D.L. Huffaker, D.G. Deppe, and K. Kumar, "Native-oxide defined ring contact for low threshold vertical-cavity lasers", *Appl. Phys. Lett.*, 65, pp97-99(1994).

5. G.M. Yang, M.H. MacDougal, and P.D. Dapkus, "Ultralow threshold current vertical-cavity surface-emitting lasers obtained with selective oxidation", *Electron. Lett.*, Vol.31, No.11, pp886-888, (1995).

6. K.D. Choquette, R.P. Schneider Jr., K.L. Lear, and K.M. Geib, "Low threshold voltage vertical - cavity lasers fabricated by selective oxidation", *Electron. Lett.*, vol.30, pp.2043-2044 (1994).

7. F.A.Kish, S.A.Maranowski, G.E.Höfler, N.Holonyak,Jr., S.J.Caracci, J.M.Dallesasse, and K.C.Hsieh, "Dependence on doping type (p/n) of the water vapor oxidation of high-gap $Al_xGa_{1-x}As$", *Appl. Phys. Lett.*, 60,pp3165-3167(1994).

8. H. Zhao, M.H. MacDougal, P.D.Dapkus, K. Uppal, Y. Cheng, and G.M. Yang, "Submilliampere threshold current InGaAs/GaAs/AlGaAs lasers and laser arrays grown on nonplanar substrates," *Journal of Selected Topics in Quantum Electronics*, Vol.1, No.2, pp196-202, June 1995.

Tunnel-injection laser based on type II broken-gap p-GaInAsSb/p-InAs single heterojunction.

M.P.Mikhailova, K.D.Moiseev, O.G.Ershov, G.G.Zegrya, Yu.P.Yakovlev.

A.F.Ioffe Physical Technical Institute, Russian Academy of Sciences, St.Petersburg, 194021, Russia. Fax (812) 247-1017.

We present a new physical approach for the designing of III-V middle-infrared lasers promising for the increase of the operating temperature.

Main features of the novel laser are tunnelling-injection mechanism and indirect radiative recombination of spatially separated carriers at the interface of type II p-p heterojunction (HJ) which was placed in an active layer.

Wide-gap lattice-matched p-GaInAsSb layers (E_g=0.63 eV at T=77 K, p=5x10^{16}-10^{17} cm^{-3}) were grown by liquid phase epitaxy on p-InAs (100) substrats. We found that [1] GaInAsSb/InAs heterojunction is type II one with a broken-gap alignment [1], with a gap between valence band of quaternary layer and conductivity band of InAs is about Δ=60-100 meV.

Surprisingly intensive electroluminescence (EL) have been observed for the first time in the isotype p-GaInAsSb/p-InAs structure in the range of T=77-300 K at "reverse" bias, (a negative potential at the p-InAs substrate) [2]. Two very narrow emission bands 1 and 2 with photon energies less than E_g of InAs were found in EL spectra at T=77 K, $h\nu_1$=316 meV and $h\nu_2$=378 meV, with full width of half maximum (FHWM) 10 and 20 meV, respectively. Fig.1 represents EL spectrum at direct drive current.A "blue shift" of photon energy maxima of the emission band was observed.

The unusual electroluminescence in p-p GaInAsSb/InAs HJ was explained by the indirect (tunnel) radiative recombination of 2-D electrons localized at levels E_1 and E_2 in quantum well at the InAs-side with holes confined in the quaternary layer. Inset in Fig.1 demonstrates the energy band diagram of the "reverse"-biased p-GaInAsSb/p-InAs heter-

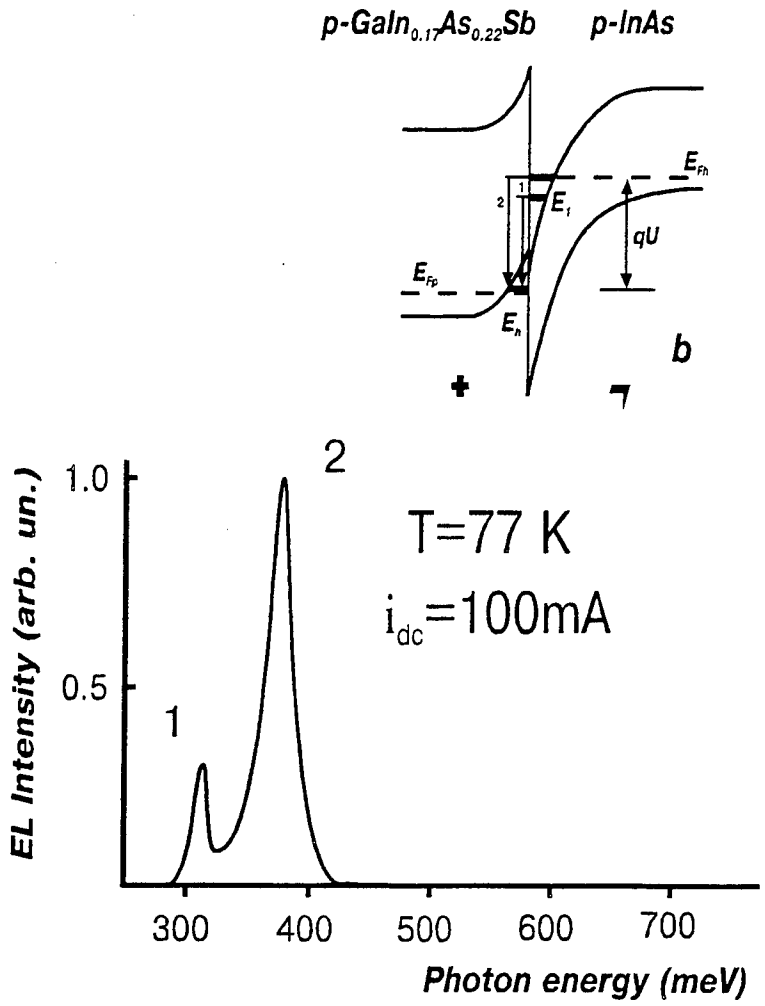


Fig.1. Electroluminescence spectrum of p-GaInAsSb/p-InAs single heterojunction at dc drive current i=100 mA. T=77 K. Emission bands 1 and 2 (see text).
Inset: energy band diagram of the "reverse" biased p- type II broken-gap HJ ("-" on p-InAs).
Arrows 1 and 2 correspond to radiative recombination transitions of confined electrons and holes by tunneling through the interface.

ostructure. Arrows 1 and 2 indicate possible radiative recombination transitions due to tunneling through the interface those correspond to emission bands 1 and 2.

Electrons appear at the interface of the type II broken-gap p-GaInAsSb/p-InAs heterostructure due to transfer (at zero bias) from the valence band of quaternary layer to the conduction band of InAs. At applied "reverse" bias there is a strong band-bending at the interface and quantum well at p-InAs-side becomes narrower and deeper. In this conditions there are no free holes near the interface to recombine with electrons in the well.

When quasi-Fermi level in InAs coinciding with an acceptor level in the region of the flat-bands crosses the discrete electron levels E_1 and E_2, electrons can inject from the acceptor level due to resonant tunneling and populate levels in the well. Existence of an electron channel at the interface in p-GaInAsSb/p-InAs heterostructure was established by Shubnikov-De Haas oscillations of longitudinal magnetoresistance as well as visually by scanning tunnel microscopy measurements.

Using effect under study we proposed and realized a new laser structure on the base of type II broken-gap p-p heterojunction.

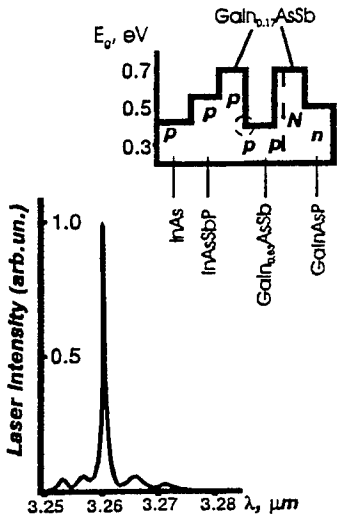


Fig.2. Single-mode lasing of laser structure shown in inset. T=77 K. Pulse regime. I_{th}=2 kA/cm^2.

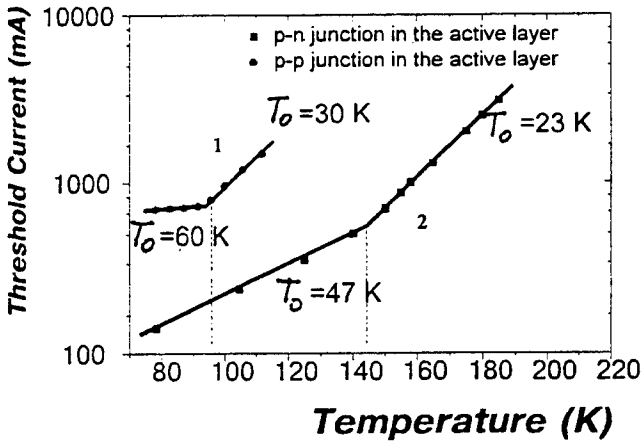


Fig.3. Temperature dependence of threshold current for two laser structures with type II broken-gap heterojunction in an active layer.

A laser structure with separated electron and optical confinement grown by LPE on p-InAs substrats and contained 6 layers as it is shown in Fig.2. Mesa-stripe diodes with a stripe width 60 μm and cavity length about 350 μm were made. There is type II p-p heterojunction in the active region that consists of the wide-gap and narrow gap quaternary GaInAsSb layers with energy gaps E_g=0.630 and 0.390 eV at T=77 K (In content 17 and 30%, respectively) forming broken-gap alignment.Wide-gap GaInAsSb p-n junction was made in the cap confined layer to provide an additional electron injection. Big value of band offset at the interface (ΔE_c~0.6 eV) allows to get a good electron confinement. For improvement of the optical confinement n- and p-type wide-gap InAsSbP layers (E_g=510 meV) were used.

Single-mode coherent emission have been obtained with λ=3.26 μm at T=77 K (Fig.2). It is important to notice that coherent emission in the laser structure aroses at the shortwavelength edge of the spontaneous EL spectrum. Two kinds of laser structures were designed and studied: (1) with p-p type II broken-gap heterojunction and (2) with the p-n one in an active region. Threshold current temperature dependence for both laser structures is represented in Fig.3.(curves 1 and 2). It was found that threshold current weakly depends on temperature in the region of 77-110 K for the structure 1, and in the region of 77-140 K for the other structure. Characteristic temperatures were achieved for these lasers: T_0=60 and T_0=45 K. It is the highest T_0 value reported for InAs-based lasers [3]. Lasing was observed for an improved novel laser structures up to 185 K.

By our opinion, this imprtant result is due to using the interface radiative recombination transitions at the type II heteroboundary.

As it was shown in [4] Auger-recombination rate can be suppressed, and have a weaker temperature dependence at type II heterointerface, in comparing with type I heterostructures. It connects with the fact that matrix element for non-radiative Auger recombination transition at the type II heteroboundary has an additional infinitesmal unlike the type I HJ, that is proportional to $(T/\Delta E_c m_h/m_c)<<1$. The ratio of the Auger-recombination rates is $G^{II}{}_A/G^{I}{}_A \sim (T/\Delta E_c m_h/m_c)^{3/2}$. Due to this result, the Auger-recombination rate decreases at the type II heterointerface. With using parameters of the p-p heterostructure under study, ΔE_c=640 meV, m_c=0.026 m_0, m_h=0.41m_0, T~10 mV (~100 K), we obtain the ratio $G^{II}{}_A/G^{I}{}_A \sim 0.15$. However, radiative recombination rates R^{II} and R^{I} in both types of heterostructures are comparable, $R^{II}/R^{I} \sim 1$ [4]. It means that internal quantum efficiency must be higher for the type II HJs. High intensity of the interface spontaneous emission observed experimentally in the p-p structures under study is in agreement with this confirmation. So, we can conclude, Auger-recombination suppression leads to the weaker temperature dependence of the threshold current density in the laser structure based on type II heterostructures.

These results open the way for the designing mid-infrared lasers operating at room temperatures.

Acknowledgement. This work is supported in part by International Science Foundation and Russian Government Grant **R 46300**, and by AF Phillips Lab. through the EOARD Contract N **F6170894C0011**.

References

1. Mikhailova, I.A.Andreev, T.I.Voronina,K.D.Moiseev, T.S.Lagunova, Yu.P.Yakovlev. Semiconductors 29, **353** (1995).
2. Mikhailova, G.G.Zegrya, K.D.Moiseev, I.N.Timchenko, Yu.P.Yakovlev. Semiconductors, v.29, **676** (1995).
3. A.N.Baranov, A.N.Imenkov, V.V.Sherstnev, Yu.P.Yakovlev / Appl.Phys.Lett., 64, **2480** (1994).
4. G.G.Zegrya, A.D.Andreev. Pisma v Zhurnal Experimentalnoii i Teoreticheskoi Fiziki (JETP Lett.) 61, **754**, (1995).

Blue Lasers using Frequency Doubling in Optical Waveguides

John D. Bierlein
Central Research and Development
E. I. du Pont de Nemours and Company
Experimental Station
Wilmington, DE 19880-0356
(Phone) 302-695-4173 (fax) 302-695-8207

Abstract

Frequency doubling using optical waveguide structures show promise for obtaining compact blue lasers that can be used in many applications. Using a segmented KTP optical waveguide over 50 mW output at 490 nm has been demonstrated. This paper reviews these type systems and discusses their advantages and current limitations.

Summary

Low-cost, efficient, compact coherent sources operating from the near ultraviolet to the green regions of the spectrum are required for a broad range of applications ranging from reprographics to data storage and biomedical diagnostics. Several technical approaches are being pursued for achieving these sources including II-VI and III-V semiconductor diodes, rare earth upconversion, and nonlinear optic frequency conversion. One of the more promising candidates for such a source is frequency doubling an infrared laser diode using an optical waveguide. There are currently three main materials, $LiNbO_3$, $LiTaO_3$, and $KTiOPO_3$ (KTP), being evaluated for optical waveguide doublers. Of these KTP has been the most thoroughly evaluated and, hence, will be to primary focus of this paper.

There are two important conditions for efficient SHG generation of a laser diode using an optical waveguide, high SHG conversion efficiency and stable laser diode properties. The first condition is achieved by using relative small cross section optical waveguides to ensure high fundamental power intensity in the guide and by using a quasi phase matched SHG scheme that permits the utilization of a high nonlinear optic coefficient of the material. The second condition

has been achieved using various diode stabilization schemes such as external grating feedback, DFB laser diodes, very narrow band filters located between the diode and waveguide and Bragg reflection from the optical waveguide.

We have reported previously on a blue laser that uses a KTP waveguide consisting of an initial waveguide section designed for quasi phase matched SHG of the laser diode followed by a Bragg reflection waveguide section which is used to provide feedback to lock the laser diode to the wavelength needed for SHG.[1] Such a waveguide was lens coupled to an AR coated laser diode to produce 1.6 mW at 425 nm. We also reported on the development of a butt-coupled KTP SHG laser that generates 3 mW output at 425 nm.[2] The basic configuration is shown in Fig. 1. The KTP waveguide design was similar to that described earlier[3] and consisted of an 8 mm SHG section followed by a 2 mm Bragg section. The waveguides were fabricated using Rb/Ba ion-exchange processing conditions which were also similar to those reported previously. Improvements in photolithography and in ion-exchange processing optimization and reproducibility now allow such waveguides to be routinely fabricated with internal conversion efficiencies of about 250 %/W-cm^2 and, in some cases, with efficiencies in excess of 600%/W-cm^2.

An SDL 5422 C-block packaged laser diode with AR coating (less than 0.5% reflectivity) was directly coupled to the input face of the KTP waveguide. Both faces of the KTP waveguide are also AR-coated (reflectivities less than 0.5%) to reduce Fabry-Perot reflections and to minimize other spurious reflections reducing diode stability. By precise, sub-micron alignment a diode-to-waveguide coupling efficiency of 56% was achieved. This KTP blue laser has an RIN noise of less than -140 dB/Hz and the beam is diffraction limited which makes it suitable for reading high density optical discs.

In more recent work using a Ti:Al_2O_3 laser we have demonstrated SHG outputs in excess of 100 mW at about 490 nm from an 8 mm long waveguide. These waveguides also showed good long term stability at 50 mW, the highest power tested over long times. When suitable high power single mode IR laser diodes are available similar powers are expected from a directly coupled diode/waveguide system as well.

This paper will review the various diode/waveguide doubling systems currently under development and will particularly emphasize both waveguide material and IR laser diode limitations.

References

1. M. G. Roelofs, J. D. Bierlein, and F. Laurell, "Second harmonic generation from diode lasers in KTP waveguides, Compact Blue-Green Lasers Technical Digest, 1992 (Optical Society of America, Washington, DC. 1992), Vol. 6, p. 127.

2. T. Tohma and J. D. Bierlein, "KTP blue laser for optical storage", Presented at the Topical Meeting on Nonlinear Guided Waves and their Applications, Dana Point, Calif., Feb. 23-25, 1995.

3. J. D. Bierlein, M. G. Roelofs, J. B. Brown, T. Tohma, and S. Okamoto, "$KTiOPO_4$ blue laser using segmented waveguide structures", Compact Blue-Green Lasers Technical Digest, 1994, PD 7, 1-4.

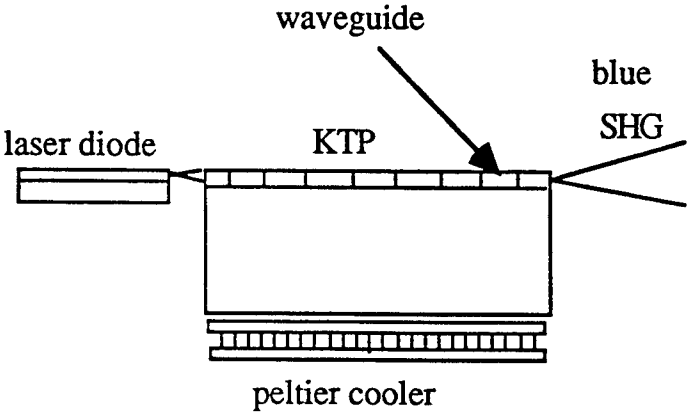


FIG. 1 The basic configuration of the butt-coupled KTP SHG laser

Polarization Sensitive Photodetector Arrays

M. S. Ünlü and B. Onat
Boston University, Department of Electrical, Computer, and Systems Engineering
44 Cummington Street, Boston, MA 02215, Tel: (617) 353–5067

H. P. Zengingönül
University of Illinois at Urbana-Champaign, Department of Electrical and Computer Engineering
Urbana, IL 61801

R. Henderson and E. Towe
University of Virginia, Department of Electrical Engineering,
Charlottesville, VA 22903

A photodetector structure is described which is sensitive to the polarization of the incident radiation. The principle of operation is based on the resonant cavity enhanced (RCE) photodetectors [1]. This structure does not require any external polarization filters or beam splitters. Sensitivity of discrete devices can be controlled by recessing the top surface of the detector allowing for the monolithic fabrication of detector arrays with varying sensitivities to TE(s) and TM(p) polarizations. A detector array of two detectors can be used to measure the polarization of the incident light. Below we discuss the concept and preliminary analysis. The presentation will include a more detailed theoretical analysis and experimental results.

Over the past five years, a new family of optoelectronic devices has emerged whose performance is enhanced by placing the active device structure inside a Fabry-Perot resonant microcavity [2]. The RCE structure consists of a thin absorption region placed in an asymmetric Fabry-Perot cavity. The cavity is formed by top and bottom reflectors which can be fabricated by various methods (for example, alternating layers of quarter-wavelength dielectrics, i.e., Distributed Bragg Reflectors). The quantum efficiency for a RCE detector can be expressed as

$$\eta = \left\{ \frac{(1 + R_2 e^{-\alpha d})}{1 - 2\sqrt{R_1 R_2} e^{-\alpha d} cos(2\beta L + \psi_1 + \psi_2) + R_1 R_2 e^{2\alpha d}} \right\} \times (1 - R_1)(1 - e^{-\alpha d}) \quad (1)$$

where α and d are the absorption coefficient and thickness for the thin absorber, β is the optical propagation constant, L is the length of the cavity, and R_1, ψ_1 and R_2, ψ_2 are the amplitude and phase of the top and bottom reflectors, respectively. If the light is incident to the surface at an angle θ with the normal, L is replaced by $L/\cos\theta$.

When the optical length of the cavity satisfies the resonance condition, the cavity enhances the optical fields and the detector response is drastically increased. If the length of the cavity is altered (for example, by surface recessing) then the sensitivity is reduced below that of a conventional detector structure without the cavity. The enhancement/reduction in the detector response depends strongly on the top reflectivity (R_1) [2].

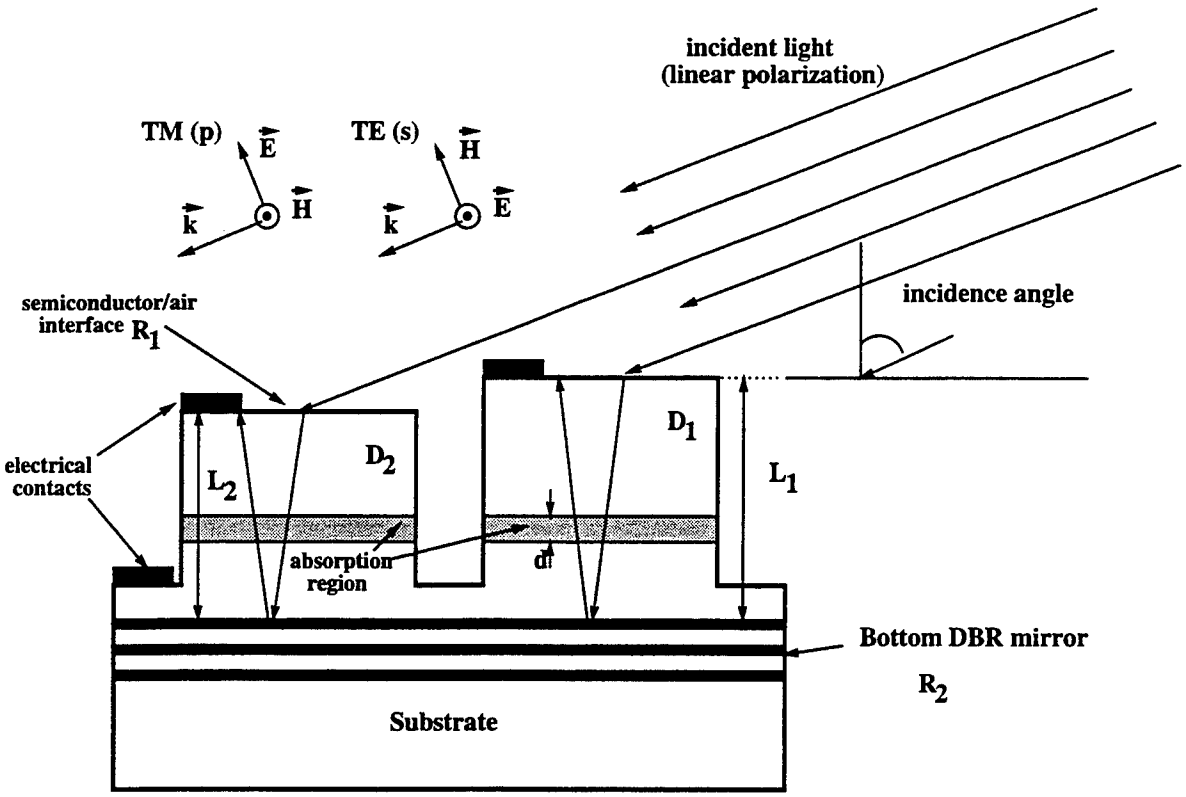


Figure 1: Conceptual representation of the polarization sensitive photodetector array.

The concepts described below are applicable to most material systems and detector structures at various wavelength (λ) regions. The discussion will focus on the theoretical and experimental results based on a GaAs/AlGaAs/InGaAs photodetector structure at around λ=900 nm.

Figure 1 shows a conceptual representation of the polarization sensitive detector array consisting of two monolithic RCE photodetectors with different cavity lengths (L_1 and L_2). The interface between semiconductor and air is used as the top reflector. At normal incidence, GaAs/air interface provides a reflectivity of 0.32. This reflectivity is a strong function of incidence angle and polarization as shown in Fig. 2.

At Brewster's angle ($\sim 74°$ for GaAs), TM reflectivity vanishes and TE reflectivity is about 0.75. Therefore, sensitivity is a strong function of the cavity length for TE polarization and can be controlled by recessing the top surface, while the sensitivity for TM is invariant. The detectors #1 and #2 in Fig. 1 can be made to have very different sensitivities for TE polarization while their responses to TM polarization are equal.

Figure 3 shows the calculated dependence of the detector response on the surface recess for TE and TM polarizations. A maximum cavity length of $L_{max} = 2.5\mu$m is considered. By selecting the two recess values corresponding to the maximum and minimum of the TE quantum efficiency, a sharp contrast in TE–response can be achieved. The length of detector #1 (in Fig. 1) is adjusted to achieve the maximum sensitivity of the resonant cavity for TE polarization for the selected incidence angle. The surface of detector #2 is recessed such that the incident TE polarized light is rejected.

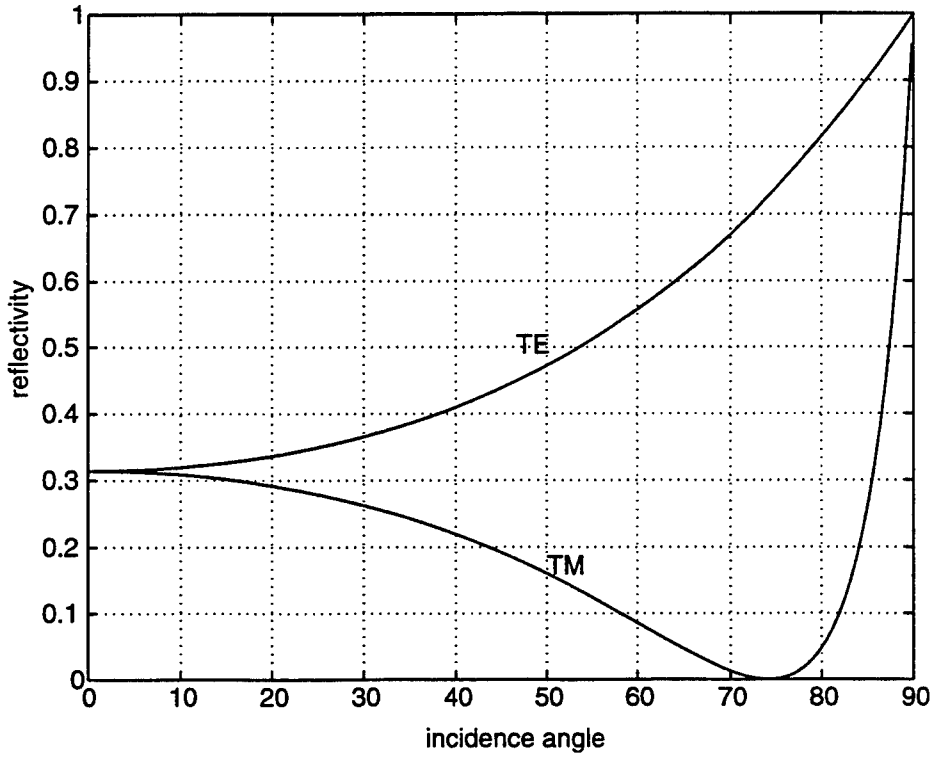


Figure 2: Incidence angle dependence of the reflectivity at GaAs/air interface for TE(s) and TM(p) polarizations. At the wavelength of interest (λ=900 nm), the refractive index of GaAs is $n = 3.55$.

The detector responses D_1 and D_2 can be expressed as

$$\begin{bmatrix} D_1 \\ D_2 \end{bmatrix} = \begin{bmatrix} S_{1,TE} & S_{1,TM} \\ S_{2,TE} & S_{2,TM} \end{bmatrix} \cdot \begin{bmatrix} TE \\ TM \end{bmatrix} = [S] \cdot \begin{bmatrix} TE \\ TM \end{bmatrix} \tag{2}$$

where $S_{i,TE}$ and $S_{i,TM}$ represent the sensitivity of the two detectors to different polarizations. For the described device structure, there is a big contrast in the response to different polarizations. Therefore, [S] can be inverted and TE and TM powers can be evaluated from the detector signals as:

$$\begin{bmatrix} TE \\ TM \end{bmatrix} = [S]^{-1} \cdot \begin{bmatrix} D_1 \\ D_2 \end{bmatrix} \tag{3}$$

For the device parameters of Fig. 3, $S_{1,TE} = 0.98$, $S_{2,TE} = 0.03$, and $S_{1,TM} = S_{2,TM} = 0.33$, we obtain:

$$\begin{bmatrix} TE \\ TM \end{bmatrix} = \begin{bmatrix} 1.053 & -1.053 \\ -0.096 & 3.126 \end{bmatrix} \cdot \begin{bmatrix} D_1 \\ D_2 \end{bmatrix} \tag{4}$$

We have designed and fabricated RCE detector structures in GaAs/(In,Al)GaAs material system. The bottom reflector is formed by 15 period GaAs/AlAs DBR mirror. Active absorption region consists of $In_{0.1}Ga_{0.9}As$. We are in the process of characterizing these

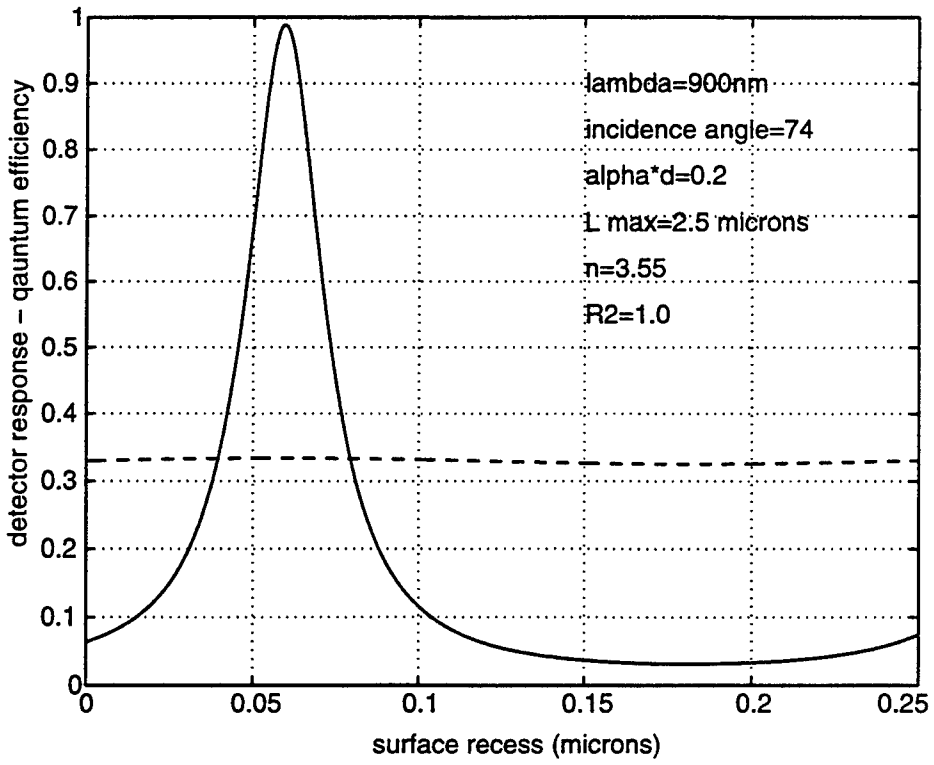


Figure 3: Dependence of quantum efficiency for a RCE-detector

samples by reflectivity measurements and fabricating detector arrays. We will present experimental results, analysis of these detector arrays and dependence of performance on various parameters.

This work is supported by the National Science Foundation under the contract No: ECS-9309607. We would like to thank Prof. M. Ruane for fruitful discussions.

References

[1] M. S. Ünlü, K. Kishino, J.I. Chyi, L. Arsenault, J. Reed, S.Noor Mohammad, and H. Morkoç, "Resonant Cavity Enhanced AlGaAs/GaAs Heterojunction Phototransistors with an Intermediate InGaAs Layer in the Collector," *Appl. Phys. Lett.*, Vol. 57(8), pp. 750-752, (1990).

[2] M. S. Ünlü and S. Strite, "Resonant Cavity Enhanced Photonic Devices," *Appl. Phys. Rev., J. Apply. Phys.*, Vol. 78(2), pp. 607-639, (1995).

Correlation of optical pulses with a low-temperature-grown GaAs photoconductor

S. Verghese,[1,2] N. Zamdmer,[1] E. R. Brown,[2] A. Förster,[3] and Qing Hu[1]
[1]Department of EECS and Research Laboratory of Electronics,
Massachusetts Institute of Technology, Cambridge, MA
[2]MIT Lincoln Laboratory, Lexington, MA
[3]Institut für Schicht- und Ionentechnik (ISI), Forschungszentrum Jülich, Germany

A novel sampling correlator is described which is useful for characterizing optical pulses with subpicosecond temporal resolution. The correlator exploits the ultrafast nonlinear response of a photoconductor made of low-temperature-grown (LTG) gallium arsenide, which is connected to a coplanar-waveguide transmission line. Unlike commercially available correlators, the LTG-GaAs correlator (LTGGC) does not require a nonlinear crystal for second-harmonic generation. Instead, the LTGGC uses a nonlinearity which is associated with the transmission line and photoconductor functioning as a voltage divider. The resulting nonlinearity is used to measure $g^{(2)}(\tau)$, the second-order intensity autocorrelation function [1].

Figure 1 schematically shows the LTG-GaAs photoconductor in a transmission line geometry. On time-scales of $\sim 1\,\mathrm{ps}$, the current-response $i_{pc}(t)$ to an intensity pulse $I(t)$ is effectively instantaneous.

$$i_{pc}(t) = \frac{v_o}{Z_o + G(t)^{-1}} \,. \tag{1}$$

Here v_o is the dc bias voltage, Z_o is the characteristic impedance of the transmission line ($\sim 100\,\Omega$), and $G(t) \propto I(t)$ is the photoconductance [2]. For small $I(t)$, the photocurrent $i_{pc}(t)$ is linear in $I(t)$ since $G(t)^{-1} \gg Z_o$ and the photoconductor is voltage-biased. For larger $I(t)$, however, the photoconductor is no longer voltage-biased—it is biased through a load impedance Z_o and responds nonlinearly in $I(t)$ when $Z_o \approx G^{-1}$.

This nonlinearity is exploited by the LTGGC to measure $g^{(2)}(\tau)$ as follows. Phenomenologically, the lowest order nonlinearity is given by $i_{pc}(t) \approx S_I^{(2)} (I(t))^2$, where $S_I^{(2)}$ is the second-order nonlinear current responsivity in units of $\mathrm{A/(W\,cm^{-2})^2}$. For two cross-polarized beams which are separated by a variable time-delay τ, the incident intensity at the LTG-GaAs photoconductor is $I_T(t) = I(t) + I(t+\tau)$. The time-averaged photocurrent in response to $I_T(t)$ gives a cross-term which depends on τ.

$$< i_{pc}(\tau) >_t = 2S_I^{(2)} < I(t)I(t+\tau) >_t + \mathrm{const}\,. \tag{2}$$

Neglecting the constant term, $< i_{pc}(\tau) >_t$ is proportional to the second-order intensity autocorrelation $g^{(2)}(\tau)$ in the limit that the photoconductor nonlinear responsivity $S_I^{(2)}$ depends weakly on $I(t)$—a condition which is satisfied when the intensity is chosen such that $Z_o G \approx 0.1$. Therefore, $g^{(2)}(\tau)$ can be measured from the dc photocurrent as a function of the time-delay τ.

An example illustrates typical parameter values for the LTGGC. Consider a photoconductor integrated into a coplanar waveguide as shown in Fig. 1 with a $5 \times 5\,\mu\mathrm{m}$ active area. Assume the quantum efficiency is $\eta = 0.5$, $\hbar\omega = 1.5\,\mathrm{eV}$, the photoconductive response time is $\tau_r = 100\,\mathrm{fs}$, $\mu_e = 100\,\mathrm{cm^2V/s}$, and $\mu_h \ll \mu_e$. For a $100\,\Omega$ transmission line, the optimum

operating condition $Z_oG \approx 0.1$ occurs for a peak intensity $I(t) = 7 \cdot 10^7$ W/cm^2. This corresponds to an average power of 0.1 mW for a mode-locked Ti:sapphire laser which produces ~ 80 fs pulses at a repetition rate of 82 MHz. This power is much lower than that required for a similar signal-to-noise ratio for conventional autocorrelators (typically ~ 10 mW) [3].

The temporal resolution of the LTGGC is determined by the time required for the LTG-GaAs photoconductor to return to a high resistance state after brief illumination. This recovery time is referred to as τ_r—which accounts for recombination and trapping of photo-excited electrons and holes. Time-domain reflectivity measurements were used to measure τ_r in a LTG-GaAs sample. In such measurements, a short intense pulse induces a change in the reflectivity ΔR which then decays exponentially with time-constant τ_r. The lifetime τ_r measured for our sample was ~ 650 fs.

We recently demonstrated the feasibility of the LTGGC using this photoconductor sample. The temporal resolution of this particular LTGGC is limited by τ_r and is adequate for measuring intensity envelopes with modulation features on time-scales longer than ~ 1 ps. A $10 \times 3\,\mu$m LTG-GaAs photoconductor was integrated into a high-frequency coplanar waveguide patterned from a Au:Ti metal film. An audio speaker with a retroreflector driven at 30 Hz swept the time-delay τ between two trains of ~ 80 fs pulses from a Ti:sapphire laser. The two pulse trains were coupled to the LTG-GaAs photoconductor through a length of single-mode optical fiber. The optical fiber dispersed the ~ 80 fs pulses to picosecond time scales. Figure 2a shows a measurement of $i_{pc}(\tau)$ versus time-delay τ for two ~ 80 fs optical pulse trains ($\lambda = 810$ nm) which have propagated through 43 cm of single-mode optical fiber. The shape of this curve is similar to autocorrelation curves measured for dispersed pulses with a conventional autocorrelator [4]. The sharp peak in the center is a coherence peak whose width is approximately the inverse of the pulse's optical bandwidth. The coherence peak contains no information about the time-scale of the modulated intensity and can be eliminated by coupling the two optical pulses with crossed polarizations through a polarization-maintaining optical fiber. The rounded shoulders on either side of the coherence peak contain information about the temporal width of the dispersion-broadened pulse. The full width half maximum (FWHM) of the rounded shoulders is 2 ps for Fig. 2a. Deconvolution, assuming a $\mathrm{sech}^2(t)$ pulse-shape, then yields a temporal width of 1.3 ps for the dispersed optical pulse. Figure 2b shows a similar measurement, but with a longer length of fiber (94 cm). Deconvolution in this case yields a width of 1.9 ps for the dispersed pulse. The curves in Fig. 2 clearly demonstrate the operation of the LTGGC on the picosecond time-scale. Note that the coherence peak has the same width in both traces. This indicates that the bandwidth has been preserved and that the LTGGC is not measuring a change in coherence—it is measuring the additional dispersion of the intensity envelope caused by the longer optical fiber.

Compared to conventional autocorrelators which use nonlinear crystals, the LTGGC allows for simplified and compact measurement of the intensity-intensity autocorrelation function of picosecond optical pulses. Faster LTG-GaAs photoconductors are being developed with τ_r approaching 100 fs [5]. Such a photoconductor would conceivably make the LTGGC useful for characterizing optical pulses produced by femtosecond lasers. This work was supported in part by the MRSEC program of the National Science Foundation under award number DMR-9400334, and by the U.S. Air Force under grant number F-19628-95-C-0002.

References

[1] E. P. Ippen, C. V. Shank, "Techniques for measurements," in *Ultrashort light pulses*, S. L. Shapiro Ed., New York: Springer-Verlag, pp. 83-122, 1977.

[2] E. R. Brown, K. A. McIntosh, F. W. Smith, M. J. Manfra, C. L. Dennis, "Measurements of optical-heterodyne conversion in low-temperature-grown GaAs," *Appl. Phys. Lett.*, vol. 62, pp. 1206-1209, 1993.

[3] See, for example, the Model 5-14 autocorrelator, Inrad Corp., 181 Legrand Ave. Northvale, NJ 07647.

[4] K. L. Sala, G. A. Kenney-Wallace, G. E. Hall, "CW autocorrelation measurements of picosecond laser pulses," *IEEE J. Quant. Elec.*, vol. QE-16, pp. 990-996, 1980.

[5] McIntosh, K. A., *private communication.*

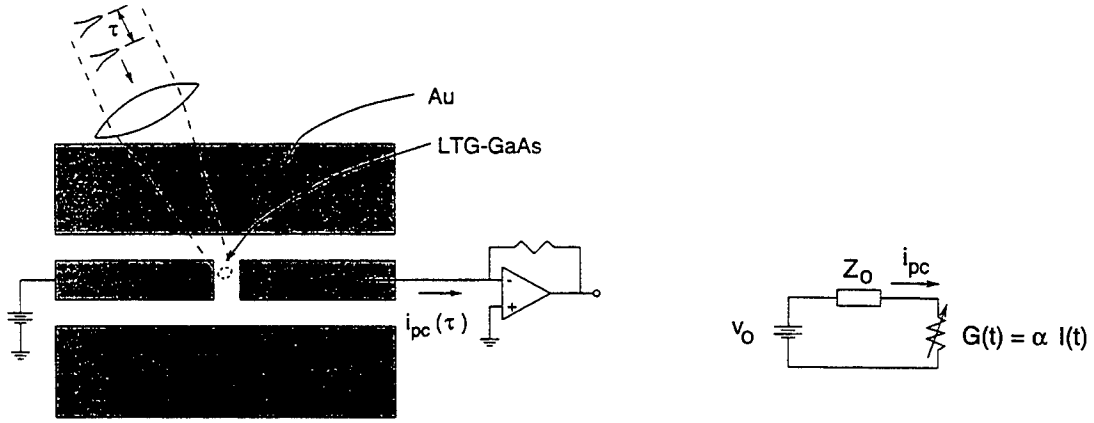


Figure 1: Schematic diagram of the LTG-GaAs photoconductor embedded in a coplanar-waveguide transmission line. A transimpedance amplifier is used as a read-out for the dc photocurrent $i_{pc}(\tau)$. The equivalent circuit models the high-frequency response of the LTGGC to an intensity pulse $I(t)$.

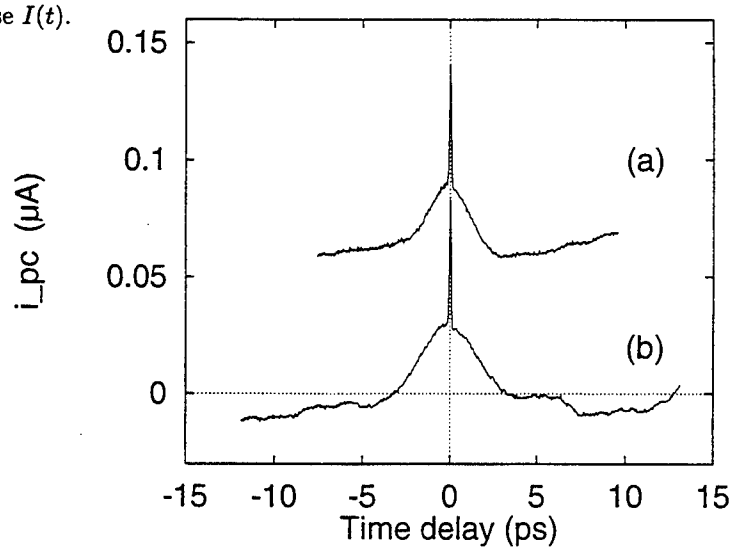


Figure 2: Demonstration of the LTGGC used to measure dispersion on the 1 ps time-scale. (a) Measured values of $i_{pc}(\tau)$ versus time-delay τ for two optical pulses which have been dispersed by propagating through 43 cm of single-mode optical fiber. (b) Measured values of $i_{pc}(\tau)$ versus τ for two optical pulses which have propagated through 94 cm of fiber. The LTGGC clearly measures the increased dispersion produced by the longer fiber.

Direct Broadband (130 MHz to 20 GHz) Amplitude Modulation-Frequency Response Measurements of InGaAsP Optical Amplifiers at a Wavelength of 1.55μm

Timothy U. Horton and Gregory E. Stillman
Center for Compound Semiconductor Microelectronics
University of Illinois at Urbana-Champaign, Urbana, Illinois 61801

Optical amplifiers are becoming increasingly important components in lightwave communication systems [1,2]. Specifically, diode-pumped erbium-doped fiber-optic amplifiers have been demonstrated as effective replacements for many repeaters and and regenerators in long-haul fiber communication links [1]. In addition, semiconductor optical amplifiers have also been extensively studied and demonstrated to function as both repeater replacements [2] and as optical preamplifiers [3,4].

Considerable effort has been devoted to studying travelling-wave InGaAsP/InP optical amplifiers for application as 1.55μm preamplifiers [3,4]. In particular, researchers have worked to develop monolithically integrated preamplifier/detector combinations [3]. A key requirement for optical preamplifiers in these applications is flat amplitude modulation response up to high frequencies [5].

Little has been previously reported concerning direct experimental measurement of the AM frequency response of an InGaAsP optical amplifier. For this reason, we have performed frequency response measurements from 130 MHz to 20 GHz on an InGaAsP semiconductor optical amplifier at 1.55μm using an HP Lightwave Test Set as shown in the schematic of Figure 1 below. The experimental results include an expected frequency response minimum at high frequency (approximately 15 GHz) due to the residual facet reflectivity of the amplifier, as well as a separate low-frequency response degradation which is attributable to the time-dependent coupling between the photon density and the free carrier densities within the active layer of the amplifier.

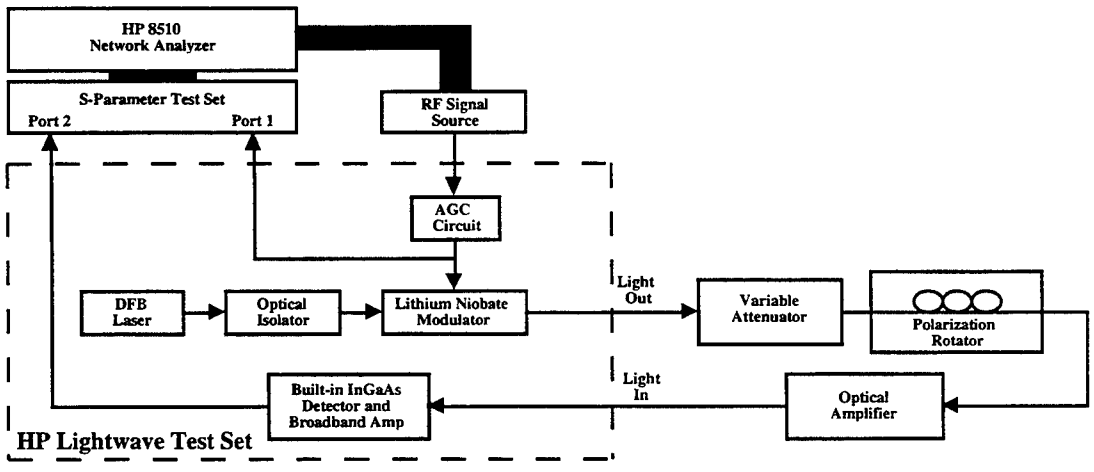


Figure 1. Schematic of the experimental setup for measuring the modulation frequency response of an optical amplifier using the HP Lightwave Test Set

Referring to Figure 1, the Lightwave Test Set adjusts the RF level applied to a $LiNbO_3$ modulator so that the output of an internal DFB laser (1.55μm wavelength and 60 MHz spectral linewidth) is amplitude-modulated to a depth of about 20% independent of frequency. The modulated light signal is routed through single-mode fiber to an optical attenuator and polarization controller, and is then coupled through an anti-reflection coated lens to the input facet of the optical amplifier. The output of the amplifier is similarly coupled into a second fiber which routes the amplified light signal back to a fast photoreceiver inside the Lightwave Test Set.. The S-Parameter Test Set compares the amplitude and phase of the RF output from the photoreceiver to the RF signal driving the $LiNbO_3$ modulator. In order to isolate the modulation frequency response of the optical amplifier, the combined transfer functions of the $LiNbO_3$ modulator and internal photoreceiver are measured directly with the optical amplifier removed from the setup.

The optical amplifier is powered by a current source at DC levels up to 200 mA and is mounted on a heat sink with a thermoelectric cooler which maintains the device temperature at approximately 20°C. Figure 2 shows a simple schematic of the specific amplifier layer and device structure which we tested. The layers form a bulk InGaAsP/InP double heterostructure gives peak emission at 1.58μm. The device structure is similar to a ridge-waveguide laser with the 3μm-wide ridge oriented 10° off-axis (yielding an effective reflectivity at the facets on the order of .01%) and with a device length of approximately 1mm. This amplifier was provided by researchers at HP Laboratories who have used it within an external cavity for tunable laser applications.

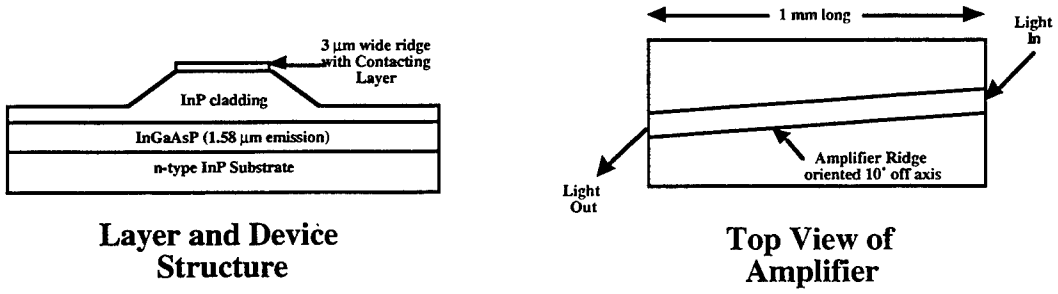


Figure 2. Simplified schematic of InGaAsP optical amplifier device

Figure 3 shows measured fiber-to-fiber unsaturated gain versus frequency data for this optical amplifier with TE excitation as drive current is varied from 70 mA to 200 mA in 10 mA steps. Gain here is defined as the optical power gain supplied by the InGaAsP amplifier and represents directly the amplification of the fundamental frequency component in the intensity modulation. The modulation frequency response is flat to within 1.5 dB over this frequency range for all drive currents, which is desirable for analog preamplification schemes [5]. From Figure 3, the maximum fiber-to-fiber gain is about 19 dB at 200 mA of drive current. The fiber-to-amplifier coupling loss was independently measured to be about 5 dB per facet, yielding a maximum device gain of nearly 30 dB at 200 mA.

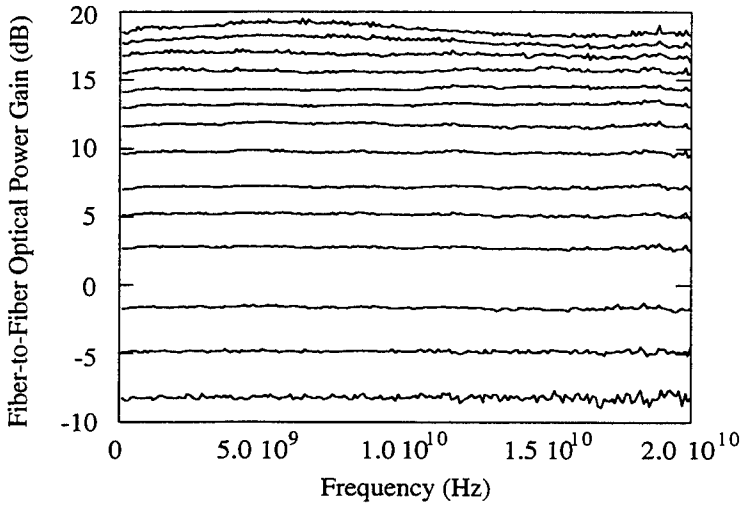


Figure 3. Unsaturated fiber-fiber TE mode gain vs. modulation frequency for amplifier drive currents from 70 mA - 200 mA in 10 mA steps (gain increasing with increasing current)

Even though the gain fluctuations in Figure 3 are small for all drive currents, the 180 mA, 190 mA, and 200 mA curves display a measureable ripple in the frequency response. This is more clearly seen in Figure 4 which shows the 200 mA curve with an expanded vertical scale.

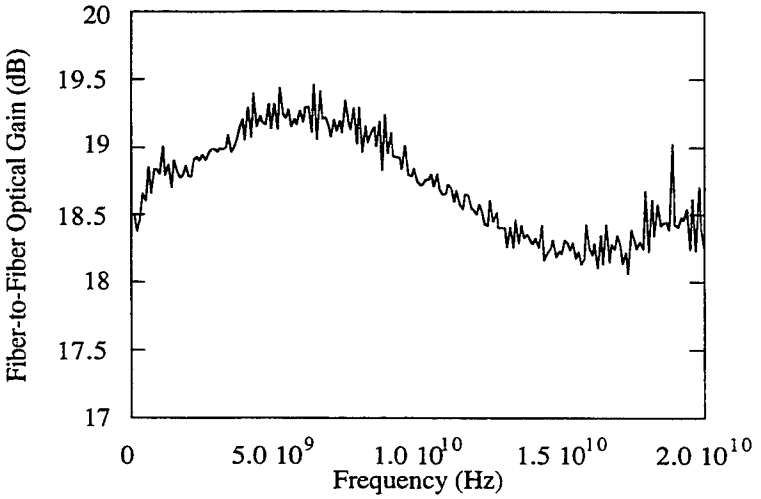


Figure 4. Unsaturated fiber-fiber TE mode gain vs. modulation frequency for 200 mA current showing response minimum near 15 GHz due to facet reflectivity as well as low-frequency degradation due to coupling between carrier and photon densities.

A frequency response minimum occurs at about 15 GHz, and an additional low-frequency degradation is evident below about 5 GHz. The minimum at 15 GHz can be attributed to the amplified optical feedback which occurs due to non-zero facet reflectivities and is directly related to the well documented ripple that is seen in the spontaneous emission spectra of optical amplifiers under high gain conditions [2]. In addition, the low-frequency degradation can be attributed to time-dependent interactions within the active layer between photon densities and free carrier populations which create negative nonlinear feedback for the gain. This result (in terms of degraded low-frequency amplitude modulation response) has been explicitely predicted by a theoretical model which accounts for these interactions in a coupled rate equation analysis [5,6], but to our knowlege has not been reported experimentally. That model predicts the degradation to occur at frequencies below a value roughly equal to the inverse recombination time in the active layer. For our data the frequency at which degradation begins is close to 5 GHz which yields a reasonable recombination time estimate of 200ps. The low-frequency degradation beginning around 5 GHz is also consistent with both modelling and experimental data that has been published demonstrating repetition-rate-dependent gain compression in an InGaAsP 1.3μm amplifier injected with ultra-short optical pulses [7]. That research found that for pulse repetition rates higher than 3 - 6 GHz the gain in the active layer maintained a steady-state value dependent only on the average optical power, whereas for repetition rates lower than this the gain demonstrated a negative exponential-like transient response to each pulse individually.

In summary, we have performed amplitude modulation frequency response measurements on an InGaAsP travelling-wave optical amplifier. The results demonstrate that in addition to the frequency response minimum that is introduced by residual facet reflectivity, there is also low-frequency degradation related to time-dependent coupling between the photon densities and the free carrier densities within the active layer.

The authors wish to acknowlege Dr. Rangu Ranganath of HP Laboratories for providing us with the optical amplifier and the Center for Compound Semiconductor Microelectronics for the use of its excellent measurement facilities. This work was supported by AASERT Grant #N00014-93-1-1075 and JSEP Grant #N00014-90-J-1270.

References:

[1] J.-M. P Delavaux, "Multi-Stage Erbium-Doped Fiber Amplifier Designs," *J. Lightwave Tech.*, vol. 13, no. 5, pp. 703-720, 1995.

[2] M. J. O'Mahoney, "Semiconductor Laser Optical Amplifiers for Use in Future Fiber Systems," *J. Lightwave Tech.*, vol 6, no. 4, pp. 531-544, 1988.

[3] D. Wake, "A 1550-nm Millimeter-Wave Photodetector with a Bandwidth-Efficiency Product of 2.4 THz," *J. Lightwave Tech.*, vol. 10, no. 7, 1992.

[4] H. Nakano, S. Tsuji, K. Uomi, S. Sasaki, and K. Yamashita, "10 Gbit/s, 100km nonrepeatered fibre transmission experiment using a high-sensitivity semiconductor optical preamplifier," *Electron. Lett.*, vol. 26, pp. 1364-1366, 1990.

[5] J. A. Constable, I. H. White, A. N. Coles, D. G. Cunningham, "Harmonic and phase distortion of analogue amplitude-modulated signals in bulk near travelling-wave semiconductor optical amplifiers," *IEE Proceed.-J Optoelectron.*, vol. 139, no. 6, pp. 389-398, 1992.

[6] P. N. Pennington and R. F. Ormondroyd, "Large-signal modulation response of monolithic active integrated-optic waveguides," *IEE Proceed.-J Optoelectron.*, vol. 137, no. 1, pp. 11-20, 1990.

[7] P. B. Hansen, J. M. Wiesenfeld, G. Eisenstein, R. S. Tucker, and G. Raybon, "Repetition-Rate Dependence of Gain Compression in InGaAsP Optical Amplifiers Using Picosecond Optical Pulses," *IEEE J. Quantum Electron.*, QE-25, no. 12, pp. 2611-2620, 1989.

Surface-Normal Optical Pixels For Optical Interconnects

Yoshimasa Sugimoto and Kenichi Kasahara

Opto-Electronics Research Laboratories, NEC Corporation
34 Miyukigaoka,Tsukuba, Ibaraki 305, Japan

Abstract - **A surface-normal optical device with low power consumption and temperature-insensitive light output characteristics is desired for optical interconnects in switching and computer. We show a surface-emitting laser (VCSEL) and VCSEL-based electrophotonic pixels being fabricated for this purpose. These pixels have functions of optical signal routing etc.. This paper also describes the technology to fabricate optical pixels for wavelength division multiplex applications.**

I. Introduction

The advantage of surface-normal optical devices such as vertical-cavity surface-emitting lasers (VCSELs) [1,2] and VCSEL-based devices, for example, VC-VSTEP (vertical-cavity vertical-to-surface transmission electrophotonic device) [3] is low threshold current and ease of array fabrication. In VCSEL applications, high wall-plug efficiency, temperature-insensitivity, uniformity in the electrical and optical characteristics are important. To obtain higher performance, we fabricated VCSELs which had a 5/4-λ-thick contact layer [4], and broad gain bandwidth. It was also possible to stabilize the polarization direction by making the mesa shape of rectangular.

Another features in VCSELs is their single-mode operation is possible, which makes multiple-wavelength VCSEL arrays useful for wavelength division multiplexing (WDM) application. To fabricate monolithically integrated multiple-wavelength arrays, we have developed a new mask molecular beam epitaxy (MBE) technique [5] in which a shadow mask is placed on a wafer during epitaxial growth [6]. This technique allows changing selective and nonselective growth mode in a MBE chamber. Varying the cavity thickness at selective areas grown by the mask MBE enables multiple-wavelength VCSELs to be monolithically integrated.

Optical signal routing for photonic switching and network computing is possible with VCSEL-based electrophotonic pixels. We have propose a distributed fiber switch that consists of VCSELs with an addressing circuit and an optical cross connector.

II. VCSEL device structure and characteristics

The structure of InGaAs/AlGaAs bottom emitting lasers grown by MBE was shown in Fig. 1. The bottom mirror consisted of a 18.5 period Si-doped AlAs/GaAs distributed Bragg reflector (DBR). The l-thick spacer region consisted of active layers and $Al_{0.5}Ga_{0.5}As$ confinement layers. The top mirror was composed of a 16 period Be-doped AlAs/GaAs DBR. The active region was surrounded by a highly resistive proton-implanted region. The back of the substrate was anti-reflection (AR)-coated.

On our proposed device, the active layer consisted of multiple types of InGaAs quantum wells to achieve a broad gain bandwidth [11]. The quantum wells were sandwiched with a $Al_{0.25}Ga_{0.75}As$ barrier layer. The gain peaks for this proposed device were

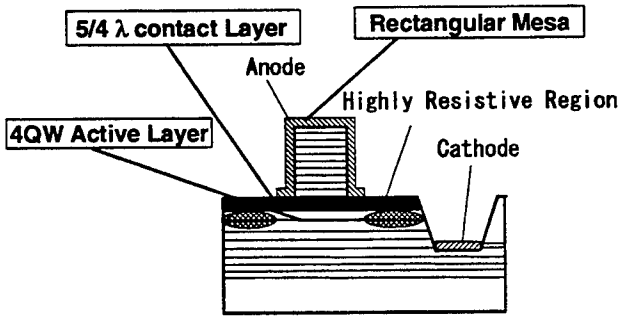


Fig. 1 Structure of the proposed VCSEL

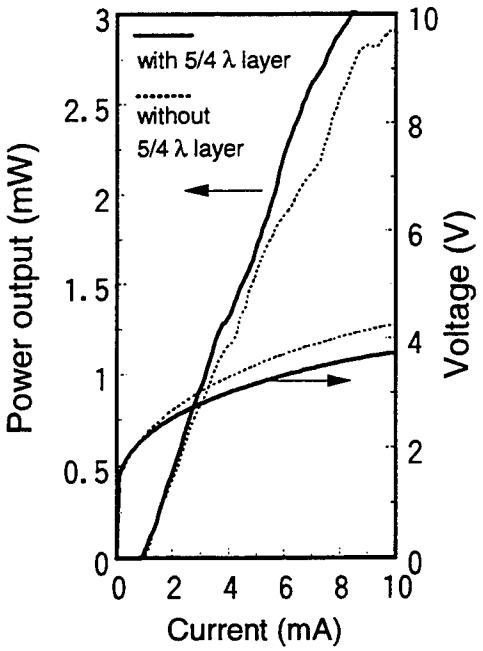


Fig. 2 I-L and I-V characteristics (CW, RT). Solid lines: with 5/4-λ layer, dotted lines: without 5/4 -λ layer.

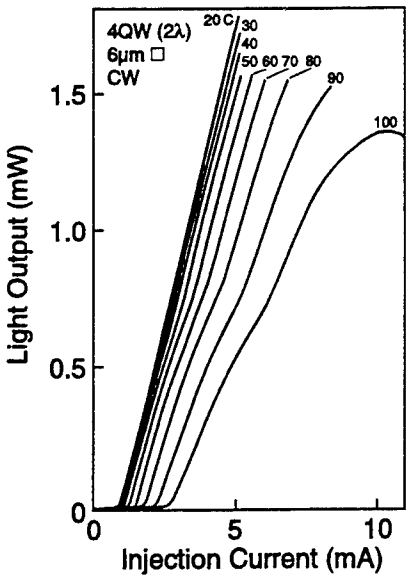


Fig. 3 I-L characteristics of the VCSEL with temperature as a parameter.

set at 960, 960, 940, and 920 nm from the p-side, sequentially. This arrangement of the active layers was optimized from a simulation [11]. The cavity peak was set at 960 nm. In addition, a 5/4-λ-thick GaAs layer is inserted in the bottom of the p-type DBR to reduce the sheet resistance of the contact layer [4]. This improves the current versus voltage (I-V) characteristics and results in both high light output power and high wall-plug efficiency.

Solid lines in Fig. 2 show the current versus light-output (I-L) and current versus voltage (I-V) characteristics at room temperature CW operation. For comparison, those for a conventional VCSEL with a top DBR without the 5/4-l-thick GaAs layer are also shown in Fig.2 (dotted lines). The threshold current for the proposed VCSEL was 1.2 mA and the slope efficiency is 0.5 W/A. The threshold voltage was 2.2 V. Introducing the 5/4-λ contact layer reduced the driving voltage at 1mW light output to 2.8 V from the 3.2 V of a conventional VCSEL structure. Note also that the voltage reduction is greater at higher voltages. Maximum output power was also improved to more than 5mW by introducing the 5/4-λ contact layer. The average wall-plug efficiency was 11±0.4% in an 8×8 array, and all elements showed the high efficiency over 10% with the exception of one VCSEL. Such high efficiency is due to both the reduction in the driving voltage and the high slope

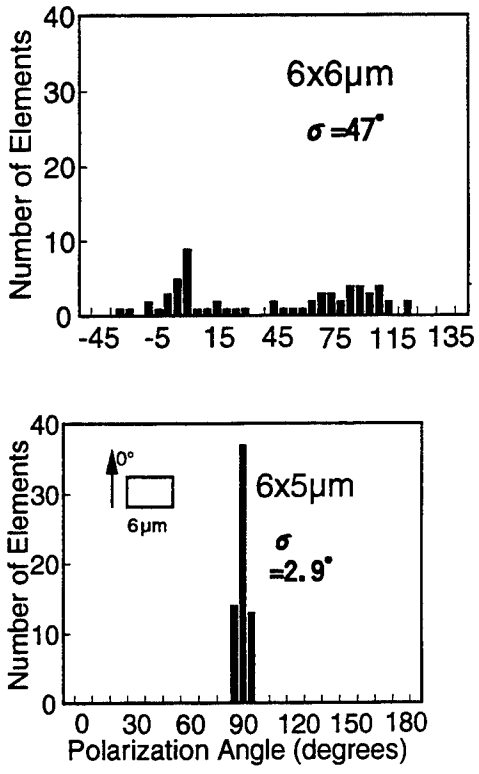


Fig. 4 Polarization angle of the 6×6 μm size polarization uncontrolled array and the 6×5 μm polarization controlled array. The deviation angle is only 2.9° for the 6×5 μm array

efficiency of about 0.5W/A.

Figure 3 shows the temperature characteristic of the VCSEL [7]. The temperature dependence of VCSELs is due to shifts in the DBR mirror resonance and the gain bandwidth to longer wavelengths at different rates as temperature increases. Active layer with broad band gain width improve the temperature characteristics, and light output power of more than 1 mW was obtained even at 100 °C (Fig. 3).

Polarization control is also important for noise reduction and polarization sensitive applications. To align polarization to one direction, the top mesas of some devices were made rectangular, which causes a difference in the gain for two orthogonal directions. When the top mesa size is made small and approaches the single lateral mode region, the dependence of modal gain on the top mesa size becomes larger, which allows a large difference in the modal gain for two orthogonal directions. Figure 4 shows the distribution of polarization angles for a 6×6-μm polarization uncontrolled VCSEL array and a 6×5-μm polarization controlled array [8]. The polarization angle distribution clearly decreases for the 6×5-μm array. Furthermore, the polarization angle distribution of all the 6×5-μm VCSELs is suppressed within only 12° with a deviation of 2.9°, which is comparable to the measurement error. This method of using slightly rectangular shape to control polarization direction is simple and needs not extra costs.

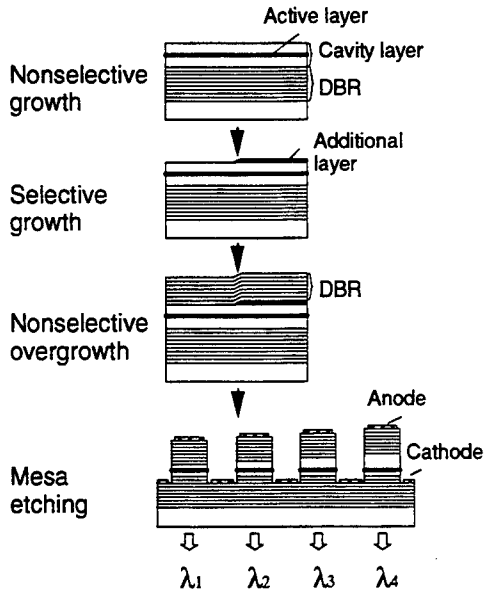


Fig. 5 Integration process for four-wavelength VCSELs by using mask MBE.

III. Monolithic integration of multiple wavelength VCSEL by mask MBE

We fabricated a monolithically integrated four-wavelength VCSEL array with a 2-nm wavelength separation. The integration process [5] for four wavelength is shown in Fig. 5. The bottom DBR layer and the cavity layer including InGaAs QW active layers were first grown on the substrate. Then the mask was placed on the substrate. An additional layer was grown only on selected areas to supplement the cavity layer thickness. After the first additional layer for the cavity was grown on stripe areas, the mask was rotated 90° and a second additional layer was grown perpendicular to the first layer. Finally, the mask was moved away from the substrate and the top DBR layer was overgrown on the whole area. Because the mask had 500-μm striped windows with 500-μm spaces, four lasers with different wavelength were displaced from each other laterally by 500-μm.

Figure 6 shows the lasing spectra of 6 mA CW operation. The lasing wavelengths were 962.4, 964.3, 966.4, and 968.4 nm. The lasers have threshold current densities of 800 A/cm^2, a range comparable to that of a VCSEL with the same structure grown by conventional MBE. This indicates the good quality of the device grown by mask MBE.

IV. Optical Cross Connectors for Distributed Fiber Switches

VCSELs are promising for achieving low-cost optical interconnections. To realize them, alignment-tolerant and low-cost optical assembling techniques become important in addition to performance improvements in VCSELs. To reduce the alignment difficulties during fiber assembly, we are attempting to

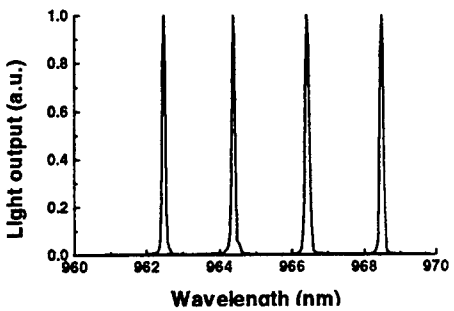


Fig. 6 Lasing spectra of the four-wavelength VCSELs during 6mA CW operation. The lasing wavelengths were 962.4, 964.3, 966.4, and 968.4 nm.

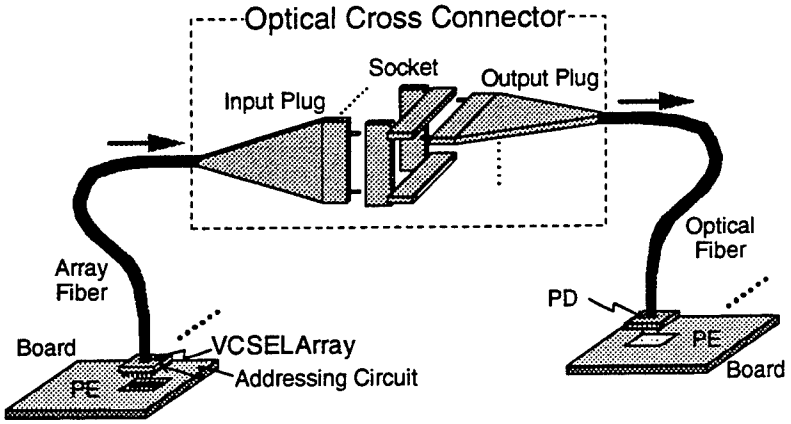


Fig. 7 Distribution fiber switch consists of VCSELs with an addressing circuit and an optical cross connector using PCFs

use large-core plastic cladding fibers (PCFs) [9] with VCSELs. We propose and fabricate a distributed fiber switch (DFS) that consists of VCSELs with an addressing circuit and an optical cross connector (OCC) using PCFs as shown in Fig. 7.

In the DFS system, each VCSEL in an array corresponding to the desired destination, is selectively switched on by the addressing circuit. The light from the VCSEL is transmitted through one of the array fibers which is two-dimensionally aligned at the VCSEL side. These fibers are one-dimensionally rearranged at the input plug. The input plugs are perpendicularly connected to the output plugs. The lights coming into the same output plug are combined into an optical fiber which reaches the photodetector. The advantages of DFS when compared with concentrated switches are high band width, low latency and contention-free connection.

V. Conclusion

We have developed VCSELs which provide high wall-plug efficiency, good temperature characteristics, high uniformity, and controlled polarization directions. The wavelength of these VCSELs were changed over a substrate using mask MBE. This technique can produce arrays that have the desired wavelength separation and that are useful in WDM applications. These VCSELs, in combination with large-core fibers such as PCF, are suitable for achieving low cost optical interconnection systems. We have also developed optical cross connectors for distributed fiber switches which should become key components for parallel processing and network computing.

REFERENCES

[1] Y. H. Lee, J. L. Jewell, A. Scherer, S. L. McCall, J. P. Harbison, and L. T. Florez, Electron. Lett. vol. 25, pp. 1377-1378, 1989.

[2] R. S. Geels, S. W. Corzine, and L. A. Coldren, IEEE J. Quantum Electron. vol. 27, pp. 1359, 1991.

[3] T. Numai, K. Kurihara, I. Ogura, H. Kosaka, M. Sugimoto, and K. Kasahara, IEEE Photon. Tech. Lett., vol. 5, pp. 136-138, 1993.

[4] K. Kurihara, T. Kawakami, H. Kosaka, T. Yoshikawa, H. Saitoh, M. Kajita, A. K. Dutta, I. Ogura, Y. Sugimoto, and K. Kasahara, Proc. 10th IOOC, Hong Kong,vol.1 pp. 28-29 1995

[5]H. Saito, I. Ogura, Y. Sugimoto, and K. Kasahara, Appl. Phys. Lett. vol. 66, pp. 2466-2468, 1995.

[6] W. T. Tsang and M. Ilegems, Appl. Phys. Lett. vol. 35, pp. 792-794, 1979.

[7] M. Kajita, T. Kawakami, M. Nido, A. Kimura, T. Yoshikawa, K. Kurihara, Y. Sugimoto, and K. Kasahara, IEEE Journal of Selected Topics in Quantum Electronics, vol. 1, pp. 654-660, 1995

[8] T. Yoshikawa, H. Kosaka, K. Kurihara, M. Kajita, Y. Sugimoto, and K. Kasahara, Appl. Phys. Lett., vol. 66, pp. 908-910, 1995.

[9] H. Kosaka, A. K. Dutta, K. Kurihara, Y. Sugimoto, and K. Kasahara, IEEE Photon. Technol. Lett., vol.7, pp. 926-928, 1995.

Intersubband Absorption in OMVPE Grown Delta-Doped GaAs/AlGAs Quantum Wells

Charles R. Lutz, Jason Kanaley, and Kei May Lau,
Department of Electrical and Computer Engineering
University of Massachusetts, Amherst, MA 01003

1.0 Introduction

High performance GaAs/AlGaAs quantum well infrared photodetectors (QWIPs) have been previously demonstrated [1]. Most of these have been grown by molecular beam epitaxy (MBE) with only a few studies involving devices grown by organometallic vapor phase epitaxy (OMVPE) [2,3]. Of these, all the structures investigated utilized uniformly doped wells. In this paper the dependence of the intersubband absorption characteristics of δ-doped GaAs/AlGaAs multiquantum well structures grown by OMVPE is investigated. Several samples with different doping levels and periods were grown over a period of several months. In addition an identical structure in which the wells were uniformly doped to 10^{18} cm^{-3} was grown and its absorption characteristics measured in order to assess the effects of varying the δ-doping parameters.

2.0 Experimental

All the samples used in this study were grown by atmospheric pressure OMVPE at 700° C on (100) semi-insulating GaAs substrates oriented 2° off toward (110). The epitaxial structure, shown schematically in Figure 1, consisted of a 0.3 μm GaAs buffer layer followed by a 1 μm n^+ ohmic contact layer. Next, a series of identical 60 Å wide multiple GaAs quantum wells separated by 200 Å $Al_{0.38}Ga_{0.62}As$ barriers were grown, forming the active IR absorption section of the devices. A planar doping layer was incorporated at the center of each well in order to populate the ground state. Finally, a second 0.5 μm n^+ GaAs cap layer formed the top ohmic contact of the structure. The reactant sources used were trimethylgallium (TMG), trimethylaluminum (TMA), 100% arsine, and H_2 diluted silane (SiH_4) for the n-type doping. Growth interruptions of ten second duration were employed between consecutive layers within the active region. The total number of periods in the stack ranges from two to twenty-four. For all the samples, the SiH_4/III ratio was maintained constant and the effective carrier density in the QW was controlled by

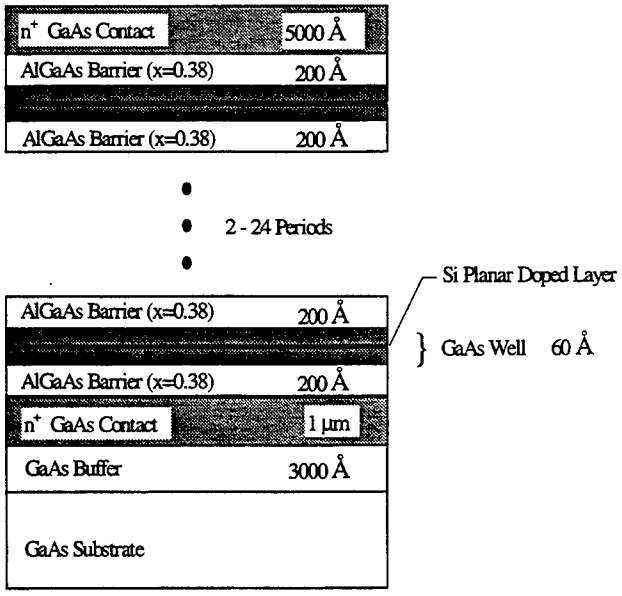


Figure 1. Schematic of the device layer sequence.

interrupting the well growth and injecting SiH_4 for a duration of between five to twenty-five

seconds. With this technique it was possible to obtain a delta-doping profile in the GaAs well in spite of the high growth temperatures (as compared to those typically used for MBE growth). Clearly the possibility of impurity diffusion cannot be ignored. Capacitance-Voltage profiling of a separate single-well calibration sample was performed. To within the limits of the measurement apparatus, the impurity profile exhibited a delta-like distribution. Using the nominal growth parameters, calculations show the well to contain two bound states with confinement energies of 63 meV and 237 meV.

The room temperature intersubband absorption characteristics of the structures were measured using a Bruker IFS 66V Fourier transform spectrometer (FTS). Multi-pass waveguide samples were prepared by cleaving the as-grown wafer into rectangular sections of approximately 14 mm x 4 mm and polishing 45° facets on opposing edges [1]. IR light from a globar was coupled to the sample and the transmitted energy detected by a cooled MCT detector after passing through a polarizer. The absorption spectra were measured by collecting two successive scans; one in which the polarizer was oriented so that the electric field vector was in the plane of the wells (s-pol) and a second for which it was perpendicular (p-pol) to the wells. The reference signal was obtained by using the s-pol measurement from the sample. This resulted in minimal error in the measurements which would have otherwise been encountered in using a separated reference crystal (e.g. SI-GaAs).

3.0 Results and Discussion

Typical room temperature absorbance spectra measured with a sixteen-pass waveguide sample are plotted in Figure 2. The light-colored curve was obtained by measuring the uniformly doped sample while the solid curve is from one of the planar doped structures. This particular device consisted of a five period MQW stack in which the SiH_4 injection time was fifteen seconds.

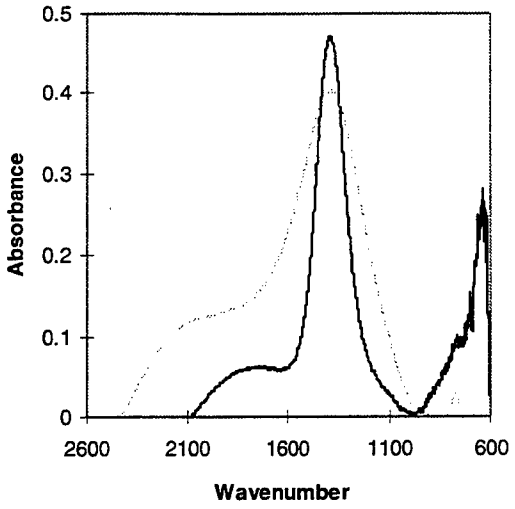


Figure 2. Room temperature FTS absorbance spectra. The solid curve is from a δ-doped sample while the light colored plot is the characteristic measured for a uniformly doped well.

The peak absorbance (arbitrary units) of the δ-doped sample is 0.45 and occurs at 1383 cm^{-1} (172 meV). This value agrees well with the expected transition energy of 174 meV. The linewidth of the resonance is approximately 165 cm^{-1} (20 meV) and corresponds to a fractional spectral bandwidth, $\Delta\nu/\nu$, of around 12 %. This result compares favorably with MBE grown bound-to-bound QWIP structures previously reported [1]. An additional small peak appears at ~ 1800 cm^{-1} in the δ-doped sample and may possibly correspond to a transition involving a continuum state near the top of the barrier. This feature is only present in a small fraction of the samples and predominately in the most recent growth runs. This could be indicative of a slight baseline shift in the OMVPE growth parameters. It has been observed that small changes in either the well or barrier parameters can significantly

alter the absorption characteristics of bound to continuum transitions [4]. The absorption peaks for the remaining samples were in the range of 1400 cm^{-1} to 1580 cm^{-1}. Growth runs which were performed on the same day tended to be more consistent, typically within 25 cm^{-1}. For comparison, the peak absorbance of the uniformly doped well was slightly smaller, around 0.4. In addition, the linewidth has broadened considerably to 324 cm^{-1} (40 meV) resulting in a fractional bandwidth for the transition in excess of 22%. The intersubband absorption characteristics and its dependencies on the incorporated sheet charge in the well as well as the total number of periods within the active MQW stack are summarized for several samples in Figures 3 and 4.

Figure 3a shows the dependence of the absorption strength and the linewidth, $\Delta\nu$, of the transition as the SiH_4 injection (exposure) time is varied. In order to draw a valid comparison all the points plotted in this graph are for samples which contain the same number of periods (in this case five) of the MQW structure. As this plot indicates the peak absorbance initially increases in a linear fashion for short injection times. Eventually a point is reached at which the absorbance "clamps" and a further increase in dopant injection has no effect. The transition linewidth also exhibits a general linear dependence over most of the range of injection times investigated. The linewidth for the twenty-five second sample however, appears to be an exception for reasons which are not presently clear. The fractional spectral bandwidths, $\Delta\nu/\nu$, and the integrated absorption fractions (i.e. absorption integrated over photon energy), IAF, for the same samples are plotted in figure 3b. The IAF has, in this case, been approximated by multiplying the peak absorbance by the transition linewidth. This value slightly underestimates the true IAF due to the contribution of the wings on the lineshape. The trends exhibited in this data show a pronounced linear behavior. As has been previously reported, the IAF is expected to be proportional to the doping density [5]. For

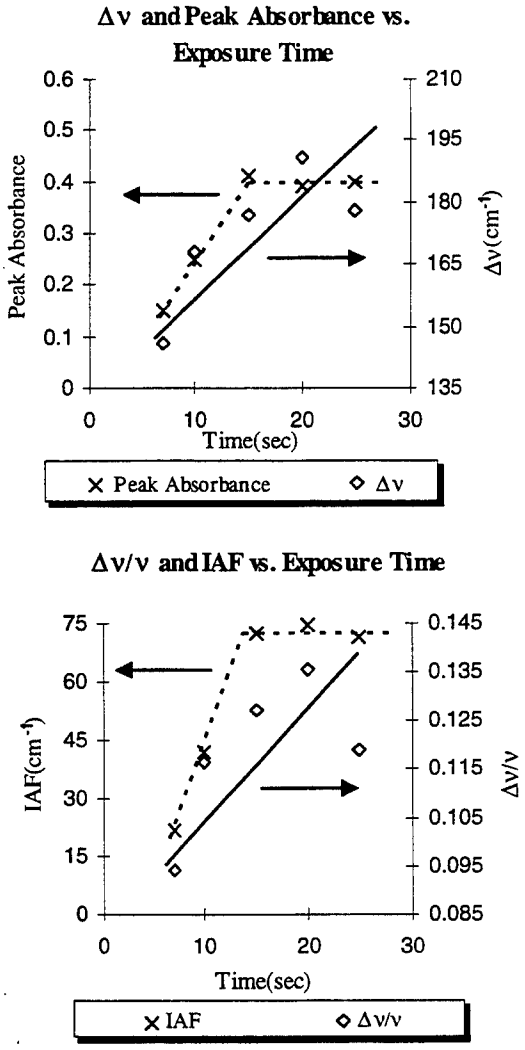
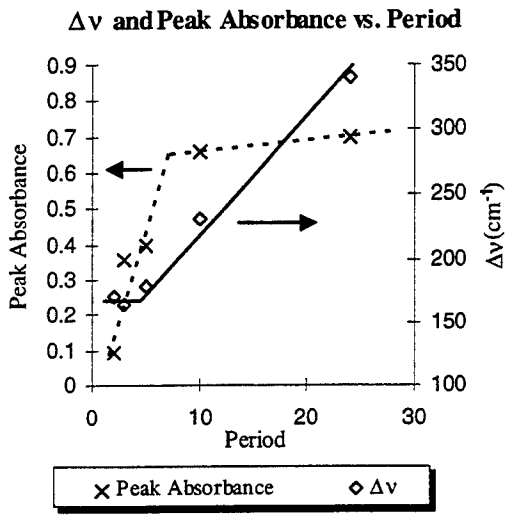


Figure 3. (a) Resonance linewidth and peak absorbance plotted as a function of SiH_4 injection time. (b) Plot of fractional spectral bandwidth and integrated absorption fraction. The lines have been added as a guide

short injection times the IAF appears to be proportional to the dopant density incorporated in the well (assuming charge density scales with injection time). The increase in transition bandwidth may be due to

diffusion of the Si dopant atoms in the well, resulting in an impurity distribution which approaches that of the uniformly doped structure.

Figure 4 shows the absorption characteristics for samples in which the number of periods was varied while maintaining a constant SiH_4 injection time (25 seconds). The absorbance intensity demonstrates a distinct nonlinear dependence, increasing abruptly as more periods are added and finally reaching a maximum value beyond which no significant gains are realized. This result is in sharp contrast to a previous study in which the absorption was shown to increase linearly [6]. The transition linewidth, for reasons which are not understood at this time, also shows a strong dependence, increasing markedly when more than five periods are incorporated in the MQW stack.



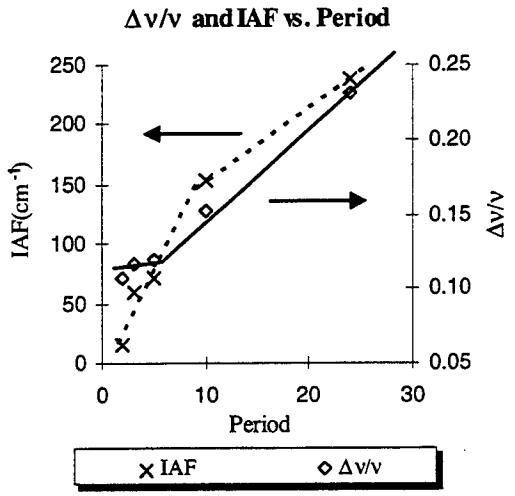


Figure 4. (a) Measured intersubband absorbance linewidth vs the total number of periods in the MQW stack. (b) Plot of fractional spectral bandwidth and integrated absorption fraction. The lines have been added as a guide.

4.0 Summary

We have carried out an investigation of the effect of planar-doping on the intersubband absorption characteristics of GaAs/AlGaAs MQW QWIP structures. All of the δ-doped samples exhibited improved absorption characteristics (i.e. a reduced fractional bandwidth) as compared to an identical structure in which the wells were uniformly doped to 10^{18} cm^{-3}. The absorption strength and transition linewidths exhibit a marked dependence on both the injection times as well as the number of periods in the structure.

5.0 References

[1] B.F. Levine, R. J. Malik, J. Walker, K. K. Choi, C. G. Bethea, D. A. Kleinman, and J.M Vandenberg, Appl. Phys. Lett, 50, 273, (1987)

[2] S. D. Gunapala, B. F. Levine, R. A. Logan, T. Tanbun-Ek, and D.A. Humphrey, Appl. Phys. Lett., 57, 1802, (1990)

[3] A. Zussman, B. F. Levine, and W. S. Hobson, J. Elect. Mat., 21, 799, (1992)

[4] A. Zussman, B. F. Levine, J. M. Kuo, and J. de Jong, J. Appl. Phys., 70, 5101, (1991)

[5] S. D. Gunapala, B. F. Levine, L. Pfeiffer, and K. West, J. Appl. Phys., 69, 6517, (1991)

[6] A. G. Steele, H. C. Liu, M. Buchanan, and Z. R. Wasilewski, J. Appl. Phys., 72, 1062, (1992)

Intentionally Left Blank

Intentionally Left Blank

Ballistic Generatior of Terahertz Oscillations

Z. S. Gribnikov[a,b], A. N. Korshak[a], N. Z. Vagidov[a], and V. Mitin[b]

[a] *Institute of Semiconductor Physics, Pr. Nauki 45, Kiev, 252650, Ukraine*
[b] *Department of Electrical and Computer Engineering*
Wayne State University, Detroit, MI 48202

Abstract

Novel universal mechanism of oscillation generation in terahertz range — oscillations of ballistic plasma of carriers with negative effective masses (NEM) in doped narrow bases of diodes — is investigated. Prerequisites of excitation, physical peculiarities of these oscillations and mechanisms of NEM-plasma formation are considered

1. The subject of interest in this report is a ballistic transport of current carriers (either electrons or holes) with a specific dispersion relation $\varepsilon(k)$ through a narrow doped base of n^+nn^+- or p^+pp^+-diode. The specific feature of the $\varepsilon(k)$ is an existence of a region in the $\vec{k}$-space where the differential effective mass of carriers in the direction of current flow is negative: $(d^2\varepsilon/\hbar^2 dk_x^2)^{-1} < 0$ (see *Fig.*1). We show that single stationary distribution of ballistic carriers in a certain range of voltages U across the diode is characterized by long central quasineutral region where a charge of drifting carriers with negative effective masses (NEM-carriers) compensates a charge of ionized doping impurities completely. That region with NEM-carriers is located between two charged regions (a standard cathode-side region and nonstandard anode-side region [1]). The voltage increase causes an extension of the nonstandard region (*Fig.*2). A current in this range of voltages is saturated (see inset in *Fig.*2). We have obtained that the single stationary state with a given voltage is unstable and can not be realized. Instead there exists a stable nonstationary state with oscillating current and oscillating distributions of carrier concentrations and potential [2].

The domain of existence for this oscillating solution in a (U, l)-plane (l is a length of the base) appears at some critical (minimum) value $l = l_c$ and broadens with increasing $l > l_c$ (*Fig.*3). Not far from the domain edge the current oscillations are always quasilinear and one-harmonic. Both their frequency and their amplitude are determined by inner parameters of the device (i.e. parameters of the dispersion relation, doping, base length, boundary concentrations etc.) and by the only one external parameter: an applied voltage U. The voltage increase and the length of the base decrease cause the growth of the frequency. As a rule an amplitude of current oscillations does not exceed 10% of an average current for the quasilinear regime. For large values of the length l we have obtained a domain of nonlinear oscillations inside of the domain of existence (*Fig.*3). A nonlinear regime appears as a result of a large growth of linear oscillation amplitude (up to $25 - 30\%$ of an average current value; see *Fig.*4); it can show itself as biharmonic oscillations.

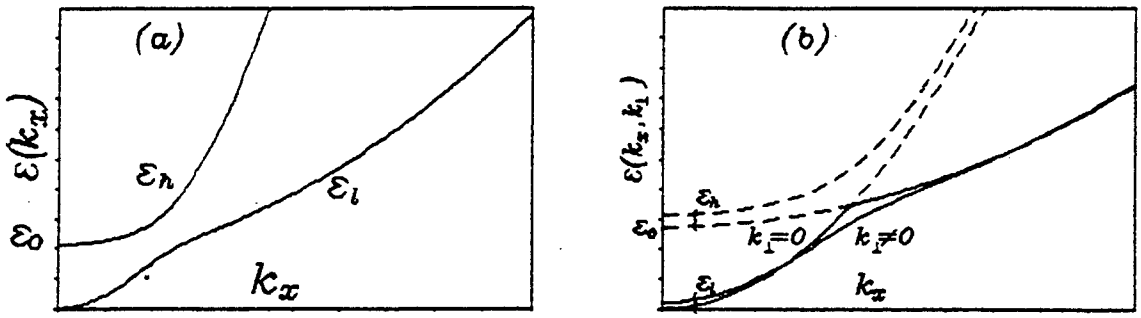


Fig.1. a—Energy spectrum in asymmetric DQW; b—Hole spectrum in uniaxially compressed semiconductor along [100] direction.

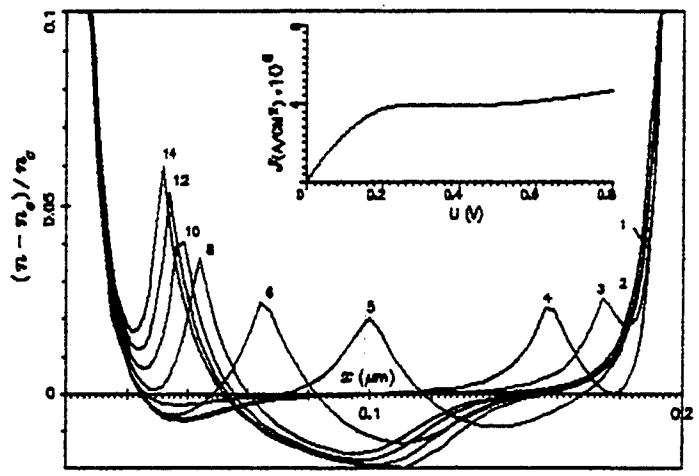


Fig.2. Stationary concentrations of the carriers in the doped bases (n_e is the equilibrium cathode concentration) for a set of voltages (U=0.1· No V, where No is the number at curve). Inset shows the JU—characteristic.

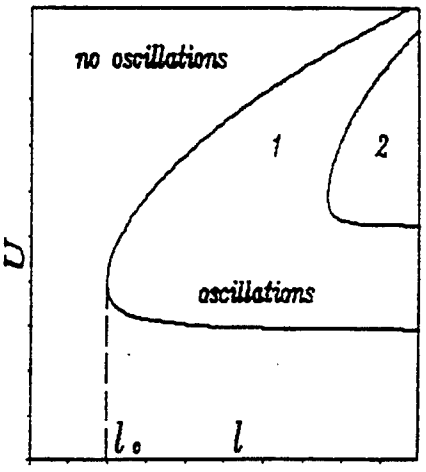


Fig.3. Domains of oscillatory regime existence:1—linear oscillations, 2—nonlinear oscillations.

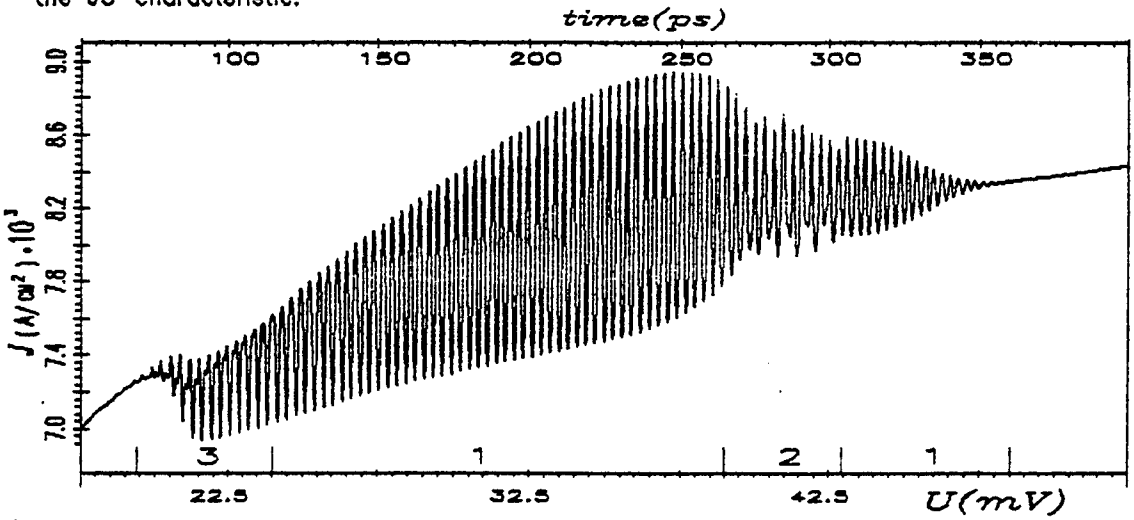


Fig.4. Typical oscillations of ballistic hole current for compressed p—Ge: T=4.2K, l =1 μm, n_o =3·10^{15} cm^{-3}, compression 0.2 %. Ranges of oscillations: 1—quasilinear, 2—regular nonlinear, 3—irregular nonlinear. Oscillations have obtained by numerical method described in detail in [2].

Besides a short-circuit regime with a given voltage U regimes with different active and reactive loads were studied. An active load diminishes an oscillation amplitude and reactive loads can affect a frequency and position of boundaries in the domain of existence. Frequency ranges in our calculations of ballistic current oscillations are from $200GHz$ to $15THz$ (depending on l, U, $\varepsilon(k)$, doping concentrations and mechanisms controlling $\varepsilon(k)$).

All these results are obtained from numerical self-consistent solutions of Poisson equation together with nonstationary kinetic equation for a given $\varepsilon(k)$. Distributions of carriers flying into the base from the cathode and anode are equilibrium with the same given Fermi-energies.

Results of numerical calculations of stationary states are in a good agreement with the preliminary analytical consideration [3,4].

2. Needed dispersion relations $\varepsilon(k)$ with NEM-parts can be implemented with different physical mechanisms. Let us remind some of them.

(i) Asymmetrical double-quantum well (DQW).

$Fig.1a$ shows the electron energy spectrum in DQW formed of two quantum wells with different electron masses m and M. The low branch of this spectrum has a part with the NEM. A simplified expression of it is

$$\varepsilon(k) = 1/2(\varepsilon_1(k) + \varepsilon_2(k) - [(\varepsilon_1(k) - \varepsilon_2(k))^2 + 4\Delta^2]^{1/2}), \qquad (1)$$

where $\varepsilon_1(k) = \hbar^2k^2/2m$, $\varepsilon_2(k) = \varepsilon_o + \hbar^2k^2/2M$, $\Delta < \varepsilon_o(M-m)/(M+m)$, $\varepsilon_o > 0$, $M > 2m$. Most of our simulations are carried out using (1) because of its simplicity. But the condition $M > 2m$ scarcely is satisfied in traditional heterosystems. Therefore more sophisticated methods of realization of the needed $\varepsilon(k)$ are considered as well.

(ii) Holes in uniaxially compressed cubic semiconductors.

Holes in semiconductors with uniaxially-compressed diamond-like or zinc-blende-like crystal lattice have a dispersion relation (in direction of compression), which reminds us the expression (1) and has a NEM-part with negative masses that depends on a transverse wave vector $k_\perp$ ($Fig.1b$). Analogous situation is realized in strained pseudomorphic layers for vertical ballistic hole transport across them. In both cases roles of m and M play light and heavy hole masses, respectively, and ε_o is proportional to deformation. We have performed numerous calculations of ballistic oscillating hole currents in $p-Ge$ and $p-InAs$-bases for two limit cases: a) small compressions, light doping, cryogenic temperatures, long bases ($\geq 1.0\mu m$), subterahertz frequencies; b) strong compressions, heavy doping, room temperatures, very short bases ($\leq 0.1\mu m$), ten-terahertz frequencies.

(iii) ΓX-mixed electrons.

It is known [5,6] that on abrupt (100)-heterojunction surface Γ - electron states can be mixed with states of X_1-valley which is expanded along [100]-axis. The X_1-

states participating in the mixture can be placed both on the same and on the opposite side of the surface (or on each of them). Two other X-valleys (X_2 and X_3) could be eliminated from consideration by suitable deformation or quantization. If mixing Γ-and X_1-states belong to the same semiconductor the needed dispersion relation $\varepsilon(k)$ is obtained in a system of isolated semiconductor layers. (Ballistic transport in similar systems was considered in [7,8]). If mixing Γ-and X-states belong to different materials (for example, to $GaAs$ and $AlAs$, respectively), we need a system of two-layer structures. Mass of Γ-electrons and transverse mass of X-electrons are similar to the masses m and M in the energy relation and ε_o is ΓX_1-splitting (with taking into account possible deformation and quantization effects).

3. In conclusion we indicate some important problems which have to be solved to implement ballistic generators of terahertz oscillations. All above considered effects could be obtained in sufficiently doped bases only. A decrease of l_c and growth of oscillation frequencies can be achieved by an increase of the doping concentration n_0 mainly. But this increase of n_0 shortens a ballistic length. This circumstance is the basic obstacle in order to extend ranges of effective generation. It can be overcome using layered bases with modulation doping. Let us note that most of the considered mechanisms of the $\varepsilon(k)$-formation stipulate an application of layered heterostructures and are in agreement with possible modulation doping.

The second problem of further analysis is our neglect of carrier transfer between low and high branches of the spectrum $\varepsilon(k)$ (see $Fig.1$). To evade these transfers a splitting between these branches has to be large enough. The frequencies of possible quantum interbranch oscillations should be greater than frequencies of quasiclassic oscillations of the ballistic plasma with the NEM-carriers which are considered here. The case of disruption of this condition is of special interest for further searches.

This research was partially supported by the Joint Fund of the Government of Ukraine and International Science Foundation, by the Ukrainian Fund of the Fundamental Researches, and by Wayne State University, College of Engineering.

1. N.Z.Vagidov, Z.S.Gribnikov, A.N.Korshak. Fiz.Tekhn.Poluprov., 29, accepted (1995)
2. N.Z.Vagidov, Z.S.Gribnikov, A.N.Korshak. Pis'ma ZhETF, 61, 38 (1995)
3. Z.S.Gribnikov, A.N.Korshak. Fiz.Tekhn.Poluprov., 28, 1445 (1994)
4. Z.S.Gribnikov, A.N.Korshak. Quantum Confinement. Physics & Applications. Electrochem. Soc., Inc. p.34 – 45 (1994)
5. T.Ando, H.Akera, Phys.Rev., B40, 11619 (1989)
6. Y.Fu, M.Willander, E.L.Ivchenko, A.A.Kiselev, Phys.Rev., B47, 13498 (1993)
7. N.Z.Vagidov, Z.S.Gribnikov, A.N.Korshak. Fiz.Tekhn.Poluprov., 28, 1873 (1994)
8. N.Z.Vagidov, Z.S.Gribnikov, A.N.Korshak. Fiz.Tekhn.Poluprov., 29, 553 (1995)

Terahertz Devices using Two Dimensional Electron Fluid: Sources, Detectors, Multipliers, and Mixers.

M. I. Dyakonov and M. S. Shur*

A. F. Ioffe Physico-Technical Institute, St. Petersburg, 194021, Russia
*Department of Electrical Engineering, University of Virginia,
Charlottesville, VA 22903-2442, USA, shur@virginia.edu
http://www.ee.virginia.edu/faculty.txt/shur.html

Abstract. We discuss how the propagation of plasma waves in a High Electron Mobility Transistor (HEMT) can be used to implement a new generation of terahertz devices, including sources, resonant detectors, broad band detectors, and frequency multipliers. Our estimates show that these devices should outperform conventional terahertz devices, which use deep submicron Schottky diodes.

Introduction.

Plasma waves with a linear dispersion law, $\omega = sk$, may propagate in a Field Effect Transistor channel. [1-3] Here ω is frequency, $s = (eU/m)^{1/2}$ is the wave velocity, e is the electronic charge, m is the electron effective mass, U is the gate-to channel voltage swing, and k is the wave vector. Allen et al. observed infrared absorption [4] and Tsui et al. observed weak infrared emission [5] related to such waves in silicon inversion layers.

The velocity of the plasma waves, s, is typically on the order of 10^8 cm/s, which is much larger than the drift velocity of the two-dimensional electrons in the FET channel. Therefore, the propagation of the plasma waves can be used for new regimes of FET operation, with a much higher frequency than for conventional, transit-time limited regimes of operation. Under certain conditions, plasma oscillations can be excited in a FET by dc current. Nonlinear properties of the plasma waves can be utilized for terahertz detectors, broad band detectors, mixers, and frequency multipliers, operating in the terahertz range.

The plasma oscillations can be coupled to electromagnetic radiation. However, since the plasma wave velocity is much smaller than the light velocity and the device dimensions are much smaller than the light wave length corresponding to the plasma frequency, standard antenna structures are needed for such a coupling.

The electron system in the FET channel is usually referred to as a 2D electron gas. In fact, as we have shown [6], for this system, the mean free path for interelectronic collisions may be often smaller than both the sample length and the mean free path for collisions with impurities and/or phonons. For example, this is the case for an AlGaAs/GaAs HEMT at 77 K for the surface electron concentration $n_s \approx 10^{12}$ cm^{-2}. In this situation, the two dimensional electrons behave as a fluid and they are described by hydrodynamic equations. The equation of motion for the 2D electron fluid (the Euler equation) is given by

$$\frac{\partial v}{\partial t} + v\frac{\partial v}{\partial x} + \frac{e}{m}\frac{\partial U}{\partial x} + \frac{v}{\tau} = 0 \qquad (1)$$

where $\partial U/\partial x$ is the longitudinal electric field in the channel, $v(x, t)$ is the local electron velocity, and τ is the momentum relaxation time. Eq. (1) has to be solved together with the usual continuity equation which (using the gradual channel approximation, $n_s = CU/e$, where C is the gate-to-channel capacitance per unit area) can be written as :

$$\frac{\partial U}{\partial t}+\frac{\partial (U\mathrm{v})}{\partial x}=0 \qquad (2)$$

These equations coincide with the hydrodynamic equations for shallow water, and the plasma waves are similar to the shallow water waves with the gate-to-channel voltage swing, U, being similar to the water level and the e/m ratio being similar to the of free-fall acceleration.

A FET serves as a resonator for the plasma waves with the fundamental frequency determined by the ratio s/L and with a quality factor on the order of $s\tau/L$, where L is the channel length.

Nonlinear eqs. (1) and (2), with appropriate boundary conditions, describe the FET physics, including the physics of the new devices, which we describe below.

Resonant detectors and mixers of terahertz radiation.

In our proposed detector [7], the incoming electromagnetic radiation induces an ac voltage at the source side of the channel. The drain side of the channel is an open circuit. This can be easily achieved using an appropriate antenna structure. This ac voltage excites the plasma waves. As mentioned above, the velocity, s, of these waves is determined by the dc gate-to-source voltage. Because of the nonlinear properties of the electron fluid and the asymmetry in the boundary conditions, a FET biased only by the gate-to-source voltage and subjected to an electromagnetic radiation develops a constant drain-to-source voltage, which has a resonant dependence on the radiation frequency with maxima at the plasma oscillation frequency $\omega_o=\frac{\pi s}{2L}$ and its odd harmonics. For the frequencies, such that $|\omega - n\omega_o| \ll \omega_o$, where n = 1, 3, 5, 7..., we found

$$\frac{\Delta U}{U_o}=\left(\frac{U_a}{U_o}\right)^2\left(\frac{s\tau}{L}\right)^2\frac{1}{4(\omega-n\omega_o)^2\tau^2+1} \qquad (3)$$

where ΔU is the dc voltage difference between the drain and source potentials, U_o is the gate-to-source gate voltage swing, and U_a is the amplitude of the ac source-to-gate voltage induced by the incoming radiation. The half width of the resonance curve is determined by the damping of the plasma oscillations caused by the electron momentum relaxation and/or the electron fluid viscosity. Thus, the FET acts as a resonance quadratic detector of electromagnetic radiation (see Fig. 1). As can be seen from the figure, this responsivity can exceed typical responsivities of standard Schottky barrier detectors (which are on the order of 1000 V/W) by many orders of magnitude.

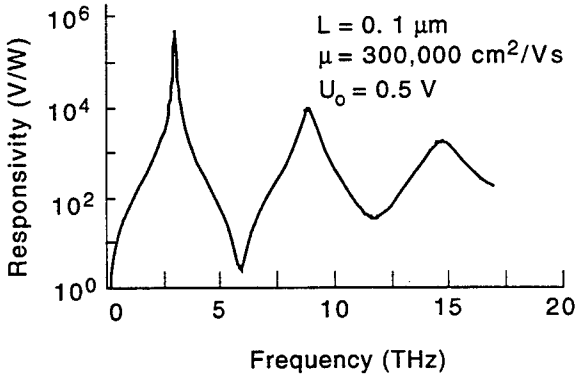


Fig. 1. Responsivity of a HEMT detector versus radiation frequency. (The viscosity of the electronic fluid is accounted for. Without viscosity, all resonance peaks would have equal magnitudes, approximately 10^7 V/W.)

In practical systems, mixing of weak incoming signal, $U_s\cos\omega_s t$ with a strong local oscillator signal, $U_{loc}\cos\omega_{loc}t$, is often more desirable because of a much higher sensitivity. For $|\omega_s - n\omega_{loc}|\tau << 1$, the equation describing the electron fluid mixer response coincides with eq. (3), where U_a^2 should be replaced with $U_s U_{loc}$.

Broad band detector.

Let us now consider an HFET detector with a longer channel, such that $s\tau/L << 1$. In this case, the plasma waves are excited by the incoming radiation near the source, provided that $\omega\tau >> 1$ but they decay before ever reaching the drain side of the channel. The analysis of this case, based on the solution of eqs. (1) and (2), shows that the dc voltage will be still developed between the drain and source, and the detector will operate as a broad band detector of the electromagnetic radiation with the responsivity

$$R=\frac{\pi}{2\varepsilon_o G c U_o}\left(\frac{1}{4}+\frac{\omega\tau}{2\sqrt{1+\omega^2\tau^2}}\right) \qquad (4)$$

where ε_o is the dielectric permittivity of vacuum, c is the speed of light, and $G \approx 1.5$ is the antenna gain factor. R is approximately 600 V/W for $\omega\tau >> 1$ and $U_o = 0.5$ V. This equation is also valid even for $\omega\tau << 1$ (when the plasma oscillations are overdamped) if a stronger inequality, $s\tau/L << (\omega\tau)^{1/2}$, is fulfilled. As can be seen from eq. (4), a long HFET should act as a broad band detector of the electromagnetic radiation. The highest frequency of detection is on the order of s/d where d is the gate-to-source spacing, since the gradual channel approximation is not valid for the plasma wavelengths shorter than d. For $s \approx 10^8$ cm/s and $d \approx 100$ Å, this corresponds to 100 THz.

Terahertz HFET multiplier.

Nonlinear properties of the 2D electronic fluid lead not only to the rectification of the incoming electromagnetic radiation but also to the appearance of the signal at the second and higher harmonics of the incoming radiation with the resonance response at the fundamental plasma frequency. [8] As expected, the second harmonic has a larger magnitude than higher harmonics. For the second harmonic, the voltage has a maximum approximately in the middle of the device channel. The amplitude of the second harmonic is roughly of the same order as the dc voltage developed in the resonance detector.

Shallow Water Wave Instability. HFET as a Terahertz Oscillator.

In a FET with a dc current flowing in the channel, the plasma waves are carried along by the electron flow. As a consequence, the plasma wave velocity in the direction from the source to the drain is s+v whereas the velocity of the plasma wave propagation from the drain to the source is s–v. As was shown in [6], this velocity difference and the asymmetry in the source and drain boundary conditions lead to the instability of the steady electron flow with respect to plasma wave generation. At small drift velocities, the increment of the instability is on the order of v/L. The decrement is caused by the electron momentum relaxation and by the viscosity of the electronic fluid. Hence, the instability occurs when v_0 (and hence, the current) exceeds a certain threshold value, which we estimated to be on the order of 2×10^6 cm/s. The plasma oscillations result in a periodic variation of the channel charge and the mirror image charge in the gate contact, i. e. to the periodic variation of the dipole moment. This variation should lead to electromagnetic radiation. The device length is much smaller than the wavelength of the electromagnetic radiation, λ, at the plasma wave frequency. (The transverse dimension, W, may be made comparable to λ.) Hence, the Ballistic FET operates

as a point or linear source of electromagnetic radiation. Many such devices can be placed into a quasi-optical array for power combining. The maximum modulation frequency is still limited by the transit time.

Electronic flute.

Plasma waves are similar to shallow water waves or to sound waves, since they have a linear dispersion law. In turn, shallow water behavior is similar to the dynamics of a gas with pressure proportional to the square of the density. Thus, the nonlinear hydrodynamic equations for the 2D electron fluid are similar to (but not identical with) the equations for a real gas, such as air. However, the linearized equations describing small-amplitude plasma waves in a FET and sound waves in a gas are identical. Since the linearized equations determine the instability threshold for a steady flow (i. e. the wave generation threshold), the instability conditions for a real gas and for a 2D electron fluid should be similar provided that the Reynolds numbers, Re, and quality factors, Q, of resonance cavities are the same. As we showed in [9], these dimensionless parameters for a HEMT structure may be of the same order of magnitude as for a conventional wind musical instrument ($Re \sim 50$ and $Q \approx 1$ - 100).

Thus, a complete similarity between the plasma waves in a FET and sound waves led us to believe in the possibility of realizing an electronic flute based on the excitation of plasma waves by a direct current in gated modulation doped structures. This electronic flute should operate in the terahertz range of frequencies and emit far infrared radiation.

Acknowledgment.

The authors are grateful to Professor Robert Weikle for useful discussions and comments. The work at the Ioffe Institute has been partially supported by the US Army through its European Research Office. The work at the University of Virginia has been partially supported by the US Army Research Office (Project Monitor Dr. John Zavada) and by the Office of the Naval Research (Project Monitor Dr. Yoon Soo Park).

References

1. A. V. Chaplik, Sov. Phys. JETP, 35, 395, (1972))

2. M. Nakayama, J. Phys. Soc. Japan, 36, 393 (1974)

3. A. Eduiluz, T. K. Lee, J. J. Quinn, and K. W. Chiu, Phys. Rev., **B11**, 4989 (1975)

4. S. J. Allen, Jr., D. C. Tsui, and R. A. Logan, Phys. Rev. Lett., **38**, 980 (1977)

5. D. C. Tsui, E. Gornik, and R. A. Logan, Solid State Comm., **35**, 875 (1980)

6. M. Dyakonov and M. S. Shur, Phys. Rev. Lett., **71**, 2465 (1993)

7. M. I. Dyakonov and M. S. Shur Detection and Mixing of Terahertz Radiation by Two Dimensional Electronic Fluid, *in the Proceedings of 22d International Symposium on GaAs and Related Compounds*, Cheju, Korea, Aug. 28- Sep. 2, 1995, to be published

8. M. I. Dyakonov and M. S. Shur, Up-Conversion, Detection, and Mixing of Terahertz Radiation by Two dimensional Electron Fluid, IEEE Transactions, Microwave Theory and Technique, submitted for publication

9. M. I. Dyakonov and M. S. Shur, Appl. Phys. Lett., **67**, 1137 (1995)

Room-temperature operating hot-electron multiquantum well microwave detector

Fabio Beltram[1,2], Stefano Barbieri[1,2], Marco Lazzarino[2], and Lucia Sorba[2]

1. Scuola Normale Superiore, Piazza dei Cavalieri, 7, I-56126 Pisa, Italy
2. Laboratorio TASC-INFM, Padriciano, 99, I-34012 Trieste, Italy

(Invited talk)

Operation and noise performance of a new hot-electron multiquantum well (MQW) microwave detector are reported [1]. The device shows responsivity and noise equivalent power analogous to commercial devices in the X and K bands. Its different principle of operation, however, yields the possibility to extend operation up to the millimeter and submillimeter bands making it an attractive alternative to available low-temperature detectors.

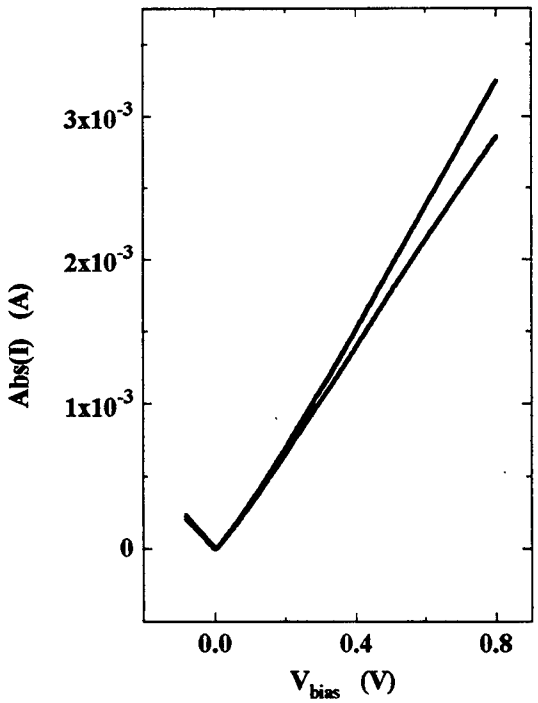


Fig. 1 Current-voltage characteristics at room temperature with and without microwave irradiation (incident power $P_i = 4 \times 10^{-5}$ W, $\theta = 0°$).

The structure was grown by molecular beam epitaxy (MBE) on an undoped GaAs substrate and consists of 20 periods of 4.5-nm thick GaAs QWs (doped n = 10^{17} cm^{-3}) and 30 nm undoped $Al_{0.3}Ga_{0.7}As$ barriers. The MQW is sandwiched between two n = 10^{18} cm^{-3} GaAs layers to which contacts were provided. Devices were fabricated by standard photolitographic techniques into circular 120-μm-diameter mesas. The structure nominal parameters were verified by direct measurement of the conduction band discontinuity via current-voltage (I-V) characterization. Samples were mounted on quartz plates and inserted through a circular hole into a waveguide. By rotating the sample this set-up allowed us to change the angle of incidence of the propagating TE_{10} mode. Microwaves of frequency ν = 10 GHz were generated by a Varian VA-58 Klystron Reflex. With the insertion of a calibrated attenuator, incident radiation intensity could be tuned from 0 to 350 mW/cm^2. I-V characteristics of the sample were recorded with a HP4142B parameter analyzer.

Calculations give in the QWs a single

confined subband whose bottom is located at $\approx$ 86 meV above the classical bottom of the QW. An Arrhenius plot of the experimental dark current divided by the temperature- and voltage-dependent factor *vs* $1/k_BT$, showed that electrons are confined by a potential barrier $\approx$ 180 $\pm$ 20 meV, in agreement with the nominal value.

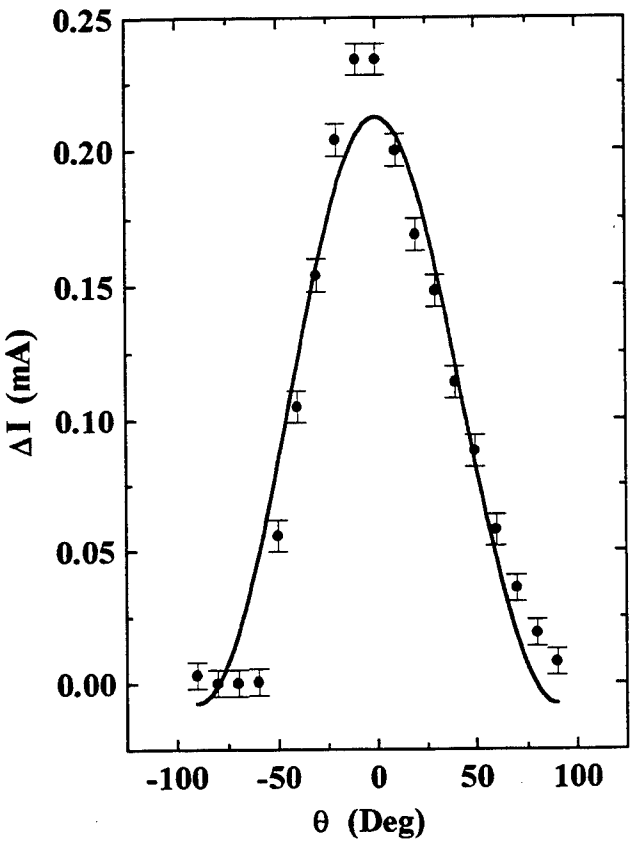


Fig. 2. Angular dependence of the photocurrent with V_{bias}=0.3 V and $P_i = 4 \times 10^{-5}$ W. θ is the angle between the electric field and the layer planes. The data were fitted with the curve $A+B\cos^2(\theta)$.

Figure 1 shows the current as a function of the applied static bias in the dark and in the presence of microwave radiation (ν = 10 GHz, incident power $P_i = 4 \times 10^{-5}$ W) at room-temperature, for the case of in-plane microwave electric field (θ = 0°). In the bias range displayed, up to 10% current increase with microwave irradiation can be observed. Competing effects such as rectification of the microwave field and spurious lattice heating will be shown not to influence the measured I-V. The incident angle dependence of the photocurrent (ΔI) will also be discussed (see Fig. 2).

At V_{bias} = 0.8 V by considering ΔI and the device differential resistance ($\approx$ 300 Ω) the value of the responsivity (R_V) of the detector was determined. We obtained $R_V \approx 2.5 \times 10^3$ V/W, a value comparable to that of conventional detectors in this frequency range.

The measured current variation will be used to estimate the electron temperature (T_e) variation yielding $\Delta T_e \approx 4$ K. The experimental value will be shown not to be accurately accounted for by a standard energy-balance-equation calculation. The discrepancy will be linked to high-field effects (in the range of interest ~ 10 kV/cm). These produce carrier impact ionization off the QWs leading to a positive feedback on the photocurrent as shown in [2].

Device operation will be reported also in the K band. Additionally it will be shown that device operation is limited by momentum relaxation rates. The detector is therefore expected to extend its operation up to ~10 THz. Particularly in the THz range this makes the present detector an attractive alternative to liquid-helium operated InSb detectors [3].

Another important parameter characterizing the operation of the detector will be presented. Noise equivalent power will be measured in the 10 Hz - 30 kHz range at room temperature (see Fig 3). The value measured is comparable to that of commercially available Schottky barrier devices. Owing to the different temperature of operation it is larger than that of liquid-helium operated InSb detectors.

For what concerns the speed of the device, as discussed in the context of MQW far-infrared detectors by Bethea [4], electron transport across the MQW produces a delay of several tens of ps indicating an interesting potential for the speed performance of the present device.

The overall performance of the new detector as compared to available devices will be discussed.

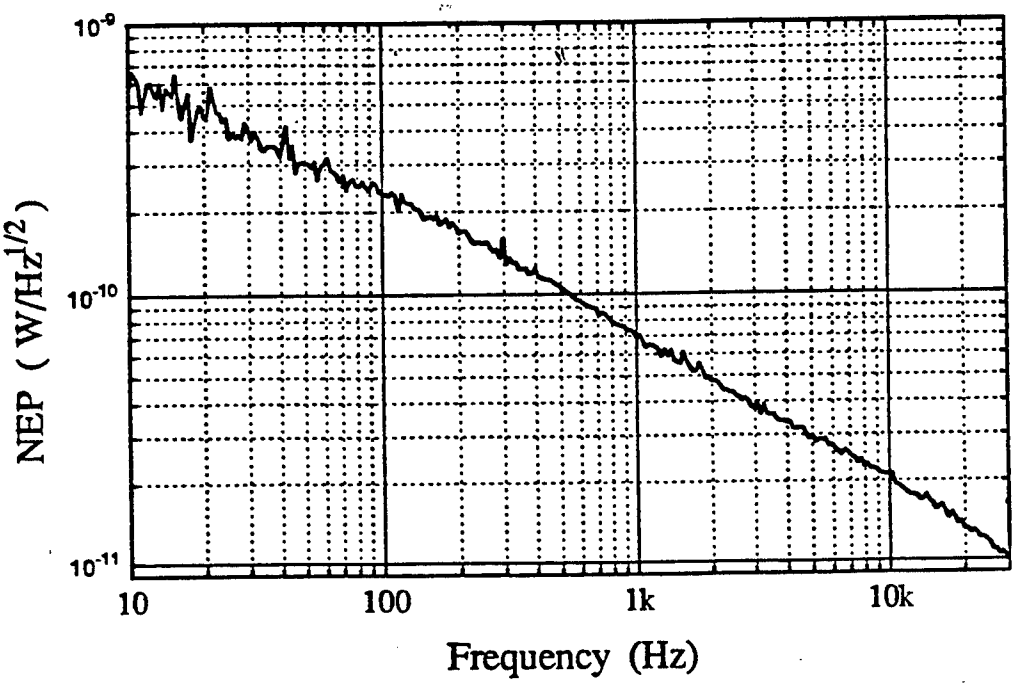


Fig. 3. Noise equivalent power for ν = 10 GHz microwave radiation (R_V = 2.5 × 10^3 V/W) and modulation frequencies in the range 10 Hz - 30 kHz.

REFERENCES:

1. S. Barbieri, F. Mango, F. Beltram, M. Lazzarino, L. Sorba, Appl.Phys. Lett. **67**, 250 (1995).

2. F. Capasso, J. Allam, A.Y. Cho, K. Mohammed, R. J. Malik, A.L. Hutchinson, and D. L. Sivco, Appl. Phys. Lett. **48**, 1294 (1986).

3. A. N. Vystavkin, V. N. Gubankov, and V. N. Listvin, FTT **8**, 443 (1966) [Sov. Phys. Solid State **8**, 350 (1966)]; A . N. Vystavkin, V. N. Gubankov, V. N. Listvin, and V. V. Migulin, Fiz. Tech. Poluprovodn. **1**, 844 (1967) [Sov. Phys. Semicond. **1**, 702 (1967)].

4. C. G. Bethea, B. F. Levine, G. Hasnain, J. F. Walker, and R. J. Malik, J.Appl.Phys. **66**, 963 (1989).

Student Paper

Micromachined Room-Temperature Microbolometers for Millimeter-Wave Detection

Arifur Rahman, Gert de Lange, and Qing Hu
Department of Electrical Engineering and Computer Science and
Research Laboratory of Electronics,
Massachusetts Institute of Technology, Cambridge, Massachusetts 02139

Over the past few years, micromachining technology has become an active area of research for fabricating very sensitive sensors and transducers [1]. Micromachining technology can also be used for building very sensitive, low-cost and compact integrated millimeter-wave detectors and focal-plane arrays [2]. For an antenna-coupled microbolometer on a thin SiN membrane (Fig. 1.) with its dimensions and the geometry optimized so that most of the thermal conduction is through the antenna leads, the lower limit of the Noise Equivalent Power (NEP) is set by its phonon noise. It is given by, $NEP=(4kG)^{1/2}T$, where $k=1.38\times10^{-23}$ J/K is the Boltzmann constant, T=300K is the operating temperature, and G is the thermal conductance of the antenna leads. For typical metallic antenna leads with a resistance of 3Ω, we obtain a thermal conductance of 2.44×10^{-6} W/K. So the NEP is $3.5\times10^{-12}\mathrm{W}/\sqrt{\mathrm{Hz}}$. This is more than two orders of magnitude lower than the commercially available pyroelectric detectors. Recently, it is shown that 1/f noise of niobium films is approximately a factor of 7 below the best reported 1/f noise of bismuth films [3]. So a Nb microbolometer, integrated with a micromachined horn antenna, has a great potential in millimeter-wave detectors and imaging systems for both military and commercial applications.

We have fabricated a room-temperature micromachined microbolometer using a niobium film as the radiation absorber and temperature sensing element. The micromachined section of the device (shown in Fig. 1.) consists of a .37λ gold dipole antenna suspended on a thin (1 μm) Si_3N_4 membrane inside a pyramidal cavity. This pyramidal cavity is bounded by the <111> planes etched into <100> silicon. Normal active area of the bolometer is $2\mu\mathrm{m}\times3.2\mu\mathrm{m}$, and its thickness can be varied from 10nm to 20nm for good impedance matching with the antenna. During the fabrication process, the original niobium film has transformed into a semiconductor type (possibly a composite of Nb_2O_5 and Nb) of material with a negative temperature coefficient of resistivity ($\alpha=\frac{1}{R}\cdot\frac{dR}{dT}$) -0.01 K^{-1} at 300K. Its 1/f noise level is an order of magnitude higher than the 1/f noise level of a pure Nb film. Systematic characterization of the material indicates that it is not a pure semiconductor film, and the conduction process is probably due to thermally activated hopping, as indicated by the approximate $R = R_0\exp(T_0/T)^{1/2}$ relation shown in Fig.2. in the high temperature region 0.055 $K^{-1/2}<T^{-1/2}<0.1$ $K^{-1/2}$, which corresponds to

100K<T<330K. At a temperature lower than 100K, the conduction is probably dominated by tunneling, and therefore resistance of the device shows weak temperature dependence. Moreover, the relatively low roll off frequency (Fig. 3.) of the device response rules out that the detected signal is due to rectification of possible Schottky barriers formed between the gold contacts and the film. So, the detection scheme is purely bolometric.

A typical I-V curve and its first derivative (dV/dI) vs. bias voltage is shown in Fig. 4. We have calculated the electrical responsivity S_E (Fig. 5.) of the device from the I-V curve by using the Jones' expression [4,5],

$$S_E = (Z - R)/ 2IR$$

where Z = dV/dI and R = V/I. Jones' expression is generally a useful, but less accurate technique to estimate the response of a bolometer to changes in the electrical power dissipation because it does not take into account any type of nonthermal nonlinearity. An important figure of merit of any detector is its NEP. To determine the NEP, we have measured the noise voltage ($V/\sqrt{Hz}$) across the device by biasing it with a current source. The noise voltage is first amplified by a low-noise BJT pre-amplifier (gain = 100, $e_n = 1.1 \times 10^{-9} V/\sqrt{Hz}$, $i_n = 3 \times 10^{-12} A/\sqrt{Hz}$) and then by a PAR 113 amplifier (gain = 10, $e_n = 6.5 \times 10^{-9} V/\sqrt{Hz}$.) The NEP is calculated from dividing the noise voltage by the voltage responsivity of the bolometer. Using this device, we have achieved an electric NEP of $8 \times 10^{-10} W/\sqrt{Hz}$ at 5 kHz with an optimum bias current of 3.6 mA. At this bias current, electrical responsivity of the device is maximum, but with a lower bias current we can improve the NEP sacrificing the electrical responsivity. The NEP of the microbolometer at various bias currents is shown in Fig. 6. Unlike a Nb microbolometer, where the lower limit of the NEP is set by either phonon noise or Johnson noise [3], the NEP of our device is limited by the 1/f noise. This may be attributed to the poor quality of the thin film. Further improvement of NEP is being pursued by optimizing the geometry of the SiN supporting membrane and improving the quality of the Nb films to reduce the 1/f noise level.

We would like to thank Earl Macedo, Janen Deneeno and Dan Baker at MIT Lincoln Laboratory for their technical assistance during the fabrication of the microbolometer. We would also like to thank R.Ralston at MIT Lincoln Laboratory for access to the fabrication facilities in his group. This work was supported by ARPA (through the Consortium for Superconducting Electronics) under contract no. MDA972-90-C-0021.

[1] K. E. Petersen, Proc. of the IEEE, vol. 70, no. 5, pp 420-460, May. 1982.
[2] G.M. Rebeiz, D.P. Kasilingam, P.A. Stimpson, and D.B. Rutelage, IEEE - Tran. Antenna Propagation, vol. AP-38, pp.1473-1482, Sept. 1990.
[3] M. E. MacDonald and E. N. Grossman, IEEE - Trans. on Microwave Theory and Techniques, vol. 43, no. 4, pp 893-896, April. 1995.
[4] P. L. Richards, J. Appl. Phys., vol. 76, no 1, July 1, 1994.
[5] R. Clark Jones, J. of the Optical Society of America, vol. 43, no. 1, Jan. 1953.

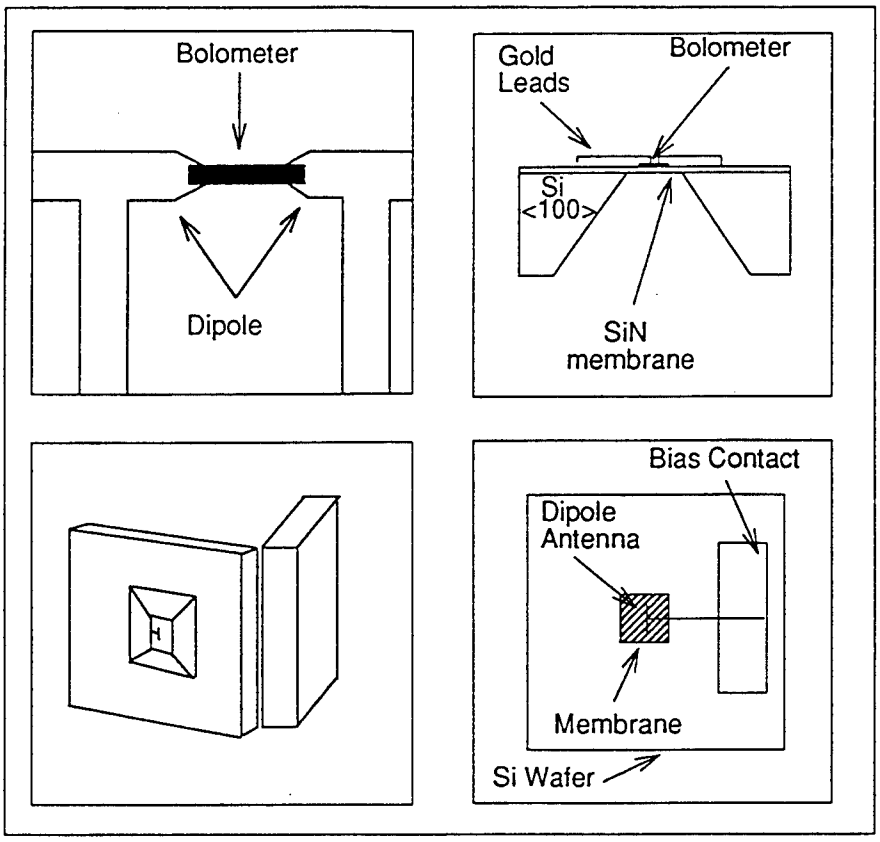


Fig. 1. Schematic of the microbolometer and the micromachined horn section.

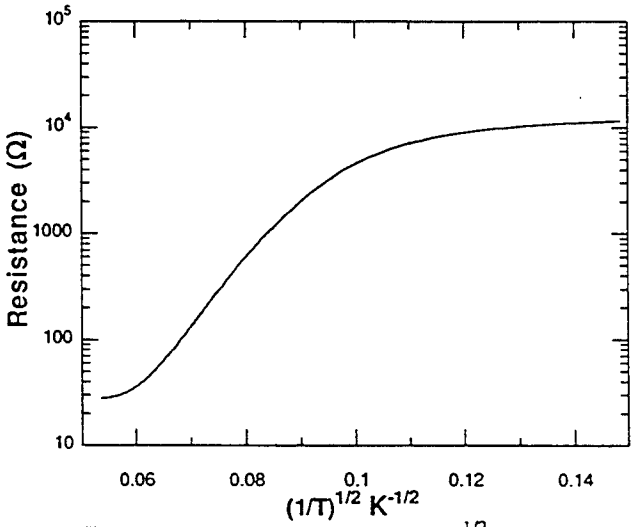


Fig. 2. Resistance vs. (temperature)$^{-1/2}$ of a 20nm microbolometer.

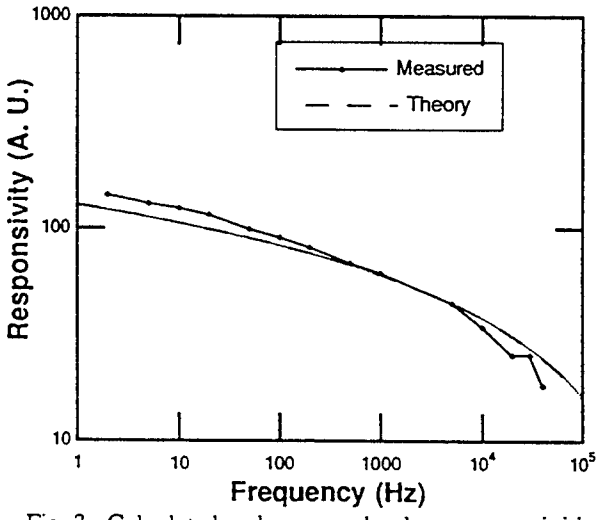


Fig. 3. Calculated and measured voltage responsivities of a 10nm thick microbolometer.Theoretical values were calculated by assuming a 2-D point source radiating heat in the membrane along the radial direction.

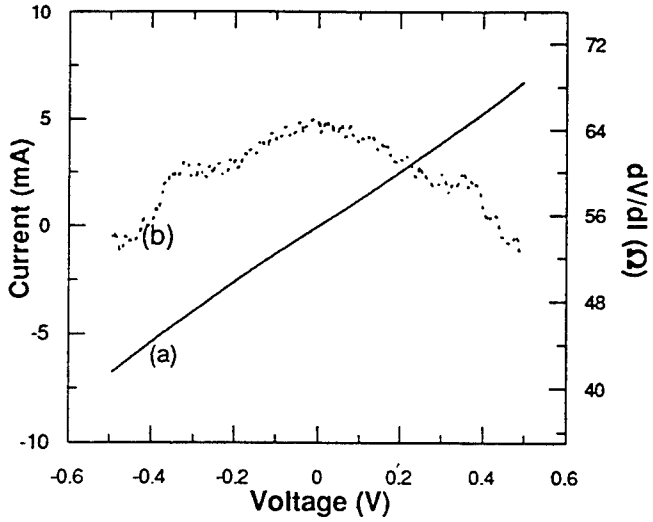


Fig. 4. I-V curve (a) and dV/dI (b) of a 10nm microbolometer.

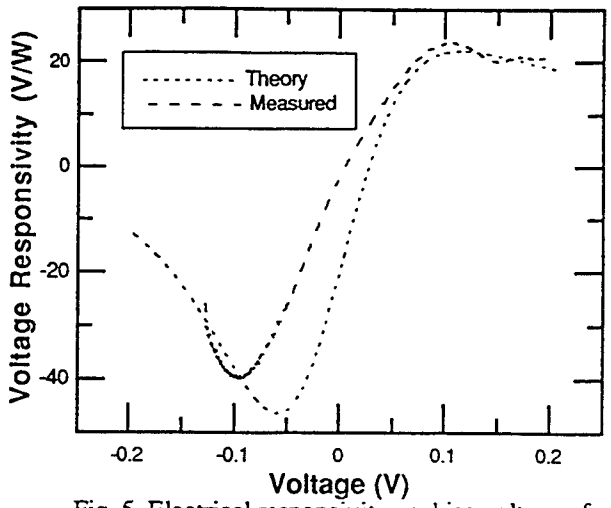


Fig. 5. Electrical responsivity vs. bias voltage of a 10nm microbolometer. Theoretical values were calculated by using the Jones' expression.

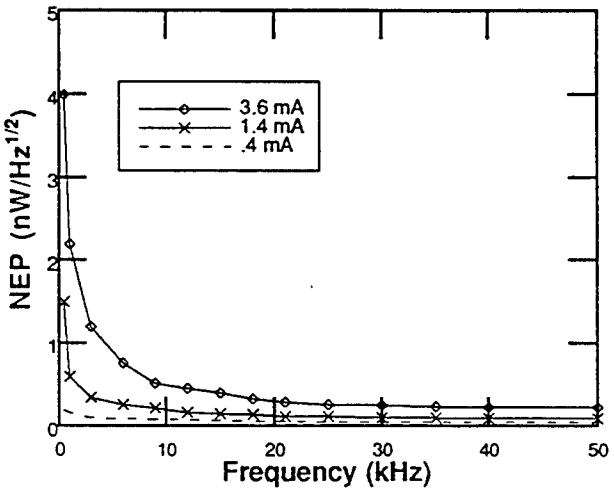


Fig. 6. Electric Noise Equivalent Power (NEP) of a 10nm thick microbolometer at various bias current.

InGaAs/InP PIN Diodes for Microwave and Millimeter-Wave Switching and Limiting Applications

Egor Alekseev, Kyushik Hong, Dimitris Pavlidis, Don Sawdai, Apostolos Samelis
Solid State Electronics Laboratory
Department of Electrical Engineering and Computer Science
The University of Michigan, Ann Arbor, MI 48109-2122

Abstract: InGaAs/InP PIN diodes were fabricated on epitaxial layers grown by MOCVD. DC and microwave characterization of the PIN diodes demonstrated low turn-on voltage (0.46 V), low insertion loss (< 1.2 dB up to 38 GHz), and high switching cutoff frequency (17 THz), as necessary for microwave and millimeter-wave switching and limiting applications.

I. INTRODUCTION:

PIN diodes are key elements for microwave switching and optical signal detection. Most results reported today refer to microwave PIN switches fabricated on GaAs[1,2] and optical PIN detectors[3] using InP-based materials. The use of InP-based PINs for microwave applications has drawn less attention, but offers unique and very attractive features, namely low insertion loss, due to the high mobility of InGaAs layers, reduced ohmic contact resistance on such materials, and low turn-on voltage, as necessary for limiting applications of low-power InP-based electronics. Moreover, InP- based PIN diodes can be used for switching functions and are compatible with InP HBT and HEMT millimeter wave technology. This paper addresses these features by evaluating the discrete characteristics of InP-based PIN diodes and examining their use as microwave switches.

II. EXPERIMENTAL RESULTS AND DISCUSSION:

The diodes were fabricated on PIN layers grown by our-in-house MOCVD facility. Starting from the substrate a 1 μm thick n^+-InGaAs layer ($2x10^{19}$ cm^{-3}) was grown followed by 1 μm of NID-InGaAs (~ $1x10^{15}$ cm^{-3}) and 0.15 μm of p^+-InGaAs ($2x10^{19}$ cm^{-3}). TMIn, TMGa and 100% AsH_3 were used for growth. *n*- and *p*-doping were introduced using DEZn and Si_2H_6. All layers were grown at 60 torr and susceptor was rotated at 100 rpm, which leads to good thickness and compositional uniformity of InGaAs. *n*- and NID InGaAs were grown at 570°C while *p*-InGaAs was grown at rather lower temperature (530°C) to enhance maximum Zn incorporation and to reduce Zn diffusion into the underlaying NID layer. The diodes were defined by 5 and 8 μm circles on the *p*-layer and wet etching was used to form the mesas. Air bridge technology was used to contact the top *p*-layer. An SEM photograph of a typical PIN diode is shown in *Fig. 1*. In addition to discrete diodes, a single pole single throw (SPST) switch was fabricated and studied.

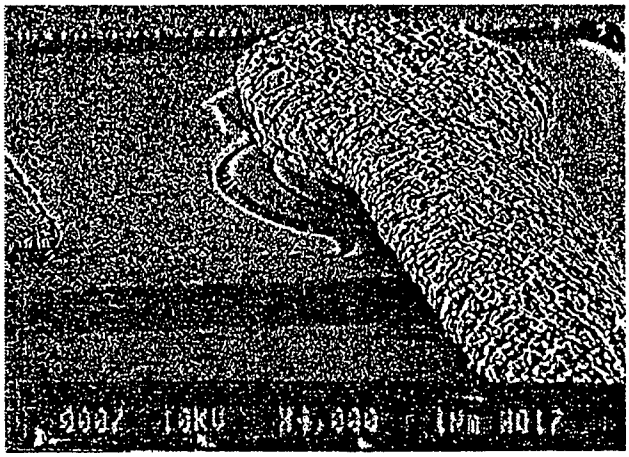


Figure 1. Scanning electron micrograph of fabricated InGaAs/InP PIN diode

The impact of *i*-layer thickness on OFF-state capacitance (C_d) was studied theoretically and experimentally. The 8 μm diameter diodes with 0.3 μm thick *i*-layer resulted in C_d values of 30 fF. By increasing the *i*-layer thickness up to 1 μm and reducing the diode diameter to 5 μm, C_d was reduced to 2 fF. The latter design was chosen for switching studies since it offers small displacement current, thus minimizing the losses, as well as, higher operating capability due to its smaller RC time constant. Further increase in the thickness of the *i*-layer was found to be unnecessary due to the diode parasitics becoming of the same order as the *i*-layer capacitance.

DC characterization of the PIN diodes (see *Fig. 2*) revealed a turn-on voltage of 0.46 V at I=10 μA. This value is smaller than that obtained using GaAs PINs where the threshold voltage is typically 0.7 to 0.8 V. The reverse characteristics of the diodes showed a breakdown voltage of 23.5 V at 10 μA current.

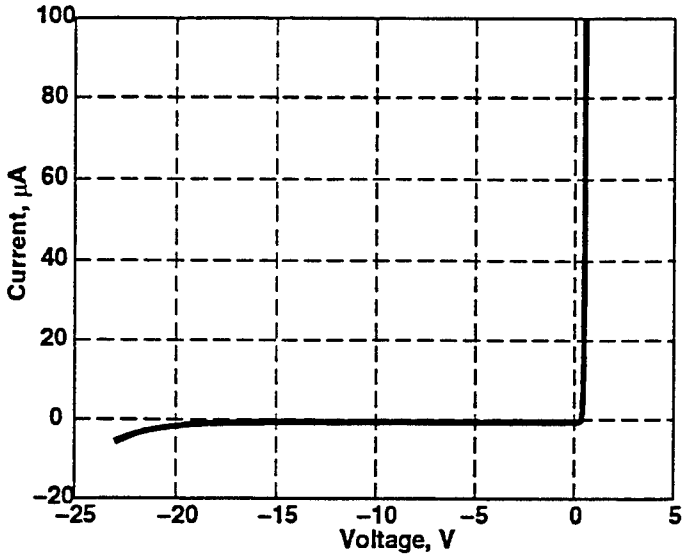


Figure 2. I-V characteristic of InGaAs/InP PIN diode

The diodes were characterized at high frequency by on-wafer probing. Equivalent circuits were extracted for the ON- and OFF-states and are shown in *Fig. 3*. L_s, R_s, C_p represent here the diode parasitics, while R_d and C_d represent *i*-layer characteristics. By changing the 5 μm diode state from ON (I=30 mA) to OFF (V=-10 V) the *i*-layer characteristics were found to vary from capacitive (C_d=2 fF) to resistive (R_d=4 Ω). The access resistance R_s was 0.5 Ω and the air bridge inductance was 21 pH in both states. The parasitic capacitance of the diode was estimated to be 4 fF.

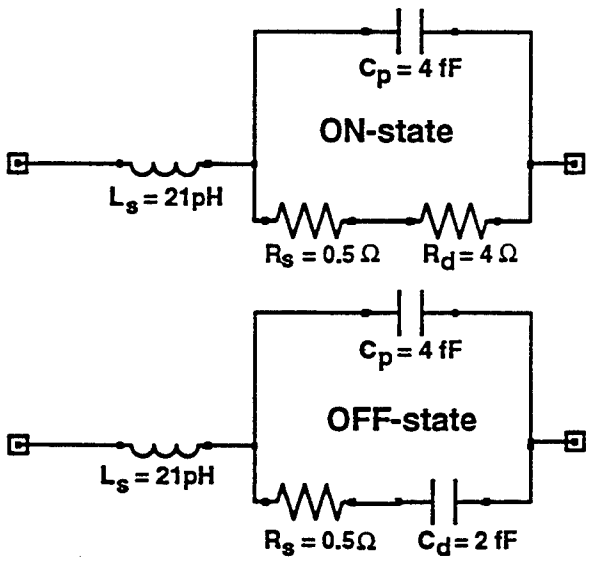


Figure 3. Equivalent circuit of 5 μm InGaAs/InP PIN diode in ON- and OFF-states.

Based on the above equivalent circuit one can estimate useful parameters of the InP-based PIN diodes

indicating their high frequency potential. The switching cutoff frequency of the PINs was estimated from

$$f_{cs} = \frac{1}{2 \cdot \pi \cdot C_d \cdot (R_s + R_d)}$$

where (R_s+R_d) is series resistance in the low impedance state and C_d is capacitance in the high impedance state. f_{cs} was found to be of the order of 17 THz for the 5 μm diameter diode. Considering that PIN diodes are used at 1/100 to 1/50 of their switching cutoff frequency one can estimate that the InGaAs/InP PIN diodes of this work can be used up to 170-340 GHz range. This indicates millimeter-wave capability and improved high frequency operation compared with estimated values 3.6 and 1.6 THz for high performance 20 and 9 μm diameter GaAs PINs respectively[1,2].

The quality factor of the PIN diodes is given by

$$Q = \frac{|Z_{ON} - Z_{OFF}|}{\sqrt{(R_1 \cdot R_2)}}$$

and is related to its impedance $Z_{ON} = (R_1 + j\,X_1)$ and $Z_{OFF} = (R_2 + j\,X_2)$ in the ON and OFF states respectively. Evaluating the quality factor of the InP based PIN diodes at 35 GHz one find a value of 1500 which again suggests the high superiority of the InGaAs/InP approach compared with other material systems and designs.

Since PIN diodes are used for switching and limiting applications, it is highly important to evaluate their large-signal characteristics. The large-signal microwave input impedance of the diodes was measured at different power levels in order to evaluate their power handling capabilities. An on-wafer testing system with electro-mechanical tuners was used for this purpose. The diode impedance was found as the complex conjugate of the 'pull' tuner impedance resulting in minimum power reflected from the diode. In this fashion, the large-signal impedances at 10 GHz were determined for different power levels and are shown in *Fig. 4*. PIN diodes switched into ON-state demonstrated no significant variations up to 17 dBm input power delivered to the device. On the other hand, the large signal impedance of the 'Zero-bias' OFF-state changed from a capacitive to the self-biased inductive ON-state when the input power was increased.

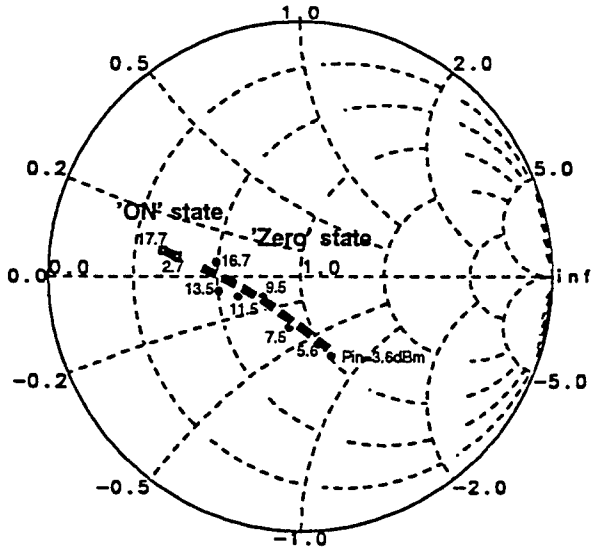


Figure 4. Large-signal characterization of InGaAs/InP PIN diode

An SPST switch was finally realized by implementing the above described diode in a 50 Ohm coplanar waveguide which was integrated on the same SI InP substrate. The diodes were switched from ON- to OFF-state and their isolation and insertion loss characteristics were measured and shown in *Fig. 5*. When the switch is turned on, the insertion loss was less than 1.2 dB and the return loss was better than 16 dB for frequencies up to 38 GHz. When the switch was turned off the return loss was less than 0.6 dB and the isolation was larger than 17 dB up to 37 GHz.

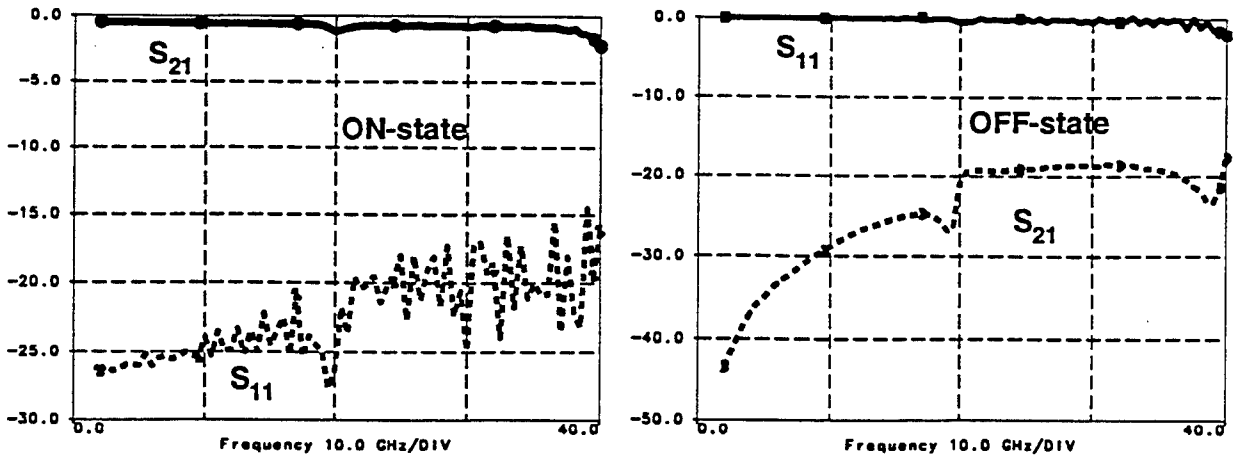


Figure 5. Performance of InGaAs/InP PIN SPST switch:
insertion loss and return loss in ON-state; reflection loss and isolation in OFF-state

III. CONCLUSIONS:

In conclusion we have grown and fabricated 5 μm diameter InGaAs PIN diodes with low turn-on voltage of 0.46 V, high breakdown voltage of 23.5 V, and low insertion loss of 1.2 dB as demonstrated by SPST switch performance evaluation up to 38 GHz. A high switching cutoff frequency of 17 THz and a high quality factor of 1500 at 35 GHz were evaluated for these devices. These excellent high frequency characteristics, compared with GaAs devices, are due to the high electron mobility and low ohmic contact resistance of the MOCVD grown InGaAs epitaxial layers.

ACKNOWLEDGMENT: The authors are grateful to Mr. Steve Robertson for the assistance in high frequency characterization.

Reference:

[1] J.Putnam, M.Fukuda,P.Staecker,Y.Yun, "A 94 GHz Monolithic Switch with a Vertical PIN Diode Structure", GaAs IC Symposium, pp. 333-336, 1994.

[2] K.W.Kobayahi, L.Tran, A.K.Oki, D.C.Streit, "A 50MHz-30GHz Broadband Co-Planar Waveguide SPDT PIN Diode Switch with 45-dB Isolation", Microwave and Guided Wave Letters, Vol.5 No.2 February 1995, pp.56-58

[3] A.L.Gutierrez-Aitken, J.Cowles, P.Bhattacharya, G.I.Haddad, "High bandwidth InAlAs/InGaAs PIN-HBT monolithically integrated photoreceiver", Proceedings of the 6th International Conference on Indium Phosphide and Related Materials, pp. 247-250, 1994

This work is supported by US Army Research Office (Contract no. DAAL-03-92-G-0109)
and Daimler Benz AG.

Microwave Pulse Power Measurement Employing Semiconductor's Resistance Change in a Strong Electric Field

Mindaugas Dagys, Žilvinas Kancleris, Vladislav Orševskij and Rimantas Simniškis
Semiconductor Physics Institute, A. Goštauto 11, Vilnius 2600,
Lithuania, tel.: (370 2) 619808, fax.: (370 2) 627123, e-mail: kancleris@uj.pfi.lt

1. Introduction Point contact or Schottky diodes are basically used to detect the envelope of microwave pulse. The main disadvantages of these devices lie in the following: (i) they can handle only a small amount of power (no more than 1 W) and (ii) they produce sufficiently small output signal. Therefore to measure high power microwave pulses with the help of the diodes direct couplers or attenuators with high level of attenuation has to be used. On the one hand, high attenuation results in the decrease of the measurement accuracy. On the other hand, a small signal is detected by the diode, and some complications could arise to measure this DC pulse in the presence of the hard stray pick up and the electromagnetic field interference which are usual at a high pulse power microwave generators. Therefore the problem of great importance is to develop the sensors that are able directly detect high power short microwave pulses and produce high output signal..

In this report the resistive sensor being one of the most perspective devices for microwave pulse measurement in the high and intermediate power range is presented. The transfer function and the possibility of independent calibration of the resistive sensor are considered. A few types of the resistive power heads for high power measurement in the waveguide are presented. Using the resistive power head together with a horn antenna microwave pulse power density measurement in a free space has been performed.

2. The performance of the resistive sensor. When a semiconductor is subjected to a strong electric field, electrons gain some additional energy and a new steady state occurs with mean electron energy greater than equilibrium one. As a rule, heated electrons are more frequently scattered by lattice imperfections, therefore the specific resistance of the semiconductor increases [1]. This effect is put on a basis for the resistive sensor performance. The general sketch of the resistive sensor mounted in the waveguide is shown in Fig. 1. It is seen that the sensor is a bar shaped piece of semiconductor with Ohmic contacts in the ends which is also connected into DC circuit together with current source. The electric field of the electromagnetic wave heats electrons in the semiconductor bar, its resistance changes, and DC pulse appears. The amplitude of that pulse can be expressed as follows:

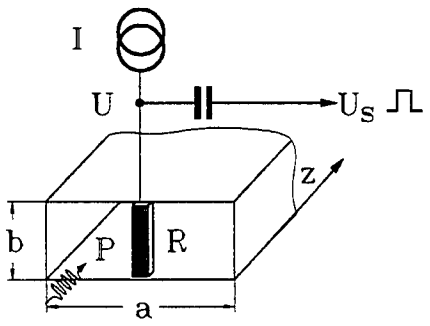


Figure 1. Resistive sensor in the rectangular waveguide

$$U_s = \varphi(E)\, U, \qquad (1)$$

where U is the DC voltage fall on the sensor, E is an amplitude of the microwave electric field strength averaged within the sensor and φ is relative sensor's resistance change in microwave electric field due to electron heating effect. In the limit of a low electric field (this interval of electric field strength is called warm electron region) relative resistance change is given by the first term of the expansion in power series of the electric field strength

$$\varphi(E) = \frac{3}{2}\beta E^2 \qquad (2)$$

where β is a coefficient describing current voltage characteristic deviation from Ohm's law. This coefficient is called warm electron coefficient and its value is of the order of 10^{-11} m^2/V^2 for n-Si at a room temperature. Warm electron region extends up to electric field strength 10^5 V/m. Our investigation revealed that at higher electric field strength relative resistance change can be described by the following empirical expression

$$\varphi(E) = \frac{\sqrt{1 + 6 k_n \beta E^2} - 1}{2 k_n}, \tag{3}$$

where k_n is an additional dimensionless coefficient has to be determined from experimental data.

It is easily seen that in the limit $E \to 0$ (2) and (3) expressions coincide with each other. Current voltage characteristic investigations performed for n-Si at a intermediate electric field strength revealed that (3) expression fairly well describes experimentally determined values of φ up to the electric field strength when relative resistance change is of the order 60-70%. It was found that at a room temperature k_n slightly depends on specific resistance of n-Si and its value lies in the interval 3-4.

To determine microwave pulse power P in the transmission line one has to express average electric field in the sensor as a function of P. In the case of bar shaped semiconductor in the rectangular waveguide it can be done in the common way:

$$E = \chi \left[\frac{2\sqrt{\mu_a / \varepsilon_a}}{\sqrt{ab}\sqrt{1 - (f_c / f)^2}} \right]^{1/2} P^{1/2}, \tag{4}$$

where f_c is a cutoff frequency, a and b are dimensions of the waveguide, μ_a and ε_a are permeability and permititivity of gas inside the waveguide and parameter $\chi = E / E_{em}$ (E_{em} is an electric field strength in an empty waveguide) accounts for perturbation of the transmission line by the semiconductor bar. From (1)-(4) it is seen that in a warm electron region output signal of the resistive sensor is proportional to P, while at a higher power levels nonlinear dependence of the output signal on P is characteristic to the resistive sensor.

3. Calibration. Bar shaped resistive sensor can be independently calibrated in the warm electron region making use of the resistive sensor as a thermistor bolometer. To determine electric field strength in the sensor the method of power replacement is used.

If a sequence of microwave pulses with pulse duration τ and period T is applied to the sensor, its resistance change can be observed due to average heating up of the sensor. Naturally, that resistance change depends on the microwave electric field strength and on the ratio τ / T. The same resistance change can be achieved applying to the sensor DC electric field E_0 . If $\tau, T \gg \tau_h$, where τ_h is characteristic time of the energy exchange between the resistive sensor and environment, the following relation binding microwave and DC electric fields based on the energy balance equation can be written down [2]

$$E = E_0 \sqrt{2\tau / T}. \tag{5}$$

Combining (4) and (5) microwave power in the transmission line can be expressed as follows

$$P = \frac{U_0^2 a \sqrt{2\tau / T}\sqrt{1 - (f_c / f)^2}}{2\chi^2 b \sqrt{\mu_a \varepsilon_a}} \tag{6}$$

where U_0 is the DC voltage applied to the sensor. Choosing dimensions and specific resistance of the sensor the value of χ can be got close to unity [3]. Thus, as follows from (6), microwave power in the transmission line can be determined by measuring DC voltage and relative microwave pulse duration. Since coefficients k_n and β can be measured independently, power head calibrated in a warm electron region can be used at higher power levels as well.

4. Resistive power heads For the intermediate microwave pulse power measurement the resistive sensor which length is equal to the narrow wall of the waveguide is used. By choosing specific resistance and dimensions of semiconductor bar the sensor's frequency response is optimized [3]. The

linear part of the output signal dependence on microwave power is employed, so intermediate power level up to 100 W and pulses with duration from 1 to 300 μs are measured.. Using meander modulated microwave signal the method of sensor calibration described above was realized in X-band. Calibrated head was compared with former Soviet Union microwave pulse standard being held in Moscow Institute of Metrology (VNIIFTRI). It is found that the deviation of our power head reading from standard pulse power meter is less than 4%.

A few calibrated power heads of this type were permanently compared with the standard since 1982. The last comparison was made in 1994. During this long-term experiment we did not observe any aging of the parameters of the resistive sensors. The relative deviation from the standard pulse power meter was found in the range of ±4 %.

Wishing to improve sensor's thermal characteristics and broaden its application for high microwave pulsed power measurement the diaphragm type resistive sensor has been developed. The sensor's height corresponds roughly $a / 10$ and it is placed between the broad wall of the waveguide and the metal diaphragm which is located in the waveguide's H-plane. Dimensions of the sensor and the diaphragm as well as the specific resistance of n-Si are chosen making an optimization of the frequency response of the sensor, decreasing electric field perturbation in the transmission line and improving thermal characteristics of the sensor.

Two modifications of the diaphragm type power heads were designed. SF series is devoted to

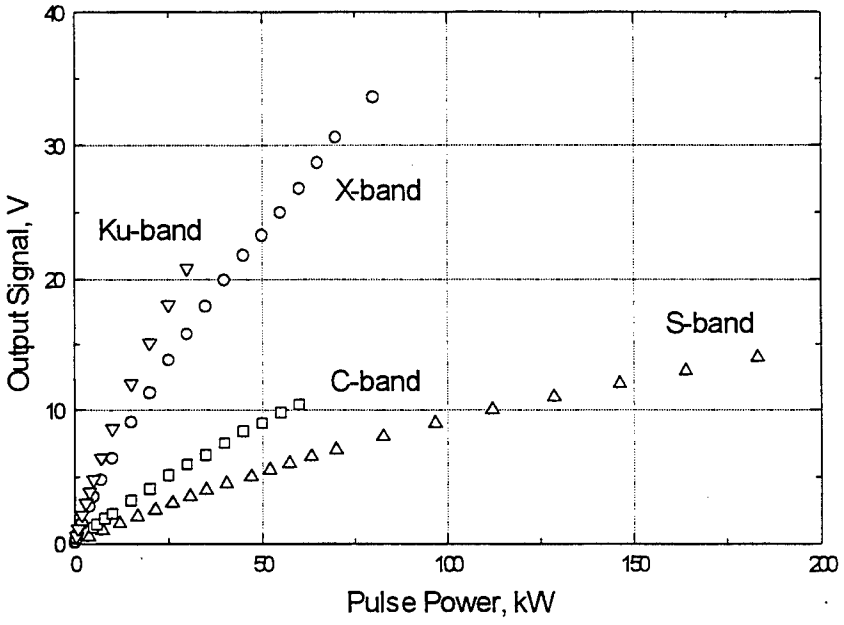


Figure 2. Output signal dependencies on microwave pulsed power for the heads of SF series..

detect short microwave pulses, the duration of which lies in the interval from 5 to 100 ns. The response time of that heads is of the order of 1 ns. Low specific resistance of n-Si is used for the resistive sensor's manufacturing, so the resistance of it is of the order of 20 Ω. To avoid lattice heating pulse DC supply is used. As it is seen from Fig. 2, the output signal of the order of a few tens of volts on 50 Ω matched load is obtained without any amplification for the power heads of SF series.

The resistive sensor made from higher specific resistance of n-Si is used in the heads of IA series, so they are employed to detect high power microwave pulses the duration of which lies in the range of 0.5-300 μs. Double shielded and located close to resistive sensor DC pulse preamplifier is employed. An additional temperature sensor and electronic circuitry are used to compensate the

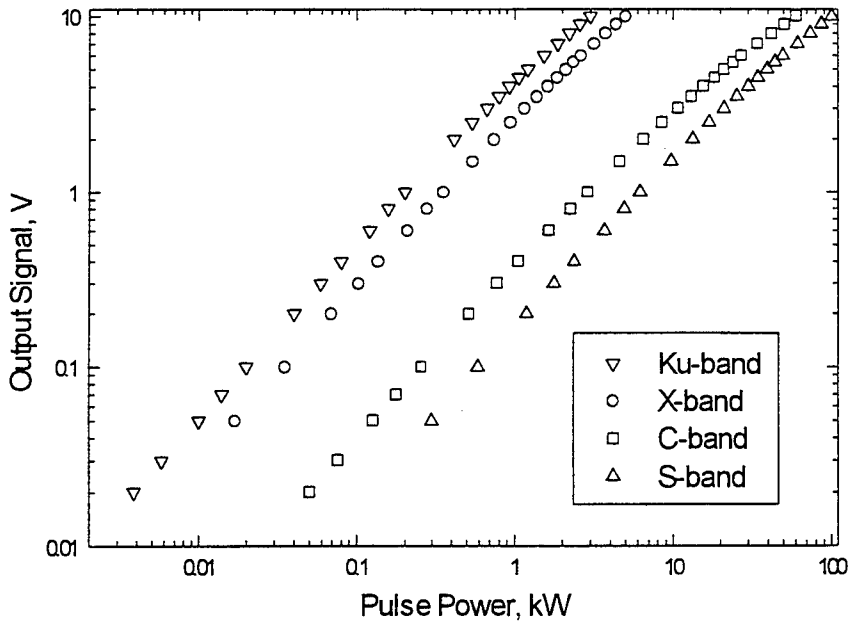


Figure 3. Output signal dependencies on microwave pulse power for the heads of IA series. The heads are calibrated up to 3, 5, 60 and 100 kW in Ku, X, C and S band, respectively.

temperature dependence of the output signal. The maximum output signal at the preamplifier output was 10 V. Microwave pulse power measurement accuracy of IA heads is ±12% in the waveguide's frequency band and in the temperature range -20 +50 C. It can be done even lower for a fixed frequency (usually high level microwave sources generates at a fixed frequency or in a narrow frequency band). Power heads of IA series for various waveguide's dimensions were designed. Output characteristics of the heads for S, C, X and Ku bands are presented in Fig. 3.

Both types of heads were tested in free space. The power head proceeded by a horn antenna and followed by a matched load comprise a unit for microwave pulse power density determination in free space. Switching off the DC supply of the sensor we examined the magnitude of the parasitic signal induced in the head by the external electromagnetic field. It was obtained that our heads can measure pulse power density up to a few MW/m^2, while the parasitic signal was less than 1% of the direct signal.

5. Conclusion The following advantages of the resistive sensor in comparison with Schottky or point contact diode have to be mentioned: (i) possibility to measure high microwave pulse power directly in the transmission line without using direct coupler or attenuator, (ii) high value of output signal from the sensor is available (up to a few tens of volts), (iii) high reliability and overload resistance is characteristic to the resistive sensor, (iv) switching off DC supply of the resistive sensor the parasitic signal induced in the measurement circuit by the external electromagnetic field can be determined. These features made resistive sensor irreplaceable for high level microwave pulse measurement at a hard external conditions.

REFERENCES

[1] E. M. Conwell, *High Field Transport in Semiconductors.* New York: Academic Press, 1967.

[2] V. Dienys, Ž. Kancleris and Z. Martūnas, *Warm electrons.* Vilnius: Mokslas, 1983 (in Russian).

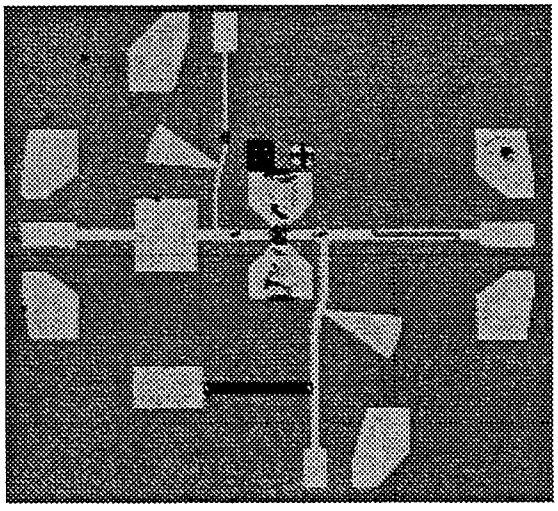
[3] R. Baltušis, M. Dagys, R. Simniškis, "Resistive sensors for high pulse power microwave measurement," in *Proc. 22nd Euro. Microwave Conf.*, Helsinki, Helsinki University of Technology, 1992, pp.169-173.

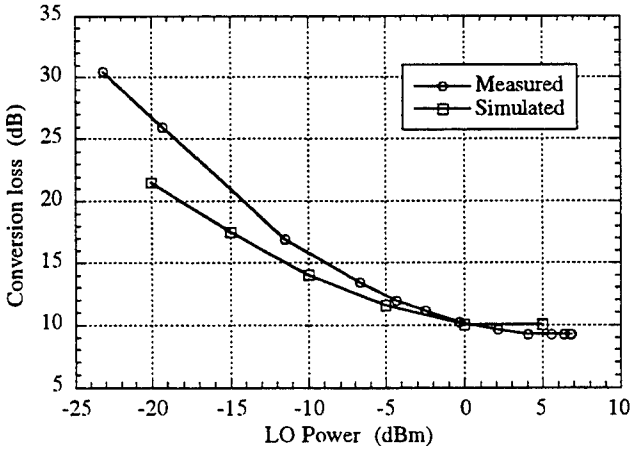
RESISTIVE MIXERS BASED ON THE HETEROSTRUCTURE FIELD EFFECT TRANSISTOR

Herbert Zirath, Chalmers University of Technology
Department of Microwave Technology
S-412 96 Göteborg SWEDEN

Abstract

This paper describes recent work on frequency mixers based on resistive mixing by modulating the charge density in the channel of a heterostructure field effect transistor (HFET). The HFET is acting as a variable resistance, controlled by the gate voltage. A local oscillator signal (LO) is applied to the gate which causes the channel resistance to vary periodically with the LO. By applying a signal (RF) between the source and the drain, different mixing products will appear across the drain and source. Normally the difference frequency f_{LO}-f_{sig} (the intermediate frequency, f_{if}) is of interest and extracted from the drain through a filter. HFETs based on both GaAs and InP have been studied and the mixing properties of both types were investigated. Also different types of subharmonically pumped HFET resistive mixers have been investigated and will be presented. The most important advantages of HFET resistive mixers are i.) electrical stability due to the passive operation of the device, ii.) the LO-port and the RF port are separated , iii.) the mixer consumes no DC-power, iv.) monolithic integration with other circuits like amplifiers etc is easy, v.) the intermodulation properties are usually better compared to the diode mixer, vi.) relatively low LO-power is required. As an example, a monolithically integrated mixer working at 100-120 GHz is described in Fig.1. The LO is applied to the left probe pad , the RF-signal to the right, and the IF-signal through the bottom probe pad. The transistor is located in the middle of the circuit. The device is a single delta doped AlInAs-GaInAs HFET lattice matched to InP.





The measured and modeled conversion loss versus the local oscillator power is also shown in the figure. At 112 GHz we measure a conversion loss of better than 9 dB with a local oscillator power of 5 dBm. At 50 GHz, a conversion loss below 6 dB was measured on a hybrid version of a similar mixer.

Micromechanical Sliding Planar Backshorts

Victor M. Lubecke,[1] William R. McGrath,[1] and David B. Rutledge[2]

[1] Jet Propulsion Laboratory, California Institute of Technology, Pasadena CA 91109, USA

[2] Department of Electrical Engineering, California Institute of Technology, Pasadena CA 91125, USA

***Abstract*—A micromechanical tuning element which can be fabricated as an integral part of a planar transmission line, has been developed and demonstrated in a fully monolithic 620 GHz integrated circuit. The design of this integrated device, called a *sliding planar backshort* (SPB), is based on a discrete SPB, previously demonstrated at 100 GHz. Its fabrication involves a unique application of sacrificial-layer and molding techniques, to materials and processes which are compatible with the fabrication of a wide range of MMIC's.**

I. Introduction

At millimeter and submillimeter wavelengths, the performance of common semiconducting and superconducting devices is severely degraded by the effects of parasitic reactances inherent in their geometries [1,2]. These effects are not easily characterized, and adjustable impedance matching circuits are typically needed to make practical use of such devices. A common approach is to embed the device in a waveguide circuit and employ mechanically adjustable waveguide backshorts as tuning elements which serve to optimize the device performance by compensating for the parasitic reactance [3]. The critical dimensions for these circuits are very small, decreasing in size as the frequency of interest increases. This makes fabrication of such waveguide circuits exceedingly costly and difficult, and has motivated interest in alternative planar approaches.

Monolithic integrated circuit technology promises a practical means for realizing reliable and reproducible planar millimeter and submillimeter wave circuits. Planar circuits are fabricated through photolithographic techniques, which allow for the cost-effective production of intricate designs not possible with waveguide technology. These circuits, however, must also provide compensation for parasitic device reactances. Conventional planar technology allows for only fixed tuning elements, providing no means for post-fabrication optimization of performance [4]. This makes characterization of the component elements critical, and it is not usually possible to achieve satisfactory results without multiple iterations.

An adjustable planar tuning element, which functions in a planar circuit analogously to a backshort in a waveguide circuit, has been developed, along with a process for its fabrication as an integral part of a submillimeter wave monolithic circuit. It is called a *sliding planar backshort* (SPB). It can be used in developmental circuits as an aid for device characterization, or as a means to optimize in-use performance for a variety of submillimeter wave integrated circuits.

II. The Sliding Planar Backshort

The SPB consists of a rectangular metal plate, with appropriately sized and spaced holes, which rests on top of a dielectric-coated planar transmission line, as shown in Fig. 1. The impedance of the sections of line covered by metal is greatly reduced, while the uncovered sections retain their higher impedance. Each of these sections is approximately one quarter-wavelength long, and the cascade of alternating low- and high-impedance sections results in an extremely low-impedance termination. This termination can be moved to vary the electrical length of a planar transmission line tuning stub, by simply sliding the metal plate along the length of the line. The semiempirical design of the SPB was carried out on a 2 GHz scale model [5], and the SPB has been successfully demonstrated as a discrete component at frequencies up to 100 GHz [6].

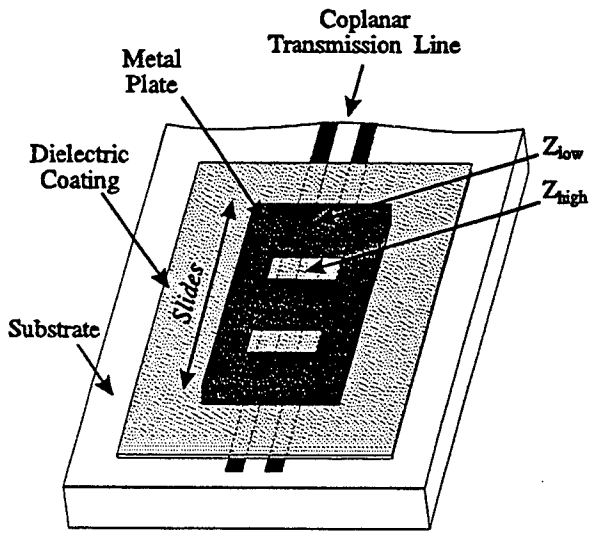


Fig. 1. Conceptual illustration of the SPB. A patterned metal plate slides over a dielectric-coated planar transmission line to vary the electrical length.

A quasi-optical, 620 GHz, direct-detection integrated circuit was developed to demonstrate the operation of an integrated SPB. This circuit used a dielectric-filled parabola to focus radiation onto a slot antenna, and coupled this radiation to a bismuth detector [7] by means of two coplanar waveguide (CPW) transmission lines, each with integrated SPB's. One SPB creates a variable reactance in series between the antenna and the detector, potentially serving to compensate for any unwanted reactance when the slot is not resonant. The other SPB creates a variable susceptance in parallel with the detector, and could be used to compensate for the parasitic capacitance found in some otherwise desirable submillimeter wave devices. The circuit is illustrated in Fig. 2.

The critical dimensions for the 620 GHz SPB, CPW lines, and dielectric-coating were scaled from an optimized 2 GHz model. The three conducting sections of the SPB each covered approximately 80 μm of the CPW line, with a 65 μm space after the first section and a 75 μm space after the second. An additional space and conducting section was added to the micromechanical SPB to better facilitate its manipulation with a mechanical probe. The CPW line consisted of a 16 μm wide center-conductor with 8 μm gaps on either side. The appropriate thickness of the dielectric-coating was determined to be slightly less than 1000 Å for silicon-dioxide at 620 GHz.

The photolithographic fabrication of microelectromechanical systems (MEMS) with submillimeter dimensions has been demonstrated, and is now a growing field with great potential [8]. Much of this work involves the fabrication of movable captivated structures by the *surface micromachining* of silicon. In this process a photopatterned polysilicon structure is deposited on a silicon substrate between two sacrificial oxide layers. A second photopatterned polysilicon structure is then deposited, overlapping the oxide-coated structure and anchoring to the substrate. The sacrificial oxide layers are then etched away, releasing the first polysilicon structure to move within the constraints of the second. A more recent MEMS fabrication technique, known as LIGA (a German acronym meaning litography, plating and molding), allows for the fabrication of microstructures with larger vertical aspect ratios (over 100 to 1), and the use of materials other than silicon. This technique is used for the batch production of three-dimensional structures within a microfabricated cast or mold.

The dimensions for a 620 GHz SPB are comparable to that of common MEMS. However, neither of the techniques previously described can be used by itself as a practical means of fabricating a suitable SPB; some of the materials and processes involved are inappropriate for, or incompatible with, those often needed in a submillimeter wave circuit. Fortunately, key features from both techniques can be suitably combined in a process which allows for the fabrication of SPB's in a variety of submillimeter wave circuit applications.

III. The Fabrication Process

The procedure used for fabricating the micromechanical SPB's in the 620 GHz integrated circuit is illustrated in Fig. 3. The circuit was fabricated on a fused-quartz wafer, and the first two thin-film circuit layers, 1000 Å of gold and 1000 Å of silicon-dioxide, formed the dielectric-coated transmission line.

A photoresist lift-off stencil was applied, and photopat-

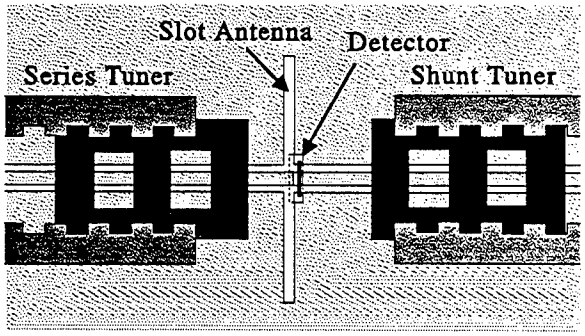


Fig. 2. The 620 GHz integrated circuit. Two micromechanical SPB's on dielectric-coated transmission lines form the adjustable impedance matching circuit.

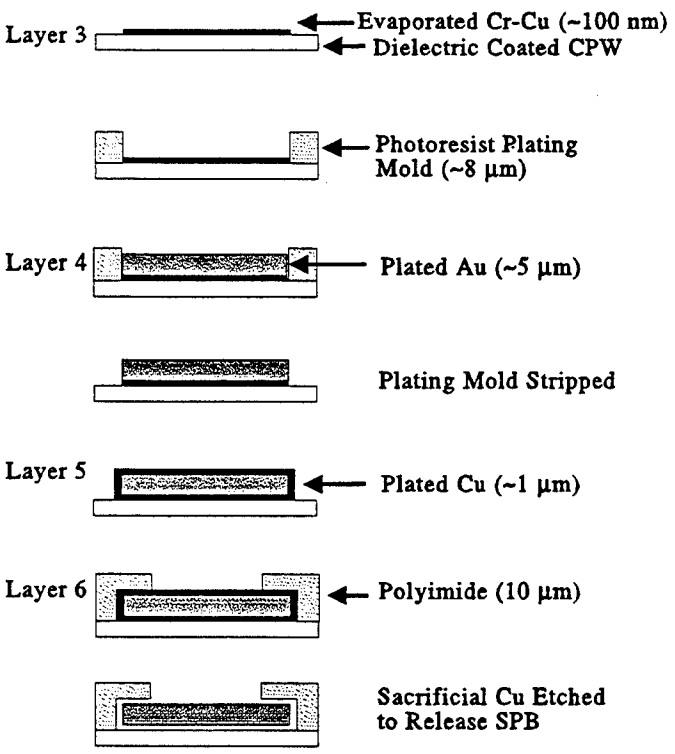


Fig. 3. Simplified illustration of the SPB fabrication process. Sacrificial layers are used to form an SPB which is constrained by guide-structures.

terned to define a sacrificial-seed layer. This pattern consisted of a rectangular strip over the coplanar lines, as wide as the SPB (200 μm) and extending to the edge of the substrate to allow for electrode connection. This third layer was formed by depositing a 1700 Å layer of copper over a 70 Å chrome adhesion layer through electron-beam evaporation, and then lifting the stencil and unwanted film in acetone.

Next, an 8 μm layer of photoresist was applied to the circuit, patterned to form a mold layer, and hard-baked. This layer defined the shape of each SPB, several sacrificial pieces used to define the region into which each SPB would slide, and two 1mm^2 patches. These patterns were all formed over the sacrificial-seed layer to allow for electroplating, with the large square patches serving to increase the plating area and allow for the use of a maintainable plating current. The wafer was then dipped in gold electroplating solution where 5 μm-thick patterned gold structures were plated within the mold, forming the fourth circuit layer.

The mold layer was then striped in N-methyl 2-pyrrolidone, and a 1 μm sacrificial copper coating, Layer 5, was applied to the SPB's by connecting the circuit to an electrode and immersing it in copper electroplating solution. A 13 μm layer of photosensitive polyimide-precursor was then spun onto the circuit, and patterned form two digitate strips, each overlapping one side the copper coated gold structures. The strips were then cured to form 9 μm-thick polyimide guide-structures.

Finally, the copper plating and sacrificial-seed layers were removed in a wet etch, releasing the gold SPB structures to slide along the substrate within the polyimide guide-structure. An SEM of the circuit is shown in Fig. 4.

The illustration in Fig. 5 shows a close-up view of the guide structure with an SPB under it as fabricated (a), and as seen after sliding the SPB to another position (b).

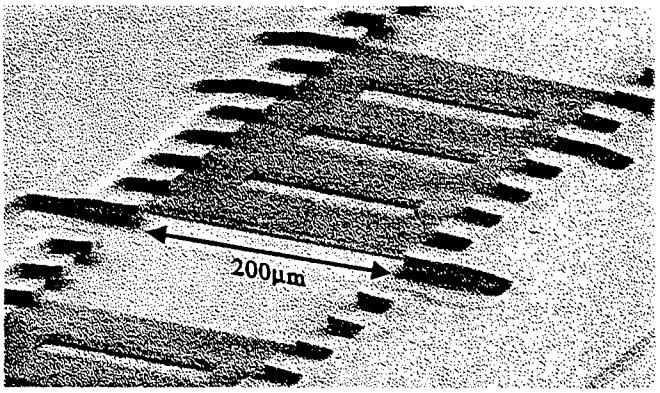


Fig. 4. SEM of the integrated circuit with with two SPB's. Each SPB controls the electrical length of a CPW line on either side of a slot antenna.

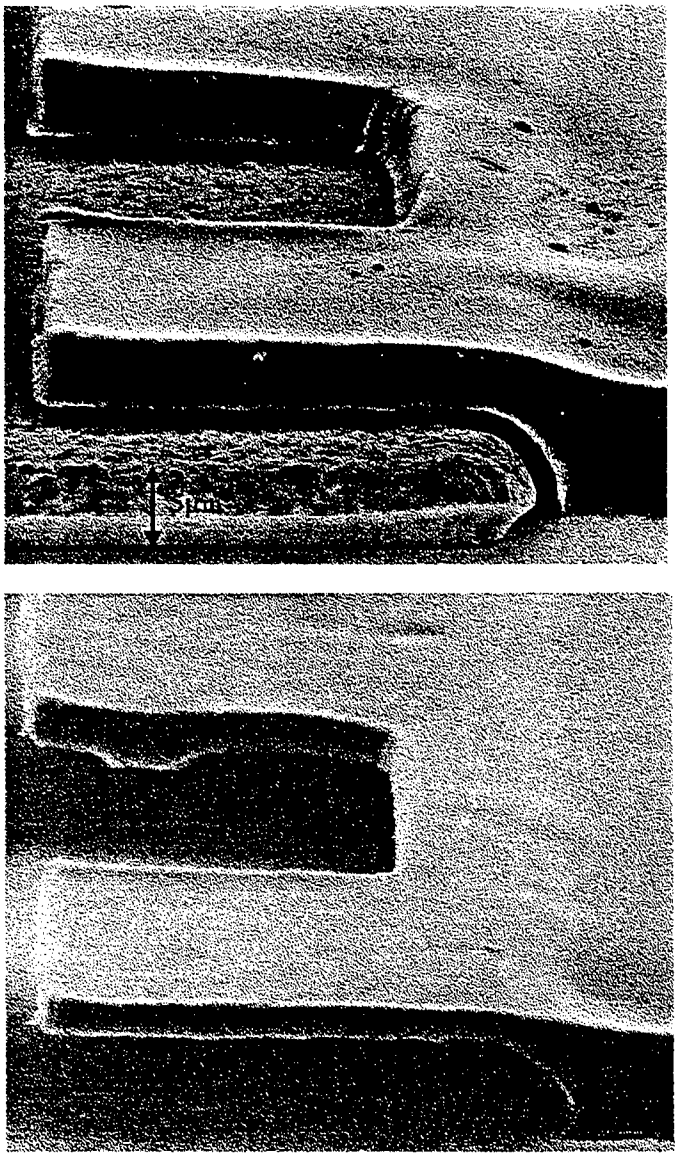


Fig. 5. Close-up SEM of one side of an SPB. The polyimide guide-structure is shown with (a) and without (b) the SPB beneath it.

IV. Performance

The integrated circuit was completed by depositing a small rectangular patch of bismuth through evaporation and lift-off, and mounting the finished wafer over a substrate lens [9] to allow for quasi-optical performance measurements.

An theoretical model was derived for the 620 GHz integrated circuit and used to predict its performance. Impedances for the antenna (24 Ω) and CPW lines (78 Ω) were calculated [10,11] along with expected ohmic, dielectric, and radiative losses [12]. The measured value for the DC resistance of the bismuth detector (18.5 Ω) was used, and measurements made using a 2 GHz scale model indicated that $|s_{11}|$ should be −0.06 dB.

The performance of the integrated SPB's was demonstrated by using them to vary the power delivered from the slot antenna to the bismuth detector by altering the impedance match between them. The measurements were carried out at 620 GHz using a backward wave oscillator as a source, and the circuit response was successfully varied over a 15 dB range by manually positioning the SPB's with an ox-hair probe. The results for independent position sweeps for each SPB agreed very closely with theory.

V. Acknowledgements

The authors would like to thank Dr. P.A. Stimson and Prof. Y.-C. Tai for their generous assistance. The research described in this paper was sponsored by NASA in the form of a Graduate Student Researchers Program fellowship as well as a contract provided through the Jet Propulsion Laboratory.

References

[1] I. Mehdi and P.H. Siegel, "Effect of Parasitic Capacitance on the performance of Planar Subharmonically Pumped Schottky Diode Mixers," *Fifth International Symposium on Space Terahertz Technology - Symposium Proceedings*, pp. 379–393, May 1994.

[2] R. Blundell and C.-Y.E. Tong, "Submillimeter Receivers for Radio Astronomy," *Proceedings of the IEEE*, vol. 80, no. 11, pp. 1702–1720, November 1992.

[3] M. Salez, P. Febvre, W.R. McGrath, B. Bumble, and H.G. Leduc, "An SIS Waveguide Heterodyne Receiver for 600 GHz-635 GHz," *International Journal of Infrared and Millimeter Waves*, vol. 15, no. 2, pp. 349–368, February 1994.

[4] J. Zmuidzinas, H.G. Leduc, J.A. Stern, and S.R. Cypher, "Two Junction Tuning Circuits for Submillimeter SIS Mixers," *IEEE Trans. on Microwave Theory Tech.*, vol. 42, no. 4, pp. 698–706, April 1994.

[5] V.M. Lubecke, W.R. McGrath, and D.B. Rutledge, "Sliding Backshorts for Planar Circuits," *International Journal of Infrared and Millimeter Waves*, vol. 12, no. 12, pp. 1387–1397, December 1991.

[6] V.M. Lubecke, W.R. McGrath, and D.B. Rutledge, "A 100 GHz Coplanar Strip Circuit Tuned With a Sliding Planar Backshort," *IEEE*, vol. 3, no. 12, pp. 441–443, December 1993.

[7] D.P. Neikirk and D.B. Rutledge, "Self-heated Thermocouples for Far-Infrared Detection," *Applied Physics Letters*, vol. 41, no. 5, pp. 400–402, September 1992.

[8] J. Bryzek, K. Peterson, and W. McCully, "Micromachines on the March," *IEEE Spectrum*, pp. 20–31, May 1994.

[9] P.H. Siegel and R.J. Dengler, "The Dielectric-Filled Parabola: a New Millimeter and Submillimeter Wavelength Receiver/Transmitter Front End," *IEEE Transactions on Antennas and Propagation*, vol. 39, no. 1, pp. 40–47, January 1991.

[10] G.V. Eleftheriades and G.M. Rebeiz, "Self and Mutual Admittance of Slot Antennas on a Dielectric Half-Space," *International Journal of Infrared and Millimeter Waves*, vol. 14, no. 10, October 1993.

[11] K.C. Gupta, R. Garg, and I.J. Bahl, *Microstrip Lines and Slotlines*, Dedham, MA: Artech House, 1979.

[12] M.Y. Frankel, S. Gupta, J.A. Valdmanis, and G.M. Mourou, "Terahertz Attenuation and Dispersion Characteristics of Coplanar Transmission Lines," *IEEE Trans. on Microwave Theory Tech.*, vol. 39, no. 6, pp. 910–916, June 1991.

A Tri-Layer Filter Structure for Individual Device Biasing of Subharmonically-Pumped Mixers Employing Antiparallel-Pair Diodes

T. H. Lee, I. Mehdi, R. J. Dengler, A. Pease, and P. H. Siegel
Jet Propulsion Laboratory, California Institute of Technology

Abstract

Antiparallel Schottky diodes, in both whisker contacted and integrated planar chip packages, have been utilized to produce millimeter-wave subharmonically-pumped (SHP) mixers for many years [1-5, e.g.]. SHP mixers have the advantage of operating with a local oscillator (LO) at one half of the signal frequency and have been shown to yield conversion loss and noise temperatures only slightly higher than conventional single-ended mixers [1,5]. However, the required LO power for these demonstrated SHP mixers is many times that of a single diode circuit. This is due to the difficulty involved in incorporating individual diode bias circuitry with the antiparallel pair and is the most limiting factor in scaling SHP mixers up to higher submillimeter-wave frequencies. In this paper the authors describe a very compact multiple layer bias circuit for an antiparallel-pair diode arrangement which can be implemented in microstrip. The concept was first proposed by the millimeter-wave development group at Rutherford Appleton Labs in the U.K., but, to our knowledge, has not yet been successfully implemented [6]. We report on the design and testing of a multiple layer transmission line bias structure which has been used with our Quartz Upside-down Integrated Device (QUID) process to produce a working SHP circuit which we have tested in a waveguide mixer block at 200 GHz. The addition of the bias circuit reduces the LO power by 50% without significant increase in the mixer conversion loss or noise temperature. The design is currently being implemented at 640 GHz for a NASA space Earth remote sensing instrument - Microwave Limb Sounder.

Extended Summary

The idea of separately biasing each diode of an antiparallel pair to reduce the turn-on voltage and, hence, the required LO power is not new and has been used in both waveguide-based and MMIC-based circuitry [7,8]. However, past implementations have required extra ports for isolating the two devices and bringing in the second bias line. This makes the implementation especially difficult in high-frequency waveguide structures where additional circuit elements are often added at a tremendous price. A very compact bias circuit arrangement was recently demonstrated in an open structure quasi-optical SHP mixer system at 180 GHz [3]. This arrangement utilizes a gap-cap configuration on one side of the two diodes and requires that there be a split in the feed lines going to the devices on this side of the circuit. Such an arrangement is not practical in a waveguide SHP circuit where there is generally not enough space to implement the feed line gap. The design presented here utilizes the vertical space within the existing filter circuitry to implement a multi-layer transmission line structure which isolates the two diodes of the antiparallel pair. It requires no additional

space and has been incorporated into an existing mixer circuit design [4] and tested at 200 GHz.

The bias circuitry is formed at the same time as the diodes and IF and RF transmission line filters using the QUID process which integrates the planar diodes with the filters and then transfers everything from the GaAs host wafer to a low-loss quartz substrate [5]. The center portion of the drawing of the lower half split-block waveguide mount with the diode bias and microstrip circuitry is shown in Figure 1.

The details of the biasing scheme near the anode region are shown in Figure 2. The filter on one side of the diode pair is duplicated and overlayed with its twin using a thin layer of nitride for DC isolation. During processing, each of the metallic filter layers is coupled to a different active device, thus electrically isolating the two diodes. The strong capacitive coupling between the filter layers preserves the AC performance. Details of the fabrication process follow.

The stacked filters are formed from a metal/nitride/metal tri-layer. The metal layers are titanium/gold deposited by electron-beam evaporation and have a total thickness of 9000 Å. The intermediate nitride layer is deposited by an electron cyclotron resonance (ECR) dielectric deposition system to a thickness of 8000 Å. The nitride layer has to have low pin-hole density and good step coverage. The deposition was performed in a high-pressure (20 mTorr) environment with the use of an etch-back process. The thickness of nitride determines the coupling capacitance required for proper filter performance. For our particular circuit, 6000 Å of nitride results in approximately 1 ohm impedance at the lowest mixer IF frequency of 1.5 GHz. However, it was necessary to use a slightly thicker nitride layer (8000 Å) to improve the processing yield.

A prototype circuit using optically-formed diodes with 2 μm diameter circular anodes was fabricated for insertion into our existing mixer block design. The measured DC parameters for the diode pair are given in Table 1. A higher turn-on voltage in the second diode, causing nonsymmetry in the I-V characteristics, can be compensated through different bias voltages at the two diodes. Due to the larger than average anode area and high series resistance, we did not expect to have extremely good mixer performance in the existing waveguide blocks. Indeed, the best mixer performance results, obtained at 195 GHz, yielded a double sideband (DSB) noise temperature of 2380 K with 16 mW of LO power required when no external bias was applied. With the application of separate bias in the two devices, we were able to decrease the required LO power to 8 mW with a subsequent increase in noise temperature to 2730 K. Bias current in the two devices was 800 μA. The DSB conversion losses were 10.1 and 10.9 dB, in the former and latter cases respectively. The IF output impedance at optimum RF performance was around 80 Ω, regardless of the bias conditions. The results translate to 0.7 dB degradation in noise performance with a 3 dB LO power reduction. Figure 3 shows the noise temperature and conversion loss at several LO frequencies, with the same device with no external bias, and with a bias condition which requires 3 dB less LO power.

The measured mixer performance is not nearly as good as that obtained with other devices in the same blocks. We believe this is largely the result of the anode size which is not optimum

for this circuit at this frequency. However, these early results do demonstrate the feasibility of the multi-layer bias concept and encourage our ongoing efforts of making smaller diodes for higher operating frequencies using this configuration.

References

[1] M. V. Schneider and W. W. Snell, "Harmonically Pumped Stripline Down-Converter," *IEEE Trans. Microwave Theory Tech.*, vol. 23, no. 5, pp. 271-275, Mar. 1975.

[2] M. Cohn, J. E. Degenford, and B. A. Newman, "Harmonical Mixing with an Antiparallel Diode Pair," *IEEE Trans. Microwave Theory Tech.*, vol. 23, no. 8, pp. 667-673, Aug. 1975.

[3] T. H. Lee, J. R. East, C. Y. Chi, G. M. Rebeiz, and G. I. Haddad, "A Novel Biased Anti-Parallel Schottky Diode Structure for Subharmonic Mixing," *IEEE Microwave and Guided Wave Letters*, vol. 4, no. 10, pp. 341-343, October, 1994.

[4] P. H. Siegel, R. Dengler, I. Mehdi, J. Oswald, W. Bishop, T. Crowe, and R. Mattauch, "Measurements on a 215 GHz Subharmonically Pumped Waveguide Mixer Using Planar Back-to-Back Air-Bridge Schottky Diodes," *IEEE Trans. Microwave Theory Tech.*, vol. 41, no. 11, pp. 1913-1921, Nov. 1993.

[5] I. Mehdi, M. Mazed, R. Dengler, A. Pease, M. Natzic, and P. Siegel, "Planar GaAs Schottky Diodes Integrated with Quartz Substrate Circuitry for Waveguide Subharmonic Mixers at 215 GHz," *IEEE MTT-S Int. Microwave Symp. Digest*, pp. 779-782, 1994.

[6] B. Ellison, B. Maddison, and D. Matheson, private communication.

[7] J. W. Archer, R. A. Batchelor, and C. J. Smith, " Low-Parasitic, Planar Schottky Diodes for Millimeter-Wave Integrated Circuits," *IEEE Trans. Microwave Theory Tech.*, vol. 38, no. 1, pp. 15-22, Jan. 1990.

[8] P. H. Siegel, S. Weinreb, S. Duncan, W. Berk, A. Eskandarian, and D.-W. Tu, "Design and Measurement of a 210 GHz Subharmonically Pumped GaAs MMIC Mixer," *IEEE MTT-S Int. Microwave Symp. Digest*, pp. 603-606, 1992.

Figures and Tables

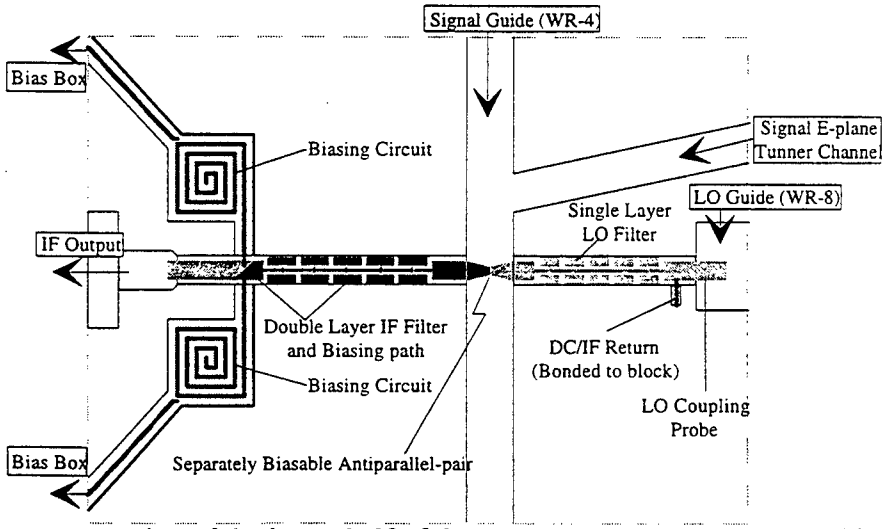


Figure 1. The center portion of the lower half of the mixer split-block that houses biasable diodes and microstrip circuits.

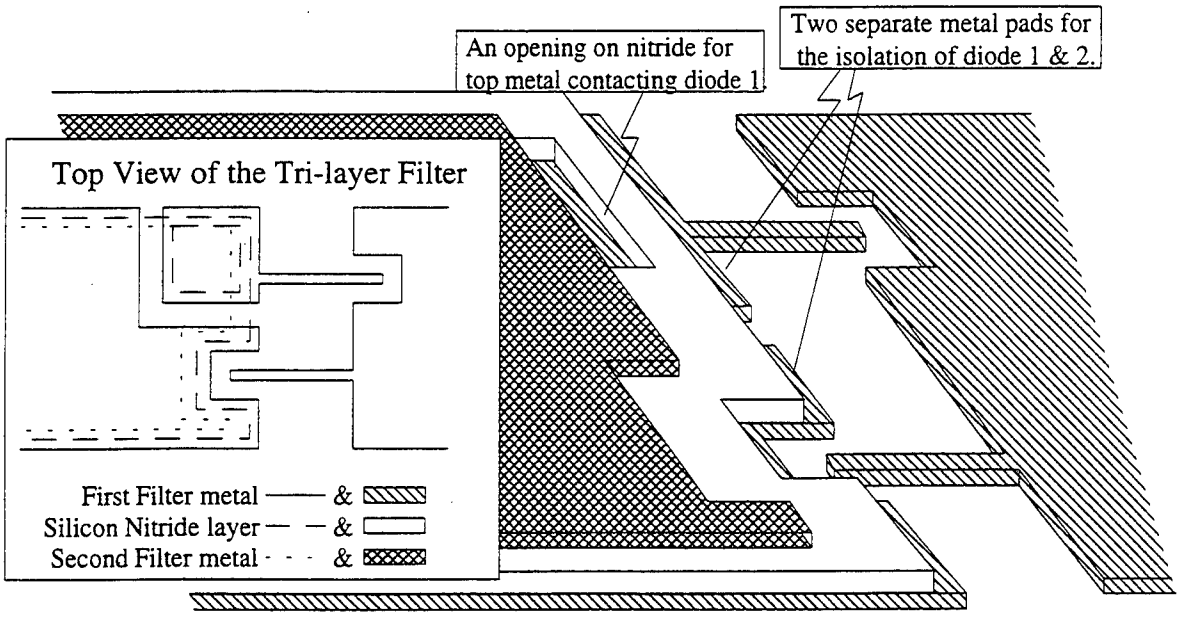


Figure 2. A tri-layer IF filter and a single layer LO filter near the anode region. The vertical structure on the IF side provides a compact way of biasing individual diodes.

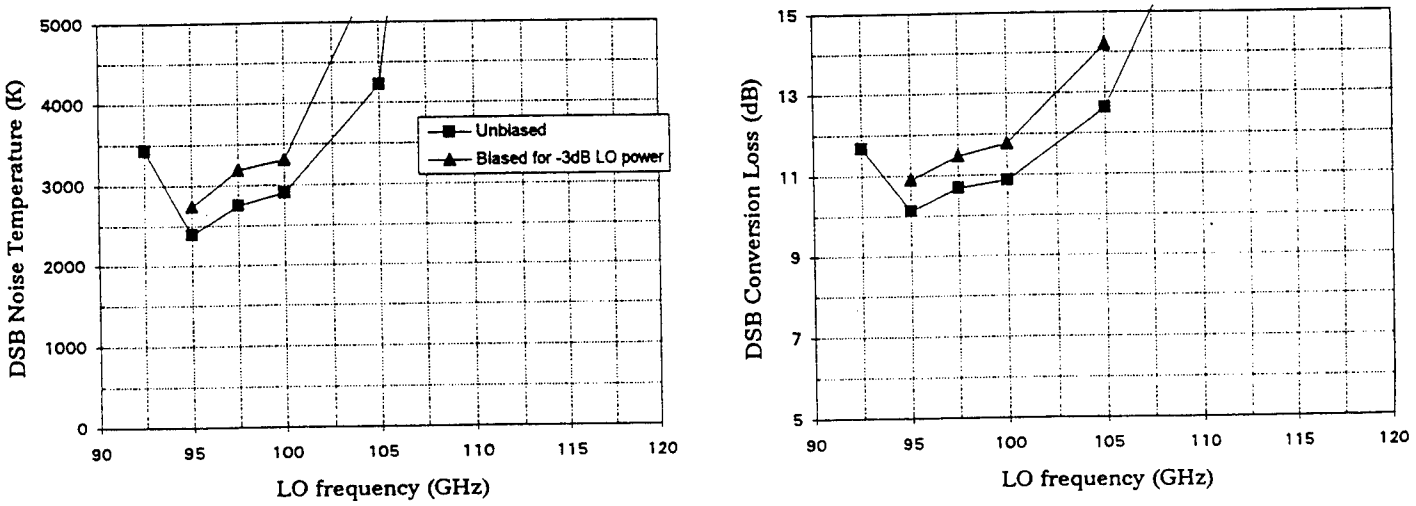


Figure 3. DSB noise temperature and conversion loss vs. LO frequency for the device with no external bias and for the same device biased to require only one-half of the LO power.

Parameters	R_s (Ω)	η	I_s (A)	$\Phi_{barrier}$ (V)
Diode 1	8	1.23	1.2×10^{-13}	0.735
Diode 2	13	1.25	1.4×10^{-13}	0.730

Table 1. Diode DC parameters measured from the separately biasable Schottky diode pair.

WAVEGUIDE AUGMENTED INTEGRATED CIRCUIT

X.J. LU, D.L. RHODES AND D.L. WOOLARD

U.S. Army Research Laboratory, Physical Sciences Directorate, Fort Monmouth, NJ 07703-5601

ABSTRACT

Electronic technology with the capacity for operation at sub-millimeter and terahertz frequencies has a number of valuable applications including: (i) detection and analysis of gas species; (ii) space communications; (iii) short range guidance and surveillance; and (iv) wireless computer networking. The push towards higher frequencies, however, strains not only active device technology but also interconnection technologies. Typical monolithic microwave integrated circuit (MMIC) on-chip interconnects, including microstrip and co-planar connections, experience higher losses with increasing frequency due to increasing loss tangents and metal losses. Rectangular, fundamental-mode waveguide, however, has much lower loss and offers additional benefits as well.

This paper reports on a new fabrication technology which results in an air-filled micro-waveguide structure, directly integrated on a MMIC, capable of guiding electromagnetic energy. As with "traditional" waveguides, this technology can be used for device to device interconnection, RF filtering functions, off-chip (antenna) connections, power combining/ splitting, etc. As losses are minimal between active devices and the RF transmission media (the waveguide), improvements in transmitter/receiver noise figures are expected.

The example design presented is aimed at the 200 GHz range, but the technique is generally applicable to frequencies where waveguide dimensions are suitable (not too large) to MMICs. This nominally includes 100 GHz to well over 1 THz. In fact, the method is better suited to the higher frequency ranges but 200 GHz was chosen due to testing limitations at higher frequencies.

The overall process makes use of a patterned thick film to form an approximately rectangular waveguide over a MMIC or other substrate. This material is then removed leaving the waveguide as air filled and hence free from dielectric loss. Both polymer and

polyimide films were used, but the polyimide version is discussed here. More specifically, a 0.2 THz waveguide structure was fabricated on a Duriod substrate using a photo-sensitive polyimide as a forming material. Here, photolithographic techniques are used to define a rectangular section (approximately 1 cm long) of the polyimide material on top of the Duriod substrate. This rectangular section is then gold over-plated; hence, serving as a mold to define the top and sides of the micro-waveguide structure. An immersion process is then used to dissolve-out the polyimide which remains inside the formed cavity. One of the advantages of this on-substrate waveguide is that it can be conveniently integrated with other passive and active devices at low cost. With this in mind, we also designed and simulated a compatible waveguide-microstrip mode launching structure to achieve lower insertion loss and larger transmission. This planar approach is very desirable since it is much easier to fabricate than more traditional post-in-waveguide designs.

A detailed description of the waveguide fabrication process (see Fig. 1) begins with coating the substrate with polyimide followed by a softbake. In order to achieve the desired coating height of 100 μm, a 750 rpm spin-speed and 25 sec. spin-time were employed. The photosensitive polyimide was then imaged into a rectangular pattern using a UV light-source mask aligner. The unexposed portion of polyimide was then removed using a developer provided by the polyimide manufacturer. In this case, Porbimide 414 polyimide and QZ3301 developer from Olin Ciba-Giegy (OCG). Note, for coatings thicker than 100 μm a simple immersion step is insufficient. Hence, additional mechanical means (spray/spin and ultra-sonic development) were employed.

To electroplate the guide structure, a seed layer of gold was sputtered onto the polyimide material. The electroplating of gold was carried out in the typical fashion, with the substrate at the cathode of the electroplating cell. A gold-layer 25 μ m thick was employed for this structure. After electroplating, the polyimide was immersed again to remove the polyimide inside the waveguide.

As a next step, the interconnection structure connecting devices to the waveguide have been investigated. While the technology is aimed at placement of devices directly within the waveguide, the design reported here moves the device outside the waveguide for testing purposes. This includes a planar antenna coupling the waveguide to a microstrip transmission line through a side opening in the waveguide (see Fig. 2). This design has been

simulated using a three dimensional EM analysis tool (HP's HFSS package). The geometry of the interconnection was designed to achieve optimum transmission. In this design, the side outlet was actually placed in the side of the waveguide one-quarter wavelength away from the input-end. The microstrip is connected to the bottom of the waveguide via an impedance transformer structure. Thus far, the best $|S_{12}|$ design result is 0.4 (approximately -8 dB) at 200 GHz. Note, the implementation of a closed waveguide system is necessary since at THz frequencies the radiation-frequency limit of a microstrip has been far exceeded (e.g. for dielectric material with $\varepsilon_0 = 10$ and microstrip width of 0.1 mm, $F_M = 25$ GHz). After measurement verification, the subsequent design will place the device and coupling structure directly in the waveguide. In this case, coupling losses are expected to be less than 1 dB, which would compare quite favorably to an alternative design using a quarter wavelength long post (which is more difficult to integrate) to couple the device.

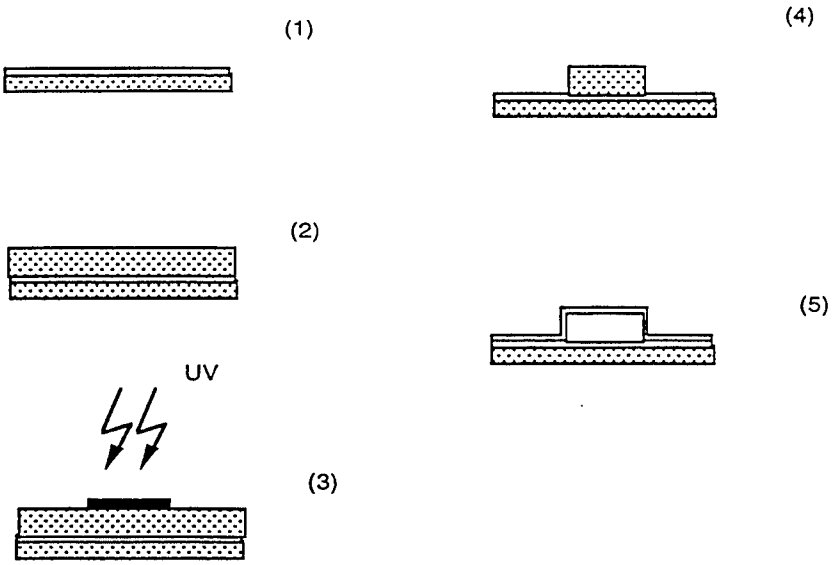


Fig. 1: The processing steps of the waveguide structure.

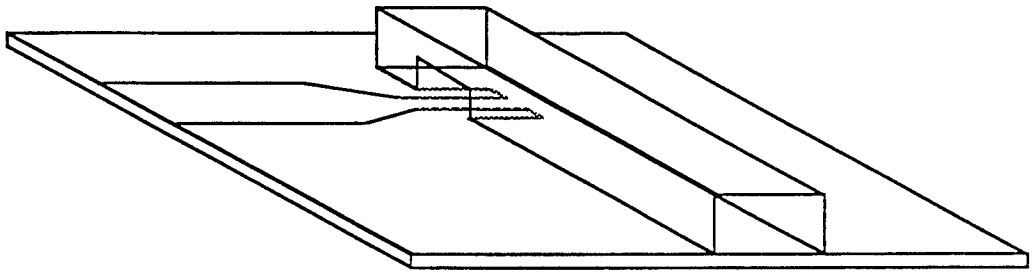


Fig. 2: The illustration of the the waveguide and microstrip interconection structure simulated by HFSS.

Quantum Cascade Lasers for the 3-5μm and 8-12 μm Atmospheric Window

J. Faist

AT&T Bell Laboratories,
600 Mountain av, Murray Hill, NJ, 07974 USA

After our first demonstration of a quantum cascade laser based on a three well active region with a diagonal transition in real space[1], we have developed a more efficient design based on a two wells active region with a vertical transition and a Bragg electron confinement[2].
This new design configuration allowed us to reduce dramatically the threshold current density to as low as 1.5kA/cm^2 at 10K. These devices also operate in pulses up to a maximum temperature of 260K. The simultaneous optimization of thermal characteristics of the structures at both 4.6μm and 8μm wavelengths allow operation in continuous wave, with a maximum with powers of 10mW at 80K to 20mW at 50K. The laser being unipolar, index guiding is natural and the lasers operate on a single longitudinal mode on most of the current and temperature range. The powers obtained on a single mode (10mW) are almost 100 times the value obtained in commercially available lead-salt lasers. These high single mode powers are very significant for possible uses which include trace-gas analysis, optical pollutant detection and industrial process monitoring.

(1.) J. Faist, F. Capasso, D. L. Sivco, C. Sirtori, A. L. Hutchinson, and A. Y. Cho, *"Quantum Cascade Lasers"* Science **264**, 477 (1994)

(2.) J. Faist, F. Capasso, C. Sirtori, D. L. Sivco, A. L. Hutchinson, and A. Y. Cho, *"A vertical transition quantum cascade laser with Bragg-confined excited state"* Appl. Phys. Lett **66**, 538 (1995)

GaSb-Based Mid-Infrared Quantum-Well Diode Lasers*

H. K. Choi and G. W. Turner
Lincoln Laboratory, Massachusetts Institute of Technology
Lexington, MA 02173-9108

1. Introduction

High-performance semiconductor lasers emitting in the mid-infrared (IR) band (2 – 5 μm) are very desirable for many applications. A variety of molecules including all hydrocarbons have strong absorption lines in this band. Single-frequency mid-IR diode lasers are ideally suited for highly sensitive detection of trace gases for such applications as pollution or toxic gas monitoring and industrial process monitoring. In addition, there are three atmospheric transmission windows in this band. High-power diode lasers emitting in these windows can be very useful for laser radars, target designation, and illumination.

In this paper, we review recent progress in mid-IR quantum-well (QW) diode lasers grown on GaSb substrates by molecular beam epitaxy (MBE). At ~2 μm, GaInAsSb/AlGaAsSb lasers have excellent room-temperature performance with cw power of 1.3 W from a 300-μm aperture.[1] At ~4 μm, InAsSb/InAlAsSb QW lasers have operated pulsed up to 165 K and cw up to 128 K, with the maximum cw power at 80 K of 30 mW/facet.[2] These results are much better than those obtained for double-heterostructure lasers fabricated from the same material system.

2. GaInAsSb/AlGaAsSb QW lasers

Since the first GaInAsSb/AlGaAsSb QW lasers were reported[3] that had room-temperature pulsed threshold current density J_{th} of 260 A/cm^2 and cw power of 300 mW/facet, the performance of 2-μm lasers has been further improved by optimizing the MBE growth conditions to get smoother interfaces.[4] The laser structure consists of the following layers: n^+-GaSb buffer, 2-μm-thick n-$Al_{0.85}Ga_{0.15}As_{0.07}Sb_{0.93}$ cladding, active region consisting of five 10-nm-thick $Ga_xIn_{1-x}As_ySb_{1-y}$ wells and six 20-nm-thick $Al_{0.25}Ga_{0.75}As_{0.02}Sb_{0.98}$ barriers, 2-μm-thick p-$Al_{0.85}Ga_{0.15}As_{0.07}Sb_{0.93}$ cladding, and 0.05-μm-thick p^+-GaSb contacting. All the layers are nominally lattice matched to the substrate, except for the active wells, which are under compressive strain of ~5 x 10^{-3}. Based on the growth parameters and the amount of strain, the best estimate for the active layer composition is x = 0.86 and y = 0.05.

Figure 1 shows the room-temperature pulsed J_{th} vs inverse cavity length L^{-1} of a 300-μm-wide broad-stripe laser. For L = 2 mm, J_{th} = 143 A/cm^2. The value of J_{th} per well is only 29 A/cm^2, which is about half the lowest value obtained for the best InGaAs/AlGaAs lasers emitting at ~1 μm. As L becomes smaller, the value of J_{th} increases gradually, to a value of 280 A/cm^2 for 300 μm. The characteristic temperature T_0 near room temperature is 95 K, which is significantly higher than 55 K obtained for InGaAs/InP lasers emitting at ~2 μm.[5] The emission wavelength at room temperature is at ~1.91 μm, and it shifts with temperature to longer wavelengths at a rate of ~1 nm/°C. The full width at half-maximum (FWHM) of the spectrum is ~5 nm.

Figure 2 shows the cw output power vs current curve for a 1000-μm-long device at a heatsink temperature of 12°C. The front and back facets were coated to have reflectivities of 4 and 95%, respectively. The threshold current is ~650 mA and the initial slope efficiency is ~0.3 W/A, corresponding to a differential quantum efficiency of 47%. The maximum output power is 1.3 W, limited by the junction temperature rise. The power conversion efficiency is as high as 15.5%.

Ridge-waveguide lasers 5 μm wide were fabricated by using reactive ion etching to form ridges.[6] One device with L = 1000 μm was coated for high reflection (HR) on the back facet and antireflection (AR)

*This work was sponsored by Phillips Laboratory, the Department of the Air Force.

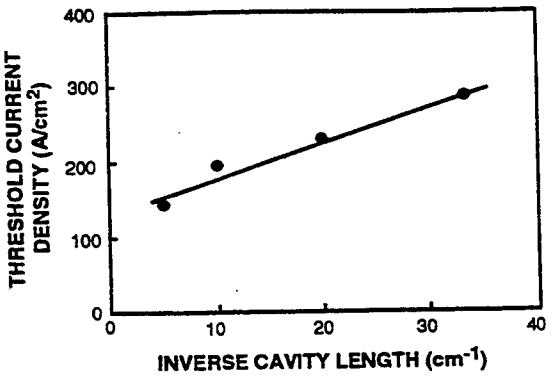


Fig. 1. Room-temperature pulsed threshold current density vs inverse cavity length of GaInAsSb/AlGaAsSb quantum-well (QW) laser at 12°C.

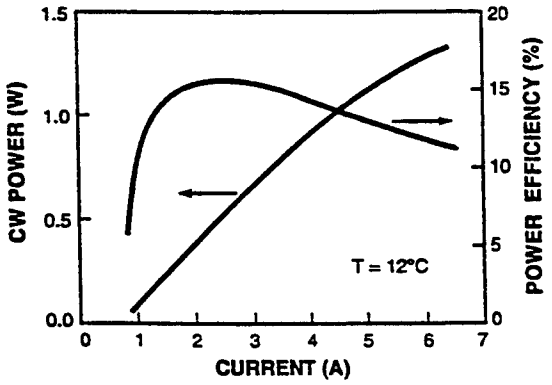


Fig. 2. CW output power vs current for a 1000-μm-long GaInAsSb/AlGaAsSb QW laser.

on the front facet. Figure 3 shows the cw output power vs current at a heatsink temperature of 20°C. The threshold current is 40 mA and the initial slope efficiency is 0.25 W/A, corresponding to a differential quantum efficiency of 39%. The maximum output power is 100 mW obtained at 525 mA, limited by the junction temperature rise. This power is substantially higher than 25 mW/facet reported for InGaAs/InGaAsP ridge-waveguide lasers grown on InP substrates with emission wavelength of ~2 μm.[7]

Figure 4 shows cw power vs current curves at several heatsink temperatures of another 1000-μm-long device with HR and passivation coatings on the back and front facets, respectively. For temperatures between 20 and 80°C, the characteristic temperature T_0 is 85 K. The slope efficiency does not change appreciably between 20 and 60°C, but becomes smaller at higher temperatures. The maximum cw operating temperature is 130°C, which is 100°C higher than that for GaInAsSb/AlGaAsSb DH lasers.[8]

The emission wavelength of GaInAsSb/AlGaAsSb QW lasers has been extended to 2.8 μm by Lee *et al.*[9] The laser structure consists of four 10-nm-thick $Ga_{0.76}In_{0.24}As_{0.16}Sb_{0.84}$ wells and five 18-nm-thick $Al_{0.25}Ga_{0.75}As_{0.02}Sb_{0.98}$ barriers, surrounded by 2-μm-thick $Al_{0.9}Ga_{0.1}As_{0.07}Sb_{0.93}$ cladding layers. Under pulsed conditions, the lasers operated pulsed up to 60°C, with T_0 of 58 K between 0 and 40°C. The threshold current density at 25°C was 1.25 kA/cm^2. These lasers operated CW up to -39°C.[10]

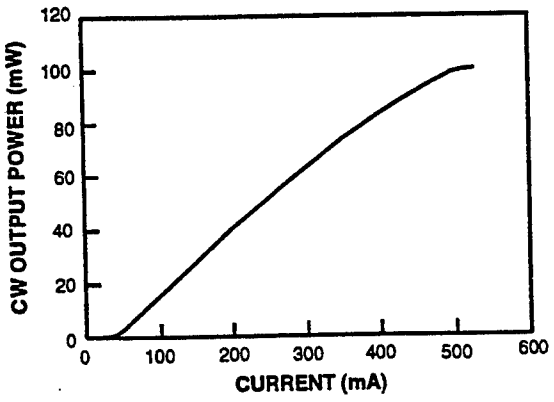


Fig. 3. CW output power vs current for a GaInAsSb/AlGaAsSb ridge-waveguide laser at 20°C. The back facet is high-reflection coated (> 95%) and the front facet is antireflection coated (< 1%).

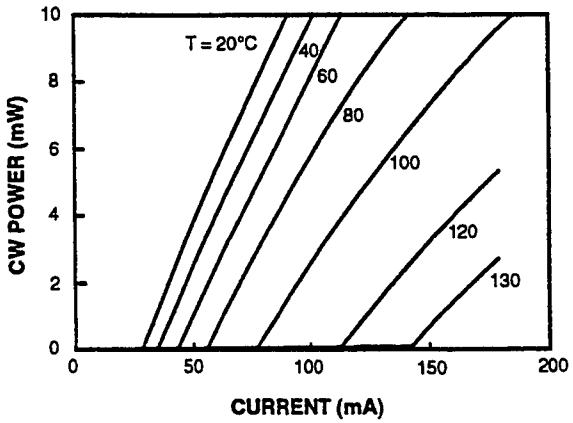


Fig. 4. CW output power vs current of a GaInAsSb/AlGaAsSb ridge-waveguide laser at temperatures between 20 and 130°C.

3. InAsSb/InAlAsSb QW lasers

For 4-μm emission, InAsSb was chosen for the active layer because it is stable at the growth temperature and is easier to grow than metastable GaInAsSb alloys with a similar bandgap energy. For the barrier, InAlAsSb was chosen because it provides adequate confinement for both the electrons and holes. Due to a lower valence-band position of InAsSb, AlGaAsSb is not suitable for the barrier. The following laser structure was grown by MBE: 1-μm-thick n-GaSb buffer, 3-μm-thick n-$AlAs_{0.08}Sb_{0.92}$ cladding, active region consisting of ten 15-nm-thick $InAs_{0.85}Sb_{0.15}$ active wells and eleven 30-nm-thick $In_{0.85}Al_{0.15}As_{0.86}Sb_{0.14}$ barriers, 3-μm-thick p-$AlAs_{0.08}Sb_{0.92}$ cladding, and 50-nm-thick p^+-GaSb cap. Double-crystal x-ray diffraction measurement of the laser structure showed some broadening of the satellite peaks, indicating that the interfaces are not very smooth.

Broad-stripe lasers 100 μm wide were fabricated by using SiO_2 patterning. Lasers were mounted junction-side up on Cu heat sinks using In, and loaded into a dewar for low-temperature measurements. Pulsed J_{th} of a 1000-μm-long device for temperatures between 80 and 165 K is plotted in Fig. 5. For comparison, data for the best DH lasers emitting at 3.9 μm are also plotted in the figure. At 80 K, the value of J_{th} for the QW device is 78 A/cm^2. The characteristic temperature T_0 up to 120 K is 30 K, which is larger than the 20 K observed for the DH lasers emitting at the same wavelength.[11] Both the lower J_{th} and higher T_0 for the QW devices indicate that the Auger recombination, believed to be the limiting mechanism for 4-μm lasers, has been decreased by the employment of the strained QW structure. As the temperature is increased above 120 K, T_0 becomes smaller. At the maximum operating temperature of 165 K, the value of J_{th} is 3.5 kA/cm^2.

Figure 6 shows the cw power vs current for the same device. The maximum power at 80 K is 30 mW/facet, which is much higher than 24 mW obtained for the DH lasers with HR/AR coatings and junction-down mounting.[11] The highest cw operating temperature is 123 K, which is higher than 105 K obtained for the 60-μm-wide DH devices mounted junction-side down. Ridge-waveguide lasers 15 μm wide were fabricated. At 80 K, the cw threshold current of a 1000-μm-long device is 35 mA. The device operated cw up to 128 K. The far-field pattern in the transverse direction has an FWHM of ~60°. In the lateral direction, the far-field pattern shows a single lobe with an FWHM of ~15°.

4. Conclusions

The maximum cw operating temperature of III-V diode lasers as a function of wavelength is plotted in Fig. 7. It is clear that the operating temperature decreases rapidly as the wavelength is increased. The performance degradation at longer wavelengths may be mainly due to Auger recombination, which increases

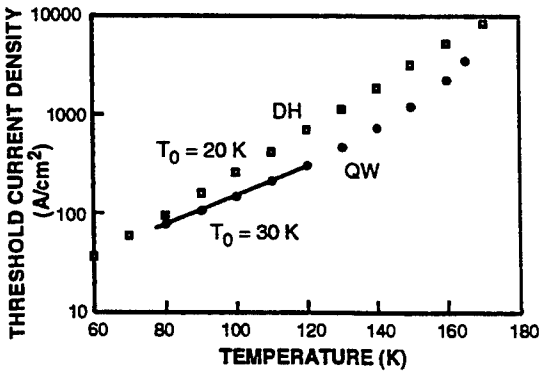


Fig. 5. Pulsed threshold current density of InAsSb/InAlAsSb QW and InAsSb/AlAsSb DH lasers as a function of temperature.

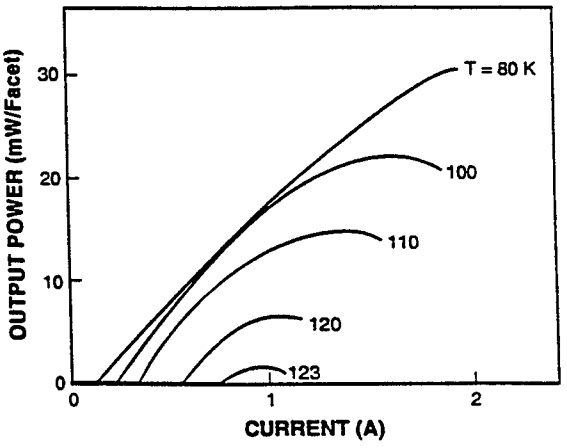


Fig. 6. CW power vs current of InAsSb/InAlAsSb QW laser at several temperatures.

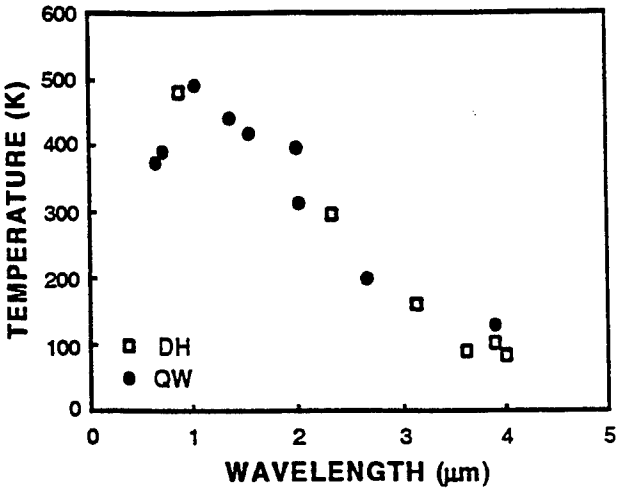


Fig. 7. Maximum cw operating temperature vs emission wavelength of III-V diode lasers.

exponentially as the wavelength is increased. The strained QW lasers have shown much higher performance than DH lasers at ~2 μm, not only in J_{th} but also in T_0. This improvement suggests that the Auger recombination is substantially reduced by the employment of the strained QW structures. At ~4 μm, work has just begun to adopt the strained QW structures. Already we have obtained modest improvements over DH lasers in both J_{th} and T_0. It should be possible to obtain much higher performance by optimizing the device structure and the growth conditions.

References

1. H. K. Choi, G. W. Turner, and S. J. Eglash, IEEE Photon. Technol. Lett. **6**, 7 (1994).
2. H. K. Choi and G. W. Turner, Appl. Phys. Lett. **67**, 332 (1995).
3. H. K. Choi and S. J. Eglash, Appl. Phys. Lett. **61**, 1154 (1992).
4. G. W. Turner, H. K. Choi, D. R. Calawa, J. V. Pantano, and J. W. Chludzinski, J. Vac. Sci. Technol. B **12**, 1266 (1994).
5. J. S. Major, Jr., D. W. Nam, J. S. Osinski, and D. F. Welch, IEEE Photon. Technol. Lett. **5**, 594 (1993).
6. H. K. Choi, G. W. Turner, M. K. Connors, S. Fox, C. Dauga, and M. Dagenais, IEEE Photon. Technol. Lett. **7**, 281 (1995).
7. J. S. Major, Jr., D. W. Nam, J. S. Osinski, and D. F. Welch, IEEE Photon. Technol. Lett. **7**, 733 (1993).
8. H. K. Choi and S. J. Eglash. Appl. Phys. Lett. **59**, 1165 (1991).
9. H. Lee, P. K. York, R. J. Menna, R. U. Martinelli, D. Z. Garbuzov, S. Y. Narayan, and J. C. Connolly, Appl. Phys. Lett. **66**, 1942 (1995).
10. D. Z. Garbuzov, R. U. Martinelli, R. J. Menna, P. K. York, H. Lee, S. Y. Narayan, and J. C. Connolly, Appl. Phys. Lett. to be published.
11. H. K. Choi, G. W. Turner, and Z. L. Liau, Appl. Phys. Lett. **65**, 2251 (1994).

Far-Infrared Germanium Cyclotron Resonance Lasers

Erich Gornik, Wolfgang Heiss, and Karl Unterrainer
Institute for Solid State Electronics
Technische Universität Wien, A-1040 Vienna, Austria

Abstract

p-type Germanium in crossed magnetic and electric fields is used as a continuously tunable laser source in the far-infrared. We are able to achieve laser action in a tuning range from 28 to 76 cm^{-1} by varying the magnetic field between 1.4 T and 3.7 T. The laser output consists of a single line having a width of 0.25 cm^{-1} and a maximum power of about 300 mW for a pulse width of 1 µsec.

p-type Germanium in crossed electric and magnetic fields as a source of stimulated tunable emission in the far infrared (FIR) has become a subject of intensive studies /1/. The cyclotron resonance (CR) laser based on light hole transitions between Landau levels exhibits a narrowband spectrum which is linearly tunable by the magnetic field; the light - heavy hole laser is based on transitions between the light and the heavy hole band and shows a broadband emission spectrum.

An important requirement for establishing a negative absorption coefficient from inverted Landau levels (LL) is an unequal energy level spacing. In the valence band of Ge this is automatically the case, since the degeneracy of the Γ_8 band gives rise to the Luttinger (or "quantum") effects /2/. The Landau level spacing in this case is influenced also by the electric field. An inverted carrier distribution in the case of streaming motion in crossed electric and magnetic fields is predicted.

In high electric E and magnetic fields B for $E/B > \sqrt{2\hbar\omega_{op}/m^h}$, where $\hbar\omega_{op}$ is the optical phonon energy and m^h is the effective heavy hole mass, *streaming motion* can appear where the heavy holes are repeatedly accelerated collisionless to the optical phonon energy and scattered back to the origin /3/. There is a finite probability for heavy holes to scatter into the light hole Landau levels where the carriers are *accumulating* and having a longer life time for $E/B < \frac{1}{2}\sqrt{2\hbar\omega_{op}/m^\ell}$. This is one of the main processes of p-Ge lasers. Streaming motion of heavy holes leads to an increase of the population of light hole LL's. A population inversion between different LL's which is necessary for the CR laser is built up due to the depopulation of low lying LL's by ionised impurity scattering or due to mixing between light and heavy hole states, which leads to a reduction of the lower LL's lifetime due to streaming motion of the heavy holes /2/.

Laser crystals with two different acceptor concentrations are used, N_A-$N_D = 8x10^{12}$ cm^{-3} and N_A-$N_D = 6x10^{13}$ cm^{-3}. The laser samples are cut from the crystals to form a parallelepiped. The length of the samples parallel to the [1 1 0] crystallographic direction is between 20 mm and 40 mm. The cross section dimensions are 7 mm and 5 mm parallel to the [1 $\bar{1}$ 0] and to the [0 0 1] directions, respectively. All faces of the samples are polished and are parallel within 0.01°. Two mirrors are mounted at the sample endfaces to form an additional external resonator. The mirrors consist of 50 µm thick Mylar sheets coated by 100 nm Gold; one mirror has a central bore (diameter 1 mm) serving as output coupler.

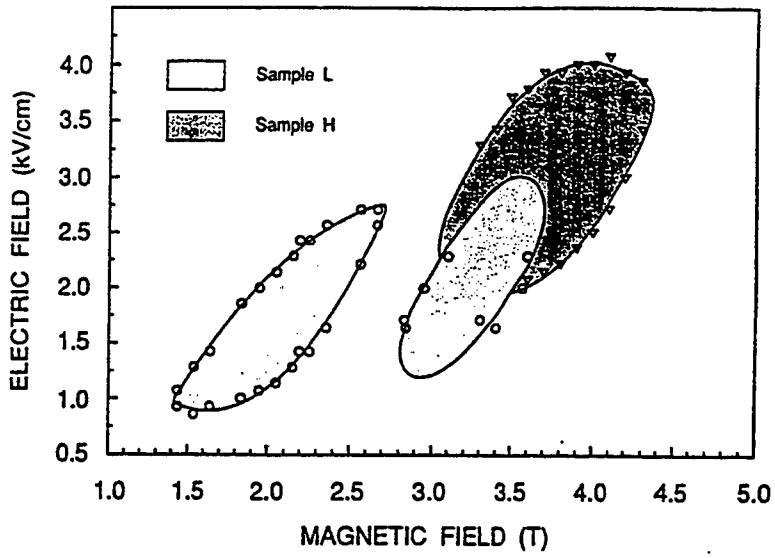


Fig. 1: Ranges of the stimulated FIR emission of low (L) and high (H) doped samples as a function of magnetic field for different electric fields.

The magnetic field is applied parallel to the [1 1 0] direction and the electric field parallel to the 7 mm wide side of the laser samples. Ohmic contacts are made by evaporating indium (with 5% gold) and alloying at 400°C /2/. The electric field is applied to the laser crystal in form of pulses with amplitudes of up to 2 kV and a duration of 1 µsec. All experiments are performed at 4.2 K , so the samples are immersed in liquid Helium at the center of a superconducting solenoid. A broadband Ge:Ga-detector with a peak sensitivity at about 90 cm^{-1} is used for the measurements of the integral emission intensity. In addition, a photoconductive GaAs/AlGaAs quantum well detector is used, which is sensitive between 10 cm^{-1} and 100 cm^{-1} . The emission spectra are analysed by a magnetic field tunable GaAs-detector. The Zeeman-split 1s-2p$^+$ shallow donor line is used for detection. This line is linearly tunable between 45 cm^{-1} and 130 cm^{-1} with magnetic fields between 1 T and 6.5 T. Due to the fact that the GaAs contains only one species of shallow donors, the absorption is extremely narrow (0.25 cm^{-1}) and thus the GaAs detector can be used as a high resolution spectrometer.

The stimulated emission from the lasers with an impurity concentration of N_A-$N_D = 8x10^{12}$ cm^{-3} is measured by a quantum well photoconductive detector. In Fig. 1 the range of the external fields where stimulated emission occurs is shown. For

electric fields higher than 1.6 kV/cm and magnetic fields higher than 2.75 T we have observed a second emission range. The stimulated emission of the second range extends up to a magnetic field of 3.7 T.

The observation of this second range was made possible by the use of a very homogeneous magnet. The magnetic field was constant within 0.3 % over a length of 4 cm. Therefore the variation $\Delta B/B$ of the magnetic field throughout the sample was smaller than the relative linewidth of the stimulated emission $\Delta\nu/\nu = 0.25\ cm^{-1}$. Thus absorption losses by non-inverted pairs of levels with a resonance energy similar to that of the inverted levels were eliminated /4/.

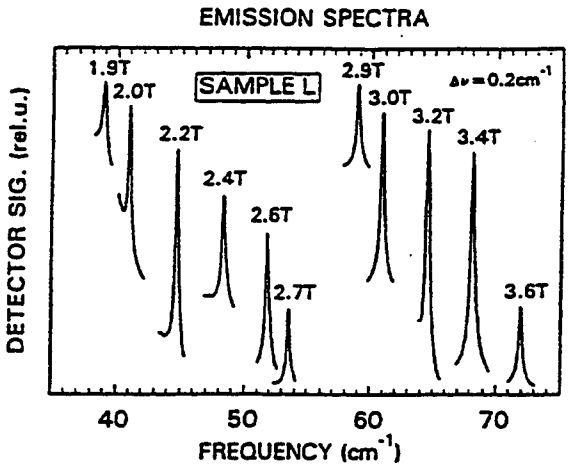


Fig. 2: Spectra of the low and high field emission range of low (L) doped lasers. The spectra consist of magnetically tunable single lines in each range. The applied electric field is varied: 1.7 kV/cm < E < 2.3 kV/cm for magnetic fields: 1.9 T < B < 2.7 T and 1.7 kV/cm < E < 2.5 kV/cm for 2.9 T < B < 3.6 T.

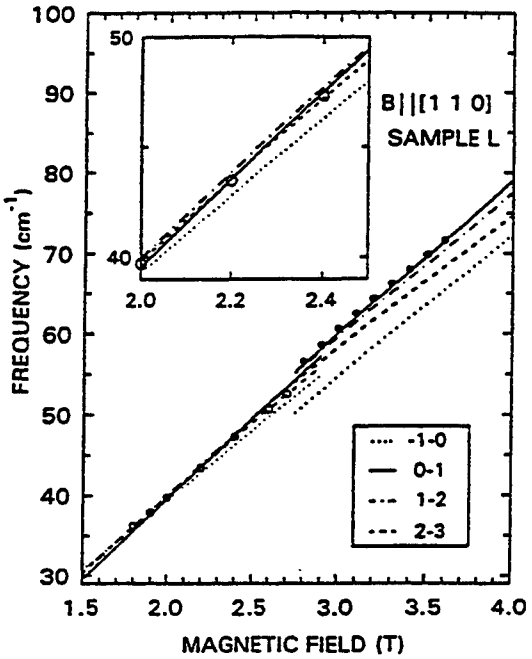


Fig. 3: Emission frequency of low doped lasers as a function of applied magnetic field. Circles indicate the experimental data. The lines show the theoretical results for n = -1 to 0, n = 0 to 1, n = 1 to 2, and n = 2 to 3 in the Landau level transitions in the b-set.

In Fig. 2 typical low and high field emission spectra are shown. For both ranges the spectra consist of a single line which tunes with magnetic field. We observe no linewidth difference, but the intensity is 2-3 times higher in the high field range. In Fig. 3 the emission frequency of sample L is plotted versus the applied magnetic field. The frequency tunes between 28 cm^{-1} and 76 cm^{-1}.

It is seen from Fig. 3 that the dependence of the emission frequency on the magnetic field shows a discontinuity between the two ranges at 2.75 T. The corresponding effective cyclotron mass m^{ℓ} (according to the expression for the CR frequency of the light holes $\hbar\omega_c = eB/m^{\ell}$) for the low range at 2.7 T is $m^{\ell} = 0.0472\ m_0$, that of the high range at 2.8 T is $m^{\ell} = 0.0461\ m_0$. It is clear that

different pairs of Landau levels are involved in the low field range (B < 2.7 T) and in the high field range (B > 2.8 T) laser transitions. Furthermore both tuning curves do not go through the origin if extended to zero magnetic field.

In samples with a high impurity concentration of N_A-N_D = 6x10^{13} cm^{-3} stimulated CR emission was found for magnetic fields between 3 T and 4.5 T (see Fig. 1). For this measurement an external resonator with two Mylar foils coated with Gold were used. The power of the stimulated CR emission for this configuration reached 150 mW. For maximum output power an external resonator consisting of a spherical mirror and a mesh output coupler is used where we have found an output power of 300 mW. In general the emission power of lasers with higher impurity concentration is one to two orders of magnitude larger than that of low doped lasers.

The maximum repetition rate for 1 µsec long pulses is 10 Hz, for 0.5 µsec pulses 25 Hz, and reaches a maximum repetition rate of 50 Hz for 0.25 µsec pulses. This upper limit for the repetition rate is caused by heating and could be improved by better heat sinking of the laser samples.

There is no linewidth difference to the spectra of the low doped lasers . The position of the line is changed in a range between 60 cm^{-1} and 90 cm^{-1} by varying the magnetic field. The emission frequency shows the same linear magnetic field dependence as that for the low doped lasers. The tuning curve, however, does not go through the origin if extended to zero magnetic field, this represents a change of the effective cyclotron mass m^{ℓ} of the light holes between 0.0467 m_0 (3 T) and 0.0469 m_0 (4 T). This increase of the effective mass is due to the non-parabolicity effect.

In addition, we have studied the influence of the direction of the electric field on the stimulated emission using laser samples with different angles between the applied field and the [1 $\bar{1}$ 0] direction. The samples are rotated by an angle of 20° and 42° to the [1 $\bar{1}$ 0] axis. In order to estimate the effective internal electric field we performed Hall measurements using samples with the same concentration and the same crystallographic orientation as for the laser crystals. In our standard laser crystals where the angle φ between the effective field and the [1 $\bar{1}$ 0] direction in the (1 1 0) plane is φ=55° stimulated emission is found for magnetic fields between 3.2 T and 4.2 T. For φ=13° and φ=35° no stimulated CR emission is found. The largest emission range is observed for φ=75°, where the range extends from 2.4 to 4.4 T. This corresponds to a tuning range from 48 cm^{-1} to 88 cm^{-1}. The emission frequency does not depend on the angle φ.

References:

/1/ "Infrared Semiconductor Lasers", ed. E. Gornik and A.A. Andronov, special issue of Opt. Quantum Electron. 23 (1991).

/2/ K. Unterrainer, C. Kremser, E. Gornik, C.R. Pidgeon, Yu.L. Ivanov, and E.E. Haller, Phys. Rev. Lett. 64, 2277 (1990).

/3/ S. Komiyama, Adv. Phys. 31, 255(1982).

/4/ K. Unterrainer, C. Kremser, C. Wurzer, E. Gornik, P. Pfeffer, W. Zawadzki, B. Murdin, and C.R. Pidgeon, Semiconductor Sci. Technol. 7, B604 (1992).

/5/ K. Unterrainer, Physica Scripta T49, 497 (1993).

Applications of Lead-Salt Semiconductor Lasers to Pollution Monitoring and Industrial Process Control

Edward A. Whittaker, Khosrow Namjou-Khaless and Chi Kong Ng
Department of Physics and Engineering Physics
Stevens Institute of Technology
Hoboken, NJ 07030

The prospect of tunable laser based instrumentation for spectrochemical analysis has tantalized the analytical community for many years but thus far few commercial instruments have appeared on the market. Methods based on tunable dye lasers have demonstrated tremendous sensitivity, including single atom or molecule detection in some cases but the expense and bulk of these devices precludes their use in all but the most specialized instruments.

In contrast, tunable diode lasers are compact and relatively low in cost compared to dye systems. From an analytical viewpoint, the most versatile such diode laser source available presently are the lead-salt devices which offer an operating wavelength which is band-gap tunable from approximately 3,000 cm^{-1} to 300 cm^{-1}. This range of frequencies makes possible the detection of many small molecules, free radicals and molecular ions of interest to such diverse fields as environmental monitoring and industrial process control.[1]

The principal drawback of the lead salt laser family is the necessity of cryogenic operation. With little likelihood for substantial improvement in this situation, lead salt lasers would seem a poor candidate for use in the development of compact, relatively inexpensive analytical instrumentation. Nonetheless, in our research we have taken the point of view that ultimately, a non-cryogenic, diode based tunable source will eventually emerge from the various diode laser research programs around the world and partially represented at this meeting. Consequently, we have focused our efforts on solving generic problems associated with the use of tunable diode lasers for highly sensitive detection of gas phase chemical species.

When contemplating the use of a laser source for sensitive analytical applications a number of issues arise. The first is to determine the best mode of detection, distinguishing first between scattering and absorptive methods. The former are exemplified for example by resonance fluorescence in which scattered laser light is detected usually at right angles to the incident light beam. Such approaches are inherently sensitive when the scattered light is

easily detected but unfortunately for infrared based detection this is not the case. We have therefore concentrated our efforts on measuring resonant light absorption.

While a number of methods are available to detect small absorbances, we have chosen to directly measure the amount of absorbed laser light using high frequency modulation spectroscopy. Using this method, absorbances as small as a few parts in 10^{-7} with a detection bandwidth of several kilohertz may be detected for suitably sharp molecular transitions.[2] The modulation approach has a number of advantages including simplicity of the optical setup, and compatibility with laser frequency locking methods.

Our efforts to translate this potential sensitivity into a practical spectroanalytic system were quickly thwarted by the presence of interference fringes induced by multiple reflections in the optical path from source, through the sample cell and onto the photodetector. To overcome the fringe limitation we developed an additional modulation scheme which combines high frequency (40 - 100 MHz) modulation for basic sensitivity with a low frequency (kHz) wavelength modulation which allows us to evade the fringes while preserving signal strength from the analyte molecule.[3] Using this method, we have demonstrated nanoTorr detection sensitivity for strong absorbers such as SF_6.[4]

Translating this figure into a fractional concentration limit of a particular species in a particular environment requires us to consider the detailed structure of the species infrared absorption spectrum, including the specific line strength of the transition, the line broadening parameters at play in the working environment, the possible blending of lines of a single species at working pressures and finally the overlap of the detected species spectrum with that of other species in the working environment.

Line blending is a particularly significant problem when detecting complex molecules such as volatile organic solvents. Many of these molecules have very strong infrared absorption lines which nevertheless blend together when detecting the molecule at atmospheric pressure as might be required for on-line analysis at a contaminated site clean-up operation. While somewhat less of a problem for Fourier Transform spectrometric analysis, line blending substantially reduces sensitivity for modulated laser methods which derive their sensitivity from detection of differential absorption. Practical detection schemes will thus most likely involve depressurizing the sample before measuring the absorption spectrum. We will present data which illustrates some of these issues.

Finally, the most problematic issue for laser based instrumentation is laser frequency measurement and control. In order to design an instrument that may reliably detect a particular species each time it is turned on, it is necessary for there to be some type of algorithm to return the laser to a known

frequency. We have explored a number of approaches to solve this problem. Our basic modulation techniques enable us to lock the laser to a particular resonance line.[5] Using this method, we have been able to lock the laser to the absorption line of a particular molecule and then track the molecule's concentration as a function of other parameters. In particular, we are able to monitor species formed in a silicon plasma etching reactor which are indicative of the state of the wafer process.[6] Such methods may prove useful for the sophisticated process control that the semiconductor industry is estimates will be required to meet projected device improvement curves.

While line locking gives us a satisfactory method to follow a particular species concentration once we have acquired the line, turn key operation of a system which reliably acquires the same line regardless of uncontrolled conditions such as environmental temperature and instrument turn on history is quite another matter. We have developed methods to find a particular line based on line pattern recognition but implementing such approaches in a reliable standalone system has proven quite difficult. We are currently exploring the use of thin film filters to improve upon this situation. Development of non-lead salt sources which take advantage of distributed feedback and other frequency control methods also offer promise in this area.

In summary, we have developed a number of generic approaches useful when employing tunable diode lasers for spectrochemical analytic applications. Using these methods we are able to detect absorption spectra free of interfering fringes caused by optical elements in the laser beam path and thereby implement practical detection schemes for use in environmental monitoring and gas phase based industrial process control. We have implemented these methods using tunable lead salt lasers but anticipate extending them to new infrared laser technology as it becomes available.

We acknowledge support from the National Science Foundation (Grant # DMI-9313320), the New Jersey Commission on Science and Technology through the Advanced Technology Center for Surface Engineering Materials, Princeton Electronic Systems, and McLaren-Hart, Incorporated.

References

1. "Optical diagnostics of low pressure plasmas", R. W. Dreyfus, J. M. Jasinski, R. E. Walkup, G. S. Selwyn, *Pure & Appl. Chem.* **57**, 1265 (1985).

2. "Quantum limited FM-spectroscopy with a lead-salt diode laser", P. Werle, F. Slemr, M. Gehrtz, C. Bräuchle, *Appl. Phys. B* **49**, 99 (1988).

3. "Novel etalon fringe rejection technique for laser absorption spectroscopy", H. C. Sun, E. A. Whittaker, *Appl. Opt.* **31**, 4998 (1992).

4. "Real-time *in situ* detection of SF_6 in a plasma reactor", H. C. Sun, E. A. Whittaker, *Appl. Phys. Lett.* **63**, 1035 (1993).

5. "Dynamic resonant peak locking scheme for diode laser modulation spectroscopy", H. C. Sun, E. A. Whittaker, *Opt. Eng.* **32**, 453 (1993).

6. "Sensitive plasma etching endpoint detection using tunable diode laser absorption spectroscopy", H. C. Sun, V. Patel, B. Singh, C. K. Ng, and E. A. Whittaker, *Appl. Phys. Lett.* **64**, 1035 (1994).

Extended Abstract (Student Paper)

Progress towards a Continous Wave Intervalence Band Germanium-Laser

A.M. Linhart, E. Bründermann and H.P. Röser
DLR, Institute for Space Sensor Technology, D-12489 Berlin, Germany
O.D. Dubon, W.L. Hansen and E.E. Haller
Lawrence Berkeley National Laboratory and University of California, Berkeley, CA 94720, USA

We are developing a compact, tunable, easy-to-operate continous-wave intervalence band (IVB) Ge laser. It will be a device suitable as local oscillator in heterodyne receivers for the study of far-infrared-emission from sources encountered in astronomy, in atmospheric physics, in material science and in chemical dynamics. The current state of development of p-Ge lasers is still far from the desired goals stated above. We will report on progress towards a cw laser involving advanced sample processing, doping, geometries and heat transfer.

I. Operating Principle and Choice of Materials

Laser action of an IVB Ge device is based on an inversion of the population of holes the light and the heavy hole bands. The Ge-laser is operated in crossed electric and magnetic field at liquid helium temperature. The electric field is pulsed, leading to a maximum emission pulse of typically 6 µs pulslength and reported repetition rates of a few Hz leading to a low duty cycle (pulslength times repetition rate) in the order of 10^{-5} [1].

The choice of the Ge-crystal material in respect to acceptor type and doping concentration strongly influences the gain of the laser. A high gain leads to a high duty cycle, large generation zone in the E-B-field-plot, high output power and short delay time until the laser pulse starts after excitation with the electric pulse. To generate a quantitative understanding of how the acceptor type and doping concentration affect the laser performance we began with characterizing the Ge-samples with variable temperature Hall-Effect measurements from 300 K to 6 K. The freeze-out-curve of the free holes gives the majority acceptor and minority donor concentrations and hence the compensation [5]. From tests with these crystals as lasers, we found that the gain increased with decreasing doping concentration, leading to a larger generation zone.

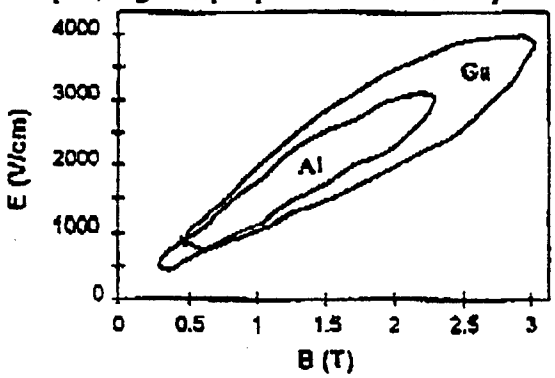


Fig 1: Generation zones of IVB-emission of a low doped Ge:Ga (N_a=4.5x10^{13} cm^{-3}) and a higher doped Ge:Al (N_a=1.4x10^{14} cm^{-3}) crystal of compurable sizes. Lower doping increases the gain.

This is illustrated by the example of a low doped Ge:Ga crystal (N_a=4.5x10^{13} cm^{-3}) and a higher doped Ge:Al crystal (N_a=1.4x10^{14} cm^{-3}) of comparable size and shape (Fig. 1). The acceptor type does not make much difference in this case, as the impurity levels of both dopant types (Ge:Ga and Ge:Al) have nearly the same energies. So far we have not arived at a lower limit for the doping. The increased gain can be explained with reduced light hole scattering, a process which depopulates the light hole band, decreasing the degree of inversion.

Growth and Characterization of PbSeTe/PbSnSeTe/PbSeTe Double Heterostructures

I-Na Chao, Shu Yuan, and Patrick J. McCann
School of Electrical Engineering
University of Oklahoma
Norman, OK 73019

The recent fabrication of III-V semiconductor quantum cascade (QC) lasers that emit beyond the near-infrared range [1] has attracted considerable attention. This interest is due in part to the potential applications for these long wavelength lasers as light sources in high-resolution infrared spectrometers. The versatility of such laser-based infrared spectrometers in uses ranging from air pollution monitoring [2] to medical diagnostics [3], however, is limited by the tuning range of the laser light source. In this respect, lasers made from IV-VI semiconductor alloys have a significant advantage over III-V semiconductor QC lasers since they can be temperature tuned at a rate of 0.46 meV per degree whereas QC lasers have shown a tuning rate of only about 0.05 meV per degree. Furthermore, IV-VI semiconductor alloy composition can be adjusted to cover regions of the infrared spectrum from 3 μm to over 30 μm. $Pb_{1-x}Eu_xSe_{1-y}Te_y$ alloys, for example, have been used to fabricate lasers covering the 3 μm to 6 μm spectral range [4], while the $Pb_{1-x}Sn_xSe_{1-y}Te_y$ alloy system shows promise for fabrication of lasers covering the 6 μm to 30 μm spectral range [5]. This article discusses growth and characterization of $PbSe_{0.78}Te_{0.22}/Pb_{1-x}Sn_xSe_{1-y}Te_y/PbSe_{0.78}Te_{0.22}$ triple-layer structures and shows that this system is suitable for fabrication of temperature tunable double heterostructure (DH) lasers.

Lattice-matched $PbSe_{0.78}Te_{0.22}/Pb_{1-x}Sn_xSe_{1-y}Te_y/PbSe_{0.78}Te_{0.22}$ triple-layer structures with different tin, x, contents in the middle layer were grown on polished (100) BaF_2 substrates, see Figure 1, using previously developed liquid phase epitaxy (LPE) growth techniques [6, 7]. A schematic diagram of the LPE growth procedure is shown in Figure 2. The first ternary layer and the second quaternary layer are undoped, while the third ternary layer is doped with thallium acceptor impurities. Based upon Hall effect characterization of single layers [8] this doping is expected to yield a p-n junction at the second heterojunction. The band diagram for this triple layer structure is shown in Figure 3.

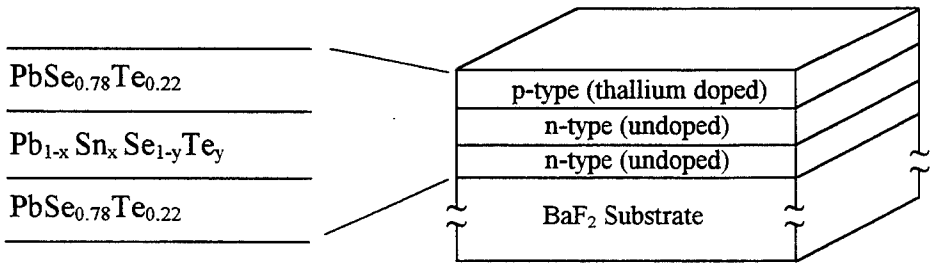


Figure 1: Lattice-matched double heterostructure (DH) grown by liquid phase epitaxy (LPE). Lasers are fabricated by removing the BaF_2 substrate and then cleaving the epilayers to form IV-VI semiconductor Fabry-Perot resonant cavities.

Growth of IV-VI semiconductor heterostructures on (100) BaF_2 substrates is motivated by the prospects of fabricating high operating temperature DH lasers. Presently the highest continuous wave (cw) operating temperature for IV-VI semiconductor DH lasers grown on PbTe substrates is 203 K [4]. Thermal modeling analysis of these lasers [9] suggests that cw operating temperatures can be increased to greater than 260 K, thus allowing thermoelectric cooling, if the thermally

resistive PbTe substrate is replaced by a copper heat sink. Growth on BaF_2 allows such laser fabrication since the BaF_2 substrate can be easily removed from the epilayer structure by dissolution in water. The resulting laser can thus have nearly ideal active region heat dissipation since the device consists of just the epilayer device structure sandwiched between two copper heat sinks. An epilayer transfer procedure that also employs a cleaving jig to form Fabry-Perot cavities [10] is presently under development at the University of Oklahoma using the LPE-grown materials discussed here. Thermoelectrically-cooled operation of IV-VI semiconductor tunable infrared lasers should be possible once this new procedure is fully developed.

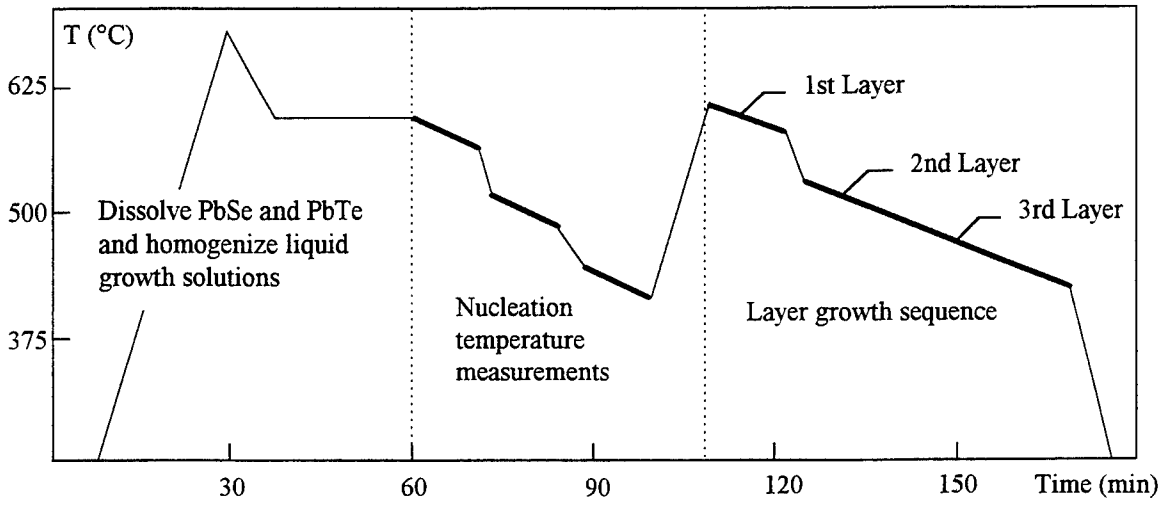


Figure 2. Schematic representation of the LPE growth sequence used in this study. A 2-degree-per-minute cooling ramp (indicated by thicker lines) is employed for growth solution nucleation temperature measurements and layer growth. The last layer is grown at the lowest temperature to minimize interdiffusion at the heterojunctions.

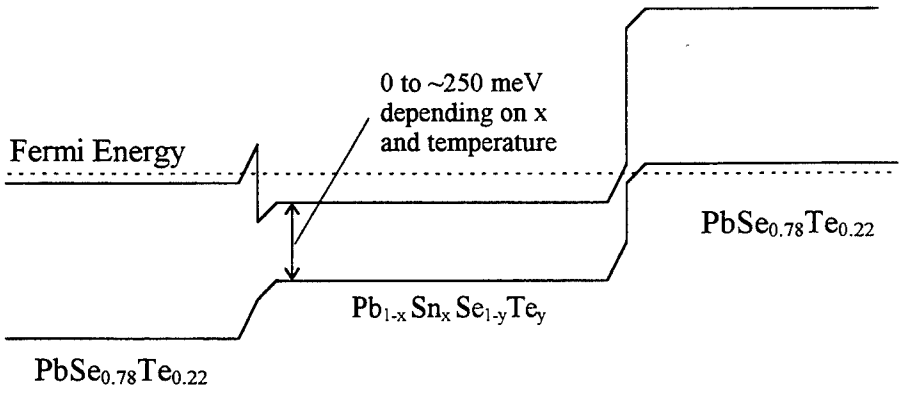


Figure 3: Equilibrium energy band diagram for the triple-layer structures. Quaternary layers with different tin contents, x, were grown for this study. Group VI vacancy defect levels in the conduction band and thallium defect levels in the valence band are believed to cause both n-type and p-type layers, respectively, to be degenerate [8].

An important factor in fabricating DH lasers from LPE-grown material is growth solution wipe-off. Good wipe-off is particularly critical for good epilayer transfer and substrate removal since solidified drops of Pb-rich growth solution on the top epilayer surface will prevent good adhesion with the copper heat sink. Considerable experimentation has shown that the key parameters to control for good growth solution wipe-off are (1) proper BaF_2 substrate preparation, which includes

a chemo-mechanical polish, and (2) maintaining a tight tolerance of between 5 and 40 microns on the clearance between the substrate surface and the slider surface. These procedures are now routinely used by a number of growers using two separate LPE systems to grow PbSeTe/PbSnSeTe/PbSeTe double heterostructures with excellent growth solution wipe-off. LPE growth yields for experienced growers at the University of Oklahoma are now well over 70%.

A vacuum bench Bruker, model IR/98, Fourier transform infrared (FTIR) spectrometer equipped with a graphite globar, KBr beam splitter, and a $Hg_{1-x}Cd_xTe$ detector having a peak detectivity at 16 μm, was used to measure transmitted radiation through LPE-grown heterostructure samples. It was not necessary to remove the BaF_2 substrate since it is transparent to infrared radiation up to ~13 μm (770 cm^{-1}). Room temperature transmission spectra for three different samples illustrating the effects of adding ternary cladding layers to a $Pb_{1-x}Sn_xSe_{1-y}Te_y$ quaternary active layer, where x is about 5%, are shown in Figure 4. The onset of absorption, which corresponds to the bandgap of the quaternary layer [11], shifts from ~200 meV for the single layer to ~220 meV for the double and triple layer structures suggesting that less tin is incorporated in the quaternary layer when the growth temperature is reduced. (Preliminary photoluminescence experiments also suggest that lower quaternary layer growth temperatures result in larger bandgaps, i.e. less tin). A lower liquid-to-solid segregation coefficient for tin at lower growth temperatures is supported by the shape of the Pb-Sn-Se phase diagram [12]. The multilayer structures in Figure 4, as well as all other multilayer structures measured so far, also exhibit a second lower energy absorption edge with an onset at ~100 meV. At this time, we believe that this lower energy absorption edge is due to excitation of confined electrons from the band edge to above the Fermi energy in the degenerate n-type quaternary layer. If so, the ~100 meV energy corresponds to the location of the Fermi energy with respect to the bottom of the conduction band of the quaternary layer at the first heterojunction, see Figure 3.

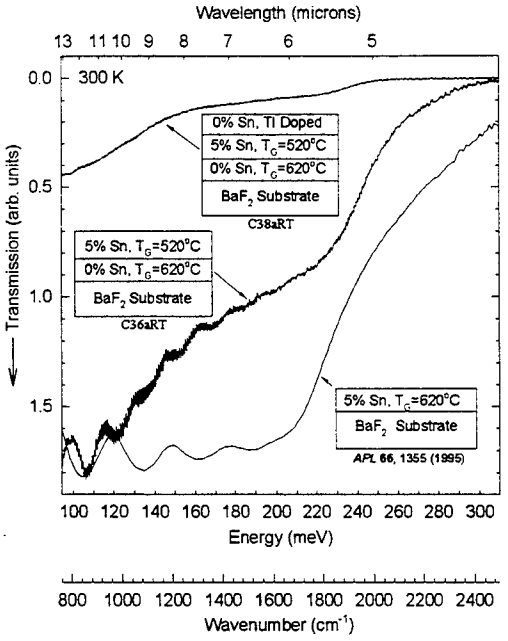


Figure 4: FTIR transmission spectra for three different LPE-grown samples. Greater absorption for the triple layer structure is probably due to more free carrier absorption. Fabry-Perot interference fringe spacing for the two layer sample yields a total epilayer thickness of 6.2 μm (total growth time=20 min). The single layer is 2.2 μm thick (total growth time=4 min) [11].

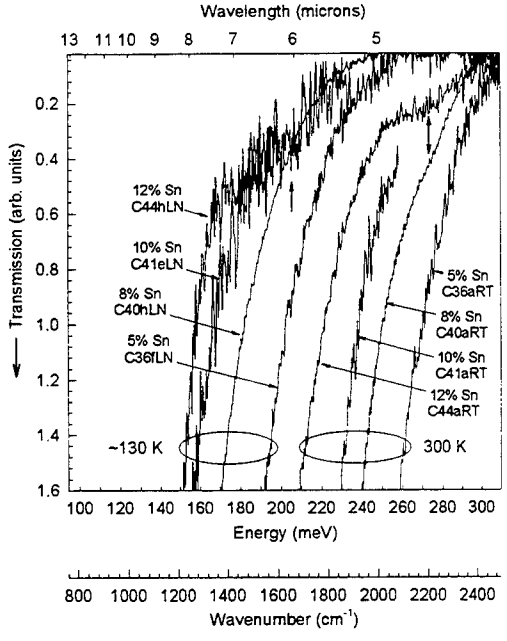


Figure 5: FTIR transmission spectra for four LPE-grown samples having different tin contents. Spectra, some of which are truncated for clarity, are grouped for measurements at 300 K and at ~130 K. Absorption edges for the larger bandgap ternary cladding layers are marked with arrows. Note the large spectral range covered by these laser structures.

FTIR transmission spectra for four different multilayer structures, where the laser active region layers (the quaternary $Pb_{1-x}Sn_xSe_{1-y}Te_y$ alloy) were grown from growth solutions containing 5%, 8%, 10%, and 12% tin, are shown in Figure 5. As expected, the absorption edges shift to lower energies as the tin content increases. This trend is present at both room temperature and at ~130 K. The strong dependence of IV-VI semiconductor bandgap on temperature is also quite apparent from these data. In addition, absorption edges corresponding to the ternary cladding layers, marked by arrows in Figure 5, can be seen in some of the spectra. Note the uniform shift in the absorption edges with temperature for both the quaternary active layer and the ternary cladding layers of the 12% Sn sample (#C44). This shows that band edge discontinuities are preserved as the temperature changes, an important consideration for good laser tuning characteristics.

In summary, lattice-matched IV-VI semiconductor $PbSe_{0.78}Te_{0.22}/Pb_{1-x}Sn_xSe_{1-y}Te_y/PbSe_{0.78}Te_{0.22}$ double heterostructures were grown by LPE on polished (100) BaF_2 substrates with excellent growth solution wipe-off. FTIR transmission experiments performed on a number of multilayer samples with different tin concentrations in the quaternary layer clearly show that adding tin as well as lowering the temperature reduces the bandgap of the quaternary active region. These data show that lasers made from the structures studied here can span the 5 μm to 8 μm (2000 cm^{-1} to 1250 cm^{-1}) spectral range with an expected tuning rate of approximately 0.46 meV per degree.

Acknowledgment

This work was supported by the National Science Foundation, grant number DMR-9416871.

References

[1] Sirtori, J. Faist, F. Capasso, D. L. Sivco, A. Hutchinson, and A. Y. Cho, "Quantum Cascade Laser with Plasmon-Enhanced Waveguide Operating at 8.4 μm Wavelength", *Appl. Phys. Lett.* **66**, 3242 (1995).

[2] M. Loewenstein, "Diode Laser Harmonic Spectroscopy Applied to *In Situ* Measurements of Atmospheric Trace Molecules", *J. Quant. Spectros. Radiat. Transfer* **40**, 249 (1988).

[3] P.S. Lee, R.M. Schreck, B.A. Hare, and J.J. McGrath, "Biomedical Applications of Tunable Diode Laser Spectrometry", *Annals of Biomed. Eng.* **22**, 120 (1994).

[4] Z. Feit, D. Kostyk, R. J. Woods, and P. Mak, "Single-Mode Molecular Beam Epitaxy Grown PbEuSeTe/PbTe Buried Heterostructure Diode Lasers for CO_2 High-Resolution Spectroscopy", *Appl.Phys.Lett.* **58**, 343 (1991).

[5] P. J. McCann and L. Li, " $Pb_{1-x}Sn_xSe_{1-y}Te_y$ Alloys Lattice Matched with BaF_2: A New Materials System for Far-Infrared Device Fabrication", International Device Research Symposium, Charlottesville, VA, December 1-3, 1993.

[6] P. J. McCann and S. Aanegola, "The Role of Graphite Boat Design in Liquid Phase Epitaxial Growth of $PbSe_{0.78}Te_{0.22}$ on BaF_2 ", *J. Crystal Growth* **141**, 376 (1994).

[7] P. J. McCann and D. Zhong, "Liquid Phase Epitaxy Growth of $Pb_{1-x}Sn_xSe_{1-y}Te_y$ Alloys Lattice Matched with BaF_2 ", *J. Appl. Phys.* **75**, 1145 (1994).

[8] P. J. McCann, S. Aanegola, and J. E. Furneaux, "Growth and Characterization of Thallium and Gold Doped $PbSe_{0.78}Te_{0.22}$ Layers Lattice Matched with BaF_2 Substrates", *Appl.Phys.Lett.* **65**, 2185 (1994).

[9] P. J. McCann and K. R. Lewelling, "Prospects for High Operating Temperature IV-VI Semiconductor Tunable Diode Lasers", International Symposium on Optical Sensing for Environmental and Process Monitoring, Air and Waste Management Association, San Francisco, CA, September 25-27, 1995.

[10] P. J. McCann, "High Temperature Semiconductor Lasers", U. S. Patent Pending, Serial Number 08/234,775, Filed April 28, 1994, Allowed May 22, 1995. To issue ~September, 1995.

[11] P. J. McCann, L. Li, J. Furneaux, and R. Wright, "Optical Properties of Ternary and Quaternary IV-VI Semiconductor Layers on (100) BaF_2 Substrates", *Appl.Phys.Lett.* **66**, 1355 (1995).

[12] P. J. McCann, J. Fuchs, Z. Feit and C. G. Fonstad, "Phase Equilibria and Liquid Phase Epitaxy Growth of PbSnSeTe Lattice Matched to PbSe", *J. Appl. Phys.* **62**, 2994 (1987).

Carrier recombination in 6H-SiC pn structures fabricated by different technological techniques: phenomena, parameters and centers

A.M.Strel'chuk
A.F.Ioffe Physico-Technical Institute, Russian Academy of Sciences, 26 Polytekhnicheskaya st., St. Petersburg 194021, Russia
Phone: (812) 247 93 14, FAX: (812) 247 10 17

In this study a review, systematization and comparative analysis of the carrier recombination phenomena (as revealed in current-voltage, photoelectrical and transient current characteristics) and carrier recombination parameters (lifetimes and diffusion lengths of non-equilibrium charge carriers) is given for characterization of recombination centers in SiC pn structures fabricated by different technological techniques. The basic material used for preparation of the pn structures was Lely substrate with ongrown n-type conductivity epitaxial layers (N_d-$N_a \approx 10^{16}$-10^{18} cm^{-3}) grown by sublimation epitaxy [1] or container-free liquid-phase epitaxy [2]. The p-type conductivity layers were prepared by sublimation epitaxy (SE structures) onto or ion-implantation (II structures) [1] into n-type sublimation epitaxial layers and, as well, by container-free (LPE structures) or low-temperature [3] liquid-phase epitaxy onto n-type layers grown by container-free liquid-phase epitaxy.

1.Current-voltage characteristics and the steady-state lifetimes. In the study of the forward current-voltage (I-V) characteristics there were identified and analyzed the currents with exponential dependence on voltage and reciprocal temperature: $J=J_0\exp[qU/(nkT)]$, $J_0 \sim \exp[-E_a/(kT)]$, where n is temperature-independent. In the current range $J \approx 10^{-6}$-10^{0} A/cm^2, usually, $n \approx 2$ for the lower portion of the I-V characteristics ($J \leq 10^{-3}$ A/cm^2) and assumes fractional values between 1 and 2 ($n \approx 3/2$ or 4/3 or 6/5) for the upper portion ($J \geq 10^{-3} A/cm^2$) [4,5]. The present study emhpasizes that in structures fabricated by different methods portions of the I-V characteristics measured at the same temperature which had identical values of n (i.e., corresponding to the identical type of current) were found to be shifted relative to each other along the voltage axis, revealing different values of J_0 (fig.1a); moreover identical current types in structures fabricated by different methods were characterized with different values of the activation energy E_a (fig.1b).

These currents were in agreement with the models of current due to carrier recombination in the space charge region of pn junction via a deep level near the middle of the band gap [6] ($n \approx 2$) or via a multilevel center with one deep and one or more shallow levels [7] (fractional values of n). Steady-state lifetime τ_s is a parameter in the models. Application to the experimental data of models [6] and [7] showed that the values of τ_s at room temperature were different in different structure types (for example, larger in LPE compared with SE and II structures) and τ_s rises with temperature at different rates in different structure types (steeper in SE and II compared with LPE structures) because of different temperature dependences of the effective capture cross-section of the recombi-

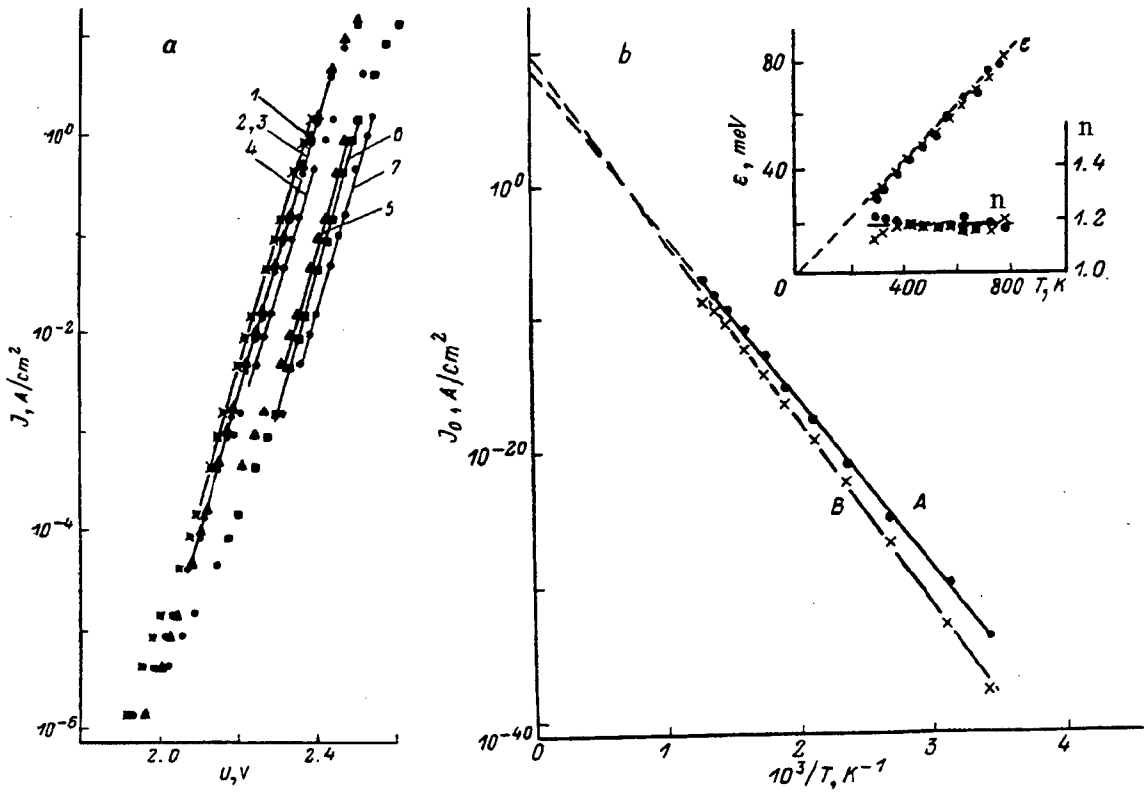


Fig. 1. a) Room temperature current-voltage characteristics $J=J_0\exp[qU/(nkT)]$ of several pn structures with n=6/5: 1-4 - II structures, 5-7 - LPE structures; b) temperature dependence of the preexponential factor J_0, of the characteristic energies $\varepsilon=nkT$, and of the coefficient n for II structure (A) and LPE structure (B) [5].

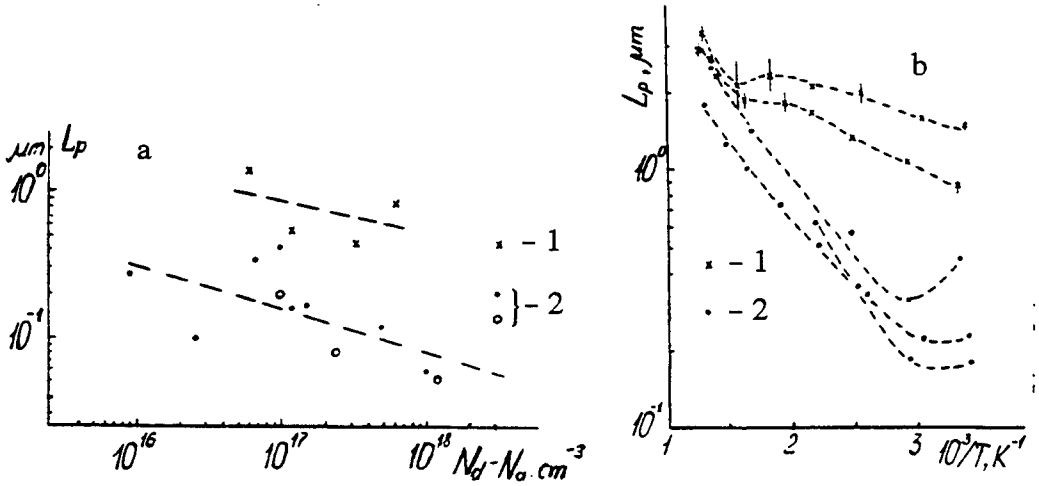


Fig. 2. Dependence of hole diffusion length in LPE structures (1) and in SE structures (2) on a) uncompensated donor concentration N_d-N_a at room temperature and b) reciprocal temperature ([8]).

nation center and/or different depths of the shallow levels of the multilevel center (this depth is roughly 100-200 meV and the levels are more shallow in LPE structures compared with SE and II structures).

2.Photoelectrical characteristics and diffusion lengths. The main results were obtained [8] from measured data on the photo current as a function of the thickness of the

space charge region of the pn junction illuminated with weakly absorbed light corresponding to the fundamental absorption edge. It was shown that for LPE structures the room temperature minority carrier diffusion length L≈0.4-1.5 μm and for SE structures L ≈0.1-0.4 μm (fig.2a; L characterizes the electrical transport and recombination in the quasi neutral region). L increased with temperature and at 800K amounted to 2-3 μm both in SE and LPE structures (fig.2b), i.e. in SE structures the rate of increase is higher. This increase in L with temperature may be explained only with an increase of minority carrier lifetime τ. The activation energies of τ deduced ignoring the temperature dependence of the carrier mobility were 240 meV at 350-800K and 100-120 meV at 300-600K for SE and LPE structures, respectively. These energies provide rough estimates of the depth value or/and the measure of the temperature dependence of the capture cross-section of a recombination center.

3.Characteristics of transient currents and the relaxation lifetimes. The relaxation lifetime τ_r was determined in a study [9] of transient currents occurring as a result of switching from the forward to reverse bias. An analysis of the experimental data (dependences of the constant-current-phase duration on the ratio of the forward and reverse currents) indicated that at room temperature $\tau_r \approx 2$ ns for the SE structures and $\tau_r \approx$ 20-30 ns for the LPE structures (i.e. the data for τ_r are similar to those for τ_s and L).

4.Conclusion. The study of the carrier recombination phenomena and carrier parameters in the SiC pn structures fabricated by different technological techniques showed that whatever the region where the recombination lifetime was measured (the space-charge region or the quasi neutral region of the structure): a) the room-temperature lifetime of non-equilibrium charge carriers is different in different structure types; b) with increasing temperature the lifetime increases in all structure types, though at a different rate; c) depending on prevailing conditions, the levels dominating the recombination process may be deep centers (near midgap) and/or the levels of a multi-level center and/or shallow levels (depth of about 100-300 meV); the temperature dependence of the lifetime is determined by temperature variation of the effective capture cross-section and/or by thermalization of shallow levels.

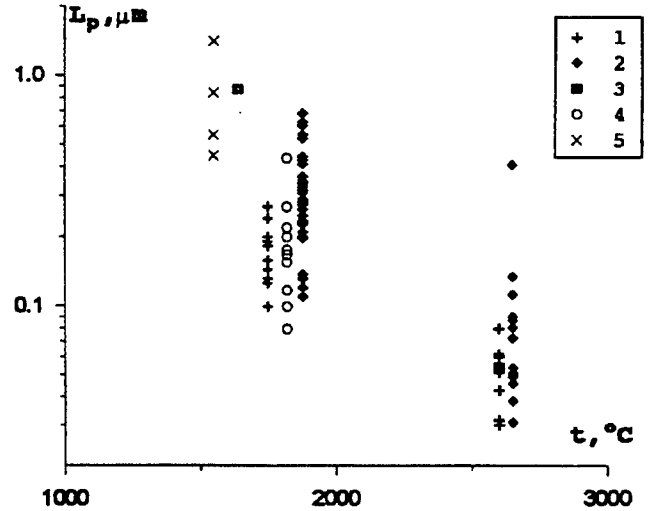


Fig. 3. Hole diffusion lengths in 6H-SiC at room temperature: 1 - following Ref.10, 2 - following Ref.11, 3 - following Ref.12, 4 - SE structures, 5 - LPE structures; the horizontal axis reprezents the characteristic temperature of the process (growth temperature of the epitaxial layer or annealing temperature).

Observations of the effect of the fabrication technology of pn structures on the carrier lifetime, lead one to suggest that a connection exists between the above parameters and one of the major characteristics of a technological process, the growth temperature of the epitaxial layer (1800-1900 °C for SE and 1500-1600 °C for LPE structures) or annealing temperature (fig.3). In particular, the lifetime is larger and its rise with temperature weaker in structures fabricated at lower temperatures. The nonradiative recombination center determining the lifetime may be tentatively considered as an intrinsic defect of the semiconductor crystal lattice.

This work was supported in part by the US Department of Defense.

References

1.Anikin M.M. et al, 1984, Pisma Zh.Tekh.Fiz., **10**, 1053 [in Russian].
2.Dmitriev V.A. et al, 1985, Pisma Zh.Tekh.Fiz., **11**, 238 [in Russian].
3.Dmitriev V.A. et al, 1992, Springer Proc. in Physics, **56**, 307.
4.Anikin M.M. et al, 1989, Sov.Phys.Semicond., **23**, 405.
5. Anikin M.M. et al, 1989, Sov.Phys.Semicond., **23**, 1122.
6.Sah C.-T. et al, 1957, Proc. IRE, **45**, 1228.
7.Evstropov V.V. et al, 1984, Fiz Tekh.Poluprovodn., **18**, 1852 [in Russian].
8.Anikin M.M. et al, 1992, Springer Proc. in Physics, **56**, 269.
9.Anikin M.M. et al, 1991, Sov.Phys.Semicond., **25**, 289.
10.Ballandovich V.S., Violina G.N., 1981, Fiz Tekh.Poluprovodn., **15**, 1650 [in Russian].
11.Sankin V.I. et al, 1982, Fiz Tekh.Poluprovodn., **16**, 1325 [in Russian].
12.Ikeda M. et al, 1979, J. Appl. Phys., **50**, 8215.

LOW-FREQUENCY NOISE IN 4H-SiC JFETs

J.W.Palmour*, M.E.Levinshtein**, S.L.Rumyantsev** and G.S.Simin**

* CREE Research Inc., 2810 Meridian Parkway, Durham, NC 27713, USA
**A.F.Ioffe Institute of Russian Ac. of Sci., 194021, St.-Petersburg, Russia

Abstract

Low frequency noise in 4H-SiC JFET has been investigated for the first time. JFETs with a buried p^+n junction gate were manufactured by CREE Research Inc. Very low noise level has been observed in the FETs. At 300 K the value of Hooge constant α is as small as $\alpha \sim 10^{-5}$ and the α value can be decreased by an appropriate annealing to $\alpha \sim 2 \cdot 10^{-6}$. It has been shown that even these extremely low noise values are determined not by the volume noise sources but by the noise at the SiC-SiO_2 interface.

I. Introduction

In recent years 4H-SiC polytype has received much attention because of its ability to be used for high power microwave devices [1-3]. The electron mobility in 4H-SiC is about twice as high as that of 6H-SiC. Additionally, 4H-SiC is practically isotropic [4], and the activation energy of the donor dopants is lower than in 6H-SiC.

For microwave devices the level of low frequency noise is one of the important parameters which determines the applicability of the device for microwave communication systems.

In this paper the low frequency noise in 4H-SiC FETs has been investigated for the first time.

II. Results and Discussion

In this research 4H-SiC FETs with a buried p^+n junction gate manufactured by Cree Research Inc. were used. The design of the devices is basically the same as that reported previously for 6H-SiC JFETs [5]. On the p^+ gate side the channel is bounded by the space-charge region of a p^+n junction. On the opposite side the channel is bounded by an oxide layer. It will be shown that the oxide is usually negatively charged and on the oxide side the channel is also bounded by a space-charge region. Hence the real thickness of the channel is $h=h^o-d_{pn}-d_o$ [5], where h^o is the geometrical thickness of the channel, d_{pn} is the thickness of the space-charge region near the gate p^+n junction, d_o is the thickness of the space-charge region near the oxide. The gate length is $L=5\mu m$, the gate width is $W=1mm$, the doping concentration is $N_d - N_a \cong 10^{17} cm^{-3}$ at 300 K.

Fig.1(a) shows the temperature dependencies of the spectral density fluctuations S_I/I^2 in the temperature range of 300 - 600 K. Unlike the 6H-SiC reported previously [4] there are no pronounced maxima on S-T dependencies . For all the frequencies of the analysis the noise increases monotonically with the increase of temperature. Fig.1(b) shows the frequency dependencies of S_I/I^2. It is clear that for all temperatures the dependence $S_I/I^2 \sim 1/f^{1.5}$ is valid. This kind of frequency dependence is rather typical for GaAs, SiC, and Si FET's [6-8].

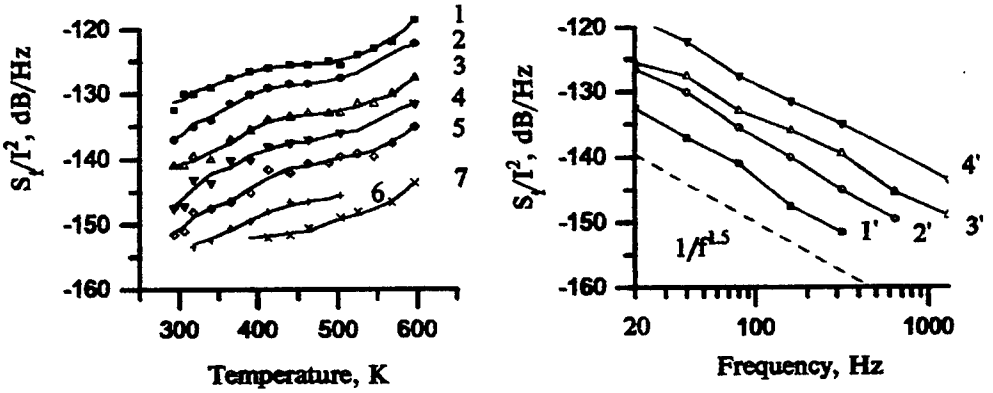


Fig.1 The temperature (a) and the frequency (b) dependencies of spectral density fluctuations S_I/I^2. V_{GS}=0 V.

a) Frequency (Hz): 1-20; 2-40; 3-80; 4-160; 5-320; 6-640; 7-1300;

b) Temperature (K): 1'-300; 2'-400; 3'-500; 4'-595.

The real thickness of the channel at $V_{GS} = 0$ V estimated from the threshold voltage $V_t \cong 2.5$ V, is equal to $h \cong 0.06$ μm. Then the total number of carriers in the channel is $N = n_0 \cdot L \cdot W \cdot h \cong 3 \cdot 10^7$ and the value of Hooge parameter is $\alpha = S_I/I^2 \cdot f \cdot N$ at 300K is equal to $\alpha \cong 3 \cdot 10^{-5}$ at f =20 Hz and $\alpha \cong 5 \cdot 10^{-6}$ at f =1300 Hz. According to the criteria established for conventional Si and GaAs FETs, such a low value of α indicates a very high degree of structural quality for the channel material and a rather small contribution of the contacts in the total noise of the device.

One can show however that even this small noise value is determined not by the volume noise sources in the 4H-SiC channel but by the fluctuations on SiC-SiO_2 interface. Fig. 2 shows the dependencies of S_I/I^2 on the channel resistance R. The resistance has been controlled by the gate voltage V_{GS}. All the measurements were made in the linear (ohmic) regime. It is seen that for all frequencies the S_I/I^2 value is proportional to R^2. The dependence $S_I/I^2 \sim R^2$ may be explained reasonably if one assumes that the volume noise of the channel is very small and that the source of the noise obtained is a surface resistance $R_s >> R$ on the channel - oxide interface. Neither the R_s value nor the amplitude of the fluctuations δR_s depends on the gate voltage V_{GS}. However the greater the value of R, the weaker it shunts the "noise" resistance R_s. For

this situation it is easy to show that $S \sim R^2$ [9]. On the other hand, if the volume noise were dominant the dependence would be $S_I/I^2 \sim R$.

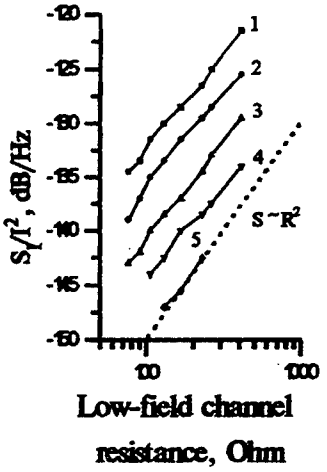


Fig. 2 The dependencies of S_I/I^2 vs low-field channel resistance R for different frequencies of analysis.
T=300 K. Ohmic regime.
The minimal value R=77 Ohm corresponds to VGS=+2V.
The maximal value R=414 Ohm corresponds to VGS = -1.5V.
Frequency (Hz):
1-20; 2-40; 3-80; 4-160;
5-320.

The noise value and the frequency dependence of the noise may be changed considerably by appropriate annealing. The noise properties of the samples are stable up to 500 K. For T>500K, the noise parameters depend on the regime of the annealing. The annealing of the samples at T~550-600 K for several hours in linear (ohmic) regime or at $I_{DS}=0$ decreases the noise level to a great extent (Fig.3, curve 2). The frequency dependence of S takes the form $S \sim 1/f$ (flicker noise). As this takes place, the Hooge α value is as small as $\alpha \cong 5 \cdot 10^{-6}$. This low noise level is retained for T≤ 500K.

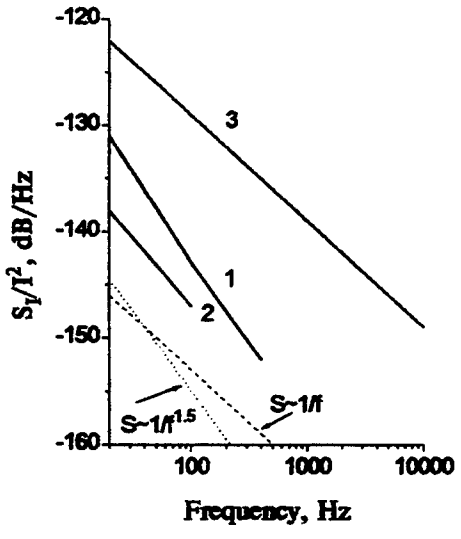


Fig.3. Frequency dependencies of S_I/I^2 for the device before (curve 1) and after (curves 2 and 3) annealing in different regimes. T=300 K.
2 - The annealing at 600 K during two hours at $I_{DS}=0$;
3 - The annealing at 600 K during two hours in saturation regime:
$V_{GS}=0$; $V_{DS}=8V$.

The annealing of the samples at T~550 - 600K for several hours at saturation regime makes quite a different effect on the noise. In this case the noise level increases considerably (Fig.3, curve 3). The frequency dependence of S again takes the form S~1/f.

During the annealing at T~550 - 600K in the saturation regime the noise level gradually increases . At the same time the current-voltage characteristic of the device $I_D(V_{DS})$ is also affected. The drain current I_D increases monotonically at constant V_{DS} value. The measurements show that during the annealing in the saturation regime the thickness of the channel increases monotonically. At high temperature a current flow of hot electrons near the channel-oxide interface recharges the oxide. The thickness of the space-charge region d_0 decreases and the thickness of the channel h grows. As this takes place, the distance between the channel and the oxide-4H-SiC interface (which is the main source of the noise) decreases and the noise increases (Fig.3, curve 3).

The annealing of the samples in the linear (ohmic) regime again decreases the noise level to values comparable with the curves 1 or 2 in Fig. 3.

To conclude, a very low noise level has been observed in 4H-SiC FETs. At 300 K the value of Hooge constant α is as small as $\alpha \sim 10^{-5}$ and the α value can be decreased by an appropriate annealing to $\alpha \sim 2 \cdot 10^{-6}$.

References

1. M.M.Anikin, P.A.Ivanov, V.P.Rastegaev, N.S.Savkina, A.L.Syrin, V.E.Chelnokov. Semiconductors, **27**, 53 (1993)

2. C.E.Weitzel, J.W.Palmour, C.H.Carter, Jr, K.J.Nordquist. IEEE Electr. Dev. Lett., **15**, 406 (1994).

3. J.W.Palmour, V.F.Tsvetkov, L.A.Lipkin, C.H.Carter, Jr. 21-st Intern. Symp. on Compound Semicond., San Diego, California, 1994, Abstract p. 17.

4. W.J.Schaffer, G.H.Negley, K.G.Irvin, J.W.Palmour. in Diamond, Silicon Carbide and Nitride Wide Bandgap Semiconductors, ed. by C.H.Carter, Jr, G.Gildenblat, S.Nakamura, R.Nemanich, MRS Symposium Proc. v.339 (MRS, Pittsburg, 1994), p.595.

5. M.E.Levinshtein, J.W.Palmour, S.L.Rumyantsev. Semicond. Sci. Technol., **9**, 2080 (1994).

6. J.R.Hellum, L.M.Rucker. Sol. St. Electr., **28**, 549 (1985).

7. N.V.Dyakonova, M.E.Levinshtein, J.W.Palmour, S.L.Rumyantsev. Semicond. Sci. Technol., 1995 (in print).

8. R.A.Spaulding. Proc. IEEE, **56**, 886 (1968).

9. M.E.Levinshtein, S.L.Rumyantsev. Sov.Phys. Semicond., **17**, 1167 (1983).

A Highly Resistive Layer in Silicon-Carbide Obtained by Vanadium Ion Implantation

M. P. Lam, K. T. Kornegay, and J. A. Cooper, Jr.

School of Electrical and Computer Engineering
Purdue University, West Lafayette, IN 47907

Vanadium (V) is known to produce a deep-level state lying near the middle of the band gap in 6H-silicon-carbide (SiC) [1]. SiC crystals with semi-insulating behavior have been successfully grown with intentionally doped vanadium using the physical vapor transport process [2]. However, it may be desirable to produce semi-insulating properties only in selected areas of the wafer for isolating active regions of certain devices. This paper reports on a high-resistivity layer produced by ion implanting vanadium in a p-type 6H-SiC Si face epilayer.

To investigate the conductivity of a V-implanted layer, we fabricated a vertical Au/V-implanted layer/p-type SiC Schottky barrier diode as shown in Fig. 1. A p-type SiC epilayer with doping of $5x10^{15}$ cm^{-3} is implanted with vanadium ions at 650°C through a 200 Å SiO_2 screen layer. A double energy of 85 keV and 190 keV is used with a total dose of $1.9x10^{13}$ cm^{-2}. After implantation, vanadium is annealed in a Lindberg tube furnace under argon at 1200°C for 12 min. An Al ohmic contact is fabricated on the back of the substrate by thermal evaporation, and subsequently annealed under argon at elevated temperature. Au is electron-beam deposited over the V-implanted epilayer. Before Au deposition, the epilayer surface is cleaned in organic solvents, aqua regia and BHF, and then rinsed in deionized water. Au Schottky contacts are patterned with an area of $1x10^{-4}$ cm^{-2}. The implant depth of V in SiC is estimated to be 0.1-0.15 μm. The precise depth will be determined by SIMS analysis. In order to compare electrical

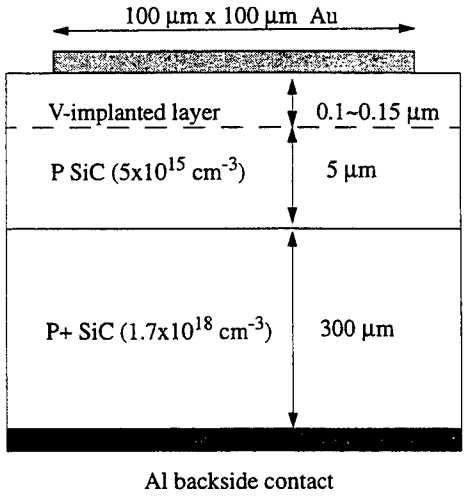


Fig. 1 V-implanted Schottky barrier diode

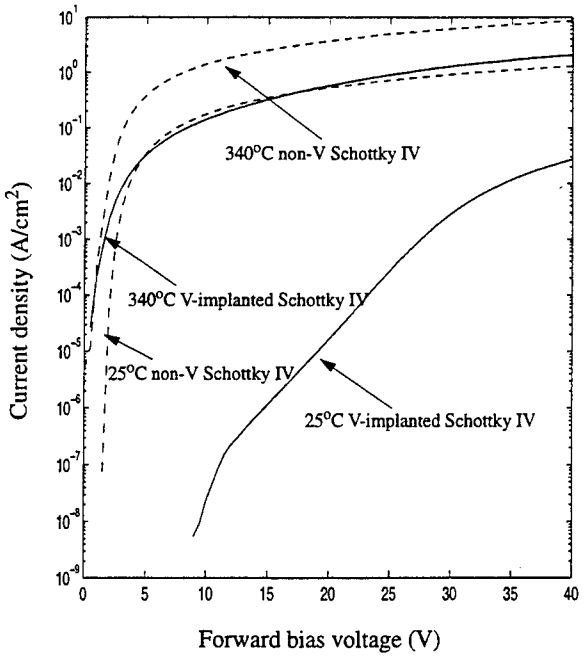


Fig. 2 Forward I-V characteristics of Au/V-implanted SiC and Au/SiC diodes at 25°C and 340°C. Area = 100 μm x 100 μm

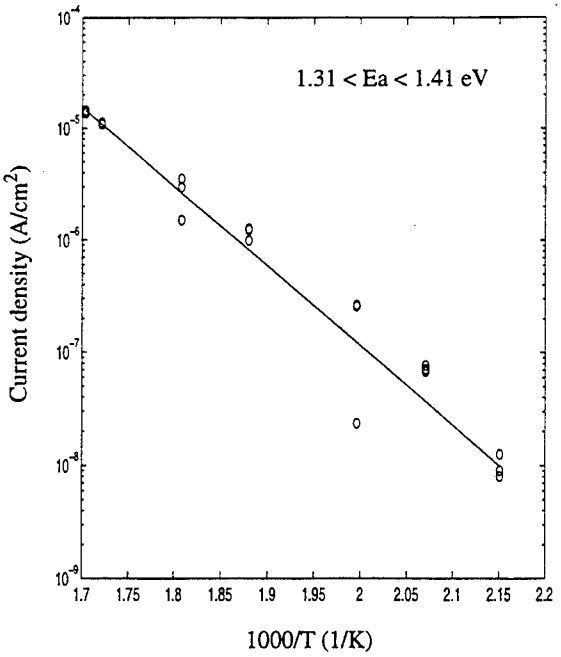


Fig. 3 Current as a function of reciprocal temperature for V-implanted 6H-SiC Schottky barrier diodes at 0.4 V.

characteristics with conventional SiC Schottky barrier diodes, we have also fabricated Schottky diodes with the same processes described above, excluding the vanadium implantation.

Forward current-voltage (I-V) measurements on Au/V-implanted SiC and Au/SiC Schottky diodes are shown in Fig. 2. Clearly, the presence of the V-implanted layer at room temperature introduces a significant reduction of current density. The reduction decreases with higher forward bias voltage and higher temperature. Since the current is too small to measure at low voltage for the V-implanted Schottky diode at room temperature, we compare its I-V characteristic with that of the non-V Schottky diode at 10 V. V-implanted SiC Schottky diodes exhibit specific differential contact resistances up to 3×10^7 ohm-cm^2 and current densities as low as 2×10^{-8} A/cm^2 at 10 V, which is six orders of magnitude less than their non-V counterparts.

Since vanadium is a deep-level trap in SiC, one can estimate its energy level from the temperature dependence of the forward current. Figure 3 shows current as a function of reciprocal temperature at a constant forward bias voltage of 0.4 V. A linear fit of the currents measured from three V-implanted Schottky diodes yields an activation energy between 1.31 to 1.41 eV, which is close to the energy levels reported for V in SiC.

The breakdown voltages for both devices at 25°C and 340°C are compared in Table 1. We note that the thin high-resistivity layer increases the breakdown voltage from 170 V to 240 V at room temperature. This effect is more significant at a higher temperature.

TABLE 1. Breakdown voltage for Au/V-implanted SiC and Au/SiC Schottky diode

Device type	V_{br} at 25°C	V_{br} at 340°C
V-implanted SiC	240 V	210 V
non-V SiC	170 V	92 V

In conclusion, this work investigates the possibility of obtaining a highly resistive layer in SiC by implanting V. Experiments are underway to make use of the high-resistivity V-implanted layer as edge termination [3] to obtain high blocking voltage SiC Schottky rectifiers. This technology can also be used as ion implant isolation for SiC MESFET circuits.

This material is based upon work supported by the National Science Foundation under grant no. 9521901-ECS, by the Ballistic Missile Defense Organization (IST) under grant no. N00014-93-C-0071, administered by ONR, and by the Semiconductor Research Corporation.

References

[1] J. Schneider, H. D. Muller, K. Maier, and F. Fuchs, "Infrared spectra and electron spin resonance of vanadium deep level impurities in silicon carbide," *Appl. Phys. Lett.*, vol. 56, no. 12, pp. 1184-1186, March 1990.

[2] H. McD. Hobgood, R. C. Glass, G. Augustine, R. H. Hopkins, J. Jenny, M. Skowronski, W. C. Mitchel and M. Roth, "Semi-insulating 6H-SiC grown by physical vapor transport," *Appl. Phys. Lett.*, vol. 66, no. 11, pp. 1364-1366, March 1995.

[3] D. Alok, B. J. Baliga and P. K. McLarty, "A simple edge termination for silicon carbide devices with nearly ideal breakdown voltage," *IEEE Electron Devices Lett.*, vol. EDL 15, no. 10, pp. 394-395, Oct. 1994.

MODELING OF EXCITONIC GAIN IN ULTRA-LOW THRESHOLD TENSILE-STRAINED ZnCdSe-ZnMgSSe QUANTUM WIRE LASERS

W. Huang and F. Jain
Electrical and Systems Engineering Department
University of Connecticut, Storrs, CT 06269-3157 (USA)

Exciton transitions play a dominant role in ZnCdSe-ZnSSe quantum well blue-green lasers reported by several investigators [1-3] during the past four years. We have computed optical gain in ZnCdSe based multiple quantum well lasers incorporating excitonic effects. The computations matched the optical gain data obtained experimentally [4] on compressively strained samples. This paper calculates the optical gain and threshold current density in ZnCdSe based quantum wire lasers including the contributions of excitonic transitions. In particular, we present computations of excitonic binding energies, optical gain, and threshold current density in ZnCdSe-ZnMgSSe strained quantum wires. The tensile-strained ZnCdSe-ZnMgSSe quantum wires [$L_z=L_y=80$Å], such as realized on InP substrates, are shown to yield an ultra-low threshold current density of 58 A/cm^2.

Quantum wire semiconductor lasers, realized in III-V material system such as AlGaAs-GaAs, have been shown [5-6] to result in lower threshold current operation. These devices are generally modeled using free carrier band-to-band transitions that are not applicable to ZnCdSe based blue-green lasers, which are known to have excitonic transitions [7].

Our calculations show (Fig.1) that excitonic binding energy is enhanced from 30 to 55 meV as we reduce the lateral dimension in quantum wells to obtain quantum wires. This increases the excitonic density of states which is enhanced over and above the larger values of free carrier density of states as we transition from well to wire. The increased excitonic density of states results in narrowing of the emission line width which in turn improves the optical gain, resulting in lower threshold current density. Fig.2 (a) and (b) show the optical gain for unstrained, compressive strained, and tensile strained active layers. Threshold current density has been found to be the lowest in the presence of tensile strain. This is similar to our previous findings on blue-green quantum well lasers [8].

The model also shows that the excitonic transitions (in comparison to free carrier transitions, such as in AlGaAs-GaAs or InGaAsP-InP lasers) would assist in reducing the threshold current density in the presence of dislocations. The exciton transitions dramatically increase the absorption coefficient as shown in Fig 3. The solid line shows a strong excitonic absorption peak appears on the lower photon energy side. The dashed line shows the absorption coefficient with band to band free carrier transition only. Since the exciton absorption peak is much stronger than band to band free carrier transition,

the estimated rate of radiative recombination [9] with excitonic transition is about 14 times larger than just free carrier transitions in ZnCdSe-ZnMgSSe quantum wire. This yields a much lower radiative life time and a higher quantum efficiency. Therefore, a reduced J_{th} value is expected. As an example, if the quantum efficiency η_q in free carrier transition system drops from 0.9 to 0.09 due to the dislocation density, the η_q value in exciton transition system would drop from 0.9 to 0.58 due to the same dislocation density. This is shown in Fig. 4. Fig. 4-(a) shows the gain coefficient as a function of injection current for η_q=0.9, Fig.4-(b) shows the increased threshold current density in the presence of the dislocation, and Fig. 4-(c) shows the enhanced threshold current density over case (b) due to excitonic transitions. This indicates that the high exciton density, resulting in high excitonic transition rate and diminishing nonradiative recombination, would assist in reducing the threshold current density which is significantly increased by the presence of dislocations and defects from processing of quantum wires.

1. C. T. Walker, J. M. Depuydt, M. A. Haase, J. Qiu and H. Cheng, "Blue-green II-VI laser diodes," Physica B. 185, pp. 27-35, 1993.
2. J. Ding, H. Jeon, T. Ishihara, M. Hagerott and A. V. Nurmikko, H. Luo, N. Samarth, and J. Furdyna, ''Excitonic gain and laser emission in ZnSe-based quantum wells," Phys. Rev. Lett. 69, pp.1707-1710, 1992.
3. Y. Wu, K. Ichino, Y. Kawakami, Shizuo. Fujita and Shigeo. Fujita, ''Optical properties of ZnCdSe/ZnSSe strained-layer quantum wells," Jpn. J. Appl. Phys. 31, pp. 3608-3614, 1992.
4. J. Ding, M. Hagerott, P. Kelkar, A.V. Nurmikko, D. C. Grillo, L. He, J. Han, and R. L. Gunshor, "Gain and dynamics in ZnSe-based quantum wells," J. Cryst. Growth, 138, pp. 719-726, 1994.
5. M. Asada, Y. Miyamoto, and Y. Suematsu, "Gain and threshold of three-dimensional quantum-box lasers", IEEE J. Quantum Electronics, QE-22, pp. 1915-1921, September 1986.
6. E. Kapon, "Quantum wire lasers," Proc. IEEE, 80, pp. 398-410, March 1992.
7. W. Wegscheider, L. Pfeiffer, K. West, R. E. Leibenguth, "Current injection GaAs/AlGaAs quantum wire lasers fabricated by cleaved edge overgrowth," Appl. Phys. Lett. 65, pp. 2510-2512, 1994.
8. W. Huang and F. Jain, "Optical gain due to excitonic transitions in ZnCdSe/ZnMgSSe strained layer quantum well blue-green lasers: Prediction of low threshold under tensile strain, Appl. Phys. Lett. 66, p.1596-1598, March 1995.
9. T. S. Moss, G. J. Burrel and B. Ellis, "Semiconductor Opto-Electronics," Butterworths, London, 1973.

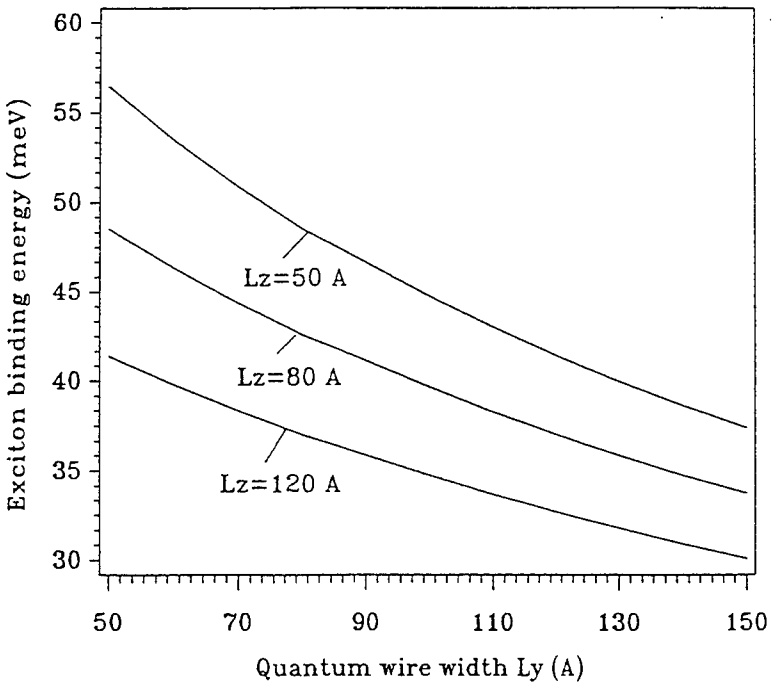


Fig. 1 Exciton binding energies as a function of wire width in ZnCdSe-ZnSSe quantum wire.

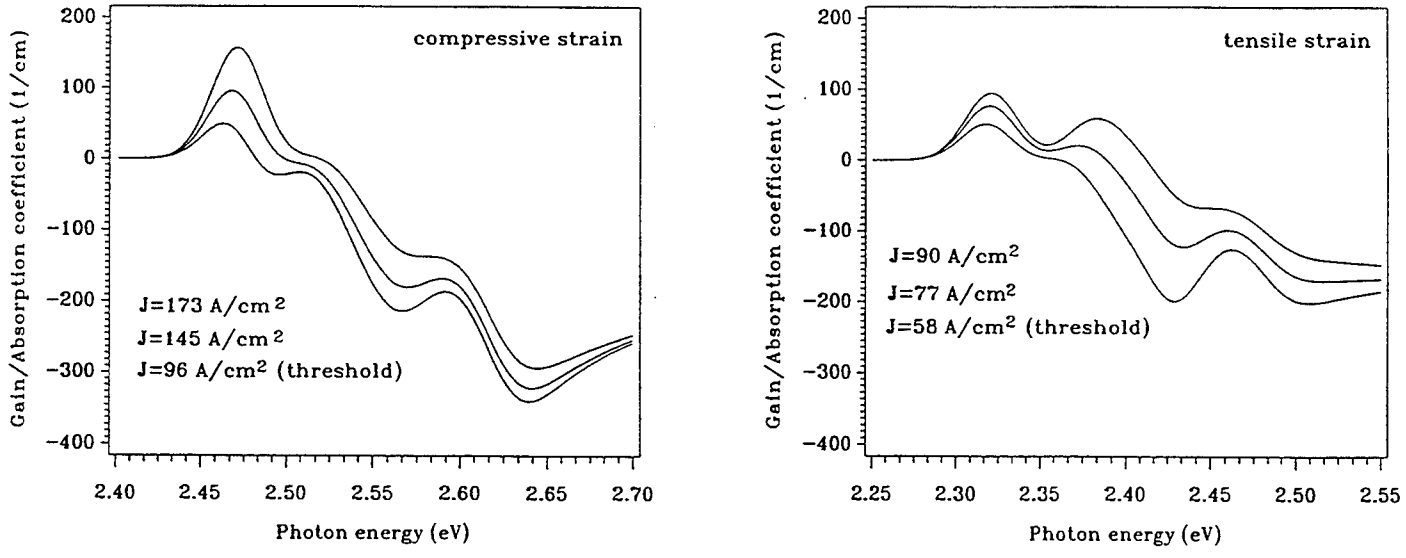


Fig. 2 Computed gain/absorption coefficient for ZnCdSe-ZnMgSSe quantum wire laser:
(a) Compressively strained active layer. (b) Tensile strained active layer

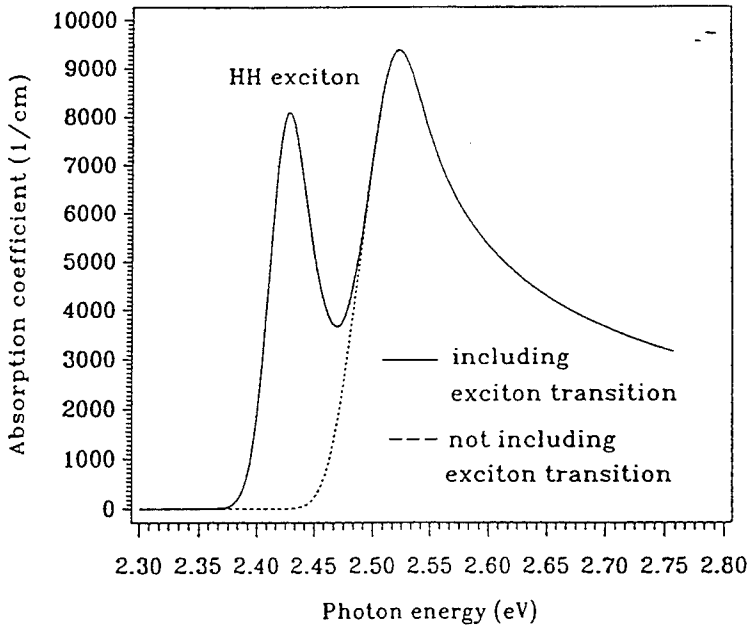


Figure 3 : Absorption coefficient for ZnCdSe-ZnMgSSe quantum wire laser (Ly=Lz=80 $\mathring{A}$)

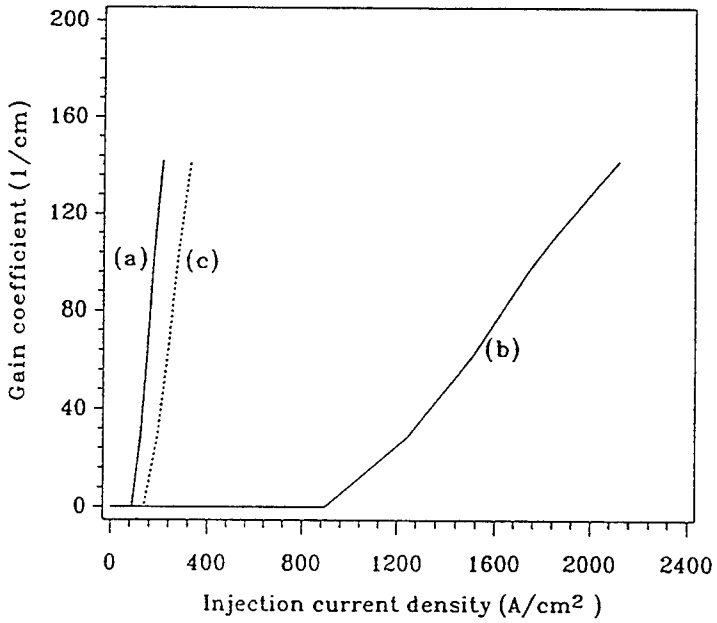


Figure 4 : Effect of exciton transitions in improving quantum efficiency and lowing of threshold current density for unstrained ZnCdSe-ZnMgSSe quantum wire laser. (a) $\eta = 0.9$, (b) $\eta = 0.09$ due to defect states, (c) improved η values in the present of excitons over (b).

OPTICAL PROPERTIES OF GaN FILMS ON SAPPHIRE SUBSTRATE

R. Zhang, K. Yang, B. Shen, L.H. Qin, S.L. Gu, Y. Shi and Y.D. Zheng
Department of Physics, Nanjing University, Nanjing 210093, CHINA

Z.C. Huang and J.C. Chen
Department of Electrical Engineering, University of Maryland Baltimore County, Baltimore, MD 21228-5398, USA

Recently the wide bandgap III-V nitrides have attracted much attention because of their great significance in both scientific research and practical applications near the short wavelength end of visible range[1]. Among them, gallium nitride (GaN) is the most interesting material because of its suitable direct energy bandgap of 3.39eV at room temperature, notable chemical inertness and great physical hardness. Those attractive properties make it not only ideally useful for fabricating blue and ultraviolet light emitting diodes (LED) and detectors, but also for application in harsh environments, such as high temperature[2,3]. High quality GaN films on sapphire substrates have been grown by metalorganic chemical vapor deposition (MOCVD)[3,4], and high performance devices, including blue LED and UV detector, have been demonstrated[5]. For most applications, the optical properties of GaN film is the key factor to influence the features of devices. In this paper, photoreflectance (PR), optical absorption, Raman scattering and x-ray diffraction (XRD) techniques were employed at room temperature to analyze the optical properties of GaN epilayers.

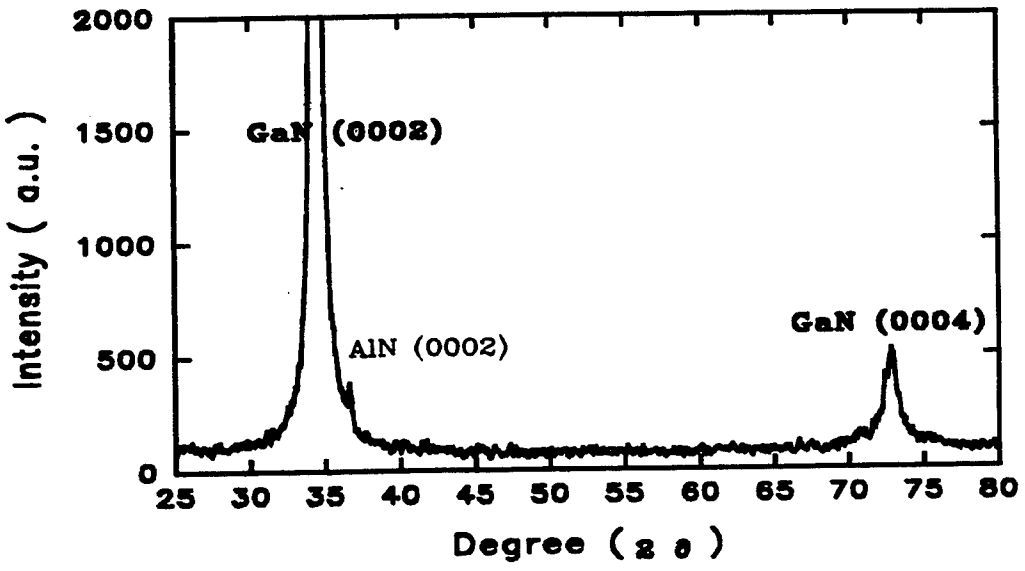


Fig.1 XRD spectrum of GaN film deposited on (0001) sapphire substrate.

Single crystal hexagonal GaN epitaxial films were grown on (0001) sapphire substrate with an AlN buffer layer by MOCVD. The thin AlN buffer layer with the thickness of 50nm was deposited at 550°C and followed by the growth of GaN at 720°C. The growth rate of GaN was about 1μm/hour, and all samples were unintentionally n-type doped.

Fig. 1 presented the typical XRD spectrum of a GaN film deposited on (0001) sapphire substrate, which showed a good quality single crystal wurtzite structure of the GaN epilayer. From the (0002) and (0004) peak position of the GaN film, we obtained the lattice constant in the direction of c-axis as 0.5188nm. The AlN(0002) peak from the buffer layer with the lattice constant c of 0.4948nm was observed. Because of the thick GaN film, the diffraction peaks from sapphire substrate was not found.

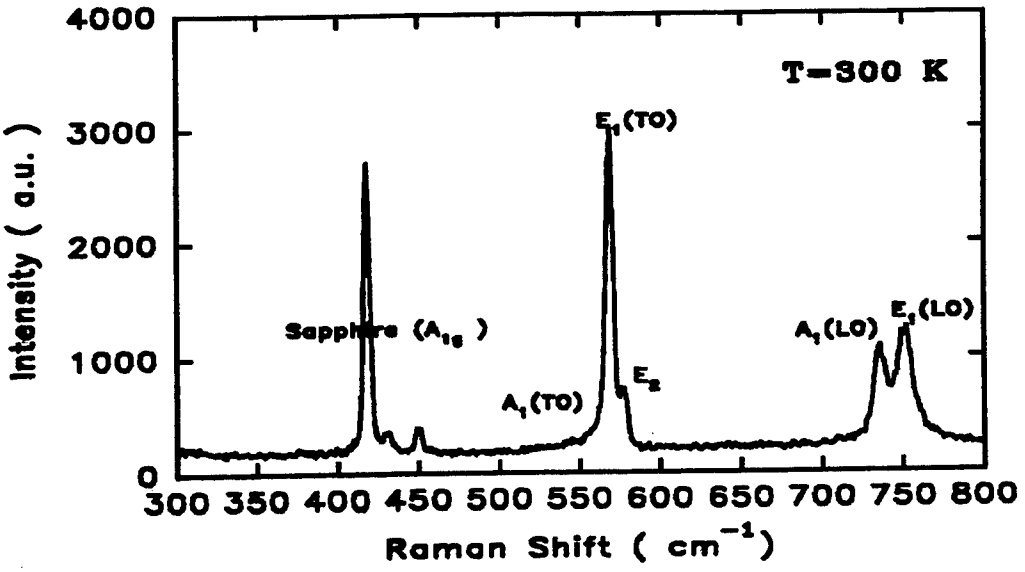


Fig.2 Raman scattering spectrum of GaN film at room temperature under 488nm argon laser excitation in backscattering configuration.

Raman spectra were used to study the phonon modes of the GaN film. Since GaN has a hexagonal structure and belongs to the C_{6v} symmetry group, there are six Raman active phonon modes: two E_2, E_1(TO), E_1(LO), A_1(TO) and A_1(LO). Fig.2 showed a typical Raman spectrum from the GaN film grown on sapphire substrate with the backscattering configuration, and E_1(TO), E_1(LO), A_1(TO), A_1(LO) and high frequency E_2 modes, with phonon frequencies as 545cm^{-1}, 569cm^{-1}, 735cm^{-1}, 750cm^{-1} and 578cm^{-1} respectively, were observed together with three modes of 418cm^{-1}, 430cm^{-1} and 449cm^{-1}, come from the sapphire substrate.

In order to determine the optical bandgap and optical functions of GaN film, the optical transmission spectrum was

measured from 0.6-4.0eV. The absorption coefficient was about $8x10^3$ cm^{-1} above the bandgap, and almost zero below the gap with a sharp line shape around the bandgap. By drawing the absorption coefficient squared vs. the spectral energy curve, α^2-hν, which was shown in Fig. 3, we determined the direct energy bandgap of 3.39eV, consistent with the results in literatures. From the interference features on the transmission data, the film thickness of this sample was determined as about 2.0μm which agreed well withthe designed value, and the refractive index n was drawn as the function of photon energy as shown in Fig. 4.

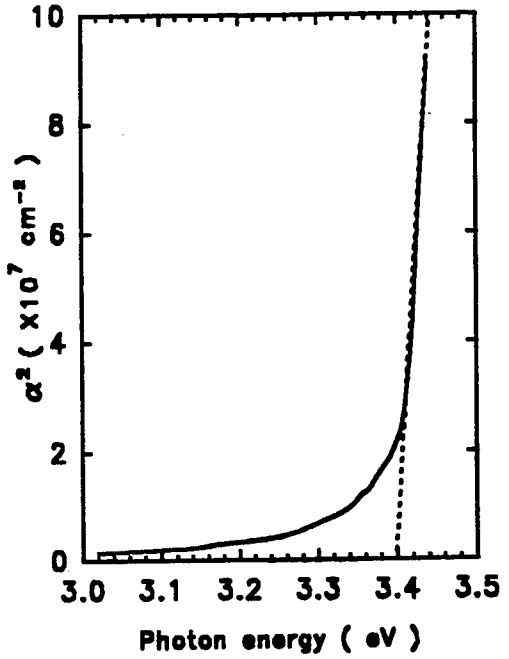


Fig. 3 Absorption coefficient square (α^2) of GaN vs. photon energy hν.

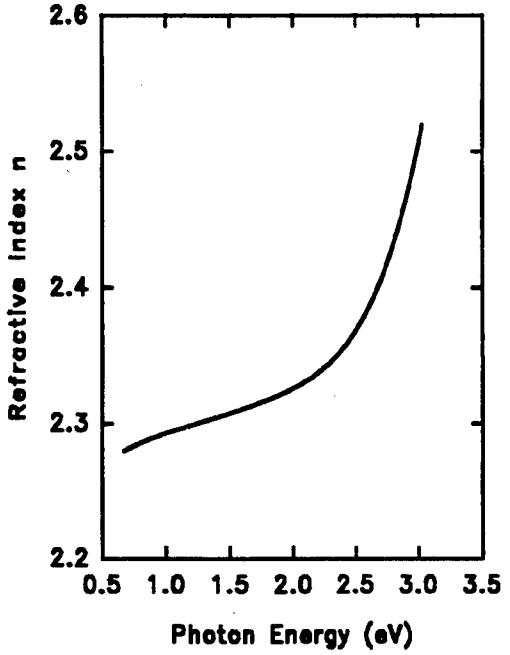


Fig. 4 Refractive index n of GaN film vs. photon energy at room temperature.

Fig. 5 showed a typical PR spectrum of the GaN film with the thickness of 6.0μm, which confirmed the direct energy bandgap and the high crystal quality of the sample. The experimental data could be fitted by the equation

$$\frac{\Delta R}{R} = Re\left[\frac{A\Gamma^{-n}e^{i\theta}}{(E-E_g-i\Gamma)^n}\right]$$

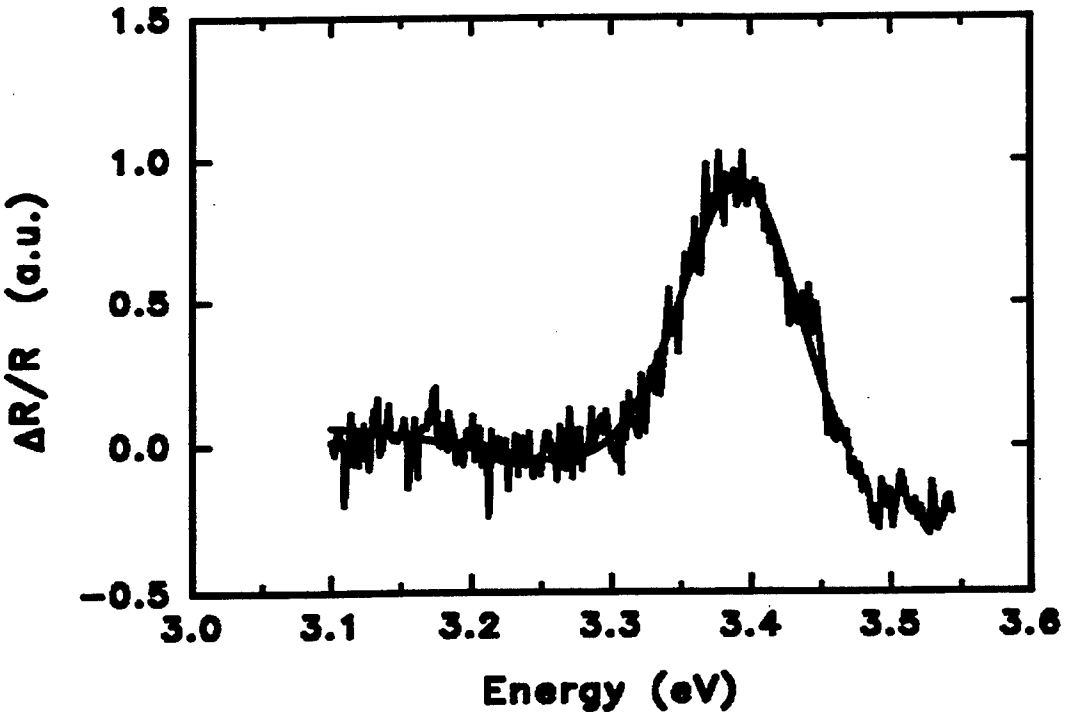


Fig. 5 Photoreflectance spectrum of GaN film on sapphire at room temperature (the rough line). The modulation beam was 488 nm line of an Ar^+ laser mechanically chopped at 20 Hz. The curve was fitted as the smooth line.

where Γ=0.124eV was the linewidth, θ was the phase, and the E_g=3.400eV was the transition energy. The exponent n was fixed at the value of 2.5, which is often used for band to band transition in the bulk samples.

In summary, we studied the optical properties of the GaN films grown on sapphire substrate by MOCVD. XRD and Raman scattering measurements showed high crystal quality, while optical absorption and PR spectra gave a direct bandgap of 3.400eV and the refractive index function.

References

[1] S. Strite and H. Morkoc, J. Vac. Sci. Technol. B10(4), 1237(1992)
[2] M.A. Khan, Microwave Journal P67, (Nov, 1993)
[3] S. Nakamura, T. Mukai and M. Senoh, Appl. Phys. Lett., 64(13), 1687(1994)
[4] K.G. Fertitta, A.L. Holmes, J.G. Neff, F.J. Ciuba, and R.D. Dupuis, Appl. Phys. Lett., 65 (14), 1823(1994)
[5] M. Razeghi, Y.H. Choi, X. He and C.J. Sun, Mater. Sci. Technol., 11, 3(1995)

GaN and AlGaN p-i-n Structures.

N.I. Kuznetsov and V.A. Dmitriev*
Cree Research Eastern European Division and A.F. Ioffe Institute, 26 Polytechnicheskaya Street, St. Petersburg, 194021 Russia
* Cree Research Inc., 2810 Meridian Parkway, Durham, NC, 27713 USA.

Recently, significant progress has been achieved on MOCVD of GaN and AlGaN layers on SiC substrates [1,2]. This report is devoted to GaN and AlGaN p-i-n structures grown on SiC. To the best of our knowledge, this is the first study of A_3N p-i-n structures.

GaN and AlGaN structures were grown on (0001) 6H-SiC wafers by MOCVD. Si and Mg were used as dopants. For n-type layers, $N_d - N_a$ was from ~$1x10^{17}$ to ~$1x10^{18}$ cm^{-3}. For p-type layers, $N_a - N_d$ ranged from ~$1x10^{17}$ to ~$1x10^{19}$ cm^{-3}. A 2 μm thick GaN n-layer with $N_d - N_a = 10^{18}$ cm^{-3} was grown first. Then GaN or AlGaN pn junctions were formed. The structures were grown such that a highly compensated region was formed between the highly doped n- and p-layers. AlN concentration in AlGaN alloy was 8 mol. %. A 0.5μm thick cap p^+-GaN layer was grown on top of the pn junction. Mesa structures of 100 - 300 μm in diameter were made by dry etching.

Current - voltage (I-V) characteristics were studied in the temperature range from 90 to 600 K. Capacitance - voltage (C-V) characteristics were also measured. Investigations of deep levels were performed using current deep level transient spectroscopy (i-DLTS) [3].

Built-in voltage determined by C-V measurements ranged from 4 to 7 V, which was caused by i-region.

Forward I-V characteristics at current densities less then $1A/cm^2$ may be expressed by $I \sim V^{\alpha}$,where α ranged from 1 to 10. At $T < 100$ K the s-shape of the forward I-V characteristic was observed, which is typical for p-i-n structures. The forward I-V characteristics followed the model [4] created for describing current transport in deep-lying impurity semiconductors. A single recombination center is assumed. The activation energy of this recombination center was extracted from the temperature dependence of the forward current. For GaN and AlGaN structures the activation energy was found to be 0.146 eV and 0.191 eV, respectively. These values are in good agreement with the Mg acceptor ionisation energy in GaN and $Al_{0.08}Ga_{0.92}N$, respectively, measured using the Hall effect [5].

Reverse I-V characteristics showed abrupt breakdown at voltages ranging from 20 to 90 V. Breakdown had a microplasmic nature. The strength of the breakdown electric field was estimated to be ~4 MV/cm and ~3 MV/cm for GaN and AlGaN structures, respectively.

Results of i-DLTS measurements indicated the presence of hole traps at energies above the valance band. The traps had activation energy of 0.142 eV for GaN and 0.20 eV for AlGaN structures. We attribute these traps to the Mg acceptor.

I-V characteristics of the p-i-n structures and result of i-DLTS investigation will be discussed in detail.

References.

1. V.A.Dmitriev, K.G.Irvine. J.A.Edmond, G.E.Bulman, C.H.Carter,Jr., A.S.Zubrilov, I.P.Nikitina, V.Nikolaev, A.I.Babanin, Yu.V.Melnik, E.V.Kalinina, V.E.Sizov, to be published in Proceedings of the 21 st5 Int. Symp. Compound Semicond. (San Diego 1994).
2. V.A.Dmitriev, K.G.Irvine, J.A.Edmond, C.H.Carter, Jr., N.I.Kuznetsov, A.S. Zubrilov, E.V.Kalinina, D.V.Tsvetkov, submitted to ICSCRM-95.
3. N.I.Kuznetsov, Semiconductors 27 (1993) 925.
4. K.L.Ashley, A.G.Milnes, J.Appl. Phys. 35 (1964) 369.
5. T.Tanaka, A.Watanabe, H.Amano, Y.Kobayashi, I.Akasaki, S.Yamazaki and M.Koike, Appl. Phys. Lett. 65 (1994) 594.

Electrical Conduction in Platinum-Gallium Nitride Schottky Diodes

K. Suzue, S.N. Mohammad, Z.F. Fan, W.Kim, O. Aktas, A.E. Botchkarev, and H. Morkoç
University of Illinois at Urbana-Champaign,
Materials Research Laboratory and Coordinated Science Laboratory
104 S. Goodwin Ave., Urbana, Illinois 61801, U.S.A.

Gallium nitride is an important wide bandgap semiconductor with highly promising characteristics for high-speed and optoelectronic devices. Electrical conduction and other related properties of Pt-GaN Schottky diodes have been investigated. These Schottky diodes were fabricated by using n-GaN grown by molecular beam epitaxy method. Both capacitance-voltage and current-voltage measurements have been carried out for a number of temperatures. The measured variation of C^{-2} with applied gate bias V for 1 MHz frequency is shown in Fig. 1. The linear nature of the variation yields the Schottky barrier height to be 1.10 eV. The measured variation of the total current with applied bias is shown in Fig. 2. At low voltages the plots show shoulders indicating significant leakage probably due to the presence of traps. Physical mechanisms underlying electrical conduction at low and high voltages and temperatures have been studied. For the study of these physical mechanisms a theoretical curve fitting method is employed. Schottky barrier height determined from the current-voltage measurements is very close to 1.10 eV. Recombination-generation, tunneling and thermionic emission were found to contribute to the total gate current.

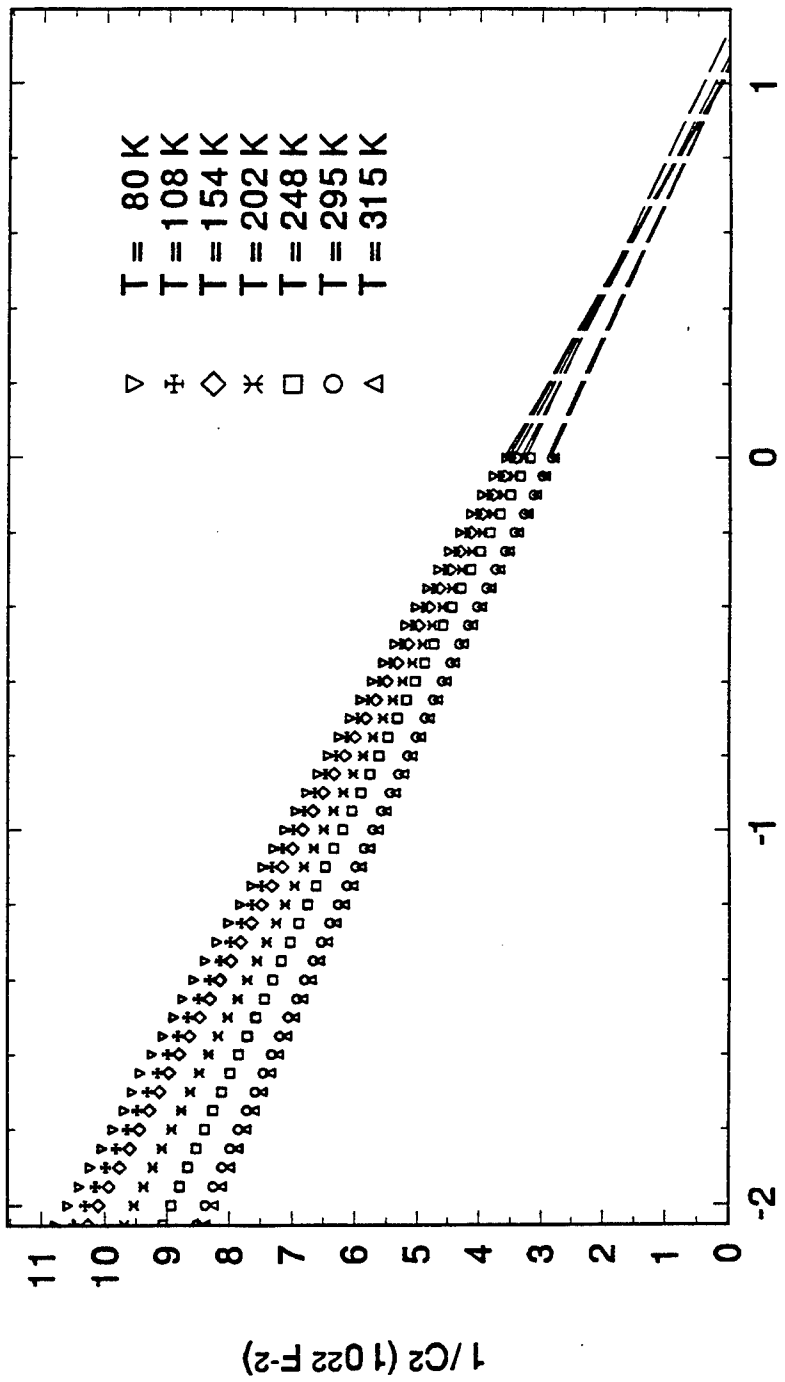


Fig.1 Measured variation of C^{-2} with applied gate bias for 1 MHz frequency at selected temperatures.

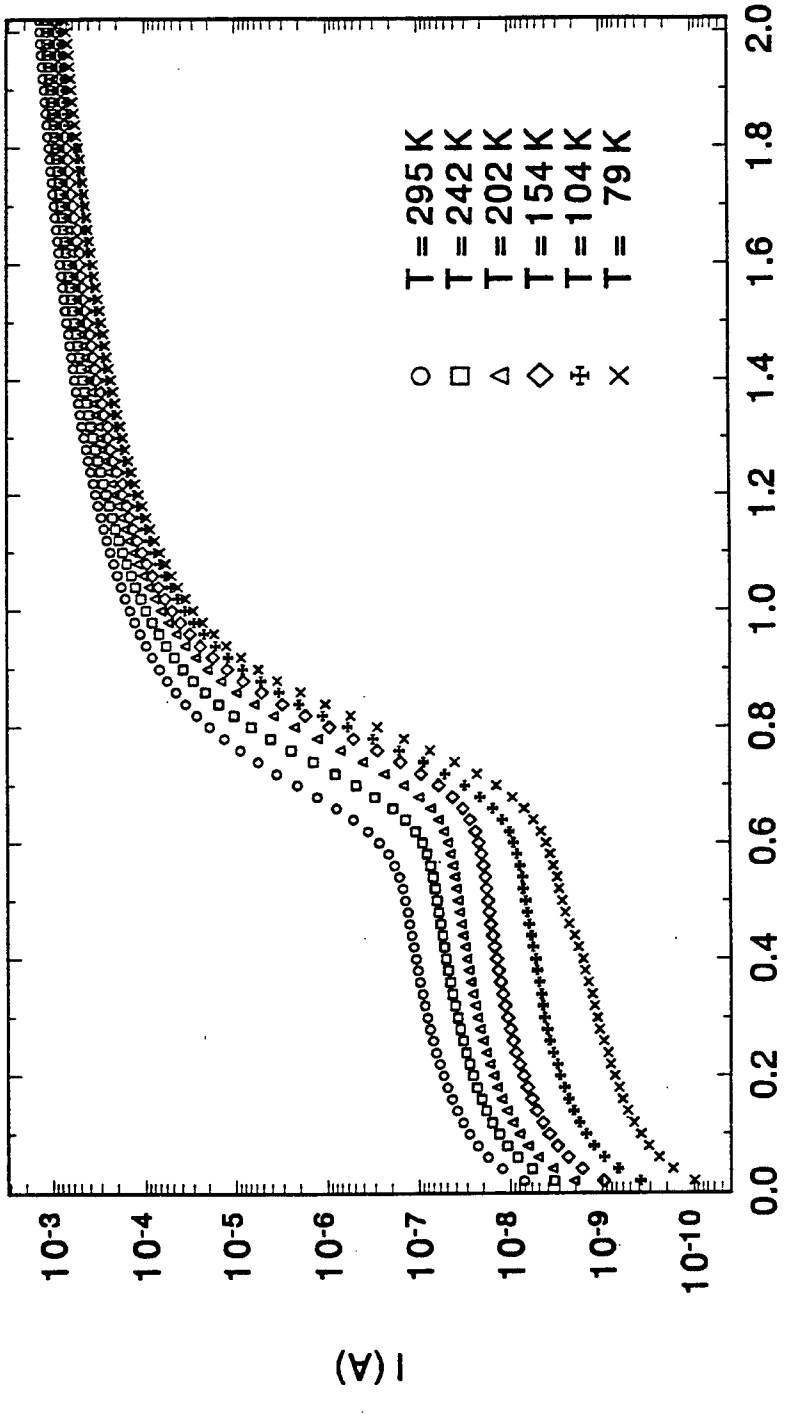


Fig.2 Measured variation of the current with applied bias voltage.

Processing and Characterization of GaN-AlGaN Based Electronic and Optoelectronic Devices

M. Asif Khan, Q. Chen, J. W. Yang and C. J. Sun
APA Optics Inc., 2950 N. E. 84 th. Lane, Blaine MN 55449.
and
I. Adesida , A. T. Ping
University of Illinois
and
M. S. Shur
Dept. of EE, University of Virginia, Chalottesville VA 22903.

Abstract: We discuss our research aimed at developing AlGaN based high power, high frequency FET and other optoelectronic devices. We discuss the processing and characterization of several devices such as InGaN-AlGaN blue LED's, GaN pn-junction UV detectors and GaN-AlGaN MESFET and HFET structures.
For the pn-junction LED's with a reactive ion etched MESA type structure intense emission is obtained at 410-450 nm. pn-junction and Schottky type UV detector structures were processed using various device geometries. These devices have a spectral responsivity sharply peaked at the bandedge wavelength for GaN (365 nm.) thereby providing a visible blind operation. Processing and dc-, rf-, and high temperature performance results will also be presented for FET devices with gate lengths ranging from 0.25 to 7 microns.

1. Introduction

AlGaN material system possesses several unique properties that make it ideally suited for electronic and optoelectronic devices. It is direct bandgap over the entire alloy composition . The bandgap can be tailored from about 2.2 eV (InN) to around 6.2 eV (AlN). This makes it an excellent candidate for optoelectronic devices in the visible-ultraviolet parts of the spectrum. AlGaN material system also has a very high breakdown voltage (>10^6 V/cm), saturated drift velocity and electron mobility (>700 cm^2/V-sec at room temperature). High quality GaN-AlGaN heterojunctions with 2-D electron gas at the junction interface have also been demonstrated [1,2,3]. The presence of 2-D electron gas with a room temperature electron mobility in excess of 1500 cm^2/V-sec and the availability of AlN with excellent insulating properties makes GaN-AlGaN superior to other wide bandgap materials for high frequency, high power transistors.

2. Epilayer Deposition and Characterization

The epilayers for the work described were deposited using low pressure MOCVD over basal plane sapphire substrates. As before we used triethylgalium, triethylaluminum and ammonia as the precursors for 'Ga', 'Al' and 'N'. Typically a growth pressure and temperature of 76 torr and 1000 C was used for the deposition of high quality GaN films

over basal plane sapphire substrates. This is similar to that described previously [1,2,3]. As deposited the GaN layers are highly resistive with a carrier density well below 10^{15} cm^{-3}. The insulating GaN layers can be doped either n- or p-type using disilane (Si) or bis-Mg (Mg) as the dopants.

The single epilayers and the heterojunctions were characterized for their electrical and optical properties. The doped channel heterojunctions exhibit room temperature electron mobilities in excess of 1200 cm^2/V-sec. These increase with decreasing temperatures reaching a peak value of 5000 cm^2/V-sec at 150 K. This high mobility value is due to the 2-dimensional electron gas at the GaN-AlGaN heterojunction interface.

3. Device Processing

Several GaN-AlGaN-InGaN based optoelectronics and electronics devices were processed. These included MESA type LED structures based on GaN-InlGaN heterojunctions or GaN pn-homojunctions. A MESA type structure with both the n- and p- type contacts on the top has been used. This is necessary due to the insulating nature of the sapphire substrate. It should be noted that this device structure is identical to a pn-junction detector where light is incident on the active region from the sapphire substrate side.

The processing of GaN-AlGaN HFETs involves several steps. This includes ohmic contacts, schottky-barriers (to n-type GaN and AlGaN) and procedures for device isolation. Being the first group to conduct GaN based electronic device research work we also developed the above processing techniques. To date we have explored several n-ohmic contact fabrication schemes. One of these most extensively used involves the use of Ti/Al bilayers for n-ohmic contacts to AlGaN and GaN. Post deposition these bilayer contacts are annealed at 350 °C for 1 minute. It is fairly routine for us to obtain a contact resistivity of $5x10^{-5}$ ohm-cm^2 for an AlGaN layer with an x-value of 0.15 and a carrier concentration of $5x10^{17}cm^{-3}$. We also have developed Ti/Au as a stable schottky barrier material for AlGaN.

AlGaN material system is very stable and hard and is nearly impossible to wet chemically etch. We have therefore developed reactive ion and chemically assisted ion beam etching as techniques for MESA fabrication for FET device isolation [4,5]. In Figure 1 we include two examples of vertical features etched in GaN using CAIBE. As seen an excellent aspect ratio is obtained. We also were the first group [6] to develop hydrogen-ion implantation as a potential device isolation technique for GaN based FETs. This is now routinely used by us for the HFET device fabrication.

4. Device Characterization

We have also fabricated GaN based photocnductive and photovoltaic ultraviolet (UV) detectors. In Figure 2 we include the current-voltage curves for such a pn-junction GaN UV detector. As seen a 1.5 V turn-on and a reverse breakdown in excess of 10 V is observed. The doping level of the p- and the n- type layers in the junction region was around $5x10^{16}$ cm^{-3}. In Figure 3 we include the responsivity of the GaN pn-junction as a function of wavelength. As seen no photoresponse is observed for wavelengths larger

than the bandgap (365 nm.). Below 365 nm. the responsivity is nearly independent of the wavelength indicating a very low surface recombination. This trend is identical to that observed in past for GaN photoconductive and schottky barrier detectors [7,8]. This visible-blind detection feature is highly desired for numerous ultraviolet detection applications.

Our group has also actively pursued the development of light emission devices based on GaN pn-homojunctions [9] and GaN-InGaN double heterojunctions. In Figure 4 we present the light emission from a GaN homojunction for a forward current of 20 mA across a 200x200 micron LED. We have also demonstrated optically pumped stimulated emission from GaN [10] and InGaN [11]. These layers were deposited over basal plane sapphire substrates. A threshold power of around 1 MW/cm^2 was measured in each case. Recently with improved material growth we have lowered these threshold values to around 200-400 kW/cm^2. In Figure 5 we present the vertical cavity PL signal from a GaN-InGaN heterojunction as a function of wavelength using a pulsed nitrogen laser (337 nm.) for pumping. As seen Fabry-Perot fringes are clearly visible on the spontaneous emission envelope. These indicate a high Q-value for the vertical cavity. As the pump powers are increased one of the modes build up nonlinearly with increasing powers. From the output versus input powers we estimate a threshold for stimulated emission to be around 200-400 kW/cm^2. However the sapphire substrates do not allow cleaving of parallel bars. Therefore we have recently deposited high quality wurtzite GaN layers over cubic (111) spinel substrates. These were measured to have a stimulated emission threshold around 500 kW/cm^2 which is superior to the sapphire grown films. The cubic spinel substrates allow for the cleaving of parallel bars of GaN films. These lateral cavities are well suited for studying optically and electrically pumped lasing. More work is underway and will be reported later.

Following the demonstration of large gate MESFETs and HFETs, we reported the operation of a submicron HFET [12]. These devices with a 0.25 micron gate length in a 2 micron source-drain opening used e-beam lithography for the T-gate fabrication. In Figure 6 we include the source-drain curves for a 150 micron wide device. As seen the series resistance was high (around 100 ohms) that limited the transconductance to 27 mS/mm and the peak currents to 53 mA/mm. In Figure 7 we include the unity current gain- and the maximum signal gain for the device as a function of frequency. From the 6-db roll-off we measured the f_t and f_{max} values of the device to be 25 and 70 GHz respectively.

6. Conclusions

We have reported on the development of high frequency high power devices based on GaN-AlGaN heterojunctions. We have also reported our work aimed at developing ultraviolet sensors and visible-UV light emission devices. For the first time we report high responsivity photoconductive and pn-junction detectors based on GaN and AlGaN. We describe the characterization of GaN homojunction and InGaN-GaN DH LED structures. Results are also presented showing intense stimulated emission from GaN and InGaN under optical pumping with thresholds superior to those previously reported.

7. References

[1] "High Electron Mobility GaN/AlGaN Heterostructures grown by LPMOCVD," M.A. Khan, J.M. Van Hove, J.N. Kuznia and D.T. Olson, Appl. Phys. Lett. 58, 2408 (1991).

[2] "Observation of a two-dimensional electron gas in low pressure MOCVD deposited GaN/AlGaN heterojunctions," M.A. Khan, J.N. Kuznia, J.M. Van Hove, N. Pan and J. Carter, Appl. Phys. Lett.60, 3027 (1992).

[3] "Two-dimensional electron gas in GaN-AlGaN heterostructures deposited usign trimethylamine-alane as the aluminium source in low pressure metalorganic chemical vapor deposition," M. A.Khan, Q. Chen, C. J. Sun, M. Shur, and B. Gelmont, Appl. Phys. Lett., Vol.67(10), 1429(1995).

[4] "Reactive ion etching of gallium nitride in silicon tetrachloride plasmas," M. Asif Khan, D.T. Olson, I. Adesida, A. Mahajan, E. Andideh, and J.N. Kuznia, Appl. Phys. Lett.63, 2777 (1993).

[5] "The characteristics of chemically assisted ion beam etching of GaN," I. Adesida, A.T. Ping, C. Youtsey, T. Dow, M. Asif Khan, D.T. Olson and J.N. Kuznia, Appl. Phys. Lett., September 1994.

[6] "A Metal Semiconductor Field Effect Transistor Based on Single Crystal GaN," M. Asif Khan, J.N. Kuznia, A.R. Bhattarai and D.T. Olson, Appl. Phys. Lett.62, 1786 (1993).

[7] "High Responsivities photoconductive ultraviolet sensors based on insulating single crystal GaN layers," M.A. Khan, J.N. Kuznia, D.T. Olson, J.M Van Hove and L. Reitz, Appl. Phys. Lett.60, 2917 (1992).

[8] "Schottky barrier photodetector based on Mg-doped p-type GaN films," M. Asif Khan, J.N. Kuznia, D.T. Olson, M. Blasingame and A.R. Bhattarai," Appl. Phys. Lett.63, 2455 (1993).

[9] "Violet LED's using high temperature RTA annealed p-type GaN Layers," M. A.Khan, Q. Chen, R. A. Skogman, and J.N. Kuznia, Appl. Phys. Lett., Vol.66(16), 2046(1995).

[10] "Vertical cavity, room temperature stimulated emission from photopumped GaN films deposited over sapphire substrates using LPMOCVD," M.A. Khan, J.M. Van Hove, D.T. Olson and J.N. Kuznia, Appl. Phys. Lett.58, 1515 (1991).

[11] "Vertical Cavity Stimulated Emission from Photo-pumped InGaN/GaN Heterojunctions at Room Temperature," M. Asif Khan, S. Krishnankutty, R.A. Skogman, J.N. Kuznia, D.T. Olson and T. George, Appl. Phys. Lett., July 1994.

[12] "Microwave performance of a 0.25 micron gate AlGaN/GaN hetero-structure field effect transistor," M. Asif Khan, J.N. Kuznia, D.T. Olson, W.J. Schaff, J.W. Burm and M.S. Shur Appl. Phys. Lett.,1121 (1994).

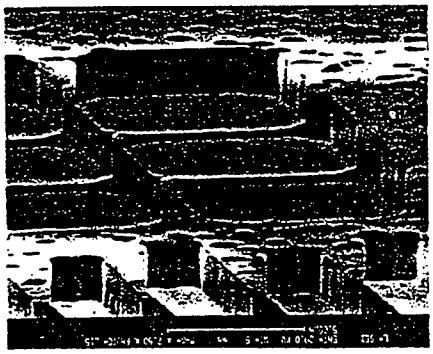


Figure 1. SEM photograph of GaN/Al_2O_3 etched by CAIBE.

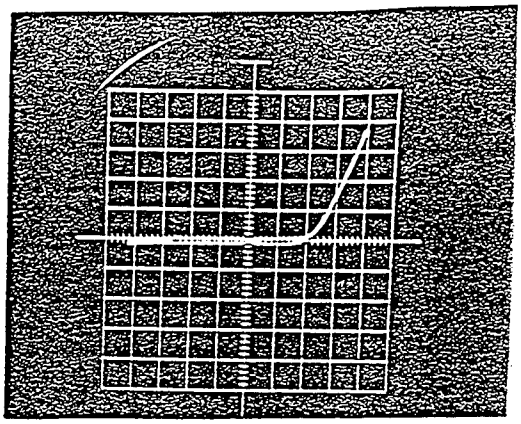


Figure 2. I-V curve of pn-junction GaN UV detector.

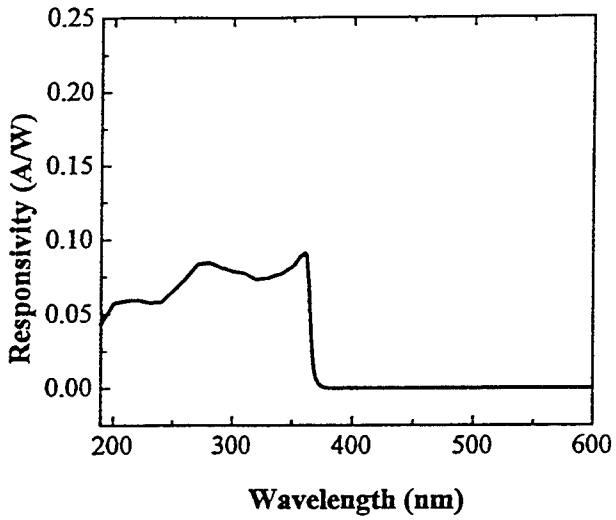


Figure 3. The photoresponsivity of GaN pn-junction vs wavelength.

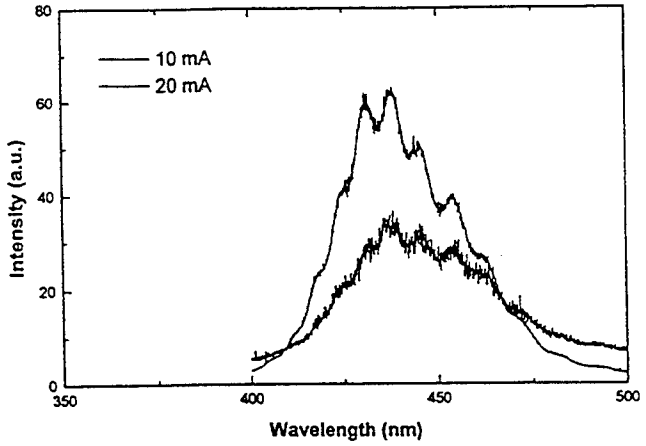
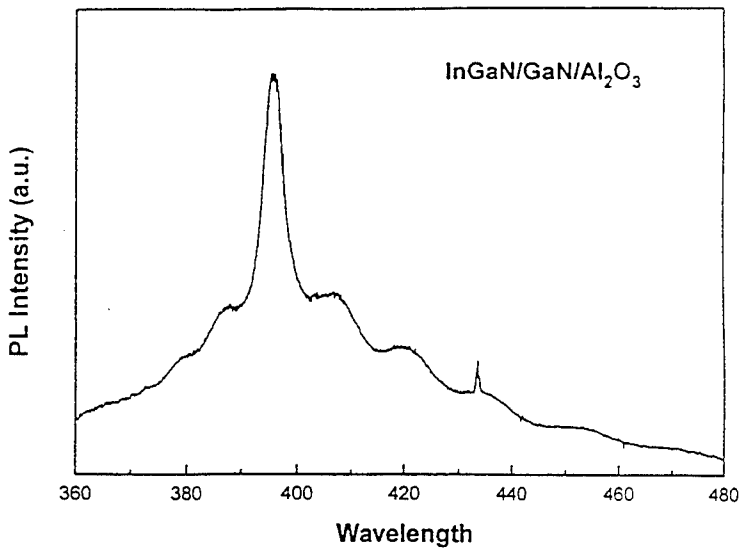


Figure 4. The emission spectrum of GaN homojunction LED at current of 20 mA.



Fugure 5. PL spectrum of InGaN/ GaN/Al_2O_3 using pulsed N2 laser as excitation source.

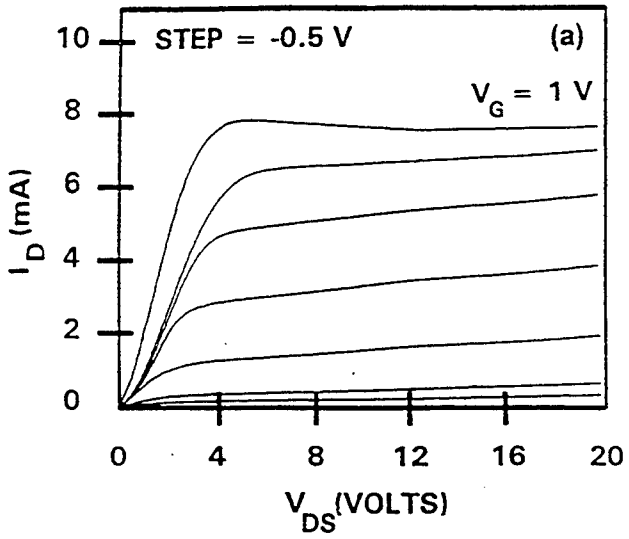


Figure 6. The souece-drain I-V curves of a 0.25 μm long gate and 150 μm wide device.

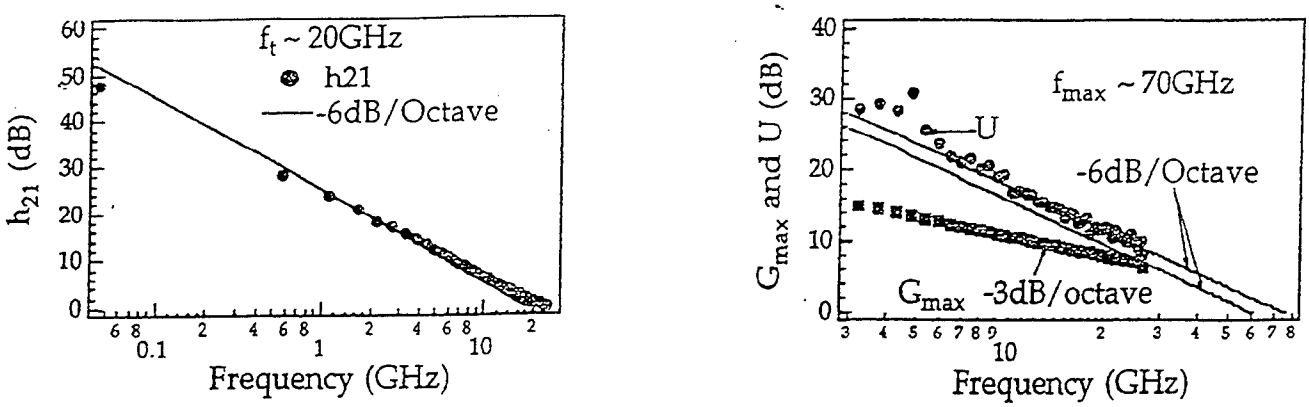


Figure 7. F_t and F_{max} values for a 0.25 μm gate transistors.

ELASTIC STRAIN RELAXATION IN GaN-AlN SUPERLATTICES

A. D. Bykhovski [a], [b], B. L. Gelmont [b], and M. S. Shur [b]

[a] *A. F. Ioffe Physico-Technical Institute, 194021 St. Petersburg, Russia*
[b] *Department of Electrical Engineering, University of Virginia, Charlottesville, VA 22903-2442, phone (804) 924-6092 fax (804) 924-8818, e-mail ab4k@virginia.edu*

I. INTRODUCTION

Layered GaN/AlN heterostructures are suitable for band gap engineering in the range of 3.4 - 6.2 eV. Compared to the solid solutions, they can allow to fabricate optoelectronic devices with lower threshold current density, lower nonradiative recombination rate, narrower emission spectra, and reduced sensitivity to temperature [1].

In GaN-AlN structures with sufficiently thin AlN and/or GaN layers, the lattice constant mismatch is accommodated by internal strains rather than by the formation of misfit dislocations. Because of the piezoelectric effect, these strains induce electric fields and may strongly affect the carrier distributions near the interfaces [2]. In order to produce a high-quality, low-dislocation density GaN- and AlN-based materials and devices, the knowledge of strain is essential.

Recently, we studied the elastic strain relaxation in GaN-AlN-GaN semiconductor-insulator-semiconductor (SIS) structures using the theory of elasticity [3]. Obtained results were in a good agreement with the data extracted from the measured capacitance-voltage characteristics. The purpose of this paper is to study the elastic strain relaxation in GaN-AlN and GaN-AlGaN superlattices using the approach developed in Ref. [3], and to compare the theoretical results with the data on fabricated GaN-AlN superlattices [1]. Also, we present the theoretical results on the piezoelectric effect in these structures.

II. ANALYSIS

The elastic strains and stresses of the GaN-AlN layered structures were calculated by considering the minimum of the deformation energy of the system. We took into account the elastic strain relaxation mechanism based on the creation of misfit dislocations. The isotropic elasticity approximation was used. To simplify the treatment, we neglected the differences between the elastic constants of GaN and AlN. Previously, we successfully used this approach to describe the elastic strain relaxation in GaN-AlN-GaN SIS structures. We have shown that it fits well the experimental data on the relaxation for a wide range of AlN film thicknesses. In particular, we have shown that the gradual relaxation process starts at AlN film thickness of approximately 30 Å, which is in agreement with our data extracted from C-V characteristics [3]. In the present work, we consider the strain in an infinite superlattice containing AlN-GaN double layers. The layer of each material has the same thickness, L. This situation was realized experimentally in Ref. [1], where up to 200 periods of AlN-GaN layers having the period thicknesses in the range of 1.5 - 40 nm were grown.

In our calculation, all interactions between dislocations were taken into account, because those are crucial for a correct determination of the energy of the system, and all related parameters, including the relative positions of dislocations [3]. The two contributions to the elastic energy come from a uniform strain due to misfit accommodation and from the misfit dislocations. In the linear theory of elasticity, the total stress is the sum of these contributions. We assume that the dislocation grids are located on every AlN-GaN interface (see Fig. 1 a, b). In the isotropic approximation, the dislocation grid at each

interface contains two perpendicular slip systems with the slip directions directed along the x and z axes (the y axis is directed along (0001) and is perpendicular to the GaN/AlN interface). Each misfit dislocation is a straight one with its Burgers vector, $\bar{b}$, in the slip direction. Further, we specified the interval between two neighbor dislocations, ℓ, and the shift along the Burgers vector, Δx, in the positions of two nearest dislocations placed on neighbor GaN/AlN interfaces which are separated by L (see Fig. 1 a, b)

In our calculation, we expressed the elastic energy density of the system, f, using the approach developed in [3]. Every stress component was a sum over the contributions from all dislocations of the system, and an initial misfit stress. (In practice, 10-20 layers were shown to be sufficient for the convergence). To obtain the energy of the layer per unit area, δF, we integrated f numerically over the volume with the exclusion of the positions of the dislocation cores, and took into account the core energy of the dislocations per unit area, F_c: $F = F_c + \delta F$ (see [3] for details of the approach, including the analytical expressions derived for the stress tensor components of a dislocation array). As in the case of SIS structures, no fitting parameters were used in our approach.

Minimizing the derived expression for the energy of the system with respect to ℓ and Δx (see Fig. 1a, b), we found ℓ and Δx as functions of L. The average elastic strain components were then expressed via stress components. In unrelaxed structure (no dislocations), the misfit strain tensor components are equal to $u_{xx}^{(0)} = u_{zz}^{(0)} = 0.5(a_1 / a_2 - 1)$, a_i is the lattice period in the hexagonal plane, i = 1, 2. In AlN layer, indices 1 and 2 correspond to GaN and AlN, respectively, and in GaN, the definition is opposite, so that xx, zz strains are negative. (In a SIS structure, unrelaxed strains are twice as large as in a superlattice with equal thicknesses of AlN and GaN layers).

III. RESULTS

In Fig. 2, we plotted the relative deformation as a function of L. In this figure, we presented our theoretical results for the superlattices. We also showed in Fig. 2 the experimental data extracted from X-ray diffraction spectra [1]. Finally, for comparison, we plotted the results for the SIS structure obtained in Ref. 3, which, in this case, corresponds to a single layer approximation. Both, our theory and the measurements show the gradual relaxation process. The experiment showed that for L = 30 Å or less, there is no misfit dislocations at the interfaces which is in agreement with obtained critical thickness L_c of about 36 Å (see Fig. 2). The layers, within the experimental error, seemed to be completely relaxed for L over 100 Å [1]. Our theory yields 80% strain relaxation (20% of strain left) over 100 Å. In terms of energy, it means ~92% relaxation. Unfortunately, in the range 30 Å < L < 100 Å, the quantitative displacements are not clear in the diffraction analysis of Ref. 1. Notice that, in a single layer (SIS) approximation, a critical thickness is almost twice as large as the multilayer result, L_c(SIS) ~ 60 Å. This is a result of the interaction of dislocations between the arrays located on the different interfaces. Namely, two factors contribute to the decreasing of stresses, and the dislocation energy: a symmetric dislocation pattern (see Fig. 1 a,b), and the opposite signs of the Burgers vectors on the neighbor interfaces. Both factors were essential in the SIS structures as well [3]. A multipole structure with $\Delta x = 0$ (Fig. 1 a) is replaced by the more uniform pattern with $\Delta x = 0.5\ \ell$, as the relaxation develops, within 50 Å < L < 60 Å. This transition, as in the case of the SIS structure, reflects the collective interactions between the dislocations within the same array, and the neighbor arrays. In Figs. 3-4, we plotted the strain-induced polarizations in GaN and AlN layers, as functions of L, and the corresponding voltage shifts. The piezoelectric constants of AlN are known [4]. In order to estimate the strain-

induced polarizations in GaN, we used the set of wurtzite GaN piezoelectric constants estimated from the data on electromechanical coupling coefficients (k^2) of GaN and AlN for the same orientations [5]. Polarizations are 10 times larger than those for GaAs-$Ga_{0.8}In_{0.2}As$ system [6]. Notice the maximum on the curve of the voltage shift versus L at L = 50 Å (see Fig. 4). A typical band structure is plotted in Fig. 6. Also, we calculated the critical thicknesses as a function of Al concentration for the GaN-$Al_xGa_{1-x}N$ superlattices (Fig. 5), and the corresponding voltage shifts (Fig. 7). The voltage shifts within the range of $1 > x > 0.13$ are increasing with the decrease of x, though the strain induced polarization is decreasing with a decrease of x. Voltage shifts ~2 V can be obtained for x~0.13.

We conclude that the gradual relaxation process in the symmetrical GaN-AlN superlattices starts at the thicknesses of the individual layer slightly over 3 nm which is in agreement with the results of X-ray analysis [1]. Also, in agreement with the experiment the relaxation fully develops when the layer thickness approaches 10 nm. According to our theory, there is a 20% residual strain at L > 10 nm. For a given misfit strain, the critical thickness in a superlattice is almost twice smaller than in a SIS structure. Due to the gradual nature of the relaxation process, the strain-induced polarization, and the corresponding voltage shifts are large even in a partially relaxed, thicker structures which should affect electronic and optoelectronic characteristics of GaN-AlN superlattices. Also, because of a substantially larger critical thicknesses achieved in the GaN-$Al_xGa_{1-x}N$ superlattices the voltage shifts ~ 2 V can be generated by the piezoelectric effect.

This work was supported by the Office of Naval Research and was monitored by Max Yoder.

REFERENCES

[1] Z. Sitar, M. J. Paisley, B. Yan, J. Ruan, W. J. Choyke, and R. F. Davis, J. Vac. Sci. Technol. B 8 , 316 (1990).
[2] A. Bykhovski, B. Gelmont, and M. Shur , J. Appl. Phys., 74, 6734 (1993).
[3] A. D. Bykhovski, B. L. Gelmont, and M. S. Shur , J. Appl. Phys., September 15, p. 3691 (1995).
[4] J. G. Gualtieri, J. A. Kosinski, A. Ballato, IEEE Trans. Ultrason., Ferroel., and Freq. Control, 41, 53 (1994).
[5] G. D. O'Clock and M. T. Duffy, Appl. Phys. Let., 23, 55 (1973).
[6] D. L. Smith, C. Mailhiot, J. Appl. Phys., 63, 2717 (1988).

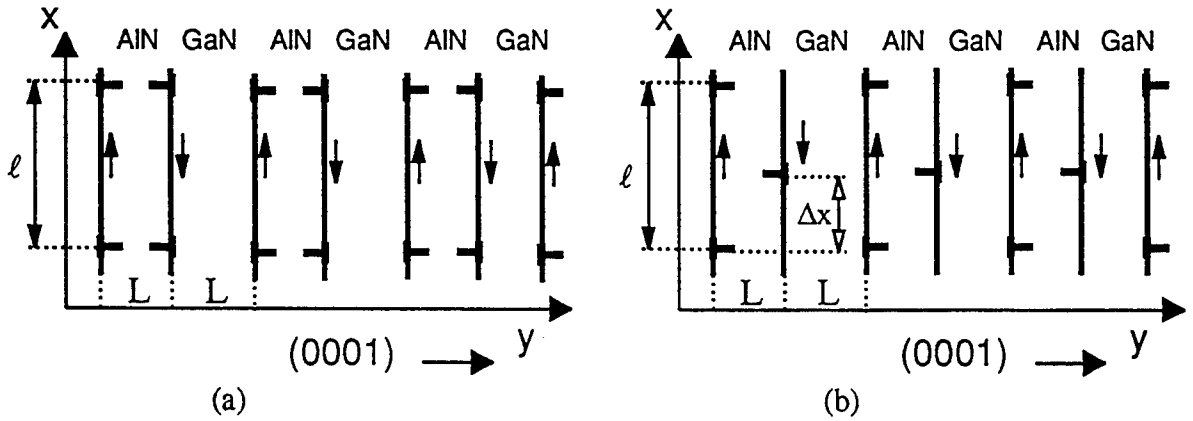


Fig. 1. GaN-AlN superlattices: low dislocation densities (a), higher dislocation densities (b). Arrows show the directions of Burgers vectors. Structure looks the same way in the yz plane.

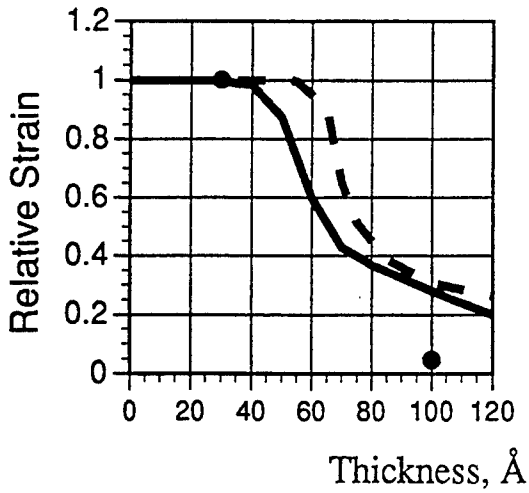


Fig. 2. Relative deformation as a function of L. The theory for a superlattice (solid line), a single layer (SIS) approximation (dashed line), and the measurements (circles).

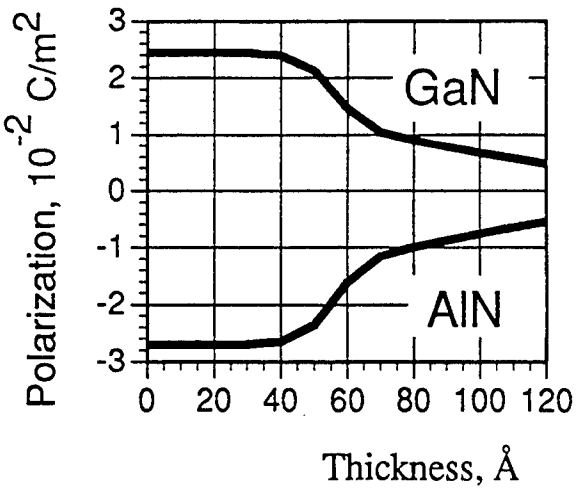


Fig. 3. Strain-induced polarization in (0001) direction as a function of L.

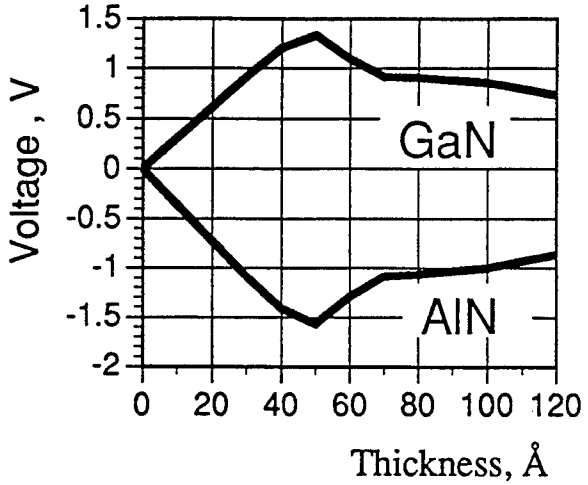


Fig. 4. Voltage shifts in AlN and GaN layers as functions of L.

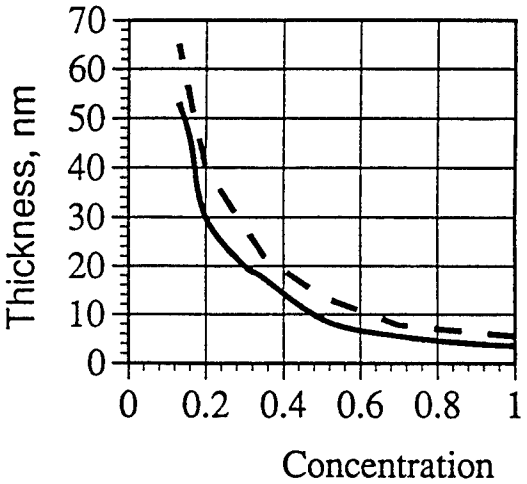


Fig. 5. Critical thickness as a function of Al concentration x: superlattice (solid line), a single layer (SIS) approximation (dashed line

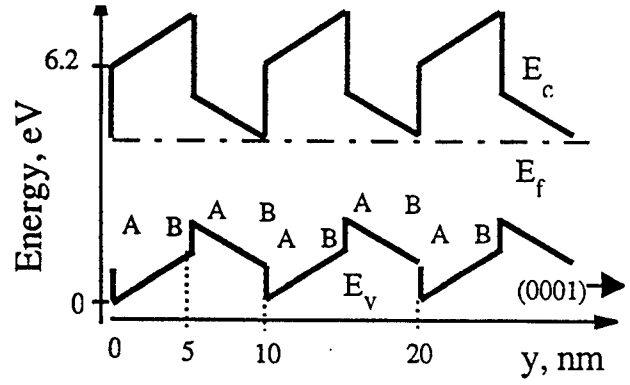


Fig. 6. AlN/GaN band structure for a low doped GaN. A is a cation face, B is an anion face.

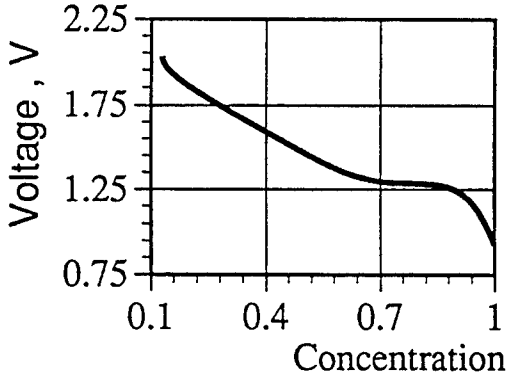


Fig. 7. Voltage shift as a function of Al concentration x.

THE INTERFACE DENSITY STATES ASYMMETRY INFLUENCE ON THE CHARACTERISTICS OF a-Si:H THIN FILM TRANSISTORS

David Bilenko, Yulia Galishnikova, Alvira Jarkova,
Olga Coldobanova, Evgenya Khasina
Saratov

The wide application of a-Si:H based transistors logical circuits and liquid crystal displays is limited by comparably low field-effect mobility and channel conductance. The possibilities of substantial parameter's increase are not exhausted.

We investigated the values and asymmetry of interface states density and position of the Fermi level in a-Si:H layers influence on the field-effect mobility - μ, channel conductance -G and threshold voltage -V_t in field-effect transistors based on single and multilayer periodic structures with thin (50-400 Å) layer's thicknesses.

The obtained results are suitable for transistors with top and bottom gate position with respect to substrate.

However, for definition all results relate to the gates,sited on substate, i.e. in a bottom position.

The calculations of field-effect mobility (FEM) and channel conductance were based on the Poisson's equation taking into account the interface states densities, similar to [1]. Reita et al [1] treated the intrinsic amorphous semiconductor with density of interface states equal at each interface. However, even if the dielectric is nominally one and the same near the both sides of semiconductor layer, interface states densities may be different. The experimental data [2,4] gives evidence that in case when a-Si:H is deposited on top of silicon nitride (bottom nitride) density of states is essentially different from that, when silicon nitride is deposited on amorphous silicon (top nitride). One of the largest values of FEM in a-Si:H TFT was achieved by Lee with coauthors on the substantially asymmetrical structure [5]. Besides, it is well known that the Fermi level position may be changed for example by doping and in the multi- layer structures it shifts towards conductivity band [6].

The calculation of G, FEM and V_t was based on selfconcerted solution of Poisson's equation with taking in account the exponential density of states distribution, consisting of deep and tail exponents [7,8]. Interface signs and values on opposite sides of a-Si:H layers were varied, density on each side was constant with energy in a-Si:H gap.

The chief results are the following:

1. The channel conductivity and field-effect mobility substantially depend on the value, sign and asymmetry of top and bottom interface states densities in a-Si:H layers in structures.The largest values of conductivity and field- effect mobility are realized when values of inter-

face states densities are not equal to zero, but with their quite definite asymmetry. The G and μ dependence on the density of states asymmetry is typical to all investigated structures and independent of a-Si:H layer thicknesses (from 50 Å to 1000 Å), a-Si:H/a-SiN_x:H number of pairs in multilayer channel and Fermi level position in a-Si:H. G and μ are influenced by asymmetry sign quite similarly in all structures.

2. The influence of interface states density is especially large in the beginning of the $G(V_g)$ and $\mu(V_g)$ characteristics, where V_g - gate voltage.As for example, for single layer structure with a-Si:H thickness - 100 Å, the change of the interface density asymmetry sign (from $N_{st}=10^{12}$ $cm^{-2}eV^{-1}$, $N_{sb}=0$ to $N_{sb}=10^{12}$ cm^{-2} eV^{-1} $N_{st}=0$) cause the change of channel conductance in $8\cdot10^3$ and field-effect mobility in 700 times as large. The favourable sign of asymmetry can essentially rise the values of parameters as compared to zero interface states densities structures with $N_{st}=10^{12}$ $cm^{-2}eV^{-1}$, $N_{sb}=0$ gives the values of G and μ, exceeding these values when $N_{st}=N_{sb}=0$ and $V_g=1V$ in 280 and 65 times respectively.

3. The influence of interface asymmetry increases, when a-Si:H layer thickness decreases; reducing of a-Si:H thickness gives rise to the increasing of channel conductance and field-effect mobility.

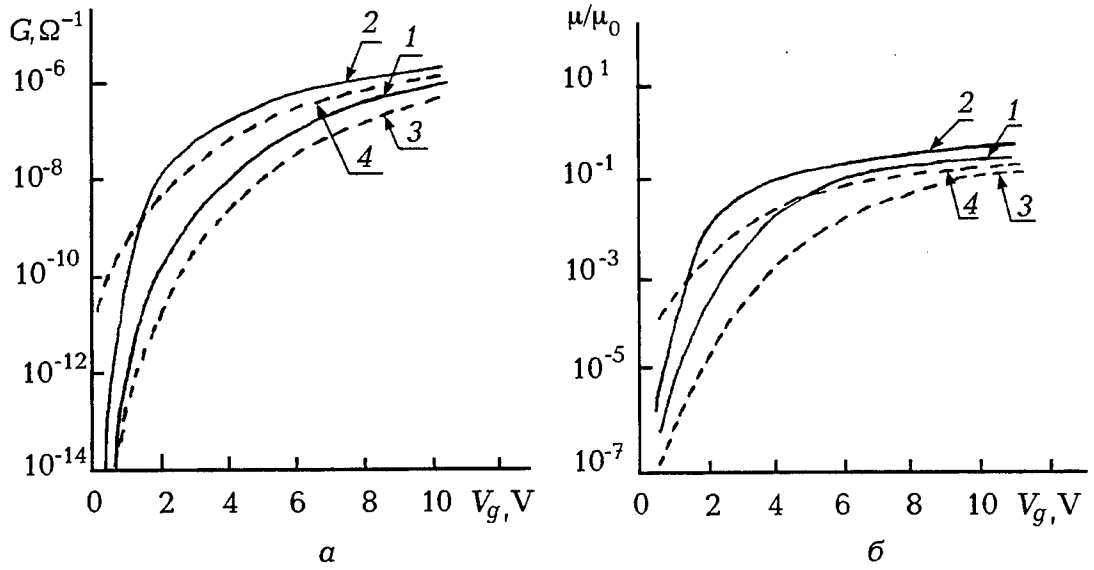
4. Comparison of the achieved values of G and μ in a single and multilayer structures with the same total a-Si:H thickness showed us that G and μ in periodic structures substantially larger, than in single layer structures. For example, field-effect mobility and channel conductance in 4-layers structure exceeds the same parameters in single layer structure by factor 2.6 - 5.3 and 5 respectively with the favourable asymmetry density interface states (Fig.1). Reduction of a-Si:H layers thicknesses in superlattice lead to the increasing of channel conductance and field-effect mobility with other things being equal.

5. Doping of a-Si:H (displacement of Fermi level towards conduction band) causes the shift of $G(V_g)$ and $\mu(V_g)$ characteristics to the area of small V_g values, and also increases the largest achievable values of G and μ/μ_0, when V_g is high, where μ_0 - the microscopic mobility in a-Si:H conductance band. When Fermi level rises the influence of interface charge and a-Si:H layer thickness reduces, while the character of G and μ dependences on interface density on states and thickness of a- Si:H layer is reserved.

6. The interface density of states asymmetry essentially influence the threshold voltage of FET. For example, the asymmetry sign change from $N_{st}=0$, $N_{sb}=10^{12}$ cm^{-2} eV^{-1} to $N_{st}=10^{12}$ cm^{-2} eV^{-1}, $N_{sb}=0$ provided all other things be equal decreases the calculated threshold voltage of FET approximately on 40 and more %.

The explanation of the revealed features of interface states density influence FET characteristics is based on combined effect of external and internal built-in fields.

The calculated dependences of potential and electric field distributions across structures demonstrate the electric field gradient



а *б*

Fig.1. Field-effect conductance (*a*) and field-effect mobility μ to free electron mobility μ_0 ratio (*b*) vs gate voltage V_g for single (- - -) and 4-layer (———) structures. Total a-Si:H thickness - 200 Å; a-SiN_x:H thickness - 50 Å; gate dielectric - a-SiN_x:H, 1000 Å, a passivating layer opposite to the gate - a-SiN_x:H, 300 Å; μ_0 = 10 cm^2 $V^{-1}s^{-1}$; *1, 3* - $N_{st} = N_{sb} = 0$; *2, 4* - $N_{st}=10^{12}$ cm^{-2} eV^{-1}, $N_{sb}= 10^{12}$ cm^{-2} eV^{-1},($Q < 0$)

and potential growth in a-Si:H layers as asymmetry transit from unfavourable to favourable for achieving the largest values of *G* and μ. Reducing of a-Si:H layer thickness influence the potential and field gradient distribution by the analogous way.

The flexibility and diversity of plasma chemical processes together with abilities of their in situ monitoring contribute to creation of multilayer structures with the designed interfaces. The essential influence of the deposition succession on the interfaces structure by optical measuring in situ is stated [9,10].

The interface states density asymmetry is revealed by in situ measuring of multilayer structure resistance change (Fig. 2). The asymmetry is shown up more sharply by in situ measurements when the different processes being made one by one. For example, in sequence - deposition of a-SiN_x:H in SiH_4/NH_3 plasma - deposition of a-Si:H in SiH_4 plasma and then modification a part of a-Si:H layer to a-SiN_x:H by nitridation in NH_3 plasma.

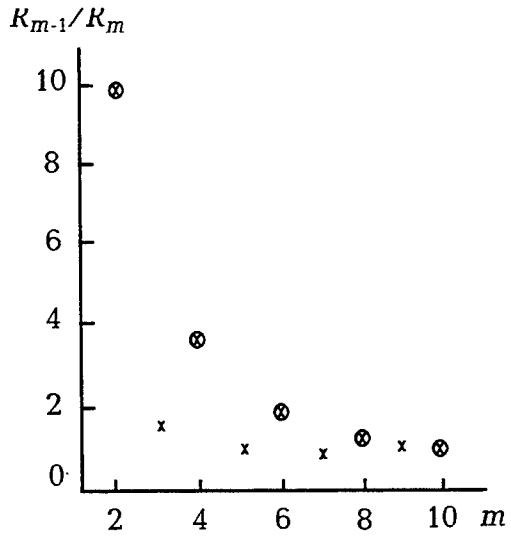


Fig. 2. Multilayer structure a-Si:H/a-SiN_x:H resistances ratio after deposition of each subsequent layer, received in situ. Even values of m are respected to structure when a-SiN_x:H is deposited on a-Si:H (top nitride); *m* - number of layers

The results show some possibilities to improve TFT's ratings on the base of structures with desired asymmetry of interface states and preserved microscopic mobility in multilayered structures with thin a-Si:H layers.

1. C.Reita, L.Mariucci, G .Fortunato. J.Appl.Phys., 29, 1634 (1990)
2. R.A.Street, M. Thompson,N.M. Johnson. Phil.Mag., 5, 1 (1985)
3. R.A.Street, M. .Thompson. Appl.Phys.Lett., 45, 71 (1984)
4. C.B.Roxlo, T.Tiedje, B.Abeles. Phys.Rev.Lett., 52, 1994 (1984)
5. J-L. Lin, W-J. Sah, S-Ch. Lee. IEEE Electron Devices L., 12,120 (1991).
6. K.Hiranako, T. Yoshimara, T. Yamaguchi, S. Yanajisawa. J. Appl. Phys., 60, 4204 (1986).
7. M. Shur,Choong Hyun, M. Hack. J. Appl. Phys., 59, 2489 (1986).
8. M. Shur, M. Hack, J.Appl. Phys., 55, 3831 (1984)
9. R. Ossikovski, H. Shirai and B. Drevillon. Appl. Phys. Lett., 64, 1815 (1994).
10. H. Shirai, B. Drevillon and R. Ossikovski. Appl. Phys. Lett., 62, 2833 (1993).

Microscopic Determination of Noise in Semiconductor Devices and its Application to Sub-μ Gate-Length Hetero-FETs

Ali Abou-Elnour and Klaus Schünemann
Tech. Univ. Hamburg-Harburg, Arbeitsbereich Hochfrequenztechnik,
D-21071 Hamburg, Germany.

Abstract

A rigorous two-dimensional Monte-Carlo physical simulator is developed to determine the non-stationary transport properties, the quantization effects, and the noise behavior in semiconductor devices. Due to the microscopic nature of the simulator, it is well suited to study the effects of device geometry, doping level, and bias voltage on device characteristics and, moreover, to determine the spatial origins of noise in the different device regions without any approximations or simplifying assumptions. As an example, the simulator is applied to accurately describe the noise behavior of submicron gate-length Hetero-FETs.

1 Introduction

It has been stated recently that "the transport properties of the two-dimensional electron gas in Hetero-FETs do not make a significant contribution to the noise reduction at high frequency operation of these devices" [1-2]. The average velocity model which has been used in [1] is, however, not suitable to take the non-stationary transport properties in subhalf-micrometer gate length MESFETs and the quantization effects in Hetero-FETs into account. Hence the accuracy of the calculated results and the validity of the interpretations are questionable. Moreover, these studies have been performed below certain frequency limits what represents another limitation of the conclusions which were drawn. On the other hand, the noise behavior of different MESFETs and Hetero-FETs has been described in [3] by using a Monte-Carlo physical simulator. In the present work, this model will be first extended and then applied to Hetero-FET structures to investigate the noise currents at the device electrodes and the noise spectra in the different device regions.

2 Model

The model is based on a self-consistent coupling of a Monte-Carlo code which simulates the non-stationary transport, with a flexiable solver of Schrödinger's equation which determines the quantization effects by using a closed-form expansion of the wave functions [4]. Hence the limitations of the conventional finite-difference models which arise from mesh size, discretization, and boundary conditions are overcome. The temporal and the spatial variations of the electric field are also taken into account by successive solution of Poisson's equation in two dimensions with a time step ΔT. This means that all variations of the physical quantities, and consequently the noise spectra, can be directly extracted without any approximations or simplifying assumptions.

The simulated semiconductor device is according to a regional approximation approach advantageously divided into different regions which are expected to have a dominant influence on its performance. An efficient choice of these regions largely depends on the understanding of the physical operation of that device. For a semiconductor device which has M electrodes and which is divided

into N different regions, the generalized noise matrix $\mathcal{S}$ which defines the noise spectral densities of the current i_{e_m} passing the m^{th} device electrode and the current i_{r_n} in the n^{th} region is given by

$$\mathcal{S} = \begin{pmatrix} S_{i_{e_1}i_{e_1}} & \cdots & S_{i_{e_1}i_{e_m}} & S_{i_{e_1}i_{r_1}} & \cdots & S_{i_{e_1}i_{r_n}} \\ \cdots & \cdots & \cdots & \cdots & \cdots & \cdots \\ S_{i_{e_m}i_{e_1}} & \cdots & S_{i_{e_m}i_{e_m}} & S_{i_{e_m}i_{r_1}} & \cdots & S_{i_{e_m}i_{r_n}} \\ S_{i_{r_1}i_{e_1}} & \cdots & S_{i_{r_1}i_{e_m}} & S_{i_{r_1}i_{r_1}} & \cdots & S_{i_{r_1}i_{r_n}} \\ \cdots & \cdots & \cdots & \cdots & \cdots & \cdots \\ S_{i_{r_n}i_{e_1}} & \cdots & S_{i_{r_n}i_{e_m}} & S_{i_{r_n}i_{r_1}} & \cdots & S_{i_{r_n}i_{r_n}} \end{pmatrix} \quad (1)$$

where the self-spectral densities $S_{i_xi_x}(f)$ and cross-spectral desities $S_{i_xi_y}(f)$ are given by [5]

$$S_{i_xi_x}(f) = 2\int_{-\infty}^{+\infty} \overline{i_x(t)i_x(t+\tau)}e^{-j\omega\tau}d\tau \quad and \quad S_{i_xi_y}(f) = 2\int_{-\infty}^{+\infty} \overline{i_x(t)i_y(t+\tau)}e^{-j\omega\tau}d\tau. \quad (2)$$

The electrode noise current $i_{e_m}(t)$ around its average value $\overline{I_{e_m}}$ is calculated from the particle counting (PC) method by: $i_{e_m}(t) = I_{e_m}(t) - \overline{I_{e_m}}$ where $I_{e_m}(t) = Q\frac{\Delta N}{\Delta T} + A\,\varepsilon\,\frac{\Delta E}{\Delta T}$, while the noise current $i_{r_n}(t)$ around $\overline{I_{r_n}}$ is given from the Shockley-Ramo (SR) theorem by: $i_{r_n}(t) = I_{r_n}(t) - \overline{I_{r_n}}$ where $I_{r_n}(t) = \frac{Q}{L}\sum_{i=1}^{N_n} v_i(t)$. In PC method, Q means particle charge, ΔN net number of particles which are crossing the m^{th} electrode, ΔE change in electric field, ΔT time step, A area of the m^{th} electrode, and ε dielectric constant, while in SR method, L means length, N_n number of particles, and $v_i(t)$ velocity of i^{th} particle in the n^{th} region. It should be mentioned that all required information for extended noise calculations, like the spatial distribution of the voltage fluctuations, can also be extracted. The required CPU time, which is mainly affected by the number of simulated particles and by the simulated time period, and storage represent the main limitations of the model. Storage itself depends on the number of both device electrodes and different device regions. These effects are, however, less important today with the ongoing progress in computational facilities.

3 Applications

The simulated Hetero-FET structure (fig.1) consists of a 30 nm thick $GaAs$ cap layer, a 42 nm $Al_{0.3}Ga_{0.7}As$ layer, and a $GaAs$ buffer layer doped with a donor concentration of $2.10^{18}cm^{-3}$, $1.10^{18}cm^{-3}$, and $1.10^{14}cm^{-3}$, respectively. A $0.15\mu m$ gate-length is recessed at a depth of 30 nm with $0.12\mu m$ separation between the gate edges and the highly doped source and drain regions. The source-gate and source-drain electrode separations are 0.3 and 1.05 μm, respectively. The simulations have been performed at temperature of 300 K. The different regions which dominate the noise performance of the device are: the source-gate, the $AlGaAs$ gate, the gate-drain, and the 2DEG regions (regions I, II, III, and IV-VI, respectively). The drain current is calculated by using both the PC and the SR method which produced almost identical results (deviations being less than 1 percent) when the simulation time is sufficiently long (fig. 2). All other interesting physical quantities, for example the percentage of the drain current which flows in the 2DEG channel, can also be determined (fig. 2).

The autocorrelation functions of the gate and drain currents are found to nearly vanish after 1 ps (fig. 3) while their spectral densities S_{i_D} and S_{i_G} (fig. 4) qualitatively show similar behavior to that described in [6]. To our best knowledge, this is, however, the first time that they are accurately calculated for Hetero-FETs by using a fully self-consistent particle simulator. The long tail oscillations of the autocorrelation functions around zero (fig. 3) increase the uncertainty in the calculated results, especially for smaller values, at lower frequencies. On the expense of CPU time, the accuracy of the results can, however, be improved by increasing the number of simulated particles, by using a smaller mesh size and smaller time steps in the Poisson solver, and by increasing the simulated time period.

To accurately interpret the measured noise behavior of MESFETs and Hetero-FETs [1-2], one must keep in mind that the improvement of the performance of Hetero-FETs is coming from the separation

of the carriers in the 2DEG channel from their parent atoms in the *AlGaAs* layer. This means that the ionized impurity scattering in a Hetero-FET is much lower than that in a MESFET. At lower frequencies of operation, however, optical phonon and intervalley scattering play a dominant role so that one can expect that the noise behavior of a MESFET should be better than that of a Hetero-FET. For higher frequencies, on the other side, the effect of the ionized impurity scattering shows a larger influence on the transport properties what improves the noise behavior of a Hetero-FET compared to a MESFET (fig. 5a). One must keep in mind that the overall noise performance is also affected by the noise generated in the source-gate and gate-drain regions which further deteriorate the noise performace at high frequencies (fig. 5b).

4 Conclusions

An accurate two-dimensional physical noise simulator is developed which takes into account the non-stationary transport properties and the quantization effects in subhalf-micrometer FETs in a better way than conventional models do. The model is capable to determine the steady-state behavior as well as the self- and cross-spectral noise densities at all device regions and electrodes. The superior noise performance of a Hetero-FET, and in particular at high frequencies, comes from the reduction of the ionized impurity scattering in the 2DEG channel. This effect depends on the current which flows through that region and its percentage of the overall current. All physical phenomena which affect the spatial and temporal fluctuations can be accurately determined what makes the model an efficient tool which can be used to analyze the noise behavior of other semiconductor materials and devices as well.

Acknowledgment

The authors are thankful to the Deutsche Forschungsgemeinschaft for financial support.

References

[1] M. Feng and J. Lasker, IEEE Trans. Electron Devices, vol. 40, p. 9, 1993.
[2] M. Feng et al, IEEE Electron Device Lett., vol. 16, p. 139, 1995.
[3] A. Abou-Elnour and K. Schünemann, Proc. of the 25th EuMC, 1995. (will be published)
[4] A. Abou-Elnour and K. Schünemann, J. Appl. Phys., vol. 74, p. 3273, 1993.
[5] A. van der Ziel, Noise in Solid-State Devices and Circuits, New York, Wiley, 1986.
[6] A. Cappy, IEEE Trans. Microwave Theory Tech, vol. 36, p. 1, 1988.

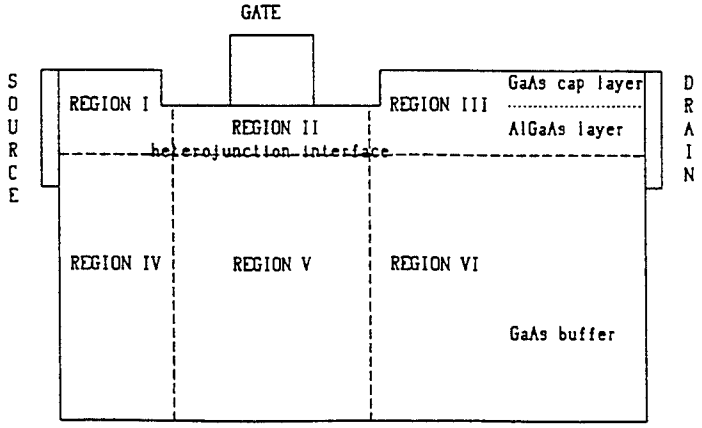


Fig.1 The simulated Hetero-FET structure with different regions.

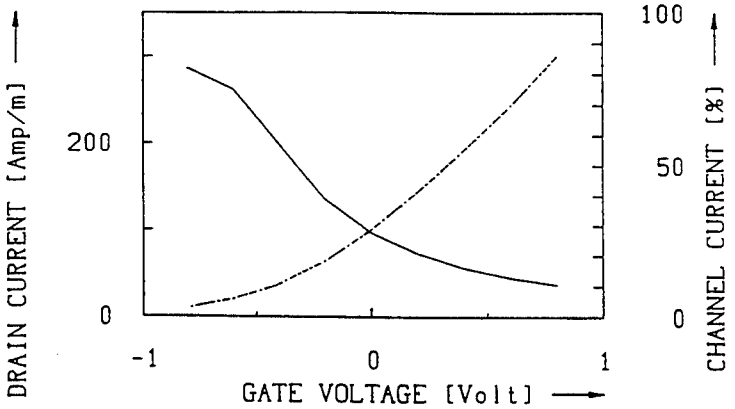


Fig.2 Drain current of the simulated Hetero-FET obtained by SR (dashes) and PC (dots) methods and its percentage (solid line) which flows in the 2DEG channel (region V).

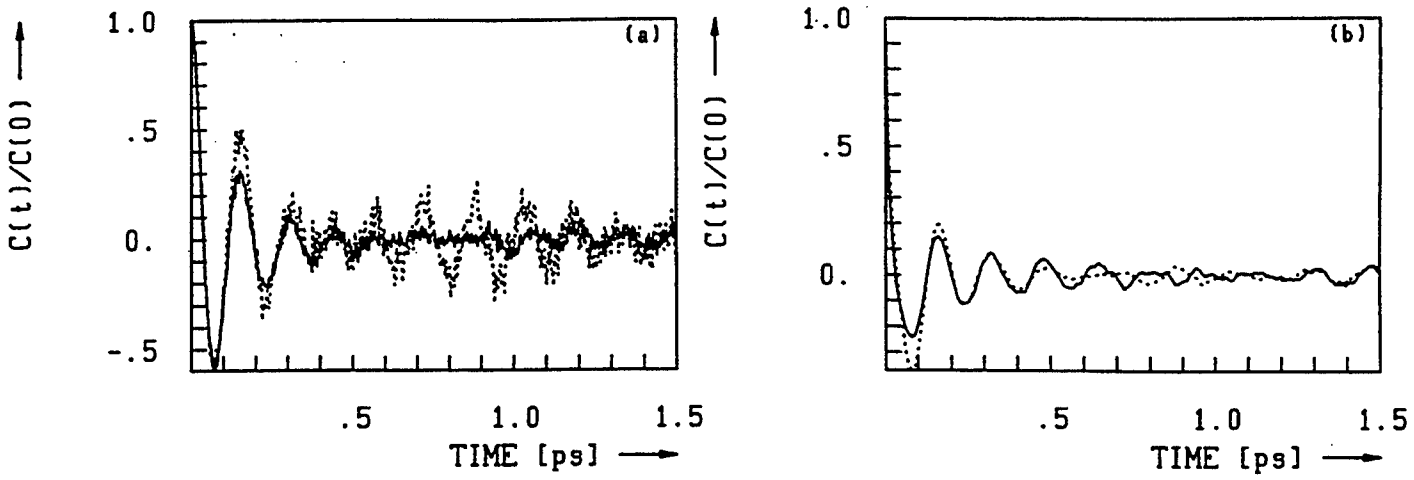


Fig.3 Drain (a) and gate (b) current autocorrelation functions. Vd=2V, Vg=.6V (solid line), Vg=-.2V (dashed line)

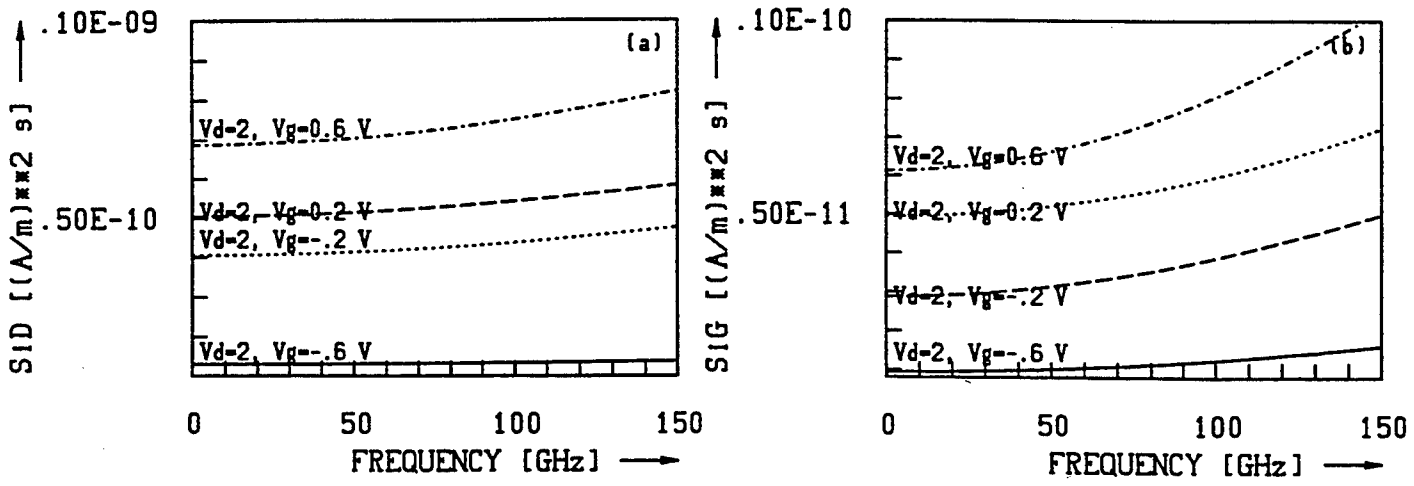


Fig.4 Drain (a) and gate (b) noise current spectral densities.

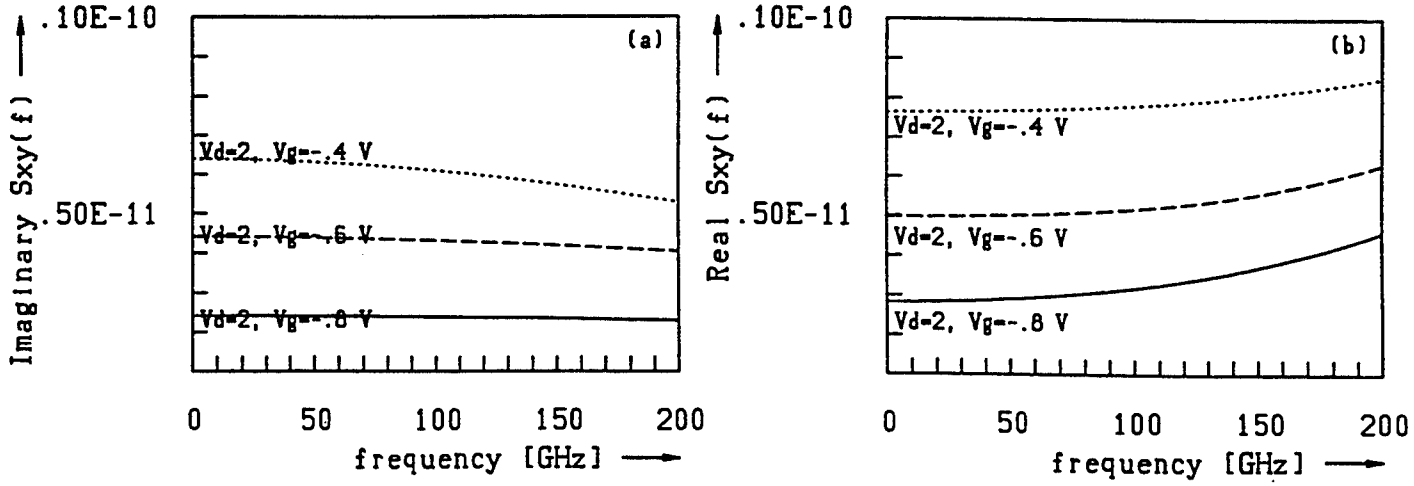


Fig.5 2DEG channel (a) and gate-drain (b) noise current spectral densities in regions V and III, respectively, of fig.1.

Electron-phonon coupling in multiply-connected quantum wires via tight-binding Green's functions

William R. Grisé
Morehead State University

This paper considers the problem of inelastic scattering due to phonons in a one-dimensional Aharonov-Bohm ring and more generally in any multiply-connected structure of quantum wires. The transmission coefficient is calculated using a recursive Green's function technique, which the author has applied to the ballistic transport problem in the same structure [1]. As in that work, the electron Hamiltonian is given by a tight-binding model, while the electrons are linearly coupled to the phonon modes. In the Aharonov-Bohm effect particularly, the role of inelastic scattering in destroying phase coherence is critical to the effect. In the model used in this work, therefore, the electron-phonon interaction is explicitly inelastic in its effect on the electron's energy.

A number of papers in recent years have analyzed the electron-phonon interaction for quantum wells [2]-[3], quantum wires [4]-[5], and resonant tunneling devices [6]-[7]. The work in [6], in which the authors went beyond the Lorentzian line shape often adopted for the elastic transmission coefficient, also uses a tight-binding recursive Green's function method to analyze the case of LO-phonon-assisted resonant tunneling. In fact, most of the authors above focus on the longitudinal optical (LO) phonon as the dominant scattering mechanism in GaAs and other III-V semiconductors. Very recently, there have been suggestions in the literature that in the transverse confining boundaries of narrow quantum wires, electron interactions with acoustic phonons also might be responsible for inelastic scattering of electrons. For the types of quantum interference devices considered here, which are often operated at low temperatures and under low bias, the present paper will compare the effects of both LO phonons and acoustic phonons on the transmission coefficient.

The tight-binding Hamiltonian for electrons only in an Aharonov-Bohm ring is:

$$H_e = \varepsilon_0 \sum_l |l\rangle \langle l| + V \left\{ \sum_l \exp\left(\frac{ie}{2\hbar c}\vec{H}\cdot\vec{r}_l \times \vec{r}_{l+1}\right) |l\rangle \langle l+1| \right. \qquad (1)$$

$$\left. + \exp\left(\frac{-ie}{2\hbar c}\vec{H}\cdot\vec{r}_l \times \vec{r}_{l-1}\right) |l\rangle \langle l-1| \right\}$$

where the phase factors apply to the perturbation indicated by the finite loop (from site 1' to M). As many have pointed out [6], by choosing $V = -\hbar^2/2m^*a^2$ and $\varepsilon_0 = -2V$, the tight-binding model can be made to replicate the effective-mass approximation. In [1], we were able to derive a closed-form expression for the transmission amplitude, t, and the transmission coefficient, T, as a function of energy and flux ratio, by taking the ratio of the matrix elements of the Green's function for the chain-loop structure to those for the infinite chain only:

$$t = \textit{transmission}\ \text{amplitude} = \frac{G(\alpha,\beta)}{G_0(\alpha,\beta)} \qquad (2)$$

When the emission and absorption of phonons is taken into account, (1) must of course be extended to include the bare phonon Hamiltonian and the electron-phonon Hamiltonian, which gives:

$$H_e = \sum_{l,n} |l,n\rangle\, \varepsilon_l \langle l,n| + \hat{V} \sum_{l,n} |l,n\rangle \langle l+1,n| + |l,n\rangle \langle l-1,n| \qquad (3a)$$

$$H_p = \sum_{l,n} |l,n\rangle \left(n + \frac{1}{2}\right) \hbar\omega_0 \langle l,n| \qquad (3b)$$

$$H_{ep} = \sum_{n,m} \sum_{l=0}^{N+1} |l,m\rangle\, \gamma Q_{mn} \langle l,n| \qquad (3c)$$

In (3a), $\hat{V}$ includes the relevant phase factors, while states labeled n and m refer to phonon states. Also, Q_{mn} is the linear displacement of the l^{th} atom in the loop region . Furthermore, in (3c), the interaction between charge carriers and phonons is restricted to the region of the loop. This approximation can only be partly justified by claiming that propagating electrons spend more time in the region of the loop where they are subject to the additional scattering occasioned by the loop itself [6]. On the other hand, in H_{ep} we have avoided mapping all the sites in the loop region onto one site. In [6], the authors do just this for the

sites in the well between the two barriers in the double-barrier resonant tunneling device. With this approximation, these authors are claiming that an electron in the well, with energy close to one resonant level, will remain far away in energy from another resonance after emission or absorption of a phonon.

To obtain the Green's function and then the transmission coefficient, we apply Dyson's equation repeatedly:

$$G = G^0 + G^0(H - H_e)G \qquad (4)$$

where we can now use our previously derived expression for the transmission amplitude (2) to write down a new $G^0(\alpha, n; \beta, n) = t_n \cdot G_{00}(\alpha, n; \beta, n)$, where G_{00} is the Green's function for the infinite chain only. We remember that G^0 is diagonal in the phonon number, and that Q_{mn} has the form

$$Q_{mn} = \sqrt{\frac{\hbar}{2M\omega_0}}\left(\sqrt{n+1}\delta_{m,n+1} + \sqrt{n}\delta_{m,n-1}\right) \qquad (5a)$$

$$= \Delta\left(\sqrt{n+1}\delta_{m,n+1} + \sqrt{n}\delta_{m,n-1}\right) \qquad (5b)$$

We will display the results for the case in which the initial state has no phonons (zero temperature), and intermediate states have up to two LO phonons. To simplify notation, we write the Green's functions matrix elements as $G_{n,m}(i,j)$, where (n,m) label the phonon states, and (i,j) label the electron states localized at sites i and j. We use $\Omega^n = (n + 1/2)\hbar\omega_0$, and repeated indices to indicate summation over the sites from 0 to N+1, or over phonon number. The results for this simple case are summarized below.

$$\left(\delta_{lk} - G^0_{0,0}(l,k)\Omega^0\right) G_{0,m}(k,\beta) = G^0_{0,0}(l,\beta) + G^0_{0,0}(l,k)\,\gamma\Delta\cdot(1)\cdot G_{1,m}(k,\beta) \qquad (6a)$$

$$\left(\delta_{lk} - G^0_{1,1}(l,k)\Omega^1\right) G_{1,m}(k,\beta) = G^0_{1,1}(l,\beta) \qquad (6b)$$

$$+G^0_{1,1}(l,k)\cdot\gamma\Delta\left[(1)\,G_{0,m}(k,\beta) + \sqrt{2}G_{2,m}(k,\beta)\right]$$

$$\left(\delta_{kj} - G^0_{2,2}(k,j)\Omega^2\right) G_{2,m}(j,\beta) = G^0_{2,2}(k,\beta) + G^0_{2,2}(k,j)\,\gamma\Delta\sqrt{2}G_{1,m}(j,\beta) \qquad (6c)$$

From this point, matrix manipulations yield the vector $G_{2,m}(k,\beta)$ in terms of $G_{1,m}(k,\beta)$. We also find $G_{0,m}(k,\beta)$ in terms of $G_{1,m}(k,\beta)$, which enables us to get a matrix equation for the $G_{1,m}(k,\beta)$. Solving these matrix equations , we can finally find the matrix element for the Green's function between sites (α,β), with the phonon states making a transition from zero phonons to m phonons. Taking

the ratio of this matrix element to the the Green's function without phonons, we define the transmission amplitude as:

$$t_{0,m} = \frac{G_{0,m}(\alpha, \beta)}{G_{0,0}(\alpha, \beta)} \tag{7}$$

In conclusion, this research has incorporated a linear coupling to phonons of the electrons in a tight-binding picture which are propagating in multiply connected quantum wires. Comparisons are made for the case of zero initial phonons and three final phonons in Figures 1 and 2, for magnetic flux ratios of $\pi/4$, and $\pi/2$, respectively. By comparison with the zero-temperature case (Figure 3), there is a greater effect on the transmission due to phonon coupling than was reported by [6]. More detailed investigations of these effects will be presented.

References

[1] W.R. Grise, C. M. Krowne, and F.A. Buot, "Ballistic transport in one-dimensional Aharonov-Bohm rings," to be submitted for publication.

[2] J. P. Leburton, "Size effects on polar optical phonon scattering of 1-D and 2-D electron gas in synthetic semiconductors," *J. Appl. Phys.*, vol. 56(10), pp.2850-2855, 1984.

[3] Lionel Friedman, "Electron-phonon scattering in superlattices," *Phys. Rev. B*, vol. 32, pp. 955-961, 1985.

[4] K.W. Kim, M.A. Stroscio, A. Bhatt, R. Mickevicius, and V.V. Mitin, "Electron-optical -phonon scattering rates in a rectangular semiconductor quantum wire," *J. Appl. Phys.*, vol. 70(1), pp. 319-327, 1991.

[5] Michael A. Stroscio, "Interaction between longitudinal-optical-phonon modes of a rectangular quantum wire and charge carriers of a one-dimensional electron gas," *Phys. Rev. B*, vol. 40, pp. 6428-6431, 1989.

[6] J.A. Støvneng, E.H. Hauge, P. Lipavský, and V. Špička, "Tight-binding approach to resonant tunneling with electron-phonon coupling," *Phys. Rev. B*, vol. 44, pp. 13595-13602, 1991.

[7] Ned S. Wingreen, Karsten W. Jacobsen, and John W. Wilkins, "Inelastic scattering in resonant tunneling," *Phys. Rev. B*, vol. 40, pp. 11834-11850, 1989.

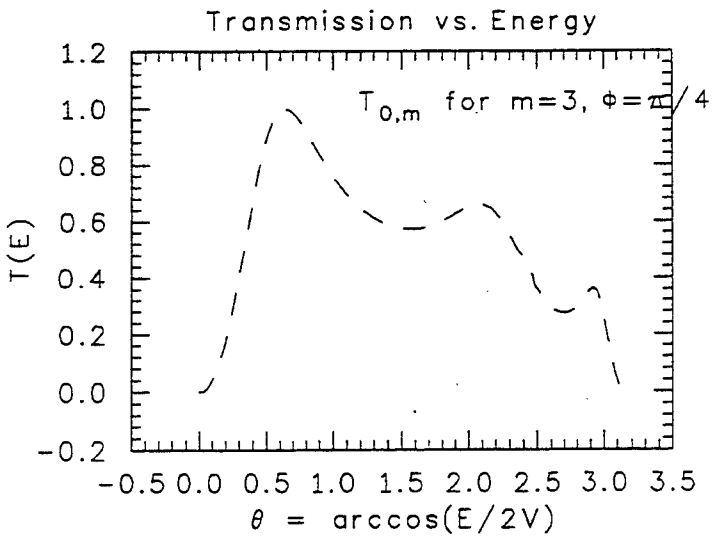


Figure 1. Transmission vs. Energy for zero initial phonons and three final phonons. Magnetic flux ratio = $\pi/4$.

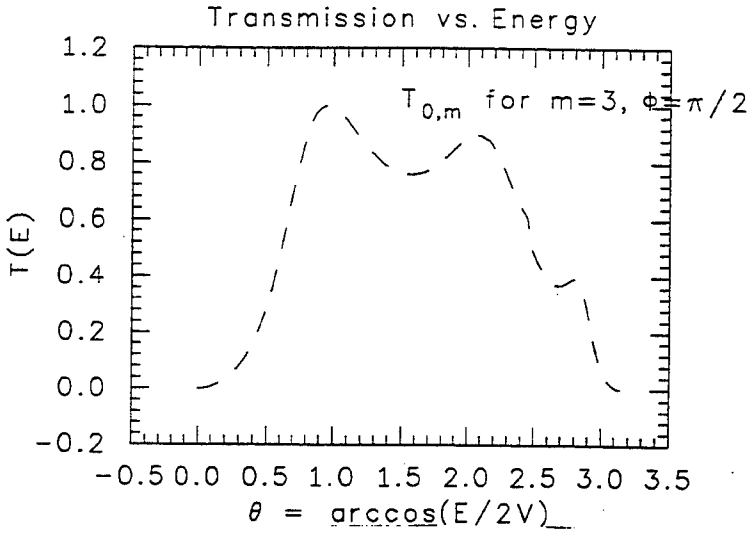


Figure 2. Transmission for same phonon numbers; flux ratio is $\pi/2$.

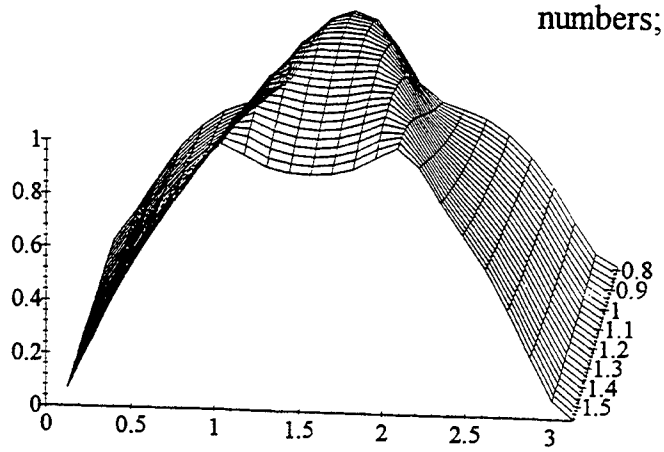


Figure 3. Transmission vs. Energy at Flux ratio, $\Phi : \pi/4 \longrightarrow \pi/2$. No phonons

Nonlinear Evolution of the Dyakonov-Shur Instability

B.Gelmont

Department of Electrical Engineering, University of Virginia, Charlottesville,

VA 22903-2442

The nonlinear evolution of the Dyakonov-Shur instability is considered in the case of small increment.It is shown that a shock wave will be formed with the discontinuity of the electric field. The coordinate where the discontinuity occurs does not depend on the initial conditions whereas the time for achieving the shock wave state is determined by the initial amplitude of the fluctuation.

1. Introduction.

Dyakonov and Shur [1] considered the behavior of electrons in a short field effect transistor at a relatively small bias when electrons experience practically no collisions with phonons and impurities during the transit time. They showed that the electron gas will be unstable if the potential is fixed at a source and the current is fixed at a drain. Usually the growth caused by instability is restricted by nonlinearity.At the first glance,it seems that the amplitude of oscillations is proportional to the square root of the increment when the increment is small [2]. We'll show that this is not the case for this instability. The amplitude will increase till the formation of a shock wave even at small increment.

2. Basic equations.

The hydrodynamic equations describing an electron fluid coincide with those for shallow water.We take a somewhat different initial system of equations which is completely equivalent to the system used by Dyakonov and Shur.We rewrite their equations for the flow ,j=CUv, and the two-dimensional charge density,Q=CU, where C is the gate capacitance, $U=U_{gc}-U_T$, U_{gc} is the gate-to-channel voltage swing, U_T is the threshold voltage,v is the drift velocity.

$$\frac{\partial Q}{\partial t}+\frac{\partial j}{\partial x}=0 \qquad (1)$$

$$\frac{\partial j}{\partial t}+\frac{\partial}{\partial x}[\frac{j^2}{Q}+\frac{eQ^2}{2mC}]=0 \qquad (2)$$

where e is the free electron charge,m is the electron effective mass.
If we introduce a new function f determined as follows

$$Q=C(L\frac{\partial f}{\partial x}+1)U_o \qquad (3a)$$

$$j=C(v_o-L\frac{\partial f}{\partial t})U_o \qquad (3b)$$

where $U_O=ms_O^2/e$ is the gate-to- source voltage swing, $j_O=CU_Ov_O$ is the drain flux equation (1) will be satisfied identically. Substituting (3a) -(3b) into (2) we obtain

$$\frac{\partial^2 f}{\partial \tau^2}+\frac{\partial}{\partial \xi}\{\frac{1}{2}(\frac{\partial f}{\partial \xi})^2+[(\frac{\partial f}{\partial \tau})^2+(\frac{\partial f}{\partial \xi})^2-\frac{\partial f}{\partial \xi}e^{-\beta}-2(1-e^{-\beta})^{1/2}\frac{\partial f}{\partial \tau}]/(1-\frac{\partial f}{\partial \xi})\}=0 \qquad (4)$$

where $\tau = ts_o$, $\xi = (L-x)/L, \exp(-\beta) = (s_o^2 - v_o^2)/s_o^2$

Since it is possible to add any arbitrary constant to function f we can let f=0 at ξ=0 . The boundary condition $\partial f/\partial\tau$=0 will be satisfied automatically. Hence, our equation has to be solved with the boundary conditions

$$f = 0 \quad \text{at} \quad \xi = 0 \quad \text{and} \quad \frac{\partial f}{\partial \xi} = 0 \quad \text{at} \quad \xi = 1 \tag{5}$$

3. Small difference between drift and "sound" velocities .

We'll analyze here the situation when the drift velocity,v_O, is very close to the "sound" velocity,s_O,i.e., β>>1. In small signal limit we obtain for β>>1

$$f(\tau,\xi) = 2\{\exp[-\xi(\beta+2\ln 2)]\cos(\pi\xi - \tau\pi e^{-\beta}/2) - [1+\xi e^{-\beta}(\beta+2\ln 2)/4]\cos(\pi\tau e^{-\beta}/2)\}$$
$$\exp[\tau e^{-\beta}(\beta/2+\ln 2) + g_o - \beta] \tag{6}$$

where g_O determines the magnitude of an initial fluctuation. The space dependence of the fluctuation has two regions .There is a sharp drop near the drain and then the slow change in the remaining domain of our device.As to the temporal dependence of our solution there is a slow growth of the magnitude.

It follows from this small signal analysis that the fluctuation satisfying boundary conditions can be presented as a sum of a fast changing function, f_r , of a coordinate with the characteristic scale $1/\beta$ and a smooth part , f_S , of the fluctuation

$$f(\tau,\xi) = f_r(\tau,\xi)\cos(\pi\xi - \tau\pi e^{-\beta}/2) - f_s(\tau,\xi)\cos(\pi\tau e^{-\beta}/2) \tag{7}$$

$$f_s(\tau,\xi) = f_r(\tau,0) + 2\xi\exp[-\beta - z(\tau,1)] \tag{8}$$

where

$$2\exp[-\beta - z(\tau,\xi)] = -\frac{\partial f_r(\tau,\xi)}{\partial\xi}, \tag{9}$$

At small amplitudes, the nonlinearity related to the spatial derivatives of the rapidly changing function f_r will be the most important. The first stage of time evolution can be described by the following approximate equation for f_r

$$\frac{3}{2}\left(\frac{\partial f_r}{\partial\xi}\right)^2 - \frac{\partial f_r}{\partial\xi}e^{-\beta} - 2\frac{\partial f_r}{\partial\tau} = 0 \tag{10}$$

This partial differential equation of the first order which is valid for $\partial f_r/\partial\ \xi$<<1 can be solved analytically

$$f_r = -3\tau\exp[-2\beta - 2z(\tau,\xi)] - 2\int_{\infty}^{\xi-\tau[1+6\exp(-z)]\exp(-\beta)/2} d\xi\exp[G(\xi) - \beta] \tag{11}$$

Function z satisfies the following functional equation

$$z = -G(\xi - \tau(1+6\exp(-z))\exp(-\beta)/2) \tag{12}$$

where G is some function which is to be determined from the boundary conditions.

This solution tends to zero at ξ-->∞ as long as $\partial f_r/\partial \xi$ tends to zero .For the determination of G, we consider the smooth part of the fluctuation ,f_S, which contains $f_r(\tau,0)$ according to eq.(8). It follows from eq.(4) that f_S can be obtained from an approximate equation

$$\frac{\partial f_s}{\partial \tau} - 2\frac{\partial f_s}{\partial \xi} = 0 \qquad (13)$$

Substituting eq.(8) we find the following relationship for $f_r(\tau,0)$

$$\frac{\partial f_r(\tau,0)}{\partial \tau} = 4\exp[-\beta - z(\tau,1)] \qquad (14)$$

From eq.(9) and eq.(11), we have

$$\frac{\partial f_r(\tau,\xi)}{\partial \tau} = \{1 + 3\exp[-z(\tau,\xi)]\}\exp[-2\beta - z(\tau,\xi)] \qquad (15)$$

Substituting eq.(15) into eq.(14), we obtain the following relationship between boundary values of the function z

$$[1 + 3\exp(-z(\tau,0))]\exp[-\beta - z(\tau,0)] = 4\exp[-z(\tau,1)] \qquad (16)$$

which permits us to find z.We can now write a functional equation for $z(\tau,0)$. Using eq.(12) we can find the dependence of z on τ and ξ

$$\xi - \{6\exp[-z(\tau,\xi)] + 1\}\exp(-\beta)\tau / 2 = -g(-z(\tau,\xi)) \qquad (17)$$

where g is a reciprocal function of G

$$G(-(g(z)) = z \qquad (18)$$

Taking eq. (17) at ξ=0, we can find the dependence of τ on $z(\tau,0)$

$$\tau = 2\exp(\beta)(6e^{-z(\tau,0)} + 1)^{-1} g(-z(\tau,0)) \qquad (19)$$

We can exclude now τ from eq. (17)

$$\xi - (6e^{-z(\tau,\xi)} + 1)(6e^{-z(\tau,0)} + 1)^{-1} g(-z(\tau,0)) + g(-z(\tau,\xi)) = 0 \qquad (20)$$

We know that g is a linear function in a small signal limit. Hence let us define a new function g_1 which characterizes a deviation from the linear dependence

$$g(z) = (g_o + z)/[\beta + 2\ln(2)] + g_1(z) \qquad (21)$$

Substituting eq. (21) into eq. (20) we obtain

$$(6e^{-z(\tau,0)} + 1)[(\beta + \ln 4)(\xi + g_1(-z(\tau,\xi))) + g_o - z(\tau,\xi)] - (6e^{-z(\tau,\xi)} + 1)[g_o - z(\tau,0) +$$

$$(\beta + \ln 4)g_1(-z(\tau,0))] = 0 \qquad (22)$$

Evaluating eq. (22) at $\xi=1$, we obtain from eq. (16) the following equation for $g_1(z)$

$$(6e^{-z(\tau,0)}+1)[\ln(1+3e^{-z(\tau,0)})-z(\tau,0)+(\beta+\ln 4)g_1(-z(\tau,1))]+6g_o[e^{-z(\tau,0)}-e^{-z(\tau,1)}]-$$

$$(6e^{-z(\tau,1)}+1)[(\beta+\ln 4)g_1(-z(\tau,0))-z(\tau,0)]=0 \qquad (23)$$

Since $\beta>>1$ and, as a consequence, $z(\tau,1)>> z(\tau,0)$ we obtain the following solution

$$g_1(z)=\{(1+6e^z)\ln(1+3e^z)+6e^z(g_o+z)\}/(\beta+\ln 4) \qquad (24)$$

Substituting eq. (24) into eq. (22), we find an equation for $z(\tau,\xi)$

$$(\beta+\ln 4)\xi+(1+6e^{-z(\tau,\xi)})[\ln(1+3e^{-z(\tau,\xi)})-\ln(1+3e^{-z(\tau,0)})+z(\tau,0)-z(\tau,\xi)]=0 \qquad (25)$$

The dependence of the z on τ and ξ can be found from (19), (21), (24), and (25).

4. Formation of a shock wave .

In this section, we show that, at some time, the discontinuity of z should develop at certain coordinate. In other words,as it follows from eq. (3a) and (9) the electric field becomes discontinious at this coordinate. Let us find the coordinate when this discontinuity should first occur.The space derivative can be determined by differentiating eq. (25)

$$\beta+\ln 4=\{(6e^{-z(\tau,\xi)}+1)[3e^{-z(\tau,\xi)}/(1+3e^{-z(\tau,\xi)})+1]+6e^{-z(\tau,\xi)}[z(\tau,0)-$$
$$z(\tau,\xi)+\ln(1+3e^{-z(\tau,\xi)})-\ln(1+3e^{-z(\tau,0)})]\}\frac{\partial z(\tau,\xi)}{\partial\xi} \qquad (26)$$

This derivative becomes infinite at z_d which can be found from the following equation

$$(1+e^{z_d}/6)[3e^{-z_d}/(1+3e^{-z_d})+1]=z_d-z(\tau,0)-\ln(1+3e^{-z_d})+\ln(1+3e^{-z(\tau,0)}) \qquad (27)$$

This first happens first time at z_{dd} where the derivative , $\partial z_d/\partial z(\tau,0)$ is zero as well

$$2=3(6e^{-z_{dd}})^2+(6e^{-z_{dd}})^3 \qquad (28)$$

Solving this equation numerically, we find z_{dd}=0.052.Using eq. (27) and (25), we obtain a coordinate corresponding to the formation of a weak shock wave

$$(\beta+\ln 4)\xi_d=1.654 \qquad (29)$$

Hence it follows from our consideration that this coordinate does not depend on the initial conditions whereas time for achieving the shock wave state is determined by the initial amplitude of the fluctuation.

I would like to thank M. Dyakonov and M. Shur for useful discussions.

References.

1.M.I.Dyakonov and M.S.Shur,Phys.Rev.Lett.,71,2465(1993)
2.L.D.Landau,E.M.Lifshitz,Fluid Mechanics,Pergamon,New York(1966)

Second And Third Order One-Dimensional Non-Quasi-Static Bipolar Transistor Models

Etienne Robilliart and Emmanuel Dubois,
Tel: (+33) 20.19.79.17 Fax: (+33) 20.19.78.84 e-mail: ero@isen.fr
IEMN/ISEN UMR CNRS 9929
Avenue Poincaré, Cité Scientifique, BP 69, 59652 Villeneuve d'Ascq Cedex, France

Introduction

The simulation of high frequency bipolar circuits requires an accurate modeling of the charge storage in the neutral base region [1]. Non-quasi-static (NQS) effects are indeed responsible for extra delay [2] and excess phase shift [3] in digital and analog circuits, respectively, due to the non-instantaneous charge redistribution in the base. This paper proposes a critical review of the existing approaches and introduces new models based on the resolution of the transport and current equations truncated to the second and third order. The model derivation is first recalled with the different truncation schemes and the device characteristics under study are given [4][5]. An extensive assessment is provided through large signal transient simulations with a special emphasis on the time-dependent charge distribution in the base. Finally, we compare several model predictions of the magnitude and phase of the current gain (h_{21}) and of the transconductance (y_{21}).

Model derivation

For the sake of simplicity, recombination is neglected and bandgap narrowing is not taken into account. The inclusion of these two important ingredients is however straightforward [6]. An exponential base doping level is assumed, $Na(x)=Na(0).\exp(-\eta.x/W_B)$ where x=0 defines the emitter edge of the quasi neutral base and W_B the thickness of the base layer . The Laplace transformation with respect to time is used to reduce the electron current and continuity equations in a p-type quasi-neutral base as follows :

$$p \cdot \mathcal{L}\{n(x,t)\} = \frac{1}{q} \cdot \frac{d\mathcal{L}\{j_n(x,t)\}}{dx} \qquad (1)$$

$$\mathcal{L}\{j_n(x,t)\} = \frac{q \cdot D_n}{N_a(x)} \cdot \frac{d\ \mathcal{L}[n(x,t) \cdot N_a(x)]}{dx} \qquad (2)$$

where p and $\mathcal{L}$ are the Laplace variable and operator, respectively. Relations (1) and (2) can be iteratively solved to obtain the two-port equation given by:

$$\begin{bmatrix} I_E(p) \\ I_C(p) \end{bmatrix} = I_0 \cdot \begin{bmatrix} A_{11}(p) & A_{12}(p) \\ A_{21}(p) & A_{22}(p) \end{bmatrix} \cdot \begin{bmatrix} \mathcal{L}\{e^{V_{BE}/V_t}-1\} \\ \mathcal{L}\{e^{V_{BC}/V_t}-1\} \end{bmatrix} \qquad (3)$$

where I_0, I_E and I_C represents the saturation, emitter and collector currents while V_{BE} and V_{BC} are the base/emitter and base/collector voltages. In forward active mode, only $A_{11}(p)$ and $A_{21}(p)$ are significant, and are defined by the following terms:

$$A_{11}(p) = -\gamma \cdot \left(\frac{\eta}{2} + z \cdot \coth(z)\right) \qquad (4)$$

$$A_{21}(p) = \frac{\gamma \cdot \exp\left(\frac{\eta}{2}\right) \cdot z}{\sinh(z)} \qquad (5)$$

where $\gamma = \dfrac{\exp(\eta)-1}{\eta \exp(\eta)}$ and $z = \sqrt{\dfrac{\eta^2}{4} + 2p\tau_f}$, with $\tau_F = W_B^2/(2D_n)$ is the usual forward transit time.Table I summarizes the various truncation schemes used in the present work (1st, 2nd and 3rd order) and also reports the approximations made in the derivation of other approaches of the charge dynamics.

Model analysis

The inspection of the current relations expressed in the Laplace domain (table I) reveals a rigourous expansion of our models to 2nd and 3rd order without combining the numerator and denominator of the transfer function. The corresponding time dependent expressions for terminals currents have been implemented in the ELDO circuit simulator [7]. In order to exercize our modeling approach on a realistic technology, comparisons have been carried out with two dimensional simulations and measurements performed on bipolar transistor of the QuBIC process [5]. Fig. 1 presents the static characteristics and the corresponding measured currents.

Large signal results

Fig. 2 compares the transient response of the collector current given by each model in forward active mode. As expected, no delay in the collector current is predicted by the Gummel-Poon [8] model while the PCB [9] model exhibits an unphysical undershoot for fast input transients. The inductance model [10] gives collector current variations in relatively good agreement with the exact solution, but still overestimate the collector current rise time. The second and third order approaches presented in this paper demonstrate the best accuracy among the discussed models. Fig. 3 and 4 show the time dependence of the transient charge flowing through the emitter terminal normalized to the total transient base charge for

different V_{BE} rise times. Only the inductance, 2nd and 3rd order models give a non constant charge ratio $Q_{ne}(t)/Q_n(t)$. Although the discrepancy remains large between the exact numerical calculation, and the different models, the 3rd order model predicts the most accurate transient charge sharing.

Small signal results

Fig. 5 and 6 present the magnitude and the phase of the small-signal current gain (h21) predicted by the different models, and compare to the exact numerical calculation, in the case of a non constant base doping profile (η=8). Beyond the cut-off frequency, the 2nd order and inductance models demonstrate analogous variations that are typical of a second order system but only the third order model gives a close agreement with the exact calculation. The major improvement of the 2nd and 3rd order model is provided for the magnitude and phase of the transcondutance (y_{21}), as illustrated in Fig. 7 and 8.

Conclusion

In summary, 2nd and 3rd order NQS models have been derived and implemented in ELDO. For large signal analysis, these models provide the best description of the non-quasi-static delay in the bipolar device under study. In the small signal domain, a better description of the transconductance is provided through modeling approaches corresponding to real 2nd and 3rd order systems.

Models	Truncation scheme in the Laplace domain
Gummel [8]	$I_C(p) = \gamma \cdot \exp\left(\frac{\eta}{2}\right) \cdot I_0 \cdot \mathcal{L}\{e^{V_{BE}/V_t} - 1\}$ $I_E(p) = -\left[1 + \left(\frac{\eta+6}{6\eta+12}\right) \cdot Z^2\right] \cdot I_0 \cdot \mathcal{L}\{e^{V_{BE}/V_t} - 1\}$
PCB [9]	$I_C(p) = \gamma \cdot \exp\left(\frac{\eta}{2}\right) \cdot \left[1 - \frac{1}{6} \cdot Z^2\right] \cdot I_0 \cdot \mathcal{L}\{e^{V_{BE}/V_t} - 1\}$ $I_E(p) = -\gamma \cdot \left[\frac{\eta}{2} + 1 + \frac{1}{3} \cdot Z^2\right] \cdot I_0 \cdot \mathcal{L}\{e^{V_{BE}/V_t} - 1\}$
Inductance [10]	$I_C(p) = \frac{\gamma \cdot \exp\left(\frac{\eta}{2}\right)}{\left[1 + \frac{1}{6} \cdot Z^2\right]} \cdot I_0 \cdot \mathcal{L}\{e^{V_{BE}/V_t} - 1\}$ $I_E(p) = -\gamma \cdot \left[\frac{\eta}{2} + 1 + \frac{1}{3} \cdot Z^2\right] \cdot I_0 \cdot \mathcal{L}\{e^{V_{BE}/V_t} - 1\}$
First Order	$I_C(p) = \frac{\gamma \cdot \exp\left(\frac{\eta}{2}\right)}{\left[1 + \frac{1}{6} \cdot Z^2\right]} \cdot I_0 \cdot \mathcal{L}\{e^{V_{BE}/V_t} - 1\}$ $I_E(p) = \frac{-\gamma \cdot \left[\eta + 2 + \left(\frac{\eta}{6} + 1\right) \cdot Z^2\right]}{\left[2 + \frac{1}{3} \cdot Z^2\right]} \cdot I_0 \cdot \mathcal{L}\{e^{V_{BE}/V_t} - 1\}$
Second Order	$I_C(p) = \frac{\gamma \cdot \exp\left(\frac{\eta}{2}\right)}{\left[1 + \frac{1}{6} \cdot Z^2 + \frac{1}{120} \cdot Z^4\right]} \cdot I_0 \cdot \mathcal{L}\{e^{V_{BE}/V_t} - 1\}$ $I_E(p) = \frac{-\gamma \cdot \left[\eta + 2 + \left(\frac{\eta}{6} + 1\right) \cdot Z^2 + \left(\frac{\eta}{120} + \frac{1}{12}\right) \cdot Z^4\right]}{\left[2 + \frac{1}{3} \cdot Z^2 + \frac{1}{60} \cdot Z^4\right]} \cdot I_0 \cdot \mathcal{L}\{e^{V_{BE}/V_t} - 1\}$
Third Order	$I_C(p) = \frac{\gamma \cdot \exp\left(\frac{\eta}{2}\right)}{\left[1 + \frac{1}{6} \cdot Z^2 + \frac{1}{120} \cdot Z^4 + \frac{1}{5040} \cdot Z^6\right]} \cdot I_0 \cdot \mathcal{L}\{e^{V_{BE}/V_t} - 1\}$ $I_E(p) = \frac{-\gamma \cdot \left[\eta + 2 + \left(\frac{\eta}{6} + 1\right) \cdot Z^2 + \left(\frac{\eta}{120} + \frac{1}{12}\right) \cdot Z^4 + \left(\frac{\eta}{360} + \frac{1}{5040}\right) \cdot Z^6\right]}{\left[2 + \frac{1}{3} \cdot Z^2 + \frac{1}{60} \cdot Z^4 + \frac{1}{2520} \cdot Z^6\right]} \cdot I_0 \cdot \mathcal{L}\left\{e^{\frac{V_{BE}}{V_t}} - 1\right\}$

Table 1 : Various Taylor's developments of the matrix terms, for small z

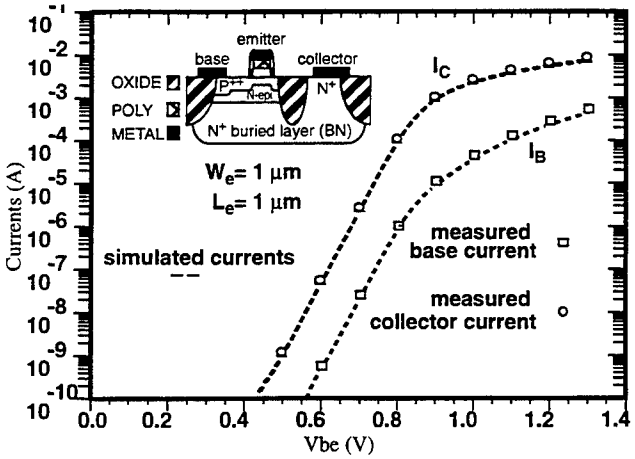


Fig 1 : Static characteristics of the simulated device compared with the measured characteristics.

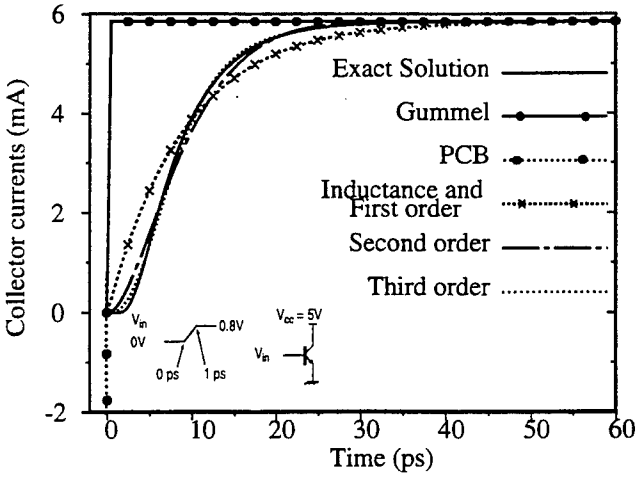


Fig 2 : Comparison of the transient variation of the collector current for the different models and the exact solution (solid line) for a Vbe rise time of 1ps

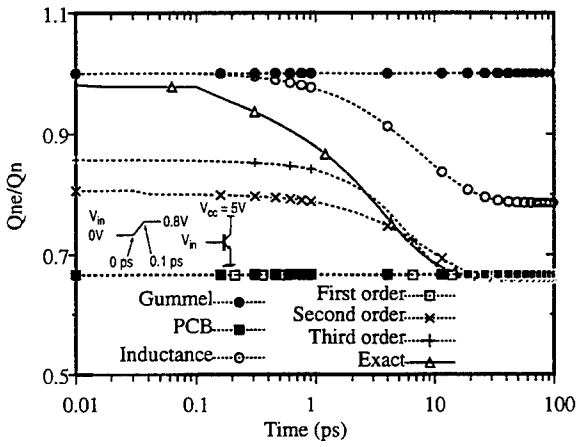


Fig 3 : Comparison of the transient variation of charge flowing through emitter terminal (Qne) for the different models and the exact solution (solid line) When Vbe increase from 0v to 0.8v in 0.1ps.

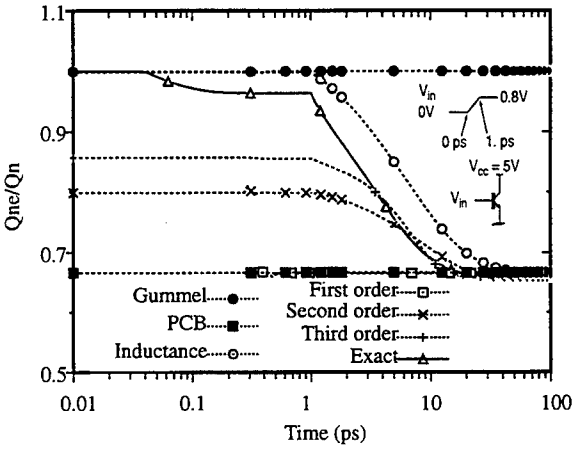


Fig 4 : Comparison of the transient variation of charge flowing through emitter terminal (Qne) for the different models and the exact solution (solid line) When Vbe increase from 0v to 0.8v in 1ps.

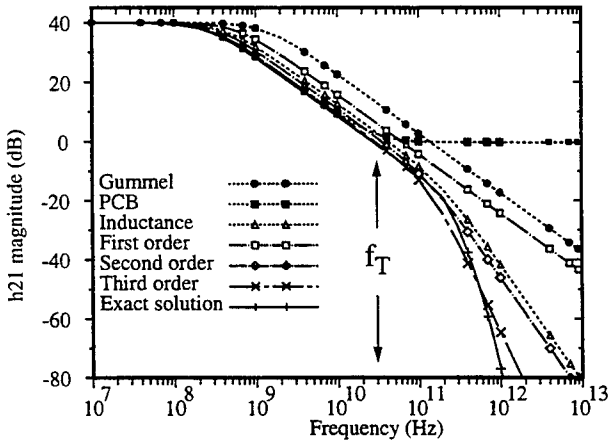


Fig 5 : Comparison of the small-signal current gain |h21| for the different models and the exact solution (solid line).
The device has an exponential base doping profile (η = 8)

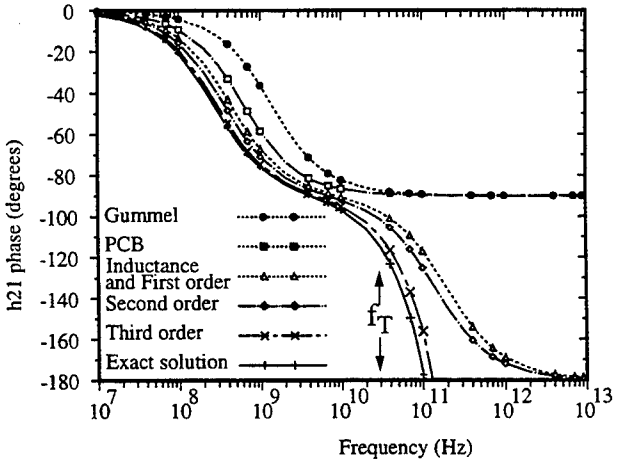


Fig 6 : Comparison of the small-signal current phase for the different models and the exact solution (solid line).
The device has an exponential base doping profile (η = 8)

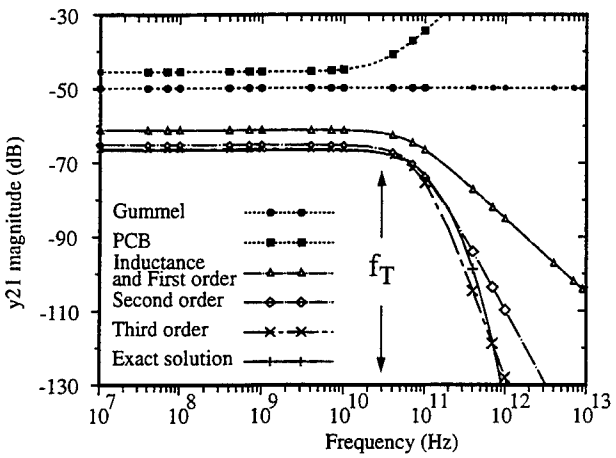


Fig 7 : Comparison of the small-signal transconductance magnitude for the different models and the exact solution (solid line). The device has an exponential base doping profile (η = 8)

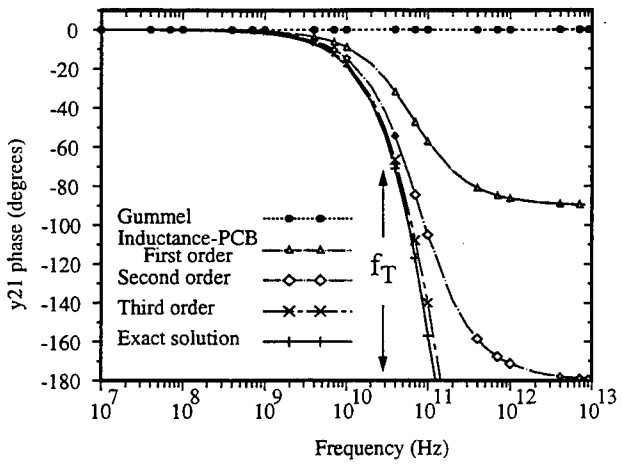


Fig 8 : Comparison of the small-signal transconductance phase for the different models and the exact solution (solid line). The device has an exponential base doping profile (η = 8)

References

[1] H.J. Huang and J.B. Kuo, *IEEE Transactions on Electron Devices*, May 1994.

[2] B.S. Wu, C.T. Chuang and P.F. Lu, *IEEE Transactions on Electron Devices*, June 1994.

[3] H.C. de Graff and F.M. Klaassen, *Springer-Verlag Wien-New York*, June 1989.

[4] E. Dubois, P.H. Bricout and E. Robilliart, *BCTM Tech. Dig.* , October 1994.

[5] C.H. Wang and J. Van Der Velden, *BCTM Tech. Dig.* , October 1994.

[6] B.S. Wu and F. A. Lindholm, *IEEE Transactions on Electron Devices*, April 1989.

[7] ELDO "User's Manual", "Dynamical System Modelling" July 1992.

[8] H.K. Gummel and H.C. Poon, *Bell Syst. Techn. J.*, vol.49, May 1970.

[9] J.G. Fossum and S. Veeraraghavan, *IEEE Electron Device Letters*, December 1986.

[10] M.K. Chen, F. A. Lindholm and B.S. Wu, *IEEE Transactions on Electron Devices*, July 1988.

Directed Vapor Deposition of Electronic Materials: Nonhydrogenated *a*-Si and Cu.

J. F. Groves[a], P. L. Ratnaparkhi[a], H. N. G. Wadley[a], T. Globus[b], S. H. Jones[b]

[a]Department of Materials Science and Engineering and [b]Department of Electrical Engineering, University of Virginia, Charlottesville, Virginia 22903-2442

Introduction

A novel physical vapor deposition (PVD) process for creating a wide variety of thin film and electronic packaging materials is being developed at the University of Virginia [1-2]. It combines supersonic gas (typically He) jets together with electron beam and/or resistive evaporation to create and transport vaporized materials for deposition onto thermally decoupled substrates. Operating at relatively high pressures (0.1-10 Torr), the inexpensive mechanically pumped system exploits high velocity inert carrier gas streams to entrain and directly transport evaporants to a wide variety of substrates. The high background pressure together with the controllable velocity of the vapor provides a new flexibility for uniformly coating large nonplanar substrates at extremely high rates with close to theoretical materials utilization efficiencies and at sometimes considerably lower substrate temperatures than those normally used during conventional PVD or chemical vapor deposition processes.

The principles of this new directed vapor deposition (DVD) system are described here and the basic relationships between deposit uniformity, structure, and controllable process conditions are outlined. Preliminary results from vapor deposition trials for nonhydrogenated *a*-Si and Cu are presented and discussed. The *a*-Si experiments have been motivated by the need for inexpensive thin film transistors and terrestrial large area photovoltaics. The copper study explores the potential of the DVD method to deposit low resistivity, electromigration-resistant interconnects in microelectronic packages [3].

Directed Vapor Deposition System and Process Parameters

The primary configuration of the DVD system (Fig. 1) utilizes a focussed, usually inert gas flow (e.g. helium) and a continuously operating e-beam gun to evaporate and deposit metal and semiconductor vapor. The small diameter (0.4 mm), high energy (60 kV) design of the system's e-beam makes possible high rate evaporation of a wide variety of materials in an unexplored low vacuum processing environment, 10^{-3} - 10 Torr. In the DVD system, target material can be evaporated either within or just beyond the exit of the carrier gas nozzle. Once evaporated, the target material is rapidly entrained in the gas flow, accelerated towards the substrate, and efficiently deposited on the substrate

To operate in a low-vacuum gas jet environment, the e-beam gun employs a specially designed gun column which prevents excessive gas flow from the low vacuum processing chamber to the high vacuum e-beam generation and focussing column while permitting free, undiminished propagation of the e-beam to the target for evaporation. Given the e-beam's sharp focus and the short propagation distance to the evaporant source, efficient heating and evaporation of many different feed stocks from a water-cooled rod-fed crucible or wire feed mechanism is possible in processing pressures up to 10 Torr or higher.

The gas flow system (Fig. 1) has been designed to produce repeatable, high quality materials synthesis conditions. Once the high purity carrier gas (e.g., six 9's He) leaves the compressed gas cylinder, it passes through a gettering system to reduce oxygen and moisture levels below one part per billion. From the purification system, the gas flows into a mass flow controller calibrated for helium and capable of controlling flows of 2.5 - 200 standard liters per minute (slm). From the mass flow controller, the gas passes into a settling chamber before being routed down the gas flow tube, through a nozzle, and into the material processing chamber. The pressures in the settling chamber and the processing chamber are monitored using gas independent capacitance manometer gauges. The pressure in the settling chamber relative to the pressure in the processing chamber can be varied by adding nozzles onto the end of the gas inlet tube or by opening and closing a throttle plate located between the processing chamber exit and the chamber pumping unit.

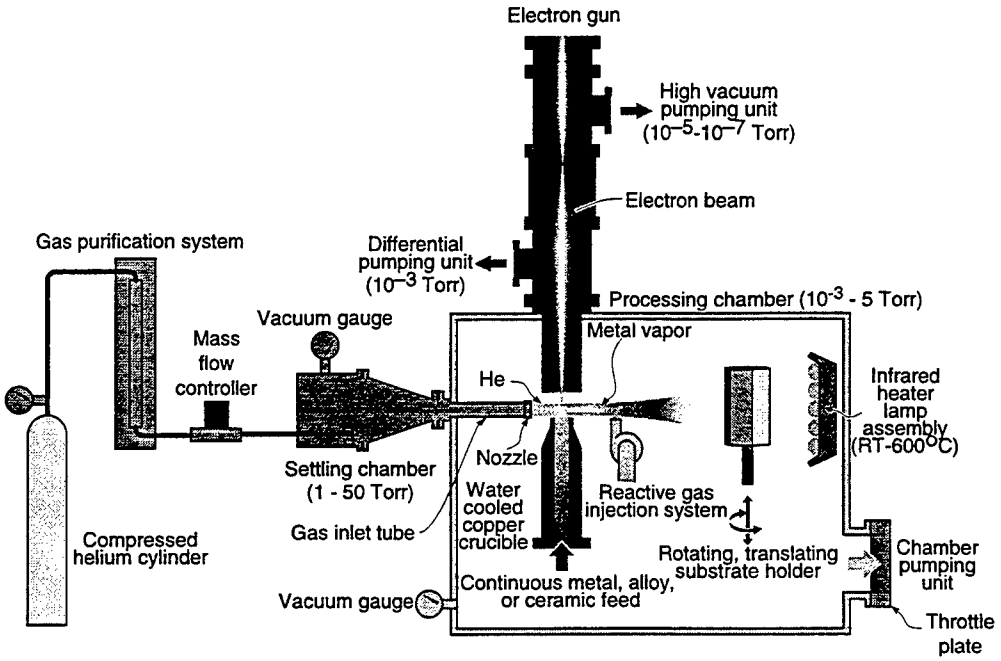


Fig. 1 The primary DVD configuration combines a purified gas flow with evaporant from an e-beam source to enable high rate vapor deposition.

For the *a*-Si deposition experiments, a solid bar (5.08 cm diameter x 2.54 cm length) of phosphorous-doped (0.1 Ω-cm resistivity) single-crystal silicon ingot was used. The *a*-Si experiments were performed using He flows of 5 and 40 slm. These gas flows led to settling chamber/processing chamber pressure ratios of 4.6/1.1 Torr and 2.6/0.1 Torr respectively. Assuming isentropic flow of fully compressible gas, the Mach number for the 4.6/1.1 Torr pressure differential is approximately 1.5, while the Mach number equals 2.8 for the 2.6/0.1 Torr pressure differential. Combined with e-beam powers in the 250-500 W range these gas flows deposited silicon vapor on unheated stationary glass substrates. Cu films were deposited on flat stationary glass slides for 30 min at a Mach number of 2.08, chamber pressure of 1.11 torr and a He gas flow rate of 20 slm. The gun wattage was 1.6 kW and deposition was conducted at either room temperature (T/Tm = 0.22), 250°C (T/T_m=0.38), or 500°C (T/T_m=0.57).

Results

Amorphous Si: Optical transmission and reflection analysis were used to determine the *a*-Si thickness and deposition rate. Measurements in the 0.6 - 2.4 μm wavelength range were made using a Cary 5E two-beam spectrophotometer. Film thicknesses were calculated in the normal way from interference fringe patterns observed in the weak absorption portion of the spectrum.

Deposition rates ranging between 0.02 and 0.44 μm/min were observed; the highest rate resulting from the 40 slm run with a substrate-to-source distance of approximately 10 cm and an electron beam energy of 500 W. The maximum thickness of deposit was 3.1 μm over approximately a 12.9 cm^2 region. The optical transmission spectra from several films were used to calculate the thin film absorption spectrum. Measurements of a PECVD hydrogenated a-Si (15% hydrogen) were made using the same spectrophotometer on material supplied by Xerox PARC. As expected, the absorption edge for the DVD *a*-Si thin films is shifted to lower energies relative to the PECVD hydrogenated *a*-Si since the DVD material is not an *a*-Si:H alloy. As a result, the absorption characteristics of the DVD material are very similar to those of crystalline silicon for energies greater than 1.4 eV. Since the dangling bonds in the DVD *a*-Si are not passivated, there is a large density of near bandgap edge states. Using the technique of Amer and Jackson we estimate this concentration of defects to be 10^{18} cm^{-3} [4]. The defect density in evaporated nonhydrogenated *a*-Si is approximately 10^{19}-10^{20} cm^{-3}.

The microstructure of several films was also investigated using transmission electron microscopy (TEM). The microstructure contains many clusters ranging from 20 to 300 nm in size. In addition, microvoids can be found surrounding the clusters; the material's porosity is approximately 1.0%. Diffuse rings in selected-area diffraction (SAD) patterns indicate that the DVD Mach 1.5 films are completely amorphous. However, several microcrystalline structures were observed in the TEM images of the films deposited at 5 slm. This suggests that some microcrystalline nucleation can be achieved without substrate heating when the average carrier gas velocity and thus particle impact energies are increased. This initial result is encouraging for the future deposition of low-temperature polycrystalline silicon.

Cu: Microstructural analysis of the deposited Cu films was performed using plan-view and cross-section scanning (SEM) and transmission (TEM) electron microscopy, Auger electron spectroscopy (AES) and X-ray diffraction (XRD).

For all of the copper experiments, the deposition rate ranged from 1 - 5 μm per minute. SEM studies revealed that Cu films deposited at room temperature ($T/T_m = 0.22$) had a classic zone I structure with the formation of tapered columns and intercolumnar porosity. Random nucleation of columns occurred near the bottom of the foil with subsequent growth of only the favorably oriented columns (which increased in diameter with increasing thickness). Increasing the temperature to 250°C ($T/T_m = 0.38$) and 500°C ($T/T_m = 0.58$) increased the lateral diffusive flux resulting in zone T and zone II microstuctures respectively. With increasing temperature the columns increased in diameter and consisted of parallel elongated grains (formed due to granular epitaxy) with a diameter of 0.6 μm and 2 μm in the 250°C and 500°C respectively. Interestingly, intercolumnar porosity (a classic zone I feature) was observed in both of these zone T and zone II films indicating discrepancies with the 'structure zone model' [5]. Zone I/zone T transition was observed to increase with increasing thickness and deposition rate. Intercolumnar voiding in all of the samples was attributed to shadowing effects and the void fraction was observed to decrease with decreasing thickness and increasing temperature. A {111} texture which initially increased with temperature was observed. This texture is believed to form due to the lower surface energy of the densely packed {111} planes. On increasing the temperature to 500°C an unexpected {110} texture was detected. The reason for the formation of such a texture in this sample is not known but such a texture has been reported in both Cu [6] and Ag films [7].

TEM studies (Fig. 2) show that at ambient temperature significant porosity exists within the deposits. Raising the deposition temperature to 500°C nearly eliminates this problem. Monte Carlo simulations have shown that this arises from enhanced adatom diffusion [8]. Cross-section TEM of the sample deposited at 250°C revealed extensive twinning on the {111} planes. This is a result

of the deposition process as vapor atoms falling on a {111} plane have a choice of two (FCC and twin) low energy sites. Molecular dynamics simulations [9] predict the experimentally observed twinning in Cu. AES results indicated that the deposited film contained approximately 500 ppm of O (comparable to the feed stock material) suggesting that high purity materials can be synthesized using this low vacuum process.



Fig. 2 Planview TEM images of Cu films deposited at settling chamber/processing chamber pressures of 11 Torr/1.11 Torr, Mach 2.08, and a gas flow rate of 20 slm. Deposition was done for 30 minutes at (a) ambient temperature and (b) 500°C.

Conclusions

A directed vapor deposition system has been developed and used for nonhydrogenated *a*-Si and Cu deposits. Both materials created using DVD show promising electronic material properties. The *a*-Si specimens were deposited at high rates and showed signs of microcrystalline structure even though deposition occurred at room temperature. Cu deposition results demonstrate the ability of substrate heating to improve film quality. Still, the microstructure and morphology of DVD Cu was different than predicted by the traditional structure zone model suggesting that a modified structure zone model should be developed for this system. The Cu results also suggest that variation of carrier gas momentum combined with limited substrate heating could lead to further Cu film quality improvements and possibly polycrystalline Si deposits at reduced temperatures.

Acknowledgements

This work was supported by the Advanced Research Projects Agency (W. Barker, Program Manager) and NASA (D. Brewer, Technical Program Monitor) through grant NAGW 1692.

References

1. Wadley, H. N. G. and Groves, J. F. "Directed Vapor Deposition of Electron Beam Evaporant." U.S. Patent Application 08/298,614 Filed August 31, 1994.
2. Groves, J. F., et al. *J. Electrochem. Soc.* 142(10), L173-L175, 1995.
3. *Thin Solid Films* (special issue dedicated to Cu based metallization), 262(1-2), June 15 1995.
4. W. B. Jackson and N. M. Amer, *Phys Rev.* B25, 5559 1982.
5. J. A. Thornton, *Ann. Rev. Mat. Sci.*, 239-260 1977
6. D. P. Tracy and D. B. Knorr, *Jnl. of Elect. Mater.* 22 pp. 611- 616 1993
7. P. K. Dutta and H. Wilman, *J. of App. Phys*, 3, pp. 839 - 853 1970
8. Y. Yang, R. A. Johnson, and H. N. G. Wadley, Acta Metall. et Mater. submitted, 1995.
9. X. Zhou, R. A. Johnson, and H. N. G. Wadley, Acta Metall. et Mater. submitted, 1995.

Reduced Lateral Diffusion of AuGe/Au and AuGe/Au/Ni Source-Drain Contacts in AlInAs/InGaAs/InP MODFET's

J.K. Zahurak[1], A.A. Iliadis[1], S. Rishton[2], W.T. Masselink[3], and T. Neil[4]

1. Department of Electrical Engineering, University of Maryland, College Park, MD 20742.
2. IBM T.J. Watson Research Center, Yorktown Heights, NY 10598,
3. Humbolt University, Physics Dept. Invaliderstr. 110, 10115 Berlin, Germany.
4. MRL, Old Annapolis Rd., Columbia, MD 21045.

Extended Abstract

Source and drain ohmic contact quality in MODFET's is of critical importance to the performance and long-term stability of the devices. In alloyed AuGe based contacts, concern is mainly focused on reducing contact resistance as much as possible and having sufficiently well controlled indiffusion to ensure contact with the active 2DEG channel. Since the indiffusing metallization front has just a few hundred Angstroms to go before reaching the active channel, lateral diffusion at the periphery of the contact can usually be neglected on the assumption that no enhanced diffusion is expected over the significantly larger lateral dimensions of the devices. Such an assumption may be justified in uniform structures, where the indiffusing front encounters no interviening boundaries to reach the active channel, but in the case of multilayered structures, where the front encounters successive boundaries of varying diffusivities, the assumption is not valid. In this case, lateral diffusion along one or more interface boundaries may become signficant enough [1,2] to alter the lateral dimensions of the device.

In this work we have investigated the source-drain contact formation on AlInAs/InGaAs/InP doped channel MODFET's (Fig. 1) of the AuGe/Au and observed significant lateral diffusion of the AuGe/Au/Ni system in this structure at the usual annealing temperature range of 300 to 400°C. Auger depth profiling of the contacts (Fig. 2) revealed that the indiffusing front (primarily Au) penetrates the AlInAs layer (250Å) of the surface, but accumulates at the second deeper AlInAs layer of the structure. Once Au (with probably some traces of Ge) is accumulated at the AlInAs layer, enhanced lateral diffusion occurs, with clear signs of encroachment as shown in Fig. 3. Both Ni containing and Ni-free contact systems had similar behaviour in terms of lateral diffusion. In order to avoid such effects and yet keep the contact resistance low, a low temperature annealing cycle was developed that resulted in equally low contact resistance ($\approx$ 0.10 Ω-mm) and no lateral diffusion. The doped channel MODFET's fabricated using the low temperature annealing cycle gave record transconductances over 700 mS/mm and drain currents of 950 mA/mm, Fig. 4.

1. H. Goronkin, S. Tehrani, T. Remmel, P. Fejes, and K. Johnson, IEEE Trans. Electron Devices, Vol. 36, p. 281, (1989).
2. D.W. Langer, A. Ezis, and A.K. Rai, J. Vac. Sci. Tech., B5(4), p. 1030, (1987).

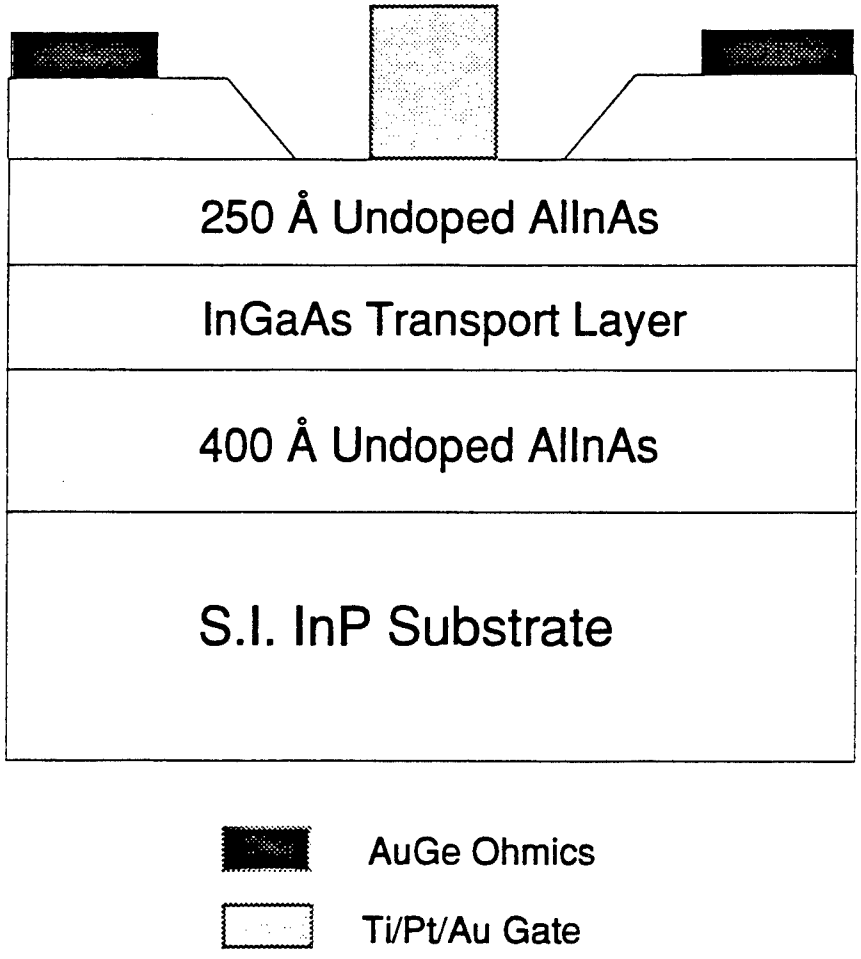


Fig. 1. Doped Channel MODFET Structure.

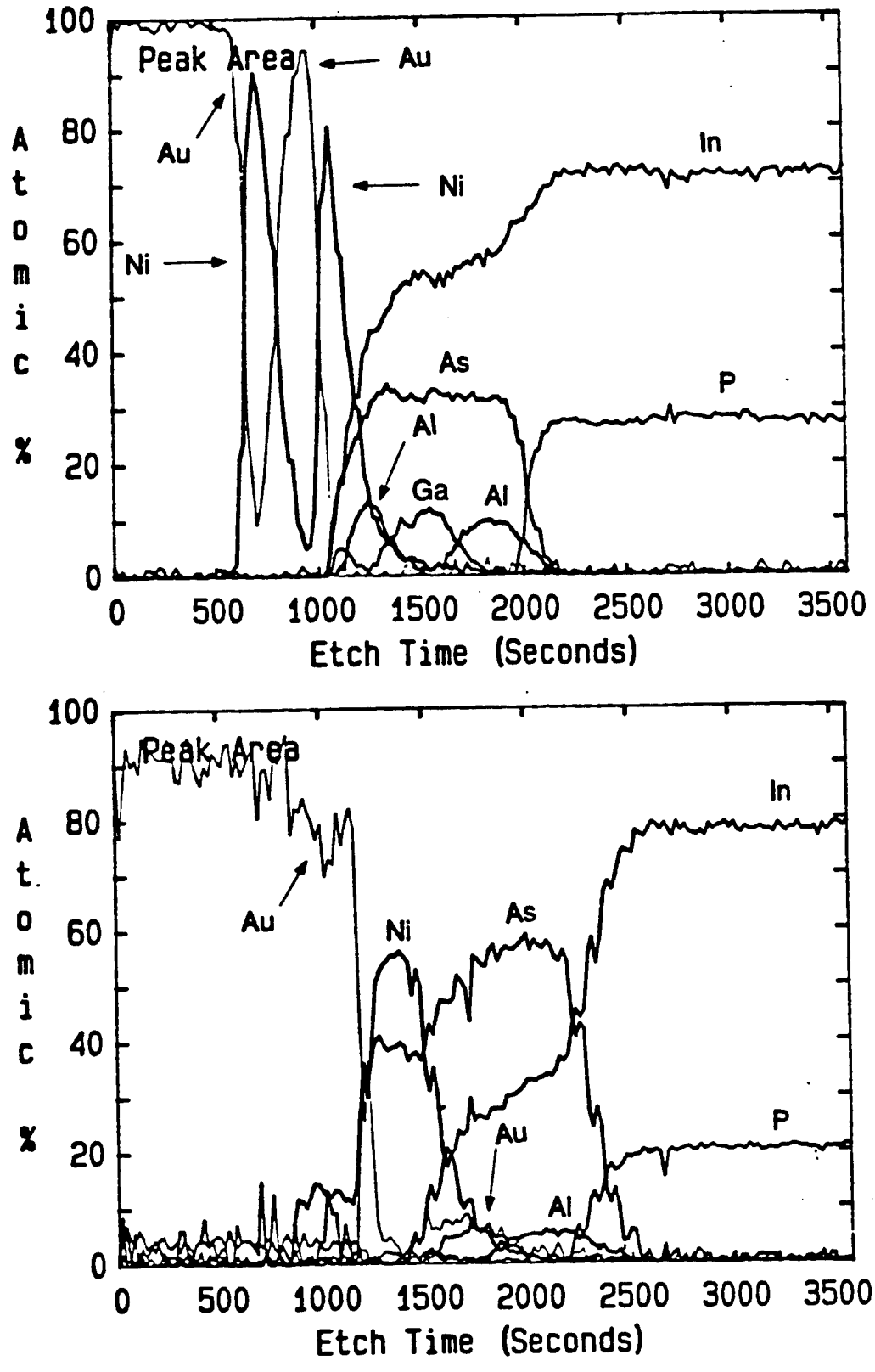


Fig. 2. Auger Depth Profile of AuGe/Au/Ni Contact.

a. As Deposited

b. Annealed at 250°C Au is beginning to accumulate before Al.

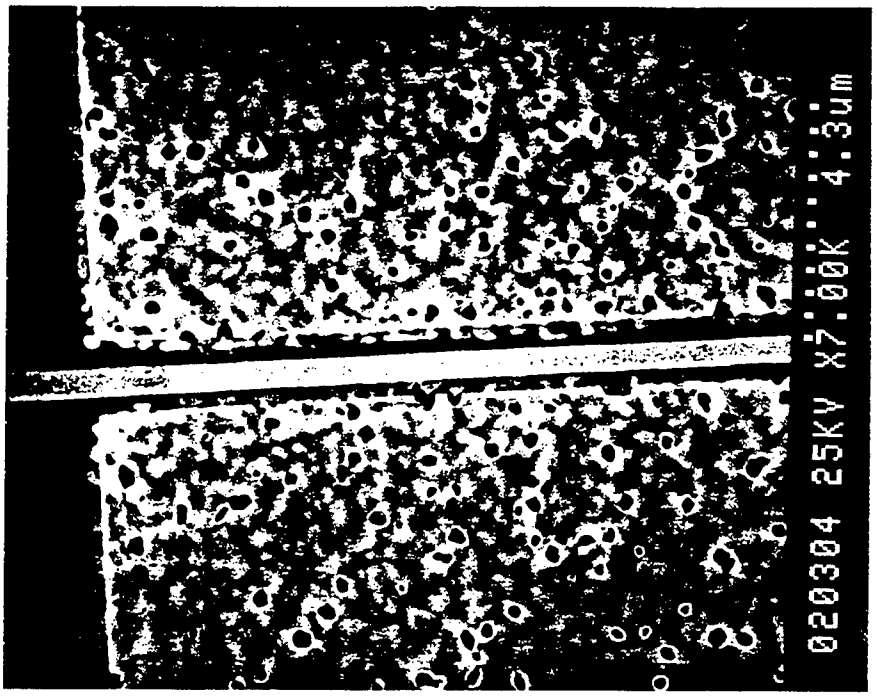


Fig. 3. SEM Picture of 0.5 microns MODFET annealed at $300°C$ showing significant lateral diffusion.

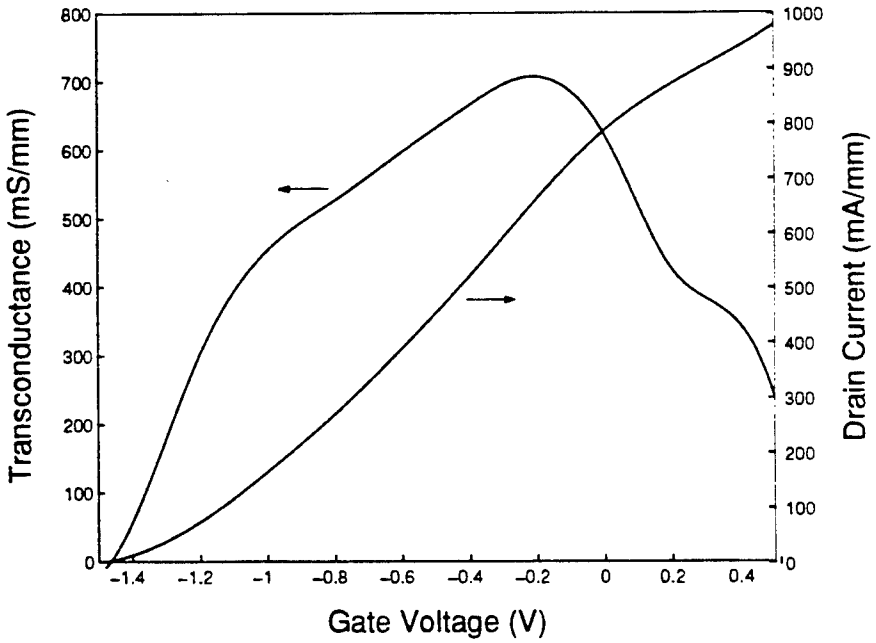


Fig. 4. Transfer characteristics of high performance MODFET.

Very low Resistance Multi-layer Ohmic Contact to n-GaN

Zhifang Fan, S. Noor Mohammad, Andrei E. Botchkarev, Wook Kim,
Özgür Aktas, and Hadis Morkoç
University of Illinois at Urbana-Champaign
Materials Research Laboratory & Coordinated Science Laboratory
104 S. Goodwin Ave.
Urbana, IL 61801

A new metallization scheme has been developed for obtaining very low ohmic contact to n-GaN. The metallization technique involves the deposition of a composite metal layer Ti/Al/Ni/Au (150Å/2200Å/400Å/500Å) on n-GaN. With annealing at 900 °C for 30 sec, contacts with specific resistivity values as low as $\rho_S=8.9\times10^{-8}\ \Omega cm^2$ for a doping level of $4\times10^{17}\ cm^{-3}$ were obtained. The specific resistivity was found to vary inversely with the doping level of the GaN sample. The physical cause underlying the realization of a very low contact resistivity is described.

Modeling of Dielectric Film Deposition by Laser CVD

Ji-Ho Ryoo, Jong-Kwan Kim, Yung-Kwon Sung
Department of Electrical Engineering, KOREA Univ.

Abstract - **A new deposition mechanism of SiO_2 film deposited by ArF(193nm) excimer laser with Si_2H_6 and N_2O gas mixture is introduced. A modeling based on the new deposition was established using deposition rate and refractive index by suggesting new precursors and film deposition mechanism. In this study, the deposition rate was first measured at the various conditions, such as source gas ratio, chamber pressure, substrate temperature, laser beam power and beam height, so as to make a new model. The simulated results were compared with the experimetal results. Trailblazing studies on modelling of SiO_2 film formation were carried out by suggesting two precursors such as SiH_2O and SiH_3OH, which almost contribute toward surface bonding and can be produced through photolysis and collision with N_2O and any other gas molecules.[3] This simulator based on the new model, makes it possible to predict the deposition rate under various condition successfully and this model has a advantage, in that it helps to understand the film deposition process more concretely.**

1. Experiment

Fig. 1 shows the set-up diagram of Laser CVD apparatus, which consists of ArF excimer laser, reaction chamber, source gas supplier, substrate heater and vacuum pump. The wavelength of ArF excimer laser is 193㎚. The beam was irradiated parallel to the substrate in the range of 0.4㎜ and 3㎜ so that the precursors and radical oxygen can be attached to the surface by diffusion. The Laser power was about 100 mJ/pulse and the repetition rate was 50Hz. The energy of Laser was condensed to 1 J/cm^2 · pulse by focusing. Source gases were Si_2H_6 and N_2O, and N_2 was used as a carrier gas. The gas flow rate was controlled by flow meter and the chamber pressure was controlled by a throttle valve.

2. Theoretical Study

In order to analyze the mechanism of film deposition, the following issues need to be considered ; i) source gas transport mechanism, ii) photolysis & reactants diffusion mechanism, iii) surface adhesion mechanism.

1) Source gas transport mechanism[6]

The gas-phase reaction of the source gas is negligible in this condition since the residence time of molecules is very short and source gases are diluted with N_2 carrier gas. In fact, no film deposition was observed without laser beam experimentally, and hence it is assumed that there is no reaction until source gases are transported to the beam.

2) Photolysis & reactants diffusion mechanism[2][3][7][8][9][10]

When using 193㎚ ArF laser, the most dominant reaction is

$$Si_2H_6 + h\nu(193㎚) \rightarrow SiH_2 + SiH_3 + H$$

and it produces products which contribute to surface reaction. Si_2H_6 source gas can be directly decomposed by 193㎚ ArF laser, so the amounts of reactants are produced in proportion to laser beam power and chamber pressure.

Produced reactants = photon flux × σ × n σ : photo absorption cross-section (3.4×10^{-18} cm^2)
n : Si_2H_6 molecule concentration (cm^{-3})

$$N_2O + h\nu \rightarrow N_2O^* \qquad N_2O^* + N_2O^* \rightarrow N_2O + N_2 + O^*$$
$$SiH_2 + N_2O^* \rightarrow SiH_2O + N_2 \qquad SiH_3 + N_2O^* \rightarrow SiH_3O + N_2$$
$$SiH_3O + SiH_4 \rightarrow SiH_3OH + SiH_3$$

However, as it can be seen in Fig. 2, intermediates(SiH_2, SiH_3, SiH_3OH) have to collide with other gas molecules(N_2O, N_2O, SiH_4) for producing precursors(SiH_2O, SiH_3OH)[2][3]

When the reactions are diffused down to the surface, the convection flow on the surface reduces the surface reaction, as be seen in Fig. 3. It shows flow direction of surface adsorption and convection flux.

While solving diffusion equation, this effect should be considered to make simulated results more accurately. A common diffusion equation is as follows;[4][10]

(3) Surface adhesion mechanism

Fig. 4 shows the overall procedure of surface reactions by two precursors of SiH_2O and SiH_3OH. As a first step, the precursors produced through photolysis and collision can cling to hydrogenated surface by substitution for Si-H bond. In addition, the radical oxygen produced by collision with N_2O provides the film with sufficient oxygen and plays a role as a bridge oxygen between precursors to enhance the film deposition. To analyze quantitatively this surface reaction, impingent flux for surface reactants was considered. it was assumed that the deposition rate is in proportion to the collision number of precursor to surface during unit time.[2][4] The effect on deposition rate by substrate temperature was also considered by adapting Arrhenius equation. Finally, the equation for the growth rate was obtained, as follows.[1]

$$<\Phi>=\frac{v<n>}{4}$$

v: thermal velocity
n': film density
α: probability to stick to substrate

$$\text{Growth rate} = \frac{v_{th}\alpha}{4n'}\exp(-E_a/kT)$$

3. Results and Discussion

Deposition rate decreases as space between the beam and the substrate becomes more distant, as seen in Fig. 5. Unfortunately, the experimental results happen to differ from the simulated results from 2㎜. This discrepancy is thought to be due to an inverse reaction and short life time of surface reactants. In the following experiments, the beam space is fixed to 0.4㎜ in order not to consider inverse reaction and life time of oxygen radicals. Fig. 6. shows the deposition rate as a function of source gas ratio(N_2O/Si_2H_6). Deposition rate has a peak about at the gas ratio of 100, which seems to be due to over 40 times smaller photo-absorption coefficient of N_2O than Si_2H_6 and short life time of radical oxygen.[5] The simulated results, which are based on the theory suggested in this study, are in good accordance with the experimental results. Refractive index of SiO_2 film according to gas ratio(N_2O/Si_2H_6) is shown in Fig. 7. As gas ratio increases, refractive index comes close to 1.46, stoichiomertric value. These results demonstrate that Si-rich film is deposited at low gas ratio and on the contrary, good quality film can be formed at high gas ratio. Fig. 8. also indicates that as gas ratio multiplies, oxygen composition increase and hydrogen composition decreases to form a better film. Deposition rate as a function of chamber pressure is shown in Fig. 9. As pressure increases, deposition rate also increases linearly, which is due to the increase of intermediates decomposed by photolysis. To derive the activation energy, the deposition rate was measured by varing substrate temperature from 150℃ to 250℃ every 50℃ apart. Fig. 10. shows an Arrhenius plot. The activation energy at low temperature(<200℃) may be 0.22eV from two points, but at the high temperature(>200℃) the activation energy is 0.61eV. This phenomena indicates that the thermal effect cannot be neglected at a high temperature. Fig. 11. shows the deposition rate as a function of laser power. In the experiment, deposition rate increases linearly with laser power. This is also in good accordance with simulated results based on direct dissociation.

4. Conclusion

A new model on film deposition by Laser CVD was suggested based on three mechanism : source gas transport mechanism, photolysis & reactants diffusion mechanism, surface adhesion mechanism.

After the experiment was carried out under various conditions, such as gas ratio, chamber pressure, substrate temperature and beam height, the simulated results were compared to the experimental results in order to establish more accurate model for Laser CVD.

Finally, this simulator based on the new model, makes it possible to predict the deposition rate under various condition successfully and this model has a advantage, in that it helps to understand the film deposition process more concretely.

Reference

[1] M. HANABUSA, Photo-induced Deposition of Thin Films, North-Holland, Amsterdam, 1987.

[2] B. Fowler, S. Lian, S. Krishnan, L. Jung, C. Li and S. Banerjee, "Modelling of Photo-Chemical Vapor Deposition of Epitaxial Silicon Using an ArF Excimer Laser", SPIE, Vol. 1598, pp108～117, 1991

[3] Carmen J. Giunta, Jonathan D. Chapple-Sokol and Roy G. Gordon, "Kinetic Modeling of the Chemical Vapor Deposition of Silicon Dioxide from Silicon or Disilane and Nitrous Oxide", J. Electrochem. Soc., Vol. 137, No. 10, pp 3237～3253, October 1990

[4] P. W. ATKINS, Physical Chemistry, 4th Edition, Oxford University Press, 1993

[5] JUNJI SHIRAFUJI, SATORU MIYOSHI and HIDEMITSU AOKI, "Laser induced Chemical Vapor Deposition and Charaterization of Amorphous Silicon oxide films", Thin Solid Films, 157, pp 105～114, 1988

[6] Brian Chapman, Glow Discharge Processes, JOHN WILEY & SON, 1976
[7] E. BOCH, C.FUCHS, E.FOGARASSY and P.SIFFERT, "Influence of Diluted in Nitrogen on the Photodissociation Processes of Silane and Disilane at 193nm", J. Appl. Surf, Sci. 43, pp17~22, 1989
[8] B.Fowler, S.Lian, S.Krishnan, L.Jung, C.Li and S.Banerjee, "ArF Excimer Laser-Enhanced Photochemical Vapor Deposition of Homoepitaxial Silicon from Disilane", J. Electrochem. Soc., Vol. 139, No. 8, pp2314~2318, August 1992
[9] S.Lian, B.Fowler, S.Krisnan, L.Jung, C.Li and S. Banerjee, "Silicon Homoepitaxial Films Grown by Photo-Enhanced Chemical Vapor Deposition from Si_2H_6", J. Electochem. Soc., Vol. 139, No. 8, pp2273~2277, August 1992
[10] William H. Press, Numerical Recipes in C, CAMBRIDGE UNIVERSITY PRESS, 1992

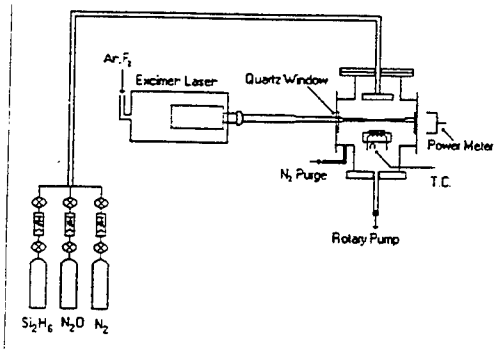


Figure 1. Experimental Apparatus

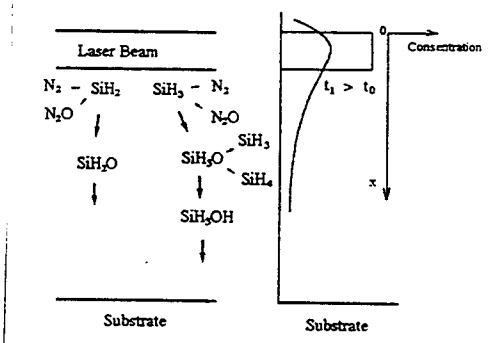


Figure 2. Diffusion of reactants

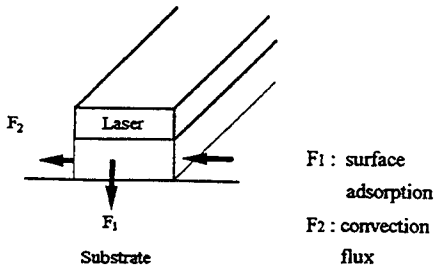
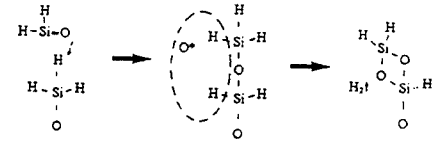
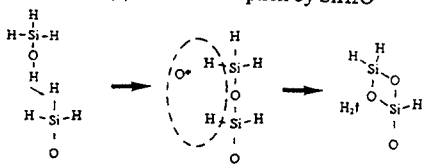


Figure 3. Flow of reactants for surface adsorption and convection flux



(a) surface adsorption by SiH_2O



(b) surface adsorption by SiH_3OH

Figure 4. Surface adsorption process

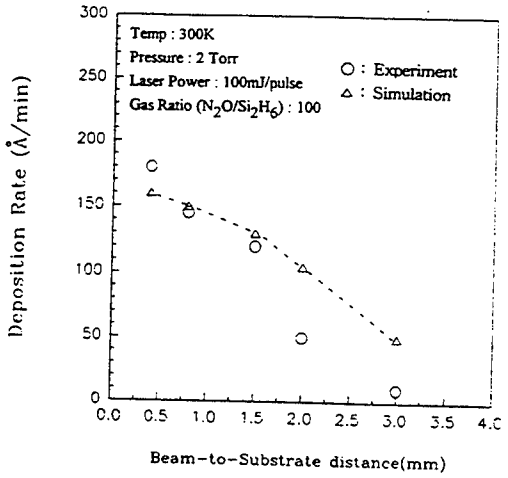


Figure 5. Deposition vs. Beam height

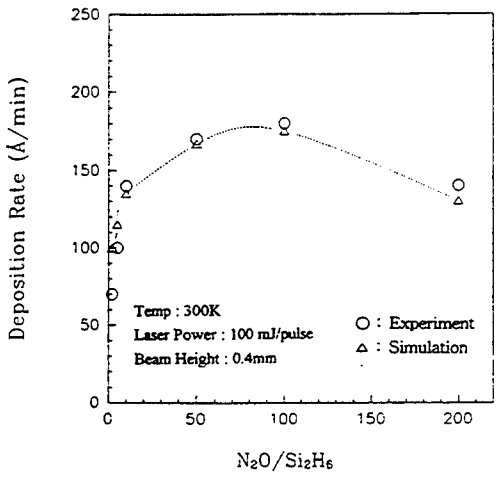


Figure 6. Deposition rate vs. Gas ratio

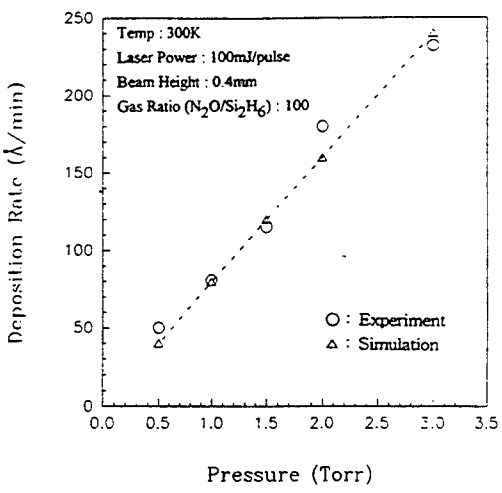


Figure 9. Deposition rate vs. Pressure

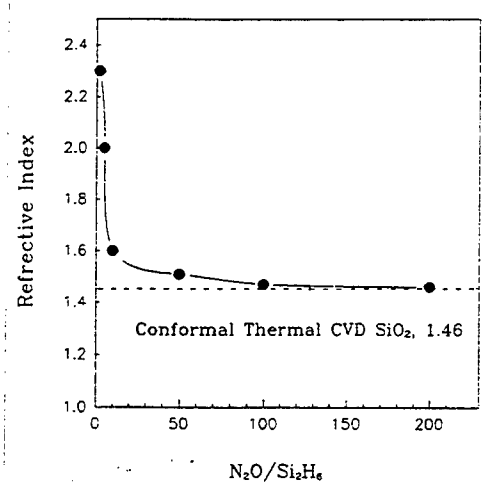


Figure 7. Refractive Index vs. Gas ratio

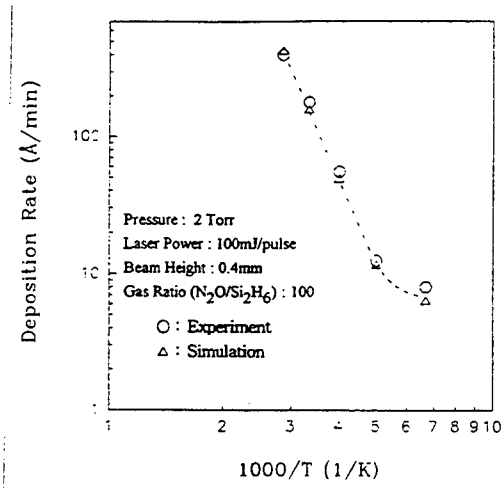


Figure 10. Deposition rate vs. Substrate temperature

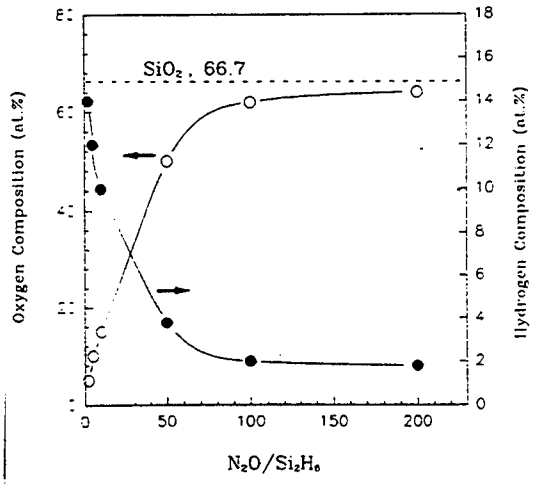


Figure 8. Oxygen & Hydrogen components vs. Gas ratio

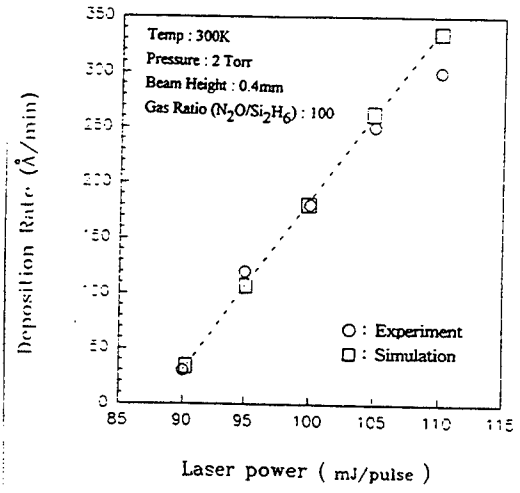


Figure 11. Deposition rate vs. Laser power

SPONTANEOUS FORMATION OF ORDERED ARRAYS OF QUANTUM DOTS

V.A. Shchukin[1], N.N. Ledentsov[1], P.S. Kop'ev[1], and D. Bimberg[2]

[1] *A.F. Ioffe Physical Technical Institute, St. Petersburg 194021, Russia*
[2] *Technische Universität Berlin, Hardenbergstraße 36, Berlin D-10623, Germany*

Spontaneous formation of ordered nanostructures on crystal surfaces is at present a subject of active research. One mechanism of formation is faceting where a planar surface rearranges to a periodic hill–and–valley structure in order to decrease the surface free energy [1]. Faceting was observed for surfaces vicinal to Si(111) [2], GaAs(100) [3], for high–index surfaces of Si [4], GaAs [5], etc. Heteroepitaxial growth on faceted surfaces may result in formation of corrugated superlattices [5].

The theory of Ref. [1] shows that a crystal surface with an arbitrary orientation $\hat{\mathbf{m}}$ is characterized by two intrinsic parameters, the surface free energy $\gamma(\hat{\mathbf{m}})$ and the intrinsic surface stress tensor $\tau_{ij}(\hat{\mathbf{m}})$. The latter implies that even the surface of a homogeneous crystal may be considered as intrinsically stressed one. For a faceted surface, the discontinuity of the intrinsic surface stress tensor τ_{ij} at the edges between neighboring facets creates a long–range strain field. The free energy of a faceted surface, defined per unit area of the reference flat surface with the normal $\hat{\mathbf{n}}$, is a sum of three terms: $E = E_{FACETS} + E_{EDGES} + \Delta E_{EL}$. Here E_{FACETS} is the free energy of tilted facets, $E_{FACETS} = A^{-1} \int \gamma(\hat{\mathbf{m}})(\hat{\mathbf{m}} \cdot \hat{\mathbf{n}})^{-1} dA$, the term E_{EDGES} is the short–range energy of edges, and ΔE_{EL} is the change of the strain energy due to elastic relaxation, termed below "elastic relaxation energy". It was shown in Ref. [1] that if the quantity $\gamma(\hat{\mathbf{m}})(\hat{\mathbf{m}} \cdot \hat{\mathbf{n}})^{-1}$ attains its minimum for $\hat{\mathbf{m}} \neq \hat{\mathbf{n}}$, the planar surface is unstable and rearranges to a periodic structure of facets.

Another mechanism of spontaneous formation of nanostructures is associated with initial growth stages on lattice–mismatched substrates. Then the planar surface of the deposited material which is stable *without external stress*, becomes unstable against long–wavelength corrugation *under external stress*, e. g., caused by lattice mismatch with the substrate [6]. This instability results in formation of coherent strained islands on the bare substrate for Volmer–Weber (VW) growth or on the wetted surface for coherent Stranski–Krastanow (SK) growth [7]. Formation of islands leads to a reduction of the strain energy and to an increase of the surface energy as compared to the planar case. The former is proportional to the volume of the island, and the latter is proportional to the surface area of the island. If the size of an island exceeds a critical size, further growth of the island becomes energetically favorable. It is generally assumed that, if the material supply is interrupted, the further growth of large islands occurs at the expense of the evaporation of smaller islands. Islands thus undergo ripening.

Heterophase growth via formation of coherent islands was studied in Ge/Si(100)–systems [8], and, more recently, in InGaAs/GaAs(100)–systems [9,10]. Surprisingly, experiments show in most cases rather narrow size distribution of islands [9,10] which does not follow from SK or VW growth modes themselves. Besides that, it was reported in Ref. 10 that coherent islands of InAs form, under certain conditions, a quasi–periodic square lattice. The lateral periodicity and the island size do not change with time.

Here we study the energetics of an array of coherent strained islands under the constraint of the fixed amount of the deposited material, assuming that all deposited material is assembled in islands. We will show that a periodic array of identical islands corresponds, under certain conditions, to the total energy minimum.

The change of the total energy due to the formation of a single island is equal:

$$\Delta \tilde{E}_{ISL} = \Delta \tilde{E}_{FACETS} + \tilde{E}_{EDGES} + \Delta \tilde{E}_{EL} \,. \qquad (1)$$

Here $\Delta\tilde{E}_{FACETS} = \int \left[\gamma(\hat{\mathbf{m}})\,(\hat{\mathbf{m}}\cdot\hat{\mathbf{n}})^{-1} - \gamma(\hat{\mathbf{n}})\right] dA$. Since the (001) surface of the deposited material without external stress is stable against faceting, the quantity $\gamma(\hat{\mathbf{m}})\,(\hat{\mathbf{m}}\cdot\hat{\mathbf{n}})^{-1}$ attains its absolute minimum for $\hat{\mathbf{m}} = \hat{\mathbf{n}} = (0,0,1)$. Then appearance of tilted facets leads to $\Delta\tilde{E}_{FACETS} > 0$. Besides the *cusped* absolute minimum for the (001) surface, $\gamma(\hat{\mathbf{m}})\,(\hat{\mathbf{m}}\cdot\hat{\mathbf{n}})^{-1}$ may have *cusped local minima* for some other facets [11], e. g. for 4 equivalent facets: (k0l), (0kl), ($\bar{\text{k}}$0l) and (0$\bar{\text{k}}$l), where the surface energy $\gamma(\hat{\mathbf{m}})$ is equal for these 4 facets. Then, under a range of conditions, the minimum of $\Delta\tilde{E}_{ISL}$ corresponds to an island bound by (k0l), (0kl), ($\bar{\text{k}}$0l) and (0$\bar{\text{k}}$l) facets, e. g. to a pyramid or to an elongated prism.

The second term in Eq.(1), $\tilde{E}_{EDGES}$, is the short–range energy of edges. The third term, $\Delta\tilde{E}_{EL}$, is the elastic relaxation energy. For lattice–mismatched systems with edges, there are two sources of the strain field, *i*) the lattice mismatch $\epsilon_0 = \Delta a/a$ (a being the lattice spacing) and *ii*) the discontinuity of the intrinsic surface stress tensor τ_{ij} at the edges. Then $\Delta\tilde{E}_{EL}$ is a quadratic function of ϵ_0 and τ. The dependence of $\Delta\tilde{E}_{EL}$ on the size of an island L is determined by scaling properties of the equilibrium equations of the elasticity theory [12]:

$$\Delta\tilde{E}_{EL} = -f_1(\varphi_0)\lambda\epsilon_0^2 L^3 - f_2(\varphi_0)\epsilon_0\tau L^2 - f_3(\varphi_0)\frac{\tau^2}{\lambda} L \ln\left(\frac{L}{2\pi a}\right). \qquad (2)$$

Here λ is a characteristic elastic modulus, geometric factors f_1, f_2, f_3 are functions of the tilt angle of facets φ, and $\varphi_0 = \tan^{-1}(k/l)$. The first term in Eq.(2) is the contribution of the lattice mismatch to the elastic relaxation energy, $\Delta\tilde{E}_{EL}^{(1)}$. The second term which is proportional to the surface of the island, is the mismatch–induced renormalization of the surface energy. The third term is the contribution of the edges to the elastic relaxation energy, $\Delta\tilde{E}_{EL}^{(2)}$. We consider islands of the size larger than the critical one, the first term in Eq.(2) being the dominant contribution to $\Delta\tilde{E}_{EL}$. We have calculated $\Delta\tilde{E}_{EL}^{(1)}$ for different shapes of an island and have shown that the square–based pyramid is energetically more favorable than the elongated prism, i. e., the "quantum dot" is more favorable than the "quantum wire" [13].

For a *dilute* system of islands, the elastic interaction between islands via the strained substrate may be neglected. Then, substituting $\Delta\tilde{E}_{EL}$ from Eq.(2) into Eq.(1), summing contributions of identical pyramid–shaped islands, one obtains the energy of the dilute system of islands *per unit surface area* as follows:

$$E_{DIL} = 6Qa\,\cot\varphi_0 \left[- f_1(\varphi_0)\lambda\epsilon_0^2 + \frac{\gamma(\varphi_0)\sec\varphi_0 - \gamma(0) - f_2(\varphi_0)\tau\epsilon_0}{L} + \frac{\eta f_4(\varphi_0)}{L^2} - \frac{\tau^2 f_3(\varphi_0)}{\lambda L^2}\ln\left(\frac{L}{2\pi a}\right)\right], \qquad (3)$$

Q being the amount of the deposited material in units of monolayers. The first term in Eq.(3) yields the contribution of the lattice mismatch to the elastic relaxation energy, $\Delta E_{EL}^{(1)}$. The second term is the renormalized surface energy of islands. The third term is the short–range energy of the edges of islands, η being the energy per unit length of the edge. The last term, which is the contribution of the edges to the elastic relaxation energy, $\Delta E_{EL}^{(2)} \sim -L^{-2}\ln L$, *always* has minimum as a function of L.

We introduce the characteristic length, $L_0 = 2\pi e^{1/2} a \exp\left[f_4(\varphi_0)(f_3(\varphi_0))^{-1}\eta\lambda\tau^{-2}\right]$, and the characteristic energy per unit area, $E_0 = 3Qa\,\cot\varphi_0 f_3(\varphi_0)\tau^2\lambda^{-1}L_0^{-2}$. Then we may write the sum of all L–dependent terms in the energy $E(L)$ as follows:

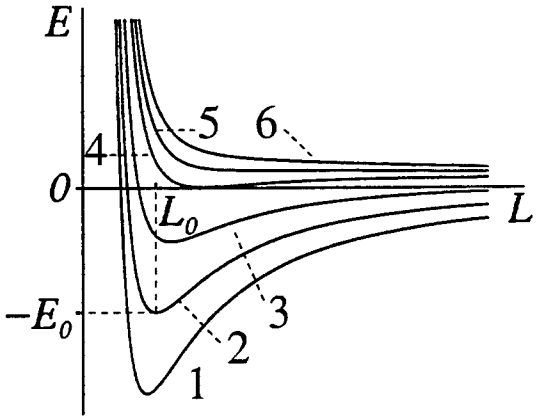


FIG. 1. The energy of the system of coherent strained islands versus the size of islands. The control parameter α is equal: 1) $\alpha = -0.5$; 2) $\alpha = 0$; 3) $\alpha = 0.5$; 4) $\alpha = 1$; 5) $\alpha = 2\,e^{-1/2} \approx 1.213$; 6) $\alpha = 1.4$.

$$E(L) = E_0\left[-2\left(\frac{L_0}{L}\right)^2 \ln\left(\frac{e^{1/2}L}{L_0}\right) + \frac{2\alpha}{e^{1/2}}\left(\frac{L_0}{L}\right)\right], \tag{4}$$

where the control parameter α is the ratio of the renormalized surface energy and of the contribution of edges to the elastic relaxation energy, $\Delta E_{EL}^{(2)}$:

$$\alpha = \left[\gamma(\varphi_0)\sec\varphi_0 - \gamma(0) - f_2(\varphi_0)\tau\epsilon_0\right] \times \frac{e^{1/2}\lambda L_0}{f_3(\varphi_0)\tau^2}. \tag{5}$$

As it is noted above, $\gamma(\varphi_0)\sec\varphi_0 - \gamma(0) > 0$. However, due to mismatch–induced renormalization of the surface energy, $-f_2(\varphi_0)\tau\epsilon$, parameter α can be of either sign.

Fig. 1 displays the dependence of E on the length L for different values of α. If $\alpha \leq 1$, there exists the absolute minimum of the energy $E(L)$ at the optimum size of pyramids L_{opt}, and L_{opt} increases with α. On the other hand, the ripening of islands would correspond to $L \to \infty$ where $E(L) \to 0$. It means that the system of islands of the optimum size L_{opt} is a *stable array*, and *islands do not undergo ripening.*

If $1 < \alpha < 2\,e^{-1/2} \approx 1.213$, there exists only a local minimum in the energy $E(L)$, which corresponds to a metastable array of islands. If $\alpha \geq 2\,e^{-1/2}$, the local minimum disappears. In both latter cases, the absolute minimum of the energy corresponds to $L \to \infty$, i. e. islands exhibit the thermodynamic tendency to ripening.

For a *dense* system of islands, the energy of elastic interaction between islands via the strained substrate, E_{INTER}, becomes essential. The system of interacting islands is then a system of stress domains where the minimum of the strain energy corresponds to a *periodic domain structure* [14]. We have calculated the energy $E_{TOTAL} = E_{DIL} + E_{INTER}$ for a 1D periodic array of elongated prisms ("quantum wires") and for different 2D periodic arrays of pyramids ("quantum dots") and have shown that 2D square array of "quantum dots" with primitive lattice vectors along "soft" directions [100] and [010] is energetically the most favorable one [13]. It should be noted that in the case of submonolayer coverage, 1D periodic arrays of wire–like elongated islands are more favorable than 2D arrays of islands of compact shape [15]. The difference of our results from those of Ref. 15 follows from the shape of individual islands which are essentially *three–dimensional* and have *well defined side facets.*

The major term in the energy E_{INTER} for 2D arrays is the energy of effective dipole–dipole elastic repulsion between islands, which yields the positive contribution to the

energy $E_{TOTAL}(L) = E_{DIL}(L) + E_{INTER}(L)$. We have shown [13] that the absolute minimum in the energy $E_{TOTAL}(L)$ persists for dense systems, if the parameter α from Eq.(5) $\alpha < 0$. The absolute minimum disappears with the increase of the coverage Q, if $0 \leq \alpha < 1$. In the latter case, islands undergo ripening.

To estimate characteristic values of α, we substitute $\tau \approx 100\text{meV/Å}^2$, $\lambda \approx 500\text{meV/Å}^3$, $L_0 \approx 100$Å, $a = 2.8$Å. The difference $[\gamma(\varphi_0)\sec\varphi_0 - \gamma(0)]$ may be of the order of $\approx$ 5–10meV/Å^2. It follows then from Eq.(5) that the parameter α for a strongly mismatched system may become negative due to mismatch–induced renormalization of the surface energy. If $\alpha < 0$, then the increase of $|\epsilon_0|$, e. g., by the increase of x for the heterophase systems $In_xGa_{1-x}As/GaAs(001)$, should result in the decrease of the size of islands L_{opt}. It agrees with experimental observations of Ref. 10.

To conclude, we have shown that coherent strained islands on the lattice–mismatched substrate may form, under certain conditions, *stable* periodic arrays of equal–sized islands. For islands which are essentially three–dimensional and have well defined side facets, 2D array of "quantum dots" is energetically more favorable than 1D array of "quantum wires". For islands on the (001)–surface of a cubic crystal, the 2D periodic square lattice with primitive lattice vectors oriented along the lowest–stiffness directions [100] and [010] is energetically preferred, due to the elastic anisotropy of cubic crystals. For practical systems, our theory predicts a narrow size distribution of islands and a periodic arrangement of islands in a 2D lattice as experimentally observed for the InAs/GaAs(001) system [10]. The dependence of the size of islands L_{opt} and of the period of the lattice D on the lattice mismatch ϵ_0 gives the possibility to control parameters of quantum dots by varying ϵ_0, e. g. by changing x for the $In_xGa_{1-x}As/GaAs(001)$ — heterophase growth.

[1] V.I. Marchenko and A.Ya. Parshin, Sov. Phys. JETP **52**, 129 (1980); V.I. Marchenko, Sov. Phys. JETP **54**, 605 (1981).
[2] R.J. Phaneuf and E.D. Williams, Phys. Rev. Lett. **58**, 2563 (1987).
[3] M. Kasu and N. Kobayashi, Appl. Phys. Lett. **62**, 1262 (1993); N.N. Ledentsov, G.M. Gurianov, G.E. Tsyrlin, V.N. Petrov, Yu.B. Samsonenko, A.O. Golubok and S.Ya. Tipisev, Semiconductors, **28**, 526 (1994).
[4] A.A. Baski and L.J. Whitman, Phys. Rev. Lett. **74**, 956 (1995).
[5] R. Nötzel, N.N. Ledentsov, L. Däweritz, M. Hochenstein and K. Ploog, Phys. Rev. Lett. **67**, 3812 (1991).
[6] M.A. Grinfield, Sov. Phys. Dokl. **31**, 831 (1986); S. Luryi and E. Suhir, Appl. Phys. Lett. **49**, 140 (1986); D. Srolovitz, Acta Metall. **37**, 621 (1989).
[7] D. Vanderbilt and L.K. Wickham, MRS Proceedings Vol. 202, p. 555 (1991).
[8] D.J. Eaglesham and M. Cerullo, Phys. Rev. Lett. **64**, 1943 (1990); Y.–W. Mo, D.E. Savage, B.S. Swartzentruber and M.G. Lagally, Phys. Rev. Lett. **65**, 1020 (1990).
[9] D. Leonard, M. Krishnamurthy, C.M. Reaves, S.P. Denbaars and P.M. Petroff, Appl. Phys. Lett. **63**, 3203 (1993); J.M. Moison, F. Houzay, F. Barthe, L. Leprince, E. André and O. Vatel, Appl. Phys. Lett. **64**, 196 (1994).
[10] N.N. Ledentsov, M. Grundmann, N. Kirstaedter, J. Christen, R. Heitz, J. Böhrer, F. Heinrichsdorff, D. Bimberg, S.S. Ruvimov, P. Werner, U. Richter, U. Gösele, J. Heidenreich, V.M. Ustinov, A.Yu. Egorov, M.V. Maximov, P.S. Kop'ev and Zh.I. Alferov, Proc. 22 ICPS, Vancouver, 1994; World Scientific, Singapore, 1995, Vol. 3, p. 1855.
[11] C. Herring, Phys. Rev. **82**, 87 (1951).
[12] V.A. Shchukin, A.I. Borovkov, N.N. Ledentsov and D. Bimberg, Phys. Rev. **B 51**, 10104 (1995).
[13] V.A. Shchukin, N.N. Ledentsov, P.S. Kop'ev and D. Bimberg, to be published.
[14] I.P. Ipatova, V.G. Malyshkin and V.A. Shchukin, J. Appl. Phys. **74**, 7198 (1993); Phil. Mag. **B 70**, 557 (1994).
[15] D. Vanderbilt, Surf. Sci. **268**, L300 (1992).

On new mechanism of lateral superlattice formation at vicinal interface

B.K. Medvedev, V.A. Petrov
Institute for Radio Engineering and Electronics the RAS, Moscow 103617, Russia
N.V. Peskov
Moscow State University, Depart. of Comput. Math. & Cybernet., Moscow 119899, Russia

The effect of lateral segregation of the Al and Ga atoms appeares when AlGaAs layers grow on a vicinal (001) face via Mobility Enhanced Epitaxy (MEE) [1]. This effect is employed for fabrication of tilted superlattices. In MEE of III-V compound semiconductors an atomic monolayer of one group is completed when the flux of another group elements is shut off. The completion of the atomic monolayer by Al and Ga in the absence of As strongly stimulates surface migration of the formers. The enhansed migration leads to Al and Ga segregation over the terrace plane. Less mobile Al atoms collect near an inner terrace edge (up step), while more mobile Ga atoms are forced out towards an outer terrace edge (down step). The kinetic of this phenomenon was investigated with the help of the stochastic model in [2].

We suppose that the difference in mobility of the third group atoms can cause their ingomogeneous distribution over a vicinal face during usual MBE process too. Consider the initial stage of MBE growth of the solid solution $A^{III}_{x}B^{III}_{1-x}C^{V}$ on the vicinal surface of $A^{III}C^{V}$. Let us suppose that the B atoms are more mobile than the A atoms. Let the MBE conditions are such that the "step flow" growth regim realizes for the B species, and the terrace nucleation growth regime realises for the A species. At the beginnig of the growth the fast B atoms will quickly reach the terrace edge and incorporate into the crystal lattice there. The slow A atoms will form clusters on the terrace surface and nucleate the new layer. Thus at the start of the first ABC layer completion ingomogeneous distribution of A and B over the terraces originates and, under the certain conditions, will be preserved until full layer completion. Therefore, there will be periodic concentration of the A and B species over the $A^{III}B^{III}C^{V}/A^{III}C^{V}$ heterojunction along certain crystallographic axis, and there will be periodic potential barrier at the interface. This periodic barrier could be used for creation the specific quantum well with the lengthwise superlatice potential.

To confirm our supposition we have performed the computer simulation of the $A^{III}B^{III}C^{V}/A^{III}C^{V}$ heterojunction MBE growth on the vicinal surface with the help of the lattice Monte Carlo model [3, 4]. This model simulates the growth process of

three-component crystal with tetrahedral lattice. The species are transfered onto the crystal surface by atomic (A and B) and molecular (C_2) fluxes. The model includes main kinetic processes on the crystal surface: the adsorption, the desorption, and the surface migration. The key parameters of the model are the bond energies of atoms in the crystal lattice. The objective of simulation was the determination of the growth conditions, under which the distinguishable and steady periodic distribution of A and B over the terraces is observed. For simplicity it was assumed that the bond energy $A-C$ and $B-C$ is equal each other as well as the bond energy $A-A$ and $B-B$, and the latter is eight times less than the former (0.8 eV and 0.1 eV). The bond energy $A-B$ was assumed to be four times less than the $A-A$ one. The hopping rate in an atom migration was calculated by the Arrhenius type formula taking into account the first and second neighbors bond energies. Under such choise of parameters the hopping rate for the B atom is about $\exp(3482/T)$ times greater the A atom hopping rate on the clear C-terminated surface of $A^{III}C^{V}$. Among all simulation variants the most significant separation of the A and B species is observed under the following growth conditions: the width of terrace located perpendicularely to the [110] axis — 16 atomic rows, the mole fraction of A — 0.5, the growth rate — 0.5 layer of ABC per second, the surface temperature — 650K. Under such conditions the B atom hopping rate is about 250 times larger than the A atom hopping rate. The simulation results obtained under described conditions are shown in the Fig.1.

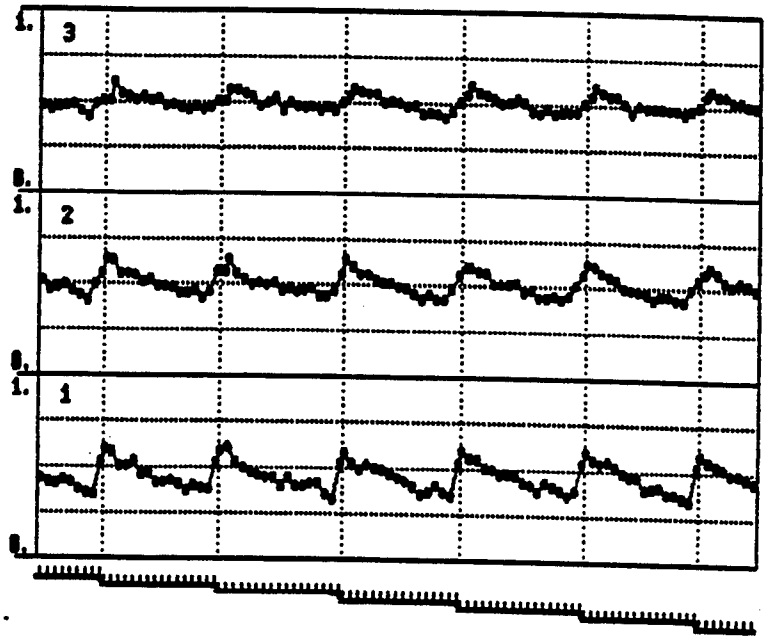


Figure 1: Concentration of the B species in three layers of ABC.

The mechanism of formation such non-unifirm distribution is explained by the Fig.2. In the leftside of Fig.2 the graph of average path length passed by an A (lower curve) and B (upper curve) atom between adsorption and incorporation into the crystal lattice is shown in dependence upon the growth time. The rightside of Fig.2 shows the distribution of B across the terraces at the successive moments of growth time: 0.1s, 0.4s, ..., 1.9s. From the Fig.2 one can conclude that about 90% of the B

atoms fallen onto the substrate in the initial 0.4s of growth time were incorporated into the crystal near the steps. During this time the average path between adsorption and incorporation for those atoms is greater than the terrace half-width while for the A atoms that path is less. The most part of A atoms have not time for reaching the terrace edge and nucleate the new layer on the terrace surface instead. When the number of nuclei becomes sufficiently large the B atoms will adjacent to them, and hence the B average path decreases. Gradually the growth regime becomes stable and the A and B concentrations steer straight.

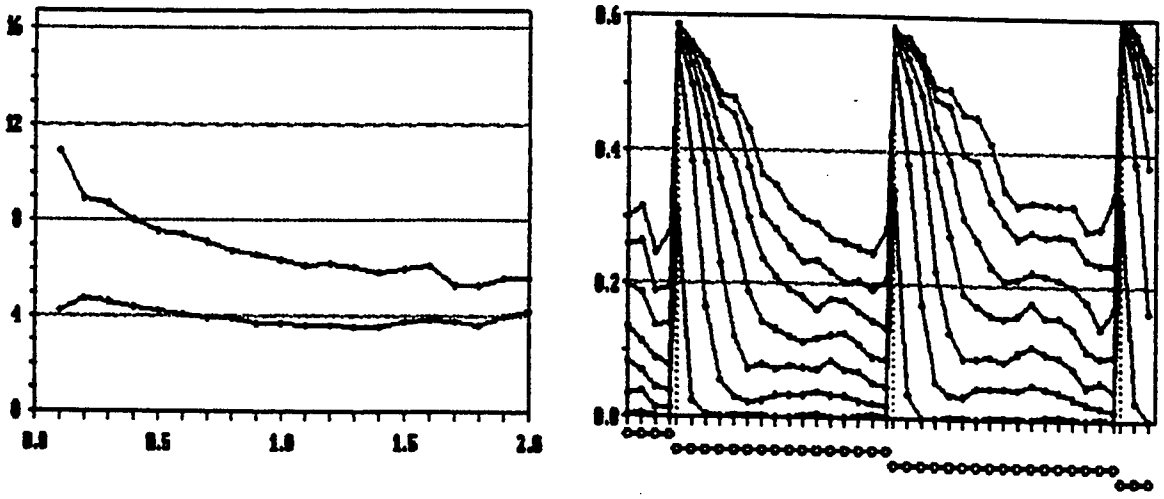


Figure 2: Leftside — the average path of A and B atoms. Rightside – the B concentration in the first ABC layer at successive time moments of growth.

We will discuss now the possible role of the ingomogeneous periodic distribution of the Al concentration considered for the formation of the minigaps in the energetic spectrum of the 2D electrons in the lateral superlattices on the vicinal heteroboundary.

As known, the existence of superlattice effects in these lateral superlattices initiates with the appearance in these systems of a new crystallographic translation period $A \gg a$ (a is the lattice constant) in the plane of quantum well [5]. The emergence in these superlattices of the periodic system of atomic steps allows to explain the appearence of the minigaps by the scattering of electrons on such gaps.

In this work we have shown that in GaAs-GaAlAs structures, the Al concentration near steps can differ significantly from its average value, defined by Al molar fraction (the difference is up to 50%). We consider that such an ingomogeneous periodic distribution of Al atoms along heteroboundary can play the role of the superlattice potential for 2D electrons in quantum well created at such heteroboundary. Indeed, since the heights of the potential barriers confinig the carrier motion in GaAs quantum well are determined by the Al molar fraction in the AlGaAs solid solution, then the heights of the potential barriers between GaAs and AlGaAs regions with various Al concentrations will differ, that is, the quantum well depth will be modulated periodically along heteroboundary. Estimations demonstrate that the change of the quantum well depth may be some tens of meV, that is, such modulating potential

can give the major contribution to the formation of the total superlattice potential exceeding the contribution of the atomic steps.

References

[1] Y. Horikoshi, H. Yamaguchi, L. Briones and M. Kawashima, J. Cryst. Growth. **105**, 326 (1990).

[2] Yan-Ten Lu and Horia Metiu, Surf. Sci. **245**, 150 (1991), Surf. Sci. **254**, 209 (1991).

[3] B.K. Medvedev, V.G. Mokerov and N.V. Peskov, Dokl. Akad. Nauk. **329**, 302 (1993) [in Russian].

[4] N.V. Peskov, Comput. Phys. Commun. **77**, 64 (1993).

[5] V.A. Petrov, Sixth All-Union Conf. on the Physics of Surface Phenomena in Simicond. Kiev, 1977; Abstr. of Paper, Kiev, 1977, part 2, p. 80; Sov. Phys. Semicond., **12**, 212 (1976).

Fabrication and RF Performance of GaAs MESFETs

Tracy Abbott, Tim Brock, Jack East, George Haddad

Center for High Frequency Microelectronics
Solid State Electronics Lab
The University of Michigan
Ann Arbor, MI 48109

Abstract

This paper describes the optimization of deep submicron GaAs MESFETs for high frequency operation. Key changes compared with earlier work, include an increased doping level in the channel layer and improvements in the electron beam lithography. The MBE grown sample has a channel layer doped with Si at 4.0×10^{18} cm^{-3} and includes a cap layer doped at 7×10^{18} cm^{-3}. Improvements in the electron beam lithography include a reduction of spot size, improved focussing techniques, and a reduction in the bilayer electron beam resist thickness.

We have fabricated GaAs MESFETs with electron beam defined "mushroom" gates with lengths of approximately 0.1 μm. Extrinsic DC results for a MESFET with a 2x45 μm wide gate in a "Π" configuration include a saturation current of 35 mA at V_{ds} = 2.5 V and V_g = 0.5 V, pinch-off voltage of -.2 V, peak transconductance of 795 mS/mm, and output conductance of around 45 mS/mm. RF characteristics include a cut-off frequency (f_t) of 103 GHz and a maximum frequency of oscillation (f_{max}) of 165 GHz. We believe that these results demonstrate state-of-the-art performance for conventional submicron GaAs MESFETs in their DC and RF characteristics.

This work is being supported by the Army Research Office under the URI program, Contract No. DAAL03-92-G-0109 and the NASA Center for Space Terahertz Technology, Contract No. NAGW-1334.

Unified Substrate Current Model for MOSFETs

Benjamín Iñíguez *, Frode Pedersen + and Tor A. Fjeldly +

* University of the Balearic Islands, Faculty of Sciences, Dpt. of Physics, Crtra de Valldemossa, Km. 7.5, 07071, Palma de Mallorca, Spain.

+ Department of Physical Electronics, Norwegian Institute of Technology, N-7034, Trondheim, Norway.

I. Introduction

As device dimensions of MOSFETs are scaled down, it becomes necessary to accurately model the substrate current. An accurate substrate current model can help designers prevent possible malfunctions of the circuits because of degradation by injection of hot carriers, and to obtain a better estimation of analog design parameters.

Some analytical models have been presented, for example, the model by Arora *et al.* [1] and the model by Tanizawa *et al.* [2]. However, the impact ionization current in weak inversion is neglected in the above works. Apart from creating a sharp transition across the threshold voltage this omission reduces the accuracy of the model for analog design in low-power applications. Likewise, it is necessary to establish a smooth transition between the saturation regime and the triode regime (where impact ionization is zero).

If the drain voltage is sufficiently high, the voltage drop across the substrate resistance (in the presence of a substrate current) will cause a reduction of the intrinsic bulk voltage (*n*-channel MOSFET). This, in turn, will lower the threshold voltage and enhance the channel current and the channel conductance. In the approach by Skotnicki [3] these effects are explicitly taken into account in the channel current expression, but only through the drift term.

The aim of the present work is to develop a unified and continuous model for substrate current in normal operation, suitable for circuit simulation. This substrate current model can be coupled to any continuous channel current model. Here it is combined with the unified model by Shur *et al.* [4] (Level 7 in AIM-Spice [5]) and to the model by Iñíguez *et al.* [6], [7]. Both models are continuous in all their derivatives. The effect of the voltage drop in the substrate resistance (when the substrate current is high enough) on the channel current is incorporated in an explicit and continuous manner.

II. Model

A. Substrate Current in Strong Inversion

In saturation the impact ionization current is obtained by integrating the impact ionization rate along the saturated part of the channel [1]:

$$I_{sub} = I_{ch} A_i \int_0^{l_{sat}} \exp(-B_i / E_l) dy \tag{1}$$

Here I_{ch} is the channel current, E_l is the lateral electric field, A_i and B_i are impact ionization rate parameters, and l_{sat} is the length of the saturated region. In the saturated region, a quasi-two-dimensional analysis gives the approximate expressions for the potential and the lateral electric field of [1]. We substitute them in (1) to change the variable of integration from y to E_l. After using the approximate solution of the resulting integral, given in [2], we finally obtain, assuming $E_m >> E_c$, E_c being the field at which carriers reach velocity saturation, V_{sat} the saturation voltage, $\eta \leq 1$ is a technology-dependent fitting parameter [1], and l_d the characteristic length,

$$I_{sub} = I_{ch} \frac{A_i}{B_i} (V_{ds} - \eta V_{sat}) \exp\left(\frac{-l_d B_i}{V_{ds} - \eta V_{sat}} \right) \tag{2}$$

B. Substrate Current Model in Weak Inversion

The impact ionization current in weak inversion is found by integrating the impact ionization rate along the length of the channel. As in the case considered above, the major contribution will come from the part of the channel where the electric field reaches a maximum, i.e., from near the drain.

From a quasi-two-dimensional analysis, Huang and Kueng [8] obtained approximate expressions for the potential and the lateral electric field distributions in the weakly inverted channel. The resulting substrate current in weak inversion, if E_m is high enough ($E_m \approx V_{ds} / l_d$), can be expressed as

$$I_{sub} = I_{ch} \frac{A_i}{B_i} V_{ds} \exp\left(\frac{-l_d B_i}{V_{ds}}\right) \tag{3}$$

C. Development of a Unified Model

We note from the above results that the substrate current generated by impact ionization in the channel can be unified in terms of the expression:

$$I_{sub} = I_{ch} \frac{A_i}{B_i} (V_{ds} - \eta V_{dse}) \exp\left(\frac{-l_d B_i}{V_{ds} - \eta V_{dse}}\right) \tag{4}$$

where $V_{dse} = V_{sat}$ in saturation above threshold; $V_{dse} = V_{ds}$ in the triode regime and $V_{dse} = 0$ in weak inversion.

Therefore, to develop a unified and continuous substrate current model, we need a smoothening function for V_{dse} that tends to the desired limit in each regime, and a unified and continuous channel current model. An appropriate function is, for example [5]

$$V_{dse} = \frac{V_{ds}}{\left[1 + \left(V_{ds} / V_{sat}\right)^m\right]^{1/m}} \tag{5}$$

From (4) it is clear that the above-threshold substrate current is critically dependent on the saturation voltage. A precise description of V_{sat} can be found based on an accurate velocity field relationship for the charge carriers. By including a smooth transition to the subthreshold regime (where $V_{dse} = 0$), we obtain

$$V_{sat} = \frac{2 q_s v_s L}{q_s \mu_{eff} - 2 c_{ox} \alpha v_s L} \tag{6a}$$

$$V_{sat} = -\frac{v_s L}{\mu_{eff}} \left(1 - \sqrt{1 - \frac{2 q_s \mu_{eff}}{c_{ox} \alpha v_s L}}\right) \tag{6b}$$

for *n*- and *p*-channel MOSFETs, respectively. Here q_s is the unified inversion sheet charge density at the source [5], μ_{eff} is the effective mobility, v_s is the saturation velocity and α is the bulk doping effect parameter [5].

The universal FET model by *Shur et al.* [4] contains a unified expression for the channel current suitable for calculating the substrate current:

$$I_{ch} = \frac{g_{che} V_{ds}}{\left[1 + \left(g_{che} V_{ds} / I_{sat}\right)^m\right]^{1/m}} \tag{7}$$

Here g_{che} is the the unified extrinsic channel conductance at small drain bias, R_t is the total drain and source series resistance and I_{sat} is the saturation current. In order to be consistent with the above expressions for V_{sate} the saturation current should be calculated using the corresponding velocity-field relationships.

The model of Iñíguez *et al.* [6] [7] can also be combined with the unified substrate current model. The channel current is expressed in terms of unified inversion sheet charge densities at the source end (q_s) and the drain end (q_d) of the channel using interpolation functions.

$$I_{ch} = \kappa v_s \frac{(q_d - q_s)(q_d + q_s + 2 \alpha c_{ox} V_{th})}{q_d - q_s + \kappa \alpha c_{ox} L_{eff} v_s / \mu_{eff}} \tag{8}$$

Here $\kappa = 2$ for nMOSFET and $\kappa = 1$ for pMOSFET.

E. Effects of Substrate Resistance on Channel and Substrate Currents

If the substrate current is high enough the voltage drop in the substrate resistance R_{sub} may cause an appreciable change of the effective substrate bias and in the depletion charge, resulting in an increase in the channel and substrate currents. A unified expression is developed for the inversion charge densities using the corresponding linear expansion in $R_{sub} I_{sub}$ in such a way that it is valid for both strong and weak inversion:

$$q_{sd} = q_{s,d}^0 \left[1 + \frac{(\alpha - 1) I_{sub} R_{sub}}{\eta c_{ox} V_{th} - q_{s,d}^0}\right] \tag{9}$$

where $q^{0}_{s,d}$ is the inversion charge density for $R_{sub} = 0$.

Substituting (9) in (8) we obtain to first order:

$$I_{ch} = \frac{I_{cho}}{1 - W(\alpha - 1)(M - 1)\mu_{eff} c_{ox} R_{sub} V_{dse} / (2L)} \tag{10}$$

where $M = 1 + (A_i / B_i)(V_{ds} - V_{dse}) \exp(-l_d B_i / (V_{ds} - V_{dse}))$, I_{cho} is the channel current when the effects of the substrate resistance are neglected.

III. Experimental Results and Discussion

The new substrate current model has been validated by comparisons with experimental results obtained from nMOSFETs and pMOSFETs of different channel lengths. The transistors came from a LDD n-well 1,2 µm process, with oxide thickness $t_{ox} = 23$ nm. For the comparisons we used the channel current and substrate current models of (8) and (4), although very similar results were also found using the universal channel current model of (7). The methods used to extract source current parameters follows in general those reported in [1]. The impact ionization rate parameters A_i and B_i can be determined using the procedure given in [5].

Comparisons of the modeled and measured substrate current versus V_{gs} for two nMOSFETs of different channel lengths are shown in Figs. 1 (a) and (b), and for a pMOSFET in Figure 2. The agreement between model and experiments is satisfactory in all regions and the new model gives a smooth transition of the substrate current from weak to strong inversion. Also we find a good agreement between the measured and calculated values of the normalized substrate transconductance, $g_{sub,m} / I_{sub}$ versus V_{gs} (Fig. 3). Note that it has a maximum plateau in weak inversion; the value of which is $1/(\eta V_{th})$, the same as that of the normalized channel current transconductance $g_{ch,m} / I_{ch}$. This confirms the validity of our model in weak inversion.

As indicated in Fig. 4 (a), we also observe a significant increase of the source current, I_{ch}, in moderate saturation because of the voltage drop on the substrate resistance, that implies an increase of the channel conductance, $g_{ch,d}$ with V_{ds} in this regime of operation, as correctly predicted by the model (Fig. 4 (b)).

IV. Summary

We have developed an analytical substrate current model for MOSFETs based on an analysis of the impact ionization in the conducting channel. In particular, we derived a new expression for the substrate current in weak inversion, which was joined smoothly to the existing model for above-threshold saturation and combined with a unified channel current model with an infinite order of continuity. The resulting continuous (unified) substrate current model is valid in all regimes of operation. The lowering of the intrinsic bulk bias because of the voltage drop in substrate resistance was also taken into account in an explicit and continuous way. Comparisons with experiments demonstrated that our unified substrate current model quite accurately reproduces the experimental data in all regimes of operation, including the continuous transitions between the regimes. Hence, the model appears to be very suitable for circuit simulation.

V. Acknowledgments

The authors wish to thank LG Semiconductor Inc., Ltd, and Professor Kwyro Lee at KAIST (Seoul, Korea) for providing the experimental devices used in this paper.

References

[1] N. Arora and M. S. Sharma, *IEEE Tr. on Electron Devices*, vol. 38, no 6, pp. 1392-1398, June 1991.
[2] M. Tanizawa, M. Ikeda, N. Kotani, K. Tsukamoto and K. Horie, *IEEE Tr. on CAD/ICAS*, vol. 12, no. 11, pp. 1749-1757, November 1993.
[3] T. Skotnicki, *Proceedings of ISDRS'93*, pp.113-116.
[4] M. Shur, T. A. Fjeldly, T. Ytterdal and K. Lee, *Solid State Electronics*, vol. 35, no.12, December 1992.
[5] K. Lee, M. Shur, T. A. Fjeldly and T. Ytterdal, *Semiconductor Device Modeling for VLSI*, Prentice-Hall, 1993.
[6] B. Iñíguez and E. G. Moreno, *IEEE Tr. on Electron Devices*, vol. 42, no. 2, February 1995.
[7] B. Iñíguez and E. G. Moreno, *Proceedings of MWSCAS'95*, August 1995.
[8] J. S. T. Huang and J. S. Kueng, *IEEE Tr. on Electron Devices*, vol. 39, no. 5, pp. 1245-1246, May 1992.

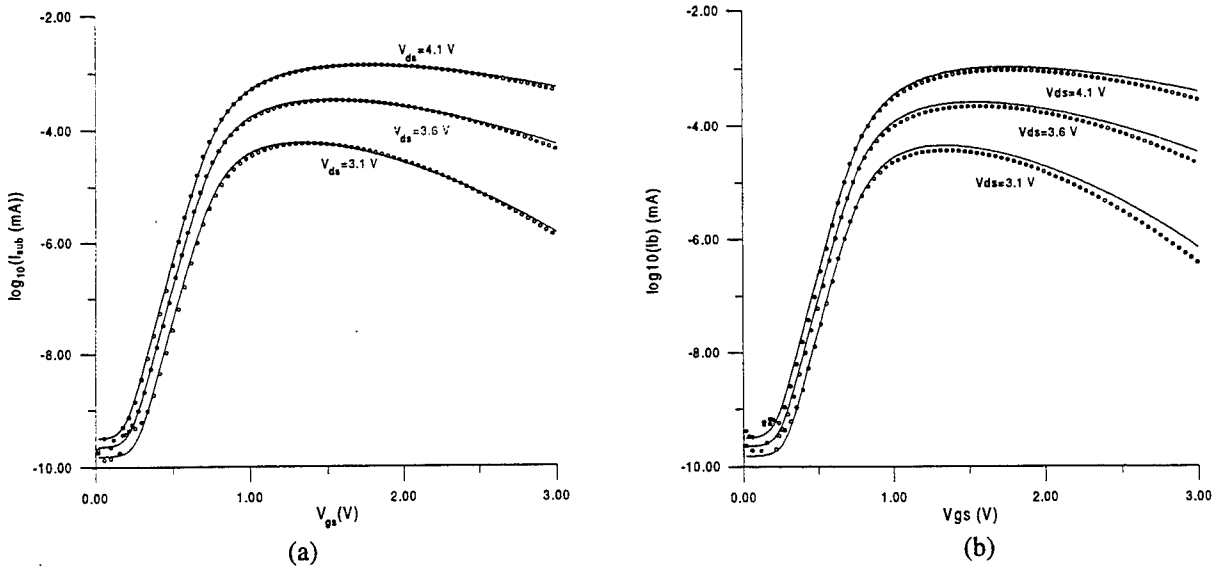


Fig. 1. I_{sub} for nMOSFETs with (a) L_m = 1.2 μm and (b) L_m = 1.5 μm. Solid line: model. Symbols: measurements.

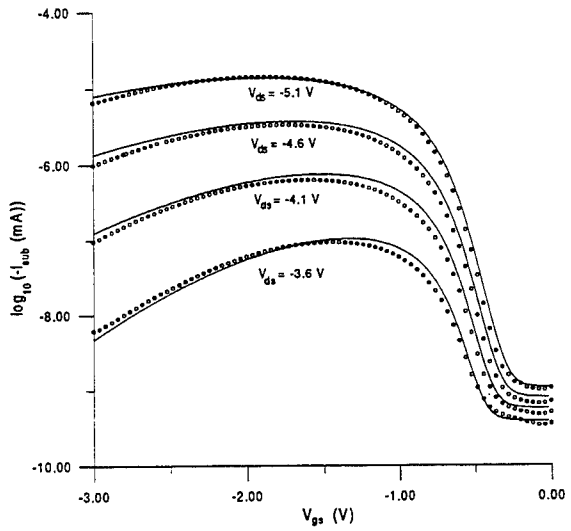


Fig. 2. I_{sub} for a pMOSFET with L_m = 1.5 μm. V_{sb} = 0. Solid line : model. Symbols: measurements.

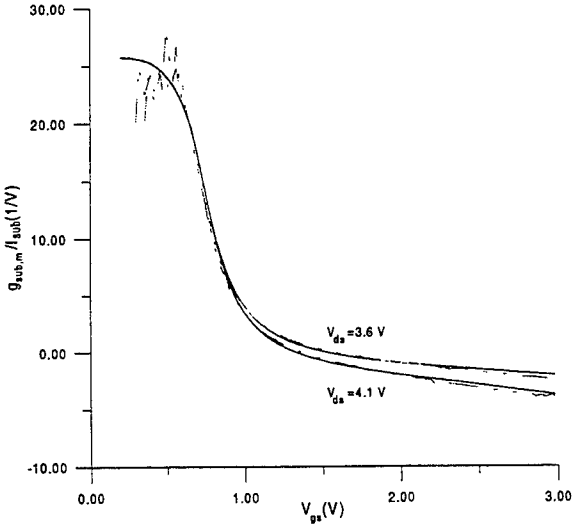


Fig. 3. $g_{sub,m}/I_{sub}$ for a nMOSFET with L_m = 1,2μm V_{sb} = 0. Solid line : model. Symbols: measurements.

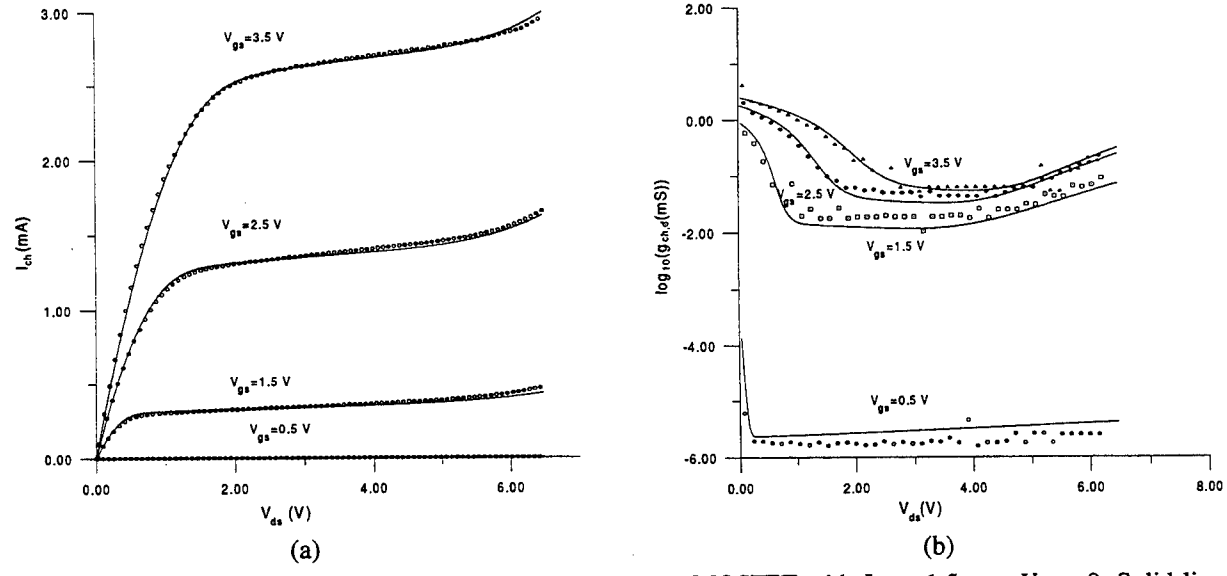


Fig. 4. Source current (a) and channel conductance (b) for a nMOSFET with L_m = 1.5 μm. V_{sb} = 0. Solid line: model. Symbols: measurements.

Differential Conductance Field-Effect Transistor Model

Alfred Phillips, Jr., Craig S. Appel, Sheldon Jordan
Cornell University, School of Electrical Engineering

We have created a Field-Effect Transistor (FET) model, based upon two postulates, that is valid for MOSFETs, MODFETs, JFETs, and MESFETs. The first postulate states that the differential channel conductance, dI_D/dV_D, consists of "adders" and "subtractors" to channel conductance. The channel conductance itself would be an "adder," as would be, for example, the influence of a buried channel in a MOSFET. The second postulate states that in a resistive material, a current existing between source and drain opposes a further increase in channel current. Drain current would, thereby, be a "subtractor." This idea can be expressed in the following equation form

$$\frac{dI_D}{dV_d} = \textit{Conductance Adders} - \textit{Conductance Subtractors}$$

The model presented here is a new approach to FET modeling. "Adders" and "subtractors" can be included to account for sophisticated devices or for use in complicated situations. These new "adders" and "subtractors" would be included on the right-hand side of the model when it is expressed in the ordinary differential equation (ODE) form given above. The resulting ODE may not always have analytic solutions. A numeric solution to it, which includes other mechanisms, would be expected to yield expected FET I-V characteristics.

This model calls into question what is implied in Shockley's *Fundamental Equation of Field-Effect Transistors.*[1] That model is valid only up to its maxima point inappropriately called saturation. (A single point is extended, by *fiat*, to account for the infinite number of points in the drain current saturation region of a FET.)

We can group FETs into two classes. First, FETs whose channel is formed by an inversion process, such as, MOSFETs and MODFETs. Second, FETs whose channel exists for zero gate voltage and is diminished by increasing the reversed-bias gate voltage, such as, JFETs and MESFETs. For the latter devices, channel pinch-off can exist, but for the former devices it cannot. Thus a valid mechanism for saturation would be pinch-off for JFETs and MESFETs, but there is no pinch-off for MOSFETs and MODFETs. All of the FET devices could saturate because of velocity saturation. Another mechanism we suggest that can cause saturation in MOSFETs and MODFETs is stated in the second postulate in this work. The saturation mechanism that is actually manifest in a FET is that which gives the lowest saturation current. We include these saturation mechanisms, as appropriate, in this model.

In this extended abstract, we will first contrast graphically the new model with the standard FET model. Next, we will compare its predictions with long channel MOSFET measurements and short channel MOSFET measurements. Following this, we consider JFETs. In this model, MOSFETs and MODFETs are similar, as are JFETs and MESFETs. Accordingly, we restrict results given in this abstract to MOSFETs and JFETs. We will discuss MODFETs and MESFETs only tangentially here; we will show specific results for these devices during the presentation of the work.

Comparison of this Model and Shockley's

Figure 1shows a comparison of the results obtained from this model (called DCM, Differential Conductance Model, on this and subsequent figures) and from the Standard Model, i.e., Shockley's - *The Fundamental Equation of Field-Effect Transistors.* Saturation currents were adjusted to have the same value. The upper curve set has a larger gate voltage than does the lower curve set. The low voltage behavior of both models is nearly identical. Drain current increases less steeply with this model than with Shockley's as saturation is approached. Empirical results tend to agree more with the new model. Shockley's model does not really behave as shown. It has an inverted parabola-like shape. With Shockley's model, the saturation current is an extension of the peak current value for drain voltages greater than that corresponding to the peak current.

Application of Model to MOSFETs and JFETs

MOSFET

The differential channel conductance of the MOSFET is given by

$$\frac{dI_d}{dV_d} = \frac{\mu_n W C_{OX}(V_G - V_T)}{2L} - \frac{2\kappa I_d}{V_G - V_T}$$

where κ is the conductance factor (usually between 1.5 and 2.5), and the other terms in this and succeeding equations have their usual meanings. We obtain after integration

$$I_d = \frac{\mu_n W C_{OX} (V_G - V_T)^2}{2L} \left(1 - e^{-\frac{2\kappa V_d}{V_G - V_T}}\right)$$

Figures 2 and 3 show the results of this model for a long channel MOSFET and a short

channel MOSFET. We obtain reasonable agreement in both cases. (In trying to test the model, we found few cases when authors published all of the data needed for modeling.)

JFET

The DCM applied to the JFET renders

$$\frac{dI_d}{dV_d} = q\mu_n N_d \frac{W}{L}\left(1 - \left[\frac{2\epsilon_S}{qN_d t^2}(\phi_j - V_D)\right]^{1/2}\right) - \frac{I_d}{V_G - V_T}$$

which is valid for the case where the channel depletion region is uniform. After integration, we obtain the following result

$$I_d = q\mu_n N_d \frac{W}{L}\left(1 - \left[\frac{2\epsilon_S}{q N_d t^2}(\phi_j - V_D)\right]^{\frac{1}{2}}\right)(V_G - V_T)\left(1 - e^{\frac{2V_d}{V_G - V_T}}\right)$$

If the channel depletion region is allowed to change with drain voltage we obtain the following ODE

$$\frac{dI_d}{dV_d} = q\mu_n N_d \frac{W}{L}\left(1 - \left[\frac{2\epsilon_S}{qN_d t^2}(\phi_j - V_G + V_D)\right]^{1/2}\right) - \frac{I_d}{V_G - V_T}$$

We have not found an analytic solution to this ODE, but our numeric solution has a similar drain current saturation characteristic to that of the analytic expression for I_D given above.

Implications for FET design

If, as it seems, the approach in this model for FETs has a measure of truth in it, then this model has implications for FET device design. From this model, we know that the "name of the game" is to maximize channel conductance. This realization may enable the imagination of device designers to have a freer rein. We will suggest, in the presentation, several FET-like devices that resulted from our consideration of maximizing channel conductance.

Other FET engineers, no doubt, knew about the importance of channel conductance in FET design. This work, to our knowledge, is the first to give a rational basis for it, especially in a quantifiable model.

The diode and the bipolar transistor are described mathematically with an exponential dependence on applied voltage(s). With this model, FETs are now described in a similar manner.

References

[1] Shockley, W., "A Unipolar Field-Effect Transistor," Proceedings of the I.R.E., Vol 40, pp. 1365, 1952.

[2] Sze, S. M., "Physics of Semiconductor Devices (2nd Ed.)," Wiley-Interscience, New York, 1981.

[3] Poon, H.C., Yau, L.D., Johnston, R.L., and Beecham, D., "DC Model for Short Channel IGFETs" Solid-State Electronics, Vol 17, p 1059, 1974.

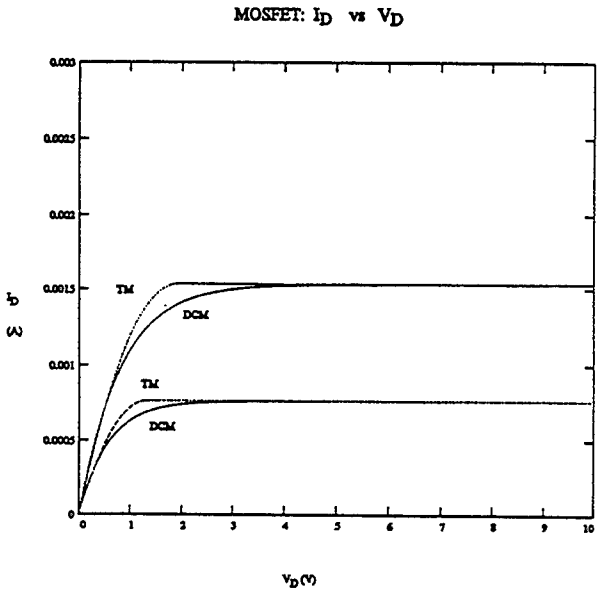


Figure 1. MOSFET I-V characteristics comparing results from the model of this work (DCM) and the standard (Shockley) model.

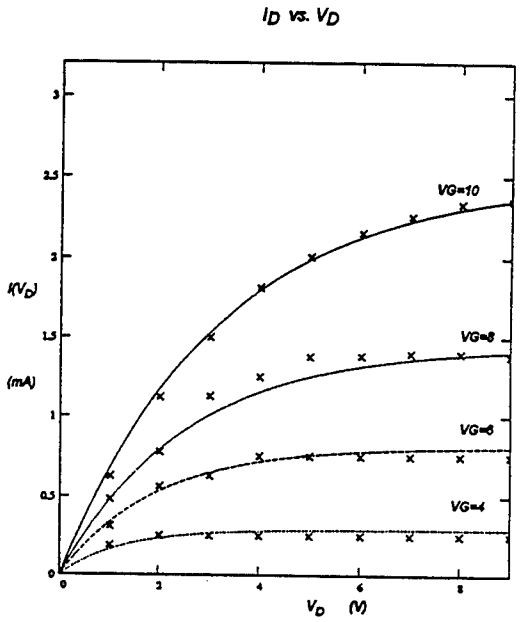


Figure 2. MOSFET I-V characteristics for model of this work, continuous curve, data (x) taken from Sze, p 445.

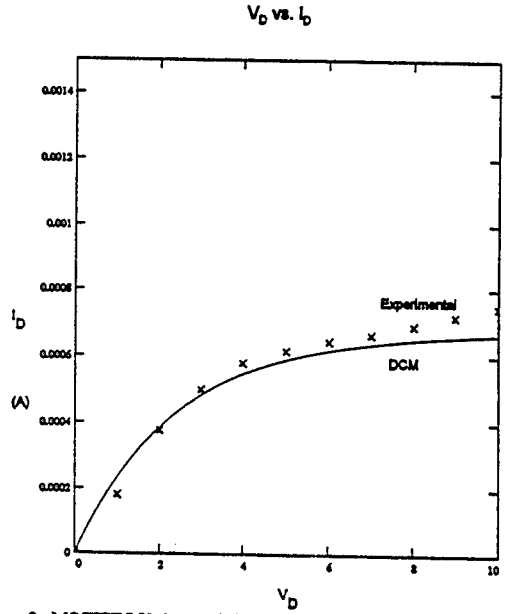


Figure 3. MOSFET I-V characteristics for model of this work, continuous curve, and data (x) taken from Poon, et al.

Simulations of the hole and current distributions in Si-Ge p-channel FETs with graded Ge profiles

S.P. McAlister and W.R. McKinnon
Institute for Microstructural Sciences, National Research Council of Canada,
Ottawa K1A 0R6, Canada.

1. INTRODUCTION

Silicon-germanium channels incorporated into silicon field effect transistors give access to improved hole mobilities and add the capability of using bandgap engineering to improve the device performance. The use of Si-Ge in field effect devices has not been as well-studied as the use of Si-Ge in bipolar npn devices, where outstanding results have been achieved [1,2]. Both n- and p-channel FETs have been reported - the n-channel devices being grown on relaxed substrates and the p-channel devices have used strained layers. p-MOSFETs have been discussed and demonstrated by workers such as König and Schäffler [3], Verdonckt-Vandebroek et al. [4], and recently Voinigescu et al. [5], and references therein. An important consideration in the design of the devices is to optimize the Ge concentration and profile.

In this paper we show the simulations of the hole and current distributions in the different layers of a p-channel Si-Ge modulation-doped FET and examine how the bias and Ge profile in the Si-Ge alters this distribution. Since a gate oxide cannot be grown directly on a Si-Ge layer a thin layer of Si is needed between the Si-Ge channel and the gate. Inevitably some current flows though this parallel channel near the surface but the band offsets, all in the valence band in strained Si-Ge, help constrain the hole current. To adjust the threshold of the device a doped layer in the Si is needed. The dopant is most conveniently located in a layer beneath the Si-Ge channel. This then separates the holes from the acceptor dopants, which reduces the hole impurity scattering. Incorporating the dopants in the capping Si spacer would require an increase in its thickness and thus the channel-gate distance, leading to a reduction in the transconductance.

2. DEVICE STRUCTURE

We have simulated p-MOSFETs with a cross-sectional design (at the n+ polysilicon gate) as follows: 5 nm SiO_2, a 5 nm Si spacer, a 15 nm Si-Ge channel, 5 nm Si (all 3 layers are doped n-type at 1×10^{15} cm^{-3}), a 10 nm p-doped (1.5×10^{18} cm^{-3}) Si layer - all of which is on an n-doped (5×10^{16} cm^{-3}) Si substrate. In our simulations the devices are 1.5 μm long with 0.4 μm source and drain contacts and a 0.5 μm gate length. Source and drain contact dopings are Gaussian-shaped with maximum of 1.5×10^{18} cm^{-3} p-type. The choice of Ge profile is constrained by the total integrated Ge dose possible within the Matthews-Blakeslee limits. In this study we have restricted our discussion to 2 Ge profiles similar to that in other work [5]. The uniform channel design has a maximum Ge composition of 0.25, with a 0 to 0.25 Ge grading over 3 nm at the edges of the channel. The triangular profile has a Ge composition of 0.4 at 3 nm from the top of the channel - which is then graded down to 0 over the remaining 0.12 nm of the channel. The two profiles have the same integrated Ge dose. The Matthews-Blakeslee limit restricts the total Ge in a layer so we have chosen the Ge dose to keep the layers from undergoing strain relaxation. Note that we have used an n+ polysilicon gate and we do not discuss the p-polysilicon case which has been mentioned in [4].

In Fig. 1 the equilibrium band diagrams for the structures are shown to overlap except in the Si-Ge channel region. The incorporation of bandgap narrowing into the calculation makes the p-doped threshold-adjust region in the Si clearly evident. One major difference between the two profiles is the built-in field in the triangular profile design which moves the holes towards the gate.

3. Simulation Results

The simulations were performed using a commercial simulation package (*Atlas/Blaze*, Silvaco International), with a mesh of approximately 3000 nodes, and using Fermi-Dirac statistics and a drift-diffusion model. The interface oxide was chosen to be defect-free for this investigation. Hole mobilities were the same as in [5]. Most parameters have the usual Si values and expressions.

The current in the Si-Ge channel is not uniform under the gate especially near pinchoff. However when the channel is sufficiently long and the device is forward biased the center of the channel can be viewed as being representative of the effects of the different layers in the device. At the end of the channel, edge effects and those from the contacts become important and can obscure some of the main features we are attempting to illustrate. In the figures we used V_{DS} = -2.5V.

In Fig. 2 we show the integrated current under the center of the gate, and the contributions from the various layers, for the triangular and uniform Ge profile devices. In effect we write

$$I_{DS} = I_{Si\ cap} + I_{SiGe} + I_{Subs}\ .$$

The contribution from the substrate includes that from the doped threshold-adjust layer, which gives the majority of the contribution to the substrate current. It is only really important at low bias. In the range of gate voltage from -0.5 to -1.5V the Si-Ge channel dominates the response, which is can also be shown in a de-convolution of the transconductance. At higher biases the parallel current in the cap layer turns on and by -3V is greater than the contribution from the Si-Ge channel. This comment also applies to the transconductance. The effect of the cap turning on is to shield the Si-Ge channel from the gate. The triangular profile is better in confining the current to the Si-Ge channel in the -0.5 to -1.5V range. This becomes clearer if the distributions are viewed as a function of distance under the center of the gate. This is shown in Figs. 3 and 4 for the triangular and uniform profile designs, respectively. The data is also plotted on a logarithmic scale to highlight regions where the current is small. The distribution for the different biases depicted in these figures at first shows the increasing contribution to the current of the Si-Ge channel and how the parallel cap layer, which represents the normal Si FET current, eventually starts to dominate. The distribution of current in the Si-Ge layers reflects the Ge profile. In the triangular Ge profile case there is a built-in field that moves the holes away from the underlying acceptor dopants under the channel to the regions where the bandgap is smallest and the hole mobility optimum. Thus the asymmetric Ge profile achieves 2 desirable features at once. The current in the channel is sharply peaked similar to that at the oxide/Si interface at the highest biases. The logarithmic plot shows linear regions which reflect the linear variation of the potential with position - in the cap layer this is because the cap layer is similar to a capacitor, whereas in the channel it is because the separation of the valence band from the Fermi energy is dependent on the bandgap, which in turn is linearly dependent on position.

In the current distribution for the uniform Ge device (Fig. 4) the current through the Si-Ge channel is initially skewed towards the lower edge of the channel. This is due to the lack of a built-in field over the uniform Ge region. As a result the transconductance is not as good as for the triangular profile design. When the negative gate bias is increased the current distribution eventually becomes

skewed towards the top of the channel before the parallel current in the Si cap layer starts to increase. Eventually this latter current dominates. This is due to the transfer of the holes from the acceptors into the Si-Ge channel and then to the Si cap - which can be envisaged to occur when the band edges are moved up on the l.h.s. in Fig. 1 when the negative gate bias is increased. The uniform design spreads the current better across the Si-Ge than the triangular profile leading to smaller peak current densities in the channel, but at the expense of the slightly reduced performance. The double-peaked nature of the uniform profile's current distribution suggests a higher Ge concentration would be needed in the center of the channel to give a more uniform current distribution, however this would still be skewed at the extremes of the gate bias range.

The current distributions are partially representative of the hole distributions. In Fig. 5 we show the cross-sectional distribution on holes, corresponding to current distributions similar to those in Fig. 3. This cross-section is at the center of the gate. For clarity we show the region down to the p-doped threshold-adjust region - the dopant scale is logarithmic. To a first approximation the hole distribution looks like the current distribution. In Fig. 6 the hole distribution along the channel is shown for different gate biases for the uniform design at 2 positions in the Si-Ge profile. The distributions are at the 2 extremes of the uniform (0.25 Ge) region of the profile, i.e. at the positions where the current density is peaked. The cross-section at the top edge (solid curve) shows the hole density being reduced at the edge of the gate near the drain. For the cross-section for the lower position there are more holes near the edge of the gate near the drain than in the center of the gate. This shows that the current at the end of the Si-Ge channel tends to be distributed towards the lower part of the channel at the drain contact. We have seen similar effects in GaAs -based devices before [6].

The high frequency performance was also simulated and confirms the superiority of the triangular profile, with similar results as [5]. The current distributions we have shown suggest that the triangular profile could be further improved by raising the Ge concentration at the lower edge of the channel, at the expense of the layer thickness, ending up with a trapezoidal Ge profile. This design should spread the current better over the Si-Ge channel, make the current distribution closer to the gate at low bias and thus channel the hole current better in the Si-Ge layer to produce higher trans-conductance.

We thank Tracey Bradford for some initial simulations and Sorin Voinigescu for his help.

REFERENCES

[1] D.L. Harame, J.H. Comfort, J.D. Cressler, E.F. Crabbé, J.Y.-C. Sun, B.S. Meyerson and T. Tice, "Si/SiGe epitaxial-base transistors - Part 1: materials, physics, and circuits," IEEE Trans. Electron Devices, vol. 42, pp. 455-468, 1995.

[2] D.L. Harame, J.H. Comfort, J.D. Cressler, E.F. Crabbé, J.Y.-C. Sun, B.S. Meyerson and T. Tice, "Si/SiGe epitaxial-base transistors - Part 2: Process integration and analog applications," IEEE Trans. Electron Devices, vol. 42, pp. 469-482, 1995.

[3] U. König and F. Schäffler, "p-Type SiGe channel modulation doped field-effect transistors with post-evaporation patterned submicrometre Schottky gates," Electron. Lett., vol. 29, pp. 486-488, 1993.

[4] S. Verdonckt-Vandebroek, E.F. Crabbé, B.S. Meyerson, D.L. Harame, P.J. Restle, J.M.C. Stork and J.B. Johnson, "SiGe-channel heterojunction p-MOSFETs," IEEE Trans. Electron Devices, vol. 41, pp. 90-101, 1994.

[5] S.P. Voinigescu, P.B. Rabkin, C.A.T. Salama and P.A. Blakey, "2D numerical investigation of the impact of compositional grading on the performance of submicrometer Si-SiGe MOSFETs," IEEE Trans. Electron Devices, vol. 42, pp. 1039-1046, 1995.

[6] Z.-M. Li, S.P. McAlister and C.M. Hurd, "Use of Fermi statistics in two-dimensional numerical simulation of heterojunction devices," Semicond. Sci. Technol., vol. 5, pp. 408-413, 1990.

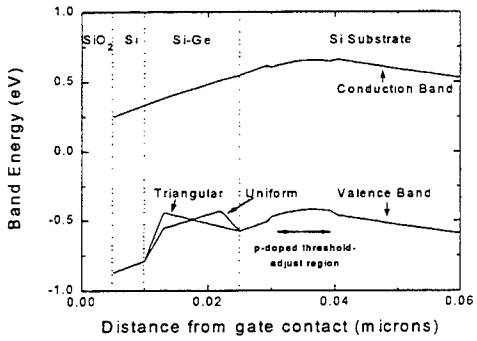


Fig. 1. Band diagram for the devices.

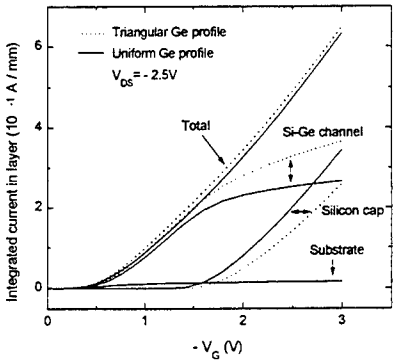


Fig. 2. Gate voltage dependence of the drain current and the contributions of the various layers to the drain current.

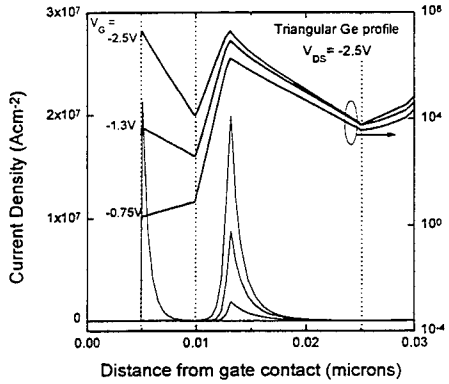


Fig. 3. Cross section of the current distribution, for the device with the triangular Ge profile, at the mid-point of the gate, at the indicated biases. Top curves use log scale on r.h.s.

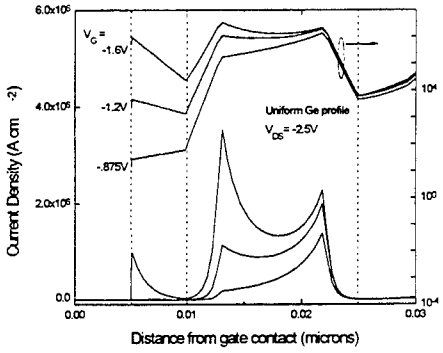


Fig. 4. Cross section of the current distribution, for the device with the uniform Ge profile, at the mid-point of the gate, at the indicated biases. Top curves use log scale on r.h.s.

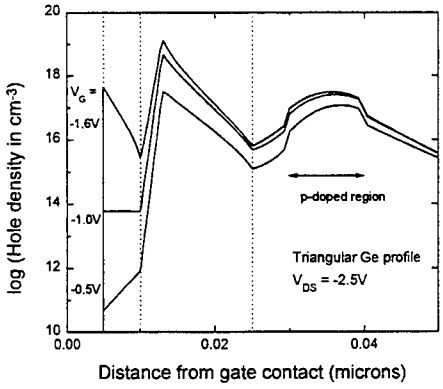


Fig. 5. Cross section of the hole distribution for the device with the triangular Ge profile, at the mid-point of the gate, at the biases indicated.

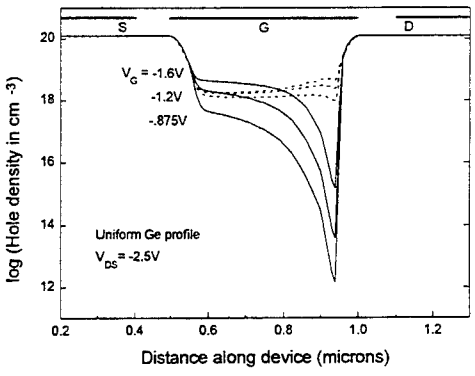


Fig. 6. Hole distribution along the channel for the uniform Ge profile device. Dotted curves are for the bottom edge of the graded region and solid ones for the top edge.

A Unified BSIM *I-V* Model for Circuit Simulation

Yuhua Cheng, Chenming Hu, Kai Chen, Mansun Chan, Min-chie Jeng*, Zhihong Liu, Jianhui Huang#, Ping Keung Ko##**

Dept. of Electrical Eng. and Computer Science, Univ. of California at Berkeley, Berkeley, CA94720
*** Cadence Design System**
**** BTA Technology Inc.,**
 # Intel Corp.
Hong Kong University of Science and Technology, Hong Kong

Abstract A physical and unified BSIM (Berkeley Short-channel IGFET Model) model, BSIM3v3 is presented in this paper. Retaining the advanced features of the previous BSIM model, the model describes current characteristics from subthreshold to strong inversion as well as from the linear to the saturation operating regions with a single *I-V* expression, and guarantees the continuities of I_{ds}, and its derivatives throughout all V_{gs} and V_{ds} bias conditions. The new model allows users to accurately describe the MOSFET characteristics over a wide range of channel lengths and widths for a wide range of technologies.

I Introduction

Several previous versions of BSIM models have been developed and implemented in SPICE for use in circuit simulation [1,2,3]. The models used separate model expressions for device operation in subthreshold and strong inversion as well as in linear and saturation regions, and can accurately describe device behavior within their own respective region of operation. However, problems could occur in the transition regions.

In this paper, we present a physical and unified BSIM model for the MOSFET's devices in analog/digital circuit simulation. This new model describes current and output conductance characteristics in all operating regions with a single *I-V* expression, and guarantees the continuities of I_{ds}, and its derivatives throughout all V_{gs} and V_{ds} bias conditions. Furthermore, the model includes the major physical effects in modern MOSFET devices, and has extensive built-in dependencies of important dimensional and processing parameters. This allows users to accurately model the MOSFET over a wide range of channel lengths and widths for a wide range of present as well as future technologies.

II Model Development

1. Unified channel charge density expression

Based on the channel charge expressions in strong inversion and subthreshold regions in previous BSIM models [1,2,3], a unified expression for the channel charge density in the channel at very small V_{ds} is introduced in the present model:

$$Q_{chs0} = C_{ox} V_{gsteff} \tag{1}$$

where C_{ox} is the gate oxide capacitance , and V_{gsteff} is:

$$V_{gsteff} = \frac{2\,n\,v_t \ln\left[1+\exp(\frac{V_{gs}-V_{th}}{2\,n\,v_t})\right]}{1+2\,n\;Cox\sqrt{\frac{2\Phi_s}{q\varepsilon_{si}N_{ch}}}\exp(-\frac{V_{gs}-V_{th}-2V_{off}}{2\,n\,v_t})} \tag{2}$$

where the parameter v_t is the thermal voltage $K_B T/q$. N_{ch} is the channel doping concentration, V_{th} is the threshold voltage of the device, ϕ_s is the surface potential and is given by $2v_t \ln(N_{ch}/n_i)$, V_{off} is the offset voltage in subthreshold regime [2], n is the subthreshold swing parameter, and can be extracted from experiments [3].

Fig. 1 shows the comparison results between the unified charge expression (1) and the charge expressions in subthreshold and strong inversion regions in previous BSIM models, as well as that from measurements . It can be seen in Fig.1 that the unified expression can well describe the channel charge characteristics, measured and predicted by the previous piece-wise charge models, in both subthreshold and strong inversion regions respectively, and has a smooth transition at the boundary of the two regions.

Based on (1), to account for the influence of V_{ds}, a unified expression for the charge density $Q_{ch(y)}$ in the channel from subthreshold to strong inversion regimes can be derived:

$$Q_{ch(y)} = Q_{chs0}(1-\frac{V_{F(y)}}{V_b}) \tag{3}$$

where $V_{F(y)}$ is the quasi-Fermi potential at any point y in the channel with respect to the source. Q_{cho} is given by (1), and $V_b=(V_{gsteff}+2vt)/A_{bulk}$., the A_{bulk} parameter is to describe the bulk charge effect in the device, and can be extracted from the I-V data.

2. Single *I-V* Expression in whole operation regions of V_{gs} and V_{ds}

With the V_{gsteff} function given above, a unified mobility model, which becomes the familiar model in strong inversion [3] and approaches a constant value in the subthreshold region, can be introduced into the model. This, in effect, ensures no mobility discontinuity in the *I-V* model. Based on the above unified channel charge and mobility models, and accounting for the influence of the major physical effects to the *I-V* characteristics in the modern MOSFETs such as (a) Short and narrow channel effects, (b) Non-uniform doping effect (in both lateral and vertical directions), (c) Mobility reduction due to vertical field, (d) Bulk charge effect. (E) Carrier velocity saturation, (f) Drain-induced barrier lowering (DIBL), (g) Channel length modulation (CLM), (h) Substrate current induced body effect (SCBE), (I) Subthreshold conduction, (J) Source/drain parasitic resistances and so on, finally we can get a unified I_{ds} expression in the whole operation region of V_{gs} and V_{ds}:

$$I_{ds} = \frac{I_{dso}}{1+\frac{R_{ds}I_{dso}}{V_{dseff}}}\left(1+\frac{V_{ds}-V_{dseff}}{V_A}\right)\left(1+\frac{V_{ds}-V_{dseff}}{V_{ASCBE}}\right) \tag{4}$$

where R_{ds} is the drain/source parasitic series resistances, I_{dso} is the unified intrinsic *I-V* expression for R_{ds}=0, V_A is the Early voltage contributed by the CLM, DIBL effects and V_{ASCBE} is the Early voltage contributed by the SCBE effect. V_{dseff} is a function, which become V_{ds} when $V_{ds}<V_{dsat}$, and tends to V_{dsat} when $V_{ds}>V_{dsat}$..

III Model Test Results

A set of benchmark tests [4] have been performed on the model discussed above to check its robustness, accuracy and performance in circuit simulation. We show below some results for the n-channel devices with the 0.5μm, 9nm, 3.3V LOCOS technology. Unless indicated in the figures, symbols represent measured data and solid lines represent the results of the model calculations.

Fig. 2 and 3 shows I_{ds}-V_{gs} characteristics of the n-channel device of W_{drawn}/L_{drawn}=20/0.5 at V_{ds}=50mV and different body biases V_{bs} (from 0 to -3.3V) in log and linear scale respectively. A good fit can be observed between the measured data and model results. To show the robustness of the model further, the G_m/I_d vs V_{gs} characteristics, are given in Fig. 4 and 5. The smoothness of the curves of G_m/I_d can be seen at different V_{ds} and V_{bs} conditions, and also the model can fit the measured data well in a wide operation conditions.

The output resistance R_{out}, which is another one of the most important parameters in the analog circuit design, is also shown in Fig. 6 for the device of W_{drawn}/L_{drawn}=20/0.5. Again, a good agreement between the model and measured data can be shown at different V_{gs} biases.

IV Conclusions

A new physical and unified BSIM *I-V* model is presented for analog/digital circuit simulation. The model describes the device current characteristics in all V_{gs} and V_{ds} condition with a single *I-V* expression, and guarantees the continuities of current and it's derivatives from subthreshold to strong inversion as well as from the linear to the saturation regimes. The model includes all major physical effects in today's MOSFETs, and builds in a lot of geometry and process parameters so that it is superior as a statistical model. The model is being implemented in circuit simulators such as Metasoftware Hspice and Cadence Spectre.

Acknowledgment: This work was supported by SRC grant BJ-324-029.

References

[1] B. J. Sheu, D. L. Scharfetter, P. K. Ko, and M. C. Jeng, "BSIM: Berkeley Short-channel IGFET Model for MOS Transistors," *IEEE J. Solid-State Circuits*, vol. SC-22, pp.558-565, 1987

[2] M. C. Jeng, "Design and modeling of deep-submicrometer MOSFETs', *ERL memorandum ERL M90/90*, University of California, Berkeley, 1990

[3] J. H. Huang, Z. H. Liu, M. C. Jeng, K. Hui, M. Chan, P. K. Ko and C. Hu, *BSIM3 Version2.0 User's Manual*, March 1994

[4] Y. Tsividis and K. Suyama, "MOSFET modeling for analog circuit CAD: Problems and prospects," *Tech. Dig.* vol.CICC-93, pp14.1.1-14.1.6, 1993.

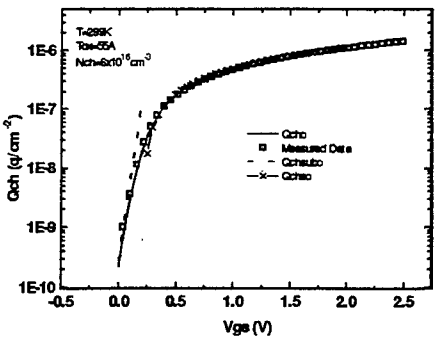


Fig. 1 Comparisons between unified charge model and piece-wise models in subthreshold and strong inversion regions. Qcho is the model result from (1), Qchso and Qchsubo are the model results from the charge expressions in previous BSIM3 model in strong inversion and subthreshold regimes respectively.

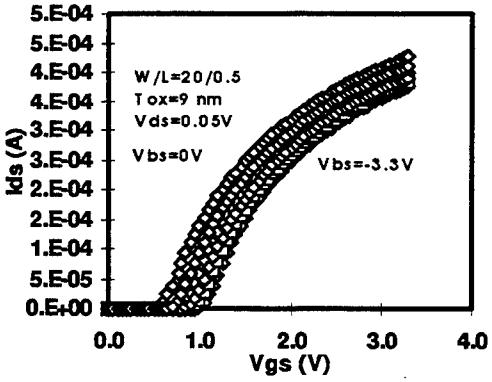


Fig. 3 Comparisons between modeled and measured Id vs Vgs curves (linear scale) at different Vbs conditions.

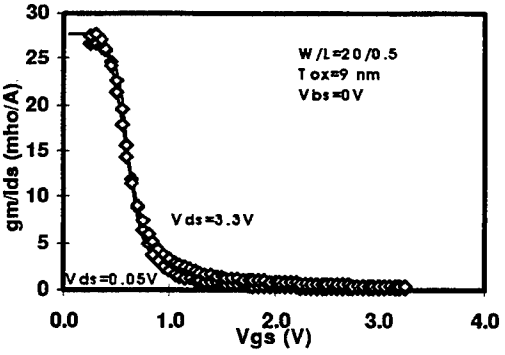


Fig. 5 Modeled and measured Gm/Id vs Vgs curves at different Vds conditions.

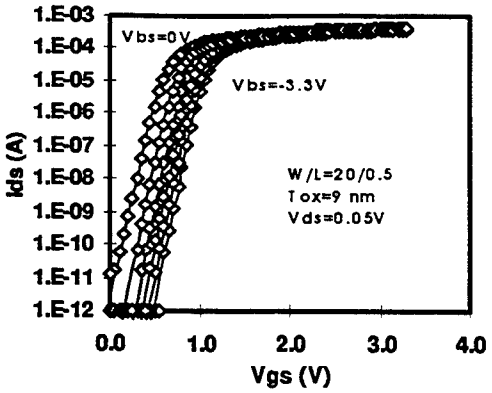


Fig. 2 Comparisons between modeled and measured Id vs Vgs curves (Log scale) at different Vbs conditions.

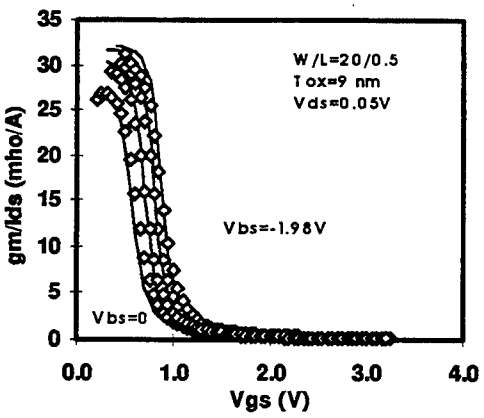


Fig. 4 Modeled and measured Gm/Id vs Vgs curves at different Vbs conditions.

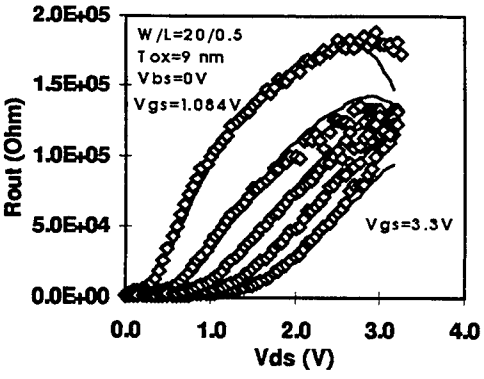


Fig.6 Modeled and measured Rout vs Vds curves at different Vgs conditions.

Universal MOSFET Carrier Mobility Model Explicitly Based on V_t, V_g and T_{ox} and Its Application in Device Modeling and Optimization

Kai Chen, Jon Duster, H. Clement Wann, Tetsu Tanaka*, Mokoto Yoshida**, Ping K. Ko and Chenming Hu

EECS Department, University of California at Berkeley, Berkeley, CA 94720, USA

*ULSI Devices Laboratory, Fujitsu Laboratories LTD., Atsugi 243-01, Japan

** Device Development Center, Hitachi, Ltd., 2326 Imai Ome-shi, Tokyo 198, Japan

I. INTRODUCTION

It is known that MOSFET's carrier mobility depends on vertical electric field, $E_{eff} = (Q_{inv}/\eta + Q_b)/\varepsilon_{Si}$ [1]-[3]. Unfortunately, this E_{eff} is not a convenient quantity for device analysis. This paper presents a new empirical mobility model based on T_{ox}, V_t and V_g. Devices used for this study are fabricated in five different laboratories with large range of T_{ox} and N_{sub}. Both surface and buried channel PMOSFETs, as well as both bulk and SOI NMOSFETs are included.

II. MODELING AND RESULTS

The strong inversion charge Q_{inv} can be expressed as $Q_{inv} \approx C_{ox}(V_g - V_t)$ and $V_t = V_{fb} + \psi_s + Q_b/C_{ox}$, where $V_{fb} + \Psi_s \approx -0.8V + 0.8V = 0$ for n^+poly gate NMOSFETs. Thus $Q_b \approx C_{ox}V_t$. Substituting η=2 for NMOSFET[2]-[4], Q_b and Q_{inv} into the E_{eff} expression in the first paragraph, we obtain:

$$E_{eff} = C_{ox}\left[\left(V_g - V_t\right)/2 + V_t\right]/\varepsilon_{si} = \left(V_g + V_t\right)/6T_{ox} \qquad (1)$$

The new E_{eff} expression of (1) is compared with its original form by measured Q_{inv} and calculated Q_b in Fig. 1-2. Good agreement is shown whereas (1) is much more convenient to use. Correspondingly, a new empirical mobility model for the NMOSFET is found as follows:

$$\mu_n = 540/\left(1+\left(\frac{E_{eff}}{0.9}\right)^{1.85}\right) \approx 540/\left(1+\left(\frac{V_g+V_t}{5.4T_{ox}}\right)^{1.85}\right) \qquad (2)$$

Figs. 3 through 6 confirm this mobility's new universality in terms of V_g, V_t and T_{ox}. The deviation from the model at low E_{eff} ($V_g < V_t + 0.6V$) is due to strong Coulombic scattering by ionized impurities or interface charges. On the other hand, the expression of E_{eff} for holes is slightly more complicated because two types of PMOSFETs, i.e., surface and buried channel devices need to be considered. In addition, the value of η for holes has been controversy even though recent studies tend to use η=3 [4][5]. We use the following method to determine η for PMOSFET from our own measurement data: similar to (1), it can be derived that $E_{eff} \approx \left(V_g - (1-\eta)V_t\right)/\left(3\eta T_{ox}\right)$. By varying V_t through V_{ts}, the relationship of V_g versus V_t for constant mobility or equivalently E_{eff} is a linear one (Figs. 7 through 9). The slope of this plot gives $(1-\eta) = -1.5$, or η=2.5 for holes. Thus for the surface channel PMOSFET, $E_{eff} = C_{ox}\left[\left(V_g - V_t\right)/2.5 + V_t\right]/\varepsilon_{si} = (V_g + 1.5V_t)/7.5T_{ox}$, where V_g and V_t are taken positive. For the n^+poly PMOSFET without boron V_t implantation, a V_{fb} difference of E_g/q=1.1V from that of p^+poly leads to $E_{eff} = (V_g + 1.5V_t - 2.5|V_{fb} - \psi_s|)/7.5T_{ox} = (V_g + 1.5V_t - 2.7)/7.5T_{ox}$. For the buried channel

PMOSFET, a small (~ 0.15V) band bending exists at the threshold condition and has to be subtracted from the n+poly's Ψ_S. Thus E_{eff} for buried channel PMOSFET becomes $E_{eff} \approx (V_g + 1.5V_t - 2.3)/7.5T_{ox}$. A single equation covering all cases of PMOSFET can then be expressed as follows:

$$E_{eff} \approx \frac{Q_p/2.5 + Q_b}{\varepsilon_{si}} \approx \frac{V_g + 1.5V_t - \alpha}{7.5T_{ox}} \qquad (3)$$

where α=0, 2.3 and 2.7 for surface, buried channel PMOSFETs with and without Boron implantation, respectively. Then the hole mobility for all types of PMOSFET observes the following universal equation:

$$\mu_p(V_g, V_t, T_{ox}) \approx \frac{185}{1+\left(\frac{E_{eff}}{0.45}\right)} \approx \frac{185}{1+\left(\left(\frac{V_g + 1.5V_t - a}{7.5T_{ox}}\right)/0.45\right)} \qquad (4)$$

Good agreement for both surface and buried channel PMOSFET is shown in Fig. 10. For the first time, the hole mobility of surface and buried channel PMOSFET is found to follow the same universal curve, not two separate ones as thought necessary before. For a given V_t, a buried channel PMOSFET has the same μ_p at a higher V_g than its p^+poly counterpart (Fig. 11). The mobility studied here is dominated by phonon scattering. The surface-roughness scattering is either insignificant or pretty identical in all the technologies studied. Additional Coulombic scattering is significant only when (V_g-V_t) is small and N_{sub} is high. Fig. 12 shows how the mobility's E_{eff} power dependence changes with E_{eff} for the realm dominated by phonon scattering.

The new mobility model can be directly and conveniently applied to device analysis and comparison. Figs. 13 and 14 show the comparison of calculated I_{dsat} with the new empirical mobility model proposed above and the measurement data. The source/drain series resistance of LDD structures have been included in the modeling. Good agreement are shown. The device and circuit performance are then predicted in Figs. 15 and 16. Fig. 15 shows that for given V_{dd} and L_{eff}, there exists an optimum T_{ox} which minimizes the propagation delay of CMOS ring oscillator.

III. CONCLUSIONS

Universal mobility that's solely dependent on device parameter T_{ox} and V_t and bias condition V_g for both NMOS- and PMOS- FETs is reported the first time. Extensive study of all types of devices, i.e., bulk and SOI NMOSFETs, surface and buried channel PMOSFETs fabricated in five different laboratories across the world confirm the correctness of the model. Its usefulness and convenience in device modeling and analysis as well as prediction for future technology is also demonstrated.

REFERENCES

[1] F. Gamiz, J. A. Lopez-Villaneva, J. Banqueri, J. E. Carceller and P. Cartujo, "Universality of Electron Mobility Curves in MOSFETs: A Monte Carlo Study", *IEEE Trans. on Electron Devices*, **vol. 42, No. 2**, pp. 258-265, February 1995.

[2] A. G. Sabnis and J. T. Clemens, *IEDM Tech. Digest*, pp.18-21, IEDM'79.

[3] M. S. Liang, J. Y. Choi, P. K. Ko, and C. Hu, *IEEE Trans. Electron Devices*, **ED-33**, 409, 1986.

[4] S. Takagi, A. Toriumi, M. Iwase and H. Tango, p. 2357-2368, *Transactions on Electron Devices, Vol.41*, No. 12, Dec. 94.

[5] K. Lee, J. Choi, S. Sim, and C. Kim, *IEEE Transactions on Electron Device*, vol. 38, No. 8, August 1991.

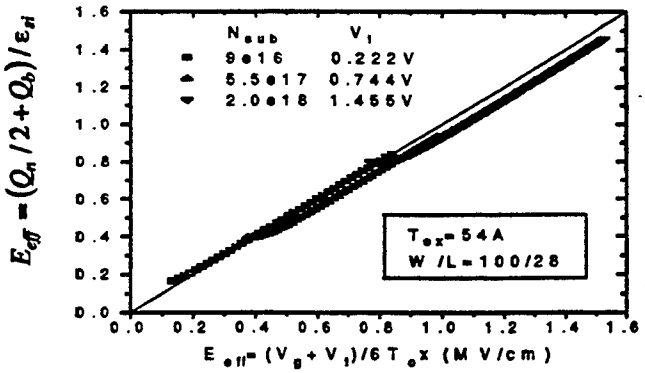


Fig. 1 Comparison of two E_{eff} equations for three different body bias.

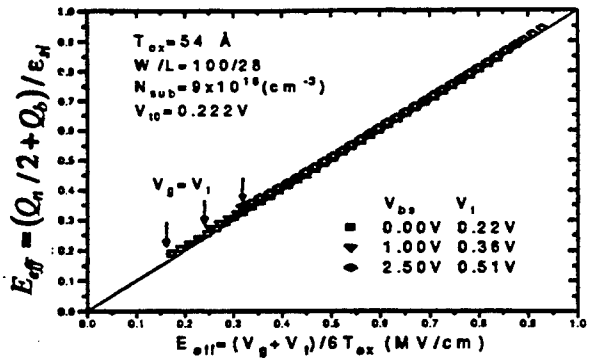


Fig. 2 Two E_{eff} comparison for three different technologies.

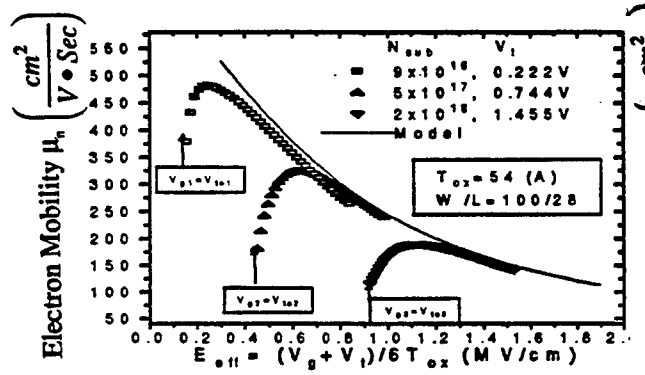


Fig. 3 NMOSFETs with different N_{sub} follow the universal mobility model.

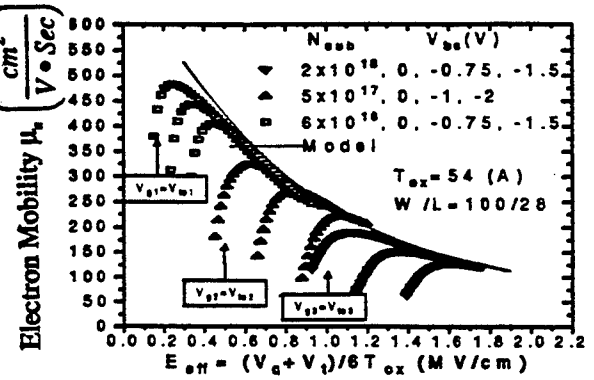


Fig. 4 NMOSFETs of different Vt (by varying V_{bs}) observe the universal model.

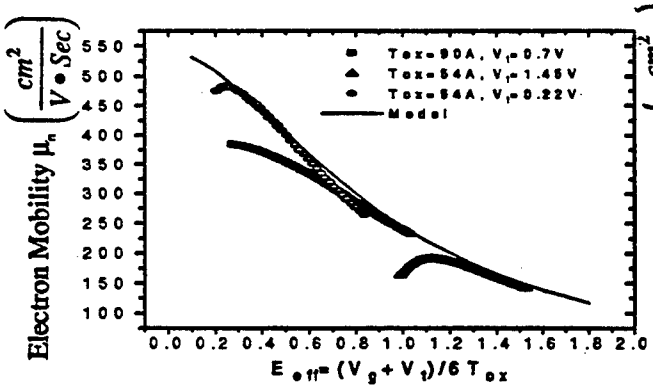


Fig. 5 NMOSFETs with different T_{ox}, N_{sub} observe the same universal mobility model.

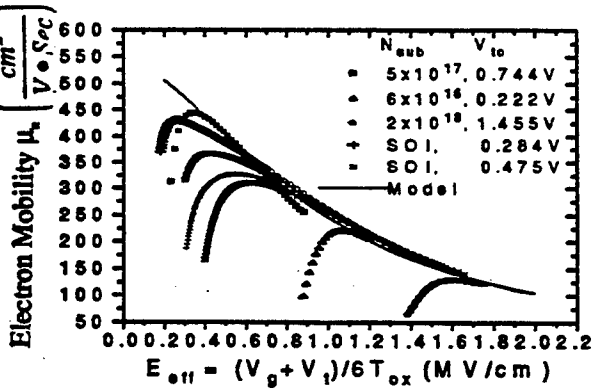


Fig. 6 Both bulk and SOI NMOSFETs with different N_{sub}, T_{ox} and V_t observe the same universal model.

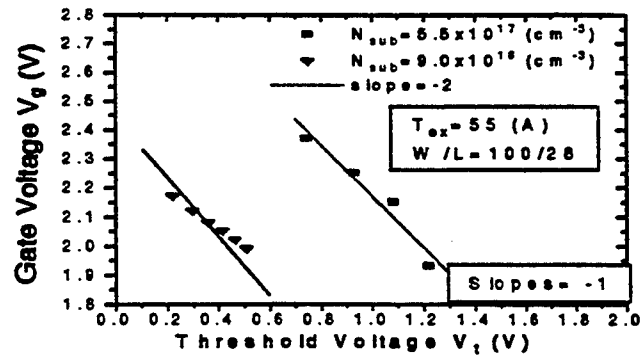


Fig. 7 The slope = -1 indicates that η=2 for NMOSFET electrons.

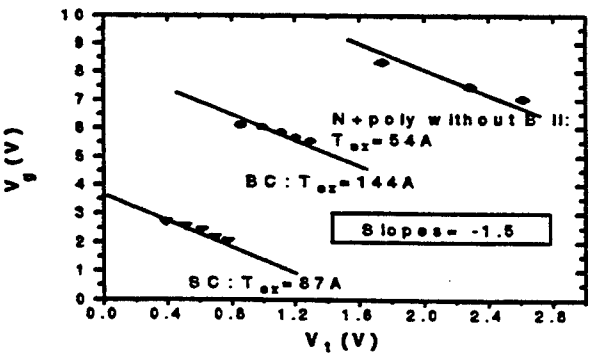


Fig. 8 The slope = -1.5 indicating that η=2.5 for PMOSFET holes.

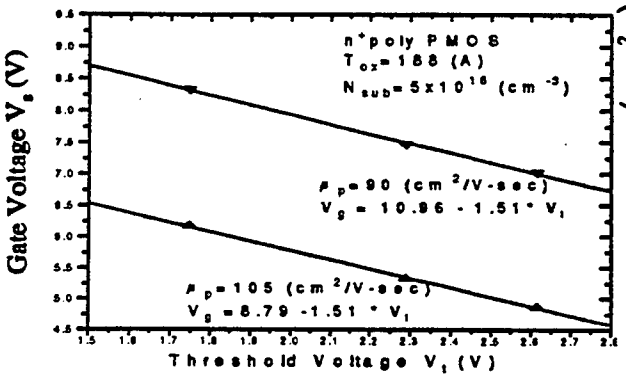


Fig. 9 The slope does not change when different mobility values are chosen for PMOS holes.

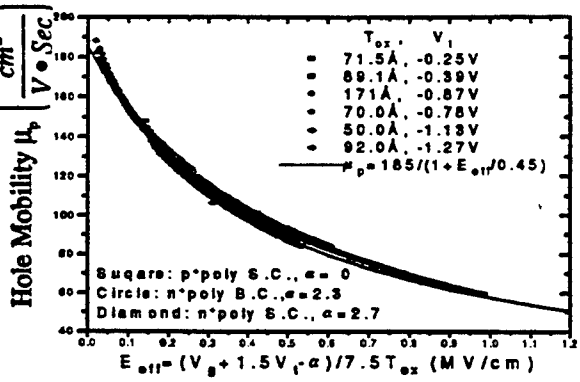


Fig. 10 6 PMOS technologies show that both SC and BC PMOS holes observe the same universal model.

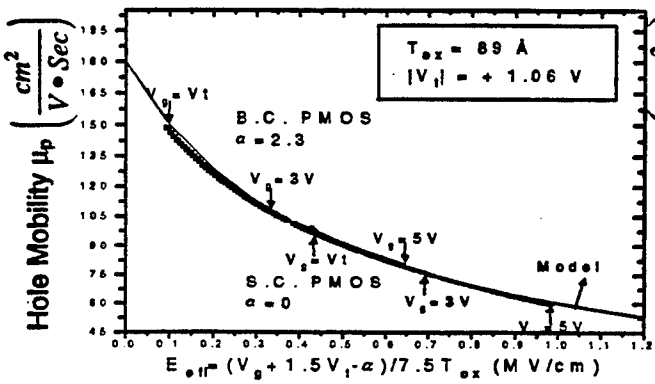


Fig. 11 SC vs.BC PMOS for the same V_t and T_{ox}:BC achieves the same μ_p at 2V lower V_g than SC PMOSFET.

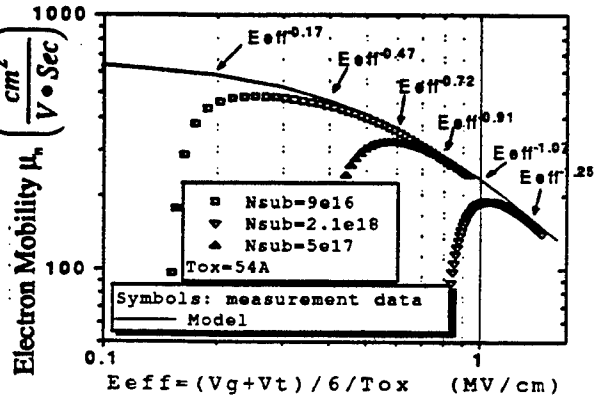


Fig. 12 Electron mobility's E_{eff} power dependence. of phnon scattering are increased with E_{eff}.

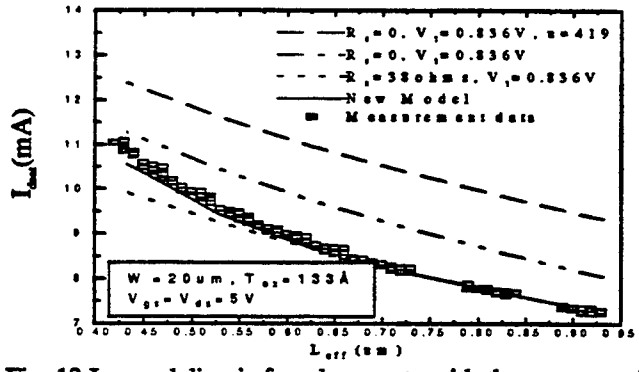


Fig. 13 I_{dsat} modeling is found accurate with the new mobility model for LDD NMOSFET.

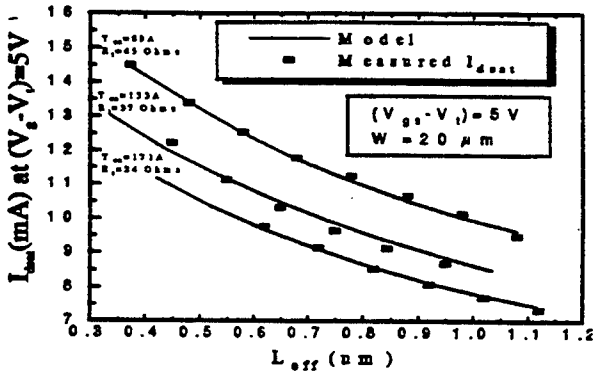


Fig. 14 I_{dsat} modeling is found accurate for different LDD NMOS technologies.

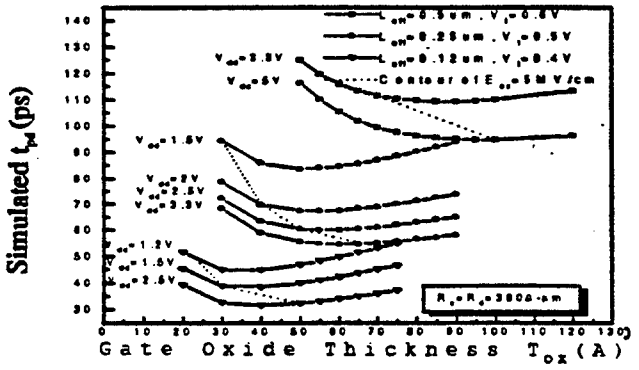


Fig.15 There exist optimum T_{ox} for given V_{dd} and L_{eff}: a new result from the mobility model.

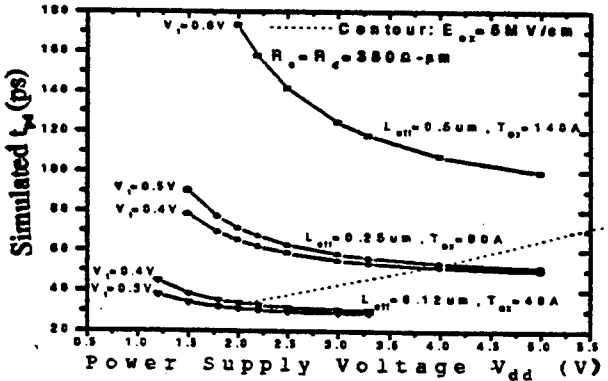


Fig. 16 Higher V_{dd} does not improve speed much beyond certain point based on the new mobility model.

Conversion Gain and Noise in the NbN Hot-Electron Submillimeter Mixer

Hans Ekström*, Boris Karasik#, and Erik Kollberg*

* Dept. of Microwave Technology, Chalmers University of Technology, Göteborg S-412 96, Sweden
# Jet Propulsion Laboratory, Caltech, Pasadena, CA 91109-8099, USA

Superconducting NbN hot-electron bolometer (HEB) mixer devices have been fabricated and measured at 350 GHz. The HEB is integrated with a double dipole antenna on an extended crystalline quartz hyper hemispherical substrate lens. Heterodyne measurement gave a -3 dB bandwidth, mainly determined by the electron-phonon interaction time, of about 680 and 1000 MHz for two different films with T_C = 8.8 and 12.5 K respectively. The measured DSB mixer noise temperature is around 3000 K at 750 MHz IF frequency. Fluctuations of the electron temperature have been shown to be the main source of electrical noise. The noise spectral density demonstrates the same frequency dependence as the IF response. The Johnson noise contribution is around 25 K. The SSB mixer noise temperature due to intrinsic noise mechanisms for the NbN device is estimated to 360 K independent of radiation frequency. The data agree with the theoretical predictions. The theoretical limit for ideal NbN HEB mixers is estimated to ~35 K SSB noise temperature along with the 3.5 GHz noise bandwidth.

I. Introduction

There is an urgent need of improved heterodyne receivers for radio astronomy at terahertz frequencies. Mainly one type of mixer device is currently in use at and above 1 THz, namely the Schottky diode mixer [1]. The sensitivity is however lower than what is required for several planned projects. The low noise InSb hot-electron bolometer mixers, used up to about 800 GHz [2], have an IF bandwidth of about 2 MHz, which is too narrow for many applications. Nb trilayer SIS quasi-particle tunnel junctions [3] are very sensitive mixer devices, but so far only for frequencies below the energy gap of Nb (≈700 GHz). There are however different types of new promising hot-electron bolometric devices under development; 2DEG devices using the temperature dependent mobility of a 2-dimensional electron gas [4], and superconducting hot electron bolometers (HEB) utilizing the electron temperature dependent resistance in superconducting narrow thin film strips [5-7]. The bandwidth of Nb devices, determined by the electron-phonon relaxation time, $\tau_{e\text{-}ph}$, is narrow (≈90 MHz) [6]. An improved bandwidth of about 2 GHz has been measured in very short Nb devices [7], where the electron diffusion time out of the device is shorter than the electron-phonon interaction time.

Another way to widen the bandwidth of superconducting hot electron mixers is to use films which made of a material with a shorter electron-phonon relaxation time. Good candidates are NbN films which can have a response time as short as 15 ps at 10 K [8]. A larger T_c and stability of the film parameters are additional advantages of such films.

In this paper we have studied a recently developed 350 GHz NbN mixer combined with a resonant double dipole antenna on a substrate lens. The bandwidth of two mixer devices has been measured at different bias points. The variation of the position of the optimal operating point with temperature has been studied as well. We have also performed a detailed study of the mixer output noise temperature spectrum and compared these data with the direct hot/cold measurements of the mixer noise temperature. The theoretical estimates of the noise temperature limit demonstrates that optimized devices can be very promising.

II. Experimental

The HEB devices were made of NbN films either 10 nm or 20 nm thick. The films were patterned to form 11 parallel, 1.5 μm wide and 5 μm long strips. The devices were integrated with double dipole antennas [9] on extended hemispherical crystalline-quartz substrate lenses [10]. The NbN-films were DC magnetron sputtered [11] on non-heated substrates and patterned by conventional photo-lithography and plasma etching (30 sccm He + 10 sccm CF_4 (incl. 8% O_2). The antenna and contacts were made of 3000 Å Nb + 1500 Å thick layer of Au, patterned by lift-off. The parameters of the devices are presented in Table I. Fig. 1 shows the superconducting transition region of the device #A. Device #B was made from the thinner (10 nm) film of higher quality (larger critical current density). However this was followed by the degradation of the transition and the rise of the "foot" structure in the $R(T)$ dependence.

The measurements were done with the mixer mounted in a LHe cooled vacuum cryostat. Signal and local oscillator (LO) were combined with a 50 μm thick Mylar beam-splitter and fed to the mixer through a

TABLE I
SPECIFICATION FOR THE SAMPLES

#	d [nm]	R_s [Ω]	R_N [Ω]	dR/dT [Ω/K]	T_c [K]	ΔT_c [K]	I_c [μA]
A	20	390	122	190	8.8	0.5	1900
B	10	500	150	110	12.6	1	3100

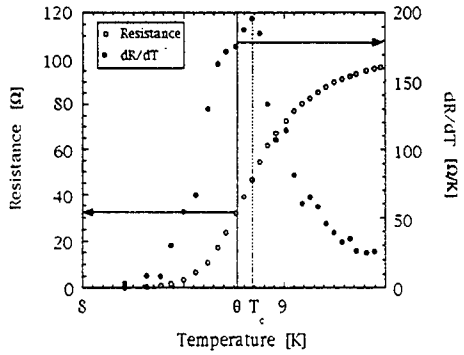


Fig. 1. R(T) and dR/dT curves for device #A.

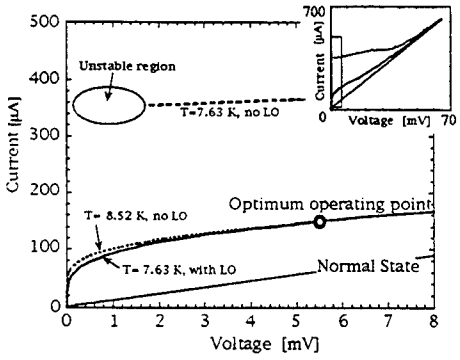


Fig. 2. Pumped and unpumped *IV* characteristics for device #A with optimum bias points at f_{IF}=750 MHz. The inset shows the characteristics on a reduced scale.

Teflon window and Fluorogold IR shield in the cryostat wall. The LO source was a 310-370 GHz BWO, and the signal was obtained from a SBV quintupler pumped by a 70 GHz Gunn oscillator. Bandwidth and output noise measurements were made with a wideband (0.02-4 GHz) room temperature IF amplifier, while for mixer noise measurements a cooled 680 to 920 MHz balanced low noise amplifier together with a cooled bias-T were included in the IF chain. The output IF signal was registered on a spectrum analyzer. We have estimated the losses on the RF-side to be roughly about 5-7 dB.

Fig. 2 shows the *IV*-characteristic for device #A. Depending on the physical temperature of the device and the intermediate frequency, it is possible to find different optimal bias points. At 4.5 K the *IV*-characteristic has a hysteretic behavior. In this case for output frequencies not too far above the IF cut-off frequency the optimal bias point is found just next to the unstable region at the transition from the resistive state to the superconducting state. For higher temperature (T=7.6 K), when the super current is suppressed, the optimum is no longer found in "one bias point", but there is a broad bias range at higher voltages. The corresponding IF spectrums also differ for these two temperatures. Whereas the spectrum at ~8 K demonstrates almost classic "one-pole" shape, the 4.5 K spectrum reveals a more gradual shape with a lower cut-off. We attribute such a behavior to the different resistive states (different thermal time constants) occurring in the film at lower and higher temperatures respectively. The low-temperature resistive state is presumably due to the normal domains with slower response to changes in electron temperature. The high-temperature resistive state is created by the flow of vortices which do not demonstrate any inertia in the scale of interest. The cut-off frequency in this case is given by the inverse electron temperature relaxation time ($\approx\tau_{e\text{-}ph}$). For device #B with higher T_c we observed the higher cut-off frequency (1 GHz) at T≈12 K.

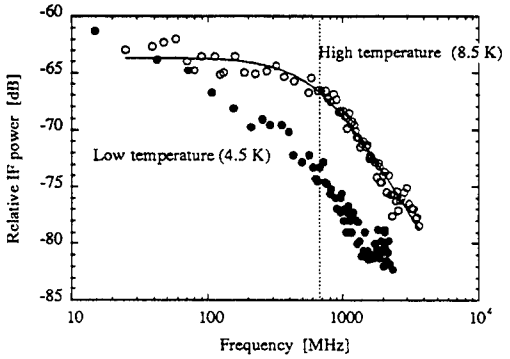


Fig. 3. IF response of sample #A at 4.5 K and 8.5 K

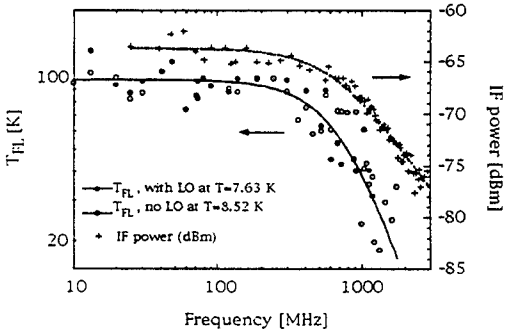


Fig.4. Frequency dependencies of the output thermal fluctuation noise temperature and IF signal power.

This qualitatively agrees with the temperature dependence of $\tau_{e\text{-}ph} \sim T^{1.6}$ [8].

The output noise of the mixer as well as the DSB receiver noise has been measured for both devices. The output noise temperature, T_{out}, was measured by comparing the noise levels obtained on a spectrum analyzer connected to the IF port of the mixer, for the device biased in the point for the maximum IF output power, with the noise level from the device at a temperature well above T_c (normal state). Thus

$$\frac{P_{noise,opt}}{P_{noise,normal}} = \frac{T_{out}(1-L)+T_{IF}}{T_J(1-L)+T_{IF}}, \qquad (1)$$

where T_{IF} is the noise contribution from the room temperature IF amplifier+bias-T etc. T_J is the Johnson noise from the device in normal state working as an ordinary resistor, and L is the corresponding mismatch loss. T_{IF} was measured by comparing the output noise levels for the device in normal state at two temperatures, 77 and 300 K.

Fig. 4 shows the typical output noise spectrum for device #A biased for maximum conversion gain at a higher temperature. The Johnson noise of the device (~8K) has been subtracted from the data ($T_{FL}=T_{out}-T_J$). One can see that T_{IF} vs IF can be well approximated by a one-pole standard dependence and that the cut-off frequency found from this curve is very close to the cut-off frequency of the mixing signal. Estimated from Eq. 2, the intrinsic conversion gain (RF coupling loss is subtracted) is -6.5±1 dB in the low frequency limit. This implies a mixer SSB noise temperature as low as 200 K.

II. Discussion of the Noise Performance of HEB Mixer.

The magnitude of the output noise temperature is much larger than the Johnson noise temperature of the device itself which is of the order of T_c. We attribute the excess noise to electron temperature fluctuations whose low-frequency analog is a well known noise mechanism in conventional bolometers. The fluctuations must demonstrate a roll-off at the same frequency as the mixing signal. The expression for the conversion gain has been given in [6]:

$$G(f) = 2C^2 \frac{R_L R}{(R_L+R)^2} \frac{P_{LO}}{P_{DC}} \frac{1}{\left(1+C\frac{R-R_L}{R+R_L}\right)^2} \frac{1}{1+(2\pi f\tau^*)^2}, \qquad (2)$$

where $C \equiv I^2(dR/d\theta)\tau_{e\text{-}ph}/c_e$ is the self-heating parameter, θ is the electron temperature, c_e is the electron heat capacity of the sample, P_{LO} and P_{DC} are the absorbed LO and Joule powers respectively and R=V/I in the bias point. The time constant τ^* in Eq. 2 is the apparent time constant which is different from $\tau_{e\text{-}ph}$ because of the feedback through the load resistor R_L and due to the self-heating of the device.

$$\tau^* = \tau_{e-ph}\left(1+C\frac{R-R_L}{R+R_L}\right)^{-1}. \qquad (3)$$

One can see that both time constants are close if $R_L=R$.

The expression for the output HEB mixer temperature due to the electron temperature fluctuations has been recently derived in [11]:

$$T_{FL}(f) = \frac{4\theta^2 c_e}{I^2\tau_{e-ph}} \frac{R_L}{(R_L+R)^2} \frac{C^2}{\left(1+C\frac{R-R_L}{R+R_L}\right)^2} \frac{1}{1+(2\pi f\tau^*)^2}. \qquad (4)$$

T_{FL} given by Eq. 4 agrees well with what we measured experimentally (see Fig. 4).

From Eqs. 2 and 4 the SSB mixer noise temperature can be derived as follows:

$$T_M = \frac{2\theta^2 c_e}{\tau_{e-ph}P_{LO}}. \qquad (5)$$

The remarkable feature of the above expression is that the mixer noise due to the thermal fluctuations depends on neither the intermediate frequency nor the conversion gain if the latter is very high. In this case the mixer noise bandwidth can be very wide, even wider than the cut-off set $\tau_{e\text{-}ph}$. Fig. 5 shows the noise contributions for ideal NbN sample. The noise bandwidth can be as large as 3.5 GHz even though the mixer bandwidth is 700 MHz.

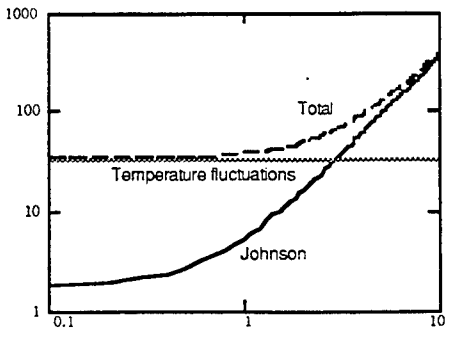


Fig. 5. SSB noise temperature vs IF for ideal NbN mixer.

To achieve such a performance one should significantly improve the conversion gain that requires $C \approx 1$. It is possible if ΔT_c is very small and critical current density is large. This automatically follows by an enhancement of the temperature fluctuations. The mixer noise temperature is reaching at the same time its physical limit which is very low and does not depend on the radiation frequency.

III. Conclusion

We have performed a study of the 350 GHz NbN hot-electron mixer. It has been shown that even a non-optimized device can demonstrate ~400 K SSB noise temperature if the RF loss has been excluded. The improvement of the film quality will allow to reduce the mixer noise temperature below 100 K. Such a performance should not depend on the radiation frequency. An increase of the noise bandwidth of the mixer is also expected.

ACKNOWLEDGEMENT

We wish to thank G. Gol'tsman and E. Gershenzon for fruitful discussions, B. Voronov and V. Siomash for manufacturing of the films. Richard Bradley at NRAO for kindly letting us borrow the 800 GHz low noise IF amplifier. This work was supported by the European Space Agency, and the RYMDSTYRELSEN the Swedish National Board for Industrial and Technical Development (NUTEK) and International Science Foundation under Grants NAF000 and NAF300.

References

[1] T.W. Crowe, R.J. Mattauch, H.R. Roser, W.L. Bishop, W.C.B. Peatman, and X. Liu, "GaAs Schottky Diodes for THz Mixing Applications," *Proc. IEEE*, vol. 80, pp.1827-1841, 1992.

[2] E.R. Brown, J. Keene, and T.G. Phillips, "A Heterodyne Receiver for the Submillimeter Wavelength Region Based on Cyclotron Resonance in InSb at Low Temperatures," *Int. J. Infrared Millimeter Waves*, vol. 6, pp.1121-1138, 1985.

[3] M.J. Wengler, "Submillimeter-Wave Detection with Superconducting Tunnel Diodes," *Proc. IEEE*, vol. 80, pp.1810-1826, 1992.

[4] J.X. Yang, F. Agahi, D. Dai, C.F. Musante, W. Grammer, K.M. Lau, and K.S. Yngvesson, "Widebandwidth Electron Bolometric Mixers: a 2DEG Prototype and Potential Low-noise THz Receivers," *IEEE Trans. Microwave Theory Tech.*, vol. 41, pp.581-589, 1993.

[5] E.M. Gershenzon, G.N. Gol'tsman, I.G. Gogidze, A.I. Elant'ev, B.S. Karasik, and A.D. Semenov, Millimeter and Submillimeter Range Mixer Based on Electronic Heating of Superconducting Films in the Resistive State," *Sov. Phys. Superconductivity*, vol. 3, pp.1582-1597, 1990.

[6] H.Ekström, B. Karasik, E. Kollberg, and K.S. Yngvesson, "Conversion Gain and Noise of Nb Superconducting Hot Electron Mixers," *IEEE Trans. Microwave Theory Tech.*, vol. 43, pp.928-947, 1995.

[7] A. Skalare, W.R. McGrath, B. Bumble, H.G. LeDuc, P.J. Burke, A.A. Verheijen, and D.E. Prober, "A Heterodyne Receiver at 533 GHz using a Diffusion-Cooled Superconducting Bolometer Mixer," *IEEE Trans. Appl. Superconductivity*, vol. 5, pp.2236-2239.

[8] Yu.P. Gousev, G.N. Gol'tsman, A.D. Semenov, E.M. Gershenzon, R.S. Nebosis, M.A. Heusinger, and K.F. Renk, "Broadband ultrafast superconducting NbN detector for electromagnetic radiation," *J. Appl. Phys.*, vol. 75, pp.3695-3697, 1994.

[9] A. Skalare, H. van der Stadt, T. de Grau, R.A. Panhuyzen, and M.M.T.M. Dierich, "Double Dipole Antenna SIS Receivers at 100 and 400 GHz," *Proc. of the 3rd Int. Symp. on Space THz Technology*, 1992.

[10] D.F. Fillipovic, S.S. Gearhart, and G.M. Rebeiz,"Double-Slot Antennas on Extended Hemispherical and Elliptical Silicon Lenses," *IEEE Trans. Microwave Theory and Tech.*, vol. 41, pp.1738-1749, 1993.

[11] B.S. Karasik and A.I. Elantev, "Analysis of the Noise Performance of a Hot-Electron Superconducting Bolometer Mixer," *Proc.of the 6th Int. Symp. on Space THz Technology*, Caltech, Pasadena, 1995.

Microwave Detection using the Photon-Activated Switch Behavior of the Single-Electron Transistor

J. M. Hergenrother, J. G. Lu, and M. Tinkham
Division of Applied Sciences and Department of Physics,
Harvard University, Cambridge, Massachusetts 02138

I. Introduction

The single-electron tunneling (SET) transistor is a three-terminal device in which a small metallic island is weakly coupled to a bias circuit through two small-capacitance tunnel junctions and a capacitive gate (Fig. 1). The total capacitance of this island to the external world, $C_\Sigma = (C_1 + C_2 + C_g) \approx 1$ fF, is so small that the characteristic charging energy, $E_C = e^2/2C_\Sigma$, typically corresponds to temperatures of a few K. Consequently, when the electron temperature T is less than E_C/k_B the behavior of the SET transistor is dominated by single-electron charging effects [1]. The gate charge, $Q_o = C_g V_g$, allows one to control the number of electrons on the island at the single-electron level. When the island is superconducting, charge transport through the SET transistor is modified dramatically in the presence of photon-assisted tunneling (PAT). In this paper, we demonstrate that under suitable bias conditions, the device acts as a photon-activated switch which automatically resets itself. As a result, the absorption of a single microwave photon switches the device from a low- to a high-current state for a time of order 1 μs, providing a new possible mechanism for very sensitive microwave detectors.

A. Sample Fabrication and Measurement

We fabricate both normal-superconductor-normal (NSN) and all-superconductor (SSS) SET transistors. In the NSN devices, normal-metal Au leads are coupled to a small (30 nm thick × 70 nm wide × 2.2 μm long) superconducting Al island through two approximately 70 nm × 70 nm AlO_x tunnel junctions. The NSN samples are fabricated as in [2]. The SSS devices are fabricated as in [3] and are similar except that the leads are Al. For the samples considered in this paper, $E_C \approx 100$ μeV (corresponding to $C_\Sigma \approx 800$ aF) and the measured tunneling resistances at high bias voltage V are approximately 100 kΩ.

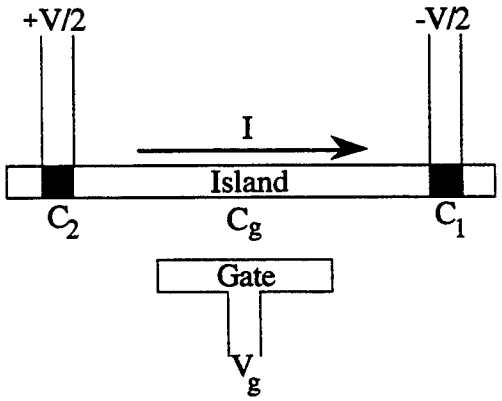


Fig. 1. Schematic of the SET transistor. The shaded squares denote the two small tunnel junctions with capacitances C_1 and C_2. The capacitance of the gate to the island is C_g. Also shown is the current I through the device.

Each sample is measured in a top-loading dilution refrigerator as in [4]. All leads are carefully filtered with conventional low-pass RC filters at room temperature and at the mixing chamber temperature, T_{MC} (≤ 50 mK for all the data presented here), as well as a Cu-powder microwave filter that is thermally anchored to the mixing chamber. The sample is protected from relatively warm (≈ 4 K) surfaces in the interior of the cryostat by 700 mK and 150 mK Cu shields. Both shields have an approximately 1.5 cm circular hole through which the slug containing the sample is top-loaded. Thus, these two Cu shields are incomplete at microwave frequencies and above. Our commercial slug also provides significant cold shielding for the sample, but there are several mm-scale gaps in this shielding. In what we refer to as the "good-shielding" case, we cover each of these gaps with a conductor such as Ag paint. If the gaps in the slug are not completely covered, then small amounts of blackbody radiation from ≈ 4 K surfaces of the cryostat can reach the sample. We have made measurements in which the gaps in the slug shielding are left uncovered (the "incomplete-shielding" case) or partially covered (the "better-shielding" case).

B. Behavior of a Well-Shielded Sample

In order to describe the effects of PAT, we must first briefly discuss charge transport in a well-shielded SET transistor. For simplicity, we restrict ourselves to the NSN case. Fig. 2(a) shows the system energy at $V = 0$ for different values of n, the number of excess electrons on the island. The charging energy term $(-en+Q_o)^2/2C_\Sigma$ in the system energy leads to a parabolic shape for each curve [1]. For odd n, the island contains exactly one quasiparticle at low T. To reflect this, the parabolas corresponding to odd n have been shifted upward by the superconducting gap Δ ($\approx 2E_C$). As a result of Δ, the island exhibits surprisingly robust even-odd electron number effects

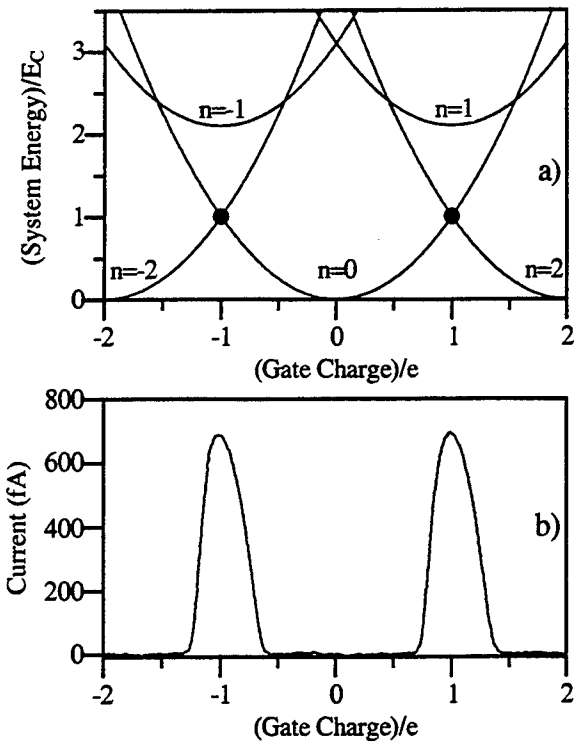


Fig. 2. (a) System energy curves for various charge states drawn for V = 0 for simplicity. (b) Experimental current versus gate charge (I-Q_o) curve for V = 125 μV and T_{MC} = 15 mK for a well-shielded NSN SET transistor. The current peaks near $Q_o = \pm e$ result from Andreev cycles which are important near the degeneracy points denoted by the solid circles in the top figure.

even when it contains approximately 10^9 conduction electrons. In islands small enough to show charging effects, these even-odd effects persist for temperatures up to 300 mK [3]. When $\Delta > E_C$, the ground state always involves an even number of electrons and SET is suppressed at low V and T. Under these conditions charge is transported exclusively through Andreev reflection (two-electron tunneling) which couples two even-n states. This Andreev current is shown clearly in Fig. 2(b). The current peaks in this figure result from a cycle involving sequential Andreev reflections at each of the two tunnel junctions. This Andreev cycle has been discussed in detail previously [2], [5], [6].

II. Effects of Photon-Assisted Tunneling

A. Comparison of Experiment and Theory

If we degrade the shielding of the device, PAT leads to a secondary Andreev peak near $Q_o = 0$ [4], [6]. The experimental data of Fig. 3(a) illustrate how this secondary peak emerges and grows as the amount of absorbed radiation increases. We have calculated the current through the NSN SET transistor by including Andreev reflections, energetically favorable and photon-assisted SET events that put a quasiparticle onto the island, and escape processes in which a quasiparticle is removed from the island. We calculate PAT rates by considering a simple model in which the environment of the SET transistor consists of a resistor of size R_{env} at temperature T_{env} in series with the two tunnel junctions. Following Martinis and Nahum [7], we consider $T_{env} >> T$. In this case, PAT greatly enhances the rates of otherwise energetically forbidden tunneling processes. In our model, we assume that R_{env} is equal to the high-frequency impedance of the sample's leads, which is real and of order 100 Ω. We also introduce a coupling parameter α such that αR_{env} characterizes how much of the ambient cryogenic blackbody radiation penetrates the shielding layers and couples to the sample through its leads. Once a value for αR_{env} has been specified, we use Eqs. (1) and (3) of [7] to determine the PAT rates.

The thin lines of Fig. 3(a) are theoretical I-Q_o curves calculated in this way. These curves correspond to T_{env} = 4 K [8], T = 50 mK, and measured junction capacitances and conductances. The theory curves agree so well with the experimental data that they are almost completely hidden by the

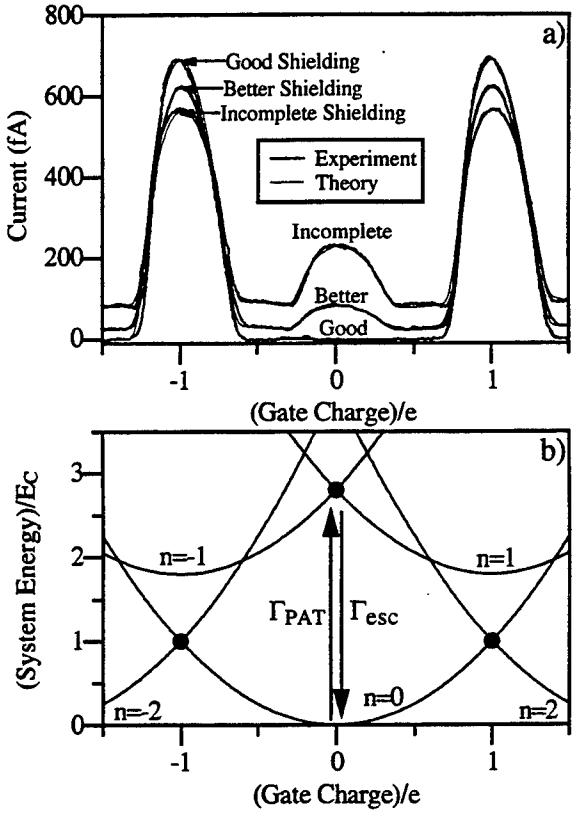


Fig. 3. (a) Three experimental I-Q_o curves for V = 125 μV and T_{MC} = 15 mK for different levels of electromagnetic shielding of the sample. Note the conspicuous secondary peak near $Q_o = 0$ that emerges as the shielding is degraded. Theoretical results (smooth, thin curves) for T_{env} = 4 K and αR_{env} = 0.99 Ω, 0.19 Ω, and 0 Ω almost perfectly coincide with the incomplete-shielding, better-shielding, and good-shielding data, respectively. (b) System energy diagram included to illustrate the origin of the secondary peak. The transition pair shown includes one photon-assisted transition (Γ_{PAT}) and one escape process (Γ_{esc}). The solid circles denote degeneracy points where an Andreev cycle occurs.

data. Note, in particular, that the theory accurately captures the height and shape of the secondary peak. The only difference among the theory curves of Fig. 3(a) is that the values of αR_{env} used [9] are changed to reflect the level of shielding. The theory curve which fits the good-shielding data uses $\alpha R_{env} = 0$, as expected in the absence of PAT. According to our simulations, about 85 aW is absorbed by this particular device in the incomplete-shielding case. The amount of power absorbed in the better-shielding case is only 19 aW.

Note that the thermal rounding at the bases of the primary Andreev peaks in Fig. 3(a) provides a useful measure of the electronic temperature T. This rounding is fit well with $T = 50$ mK regardless of the level of shielding, indicating that the absorbed microwave radiation produces minimal electron heating even at low T. Thus, the secondary peak is conspicuous in the presence of even very small amounts of microwave radiation.

B. *Photon-Activated Switch Behavior*

Fig. 3(b) illustrates that the secondary peak results when the absorption of a microwave photon provides enough energy to introduce a single quasiparticle to the island through SET. This takes the system from $n = 0$ to $n = \pm 1$, where charge is transported through the system two electrons at a time (the Andreev cycle). For the sample of Fig. 3(a), this photon must have an energy $\geq (\Delta + E_C)$, so that the device is sensitive to frequencies $f \geq (\Delta + E_C)/h \approx 80$ GHz. Without photon assistance, the introduction of a quasiparticle to the island is forbidden at the low V and T considered here. The Andreev cycle which couples the $n = -1$ and $n = 1$ states continues until the single quasiparticle escapes from the island after a relatively long "escape" time of order 1 μs [2], [10], [11]. We envision a microwave detection scheme in which the height of the secondary peak provides a direct measure of the absorbed power. This device can exceed the "quantum limit" of one electron per absorbed photon because it behaves as a photon-activated switch. The detector current is turned off when the device automatically resets itself through an escape process [12]. In the data of Fig. 3(a), the secondary peak corresponds to approximately 3 electrons tunneling through the system per absorbed photon.

III. Microwave Sensitivity

A. *Measured Samples*

Up to this point we have only considered the NSN single-electron transistor. However, the detection scheme just described also applies to the all-superconductor (SSS) single-electron transistor. In terms of detector sensitivity, the SSS device has one distinct advantage over the NSN device -- namely, a "supercurrent" which can approach 1 nA occurs at the same degeneracy points where the much smaller (pA-level) Andreev current of the NSN system occurs. This greatly increases the sensitivity of the device as a microwave detector. Fig. 4 shows an experimental I-Q_o curve for an SSS SET transistor taken in the incomplete-shielding case. For this particular device, the maximum supercurrent is about 50 pA and the escape time (inferred from sample parameters) is about 0.3 μs. Thus, at $Q_o = 0$, this device passes 50 pA of current for about 0.3 μs every time it absorbs a photon with a frequency greater than the threshold frequency. These numbers indicate that the secondary peak of Fig. 4 corresponds to (50 pA)(0.3 μs)/e ~ 100 electrons tunneling through the system per absorbed photon.

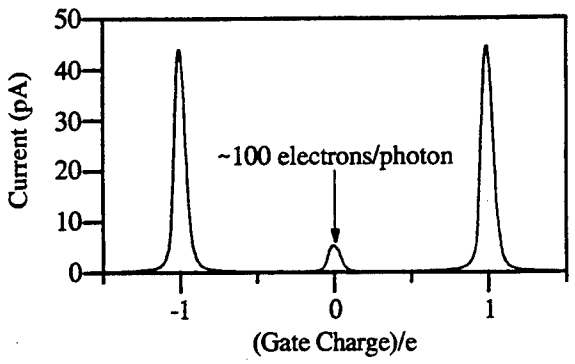


Fig. 4. Experimental incomplete-shielding I-Q_o curve for an SSS SET transistor at $V = 20$ μV and $T_{MC} = 15$ mK. Note the larger current scale in comparison with Fig. 3. Near $Q_o = 0$, this particular device absorbs about 200 aW of microwave power and this produces a sizeable secondary peak. Since the device acts as a single-photon-activated switch, the secondary peak can correspond to the tunneling of many electrons for every absorbed photon.

For the purpose of a rough sensitivity estimate, we assume that the sample is illuminated with monochromatic 80 GHz radiation. In this case, 100 electrons tunneling for every absorbed photon corresponds to a current-to-power responsivity of approximately 3×10^5 A/W. If we measure the detector current with a commercial amplifier characterized by a current noise of 10^{-14} A/$\sqrt{\text{Hz}}$, then we arrive at a noise equivalent power of 3×10^{-20} W/$\sqrt{\text{Hz}}$ (referred to the device) [13].

B. *Ultimate Sensitivity*

In order to make the device even more sensitive, we can optimize device parameters to increase both the level of the supercurrent and the escape time. By decreasing junction resistances to $R_i \approx R_Q = 6.47$ kΩ, we should obtain a nA-level maximum supercurrent. Since a single quasiparticle trapped on the superconducting island must be near one of the tunnel junctions in order to escape, the escape time is proportional to the volume of the island [10], [11].

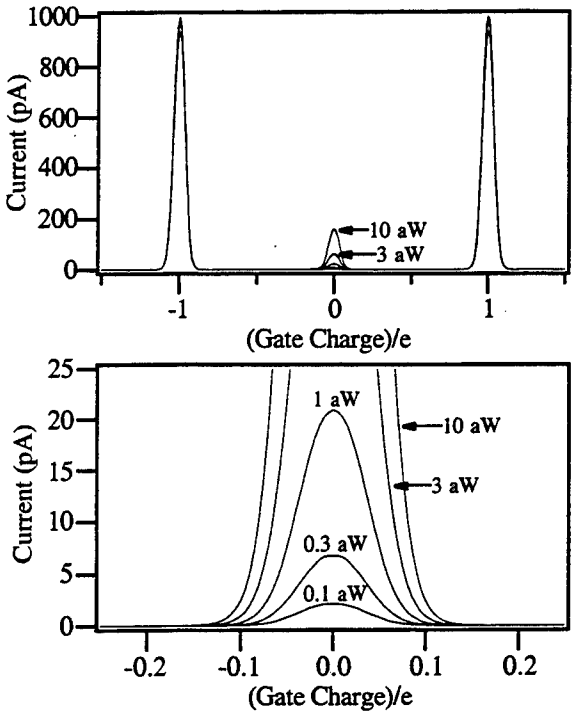


Fig. 5. (a) Theoretical I-Q_o curves for an optimal SSS SET transistor microwave detector (maximum supercurrent of 1 nA, escape time of 1 μs) for different amounts of absorbed power. These curves are calculated for $V = 20$ μV and $T = 50$ mK and are labeled by the power the device absorbs at $Q_o = 0$. (b) A blowup of the region near $Q_o = 0$. Note that the absorption of only 0.1 aW produces a 2 pA secondary peak, a current that is easily measured.

Thus, we can increase the escape time by fabricating larger islands. Although there is an upper limit on how large the island can be and still show significant charging effects, it is quite reasonable to consider an island with an escape time of 1 μs. Thus, in an optimal SET transistor microwave detector about (1 nA)(1 μs)/e ~ 10^4 electrons should tunnel for every absorbed photon. Fig. 5 shows how very small amounts of absorbed microwave power would affect such a sensitive device. Since its characteristic impedance is $2R_j$ ~ 10 kΩ, it would be difficult to couple this device efficiently to an antenna structure. However, even when one accounts for poor coupling, this device should still be significantly more sensitive than existing detectors operating in the same frequency range [14].

IV. Conclusion

We have shown that at low temperature ($T < 300$ mK), the SET transistor with a superconducting island acts as a photon-activated switch near $Q_o = 0$. Since the absorption of a microwave photon merely switches the detector current on, many electrons tunnel through the system for every absorbed photon. This makes the device an extremely sensitive and potentially useful detector of microwave radiation.

Acknowledgment

The authors wish to thank M. Tuominen and D. Ralph for valuable input over the course of this work. We also thank C. Black and R. Fitzgerald for their assistance. This work was supported in part by JSEP Grant No. N00014-89-J-1023, ONR Grant No. N00014-89-J-1565, and NSF Grant No. DMR-92-07956. JMH acknowledges support under AFOSR Grant No. F49620-93-1-0347.

References

[1] For an introduction to single-electron charging effects see *Single Charge Tunneling*, H. Grabert and M. H. Devoret, Eds., New York: Plenum Press, 1992.

[2] J. M. Hergenrother, M. T. Tuominen, and M. Tinkham, *Phys. Rev. Lett.* **72**, 1742 (1994).

[3] M. T. Tuominen, J. M. Hergenrother, T. S. Tighe, and M. Tinkham, *Phys. Rev. Lett.* **69**, 1997 (1992).

[4] J. M. Hergenrother, J. G. Lu, M. T. Tuominen, D. C. Ralph, and M. Tinkham, *Phys. Rev. B* **51**, 9407 (1995).

[5] T. M. Eiles, J. M. Martinis, and M. H. Devoret, *Phys. Rev. Lett.* **70**, 1862 (1993).

[6] J. M. Hergenrother, M. T. Tuominen, J. G. Lu, D. C. Ralph, and M. Tinkham, *Physica B* **203**, 327 (1994).

[7] J. M. Martinis and M. Nahum, *Phys. Rev. B* **48**, 18316 (1993).

[8] T_{env} = 4 K is quite reasonable because the warmest surfaces that radiate into the inner vacuum chamber of our dilution refrigerator are at this temperature.

[9] The fit values for αR_{env} are much smaller than the high-frequency lead impedance R_{env} ~ 100 Ω. This suggests that it only takes only a small fraction of the 4 K blackbody radiation to produce the observed effects.

[10] F. W. J. Hekking, L. I. Glazman, K. A. Matveev, and R. I. Shekhter, *Phys. Rev. Lett.* **70**, 4138 (1993).

[11] G. Schön and A. D. Zaikin, *Europhys. Lett.* **26**, 695 (1994).

[12] The simple picture given here breaks down for absorbed power levels $P_{abs} \geq hf\Gamma_{esc}$ because a second photon is frequently absorbed before the quasiparticle trapped on the island can escape. Although simulations can account for processes such as this, the device sensitivity is diminished when $P_{abs} \geq hf\Gamma_{esc}$.

[13] The maximum response frequency of this device ($<< \Gamma_{esc}$) will be limited by the bandwidth of this current measurement in most cases.

[14] For a general review see P. L. Richards, *J. of Appl. Phys.* **76**, 1 (1994). See also M. Nahum and J. Martinis, *Appl. Phys. Lett.* **63**, 3075 (1993).

Hot Electron Mixing in NbN at 119 Micrometer Wavelength

E. Gerecht, C.F. Musante, C.R. Lutz, Jr., Z. Wang, J. Bergendahl, K.S. Yngvesson, E.R. Mueller*, J. Waldman*, G.N. Gol'tsman**, B.M. Voronov**, and E.M. Gershenzon**

Dept. of Electrical and Computer Engineering, University of Massachusetts, Amherst, MA 01003
* Submillimeter Technology Laboratory, University of Massachusetts Lowell, Research Foundation, Lowell, MA 01854
** Department of Physics, Moscow State Pedagogical University, Moscow 119882, Russia

1.0 INTRODUCTION

Low-noise receivers in the THz range (frequencies 1-3 THz, wavelengths 100 μm -300 μm) are presently applied primarily in astronomical and remote sensing observations. The best noise temperatures in this range are obtained by Schottky-barrier diode mixers, with typical DSB values of 80-100 x hf/k, where hf/k is the quantum-limit for noise temperature [1]. At 1 THz, hf/k is roughly 50 K. An often stated goal is to develop new types of THz receivers which could demonstrate DSB noise temperatures of ten times the quantum limit [2]. At frequencies just below 1 THz, Nb tri-layer junction SIS mixers meet or exceed this criterion for low noise performance, but their noise temperature presently rises rapidly above the superconducting gap frequency of Nb, about 700 GHz. SIS mixers also have limitations due to the capacitive nature of the SIS junction device, which make it difficult to extend their performance to THz frequencies. It has been proposed [3,4,5] that the hot electron bolometric (HEB) type of mixer, which relies on bulk effect interactions in either semiconductors or thin film superconductors, and has very low parasitic reactance, can solve the problem of realizing low-noise THz receivers. Several versions of such thin film superconducting mixers have been demonstrated for frequencies up to 530 GHz [6,7,8] with DSB noise temperatures in the range 600K-1000K. Due to the low parasitics, and the fact that the HEB mixers should work well both below and above the superconducting bandgap, the noise temperature is not expected to depend strongly on frequency. Thus the above results suggest that it should be possible to reach the goal of $T_{R,DSB} = 10 \times hf/k$ in the THz range. The effort reported in this paper was aimed at obtaining direct evidence for the potential of HEB mixers as THz receivers by performing measurements in this range. We chose to use CO_2-laser pumped methanol lasers at 119 μm wavelength (frequency 2.5 THz) as both signal and LO sources for this experiment. We obtained the first evidence for HEB mixing in NbN above 350 GHz, with a best intrinsic conversion loss of 23 dB. The conversion loss is still limited by the available LO power from the laser, due to the large size of this prototype device. The conversion loss is expected to decrease very substantially in future experiments. We also present IF response curves measured at X-band for the same type of NbN devices, which were fabricated on silicon substrates. The maximum IF bandwidth obtained so far is 3-4 GHz, and is expected to be essentially unchanged when the device is used at THz frequencies. This bandwidth is wide enough for most applications of THz receivers, but is likely to be increased further, as our understanding of the properties of thin film superconductors evolves.

2.0 DEVICE FABRICATION AND OPTICAL COUPLING

The devices were fabricated from NbN films which were 30 to 70 A thick. The films were magnetron sputtered on substrates of either silicon or sapphire. It has been shown that NbN films on these substrates have higher critical temperatures (T_c), and a sharp superconducting transition (small ΔT_c), compared with NbN films on quartz. T_c is about 14 K (12 K), and the transition width may be as narrow as 0.2 K (0.3 K) for 70 A thick films on sapphire (silicon). The small ΔT_c should lead to lower conversion loss. Thinner films yield lower T_c and wider ΔT_c , and were tested to optimize the IF bandwidth. Devices as shown in Figure 1 were fabricated by reactive ion etching. They consist of 175 strips of width 1 μm, with 1 μm spacing. The size of the device was chosen to cover a typical

focal spot which could easily be obtained with the lasers. A 70 A device used in the 2.5 THz mixing experiments had a total resistance of 1.6 kΩ, i.e. 800 Ω/square. We have calculated the coupling loss to such thin film devices with a dielectric substrate backing [9]. For a resistance per square of 800 ohms, we predict a coupling efficiency of 8 % (- 11 dB). The coupling loss can be improved substantially by employing matching techniques as described by us earlier [9]. The best method appears to be to construct a "back-short" behind the device by etching the silicon substrate to a thickness of about 8.7 μm, and then depositing gold on the back side of the substrate. We are presently developing this technique.

3.0 OPTICAL SETUP

Figure 2 shows the optical setup for the two-laser measurements. Both THz lasers were pumped by a single CO_2-laser. One laser was made to oscillate at a frequency about 1 MHz away from that of the other laser by cavity tuning. The laser beams were combined with a wire grid polarizer, set at a 45 degree angle. The LO laser operated in a single waveguide mode producing a Gaussian spatial output profile with first sidelobes >20 dB down. The signal laser was an oversized half-symmetric resonator which supported more than one transverse mode (frequency). However, careful alignment produced a far-field spatial pattern which was Gaussian to a level 15 dB below the peak. An off-axis paraboloidal mirror focussed the THz radiation through a clear polyethylene window, and a black polyethylene sheet. The latter attenuated radiation at shorter wavelengths. The device was mounted on a copper post thermally attached to the bottom of the liquid helium container of the dewar. The temperature of the device could be varied by a resistive heater. For the mixing measurements we extracted the IF power through the bias tee, amplified it outside the dewar, and fed it to a spectrum analyzer. Once an optimum operating point was found, we also attempted to measure the receiver noise temperature at an IF frequency of about 1 GHz. In this case we fed the IF power through a ferrite isolator and an HFET amplifier, which were installed in the dewar. The measured IF amplifier noise temperature, including the isolator, was about 90 K. Outside the dewar, we employed a post-amplifier, detector, and a lock-in amplifier. For the noise measurements only the LO laser was pumped, increasing its output power by 3 dB. A chopped hot/cold source was substituted for the signal laser.

4.0 EXPERIMENTAL RESULTS

4.1 Mixing at 2.5 THz

Due to the relatively large size of the device, it was important to choose an operating temperature (T_{op}) for which the LO power required is minimized. Since the critical current varies with temperature, and is lower close to T_c, the operating temperature should be close to T_c. If T_{op} is too close to T_c, however, the conversion loss decreases quickly. The best choice of T_{op} is therefore typically a few times ΔT_c below T_c. If the LO power is sufficient, one will see a substantial (about a factor of two) suppression of the DC current as the LO is applied, see Figure 3. The optimum conversion loss occurs for a DC voltage range of about 0.1 to 0.3 V in this diagram. Figure 3 was recorded in an earlier experiment, when the incident laser power was 20 mW. In the mixing experiment, the incident LO power was 6 mW. The actual absorbed power can be measured by making use of the fact that along a line of constant resistance in the I-V-diagram, the electron temperature is constant, and thus the total absorbed power ($P_{DC} + P_{LO}$) is also constant. We found that the absorbed LO power was 0.16 mW, i.e. the total optical coupling loss was 15.6 dB; roughly 3 dB of this loss is due to the fact that the device fingers were oriented horizontally, whereas the polarization of the incident radiation was at 45 degrees. The uncorrected conversion loss from the incident signal laser power (0.7 mW) to the IF output port was 41.5 dB. Figure 4 shows the recorded output from the spectrum analyzer: the peak at about 1 MHz is the mixing product of the main modes of the two lasers. Other smaller peaks are due to higher order transverse modes of the signal laser, but are at least 20 dB down from the main peak. The origin of these peaks could be verified by blocking the beam of one laser. We can calculate the **intrinsic conversion loss P_{int} = 41.5 dB – 15.6 dB – 3 dB = 23 dB.** We have substracted 3 dB for the beam splitter loss, which would not

occur in an actual receiver system. Attenuating the LO by 6.2 dB, we observed a decrease in IF output power by 7 dB, which indicates that the mixer is LO starved. We expect that the intrinsic conversion loss would decrease to about the 10 dB level, typical of NbN mixers measured at 350 GHz, when sufficient LO power is available.

We also attempted to measure the noise temperature of the mixer, but were not able to do this because the chopped hot-cold signal was too small compared to the system noise level. A calculation with reasonable values for the parameters (L_C = 40 dB; T_{IF} = 100 K) yields an estimated value of $T_{R,DSB}$ of 5 x 10^5 K. This value is near the limit for measurable noise temperatures in the system. Our measurement system was checked by measuring the receiver noise temperature of a corner-cube mounted Schottky-barrier diode mixer. The result agreed well with published values for the particular diode model, measured at 2.5 THz [10]. The main factors which give rise to the high noise temperature of the NbN mixer are (1) the optical coupling loss, and (2) the fact that the mixer was LO starved. We have shown, however, that NbN HEB devices are capable of mixing at 2.5 THz. The coupled LO power needs to be increased by about an order-of-magnitude in order to lower the conversion loss to its optimum value. This level of LO power agrees with calculations based on HEB theory, as well as measurements at lower frequencies on smaller devices. Since it has been shown that the output noise temperature of a NbN device can be as low as 100 K [11], we can project a DSB receiver noise temperature of about 500 K, when the total conversion loss is brought down to the 10 dB level. The conversion loss can be decreased by (i) use of the "back-short" method described above, or (more effectively) (ii) by coupling a much smaller device through a hemisperical lens [12]. The LO power required for the smaller device would be at most a few μW. We are pursuing both of these approaches.

4.2 Bandwidth Measurements at X-band

It has been shown that microwave measurements of the IF bandpass curve for NbN mixers yield the same frequency dependence and bandwidth as when the measurement is done at 230 GHz [13]. We have employed this method in order to determine the bandwidth of NbN devices of different thickness on silicon and sapphire substrates, and at different temperatures. Complete results are not yet available, but some trends can be seen. The devices are mounted on a dipstick, which is inserted in a liquid helium storage dewar. A 30 A device, measured at 4.2 K, gave a 2 GHz bandwidth. The 70 A device on which we performed the 2.5 THz measurements, has a bandwidth of 1.2 GHz, when measured at 4.2 K, and 3-4 GHz at a temperature close to the operating temperature of the THz mixer (11.3 K) (Figure 5). The wider bandwidth at a higher temperature is expected based on the theory of HEB mixers [4,5]. Note that the 2.5 THz measurement was made for an IF frequency of 1 MHz, and that the IF response curve is essentially flat at the lowest frequencies.

5.0 REFERENCES

[1] R. Blundell and C.E. Tong, *Proc.IEEE*, **80**,1702(1992).

[2] M. Kaplan, *Proc.Sec.Intern.Symp.Space THz Technol.*,1(1991)

[3] J.X. Yang et al., *IEEE Trans. Microw. Theory Techniques*,**MTT-41**,581(1993).

[4] E.M. Gershenzon et al., *Superconductivity*, **3**,1582(1990).

[5] E.M. Gershenzon et al.,*IEEE Trans. Magnetics*, **MAG-27**, 1317(1991)

[6] Ekstrom et al., *IEEE Trans. Microw. Theory Techniques*,**MTT-43**,938(1994).

[7] Skalare et al., *IEEE Trans.Appl.Superc.*, June issue(1995).

[8] Okunev et al., *IEEE Trans.Appl.Superc.* June issue (1995).

[9] Gerecht et al., *Sixth Intern Symp. Space THz Technol.*, (1995).

[10] P.A. Wood, Ph.D. Thesis, U. Virginia, January 1994. Also *Fifth Intern. Symp. Space THz Technol.*, May 1994.

[11] H. Ekstrom and B.S. Karasik, *Appl.Phys.Lett*, **66**, 3212 (1995).

[12] Gearhart et al., *IEEE Microw.Guided Wave Lett.*, **3**, 205 (1993).

[13] Kawamura et al., *Sixth Intern Symp. Space THz Technol.*, (1995).

6.0 FIGURES

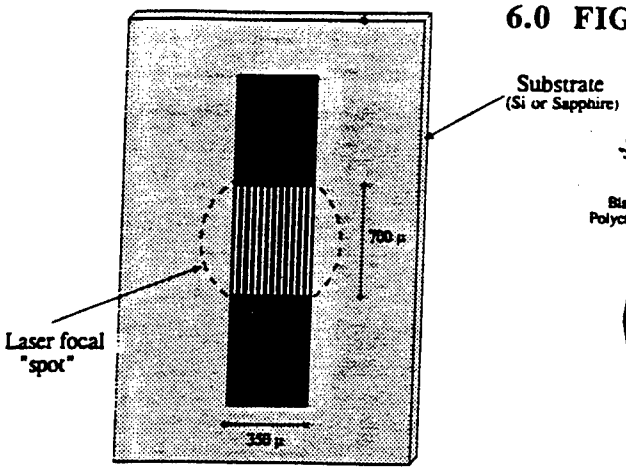


Figure 1. NbN device for the 2.5 THz mixer.

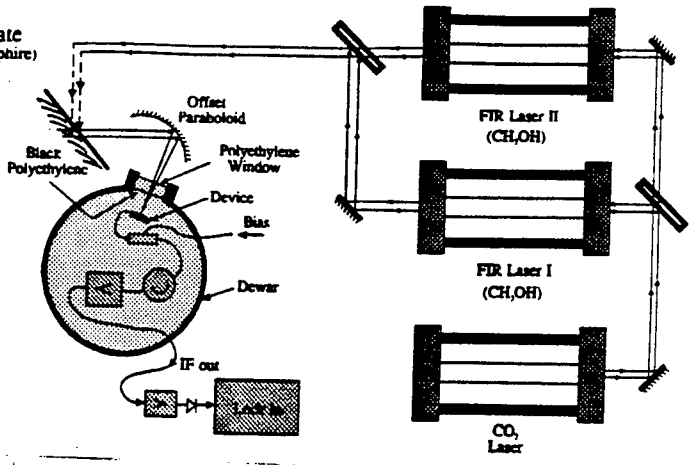


Figure 2. Optical setup for measurements on the 2.5 THz mixer.

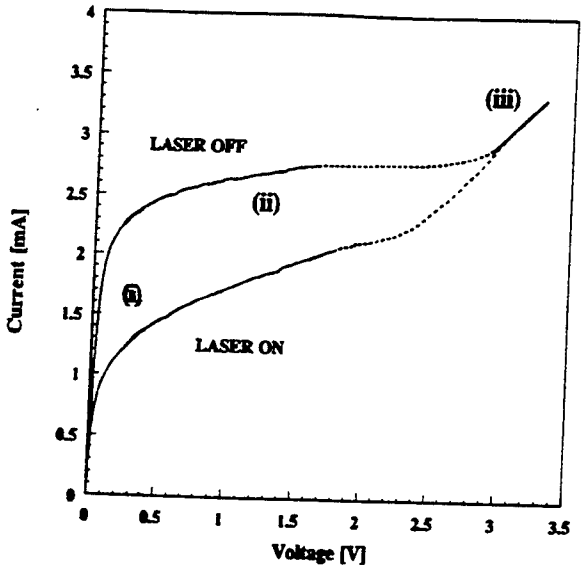


Figure 3. Measured I-V-curve for the NbN device used in the 2.5 THz mixer.

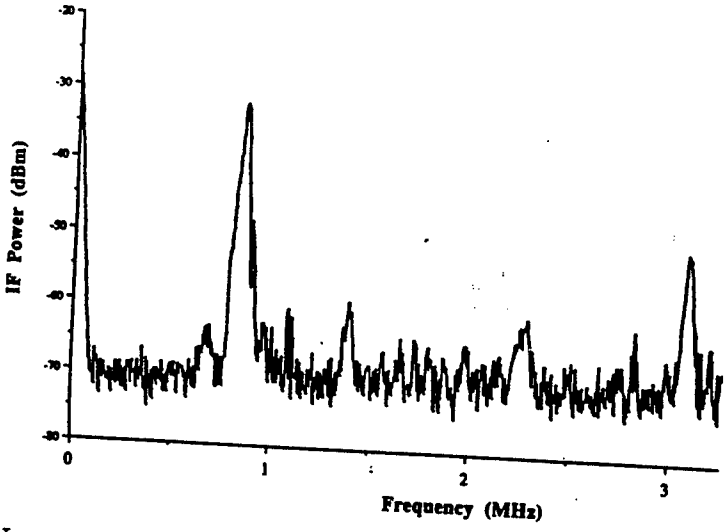


Figure 4. Spectrum analyzer recording of the IF output from the 2.5 THz mixer.

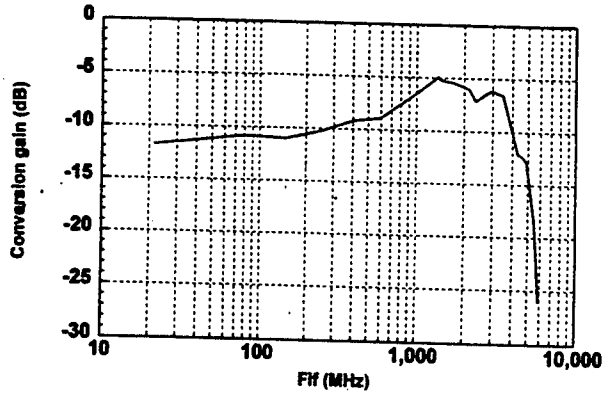


Figure 5. IF response curve for a 70 A thick NbN device, measured at X-band.

THz Parametric Oscillators Using Coupled Double Quantum Wells

I. Lyubomirsky, B. Xu and Q. Hu
Department of Electrical Engineering and Computer Science and Research Laboratory of Electronics, Massachusetts Institute of Technology, Cambridge, MA 02139

Since the early days of nonlinear optics, there have been efforts to apply optical parametric down conversion techniques to the generation of THz or far-infrared radiation [1]. But the practical realization of an optical parametric oscillator (OPO), with a tunable signal output in the THz frequencies, has been hampered by the relatively weak nonlinear susceptibility $\chi^{(2)}$ of natural crystals. Recent studies of the nonlinear optical properties of asymmetric double quantum wells using GaAs/AlGaAs heterostructures have shown that these structures posses enormous $\chi^{(2)} \sim 10^{-6} m/V$, which is four orders of magnitude greater than in bulk GaAs [2]. These quantum wells act like giant artificial atoms, whose nonlinear optical properties can be optimized by proper design [3]. Moreover, when operating near resonance, one can tune the nonlinearity using the Stark shift by simply applying a bias voltage [4, 5]. In this paper, we propose to take advantage of these properties of quantum wells to design an OPO for THz applications. The large value of $\chi^{(2)}$ will provide enough gain to overcome the losses at a reasonable level of CO_2 pump power, while the resonant Stark shift will be used for quasi-phasematching and tuning of the OPO.

A large value of $\chi^{(2)}$ can be achieved by designing an asymmetric double quantum well (DQW) structure that is doubly resonant at both the pump ω_p and signal ω_s frequencies (Fig. 1). This resonant enhancement of $\chi^{(2)}$, in addition to the large dipole matrix elements of quantum wells, leads to a strong nonlinear response and hence a large gain. If only the ground state E_1 is occupied, and when ω_p and ω_s are close to resonance [6],

$$\chi^{(2)}(\omega_s = \omega_p - \omega_i) = \frac{e^3 N}{\epsilon_0} \frac{z_{12} z_{23} z_{13}}{(\Delta E_{23} - \hbar\omega_s + i\Gamma_{23})(\Delta E_{13} - \hbar\omega_p + i\Gamma_{13})}, \qquad (1)$$

where N is the three-dimensional electron density in the wells, z_{ij}'s are the dipole matrix elements, and Γ_{ij}'s are the linewidth broadenings. In previous work [2, 3], the quantum wells were designed to maximize $\chi^{(2)}$ by maximizing the product $z_{12} z_{23} z_{13}$. However, one cannot design an OPO by simply maximizing the $\chi^{(2)}$ because this will lead to a large absorption loss of the pump and/or signal. Since the threshold condition for an OPO is determined by the balance of gain and loss, it is important to minimize the loss. The absorption loss of the signal can be avoided by designing the DQW structure to have negligible electron population in E_2. This can be achieved by using the DQW structure of Fig. 1, operating

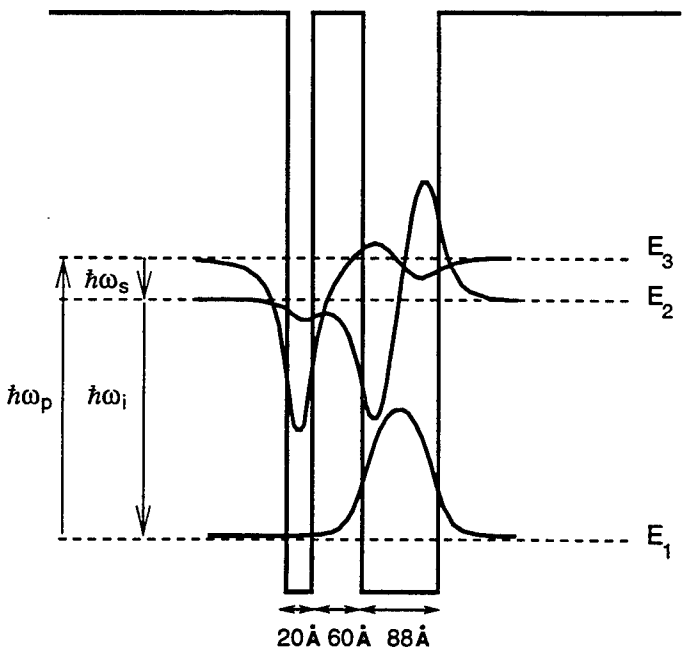


Fig. 1

at LHe temperatures and low pump power. But a large absorption loss of the pump is unavoidable for a doubly resonant quantum well and will limit the useful length of the nonlinear crystal under phasematched conditions. A good figure of merit is the ratio of $\chi^{(2)}$ to pump absorption α_p at resonance $\frac{\chi^{(2)}}{\alpha_p} \sim \frac{en_p c z_{12} z_{23}}{w_p z_{13} \Gamma}$. Thus we see that the wavefunctions must be tailored to maximize $z_{12}z_{23}$ while making z_{13} small enough to get a useful crystal length. The linewidth broadening Γ can be made small (1-5 meV) by cryogenic operations and modulation doping [2]. We designed the DQW structure of Fig. 1 to have $z_{12} = 22.5\mathring{A}$, $z_{23} = 20.3\mathring{A}$ and $z_{13} = 2.76\mathring{A}$, while the energy levels are set for double resonance at the pump $\lambda_p \sim 10\mu$ and signal $\lambda_s \sim 60\mu$ frequencies. This gives a maximum $\chi^{(2)} \sim 10^{-6} m/V$ for an electron density of $2 \times 10^{11} cm^{-2}$ in the wells. The matrix element z_{13} is made relatively small, corresponding to a depletion length of about 1 mm for the pump.

Quasi-phasematching is achieved by processing the GaAs into the periodic waveguide structure shown in Fig. 2. The periodic grid on the top face will be used for phasematching. The alternating metal strips of the grid can be biased at different voltages V_1 and V_2. The bias voltages affect the energy levels of the quantum wells through the Stark shift. Thus $\chi^{(2)}$ can be tuned to be on or off resonance. Capasso et. al. [5] have demonstrated this experimentally in the case of second harmonic generation. A periodic $\chi^{(2)}$ may be set up in the waveguide by adjusting V_1 to be on resonance while V_2 is tuned off resonance. If the period of the grating Λ is made equal to the coherence length $l_c = \frac{\pi}{\Delta k}$, the condition of

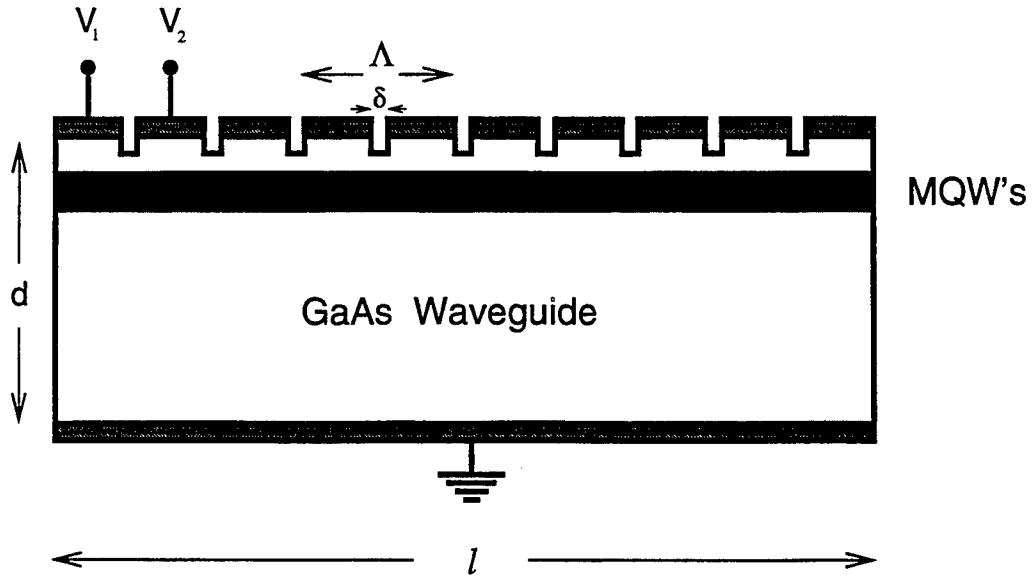


Fig. 2

quasi-phasematching results [7]. For parametric generation,

$$\Delta k = k_s - k_p + k_i = \frac{1}{c}(n_s\omega_s - n_p\omega_p + n_i\omega_i)\,. \tag{2}$$

Using the relation $\hbar\omega_p = \hbar\omega_s + \hbar\omega_i$ and with $n_p \simeq n_i = n$ and $n_s = n + \Delta n$, we obtain for the coherence length $l_c \simeq \frac{\lambda_s}{2\Delta n}$. The real part of $\chi^{(1)}$ due to intersubband transitions vanishes at resonance. In this case we only need to consider the bulk indices of refraction to estimate l_c. In GaAs $n_p \simeq n_i = 3.3$ and $n_s = 3.55$, so that $\Delta n \simeq 0.25$. Thus we must have a grating period of $\Lambda = l_c \simeq 120\mu m$. This can be easily fabricated. Imperfections in fabrication and/or our estimate of l_c can be corrected by tuning the pump frequency to be slightly off resonance so that the real part of $\chi^{(1)}$ will give a small contribution to Δn [8]. The bias electric field needed to tune $\chi^{(2)}$ off resonance can be estimated from the tight binding appriximation. In the tight binding approximation, the electrons in energy levels E_1 and E_2 are mostly located in the wide well, while the electrons occupying E_3 are located in the narrow well (see Fig. 1). Thus the change in energy spacings ΔE_{23} and ΔE_{13} can be approximated by the potential drop across the centers of the two wells. To tune $\chi^{(2)}$ off resonance, we need a bias field approximately $ez^*E_{bias} \sim \Gamma$, where $z^* \simeq 10\,nm$. This gives an estimate of $E_{bias} \simeq 10kV/cm$. While one of the electrodes (say V_2) is tuned off resonance in this way, the other V_1 is adjusted so that the desired signal frequency is exactly on resonance. This serves as a basis for tuning the OPO. Just as in a laser, the mode that will oscillate in the OPO is the one with the largest gain. Since the gain is directly proportional to $\chi^{(2)}$, we can tune the OPO by simply adjusting V_1 to a different resonance frequency.

This work was supported by the U.S. Army Research Office under Grants DAAH04-94-G-0167 and DAAL03-92-G-0251. I. Lyubomirsky acknowledges the support of the Fannie and John Hertz Foundation.

References

[1] Y. R. Shen, Progr. Quant. Electron. 4, 207 (1976).

[2] C. Sirtori, F. Capasso, J. Faist, L. N. Pfeiffer, and K. W. West, Appl. Phys. Lett. **65**, 445 (1994).

[3] E. Rosencher, and Ph. Bois, Phys. Rev. B, **44**, 11315 (1991).

[4] M. M. Fejer, S. J. B. Yoo, R. L. Byer, A. Harwit, and J. S. Harris, Jr., Phys. Rev. Lett. **62**, 1041 (1989).

[5] F. Capasso, C. Sirtori, and A. Y. Cho, IEEE J. Quantum Electron., **30**, 1313 (1994).

[6] Y. R. Shen, *The Principles of Nonlinear Optics*, (Wiley, New York, 1984).

[7] J. A. Armstrong, N. Bloembergen, J. Ducuing, and P. S. Pershan, Phys. Rev., **127**, 1918 (1962).

[8] G. Almogy, A. Shakouri, and A. Yariv, Appl. Phys. Lett., **63**, 2720 (1993).

Microwave devices based on S-N transition in high-T_c superconducting films.

V. Osadchiy, A. Swishchev, V. Sherman, M. Gaidukov, I. Vendik
St.-Petersburg Electrotechnical University, Russia

St.-Petersburg Electrotechnical University, 5 prof. Popov str., St.-Petersburg, 197376, Russia,
Fax: +7-812 234 99 83

A transition from the superconducting state to the normal one (S-N transition) under dc or pulse control current results in 3-5 orders change of a microwave surface resistance of high-T_c superconducting (HTS) films exhibiting very short switching time (10^{-10}-10^{-11}s). This looks promising for many microwave applications. Microwave switches and digital phase shifters are under consideration in this paper.

The typical configuration of the S-N switching element in single-strip and double-strip form is shown in Fig. 1. The equivalent circuit of the S-N element comprises inductance L and resistance R_S/R_N in series and two capacitances in shunt (Fig. 2). The quality of the S-N switching element can be evaluated by parameter $K=R_N/R_S$. The K parameter is temperature and frequency dependent and for $f \leq 10$ GHz and T=77 K is high enough ($K>10^4$) to provide low insertion loss in microwave switches and digital phase shifters [1].

The SPDT switch with two S-N switching elements is shown in Fig. 3a. The switching element consists of the meander form single-strip line loaded by an open stub and is connected in shunt with a 50 Ω wave impedance microstrip line. The YBCO meander lines were manufactured on a separated sapphire substrate (Fig. 3b.) and then mounted between the transmission line and the open stub on alumina substrate. The frequency dependence of transmission coefficients S_{21} and S_{31} are shown in Fig. 4. The switch exhibits low insertion loss (S_{21}) and high isolation (S_{31}).

Based on the SPDT switch structure the rat-race ring 180^0 digital phase shifter (Fig. 5) was designed, manufactured, and measured. The phase shift is determined by the difference between path lengths for the traveling wave from input to output while switching the S-N meander elements. The insertion loss and the phase shift versus frequency are presented in Fig. 6. The insertion loss level is determined by attenuation in copper microstrip line on alumina substrate, and is negligible small in both S-N switching elements.

In order to widen the frequency band the low-inductance double-strip S-N switching elements were used. Two YBCO strips 0.3 mm long an 5 μm wide with 0.2 nHn inductance form the S-N switching elements in loaded-line type phase shifter (Fig. 7). In order to equalize the insertion losses in both states of the phase

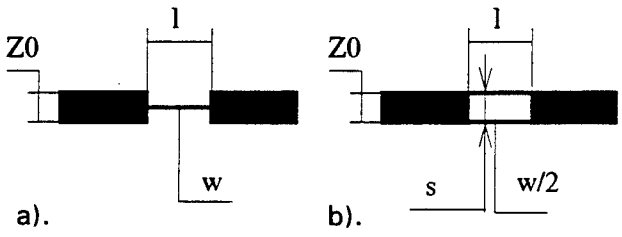


Fig. 1

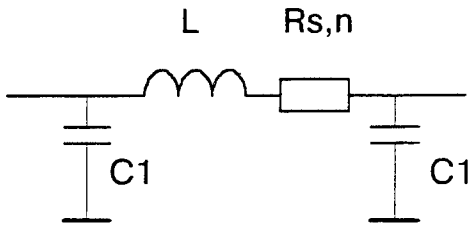


Fig.2

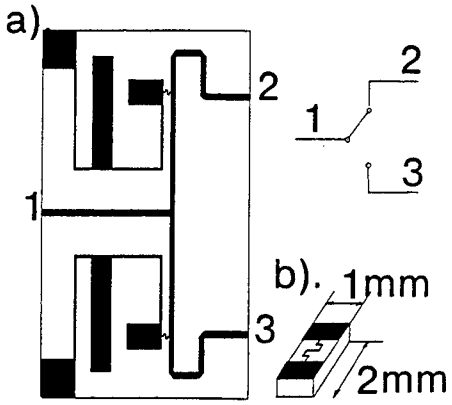


Fig. 3

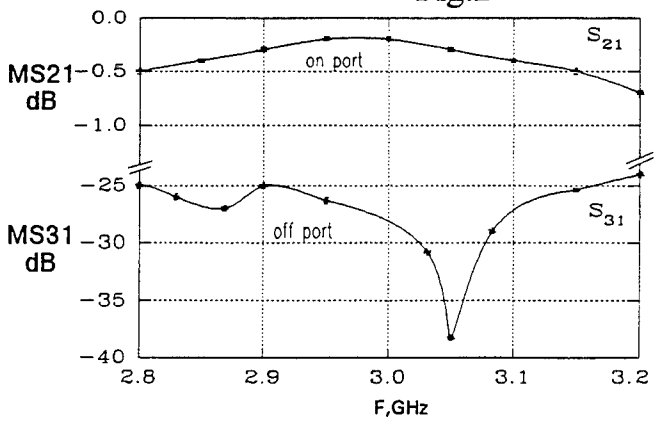


Fig. 4

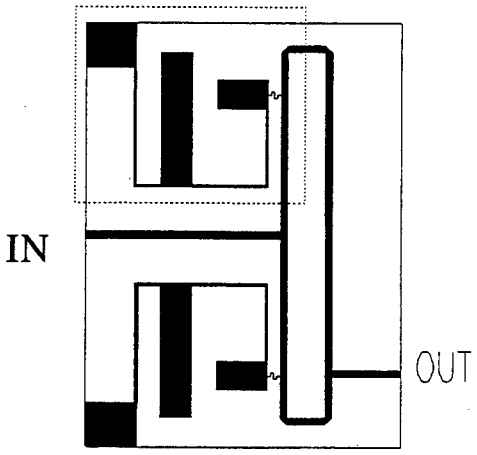


Fig. 5

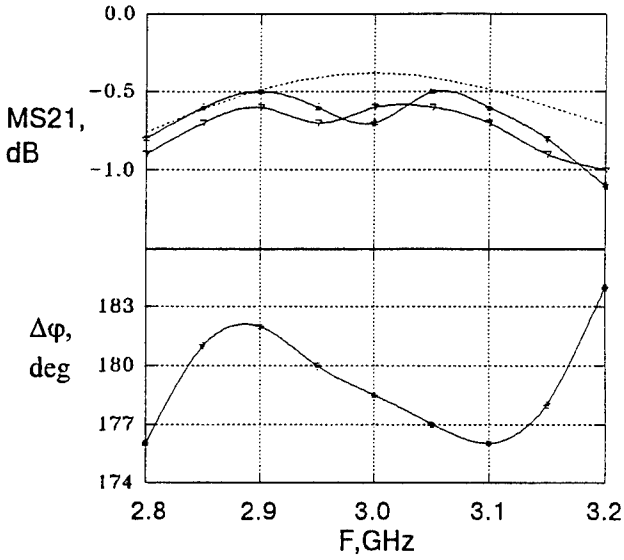


Fig. 6

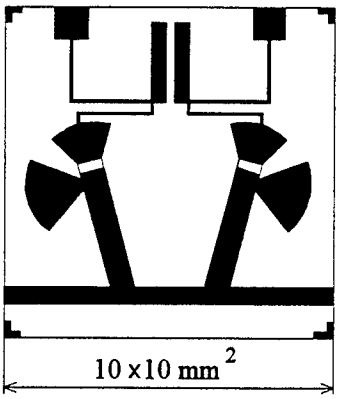


Fig. 7

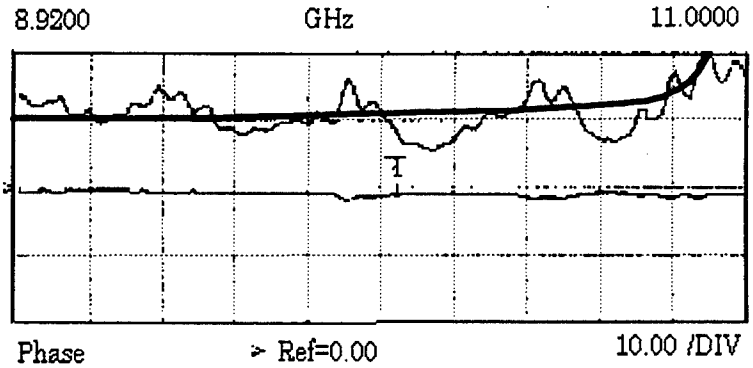


Fig. 8

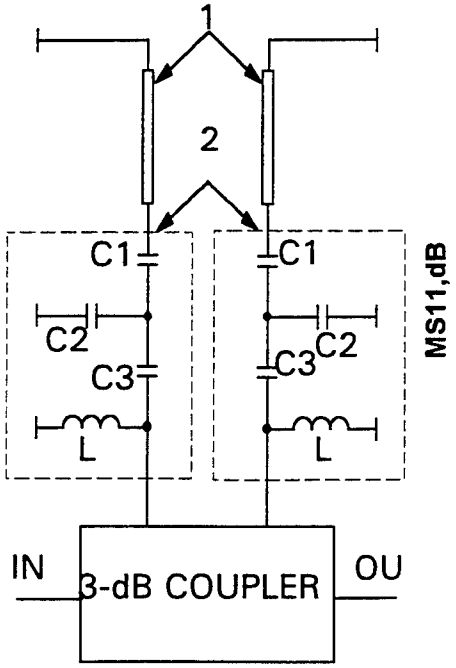


Fig. 9

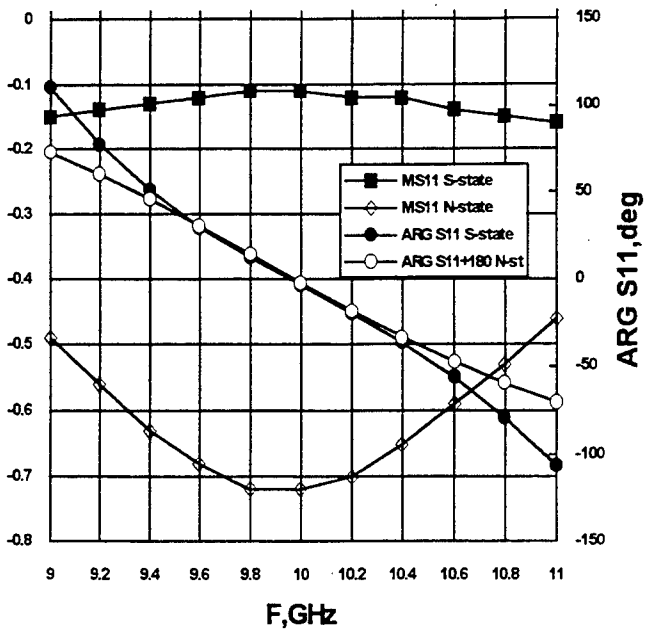


Fig. 10

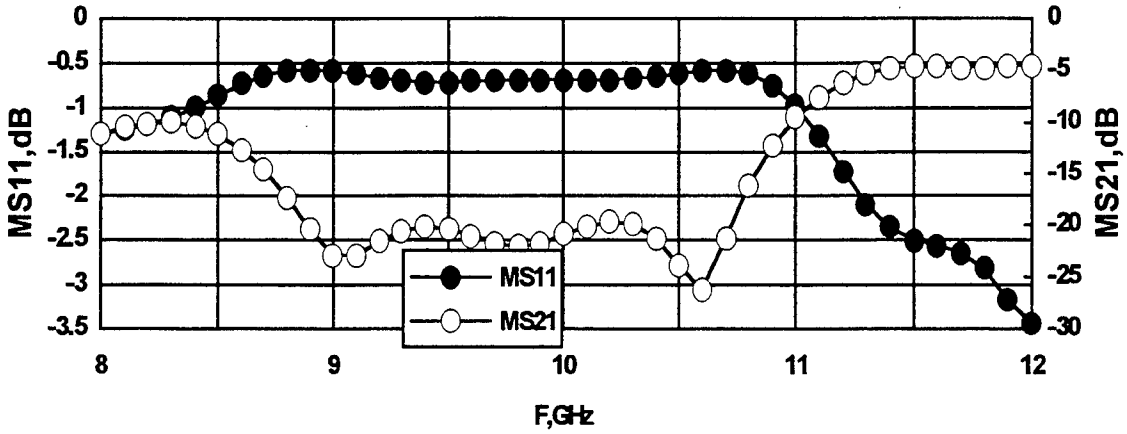


Fig. 11

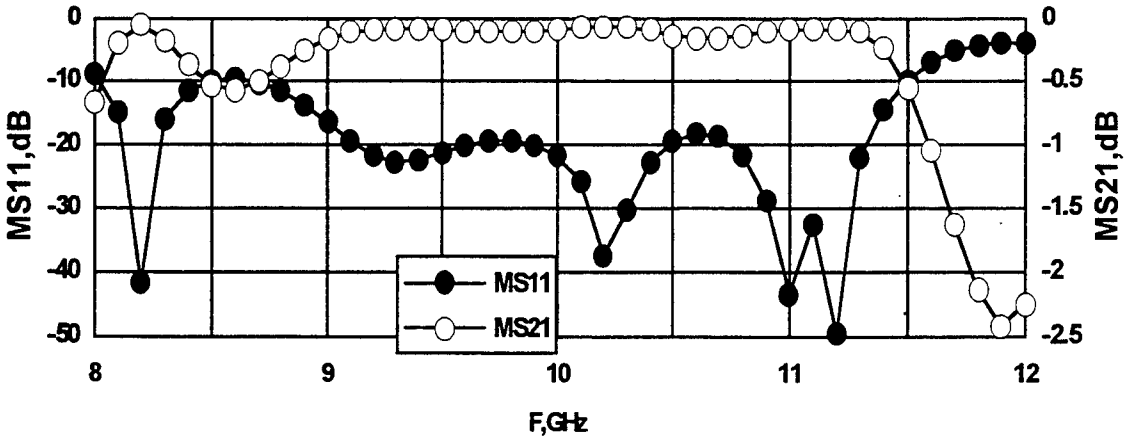


Fig. 12

shifter and to decrease insertion loss, the specially designed transformation network was used. The phase shifter ($\Delta\varphi=11^0$) is manufactured on 0.5 mm thick sapphire substrate using HTS film microstrip lines. The experimental and simulated (thick line) phase shift characteristics of the 11^0 phase shifter are shown in Fig. 8. The measured insertion loss is no more than 0.5 dB.

A wide-band S-N switch design is based on a concept of a symmetrization of the switch parameters in the N- and S-state: $|S_{11}{}^N| = |S_{21}{}^S|$. The equivalent diagram of the wide-band S-N switch is shown in Fig. 9. The switch comprises 3-dB hybrid coupler with identical terminations in two arms. The termination includes the single-strip 0.3 mm long and 10 μm thick S-N switching element (1) and a transformation network (2) which should provide matching between averaged resistance of the S-N element $R_m = \sqrt{R_n \cdot R_s}$ and 50 Ω wave impedance [2]. The modules and argument of reflection coefficient of the S-N switching element are shown in Fig. 10. It should be stressed that the phase difference between the S- and N-state reflection coefficients must be 180^0. The wide-band 3-dB branch-line hybrid with additional half-wave length transmission line sections [3] is used in the device. The device can be considered as the S-N switch, if only one termination of the 3-dB coupler is switched. The characteristics of the wide-band S-N switch in the off-state (only one S-N switching element is in the N-state under control current) is shown in Fig. 11, and in the on-state (both S-N switching element are in the S-state) is shown in Fig. 12. The main advantage of the devices under consideration is a low insertion loss. The short switching time and low noise figure should be taken into account.

Conclusion.

The low-loss switches and phase shifters based on S-N transition in HTS films were designed and measured. The devices are competitive with traditional semiconductor ones.

References.

1. I.B. Vendik, M.M. Gaidukov, D.I. Kaparkov, A.B. Kozyrev, V.V. Kuznetsov, V.N. Osadchiy, "High-T_c superconducting phase shifters", Proc. of 24th EuMC, 1994, Cannes, Nexus Business Com., V. 2, pp. 1906-1911.

2. I.B. Vendik, "The limitation of parameters of one-bit phase shifters based on S-N transition in high-$T_c$superconductors", Microwave and Optic Technology Letters, 1994, V. 7, pp. 644-646.

3. B. Mayer, R. Knochel, "Branchline-couplers with improved design flexibility and broad bandwidth", IEEE MTT-S Digest, 1990, pp. 391-394.

Cryogenic Optoelectronic Measurements of Single Flux Quantum Pulses in Superconducting Circuits

Chia-Chi Wang, Marc Currie, Douglas Jacobs-Perkins, Roman Sobolewski, Thomas Y. Hsiang, and Marc J. Feldman

Department of Electrical Engineering and Laboratory for Laser Energetics
University of Rochester, Rochester, NY 14627

The single-flux-quantum (SFQ) pulse is the basic information "bit" of several new families of digital logic employing superconducting circuits [1]. SFQ logic promises LSI clock rates of hundreds of GHz, much faster than semiconductor logic, with negligible heat generated by the circuitry.

An SFQ voltage pulse is generated when a quantum of magnetic flux, a fundamental "particle," passes through a Josephson junction. The pulse area is quantized: the integral of the voltage over time is exactly equal to h/2e, which is 2.07 mV x ps. Note the units chosen here. SFQ pulses are regularly generated, processed, and detected in many different superconducting circuits. In addition, solitonian fluxons propagating on a Josephson transmission line have been measured by a Josephson sampler, by convolution of the fluxon with the sampler's few-picosecond internal response [2]. However, because of the small amplitude and picosecond timescale, it has not been possible to experimentally observe in detail the dynamics of a Josephson junction, to map out and to delineate the SFQ pulse.

We have *directly* observed superconducting SFQ pulses. These time-domain measurements were achieved using a cryogenic electro-optic (EO) sampling system [3]. The rms noise of the measurement was less than 70 μV and the temporal resolution was 200 femtoseconds.

In our experiments a silicon metal-semiconductor-metal (MSM) photodiode with an electrode separation of 2 μm was used as an optoelectronic switch [4]. The MSM diode was mounted in-line on a Nb superconducting microstrip. With the illumination of a laser pulse, the diode produced a saw-tooth-like waveform which propagated along the microstrip to two Josephson junctions consecutively shunting the strip to the groundplane [5]. Each junction had a critical current I_c of 150 μA at 2 K and the McCumber parameter β_c of 1.5. The inductance between the junctions was estimated to be 6.5 pH. To produce SFQ pulses, the junctions were biased at about 0.7 I_c and the MSM diode was biased at 5 V and illuminated with blue light laser pulses. The SFQ pulses generated by the second Josephson junction then propagated down the microstrip. By changing the light intensity, different switching amplitudes from the MSM diode were generated and as a result different numbers of SFQ pulses were generated. The entire sample chips, including the MSM diodes, were fabricated using conventional Nb technology [6].

The time-domain observation of the SFQ pulses was made using a cryogenic EO sampling system by non-invasive measurements of the microstrip fringe field. The EO sensor was a lithium tantalate ($LiTaO_3$) crystal attached to cover the superconducting circuit [7]. A

titanium-doped sapphire mode-locked laser with ~150-fs pulses was used. The frequency-doubled (400 nm) light penetrating a dielectric coating on the $LiTaO_3$ crystal was directed at the MSM diode mounted on the device under test (DUT), acting as the switching beam. The fundamental light (800 nm) serving as the sampling beam passed through the $LiTaO_3$ crystal, experienced the birefringence\ caused by the fringe electric field from the microstrip, and was reflected to the analyzer. Both the switching and sampling beams were focused by a single microscope objective and delivered through an optical window to the DUT, which was immersed in superfluid helium.

Calibration, converting the measured fringe field to the "real" voltage transient, was accomplished using a passive superconducting microstrip that contained no Josephson junctions and was separated from the DUT by 300 μm. A known electrical signal was applied to the passive transmission line to determine the voltage scale-factor. The sampling beam was then moved back to the DUT. Sensitivities at the two measurement points were assumed equal, justified by knowing that the crystal was in uniform contact with the chip to within 250 nm (as verified by interference fringes observed through the crystal).

A sequence of experimental results is shown in the Figures. Figure 1 is the response of the Si-based MSM diode. Figure 2 shows the junctions' output for moderate light intensity; it is unambiguous -- one SFQ pulse. The measured pulse in Fig. 2 has a width of ~3.2 ps and an amplitude of ~0.7 mV. The time-integrated voltage of the pulse is shown by the dashed line. It is 2.1 ± 0.2 mV x ps, compared to the known magnitude of the magnetic flux quantum: h/2e = 2.07 mV x ps. The shape of the measured SFQ pulse in Fig. 2 agrees very well with simulations based on JSPICE [8]. Figure 2 represents ~15 minutes of data acquisition.

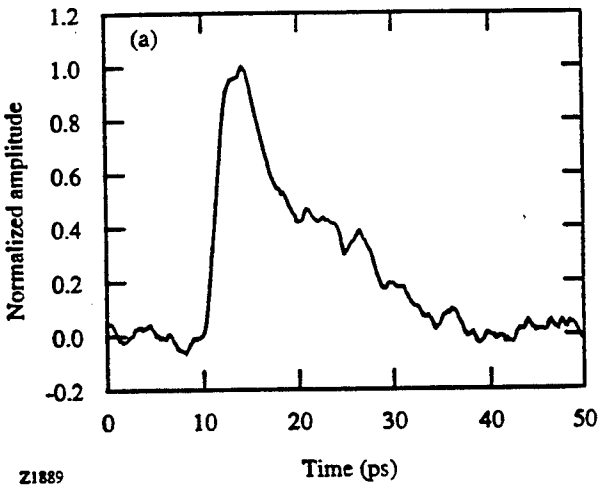


Fig. 1 Output of the Si-based MSM diode excited with a femtosecond laser pulse.

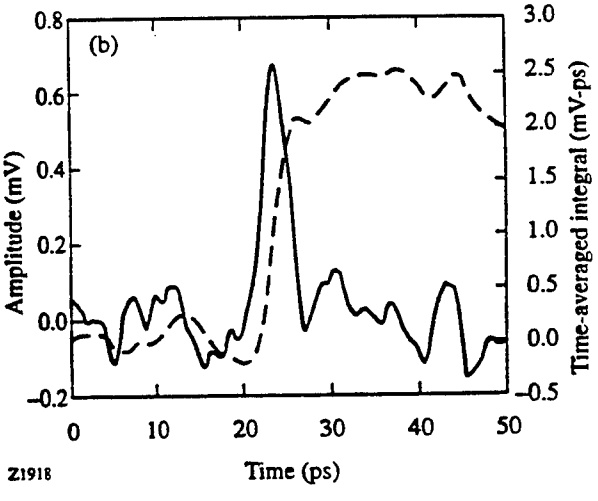


Fig. 2 Junction output voltage at low diode excitation, showing an SFQ pulse. The dashed line is the time integral of the voltage.

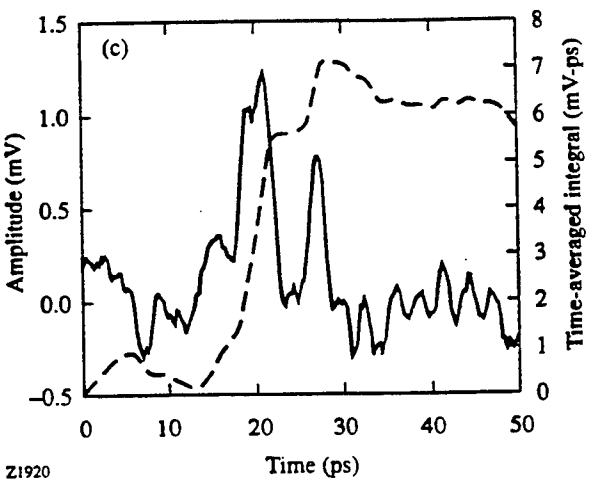


Fig. 3 Junction output at higher diode excitation, corresponding to three flux quanta.

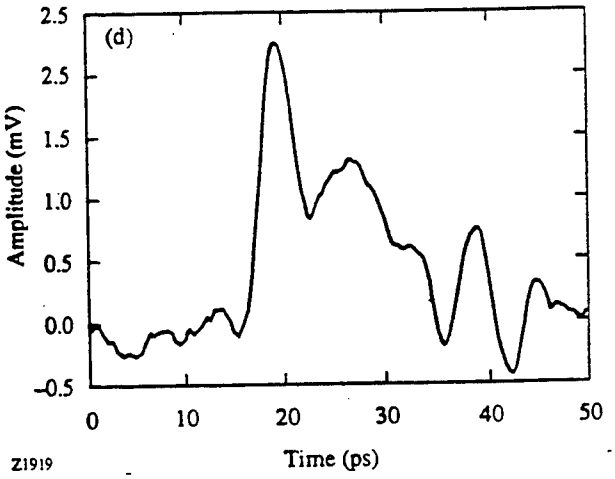


Fig. 4 Junction output with still higher diode excitation level.

With increased light intensity multiple flux quanta are generated by the Josephson junctions. In Fig. 3 we see that three flux quanta have been generated -- the time-integrated voltage is about 6 mV x ps. In this case the JSPICE simulations are less successful at duplicating the experimental result. At still higher input levels, as in Fig. 4, the output begins to acquire the overall shape of the input (Fig. 1) with the Josephson junction dynamics superimposed, even though the time-integrated voltage must still be constrained to be a multiple of h/2e.

Superconducting circuit design has relied completely on simulation tools such as JSPICE. Real Josephson junctions, however, are subject to numerous effects, many well-known and well studied, which are not included in the simple resistively-shunted junction model always used to simulate SFQ logic circuits. In addition, SFQ circuit simulations do not generally include noise, microwave effects, etc. It is crucial to determine how well standard simulations concur with actual experiments, for common circuit configurations, and whether in certain cases simulation routines must be expanded to include other effects.

Now, with the direct observation of the SFQ pulses, it is for the first time possible to examine *directly* the dynamics of ultrafast superconducting digital circuits in more detail. We will discuss the results of several experiments which have been proposed [9] and are currently in progress.

In conclusion, our cryogenic electro-optic sampling system is a powerful tool for the study of superconducting circuits. It combines temporal resolution of 200 fs and voltage resolution down to sub-hundred-microvolts with the versatility of non-invasive probing. This leads to the possibility of *nodal analysis* of superconducting circuits -- the sampling beam can be focused down to less than 2 μm and placed arbitrarily on the DUT. The instrument will also be valuable for the investigation of other electronic phenomena at cryogenic temperatures.

ACKNOWLEDGMENTS

This work was supported by the University Research Initiative at the University of Rochester sponsored by the Army Research Office grant No. DAAL-03-92-G-0112. C.-C. Wang also acknowledges the support of the Frank Horton Graduate Fellowship Program.

REFERENCES

[1] K.K. Likharev and V.K. Semenov, IEEE Trans. Appl. Superconductivity **1**, 3 (1991).

[2] A. Fujimaki, K. Nakajima, and Y. Sawada, Phys. Rev. Lett. **59**, 2985 (1987).

[3] S. Alexandrou, R. Sobolewski, and T.Y. Hsiang, IEEE J. Quantum Electron. **28**, 2325 (1992).

[4] S. Alexandrou, C.-C. Wang, T.Y. Hsiang, M.Y. Liu, and S.Y. Chou, Appl. Phys. Lett. **62**, 2507 (1993).

[5] C.-C. Wang, M. Currie, D. Jacobs-Perkins, M.J. Feldman, R. Sobolewski, and T.Y. Hsiang, Appl. Phys. Lett. **66**, 3325 (1995).

[6] HYPRES Process Design Rules Manual (available from HYPRES Inc., 175 Clearbrook Road, Elmsford, NY 10523).

[7] D.R. Dykaar, R. Sobolewski, J.M. Chwalek, J. Whitaker, T.Y. Hsiang, G.A. Mourou, D.K. Lathrop, S.E. Russek, and R.A. Buhrman, Appl. Phys. Lett. **52**, 1444 (1988).

[8] S.R. Whiteley, IEEE Trans. Magnetics **27**, 2902 (1991).

[9] M. Currie, C.-C. Wang, D. Jacobs-Perkins, R. Sobolewski, and T.Y. Hsiang, IEEE Trans. Appl. Superconductivity **5**, 2849 (1995).

The Spatial Distribution of the Critical Current Density in $YBa_2Cu_3O_7/YBa_2(Co_{0.01}Cu_{0.99})_3O_7/YBa_2Cu_3O_7$ Edge Junctions

S. C. Gausepohl†, Mark Lee† and K. Char*

†*University of Virginia, Charlottesville, VA.*

* *Conductus, Inc. 969 W. Maude Avenue, Sunnyvale, CA.*

Efforts to fabricate Josephson junctions from high-T_c superconducting materials have directed researchers to investigate weak links in $YBa_2Cu_3O_{7-\delta}$ (YBaCuO) structures. In an effort to find a reliable and reproducible fabrication technique in these YBaCuO systems, many new types of junctions have been invented over the past few years. At one time, grain boundary junctions (GBJs) seemed to be the most promising candidate to base future work on, but gross spatial inhomogeneities at the interface[1] have stalled the development of useful devices. Later, an S-N-S edge junction process[2] (see Fig. 1) was developed by Conductus, Inc. They used an artificial oxide normal metal layer with close lattice match to YBaCuO as the junction weak link. This allowed for in situ epitaxial growth. Much of the initial emphasis on weak-link materials fell on two metallic ruthenates, $CaRuO_3$ and ferromagnetic $SrRuO_3$, but devices using these oxides still showed strong inhomogeneities at the S-N interface[3]. The present design still uses an edge junction process. However, the normal metal weak link is now 1% cobalt-doped YBaCuO (YBaCoCuO). YBaCoCuO has a lower critical temperature ($T_c \approx 55$ K) than pure YBaCuO and hence acts as a weak link between 55 K and 90 K. These S-N-S devices have strong resistively shunted Josephson I-V shapes at 77 K, exhibit Shapiro steps in microwave fields, and most importantly, have cleaner I_c diffraction patterns in magnetic fields (H) than their GBJ or S-ruthenate-S predecessors. Data taken from these I_c vs. H modulation patterns suggest a critical current with far fewer spatial inhomogeneities. The emphasis of this paper is on the field diffraction experiments we performed on these junctions, and on the Fourier transform model we used to derive a consistent quantitative picture of the spatial distribution of the critical current.

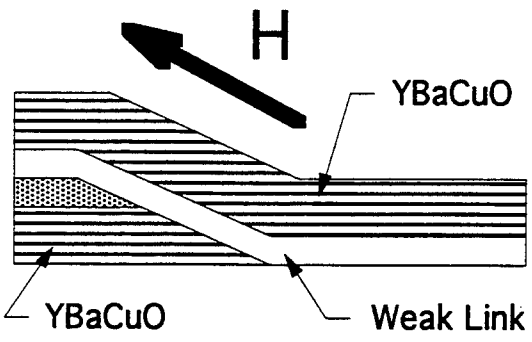


Fig. 1. A schematic cross section of an edge junction and field direction studied in this paper. The slanted interface is created by a uni-directional ion mill process. The slope is typically at a 30° to the plane of the substrate.

The YBaCuO/YBaCoCuO/YBaCuO edge junctions were fabricated using the process described in Ref. 2. Each junction we measured was 4 μm in total width. The thickness of the YBaCoCuO layer was d_N=200 Å, with 0.2 μm YBaCuO electrodes on either side of the 30° incline (see Fig. 1). We applied a field (H) in all relevant orientations: Parallel (H parallel to the substrate; perpendicular to the current), Perpendicular (H perpendicular to the substrate and hence the current), and Slant (H directed along the 30° incline of the junction). Field modulation periods of $I_c(H)$ from the Parallel and Perpendicular geometries agreed with standard models using the physical size of the devices and will be discussed thoroughly in a future paper. We concentrate here on the Slant field data, since in this orientation, the junction geometry is relatively free from unusual ramp geometry effects. The data shown in this paper were taken using an AC current bias $I(t) = I_0\cos(2\pi f t)$, where $f = 77$ Hz and $I_0 = 0.2$ mA. All of the junctions were immersed in liquid nitrogen and had a four-point finite voltage resistance $R_N \approx 0.25\ \Omega$ which was field-independent. A magnetic field up to 100 gauss could be applied using a copper coil which itself sat in a μ-metal cylinder to reduce the residual field to $\leq$ 10 mG. The voltage across the junction was monitored both on an oscilloscope and through a lock-in amplifier: I_cs could be measured directly from the scope, or from the output of the lock-in converted into current units using the scope I-V curve.

There were two distinct classes of junctions. Junctions of type "A" had a modulation field period $\Delta H \approx 0.5$ G, $I_c(0) \approx 20\ \mu$A and diffraction lobes that died away within a few gauss (as would normally be expected with a clean junction of this size). These were in stark contrast to junctions of type "B" which had a $\Delta H \approx 0.3$ G, a much larger $I_c(0) \approx 100\ \mu$A and diffraction lobes that persisted out to at least several kG.

The field periods (ΔH) of the $I_c(H)$ modulation yield information about the magnetic size of the junction[4]. Taking demagnetization factors[5] into account, the relationship is approximately $\Delta H \approx \frac{\Phi_0 t}{1.2w^2(2\lambda + d_N)}$, where λ is the London penetration depth, t and w are the thickness and width of the junction and Φ_0 is the flux quantum. From this, we find that the type B samples have an effective magnetic width $w \approx 5\ \mu$m, while the type A give $w \approx 3\ \mu$m. These numbers show that the magnetic width is comparable to the physical width of 4 μm.

The quantitative shape of the diffraction pattern gives information about how the supercurrent distributes itself in space along the face of the junction. The I_c vs. H lineshape is an absolute magnitude Fourier transform (FT) of the spatial distribution of the supercurrent density[6] $J_s(x)$, as given by the equation $I_c(H) = \left|\int_0^w J_s(x)e^{i\Phi(x)}\right|$. Here $\Phi(x)$ is the phase difference between the two superconducting electrodes and $J_s(x)$ is the supercurrent density distribution along a line perpendicular with H, integrated in the direction of the field. Since only the magnitude of the Fourier transform is measured by $I_c(H)$, this relation cannot be inverted uniquely to obtain $J_s(x)$. The next

logical alternative is to guess at a reasonable functional form for $J_s(x)$, run a Fourier transform on that assumption and match that transform against the data.

Figure 2 shows a typical modulation of I_c in field for a type A junction. The empirical result is shown as a solid line, while the computer generated fit is represented by the dotted line. The data clearly shows a strong central maximum with a 1st order lobe centered at 0.8 gauss. There is no discernible structure at fields higher than 1 gauss. The sharp decay of $I_c(H)/I_c(0)$ of a type A junction with just a single side-lobe is strongly suggestive of a "center-wedge" current (see Fig. 2 inset). The FT of this particular current profile reproduces this single secondary peak as well as the relative peak heights. At field values past the single peak, the computer model and the data show similar small variations, although at critical currents this low ($I_c <$ 3 μA) thermal fluctuations[7] at 77 K begin to smear the signal.

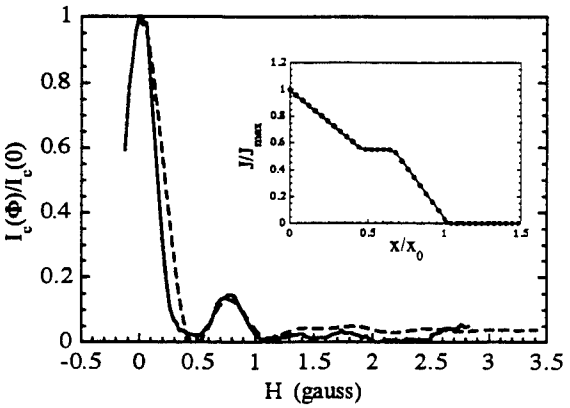


Fig. 2. Field modulations of $I_c(H)/I_c(0)$ for a type A sample at 77 K. Data is the solid line and the FT fit is the dotted line. Inset: The supercurrent distribution that the fit is based on.

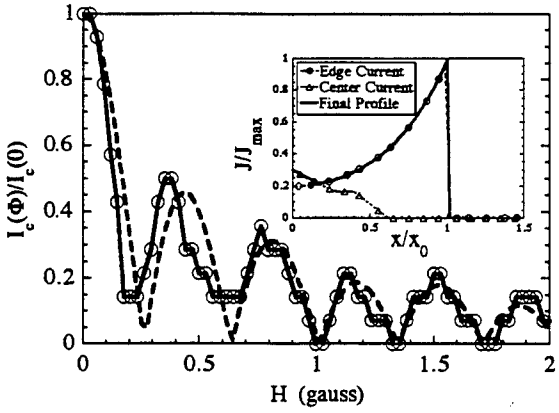


Fig. 3. Magnetic field dependence of $I_c(H)/I_c(0)$ for a type B junction at 77 K. The applied field was directed along the slant edge. Inset: Supercurrent distribution that best fits the data

The I_c vs. H pattern for a representative type B junction is found in Fig. 3. This data shows that the central maxima is now accompanied by many side lobes which continue out to high field. The decay of the I_c of type B junctions is a much slower function of field than type A, so the FT fit shown required a different current density profile. More specifically, the type B lineshape is indicative of a strong supercurrent near the junction edges. We can try to understand quantitatively both the larger $I_c(0)$, the smaller ΔH and the $I_c(H)$ shape by assuming $J_s(x)$ is a combination of the "center-wedge" distribution found in type As and an "edge-current" with a decay tailored to the peak heights in the data. After choosing functional forms[6], the two parameters of this model are the ratio of the ΔH periods and the ratio of the magnitudes of the type A and type B current profiles. Both of these parameters are constrained by the data. The width ratio is given by the ΔH for each type, and the magnitude ratio is dictated by the values of $I_c(0)$. Using these constraints, we arrive at the current density shown as an inset to Figure 3. The FT of this new profile reproduces the peak heights, shapes and their persistence in high field.

The presence of this side current in the type B junctions is more than likely a defect that needs to be corrected in future revisions of the processing technology. It is possible that the finger sides are damaged during an ion mill step used in the fabrication of these new edge junctions. This would allow for easier flux penetration along the edges, resulting in a concentration of the screening current in that area. It is also possible that weak link layer material has become oxygen deficient during the fabrication process. It is known that the T_c of YBaCoCuO rises as oxygen is lost from the crystal lattice. The prospect that these side currents are a result of a stronger superconducting link at the edges will be investigated in future experiments.

As the high T_c junctions of today get better than the early attempts at GBJs and S-N-S heterostructures, the technology quickly approaches a state reliable enough to begin the production of commercial devices. Before that point is reached, the distribution of supercurrent and the flux penetration at the interfaces must be understood. This work has presented a clear and consistent model which points to a buildup of supercurrent at the edges of these new YBaCoCuO edge junctions. Although these junctions do not possess the spatial inhomogeneities of the other high T_c junctions and are thus obviously superior devices, this edge current problem must be corrected before clean Josephson behavior can be observed.

[1]O. M. Froehlich, H. Schulze, A. Beck, B. Mayer, L. Alff, R. Gross, and R. P. Huebener, Appl. Phys. Lett. **66** (17), 2289 (1995).

[2]K. Char, M. S. Colclough, T. H. Geballe, and K. E. Myers, Appl. Phys. Lett. **62**, 196 (1993).

[3]S. C. Gausepohl, Mark Lee, L. Antognazza and K. Char, Appl. Phys. Lett. **67** (9), 1313 (1995).

[4]T. Van Duzer and C. W. Turner, *Principles of Superconductive Devices and Circuits* (Elsevier, New York, 1981).

[5]P. A. Rosenthal and M. R. Beasley, Appl. Phys. Lett. **59**, 3482 (1991).

[6]A. Barone and G. Paternò, *Physics and Applications of the Josephson Effect* (John Wiley and Sons, New York, 1982).

[7]V. Ambegaokar and B. I. Halperin, Phys. Rev. Lett. **22**, 1364 (1969).

HOT ELECTRON BOLOMETRIC HIGH-Tc MIXER:NEXT STEP

Gregory N. Gol'tsman
Department of Physics, Moscow State Pedagogical University, 119435 Moscow, Russia

Abstract -This paper describes the basic conception for the development of a hot-electron high-T_c superconducting terahertz mixer. A small bridge manufactured from a high quality thin $YBa_2Cu_3O_{7-\Delta}$ (YBCO) film may serve as a sensitive device in the receiver of submillimeter and infrared radiation. In contrast to the Schottky diode mixer, this mixer has a low and easily controllable optimum local oscillator (LO) power. The mixer can operate at liquid nitrogen (LN_2) temperatures when biased to the resistive state with transport current and LO power. Under irradiation, a nonequilibrium distribution of excited electrons arises, which may be viewed as the hot electron phenomenon. Theoretically, under such conditions a small conversion loss can be obtained. A mixer IF bandwidth of 18 GHz, limited by the measurement system, was experimentally obtained at 3 mm, 10 μm, and 1.5 μm waveranges. Whole an intrinsic limit of 100 GHz predicted. In-plane sizes of the film can be easily adjusted so as to be matched to a small antenna and also to provide the necessary dynamic range and LO power. At present the minimum attainable sizes are believed to be $0.3\times0.5\ \mu m^2$ with the film thickness ~ 10 nm. This may be estimated to correspond to 10 μW of the optimum LO power and SSB noise temperature limit due to the intrinsic mechanisms has been estimated as low as 2500 K. The spectral variation of the mixer performance is not expected to exhibit any gap peculiarities.

I.Introduction

Recently, a growing interest has been observed in hot electron bolometric HEB mixers utilizing thin superconducting films in the resistive state[1] has recently arisen in connection with prospects of terahertz applications. The potential advantage of the hot electron mixers is that they can be made simple, from the view-point of both the circuit (low or no parasitic reactances) and especially the technology. This is particularly obvious if we compare them with the superconducting SIS mixers using Nb tri-layer technology, which have demonstrated excellent sensitivity, of the order 5 times the quantum limit for the frequencies below 700 GHz. For frequencies at and above the band gap of niobium (700 GHz) the niobium SIS mixer is not expected to perform so well. Only Schottky diode mixers with the noise temperature about 100 times the quantum limit work reliably near and above 1 THz[2]. InSb mixers have a noise temperature about 20 times the quantum level in the 0.5 to 1 THz frequency range, but the bandwidth of 1-2 MHz is too narrow for most applications. Hence, there are special reasons to investigate the mixing mechanisms which do not suffer from these limitations at THz frequencies. The main superconducting materials which have been investigated for HEB mixers so far are Nb and NbN. In this paper we will concentrate on High-T_c superconductor YBaCuO.

HEB superconducting mixers have all the advantages of the bolometers, i.e. they have no conversion efficiency restriction throughout the submillimeter and infrared waverange while having a much broader IF band. As shown by the experiments with thin YBCO films[3], the IF bandwidth may even exceed 18 GHz. By extrapolating the experimental data, the IF bandwidth limitations may be estimated at ~ 100 GHz.

II.Experimental investigations.

After the high-temperature superconductivity was discovered, hundreds of papers have been published on observation possibilities and research in nonequilibrium phenomena induced by electromagnetic radiation. A considerable share of these papers is devoted to the study of the Josephson effect on a random network of weak links in granular films in contrast to the bolometric effect in the same film at $T\sim T_c$. By now, all

characteristic features of Josephson effect in HTSC are known, which permits to draw a reliable distinction between this effect and a nonequilibrium response of a different nature. In particular, the features include response dependencies on radiation frequency, power, and the magnetic field. The major part of the remaining papers especially in the fist few years after the discovery, deal with the comparison of the current or temperature dependencies of the voltage response of the film to radiation, on the one hand, and the respective dependency of the temperature derivative of resistance *dR/dT*, on the other hand. Later, some papers (e.g.[4]) showed that all peculiarities of the observed response with a time constant at nitrogen temperatures of the order of several nanoseconds are accounted for by the bolometric effect. It was discovered[5] that a much faster nonequilibrium response exists against the background of the bolometric effect, with the time constant of the order of several picoseconds.

Our group started to study the nonequilibrium processes in HTSC films, induced by electromagnetic radiation, as soon as the high-temperature superconductivity was discovered[6]. One of the most difficult experiments was the measurement of the relaxation time τ of the nonequilibrium part of resistance, as it was clear from the start that it is very small. The unique backward wave oscillator BWO technique of the terahertz range made it possible to measure the $\tau \sim T^{-1}$ law by mixing experiment[7]. We could also access the value $\tau \approx$ 1-2 ps at nitrogen temperatures. The interpretation of the studied nonequilibrium effect as the heating of the electron subsystem of the film by radiation results in the fact that τ must be interpreted as the time of its cooling, i.e. is - with the precision of a coefficient of the order of one - as the time of electron-phonon interaction $\tau_{e\text{-}ph}$.

In paper[3] we reported on the mixing of semiconductor laser radiation (λ = 1.56 μm) in an epitaxial YBCO thin film. We demonstrated an IF bandwidth of 18 GHz, which was the limit of our post-detection instrumentation and our sample mounting technique. The intrinsic IF bandwidth can be estimated from the electron-phonon interaction time to be ~ 100 GHz.

In the optical mixing experiments high quality 50 nm thick epitaxial YBCO films were laser deposited on $LaAlO_3$ substrates and patterned with photolithography and ion milling[8]. A mixer structure (20×20 μm^2 large) consisting of ten ~ 1 μm wide parallel strips, was used to reduce heating in the active region. *In situ* gold contacts provided a low contact resistance. After processing, T_c was 84.0 K, ΔT_c=1.9 K, and j_c=2×10^6 A/cm^2 at 77 K.

Two wavelength-matched InGaAsP distributed feedback quantum-well lasers emitting at 1.56 μm wavelength with 2 MHz linewidth were used in the mixing experiment. The radiation was coupled into tapered single-mode fibers and combined in a 50:50 coupler. One of the outputs of the coupler was used to monitor the optical power, while the other was fed to the mixer via an optical isolator. The lasers were connected in series and driven by a single power supply. By changing the current though one of the lasers with a resistive shunt, its wavelength could be tuned close to the wavelength of the other laser. It this way, a difference frequency from 100 MHz to 18 GHz could be selected to fit our IF

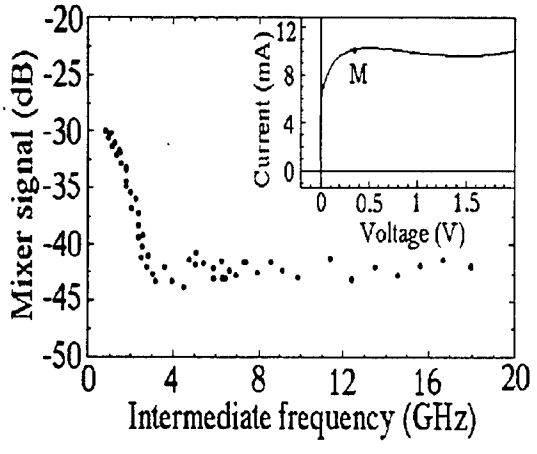


Fig.1 Measured mixer signal as a function of the intermediate frequency. The inset shows the operating point M in the current-voltage curve at 77 K.

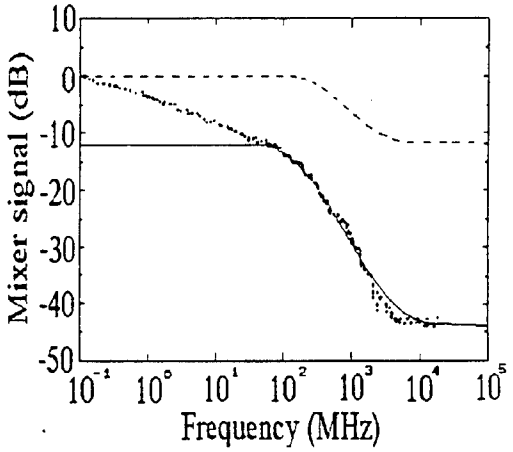


Fig.2 Measured mixer signal as a function of the intermediate frequency. The solid line is the fitted electron-heating model, and the dashed line represents the performance of an optimized mixer.

amplifiers. The amplitude was found to be stable (within ±2 dB) across the whole frequency range when checked with a calibrated 34 GHz bandwidth pin-type photodiode. The mixer was current biased to the resistive state at the point for maximum response and the signal was amplified and detected with a spectrum analyzer.

The measured frequency spectrum at 1.55 μm of the photoresponse at 77 K is shown in Fig.1 and Fig.2. As seen from the results of the 1.55 μm experiment (Fig.2), the frequency characteristic of the photoresponse above 3 GHz is almost independent of the intermediate frequency. The appearance of the plateau shows the presence of fast relaxation processes in the studied sample.

In the paper [9] the continuous wave fixed frequency CO_2 laser (LO) and PbSnTe tunable laser (signal) were used in the mixing experiment on 10 μm wavelength with the same mixer chip as for 1.55 μm radiation. The study has shown that the IF spectra for these two wavelength are identical.

Similar experiment with BWO technique has been performed[10] for 3 mm wavelength with the same mixer chip. The IF response also shows a fast bolometric effect near 100 MHz, followed by a roll-off signal. This continues to the high frequency plateau, which extends to at least 18 GHz, but for the 3 mm waverange it is located some 10-20 dB higher than on the optical curve. The nature of this plateau for the optical range is a hot electron effect. The analysis of the results for the high frequency plateau in the 3 mm wavelength shows that the mixing originates from the detection at the IV-curve nonlinearity. Within this waverange, the hot electron effect is dominating in the nonlinearity; its characteristic cut-off frequency is just above 100 GHz. Thus, a decrease in the high frequency plateau level at higher frequencies should be expected. Accordingly, one may expect that in the terahertz range the plateau is transformed into a frequency dependence identical to that for the optical spectrum.

III.Discussion.

We will now discuss a possible conversion gain of the hot electron HTSC mixer[11]. It should be noted that the working point corresponding to the maximum of the IF signal for optical mixing is situated on the current-voltage (I-V)curve near the maximum (point M on inset of Fig.1). The shape of the IV-curve is caused by the overheating of the sample and by the heat instability. The conversion gain near the maximum can even exceed unity. In our case, however, it is only possible when the IF is zero. As the difference between the conversion gains at zero IF and at high frequencies is about 40 dB for the examined sample, it can be supposed that the absolute value of conversion loss at gigahertz frequencies is ~40 dB.

Let us now consider the sources of the losses and ways to decrease them. The shape of the frequency characteristic, showed in Fig.2, was discussed previously[8]. It was found that the low frequency slope of the signal is caused by the heat diffusion in the substrate, and the steeper slope of the signal amplitude at frequencies f>80-100 MHz is caused by the thermal boundary resistance between the film and the substrate. The characteristic cutoff frequency of this process $f_0=(2\pi\tau_{es})^{-1}$, where $\tau_{es}=d/\alpha u$ is the escape time of the acoustic phonons from the film, d is the thickness of the film, u is the sound velocity, α is the acoustic transparency of the boundary between the film and the substrate. In our analysis, the nonequilibrium states of the quasiparticles will be described in terms of hot electrons.

In the operating point M (see inset of Fig.1) the sample is in the state of thermal instability. In this case we can use the following equation from bolometer theory:

$$I^2 \frac{dR}{dT_e} = G, \qquad (1)$$

where I is the bias current, $R(T_e)$ is the temperature dependence of the sample resistance in the superconducting transition region and G is the thermal conductivity between the film and the surroundings. The value G may be written as:

$$G = \frac{C_e V}{\tau_{e-ph}} \frac{1}{1+\frac{dC_e R_{bd}}{\tau_{e-ph}}+\frac{C_e V}{\tau_{e-ph}}\frac{R_{sub}}{S}} \qquad (2)$$

where V is the volume of the film, S is the film area, C_e is the specific heat of the electron subsystem, d is the film thickness, R_{sub} is the thermal resistance of the substrate, $R_{bd}=\tau_{es}/(C_{ph}d)$ is the film/substrate thermal boundary resistance, and C_{ph} is the specific heat of the phonon subsystem.

The thermal conductivity G depends on the temperature of the electron subsystem. At high frequencies, up to $f=(2\pi\ \tau_{e\text{-}ph})^{-1}$, where slow processes like the escape of the nonequilibrium phonons and the heat diffusion in the substrate are not very important, the high frequency plateau is due to the fast nonequilibrium response. In this frequency region the value G increases to:

$$G_0 = \frac{C_e V}{\tau_{e-ph}}, \quad (3)$$

which is determined only by the cooling time of the electron subsystem, $\tau_{e\text{-}ph}$. If the magnitude of the response is proportional to G^{-1}, the conversion gain is proportional to G^{-2}. Therefore, the ratio of conversion gains at low, K_0, and at high frequencies, K_{HF}, may be written as:

$$\frac{K_0}{K_{HF}} = (1 + \frac{dC_e R_{bd}}{\tau_{e-ph}} + \frac{C_e V}{\tau_{e-ph}} \frac{R_{stb}}{S})^2 \quad (4)$$

As was noted above, our measured value of this ratio is about 10^4 as was noted above. If G is enhanced by increasing the substrate heat conductivity and decreasing the film thickness, the conversion gain at low frequency will not change, but, as follows from(4), it will increase at high frequency. Consequently, a mixer made of a 100 Å thick YBCO film and having a zero thermal resistance in the substrate will have a flat intermediate frequency dependence up to ~500 MHz, τ_{es}= 0.3 ns, and the ratio K_0/K_{HF} will be about 15 dB, as shown by the dashed line in Fig.2.

As any non-linear volume devices, hot-electron superconducting mixers require an optimal local oscillator power. So, the smaller the volume of the mixing element, the lower the power. For this reason, the tendency to reduce the P_{LO} is naturally limited by the manufacturing technology of a small in-plane sized thin HTSC film. This is of course accompanied by a reduction in dynamic range. However, the two parameters are easily controlled by choosing a film of the right size. At present the minimum attainable sizes are believed to be 0.3×0.5 μm^2 with the film thickness ~ 10 nm. This may be estimated to correspond to 10 μW of the optimum LO power.

An intrinsic noise mechanisms which mainly contribute to the HEB mixer noise temperature are the Johnson noise and the thermal fluctuation noise[1].

The SSB mixer noise temperature contribution due to the Johnson noise can be estimated for high frequency plateau as[12]:

$$T_m^J = \frac{T_{c\Delta} T_c}{(T_c - T)} \frac{\tau_{es}}{\tau_{e-ph}} \frac{C_e}{C_{ph}} \approx 400K, \quad (5)$$

and the thermal fluctuation noise temperature as:

$$T_m^{FL} \cong \frac{2T_c^2}{T_c - T} \approx 2000K \quad (6)$$

By adding together these two contributions we can estimate a possible SSB mixer noise temperature at T_m≈2500 K

IV.Conclusion.

This paper argues that the hot electron bolometric mixers, which utilize thin (~ 10 nm) YBaCuO superconductive strips as the bolometric medium, have a potential for a sufficient improvement of the receiver noise temperature of heterodyne receivers for the frequency range from 1 THz to several THz, which does not need to be cooled to the liquid helium temperature range.

This research was supported by the Russian Program on Condensed Matter (Superconductivity Division) Grants No.93169 and No.94043. Additional contributions were made by the International Science Foundation (Grants No.NAF000 and No.NAE000) and mutually by the International Science Foundation and the Russian Government (Grants No.NAF300, No.NAE300).

References

1. E.M. Gershenzon, G.N. Gol'tsman, et al. , Sov. J. Superconductivity **3**, 1582 (1990).
2. T.W.Crowe, et al., Proceedings of the IEEE, **80**, N 11, pp. 1827-1842(1992).
3. M. Lindgren et al., Appl. Phys. Lett. **65**, 3398 (1994).
4. G.L.Carr et al., Appl.Phys.Lett., **57**, N25, pp. 2725-2727(1990).
5. E.M. Gershenzon, G.N. Gol'tsman, et al. , Physica C, **185-189**, pp.1371-1372 (1991).
   M.Johnson, Appl. Phys. Lett., 59, N11,pp.1371-1373(1991).
   A.D.Semenov et al., Appl. Phys. Lett., **60**, N7,pp.903-906(1992).
6. E.M. Gershenzon, G.N. Gol'tsman, et al., Sov. Phys. JETP Lett. **46**, 286 (1987).
7. E.M.Gershenzon et al., Solid State Commun. 76, 493 (1990).
8. M. Danerud et. al., J. Appl. Phys. **76**, 1902 (1994).
9. V.Trifonov et al., , EUCAS'95, Edinburgh, Scotland, 3-6 July 1995.
10. G.N.Gol'tsman et al.,ISEC'95,Nagoya, Japan,18-21 September,1995.
11. M.Zorin et al., IEEE Tran. on Appl.Superconductivity, **5**, N2,(1995).
12. B.S. Karasik and A.I.Elantev, Proc. of the Sixth Int. Symp. on Space Terahertz Technology, 21-23 March 1995, Caltech, Pasadena.

A novel method for producing the HTSC planar structures on Si.

O.V.Smolski, M.E.Gaevski, D.V.Denisov, V.P.Chalyi
Ioffe Physico-Technical Institute, Russian Academy of Sciences,
St.Petersburg, Russia.

As is well known one of the pressing tasks at present is the development of new methods for fabrication of the HTSC micron size bridges with the pure surface. It is difficult to perform this task using standard photolithographic methods because the HTSC properties of YBCO films degrade severely after contact with either aqueous solution or organic solvents.

In this paper a novel procedure is presented which allows to avoid a chemical treatment of the HTSC films. As is known the technology of preparing the YBCO HTSC films on Si substrates includes the growth of a buffer layer at the initial stage. Therefore the main idea is to etch a circuit in the buffer layer and then deposit and anneal the YBCO film. The YBCO does not grow in the places where the silicon surface is not covered with the buffer layer since the Si interacts with the deposited constituents (Y,Ba,Cu) in an oxygen environment. In the places where the buffer layer remains, the HTSC film with required configuration is formed. It is necessary to note that in this case several lithographic methods could be used because the compounds of the buffer films (ZrO_2 , YSZ , CeO_2 , Y_2O_3 etc.) are usually chemically steady.

This method was tested on Si(100)\$ZrO_2$ structures grown by the e-beam evaporation of Zr in oxygen [1].Photoresistant masks of bridges were prepared by standard photolitography and then the ZrO_2 films were etched by a collimated neutral argon beam. Thereafter the Si(100)\$ZrO_2$ planar structures prepared by this method were placed to a deposition chamber again and the YBCO films were grown by a co-evaporation using BaF_2 source followed by a two-stage annealing [1].

To investigate a local superconducting characteristics of the prepared structures a low-temperature scanning electron microscopy has been used. This technique allows visualizing the regions with various T_c and j_c as well as grain boundaries junctions [2]. Furthermore, in the present paper the current density distribution across the bridge was studied with the voltage induced by an electron beam mode (EBIV) whose spatial resolution is better than 1 μm. The measured EBIV signal is easily shown to be proportional to square of the local current density [3]. Fig.2 presents the EBIV signal versus a position of the electron probe during a scan across a bridge at 87 K .The region with higher intensity of EBIV agrees with the current localization in the ZrO_2 protected area whose width is 48 μm.

The electrical characteristics of the HTSC bridges have been measured by a standard dc four-point-probe method. The temperature dependence of the resistivity is shown in Fig.2. The superconducting transition temperature is 85 K and the width of the transition is 3 K . By using the current-voltage characteristic of bridges a critical current has been determined and is $1.3 \cdot 10^4$ A/cm^2 at 77 K .

The data obtained enable the conclusion that the new method of producing the HTSC planar structures makes it possible to efficiently limit the current in the active layers and appears promising for the fabrication of different types of devices based on HTSC. Moreover YBCO film of such structures has a pure surface that is important for a number of applications.

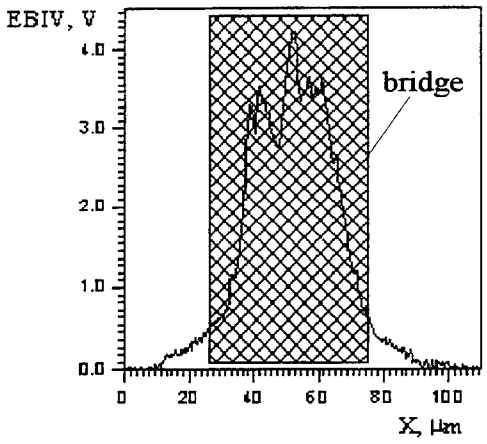


Fig. 1.

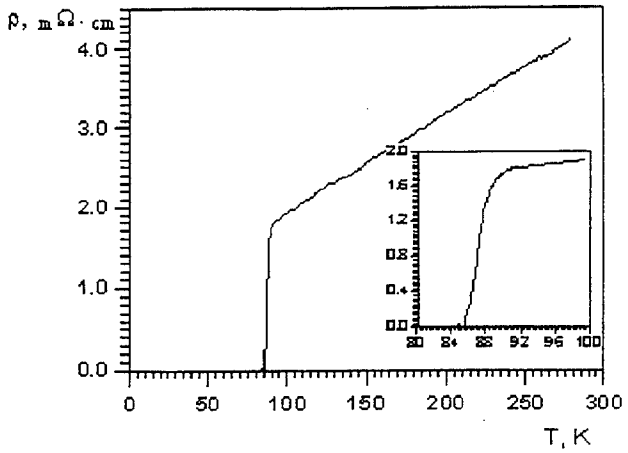


Fig. 2.

1.O.V.Smolski, A.L.Shmaev et al. Sov.Tech.Phys.Lett.(USA) **18**, 684 (1992).
2. R.Gross, D.Koelle Rep.Prog.Phys. **57**, 651 (1994).
3.A.V.Bobyl, M.E.Gaevski et al. Physica C, **246**, 314 (1995).

Modeling of low dimensional structures

D. Lippens
Institut d'Electronique et de Microélectronique du Nord
Université des Sciences et technologies de Lille
Avenue Poincaré-BP69, 59652 Villeneuve d'Ascq cedex, France

Abstract: Recent advances in low dimensional structure fabrication have made it possible to realize new devices with intrinsically quantum mechanisms for operation. In this paper, we report on simulation tools which were employed successfully to study the transport properties of this new class of devices. Two-dimensional systems involving resonant tunneling effect and one-dimensional structures under ballistic transport conditions are more specially addressed. For both cases, we will considered their operation mechanisms on the basis of wave-function calculations in order to predict their potential in terms of speed and current capability.

Introduction:

Electronic transport in confined semiconductor geometries has received increasing interest in the last decade with the potential of a new class of quantum devices whose functionality appears promising for the future[1]-[3]. Basically, two classes of device structure can be distinguished. The first one concerns structures which involve a carrier transport transverse to the heterojunctions. For such a *vertically confined geometry*, the generic structure is the double barrier heterostructure. Tunneling through the ultra-thin barriers and quantum confinement in the quantum well give rise to the so-called resonant tunneling effect which leads to a negative differential resistance region in the I-V characteristics[4].

On the other hand, progress in electron lithography techniques have made it possible to control the lateral extent of a two-dimensional gas created at the interface of a high mobility modulation doped heterostructure. In this case, the motion of carriers is restricted to one dimension so that the structure can be compared to a quantum wire. Furthermore, if the length of these quasi one-dimensional microstructures is less than the phase coherence length over which the electrons retain phase information, the transport is ballistic. Under these conditions, these *laterally confined* structures behave as electron wave guides with conduction properties solely determined by the geometry of systems. In connection with conduction properties, plateau-like structures are obtained in the conductance-voltage characteristics due to transverse quantum effects[5].

Vertically confined geometry:

The first step in the analysis is the calculation of the wavefunctions for all energy values which can be occupied by electrons. By means of this spectroscopic method, a number of basic data can be obtained namely the eigenvalues and eigenfunctions of the quantum system under consideration, revealed by energy resonances, but also the energy selectivity of phenomena. For this calculation, performed by solving the Schrödinger equation, a first difficulty is encountered. Indeed for most real structures, the heterostructure barriers block a significant part of the incoming electrons which are

spread in energy. This leads to strong band bending effects in the conduction band due to space charge effects. At this stage, to take into account these effects, one can either solve self-consistently the Schrödinger and Poisson equations or use a Thomas Fermi approach. Both methods have been reported in the literature and give realistic conduction band profiles as it is exemplified in Figure 1 which illustrates the formation of an accumulation layer in front of a double barrier heterostructure under bias[6].

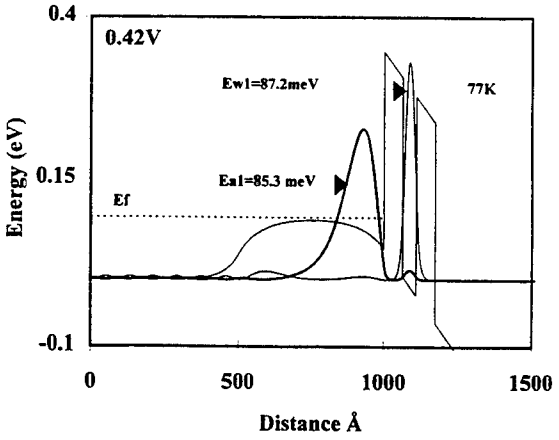


Fig. 1: Space charge effects in a double barrier heterostructure and wavefunctions.

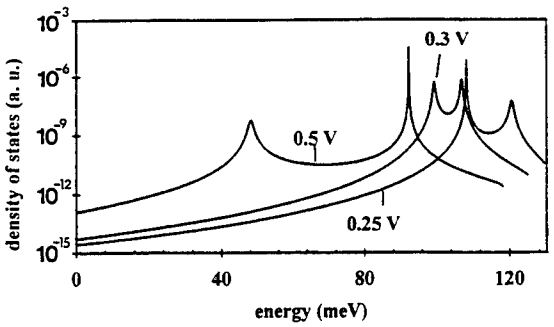


Fig. 2: Illustration of resonances in the local density of states.

When the wavefunctions are known, several methods can be used for calculating the current-voltage characteristics. The first one, widely used in the literature, is based on the calculation of the quantum transmission probabilities and the supply function. This latter function (F) reflects the energy distribution of incoming electrons and can be defined in the access regions (emitter and collector). Multiplying F times the transmission probabilities and integrating over energy for each bias conditions gives the current-voltage characteristics.

Another way for calculating the I-V curves is to use the local density of state defined as $D(E)=\int dz\ \psi(z)\psi^*(z)$[7]. Also in this case, resonance effects can be pointed out as it can be seen in Figure 2 which shows the local density of state corresponding to two quantum wells coupled to a continuum under various bias conditions[8]. However the method to calculate the current is slightly different by assuming that the current part, due to the notch states, is given by the ratio between the sheet carrier density trapped in the wells and the escaping time (τ) of this charge through the quantum structure. In practice, the relevant time τ can be determined from the energy broadening of the resonance process. Indeed, it can be shown [9] that τ is related to the full width at half maximum (Γ) of the resonant peak involved in the tunneling transitions ($\tau=\hbar/\Gamma$)

Both methods, outlined above, have been used to predict the order of magnitude of current densities flowing through various quantum structures and have been extensively used in several laboratories for optimizing the design of new devices. In addition these calculations are helpful for predicting the threshold of tunneling transitions and the time response of phenomena. However they fail to describe the peak-to-valley ratios in the negative differential resistance region because they assume a

pure coherent tunneling process. For a deeper understanding of quantum transport, including notably scattering-assisted mechanisms, it appears necessary to develop other formalisms notably those making use of the Wigner distribution functions[10].

3.Laterally confined geometry:

For these one-dimensional structure under ballistic transport conditions, it can be shown that the conductance G is a direct measure of the transmission probability of various propagating modes in the quantum wire. Indeed, the conductances are related to the transmission coefficient through the Landauer-Buttiker's formula $G= 2e^2/h \sum T^j$ (with j the mode index)[11]. Concerning the way the charges are transmitted from the feeding ports to the output ports we have the choice between several methods notably those tracking the time evolution of a Gaussian wave-packet which interacts with the quantum system. By this procedure, which requires to solve the time-dependent Schrödinger equation, resonant charge transfers can be demonstrated and the time response of mechanisms directly analyzed. In counterpart, because the Gaussian wave packet exhibits a spread in energy, the analysis of transmission properties are not straightforward. In contrast, this difficulty can be ruled out with a spectroscopic method where the quantum states of the system are analyzed by successive energy iterations. To this aim, the two-dimensional Schrödinger equation has be solved in the whole quantum system including the discontinuities which are responsible of higher-order mode excitation as observed in electromagnetic wave-guides. This means that the wave function will be locally the result of the superposition of a number of propagating or evanescent modes according to the energy considered. Subsequently, mode matching techniques[12] can be used to satisfy the continuity of solutions within the simulation domain.

To illustrate this method, which was applied successfully for various geometries, Fig. 3 gives a two-dimensional plot of the wavefunction (ψ) corresponding to a structure which consists of two electron wave guides coupled by a dual branch scheme. The feeding of the structure is by port 1 with a unitary square modulus of wavefunction. For the geometry considered here, the stream of electron is driven almost entirely towards port 3 corresponding to a real space transfer of the electrons from one electron guide to the other [13].

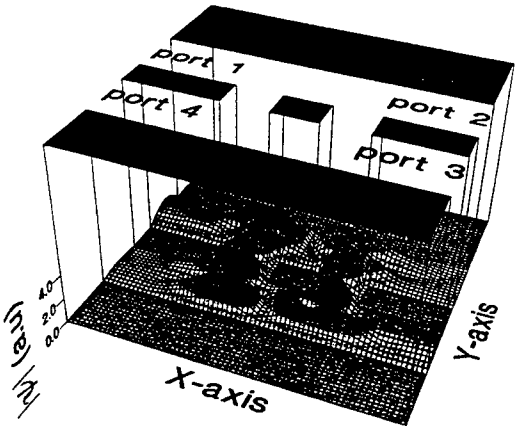


Figure 3: 3-D view of the modulus of ψ

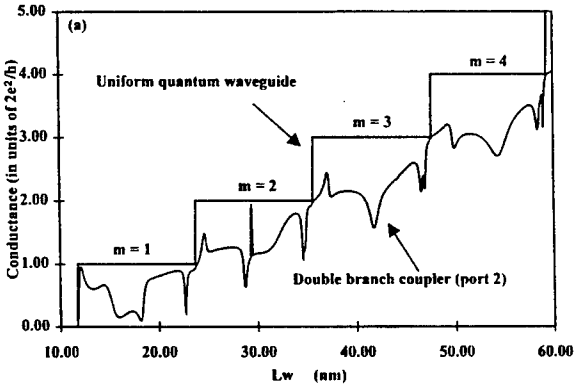


Figure 4: Conductance versus wire width example of a quantum directional coupler

It can be shown that these transfers of charge are very fast, on the subpicosecond time scale, and can occur with a very high directivity due to the interference phenomena induced by the two coupling paths[14]. Once again, resonance effects can be demonstrated in the transport properties. They correspond to the matching of the wavefunctions to the geometry of the coupling region giving rise to standing wave patterns. These resonances are clearly apparent in the plot of the conductance versus the wire width reported in Fig. 4 with apparent stop and pass energy bands and which is compared to the case of a uniform waveguide with the conventional plateau-like structures.

Conclusion:

In this rapid review of the simulations tools which can be used for the design and the analysis of low dimensional systems, we have seen that some interesting results can be obtained directly by performing a spectroscopy of quantum states. For this analysis the space charge effects has often to be taken into account either in the Thomas Fermi approximation or by using a complete self-consistent quantum calculation. These simulation codes appear relatively powerful for describing the resonance effects due to preferential paths afforded by the quantum levels. On this basis, it appears possible to derive the threshold voltage corresponding to the tunneling transitions and to have a first insight in the current capability and the time response of the quantum systems.

Acknowledgments:

Many thanks to L. Burgnies, P. Mounaix, V. Sadaune and O. Vanbésien for their contributions to the results illustrating this overview.

References

[1]F. F. Sols, M. Macucci, U. Ravaioli, and K. Hess, Appl. Phys. Lett., 54, 350(1989)
[2] J. N. Randall, M. A. Reed, and G.A. Frazier, J. Vac. Sci. Technol. B7, 1398(1989)
[3] C. Eugster, P. R. Nuytkens, J.A. Del Alamo, International Electron Device Meeting, 495(1992)
[4] See as example: *Resonant tunneling in semiconductors: Physics and Applications* edited by L.L.Chang, E.E. Mendez and C. Tejedor (Plenum, New York, 1991)
[5] B.J. Van Wees, L.P. Kouwenhoven, E.M.M. Willems, C.J.P. Harmans, J.E. Mooij, H. van Houten, C.W.J. Beenakker, J.G. Williamson, and C. T. Foxon Phys. Rev.B 43, 12431(1991)
[6] P. Mounaix, J. M. Libberecht, and D. Lippens, to be published in Solid state Electronics (1995)
[7] R. Lassnig and W. Boxleiter, Solid State Communication, 64, 978(1987)
[8] L. Burgnies, O. Vanbésien, V. Sadaune, D. Lippens, J. Nagle, and B. Vinter, J. Appl. Phys. 75, 4527(1994)
[9] C. Cohen-Tannoudji, B. Diu, and F. Laloë, in Mécanique Quantique II, p 1276 (Hermann, Paris 1986)
[10] W. R. Frensley, Rev. Mod. Phys. 62, 745(1990)
[11] M. Büttiker, Phys. Rev. Lett. 57, 1761(1986)
[12]A. Weisshaar, J. Lary, S. M. Goodnick, V. K. Tripathi, J. Appl.. Phys. 70, 355(1991)
[13] O. Vanbésien and D. Lippens, Superlattice and Microstructures, 17, 197(1995)
[14] O. Vanbésien and D. Lippens, Phys. Rev. B, to be published (15 August 1995)

Quantum Effects and the Semiconductor Law of Mass Action*

H. L. Grubin and T. R. Govindan
Scientific Research Associates, Inc.
Glastonbury, CT 06033

Introduction

A starting point in the design of semiconductor devices is the semiconductor law of mass action, which for the case of non-degenerate statistics is:

$$(1) \qquad np = N_C N_V e^{-\frac{E_G}{k_B T}}$$

The critical feature of this result is that the product is independent of background or carrier density. When Fermi statistics is considered the product *np* is dependent upon density. Critical input into the semiconductor law of mass action is that for conditions of zero current flow the density and potential are related via:

$$(2) \qquad n = N_C e^{-\left[\frac{E_C - E_F}{k_B T}\right]}$$

Equations (1) and (2) are standard undergraduate textbook expressions, and do not hold up when quantum statistical mechanical considerations are introduced. The basis of this statement derives from the work of Wigner[1], who demonstrated that carrier density, in the case of non-degenerate statistics, was not only dependent upon the *value* of the conduction band potential energy, but was also dependent upon the *shape* of the conduction band potential energy. This shape factor is introduced through a collection of potential energy derivatives.

Quantum Contributions

The consequences of shape emerge from a recasting of Schrodinger's equation in the context of a discussion by Madelung[2]. In particular if the Schrodinger equation is separated into a real and imaginary part, the real part has an ostensible classical form:

$$(3) \qquad \frac{d\mathbf{p}}{dt} = -\nabla[V + K(inetic)E(nergy) + Q]$$

where:

$$(4) \qquad Q \equiv -\frac{\hbar^2}{2m}\frac{\nabla^2\sqrt{\Psi^*\Psi}}{\sqrt{\Psi^*\Psi}}$$

is often called the Bohm[3] quantum potential. It is important to note that the quantum potential is dependent upon the shape of the real part of the wave function, rather than on its intensity; and does not necessarily fall off with distance. This additional term results in a modified Newton's Law and has the effect of introducing a driving force on the carriers

that is totally quantum mechanical in origin. When considering a collection of particles, as in the case of semiconductor devices, it is possible to relate the Wigner quantum corrections to a potential that is qualitatively similar to equation (4)

$$(5) \qquad Q \equiv -\frac{\hbar^2}{2m}\frac{\nabla^2\sqrt{n(x)}}{\sqrt{n(x)}}$$

where $n(x)$ is the density of carriers[4]. In equilibrium, equation (2) is approximately modified as:

$$(6) \qquad n(x) = N_C e^{-\frac{E_C + Q/3 - E_F}{k_B T}}$$

where the factor of 3 has been the object of some discussion. The point of equation (6) is that when similar considerations are introduced for holes, the product of the electron and hole density is no longer a constant but can include a variation that is a consequence of the quantum contributions arising from spatial variations in the charge distribution. The quantum modification of the density suggests that the product of *NP* under thermodynamic equilibrium would depend on features other than temperature. Certainly this would be expected at heterostructure interfaces, even if effective mass variations are ignored. The question addressed in this paper is: **are significant variations in the product *NP* to be expected in ostensibly classical structures** such as a bipolar transistor.

Numerical Simulations

We have investigated the semiconductor law of mass action through solutions to the quantum Liouville equation,

$$(7) \qquad i\hbar\frac{d\rho_{op}(t)}{dt} = \left[H(t), \rho_{op}(t)\right],$$

in the coordinate representation (it is related to the Wigner distribution, through the Weyl[5] transformation), under conditions of thermodynamic equilibrium. In equation (7), $\rho_{op}(t)$ and $H(t)$, are respectively the density and Hamiltonian operators. The quantum Liouville equation in the coordinate representation, under zero current conditions is given by:

$$(8) \qquad i\hbar\frac{\partial\rho(x,x')}{\partial t} = \left\{-\frac{\hbar^2}{2m}\left[\frac{\partial^2}{\partial x^2} - \frac{\partial^2}{\partial x'^2}\right] + E_C(x) - E_C(x')\right\}\rho(x,x')$$

The density is given by the diagonal component of the density matrix: $n(x) = \rho(x,x)$. A similar equation exist for holes. Solutions to the Liouville equation in the coordinate representation avoid the approximations inherent in treating the problem through the use of the quantum potential. The solutions are '*exact*', insofar as numerical simulations are exact.

To date, equation (8), when coupled to Poisson's equation, was implemented for two generically *classical* structures: *NIN* and *NPN* devices, where in all cases the *I* and *P* regions were each 50 nm in length. Non-degenerate statistics were assumed, for comparison with the classical law of mass action. (The effects of Fermi statistics will be discussed at the Symposium.) Devices of 200 nm and 400 nm were considered. Several calculations

were performed for parameters appropriate to GaAs; parametric studies were also performed. In these studies the *N* region was doped to $10^{24}/m^3$ (which is too high to strictly satisfy the non-degeneracy condition). Calculations at lower densities will be discussed at the meeting.

The results for the *NIN structures, were ordinary*; the departures from the law of mass action were negligible.

The results for the *NPN* structures, depended upon the input parameters, but some simulations yielded *extraordinary results.* Two examples are illustrated below. The first, figure 1, is for a 200 nm structure with an acceptor doping of $5x10^{23}/m^3$. Here we display the product of electron and hole density, normalized to their values at the origin. This calculation displays a modest factor of '4' departure from the mass-action law.

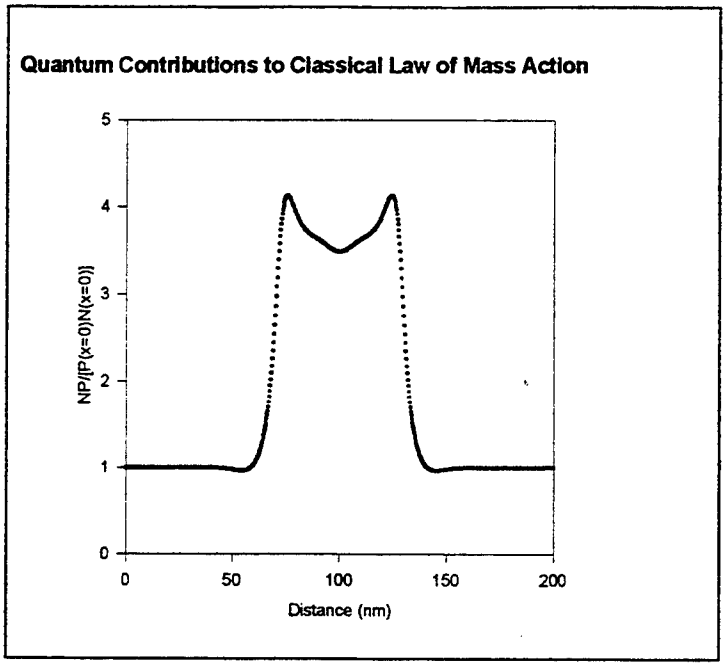


Figure 1. Product of np normalized to n(x=0)p(x=0) for a 200nm NPN structure. This calculation was performed for a band gap of 1.42 eV with electron and hole effective masses appropriate for GaAs. The doping of the P region was $0.5x10^{24}/m^3$.

The second illustration is for a 400 nm structure in which the effective mass of holes was taken to be the same as that of electrons for gallium arsenide. This is an artificial study but does illustrate the point of the violation of mass action. The results are shown in figure 2, where we see a two order of magnitude difference in the product of electron and hole densities.

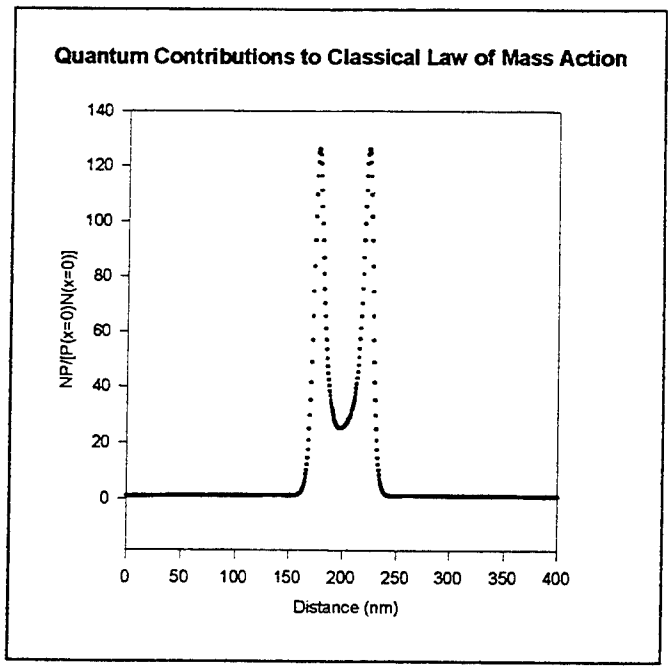


Figure 2. Product of np normalized to n(x=0)p(x=0) for a 400 nm NPN structure. This calculation was performed for a band gap of 1.42 eV with electron and hole effective masses equal to that of the electron effective mass of 0.067m. The doping of the P region was $0.9x10^{24}/m^3$.

Discussion

If we examine the results of figures 1 and 2, we notice that the departure from a constant value is greatest near the interface region, and then decreases toward the center of the device. Indeed, it is at the interface where the carriers undergo the largest change in density, and it is this change that contributes to the quantum contribution to the density. For a sufficiently long *P* region the product of electron and hole density, *within the P region*, should equal the value at the boundary region.

The implications of these results for device design have not yet been considered. But, use of one of the most frequently used relationships in the design of devices needs to be re-examined.

Acknowledgment

This work was supported by ARO and ONR.

[1] E. P. Wigner, *Phys. Rev.* **40**, 749 (1932)
[2] E. Madelung, *Z. Phys.* **40**,322 (1926)
[3] See, e.g., C. Philippidis, D. Bohm and R. D. Kaye, *Il Nuovo Cim.* **71B**, 75 (1982); and D. Bohm and B. J. Hiley, *The Undivided Universe*, Routledge, London (1993).
[4] M. A. Ancona and G. J. Iafrate, *Phys. Rev.* **39**, 9536 (1989).
[5] H. Weyl, *Z. Phys.*, **46**, 1 (1927).

Quasi-1D Coulomb potential in Quantum wires

William R. Grise
Morehead State University

This paper models the effect of a charged impurity on the electrons in a narrow quantum wire. The impurity potential is a quasi-1D Coulomb-type interaction with a long range. The wire is narrow enough that only a few transverse modes are populated. Recently, Gribi and Sigmund [1] constructed a quasi-1D Coulomb-type potential defined on a discrete lattice. For narrow energy bands, this yields an exact solution to the perturbed Hamiltonian. In this work, we use this exact solution for the Coulomb potential to study the effects of charged impurities on electrons traveling in quantum wires subject to transverse confinement potentials. The results are contrasted with previous work that models defects as either point scatterers[2],[3],[4] or as short-range scatterers [4]. We find oscillations in the electron density at distant sites from the impurity due to this potential.

The quasi-1D Coulomb potential

$$V_C(\mathbf{r}) = \frac{\alpha c}{z - z_0} \qquad (1)$$

acts only along the length of the wire. The long-range potential acting in the z direction gives rise to an infinite set of discrete energy levels.Recent theoretical work [5] suggests that in a sufficiently narrow quantum wire, the long range Coulomb interaction is not screened. Hence, the form in (1) is appropriate. Because the transverse wavevectors, $\mathbf{k}_\perp$, are still good quantum numbers, there will be a two-dimensional energy band associated with each of these discrete levels in k_z space. The overall Hamiltonian for a one-dimensional tight-binding band with the Coulomb potential is $H = H_0 + V_C$, where H_0 is the standard tight-binding Hamiltonian with nearest-neighbor hopping potentials. The Coulomb potential in the tight-binding picture is:

$$V_C = \sum_l \frac{\alpha}{l - \nu} |l\rangle \langle l| \qquad (2)$$

Here, as in (1), α denotes the strength of the interaction potential, and $\nu = z_0/a$ (a the lattice distance). We expand the discrete level eigenfunctions, $|\Phi\rangle$, in the

lattice representation:

$$\langle \mathrm{r}|\ \Phi\left(E_p\right)\rangle = \sum_n \eta_n\left(E_p\right)\phi\left(l-na\right) \tag{3}$$

The final form for the η's is:

$$\eta_n\left(E_p\right) = C_p\left(\lambda_p\right)^{-n}\sum_{m=0}^{p-1}\left(\frac{-2\alpha}{2Vp}\right)^m\binom{p}{p-m-1}\frac{1}{m!}\times\frac{n(n+1)\cdots(n+m)}{\left(\lambda_p\right)^{m+1}}, n\geq 0 \tag{4}$$

where:

$$E_p = \begin{cases} \left[4V^2+\left(\frac{\alpha}{p-\nu}\right)^2\right]^{1/2} & if \quad p=1,2,\ldots,\infty \\ -\left[4V^2+\left(\frac{\alpha}{p-\nu}\right)^2\right]^{1/2} & if \quad p=0,-1,-2,\ldots,-\infty \end{cases} \tag{5a}$$

$$\lambda_p = \frac{\left(E_p+\frac{\alpha}{p}\right)}{2V} \tag{5b}$$

$$C_p = -\frac{2\alpha}{2Vp^2}\sqrt{\frac{\alpha}{pE_p}}\cdot\left(\lambda_p\right)^p \tag{5c}$$

which is a normalization constant.

The extension of this result to the quasi-1D case is straightforward. The m^{th}-mode wavefunction in the quantum wire becomes:

$$\Phi_{p,n,m}\left(x,z\right) = \sqrt{\frac{2}{W}}\cdot\sin\left(\frac{m\pi x}{W}\right)\cdot\eta_n\left(E_p\right), n\geq 0 \tag{6}$$

The figures show the behavior of the $|\Phi_{p,n}|^2 = \sum_m |\Phi_{p,n,m}|^2$ for $\nu = 0$, and as a function of n, the lattice site, and for several values of p, the Coulomb potential quantum number. We see that already at p = 2 (Figure 1), the probability of finding the electron shows a dip quite near the origin, followed by a steady rise to a maximum at about 20 lattice sites. As p increases, the number of troughs and peaks increases, at longer distances away from the origin (Figures 2-4).

This work could be applied to the question of δ doping in superlattices. The δ doping technique uses the present ability to embed single layers of impurity atoms inside a host semiconductor [6]. Beltram and Capasso [7] have indicated the possibility of using such single layers to modulate the superlattice band structure,

advancing the possibility of increasing the miniband width by several orders of magnitude.

In conclusion, we are using an exact formulation for the Coulomb interaction in a quasi-1D structure to report on the effects of charged impurities on electrons traveling through a narrow quantum wire. The main effect seems to be an oscillation in the electron density with longitudinal distance from the site of the impurity.

References

[1] P. Gribi and E. Sigmund, "Exact solutions for a quasi-one-dimensional Coulomb-type potential," *Phys. Rev. B,* vol. 44, pp. 3537-3549, 1991.

[2] D. van der Marel and E.G. Haanappel, "Model calculations of the quantum ballistic transport in two-dimensional constriction-type microstructures," *Phys. Rev. B*, vol. 39, pp. 7811-7820, 1989.

[3] P.F. Bagwell, "Evanescent modes and scattering in quasi-one-dimensional wires," *Phys. Rev. B,* vol. 41, pp. 10354-10371, 1990.

[4] E. Tekman and S. Ciraci, "Theoretical study of transport through a quantum point contact," *Phys. Rev. B,* vol. 43, pp. 7145-7169, 1991.

[5] H. Maurey and T. Giamarchi, "Transport properties of a quantum wire in the presence of impurities and long-range Coulomb forces," *Phys. Rev. B,* pp. 10833-10843, vol. 51, 1995.

[6] Steffen Wilke and Dieter Hennig, "Theoretical approach to δ doping of GaAs with In," *Phys. Rev. B*, vol. 43, pp.12470-12476, 1991.

[7] F. Beltram and F. Capasso, *Phys. Rev. B,* vol. 38, pp. 3580, 1988.

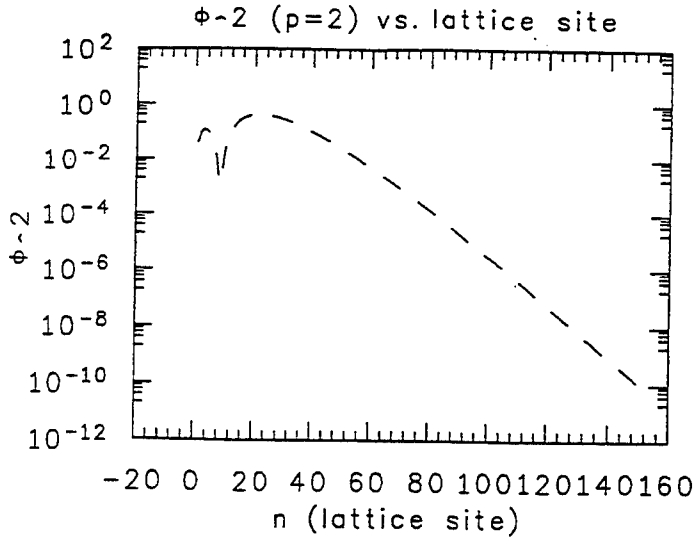


Figure 1. $|\Phi_{p,n}|^2$ as a function of n, the number of lattice sites from the source of the Coulomb potential, for p = 2.

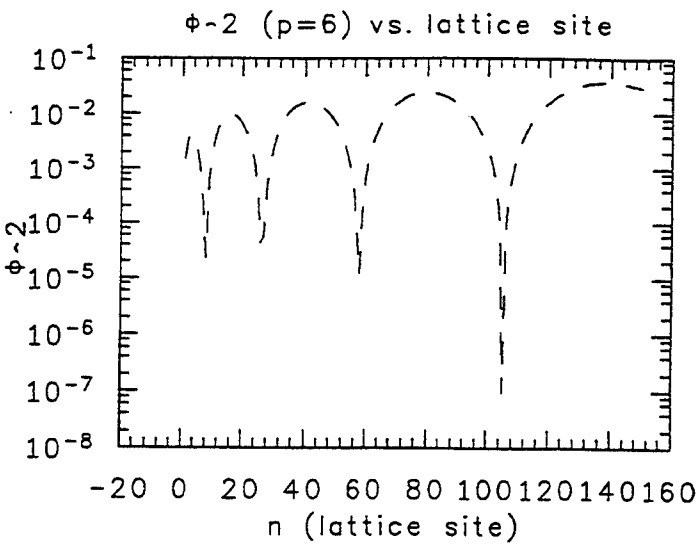


Figure 2. $|\Phi_{p,n}|^2$ vs. n, this time for $p = 6$.

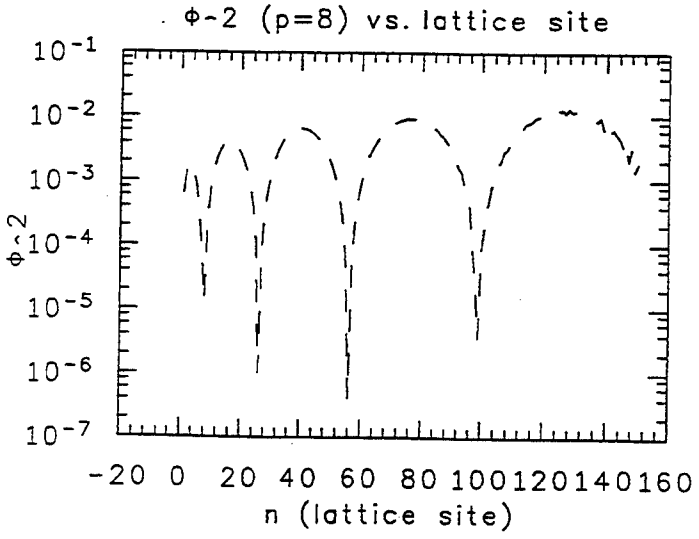


Figure 3. $|\Phi_{p,n}|^2$ vs. n, for $p = 8$. The variations in electron density, after increasing for small values of p, appear to have stabilized in number and placement of peaks in this and the following Figure.

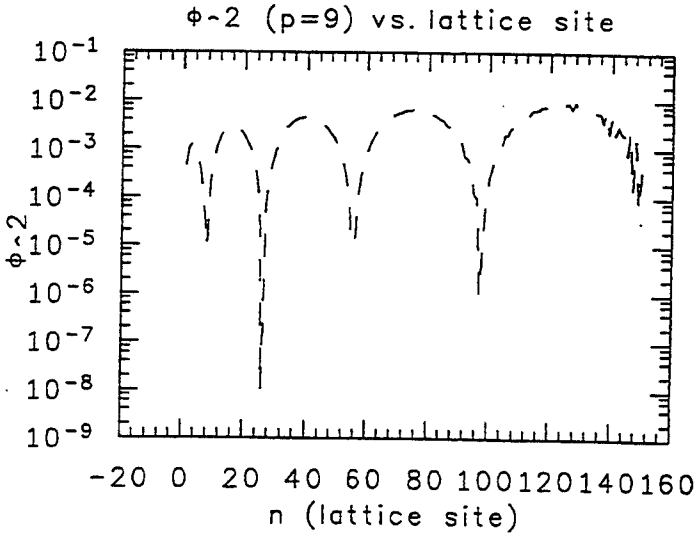


Figure 4. $|\Phi_{p,n}|^2$ for $p = 9$.

Solution of the Boltzmann Transport Equation in One-Dimensional Submicron n^+-n-n^+ Structures Based on Relaxation Scales of the Moments

Ming-C. Cheng and Liangying Guo
Department of Electrical Engineering
University of New Orleans
New Orleans, Louisiana 70148

The previously developed hydro-kinetic (HK) transport theory [1] is used to derive an efficient τ_m-scalae HK distribution function based on evolution of the distribution function under the influence of the fast varying field and scattering processes. The approach to the HK distribution function is considerably more accurate than other methods that are usually used to describe the distribution function in devices, such as the displaced Maxwellian distribution [2] or expansion of Legendre Polynomials [3]. On the other hand, the developed description is much more efficient than the Monte Carlo method [4].

In the previous studies [1,5], it has been shown that evolution of the **kinetic** distribution function $f(k)$ can be characterized by relaxation of the **hydrodynamic** parameters, including density n, average momentum $\hbar\overline{k}$, mean energy $\overline{\epsilon}$ and the higher order moments ($\overline{k^3}$, $\overline{k^4}$, ... etc). Theoretically, the exact description for the distribution function that obeys the Boltzmann transport equation (BTE) requires an infinite set of moments; namely, $f(k)=f(k;n, \overline{k}, \overline{\epsilon}, \overline{k^3}, \overline{k^4},...)$. Practically, truncation of the infinite set of moments is necessary to solve the distribution function. The truncation can be achieved based on order of magnitudes of characteristic times for the moments.

In semiconductors, $\tau_n > \tau_\epsilon > \tau_m$, where τ_n, τ_ϵ, and τ_m are carrier density, energy, and momentum relaxation times, respectively, and relaxation times of the higher order moments are assumed to be less than τ_m. Under the influence of a drastic change in electric field, dynamic information described by the smaller-scale moments will vanish faster than that given by the larger-scale moments. Consequently, after a sufficient time, information described by the higher-order moments become insignificant. $f(k)$ thus evolves into the τ_m-scale HK distribution function $f_m(k;n, \overline{\epsilon}, \overline{k})$. At time greater than τ_m, information characterized by relaxation of momentum diminishes. Therefore, $\overline{k}$ relaxes to a situation in quasi-equilibrium with mean energy, and $f_m(k;n, \overline{\epsilon}, \overline{k}) \approx f_m(k;n, \overline{\epsilon}, \overline{k}(\epsilon)) = f_\epsilon(k;n, \overline{\epsilon})$. f_m thus evolves into the τ_ϵ-scale HK distribution function $f_\epsilon(k;n, \overline{\epsilon})$. For a time greater than τ_ϵ after the drastic change in field, since $\overline{\epsilon}$ and $\overline{k}$ have relaxed to a quasi-equilibrium state, f_ϵ evolves into a quasi-equilibrium distribution $f_n(k;n)$ which can be used to derive the drift-diffusion model [6].

The distribution function at each stage of evolution characterized by a number of moments can provide information of the carrier dynamics at the relaxation scales of these moments. In submicron devices, depending on the scale of interest, f_ϵ or f_m can be taken to describe the dynamic behavior of carriers in devices. The τ_ϵ-scale HK distribution function f_ϵ has been investigated in previous papers [1,5]. In this study, a computational model for the evolution of the HK distribution from f_m into f_ϵ is presented. The evolution is taken to be a relaxation process at each time step influenced by $\overline{\epsilon}$ and $\overline{k}$ relaxation and the change in field:

$$f_m^{\ell+1}(k) = f_e^{\ell+1}(k) + \left[f_m^{\ell}(k - \Delta k_m^{\ell}) - f_e^{\ell+1}(k)\right] \exp\left(-\Delta t^{\ell} / \tau_h^{\ell+1/2}\right), \qquad (1)$$

where τ_h is the relaxation time for f_m evolving toward f_ϵ, and Δk_m is the shifted amount for f_m^ℓ in k space. For a relaxation process, the difference between f_m and f_ϵ tends to reduce and is proportional to $exp(-\Delta t/\tau_h)$ due to scattering. In addition, f_m^ℓ shifts in k space by an amount of Δk_m which accounts for changes in $\overline{k}$ within Δt caused by the field. On the other hand, f_ϵ during the evolution remains in equilibrium with mean energy. f_m can be solved from Eq. 1, if Δk_m and τ_h are determined. Evolution equations for the hydrodynamic parameters including carrier density, energy and momentum can be obtained by taking appropriately weighted integrals of the HK evolution equation given in Eq. (1). These equations are then solved together with the conservation equations. In addition to the hydrodynamic parameters, this procedure also determine Δk_m and τ_h at each time step.

The space evolution equation for f_m can be performed similarly:

$$f_m^{\ell+1}(k) = f_e^{\ell+1}(k) + \left[f_m^\ell(k - \Delta k_m^\ell) - f_e^{\ell+1}(k)\right] \exp\left(-\Delta z^\ell / \lambda_h^{\ell+1/2}\right) \qquad (2)$$

where λ_h is the relaxation length. Similar to the time evolution, Δk_m accounts for the variations in field and $\overline{k}$, and $exp(-\Delta z/\tau_h)$ includes the effects of scattering processes.

To illustrate the validity of the HK concept, time evolution of the HK distribution functions f_ϵ and f_m are shown in Fig. 1, compared with the evolution of f obtained from the Monte Carlo method for electrons in n-type *Si* subjected to a drastic increase in electric field from 2 to 70kV/cm with a rise time of 0.1psec. Average velocity of electrons is given in Fig. 2. The solid circles in Fig. 2 indicate the velocities at the instants (t_1-t_4) when f_ϵ, f_m and f are sampled and illustrated in Fig. 1.

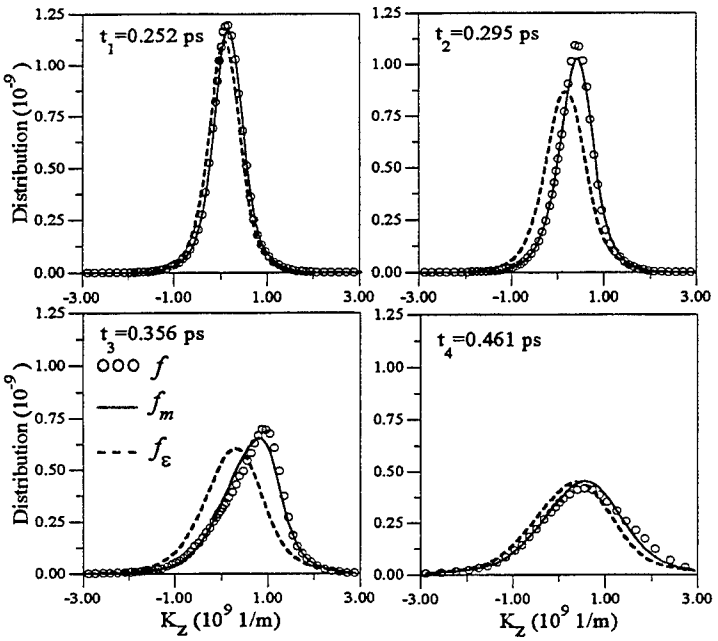


Fig. 1 Evolution of the distribution functions f_ϵ, f_m and f. The average velocities at t_1-t_4 are indicated in Fig. 2.

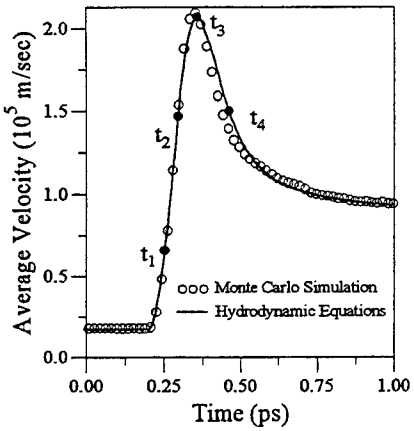


Fig. 2 Relaxation of the average velocity.

Fig. 1 clearly shows that f relaxes considerably faster than f_ϵ during the strong velocity overshoot (t_1-t_4) interval. This is because during the pronounced overshoot interval the electron dynamics is strongly influenced by velocity relaxation which is

ignored in f_ϵ. On the contrary, f_m that takes into consideration velocity relaxation evolves closely to f. It should be pointed out that a highly asymmetric distribution function in k space is clearly observed at t_3. As shown at t_3 in Fig. 1, the τ_m-scale HK distribution function f_m offers a good description to account for the non-Maxwellian nature of the electron dynamics in the extreme non-equilibrium situation.

When electrons are influenced by a slower increase in field, velocity overshoot is less pronounced. Influence of velocity relaxation on the distribution function becomes less significant, and f_ϵ can provide a reasonable description for f. To illustrate this phenomenon, a step change in field from 2 to 40kV/cm with a rise time of 0.1psec is applied to n-type Si. The peak velocity of the overshoot reduces from $2.1X10^7$ cm/s (given in Fig. 2 in the previous case) to $1.5X10^7$ cm/s. The less pronounced overshoot therefore decreases the effects of the $\overline{k}$ dependence. The distribution functions, f, f_m and f_ϵ, near the overshoot peak of velocity at this slower increase in field are shown in Fig. 3. In this case, discrepancy between f_m and f_ϵ near the overshoot peak evidently reduces, compared to that shown at t_3 in Fig. 1. Also, f and f_m are in excellent agreement at this slower increase in field.

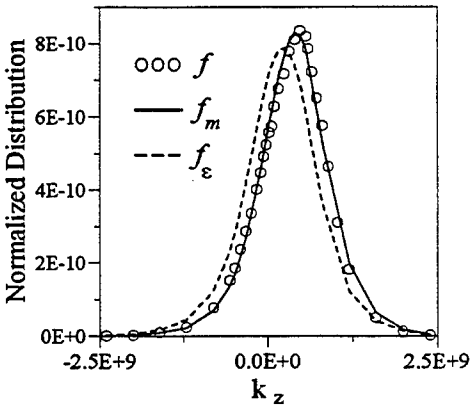


Fig. 3 The distribution near the peak of the velocity overshoot at the slower increase in field.

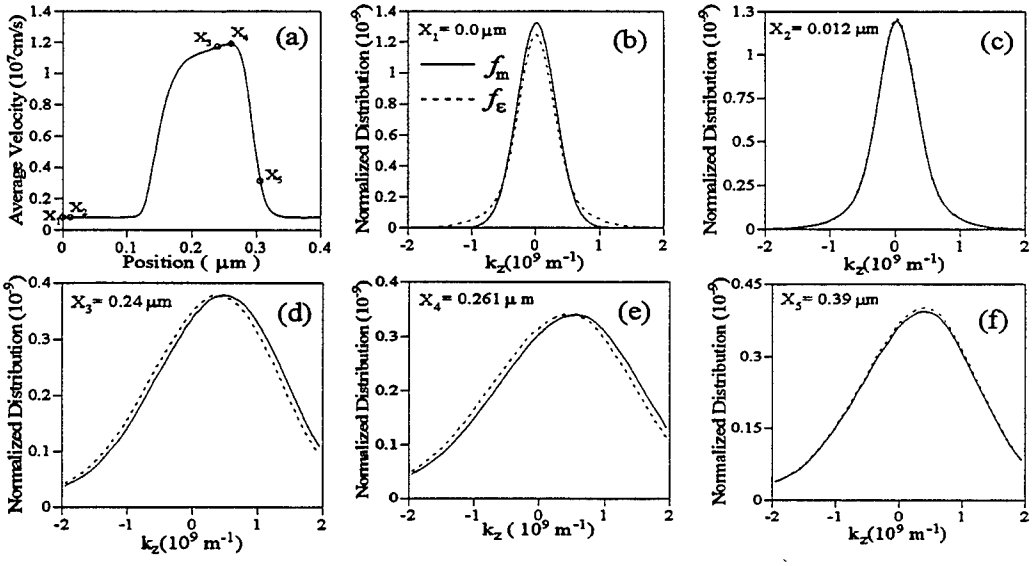


Fig. 4 (a) Average velocity profile in the device. X_1-X_5 indicate the locations where f_ϵ and f_m are calculated and shown in (b)-(f). The n-region length is equal to 0.14μm.

The developed model is applied to submicron n^+-n-n^+ structures with $N_d=10^{18}\ cm^{-3}$ in the n^+ region and $N_d=10^{16}\ cm^{-3}$ in the n region. A voltage of 1.5V is applied to the first submicron n^+-n-n^+ structure with a length of 0.14μm in the n region. The evolution of the average velocity, f_ϵ and f_m is shown in Figs. 4(a)-4(f). To start the evolution in

the device using Eq. (2), f_m at X=0 is taken to be a displaced Maxwellian distribution with the velocity and mean energy at X=0. As can be seen, f_m quickly evolves into f_ϵ at X_2. As the velocity increases in the n region, f_m starts to deviate from f_ϵ. The maximum discrepancy between f_ϵ and f_m occurs near the peak of the overshoot, as shown at X_4=0.261μm. However, the peak of the overshoot velocity is only 1.19X10^7 cm/s, and the maximum discrepancy between f_ϵ and f_m is therefore much smaller than that shown at t_3 in Fig. 1. In the n^+ region near the anode, field decreases. Large electron density and strong scattering quickly reduce velocity, and f_m evolves into f_ϵ, as shown at X_5.

A length of 0.35μm is used for the n region of the second n^+-n-n^+ structure, and the same voltage is applied to the device. Similar to the first device, a displaced Maxwellian distribution with the velocity and mean energy at X=0 is used for f_m at X=0. Fig. 5(a) shows that velocity overshoot in this case reduces to 0.97X10^7 cm/s which is just slightly greater than the steady state saturated velocity ($\sim$0.9X10^7 *cm/s* at $N_d=10^{16}$ cm^{-3}). As a result, f_ϵ and f_m shown in Figs. 5(b)-(f) are nearly indistinguishable.

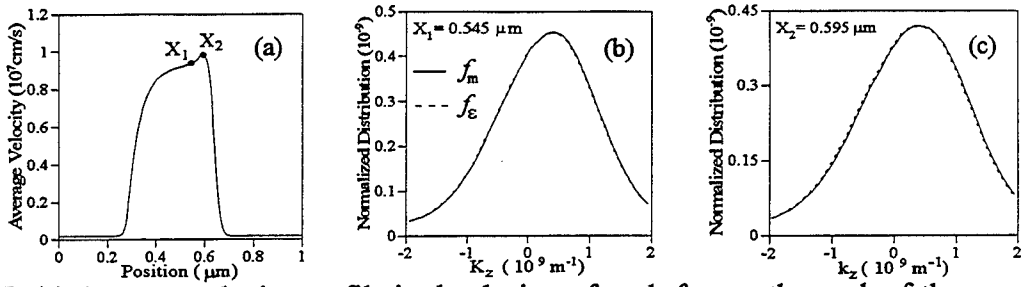


Fig. 5 (a) Average velocity profile in the device. f_ϵ and f_m near the peak of the overshoot at X_1 and X_2 are given in (b) and (c). The n-region length is equal to 0.35μm.

In conclusion, the HK transport concept has been used to develop an accurate and efficient model to determine the solution of the BTE in one dimensional submicron n^+-n-n^+ structures. When the velocity overshoot is pronounced due to the fast increase in field, the τ_m-scale HK distribution function f_m is required to account for effects of velocity relaxation during the interval of velocity overshoot. In devices where field variation is slow and the overshoot is therefore not pronounced, effects of velocity relaxation become insignificant. In this case, $f_m \approx f_\epsilon$. The study also demonstrates the validity of the HK concept to describe the evolution of the distribution function in extreme non-equilibrium situations. The developed τ_ϵ-scale and τ_m-scale HK transport models can be used to determine the distribution function in submicron devices at very low computational costs.

Acknowledgement - This work has been supported by the Nation Science Foundation under the grant number ESC-9409471.

References

[1] Ming-C. Cheng and R. Chennupati, J. Phys. D., **28**, 160 (1995).
[2] E. Bosencher, J. De. Physique, **C7**, 351 (1981).
[3] E. M. Conwell and M. O. Vassel, Phys. Rev. **166**, 797 (1968).
[4] K. Hato, IEEE Trans. Elect. Dev., **ED-35**, 1344 (1988).
[5] Ming-C. Cheng, Rambabu, and Ying Wen, J. Appl. Phys., in press.
[6] E. E. Kunhardt, M. Cheng and J. Wu, J. Appl. Phys., **64**, 1220 (1988).

Drain Current Enhancement due to Velocity Overshoot Effects and Its Analytic Modeling

Jai-Hyuk Song, Woo-Sung Choi, Young-June Park , and Hong-Shick Min

Department of Electronics Engineering and Inter-University Semiconductor Research Center
Seoul National University, San 56-1 Shinlim-Dong, Kwanak-Ku, Seoul 151-742, Korea
Phone: +82-2-880-7274, Fax: +82-2-885-4459

The main cause of the drain current enhancement due to the velocity overshoot and its analytic model are presented and verified by 2D simulations whose hydrodynamic transport model is well tuned to both the $0.12\mu m$ SOI[1] and bulk NMOSFET's.

First, it will be shown that the main cause of the current enhancement is found to be the non-local effects taking place at the source end of the channel. Figs. 1(a) and (b) compare the areal electron density(N_{inv}) and electron velocity(v_n) profiles from the hydrodynamic(HD) and drift-diffusion(DD) simulations for $0.076\mu m$ NMOSFET(type A in Table 1). N_{inv}'s near the source end are nearly same whereas $v_{n.HD}$ is enhanced appreciably over $v_{n.DD}$. Considering that the drain current can be expressed by $WqN_{inv}(y)v_n(y)$ where the y-direction is parallel to the Si/SiO_2 surface, and N_{inv}'s at the source end are not altered by the velocity overshoot effects, we can conclude that the current enhancement is caused by the enhanced velocity at the source end. Figs. 2(a) and (b) show the simulated lateral electric field(E_y) and electron mobility(μ_n) profiles, respectively, in the channel region near the source. μ_n(HD) and μ_n(DD) are different prominently at the source end of the channel where E_y(HD) and E_y(DD) are quite similar. The step-like increase of E_y in the region is considered to be responsible for the non-local effects and contributes to the current enhancement. Fig. 3 shows the correlation between the current and source-end velocity($v_n(0)$) enhancement ratios for a wide range of bias conditions for the several device structures. Excellent match in the correlation supports the reason for the current enhancement. The small deviations in the high $v_{n.HD}(0)/v_{n.DD}(0)$ region are due to the effect of source series resistance.

Based on the above observation, the current enhancement can be predicted by a proper modeling of the velocity enhancement at the source end. Since the non-local effects are caused by the spatial gradient of the field[2], the source end velocity($v_n(0)$) can be written[3] as,

$$v_{n.HD}(0) = v_{n.DD}(0)(1 + \frac{\delta(E_y)}{E_y}\frac{dE_y}{dy}), \tag{1}$$

where $\delta(E_y)$ is the characteristic length of the field gradient effects[2]. The above model has been reported to be reasonable when the field magnitude is not large, which is the case for the source end. Using the piecewise model[3] for the velocity-field relation and $v_{sat} = \mu_0 E_{sat}/2$, μ_0 and E_{sat} being the low field mobility and saturation electric field, $\delta(E_y)$ at the source region can be expressed[3] with the energy relaxation time(τ_w) and the saturation velocity(v_{sat}) as,

$$\delta(E_y) = \frac{E_y}{E_{sat}} v_{sat}\tau_w. \tag{2}$$

By applying Gauss's law to a rectangular box with height of the depletion width and infinitesimally small length Δy in the source region, dE_y/dy can be related with the threshold voltage shift(ΔV_T)[4] due the the short-channel effects as,

$$\frac{dE_y}{dy} = \frac{\eta C_{ox}}{\epsilon_{si}}\sqrt{\frac{qN_{ch}}{4\epsilon_{si}\phi_f}}\Delta V_T, \tag{3}$$

where η is a fitting parameter[4]. It is interesting to notice that dE_y/dy is the cause of ΔV_T and the velocity overshoot in the source end. Now, the current enhancement factor F_{ov} can be simply expressed as

$$F_{ov} \equiv \frac{v_{n.HD}(0)}{v_{n.DD}(0)} = 1 + \frac{\mu_0\tau_w}{2}\frac{\eta C_{ox}}{\epsilon_{si}}\sqrt{\frac{qN_{ch}}{4\epsilon_{si}\phi_f}}\Delta V_T. \tag{4}$$

In this equation, we used μ_0 as the universal mobility related with the vertical effective field including the coulombic scattering[5]. The effects of the device parameters, such as gate oxide thickness(T_{ox}) and channel doping concentration(N_{ch}), on the current enhancement can be readily found in the above expression. Also, the source, drain doping concentration(N_{sd}), junction depth(x_j) and effective channel length(L_{eff}) affect the current enhancement via ΔV_T.

In order to verify the model, HD simulation and the analytic model are compared in terms of the current enhancement for the several device structures. As a reference, the drain current from the DD simulation is used. For the calculation of F_{ov}, the simulated and measured ΔV_T(ΔV_T from V_T of the long channel device at the low drain voltage) and η of 0.33 are used. Figs. 4 and 5 show the simulated $I_{DS}(HD)/I_{DS}(DD)$ and model of (4) as a function of T_{ox} and N_{ch}, respectively. As T_{ox} increases, F_{ov} increases due to the decrease of C_{ox} and increse of ΔV_T and μ_0. Also, it can be seen that F_{ov} is relatively insensitive to N_{ch}, since the decrease of ΔV_T with the increase of N_{ch} cancels the increase of the squareroot term in (4).

In order to check the validity of our model in other device, the device type D has been considered. The type D NMOSFET has the device parameters such as $T_{ox} = 20nm$, $N_{ch} = 1 \times 10^{16}/cm^3$, $N_{sd} = 5\times10^{20}/cm^3$, $x_j = 0.08\mu m$ and $L_{eff} = 0.452 \sim 0.952\mu m$. The device structure has the relatively small channel doping concentration and thick gate oxide thickness so that ΔV_T is large. Fig. 6 shows the relation between the simulated ΔV_T's and $I_{DS}(HD)/I_{DS}(DD)$'s for the device type A and D. Even though ΔV_T's of the device type D are large, the velocity overshoot effects are not expected to be appreciable in this long channel regime. Indeed, this is the case in our model where the small values of N_{ch} and C_{ox} make the F_{ov} negligible. From the above results, it can be argued that the model of F_{ov} predicts the influence of T_{ox}, N_{ch} and L_{eff} on the current enhancement due to the velocity overshoot effects reasonably well.

Fig. 7 shows the maximum transconductances($gm_{sat.max}$'s) from the HD, DD simulations and model as a function of L_{eff} for the device type A. The $gm_{sat.max}$'s from the HD simulation increase over the value of $WC_{ox}v_{sat}$ which is the maximum value predicted by the DD simulation. As shown in Fig. 7, the analytic model of F_{ov} can predict the transconductances well.

As a final data, we show the data for $0.12\mu m$ SOI NMOSFET. Fig. 8 compares the measured I_{DS}[1] with the simulated $I_{DS}(HD)$, $I_{DS}(DD)$ and $F_{ov}I_{DS}(DD)$. In the measurements, the back gate is used as the gate electrode in order to obtain the constant channel field[1]. In this channel length regime, the $I_{DS}(DD)$ cannot expect the measured one[1], whereas $I_{DS}(HD)$ and $F_{ov}I_{DS}(DD)$ show the good agreement with the measurement.

In summary, from the analysis of the simulation results, we reported that the current enhancement due to the velocity overshoot effects is caused by the velocity enhancement at the source end. From the observed phenomena, we proposed a simple analytic model for the overshoot factor F_{ov} and showed that the model predicts the current enhancement due to the velocity overshoot effects reasonably well. With a proper model of ΔV_T such as reported in [6], the model of F_{ov} can be easily implemented in the circuit simulator.

This work was supported by SamSung Electronics Co. ltd. and ETRI(Electronic Telecommunication Research Institute).

[1] W. S. Choi, et al., *IEEE EDL.*, p.333, 1995.
[2] P. J. Price, *J.Appl.Phys.*, p.4718, 1988.
[3] K. Sonoda, et al., *IEEE Elect. Dev.*, p.2662, 1991.
[4] M. M. Mattausch, *IEEE CAD.*, p.610, 1994.
[5] S. Takagi, et al., *IEDM Tech. Dig.*, p.398,1988.
[6] Z. H. Lui, et al., *IEEE Elect. Dev.*, p.89, 1993.

Table 1: Device Parameters of the simulated MOSFET's.

Effective channel length(L_{eff}) [μm]			0.076
Channel width [μm]			10.0
Extended S/D junction depth [μm]			0.04
Extended S/D surface doping conc. [/cm^3]			1×10^{20}
	Type A	Type B	Type C
Channel doping conc.(N_{ch}) [/cm^3]	3×10^{17}	5×10^{17}	3×10^{17}
Gate oxide thickness(T_{ox}) [nm]	3.5	3.5	6.0

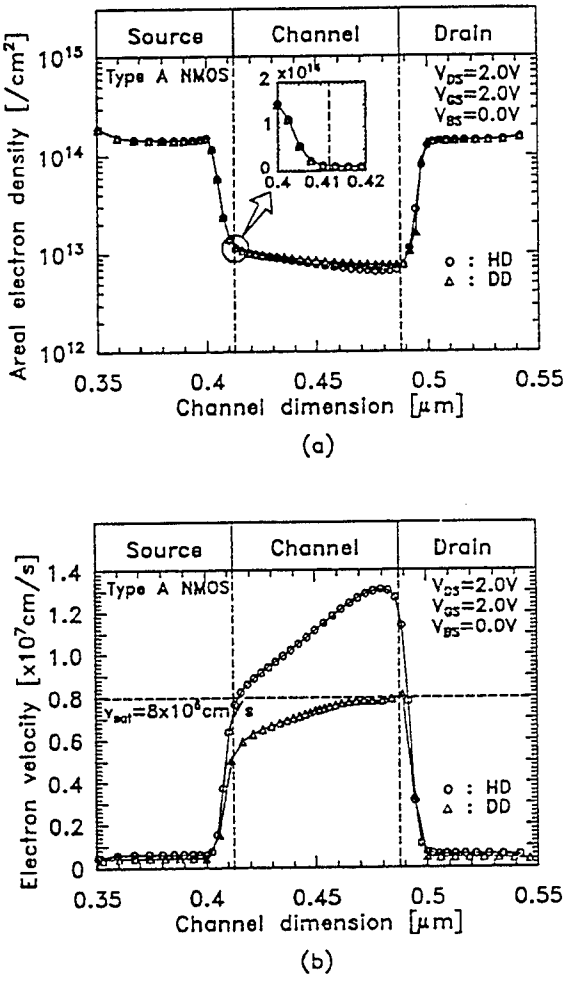


Figure 1: (a) The profiles of the areal electron density(N_{inv}) and (b) electron velocity(v_n) from the HD and DD simulations.

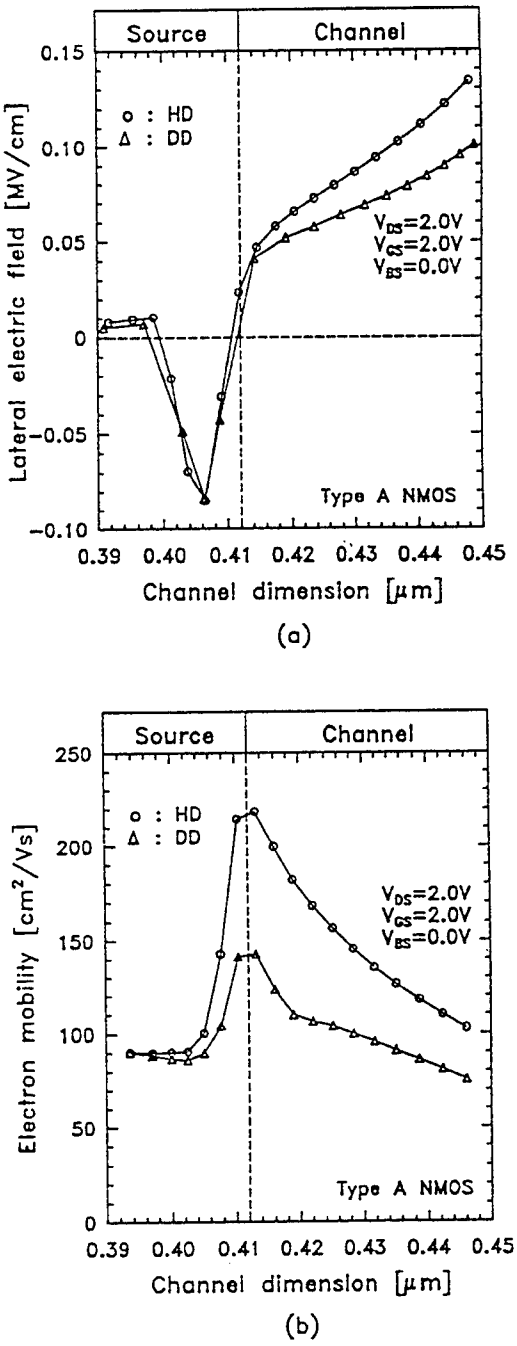


Figure 2: (a) The profiles of the lateral electric field(E_y) and (b) electron mobility(μ_n) in the source region from the HD and DD simulations.

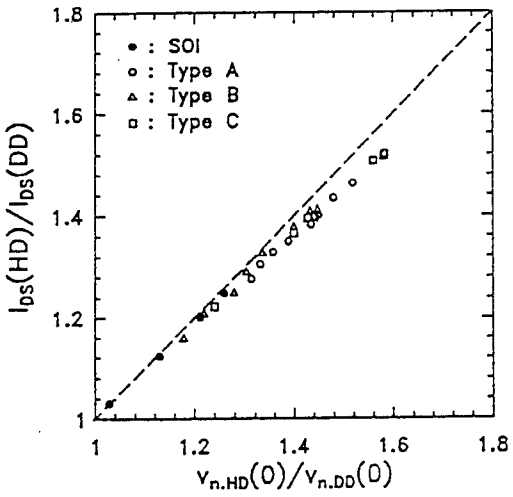


Figure 3: Relation between the simulated $v_{n.HD}(0)/v_{n.DD}(0)$ and $I_{DS}(HD)/I_{DS}(DD)$ for a wide range of bias conditions for the several device structures

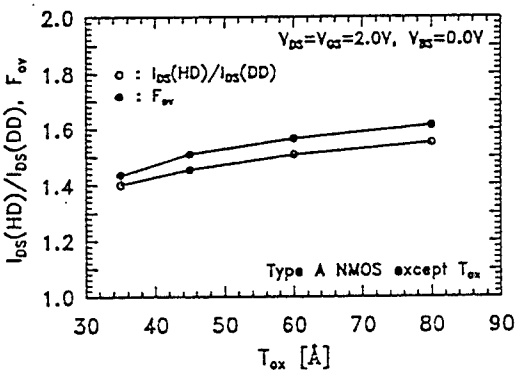


Figure 4: Relation between the calculated F_{ov} and simulated $I_{DS}(HD)/I_{DS}(DD)$ as a function of T_{ox}. For the calculation of F_{ov}, ΔV_T's are obtained from the simulations.

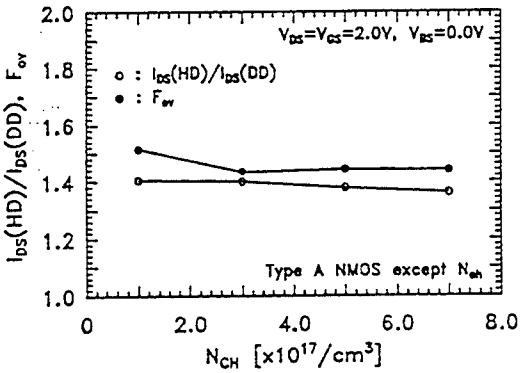


Figure 5: Relation between the calculated F_{ov} and simulated $I_{DS}(HD)/I_{DS}(DD)$ as a function of N_{ch}. For the calculation of F_{ov}, ΔV_T's are obtained from the simulations.

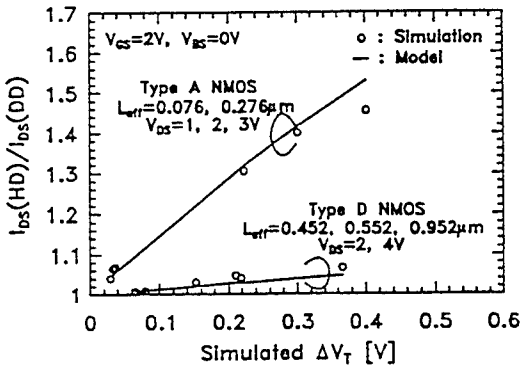


Figure 6: Relation between the simulated ΔV_T's and $I_{DS}(HD)/I_{DS}(DD)$'s.

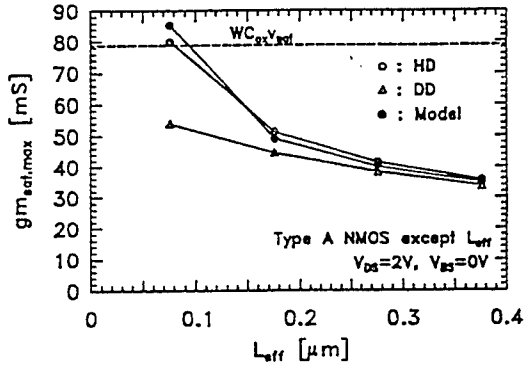


Figure 7: HD, DD simulated and model expected $gm_{sat.max}$ as a function of L_{eff} for type A NMOSFET.

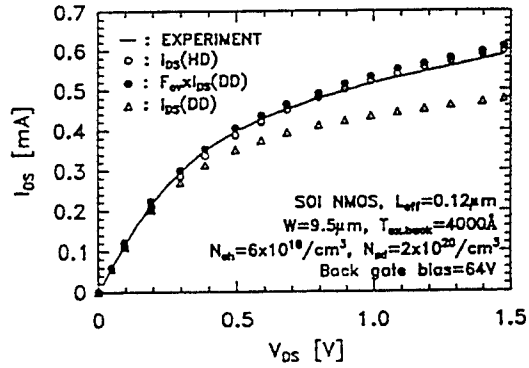


Figure 8: Measured I_{DS}, simulated $I_{DS}(HD)$, $I_{DS}(DD)$ and $I_{DS}(DD)$ mutiplied by the calculated F_{ov}. For the calculation of F_{ov}, ΔV_T's are obtained from the experiment.

Effect of Tunneling Times on the Dynamic Response of Semiconductor Resonant Tunnel Diodes

S.A.Mikhailov, D.V.Posvyanskii and V.A.Volkov*

Institut of Radioenginering & Electronics of RAS, Mokhovaya str. 11, 103907 Moscow, Russia
* e-mail: volkov@frfl.msk.ru

1.Introduction

In general, the dynamic response of semiconductor tunnel structures is determined by two factors, the dynamic processes in tunnel junction itself (with characteristic times of the order of a tunneling time) and the processes of Maxwellian relaxation in semiconductor regions after tunneling. The theory would include the formulation of self-consistent field effects and quantum mechanical time-dependent aspects of electron tunneling to account for both factors. In such complete formulation the problem of linear AC response of the tunnel structure is not solved yet.

We tried to solve this problem using two complementary approaches.

a). *Semiclassical approach.*

Let the tunnel junction occupices the region $-d < z < 0$ and separates two semiconductor regions at $z \geq 0$ and $z \leq -d$. The kinetics of electrons in semiconductor regions is considered within the framework of Boltzman equation for electron distribution function $f_p(\vec{r},t)$ in relaxation time approximation. To describe an electron tunneling through the barrier we postulated the boundary conditions for $f_p(\vec{r},t)$ of the special type [1], which are the AC generalization of the boundary conditions used in [2]. The boundary conditions take into account the finite probability and finite tunneling time and contain a set of phenomenological tunnel parameters, such as transparency (T) and reflection (R) coefficients, reflection or transmission delay times and so on. The kinetic equation is then self-consistently solved with the Poisson equation. The proposed approach is valid for the single and double barrier structures.

It is proved that AC response of the tunnel structure is determined by the properties of low-frequency plasma waves (junction plasmons -JP[3]) running along the interface boundaries in tunnel junction. JP spectrum is defined from the poles of response function. So, as the first step, JP spectrum was derived and, after that, the response function of the structure was obtained. It is shown that it could be described by the equivalent circuit in which a additional quantum (tunnel) capacity C_Q is connected in parallel with the classical one and the tunnel Esaki conductance. The capacity C_Q is proportional to the product of a tunnel time and the bulk plasma frequency.

b) *Quantum mechanical approach.*

In order to find out what is the tunnel time determining the response function and the properties of JP, we calculated JP spectrum in the frameworks of non-local random phase approximation. After comparison of the quantum results with the semiclassical ones we can conclude that a tunnel time involved in semiclassical approach is the transmission/reflection phase time [4].

2.Semiclassical approach

To solve the JP problem in the case of arbitrary transparency, we developed an approximate method which is valid under conditions

$$qv_F << |\omega + i\gamma| << \omega_p \tag{1}$$

The frequency and the damping of the JP running along the interface boundaries in tunnel junction are determined by the equation

$$\omega_{1,2} = \pm\sqrt{\frac{\omega_p^2 q(d/2+\lambda_{TF})}{1+C_Q/C_{cl}} - \left(\frac{\Gamma_1-\Gamma_2}{2}\right)^2} - i\frac{\Gamma_1+\Gamma_2}{2}, \tag{2}$$

where $q=(q_x,q_y)$ is 2D wavevector of JP in the plane of junction, ω_p is the bulk plasma frequency of electrons in the semiconductor regions, λ_{TF} is the Fermi-Thomas screening length, $\Gamma_1 = 1/\tau$ is the inverse momentum relaxation time, $\Gamma_2 = G/(C_{cl}+C_Q)$, G is the tunnel Esaki conductance (per unit area), $C_{cl} = \kappa/4\pi(d+2\lambda_{TF})$ is the classical capacity of the junction (per unit area), κ is the dielectric permittivity of semiconductor and C_Q is the additional quantum tunnel capacity due to the finite delay times (upon reflection τ_R and transmission τ_T, $\tau_R = \tau_T$ for the symmetric structure under consideration).

The quantum capacity C_Q is proportional to a tunnel time, averaged in a special way over the Fermi distribution f^0:

$$C_Q/C_{cl} = \frac{\sqrt{3}(1+d/2\lambda_{TF})\omega_p}{4}\frac{\sum_p \tau_T(p)|v_z|(R-T)\,\partial f_p^0/\partial E_p}{\sum_p |v_z|\,\partial f_p^0/\partial E_p} \tag{3}$$

It has two terms, one represents the influences of reflected and another of transmitted electrons. Reflected (transmitted) electrons give the positive (negative) contribution to C_Q. Owing to the contribution of reflected electrons, the tunnel capacitance C_Q has a relatively large value (comparable with the classical one) even for the structures with non-transparent barriers. This, in general, gives opportunity to determine the phase tunnel time from experiments on JP spectrum and/or electromagnetic response in the structures with classical (non-transparent) barriers.

Then we calculated the tunnel junction dynamic impedance with account of as quantum mechanical reflection/transmission coefficients, as deviations of electron distribution function from the local equilibrium one. The low-frequency linear electromagnetic response of the structure "metal-semiconductor -tunnel junction -semiconductor-metal" is described by the equivalent circuit in which the tunnel capacity C_Q is connected in parallel with the tunnel Esaki conductance G and classical capacity C_{cl}. The tunnel junction is, thus, described by the complex conductance $\left(Z^{-1}\right)_{tun}(\omega) = G - i\omega(C_Q + C_{cl})$.

3.Quantum mechanical approach

The semiclassical model has some obvious advantages like simplicity, possibility of improvement, but has one (very important) deficiency: the boundary conditions for distribution function (which contains information about noninstantaneous character of reflection/tunneling and about finite transparency of barrier) can not be obtained in the framework of this approach. In order to check the results of semiclassical approach, we used quantum-mechanical approach (random phase approximation - RPA) in JP spectrum calculation.

In order to calculate the spectrum of collective excitations, we used the general RPA equation for the response of the induced potential $\phi(r)$ in the case of "clean" semiconductors

$$\phi(r) = \int dr' \int dr'' G(r-r'') \Pi(r', r'', \omega) \phi(r') \tag{4}$$

where $G(r-r'')$ is Green function of the Poisson equation and

$$\Pi(r, r', \omega) = \sum_{a,a'} \frac{f_{a'}^0 - f_a^0}{E_{a'} - E_a + \hbar\omega + i0} \Psi_a^*(r) \Psi_{a'}^*(r') \Psi_a(r') \Psi_{a'}(r),$$

where the indexes a, a' enumerate electron states, f^0 is the Fermi-Dirac distribution function, Ψ_a is the basis function of the problem of scattering. We restricted our consideration to an almost completely reflecting rectangular barrier with height V and supposed that the condition $\kappa d >> 1$ takes place, where $\kappa = \left(2m(V - E_F)\right)^{1/2} / \hbar$ and $V >> E_F$. After substitution of Ψ_a into integral equation (4) we obtained at $z \geq 0$:

$$\begin{aligned} \phi(z) = & \int_0^\infty dz' \left(\Lambda(z-z') + \Lambda_R(z+z') - \Lambda_T(z+z')\right)\phi(z') - \phi(0)\coth(qd/2)e^{-qz} - \\ & - e^{-qz} \int_0^\infty dz' \left(\frac{d\Lambda(z')}{dz'} - \frac{d\Lambda_R(z')}{dz'} + \frac{d\Lambda_T(z')}{dz'} \right) \phi(z') \end{aligned} \tag{5}$$

$$\Lambda_\alpha(z) = 4\pi e^2 \int_{-\infty}^{\infty} \frac{dk_\parallel}{(2\pi)^2} \int_0^\infty \frac{dk dk'}{(2\pi)^2} \frac{f_{k';k_\parallel+q}^0 - f_{k;k_\parallel}^0}{E_{k',k_\parallel+q} - E_{k,k_\parallel} + \hbar\omega + i0} \left(\frac{\left(\alpha_k \alpha_{k'}^* e^{i(k-k')z} + c.c\right)}{(k-k')^2 + q^2} \right)$$

where α=1,r,t; $r = \sqrt{R} e^{i\theta}$, $t = \sqrt{T} e^{i\vartheta}$. In bulk semiconductor (α=1) the Fourier transformation of $\Lambda_1(|z|)$ is the polarizability of homogeneous electron gas $\chi(q, q_z, \omega)$.

We analyzed the JP dispersion law under the condition $qv_F << \omega << \omega_p$ and neglected by the bulk Landau damping of plasmons in the semiconductor regions.

We solved integral equation (5) in this case. Let us consider the results in simplest limit $T = 0$, $V < \infty$ (transparency of the barrier is zero, but the barrier has a finite height) .Then the JP spectrum is

$$\omega_{1,2} = \pm\omega_p \sqrt{\frac{q(d/2 + \lambda_{TF})}{1 + \frac{\sqrt{3}}{2}\omega_p \tau_R(E_F)(1 + d/2\lambda_{TF})}}, \tag{6}$$

where $\tau_R(E_F) = 2/v_F\kappa$ is the phase tunnel time ($\tau_R \equiv \hbar\partial\theta/\partial E = \tau_T \equiv \hbar\partial\vartheta/\partial E$) on Fermi level in one barrier case [4]. In this case let us compare equations (2) and (6).

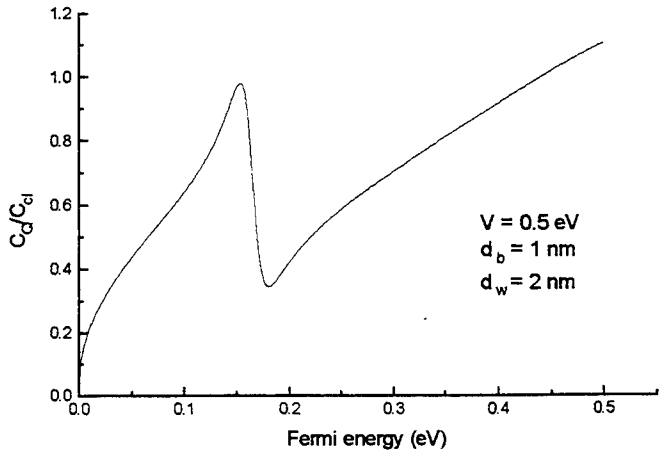
Let us suppose that $\tau_T(p)\left[= \tau_R(p)\right]$ in Eq.(3) is the phase time, then Eq.(3) could be reduced to the form

$$C_Q / C_{cl} = \frac{\sqrt{3}(1 + d/2\lambda_{TF})}{2} \omega_p \tau_R(E_F) \tag{7}$$

Accounting for (7), expressions (2) and (6) fully coincide in the case of $\Gamma_1 = \Gamma_2 = 0$. *So, the tunnel time which was used in semiclassical approach is phase time of reflection (or transmition).*

We have calculated the Fermi energy dependence of tunnel capacity C_Q in single and double tunnel junctions cases with different widths d and heights V of barriers. In a single barrier structure, the ratio C_Q / C_{cl} increases with E_F and d and decreases with V. In a double barrier structure, the dependence of C_Q / C_{cl} on E_F displays the δ'-like peculiarity near the tunnel resonance.

In figure the normalazed quantum capacity is shown versus Fermi energy in double barrier tunnel structure with the barrier height 0.5 eV, the well width 2 nm and the barrier widths 1 nm (d=4nm). The figure shows that quantum capacity can be comparable with the classical one near the tunnel resonance $E_F^{res} = 0.17$ eV.



4.Conclusions

We developed semiclassical and quantum mechanical approaches to the problem of the dynamic response of semiconductor tunnel devices. It is shown that account of tunnel times leads to an additional quantum capacity of junction connected in parallel with the classical one. Quantum capasity is proportional to the phase time of transmission or reflection and does not vanish in the limit of non-transparent barrier and can be comparable with the geometry capacity. In the case of resonance tunnel diode, it has resonance behaviour near the resonance of transmission coefficient.

5.Acknowledgement

This work was partially supported by the Russian Foundation of Fundamental Research, Grant No 93-02-15406.

References

1. S.A. Mikhailov, V.A. Volkov, JETP Lett., **61**, 524, 1995
2. B.Laikhtman, S.Luryi, Phys.Rev., **B49**, 17177, 1994
3. Z.Szentirmay, Prog.Quant. Electr., **15**, 175,1991
4. T.E.Hartman , J.Appl.Phys., **33**, 3427, 1962

Resonant Tunneling Diode I(V) Lineshapes: Analytical Formula

J. N. Schulman* and H. J. De Los Santos†

*Hughes Research Laboratories, Malibu, CA 90265

†Hughes Space and Communications Company, Los Angeles, CA 90009

1.0 Introduction

The development of resonant tunneling diodes (RTD's) has achieved a level of maturity such that a variety of circuit implementations have been proposed and prototype circuits have been fabricated and tested. To predict and explain circuit behavior, attempts have begun to incorporate the RTD negative resistance into circuit simulation models, usually based on SPICE-type CAD tools. Examples and further references can be found in Ref. [1]. At the same time, detailed quantum mechanical models have also made significant progress over the past decade in investigating the essential features that determine RTD behavior. However, models which include more physics, e.g., multiple bands or phonon scattering, can be quite computationally intensive.

The current versus voltage, I(V), characteristic of the diode is the quantity that determines the DC circuit behavior. The features of the I(V) curve which are most important are dependent on the circuit design of interest. For example, a high peak to valley current ratio may be critical in one application, but high peak currents with moderate peak to valley ratios may be more important in another. The voltages at the peak and valley currents can also be very significant. The design of the RTD heterostructure must try to optimize these quantities. For this the SPICE-level calculation should be able to take the calculated I-V curve and predict quantities related to circuit analysis such as speed, power levels, and sensitivity to fabrication induced variations in the I(V) curve.

There is a gap between the quantum mechanical models and circuit simulation that this paper attempts to bridge. There are two challenges to be met. First, the quantum mechanical models are too computationally intensive to be called directly from a circuit simulator. Second, even if they could be called in this way, this would be undesirable because they do not adequately predict the measured data at this time. This is partly due to a lack of a full understanding of the physics involved, but also due to unavoidable uncertainties in fabrication. What is needed is an analytical form with the following properties. It should be a simple formula that can be easily incorporated into the circuit simulator, avoiding discontinuities that can cause lack of convergence [1]. It should be closely related to a quantum mechanical model so that it reflects physical reality. Lastly, it should have adjustable empirical parameters so that measured I(V) curves can be reproduced. It is important that these empirical parameters should be linked as closely as possible with real physical quantities and not just be arbitrary curve-fitting parameters. In the following we derive and demonstrate the use of a proposed form for the I(V).

2.0 Derivation

The philosophy of the following procedure continues from the work of Coon and Liu [2] and Chang, et al [3]. Coon and Liu derived a simple formula for the I(V) without arbitrary parameters for the zero temperature limit. Chang, et al, introduced arbitrary parameters into a variation of Coon and Liu's result. This allowed them to create a fair reproduction of the experimental I(V) data for their device of interest. Here we start from the standard formula for the current in the effective mass approximation assuming the transmission is independent of electron in-plane momentum and keeping Fermi statistics:

$$J = \frac{e m^* kT}{2\pi^2 \hbar^3} \int_0^\infty dE \mathrm{T}(E,V) \ln\left[\frac{1+e^{(E_F-E)/kT}}{1+e^{(E_F-E-eV)/kT}}\right]$$

The transmission coefficient is approximated by a Lorentzian:

$$\mathrm{T}(E,V) = \frac{(\Gamma/2)^2}{\left[E-(E_r-eV/2)\right]^2+(\Gamma/2)^2}$$

E is the energy measured up from the emitter conduction band edge. E_r is the energy of the resonant level relative to the bottom of the well at its center. Γ is the resonance width. This formula assumes equal width barriers and that half the voltage drop falls from the emitter to the center of the well. This is certainly not always the case. Then, eV/2 could be replaced here and in the following equations by eVn with n

determined from analysis or from fitting the I-V curve.

The next step contains the approximation. For small Γ, the transmission coefficient is negligible except when E is close to the resonance, i.e., $E \cong E_r - eV/2$. Calculations show that Γ is on the order of an meV or less for even quite thin barrier widths [4]. This is much less than kT at room temperature. Therefore the substitution $E = E_r - eV/2$ can reasonably be made in the log term and it can be taken outside the integral. The result is:

$$J = \frac{e m^* kT}{2\pi^2 \hbar^3} \ln\left[\frac{1+e^{(E_F - E_r + eV/2)/kT}}{1+e^{(E_F - E_r - eV/2)/kT}}\right] \times \int_0^\infty dE \frac{(\Gamma/2)^2}{\left[E-(E_r - eV/2)\right]^2 + (\Gamma/2)^2}$$

This integral can be done and the result is:

$$J = \frac{e m^* kT\Gamma}{4\pi^2 \hbar^3} \ln\left[\frac{1+e^{(E_F - E_r + eV/2)/kT}}{1+e^{(E_F - E_r - eV/2)/kT}}\right] \times \left(\frac{\pi}{2} + \tan^{-1}\left(\frac{E_r - eV/2}{\Gamma/2}\right)\right)$$

The simplification of using $\pi/2 + \tan^{-1} x = -\cot^{-1} x$ is not used, because the proper quadrant is then not found using standard conventions.

This formula can be regarded as providing the correct *form* for the lineshape, but calculated in an oversimplified way. The physical quantities can be allowed to depart from their actual values so as to compensate for the approximations and omissions in the model. The following form is the result, where the initial guesses for A, B, C, D, and n_1 can be determined by comparison with the above, and then adjusted for match with experiment.

$$J_1(V) = A \ln\left[\frac{1+e^{(B-C+n_1 V)e/kT}}{1+e^{(B-C-n_1 V)e/kT}}\right] \times \left(\frac{\pi}{2} + \tan^{-1}\left(\frac{C-n_1 V}{D}\right)\right)$$

So far this form produce a peak current but there is no valley current. The current continuously decreases with voltage after the peak. Tunneling and thermal excitation through and over higher resonances and the barrier itself are not included yet, or are scattering processes. The simplest way to add this in would be to give it the form of tunneling through a single higher resonance. For reasonably small higher resonance widths, and voltages well below this second resonance, the argument of the arctan is large and the arctan becomes just $\pi/2$ independent of voltage. A second resonance can thus be included using a term of the form:

$$J_2(V) = H_1 \ln\left[\frac{1+e^{(-G+n_2 V)e/kT}}{1+e^{(-G-n_2 V)e/kT}}\right] .$$

Using G>>V, this can be approximated as

$$J_2(V) \approx H_2\left(\cosh(n_2 eV/kT) - 1\right) \approx H\left(e^{n_2 eV/kT} - 1\right) .$$

The last form assumes eV>>kT and is probably adequate for most purposes.

3.0 Results

Figure 1 shows a comparison between measured data and a fit using the sum of the two formulas, $J_1(V)+J_2(V)$:

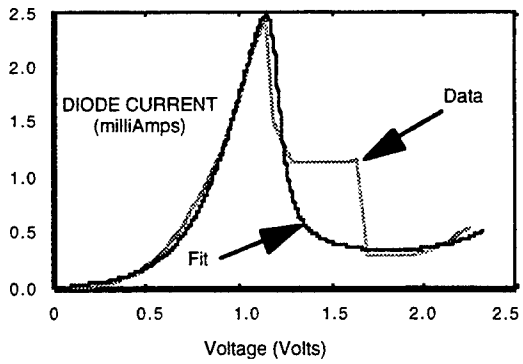


FIGURE 1. Comparison of measured RTD I(V) and fit to model.

The RTD is made from InGaAs/InAlAs with 9 monolayer barriers and a 16 monolayer well. The doping was 10^{18} with 265Å low doped spacer layers. This sample was chosen for its low series resistance voltage drop, and is not particularly suitable for high speed application. The fitting parameters used were: A=0.001, B=0.022, C=0.162, D=0.00646, n_1=0.1331, H=1.1839x10^{-8}, n_2=0.1095. The fit is excellent. In particular, the low voltage turn on, the shape of the maximum, the peak width and the form of the valley current are all well reproduced. The plateau region after the peak is well understood as due to oscillations in the negative resistance region and not the true DC characteristic.

Here we demonstrate the application of the I-V equation derived above by presenting results for an InGaAs/InAlAs HBT-driver/RTD-load bipolar inverter simulated using SPICE3f5. The RTD is modeled by a resistance in series with a parallel combination consisting of a non-linear dependent current source and a non-linear capacitor. For the RTD capacitance, the functional form $C_{jo}/(1+V/V_{bi})^M$, with C_{jo}=0.03pF, V_{bi}=0.0368V, and M=0.19 was used, where the parameters were obtained from a fit to capacitance calculations based on our self-consistent numerical two-band model. Figure 2 displays a plot of the inverter's transient response.

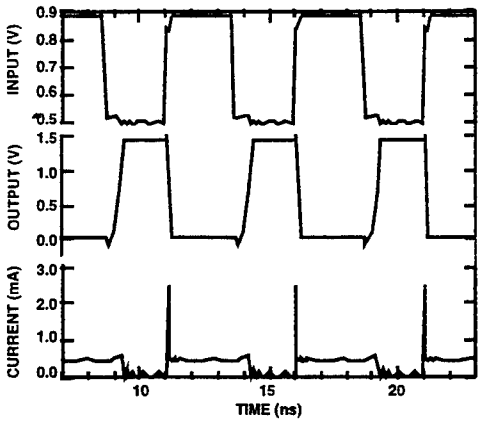


Figure 2. InGaAs/InAlAs HBT-driver/RTD-load bipolar inverter transient analysis response.

4.0 Analysis

The small value for the parameter n_1 above serves to stretch out the voltage scale. In actuality, there is a significant voltage drop over the collector spacer layer which causes the stretching. This is not explicitly included in the above derivation, but is mimicked by the low value for n_1. The band bending can be a large effect, especially if the spacer layer is wide and its doping small. The formula can be made more realistic by adding in an explicit simple form for the band bending in the total depletion approximation. Then, it can be included as a series voltage drop. The total depletion approximation gives

$$V_c = \varepsilon\varepsilon_0 F^2 / 2eN_d$$

for the collector voltage drop. F is the electric field and is just V/d, where d is the thickness of the barriers and wells together. This result then just has the form of $V_C=\beta V^2$. The total voltage across the device is then $V_t=V+V_C$, where V is the voltage used in the above formulas. The new parameter β can be used as a replacement for or in addition to n_1, which should return to a more physically realistic value (0.5 in the simplest approximation).

There are additional physical effects which the above formulas omit, but which are more difficult to devise simple formulas for. They affect the shape of the negative resistance region itself, and in particular the difference of the valley and peak voltages. In the simplest approximation, the characteristics of this region are determined by the bottom of the emitter conduction band passing through the resonance. A sudden drop-off, determined by the resonance width, Γ, would determine the slope here. However, this approach is too simple and not useful. Even in the ideal case, ignoring growth non-uniformities, there are at least two effects that predominate.

First, the dependence of the transmission coefficient on the electron momentum parallel to the layers is important here, even for Type I heterostructures. The difference in the effective masses in the well and barriers imply that the resonance energy itself depends on parallel momentum. This shifts the effective resonance position as the voltage is varied, thereby significantly decreasing the negative resistance slope. This is illustrated in Figure 3, which plots the data and two different theoretical models. Curve (b) is a calculation using a two band model [5] including the parallel momentum effect. This is to be compared with curve (c) which is also a two band model, but in which the variation on parallel momentum is ignored. The calculation was done for a structure with 8 monolayer barriers instead of the nominal 9 determined by MBE dead reckoning. This level of uncertainty is unavoidable at present and the fit is improved considerably by using 8 monolayers.

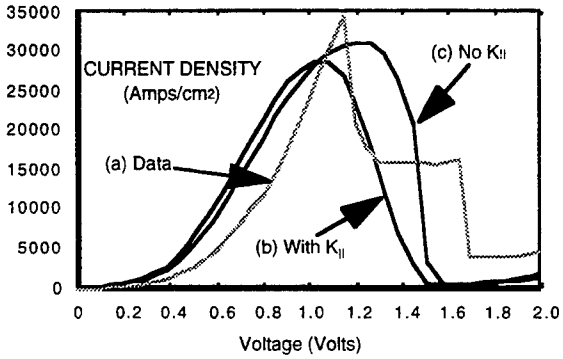


FIGURE 3. Comparison of measured RTD I(V) with two models.

It can be seen that including the parallel momentum effect significantly spreads out the negative resistance region, giving a closer approximation to the actual voltage difference between the valley and peak

voltages. It also decreases the peak voltage considerably [6].

The second effect which is important, but not yet included explicitly, is the decrease in the transmission as the resonance approaches, but is still above, the emitter conduction band edge as the voltage is increased. In other words, the current maximum does not occur when the edge lines up with the resonance. This is obvious from considering that an electron with zero kinetic energy does not transmit. The actual peak voltage is smaller and results from the tradeoff between this decrease in transmission as the resonance approaches the conduction band edge versus the increasing number of electrons available to tunnel through the resonance due to the Fermi distribution [6,7]. This tends to decrease the peak voltage, and to round off the peak. The simple formula

$$T_{MAX} = \sqrt{1-\left(eV / 2E_r\right)^2}$$

gives an excellent approximation for the decrease of the Lorentzian transmission peak to zero as the applied bias approaches the resonance condition [6].

As is well known, there is one more important quantity to include when comparing any model to data: series resistance. Hopefully, the series resistance can be measured and can be put in directly as an additional resistor in the circuit simulation. If not, the resistance is an additional parameter to be determined. The above sample was purposely chosen to have a relatively small current to avoid this issue. For high speed RTD's in which the current is larger, this issue cannot be ignored.

5.0 Summary

We have developed a framework for bridging the gap between quantum mechanical models of resonant tunneling, circuit simulation models, and measured data. The formula we have derived involves variables which can be regarded as representing their true physical values, or these values can be considered to be starting points for an empirical fit. Additional physical effects can be added in as necessary in a realistic way. Several challenges remain, especially the modeling of the negative resistance region itself and the application of this strategy to Type II resonant interband tunneling diodes.

6.0 References

[1] S. Mohan, J. P. Sun, P. Mazumder, G. I. Haddad, *IEEE Trans. Computer-Aided Design.*, **14**, 6 (1995), pp. 653-662.

[2] D. D. Coon and H. C. Liu, *App. Phys. Lett.* **49**, (1986), pp. 94-96.

[3] C. E. Chang, P. M. Asbeck, K.-C. Wang, E. R. Brown, *IEEE Trans. Electron Dev.* **40**, 4 (1993), pp. 685-691.

[4] D. H. Chow, J. N. Schulman, E. Özbay, and D. M. Bloom, *App. Phys. Lett.* **61**, (1992), pp. 1685-1687. See Table 1.

[5] J. N. Schulman and M. Waldner, *J. Appl. Phys.*, **60** (1986), pp. 3954-3958. J. N. Schulman, *J. Appl. Phys.*, **63** (1988), pp. 2859-2861.

[6] J.N. Schulman, in preparation.

[7] T.B. Boykin, R.E. Carnahan, and K.P. Martin, *Phys. Rev. B*, **51** (1995), pp. 2273--2281. See Figure 3.

A Systematic Extraction Method for Noise Sources and Correlation Coefficient in MESFET

Jong-Hee Han, *Student Member, IEEE*, and Kwyro Lee, *Senior Member, IEEE*

Department of Electrical Engineering, KAIST,
373-1, Kusong-dong, Yusong-gu, Taejon, Korea 305-701.

Abstract - A systematic extraction method for noise sources and correlation coefficient in the noise equivalent circuit of GaAs MESFET is proposed. It is based on the linear regression, which allows us to extract physically meaningful parameters from the measurement. The confidence level of the measured data can be easily examined from the linearity, y-intercept of the linear regression, and the scattering from the regression line. Furthermore, it is found that the time delay of correlation coefficient whose value is almost the same as that of the transconductance should be considered to model noise parameters accurately.

I. Introduction

The noise characteristics of a linear two-port system can be completely described by 2-port parameters such as Y, Z, S-parameters and the additional four noise parameters. There are several equivalent sets of these four noise parameters, depending on how to represent the two-port circuit[1]. In H-representation, the noise current source at the input in Y-representation is replaced by the noise voltage source. Generally speaking, the correlation between the noise sources has to be taken into account in any representation and the values of the 4 noise parameters should be determined from noise measurement at every bias point for each device.

Pospieszalski[2] assumed that the gate noise voltage and drain noise current sources are independent of each other. But, that assumption is not proved yet. Granted it is true in the intrinsic device, the parasitic gate-source capacitance, C_{gsp}, invokes the correlation between gate noise voltage and drain noise current sources[3]. Since it is very difficult to discriminate C_{gsp} from the intrinsic capacitance, C_{gsi}, by S-parameter measurement, the correlation coefficient has to be considered in the noise equivalent circuit.

Usually a numerical optimization technique is used for extracting the noise sources from the measured noise characteristics by minimizing the error between the measurement and model. Though conceptually accurate, numerical optimization often gives wrong answer due to the local extrema. This is especially true for the noise data since the data itself is very noisy. Furthermore, it is hard to figure out the confidence level of the extraction result. In this paper, we propose a new systematic method to determine the noise sources from the measurement by linear regression.

II. Noise modeling of MESFET

Fig.1 shows MESFET small signal equivalent circuit with H-representation noise sources whose correlation coefficient is C_{II}. Here, C_{II} is defined as $\langle v_{gn}\, i_{dn}{}^{*} \rangle$ over $\sqrt{\langle v_{gn}{}^{2} \rangle \langle i_{dn}{}^{2} \rangle}$, which is a complex number in general. Note that C_{gs} in Fig.1 is the sum of C_{gsp} and C_{gsi}. The input equivalent noise voltage, v_{in}, and the noise current sources, i_{in}, can be derived in the intrinsic equivalent circuit(inside the dotted box in Fig.1) as follows. v_{in} is the input equivalent noise voltage source which generates the same output noise when the gate is short to ground in AC, given by

$$v_{in} = v_{gn} + \frac{1 + j\omega C_{gs} R_i}{g_m e^{-j\omega\tau}} i_{dn} . \qquad (1)$$

i_{in} is the input equivalent noise current generating the same output noise when the gate is open in AC, which can be written as

$$i_{in} = -\frac{j\omega C_{gs}}{g_m e^{-j\omega\tau}} i_{dn} . \qquad (2)$$

Noise conductance, G_n can be obtained by normalizing $\langle i_{in}^2 \rangle$ by $4kT\Delta f$ as following

$$G_n = \frac{1}{4kT\Delta f}\frac{\omega^2 C_{gs}^2}{g_m^2}\langle i_{dn}^2 \rangle \quad . \tag{3}$$

The correlation impedance between v_{in} and i_{in}, Z_c, defined by $\langle v_{in}\, i_{in}* \rangle$ over $\langle i_{in}^2 \rangle$ can be derived using Eqs.(1)-(2) as follows.

$$Z_c = -R_i + \frac{j}{\omega C_{gs}} + \frac{j g_m e^{-j\omega\tau} C_H}{\omega C_{gs}}\sqrt{\frac{\langle v_{gn}^2 \rangle}{\langle i_{dn}^2 \rangle}} \quad . \tag{4}$$

C_H can be assumed to have only the real part in MESFET at low frequency, but the imaginary part of C_H increases at higher frequency. Ignoring the imaginary part of C_H gives rise to the large discrepancy in noise characteristics between measurement and model especially at high frequency as in Sec.IV. We found from the measurement that the angle of C_H is proportional to the frequency, and that its proportional constant can be approximated by g_m time delay, τ. Then C_H is can be written as $C_H e^{j\omega\tau}$. Then, the imaginary part of the optimum impedance, X_{opt}, can be written as

$$X_{opt} = \frac{1}{\omega C_{gs}}\left(1 + g_m C_H \sqrt{\frac{\langle v_{gn}^2 \rangle}{\langle i_{dn}^2 \rangle}}\right) . \tag{5}$$

Note that X_{opt} is inversely proportional to ωC_{gs}, and that its proportional constant is dependent on C_H. On the other hand, the real part of the optimum impedance, R_{opt}, can be easily derived as

$$R_{opt}^2 = R_i^2 + \left(1 - C_H^2\right)\frac{\langle v_{gn}^2 \rangle}{\langle i_{dn}^2 \rangle}\left(\frac{\omega_T}{\omega}\right)^2 , \tag{6}$$

where ω_T is the unit current gain frequency given by g_m / C_{gs}. It is very interesting to notice that $R_{opt}^2 - R_i^2$ is inversely proportional to the square of frequency.

III. Extraction method of noise sources from measurement for MESFET

Three noise parameters, $\langle v_{gn}^2 \rangle$, $\langle i_{dn}^2 \rangle$, and C_H are extracted from the frequency dependent noise measurement. The combinations of these three parameters have relations with G_n(Eq.(3)), X_{opt} (Eq.(5)), and R_{opt}^2(Eq.(6)). Therefore, we can extract them from three plots summarized in Table below. Therefore, we can extract three unknown noise parameters from the slopes of plots using linear regression. The inherent advantages of the linear regression are :

i) there is no danger to go into local extrema, and

ii) the confidence level of the extraction results can be checked easily from the linearity of the plots, i.e., slope, y-intercept, and the scattering from the regression line.

The examples of the extraction plots are shown in Figs.2~4. Note that the slope of X_{opt} vs. $1/\omega C_{gs}$ is not 1. In the Pospieszalski's model where C_H is zero, X_{opt} should be exactly the same as $1/\omega C_{gs}$, which means the slope should be 1. But, as shown in Fig.3, the slope is 1.2, and the slope goes upto ~1.4 at some bias conditions.

Graph	G_n vs. $(\omega/\omega_T)^2$	X_{opt} vs. $1/\omega C_{gs}$	$\left(R_{opt}^2 - R_i^2\right)$ vs. $(\omega_T/\omega)^2$
Slope	$\dfrac{\langle i_{dn}^2 \rangle}{4kT\Delta f}$	$1 + g_m C_H \sqrt{\dfrac{\langle v_{gn}^2 \rangle}{\langle i_{dn}^2 \rangle}}$	$\left(1 - C_H^2\right)\dfrac{\langle v_{gn}^2 \rangle}{\langle i_{dn}^2 \rangle}$

Table1. Three plots for the extraction of the noise parameters, and their idealized slopes.

IV. Comparison of model with measurement

The measured device is an ion-implated GaAs MESFET, whose geometry is $0.5 \times 300 \mu m^2$. The minimum noise figure, the optimum impedance, and the noise resistance of our proposed model are compared with those of measurement. In addition to our model, we compare two more cases. One is when C_{II} is assumed to have only real part in noise parameter calculation, and the other is when C_H=0, i.e., Pospieszalski's model. The noise sources in Pospieszalski's model are extracted from the slopes in the plot of G_n vs. $(\omega/\omega_T)^2$ and $\left(R_{opt}{}^2 - R_i{}^2\right)$ vs. $(\omega_T/\omega)^2$. Comparison is performed at two bias conditions in Figs.5~6, both at 45 mA(V_{GS}=0.0V) and at 15 mA(V_{GS}=-0.8V) with V_{DS}=3.0V, respectively. Figs.5~6 show that our model has much better accuracy than the other two models in explaining frequency dependence of all four noise parameters.

V. Conclusion

A new extraction method for noise sources and correlation coefficient in the noise equivalent circuit of GaAs MESFET has been proposed. Since the extraction of noise sources and correlation coefficient is based on the linear regression, it allows us not only to extract physically meaningful parameters from the measurement in a systematic and straightforward way, but also to examine easily the confidence level of the measured data from the linearity of three plots and the scattering from the regression lines. The comparison of noise figure, optimum impedance, and noise resistance between our model and measurement shows excellent agreements both at high and at low drain current bias for a typical MESFET device studied in this paper.

Acknowledgment

The authors thank Dr. Chul-Soon Park at ETRI and Dr. Woong-Sik Cho at LG Electronics Inc. for their help in noise measurement.

References

[1] K. Hartmann, "Noise Characterization of Linear Circuits," *IEEE Trans. Circuit Syst.*, vol.CAS-23, no.10, pp.581~590, Oct. 1976.

[2] M. W. Pospieszalski, "Modeling of Noise Parameters of MESFET's and MODFET's and Their Frequency and Temperature Dependence," *IEEE Trans. Microwave Theory Tech.*, vol.MTT-37, no.9, pp.1340~1350, Sep. 1989.

[3] F. Danneville, *et al.* "Microscopic Noise Modeling and Macroscopic Noise Models : How Good a Connection?," *IEEE Trans. Electron Devices*, vol.ED-41, no.5, pp.779~786 , May 1994.

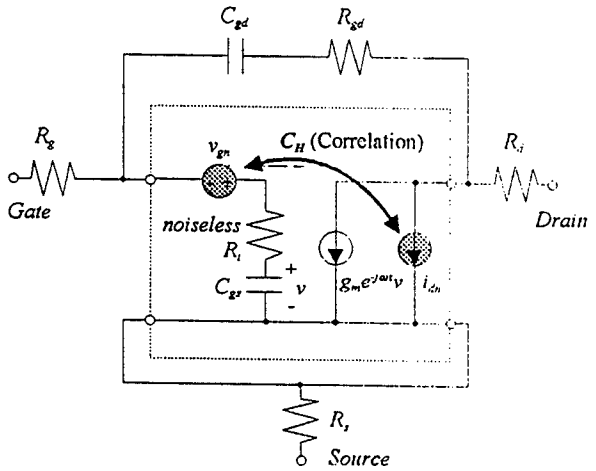


Fig. 1. A noise equivalent circuit in H-representation for MESFET.

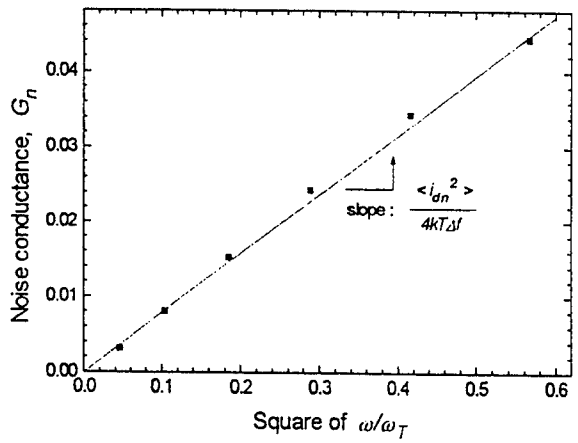


Fig.2. G_n vs. $(\omega/\omega_T)^2$ plot at V_{GS},V_{DS}=0.0, 3.0V.

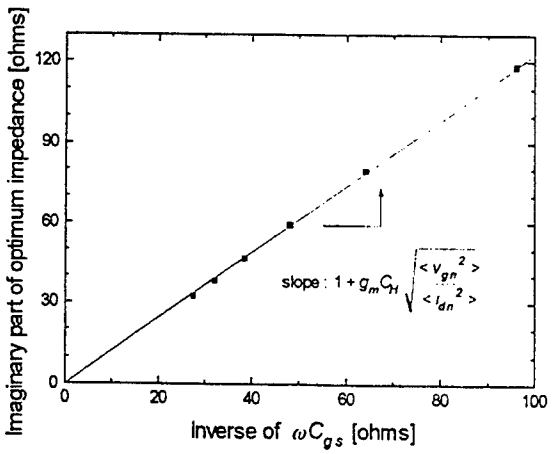


Fig. 3. X_{opt} vs. $(\omega_T / \omega)^2$

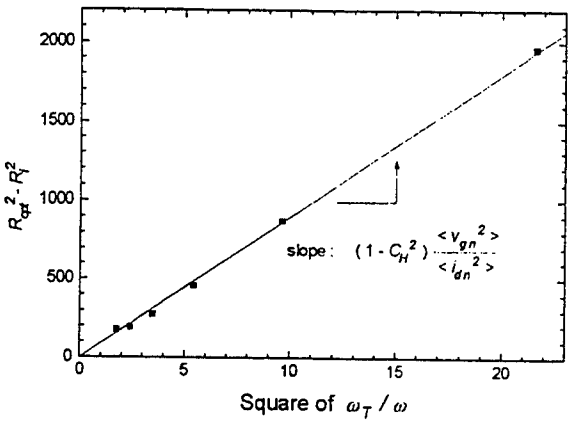


Fig. 4. $\left(R_{opt}^2 - R_i^2\right)$ vs. $(\omega_T / \omega)^2$

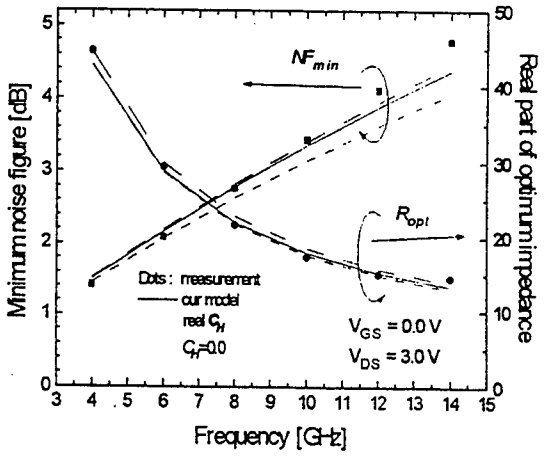


Fig.6 (a) $NF_{\min}$ and R_{opt} at V_{GS},V_{DS}=0.0, 3.0V

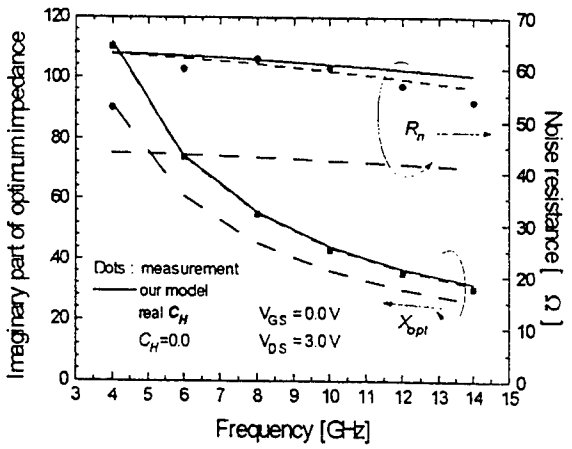


Fig.6(b) X_{opt} and R_n at V_{GS},V_{DS}=0.0, 3.0V

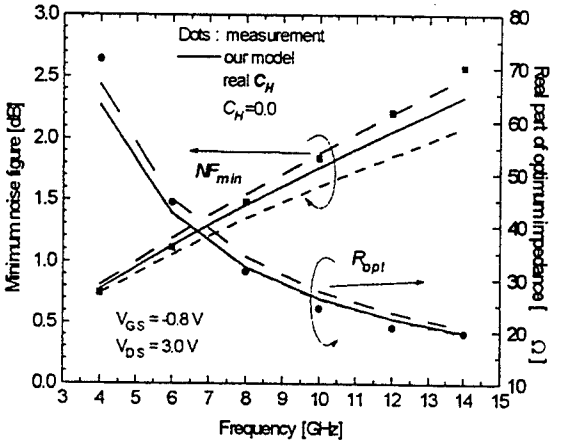


Fig.7 (a) $NF_{\min}$ and R_{opt} at V_{GS},V_{DS}=0.0, 3.0V

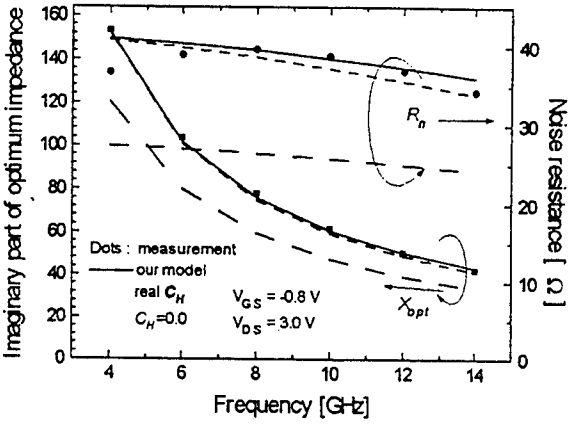


Fig.7(b) X_{opt} and R_n at V_{GS},V_{DS} = 0.0, 3.0V. Dots are measured data. Solid lines are calculated one using our model, the short and long dashed lines are those with real C_H and zero C_H.

An Efficient Current-Voltage Model of the SRH Generation-Recombination for $Al_xGa_{1-x}As$/GaAs N-p Heterojunction Diode

JaeHong Choi, HyeongRae Kim, SangDong Yoo, ByeongGeun Song, NamHong Jo, KaeDal Kwack

Abstract

An efficient and general model for analyzing the I-V(current-voltage) characteristics of N-p $Al_xGa_{1-x}As$/GaAs heterojunction is presented by using the SRH(Shockley-Read-Hall) G-R(generation-recombination) equation. The I-V equations are further classified in order to obtain the more general and precise characteristic equations according to the various biased conditions. The density and level of the traps are also considered.

The validity of the presented model is verified by comparing the results of simulation with those of experimental data and numerical analysis.

I. Introduction

The $Al_xGa_{1-x}As$/GaAs compound semiconductors making up the heterojunction have larger bulk defect densitiy and poorer surface qualitiy in comparision with those of homojunction device. They operate as the G-R traps and thereby produce a junction current. The trap is one of the most important factors in G-R mechanism at low temperature, reverse bias and small forward bias.

Also, because the energy gap of $Al_xGa_{1-x}As$/GaAs is large, the G-R current in the SCR is more important than that of other materials, due to the small intrinsic carrier density in $Al_xGa_{1-x}As$/GaAs[1].

Therefore, to predict accurately these device's characteristics and to design optimally these circuits, it is prerequisite to set up the precise I-V characteristic models of G-R. A few basic models on these topics were issued recently, but they did not analytically characterize the effects of trap with the various parameters of trap[2-4]. Not only these simple characteristic models result in limiting the significant material parameters, but also they don't give satisfactory results regarding the analysis of G-R due to the assumption of the sensitive paremeters such as E_t (trap level), E_i (intrinsic level), N_t (trap density), τ_n(electron life time) and τ_p(hole life time). In these papers, the conditions of $\tau_n = \tau_p$ and $E_t = E_i$ are asumed. These assumptions are the most effective G-R trap, but these assumed models are strictly valid for the middle trap level and they could not generally include the variational parameters as mentioned above. Moreover, the $Al_xGa_{1-x}As$/GaAs material has less effective G-R traps ($E_t \neq E_i$).

In this paper, the analytical G-R model for the heterojunction is presented and discussed in consideration of the trap density and level which existed in $Al_xGa_{1-x}As$/GaAs compound semiconductor within the SCR.

II. G-R Current-Voltage Model

The fundamental SRH(Shockley Read Hall) recombination rate U is given by

$$U = \frac{\sigma_n \sigma_p (p\,n - n_i^2) N_t}{\sigma_n (n + n_i \exp((E_t - E_i)/kT)) + \sigma_p (p + n_i \exp(-(E_t - E_i)/kT))} \quad (1)$$

Eqn. (1) can be written as

$$U = \frac{n_i}{\sqrt{\tau_n \tau_p}} \frac{\sinh\left(\frac{F_n - F_p}{2kT}\right)}{\cosh\left[\frac{1}{kT}\left(\frac{F_n + F_p}{2} - E_i\right) + \frac{1}{2}\ln\frac{\tau_p}{\tau_n}\right] + b} \quad (2)$$

while b in eqn. (2) is a function of the trap parameters and can be written as follow

$$b = \exp\left(-\frac{F_n - F_p}{2kT}\right)\cosh\left\{\frac{1}{kT}(E_t - E_i) + \frac{1}{2}\ln\frac{\tau_p}{\tau_n}\right\} \quad (3)$$

where F_n and F_p are the Quasi-Fermi level. The G-R currents can be obtained as

$$J_{SRH} = q\int_{-x_n}^{x_p} U dx = q\int_{-x_n}^{0} U dx + q\int_{0}^{x_p} U dx = J_{SRH(n)} + J_{SRH(p)} \quad (4)$$

The heterojunction energy band diagram and matreial parameters are shown in Fig. 1.

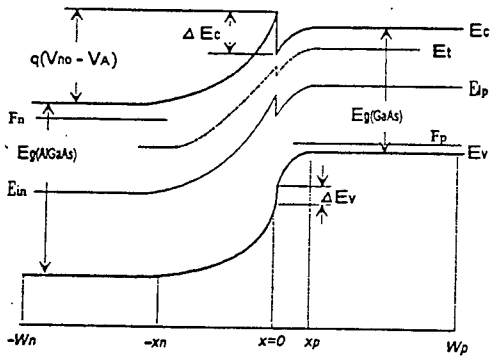


Fig. 1. The heterojunction energy band diagram and matreial parameters

By combining the material parameters and the shape of heterojunction energy band shown in Fig. 1, the expression for the hyperbolic cosine term in eqn. (2) is derived as eqn. (5)

$$\frac{F_n+F_p}{2}-E_{in}=q\left[V_{no}-\frac{V_A}{2}\right]+\frac{\Delta E_g}{2}+kT\ln\frac{n_{ip}}{p(x_p)}-\frac{q^2N_d}{2\varepsilon_n}(x+x_n)^2 \quad (5)$$

Substituting eqn. (5) into eqn. (2) yields eqn. (6)

$$U=\frac{n_{in}}{\sqrt{\tau_n\tau_p}}\frac{\sinh\left(\frac{qV_A}{2kT}\right)}{\cosh\left[\Sigma_n-\frac{q^2N_d(x+x_n)^2}{2\varepsilon_nkT}\right]+b} \quad (6)$$

where, $$\Sigma_n=\frac{q}{kT}\left[V_{no}-\frac{V_A}{2}+\frac{\Delta E_g}{2q}\right]+\ln\frac{n_{ip}}{p(x_p)}+\ln\frac{\tau_p}{\tau_n} \quad (7)$$

Therefore, the G-R I-V relation is obtained by integration in the n-AlGaAs SCR

$$J_{SRH(n)}=q\frac{n_{in}}{\sqrt{\tau_n\tau_p}}\sinh\left(\frac{qV_A}{2kT}\right)\int_{-x_n}^{0}\frac{dx}{\cosh\left[\Sigma_n-\frac{q^2N_d(x+x_n)^2}{2\varepsilon_nkT}\right]+b} \quad (8)$$

To obtain analytic integration of $(x+x_n)^2$, we can approximate it to linear formulation as $x_n(x+x_n)$. The integral term can be rearranged and the eqn. (8) is written as

$$J_{SRH(n)}=H_n\sinh\left(\frac{qV_A}{2kT}\right)T_n(b) \quad (9)$$

where, $$H_n=-\frac{4\varepsilon_nkT}{qN_dx_n}n_{in} \quad (10)$$

$$T_n(b)=\frac{1}{\sqrt{\tau_n\tau_p}}\int_{z_a}^{z_n}\frac{1}{z_n^2+2bz_n+1}dz_n \quad (11)$$

where H_n has the general parameters of heterojunction, $T_n(b)$ has the relation with the trap parameters such as E_t, E_i, τ_n, τ_p. It is very useful function that the SRH equation is divided into general parameter H and trap related parameter T of the heterojunction. After all, treatments of T may be most important in this paper.

Following the same procedure, the G-R current in p-GaAs SCR ($J_{SRH(p)}$) can be obtained,

$$J_{SRH(p)}=H_p\sinh\left(\frac{qV_A}{2kT}\right)T_p(b) \quad (12)$$

$$H_p=-\frac{4\varepsilon_pkT}{qN_ax_p}n_{ip} \quad (13)$$

$$T_p(b)=\frac{1}{\sqrt{\tau_n\tau_p}}\int_{z_a}^{z_p}\frac{1}{z_p^2+2bz_p+1}dz_p \quad (14)$$

If the trap levels were assumed to be in the middle trap, many parameters (E_t, E_i, τ_p, τ_n and even N_t, σ_n, σ_p) of the derived equations could be eliminated in previous procedure.

III. Calculations of the G-R Current-Voltage

The G-R current equations (J_{SRH}) depends on the classification of b. Therefore, to obtain the accurate characteristic equations, it is necessary to calculate the G-R I-V equation according to the classified conditions as the below case.

Case 1. $V_A < 0$ (Reverse Bias)

Trap related parameter $T_{n,p}(b)$ expressed as

$$T_{n,p}(b^2>1) = \frac{1}{\sqrt{\tau_n \tau_p}} \left[-\frac{1}{\sqrt{b^2-1}} \tanh^{-1}\left(\frac{b+z_{n,p}}{\sqrt{b^2-1}} \right) \right]_{z_{n,p}1}^{z_{n,p}2} \quad (15)$$

Then the generation current in n-SCR and p-SCR is derived, the resulting equation is

$$J_{SRH} = [H_n T_n(b^2>1) + H_p T_p(b^2>1)] \sinh\left(\frac{qV_A}{2kT} \right) \quad (16)$$

Case 2. $V_A > 0$ (Forward Bias)

It can be divided into several cases. The critical point of the division is the case at $b^2=1$ and the applied bias is V_C .

$$V_c = \frac{kT}{q} \ln \cosh^2 \left[\frac{E_t - E_i}{kT} + \frac{1}{2} \ln \frac{\tau_p}{\tau_n} \right] \quad (17)$$

a) : $b^2>1$

As the case of small forward bias ($0< V_A< V_C$), the variations of the trap parameters have an serious effect on the current. Total recombination current can be obtained similarly by eqn.(16).

b) : $b^2=1$

In case of the critical bias between the small and the large forward bias ($V_A= V_C$), and the values of $T_{n,p}(b)$ obtained by

$$T_{n,p}(b^2=1) = \frac{1}{\sqrt{\tau_n \tau_p}} \left[-\frac{1}{b+z_{n,p}} \right]_{z_{n,p}1}^{z_{n,p}2} \quad (18)$$

Then, the total G-R current is

$$J_{SRH} = [H_n T_n(b^2=1) + H_p T_p(b^2=1)] \sinh\left(\frac{qV_A}{2kT} \right) \quad (19)$$

c) : $b^2<1$

In case of the large forward bias ($V_A > V_C$), the diffusion curent is greater than the recombination current. So the G-R current is negligible in comparision with the diffusion current. The G-R currents, however, are expressed as following

$$J_{SRH} = [H_n T_n(b^2<1) + H_p T_p(b^2<1)] \sinh\left(\frac{qV_A}{2kT} \right) \quad (20)$$

where, $$T_{n,p}(b^2<1) = \frac{1}{\sqrt{\tau_n \tau_p}} \left[\frac{1}{\sqrt{1-b^2}} \tan^{-1}\left(\frac{b+z_{n,p}}{\sqrt{1-b^2}} \right) \right]_{z_{n,p}1}^{z_{n,p}2} \quad (21)$$

IV. Results and Discussions

The Fig.2 shows the I-V simulation results as a function of bias under the various temperature from 150K to 350K in comparision with experimental data, which is in good agreement. But below 0.8V in high temperature 350K and above the range of 1.0 - 1.2V in low temperature, a small deviation occurs. These phenomena are due to neglecting both the high and low temperature effects and current components by tunneling effects. However, the model of this paper is well agreement with experimental data in proper operational temperature and bias.

In the reverse bias, the results of presented model are compared with those of models under the condition of middle trap ($E_t= E_i$ and $\tau_n= \tau_p= 10^{-9}$ [s]) as shown in Fig.3. In this paper, the simulation is performed at the trap level of 0.13 [eV], because the further deviation from the middle level of trap results in elucidating the trap level effect. Although the difference from both results is not large, the G-R under the assumption of middle trap is differ from the presented model. Therefore, in order to consider the traps in $Al_xGa_{1-x}As/GaAs$ heterojunction, not only the presented model may be a more useful and accurate I-V relation than the assumed model, but also it is able to analyze an I-V relation according to the variation of trap parameters even though other materials.

To find the effect of the trap density on current components, Fig. (4) is shown. The more trap density increases in forward and reverse bias, the more G-R currents increases. As a result, the trap density gives a great influence on the generation current in reverse bias and the recombination current in small forward bias. And the reason why the trap density does not affect the magnitude of current in high bias(above 1.0 [V]), is the large diffusion current in this region.

Comparing the results of presented model with those of numerical simulation (the mole fraction of Al : $x=0.25$) in Fig.(5), the results well coincide with each other in all of the applied bias and doping. Especially, agreements with both results in reverse and small forward bias are well informed that the presented model take well account of the trap parameters for the G-R I-V characteristics. Therefore, the proposed model can be used not only $E_t = E_i$,but $E_t \neq E_i$.

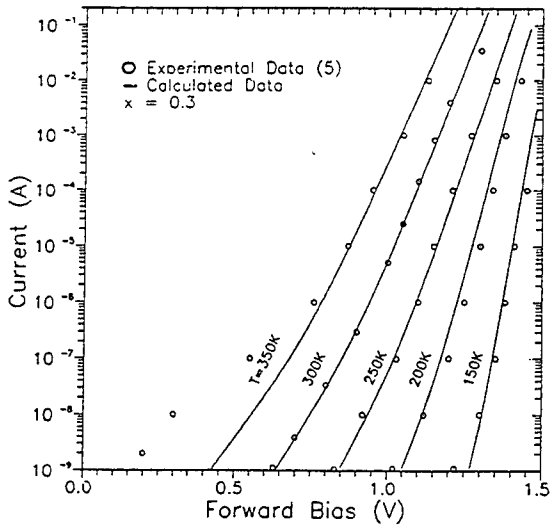


Fig.2. Current-voltage characteristics for the various temperature under forward bias.

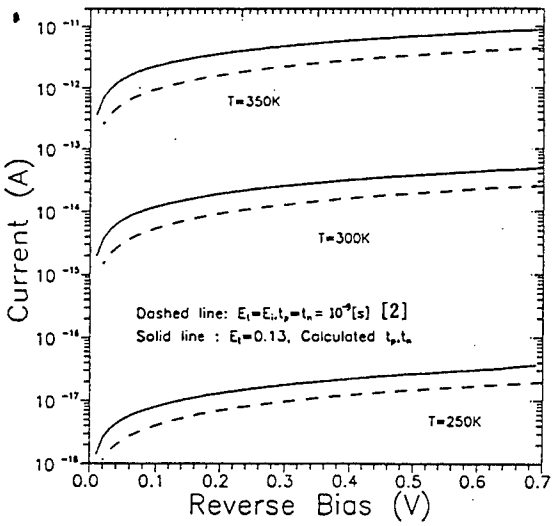


Fig.3. Current-voltage characteristics for the temperature and trap under reverse bias.

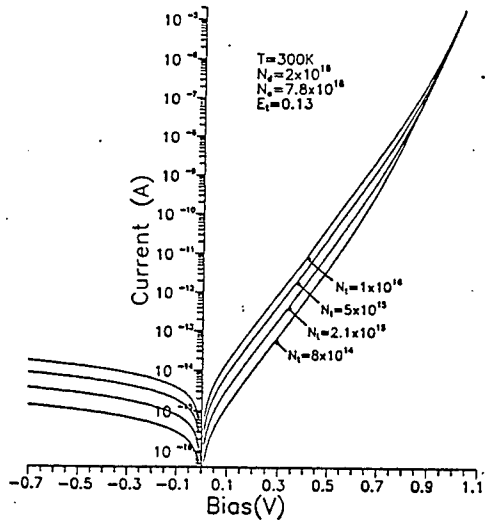


Fig.4. Characteristics of the current variation for the trap density in temperature 300K.

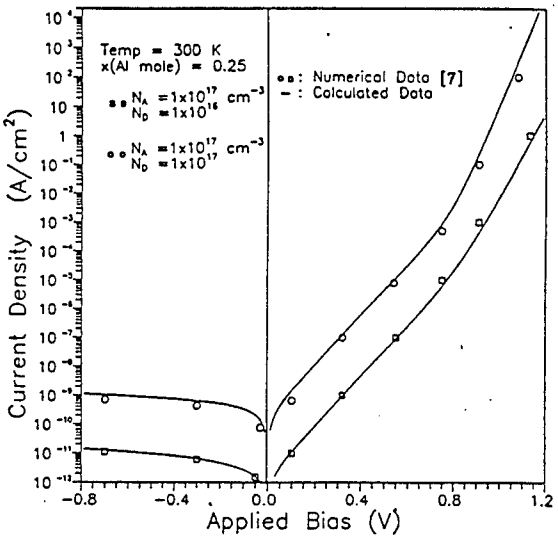


Fig.5. Characteristics of the current variation for the doping density in Al mole fraction 0.25

V. Conclusion

In this paper, we analyze the characteristics of G-R $Al_xGa_{1-x}As$/GaAs N-p heterojunction through the variation of temperature and trap level and density using by simple analytic method. The further classified I-V equations give the more precise and general characteristic equations. The validity of the proposed model is verified by comparing the simulation results with experimental and numerical data.

The proposed model takes well account of the variations of trap parameters and is a more efficient and general analytic model for the G-R mechanism.

References

[1]Chetan D. Parikh, Fredrik A. Lindholm, IEEE Trans. Electron Devices, vol. 39, pp. 2197-2205, 1992.
[2]K. Park, J. Choi, K. Kwack, J. of KITE, Vol. 29-A, No. 6, pp. 6-13 , 1992
[3]Hirosh Ito, Japanese J. Appl. Phys., vol. 25, no. 9, pp. 1400-1404, 1986.
[4]Kazushige Horio, Akira Oguchi and Hisayoshi Yanai, Solid-State Electronics vol. 34, no. 12, pp. 1393-1400, 1991
[5]Andrzej Rys, Ian L. C. Burrows and William M. Portnoy, IEEE Trans. Electron Devices, vol. 31, no. 4, pp. 500-505, 1984.
[6]Tetsuji Imai, Shunro Fuke, Akira Takeuchi, Tsutomu Uchida and Kazuhiro Kuwahara, Solid-State Electronics vol. 30, no. 8, pp. 865-871, 1987.
[7]Kyoung Hoon Yang, Jack R. East and George I. Haddad, Solid-State Electronics Vol. 36, No. 3, pp. 321-330, 1993.

Two-dimensional Modeling of Carrier Transport and Optimization of Graded-Base Heterojunction Bipolar Transistors

S. Ahmad Tabatabaei, Agis A. Iliadis, Colin E.C. Wood, and Dennis R. Stone

Joint Program for Advanced Electronic Materials,
Electrical Engineering Department, University of Maryland
and Laboratory for Physical Sciences, College Park, Maryland 20742

EXTENDED ABSTRACT

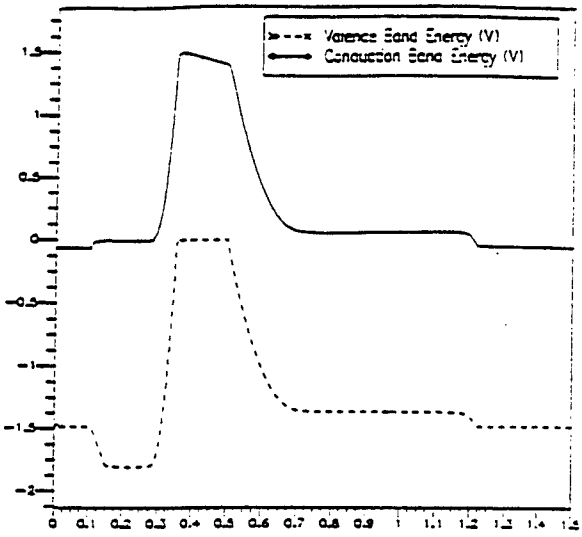
A rigorous self-consistent two-dimensional drift-diffusion and energy-balance simulation of Npn $Al_{0.3}Ga_{0.7}As$/ $Al_xGa_{(1-x)}As$/ GaAs graded base heterojunction bipolar transistors [1] has been developed to investigate the effect of compositional base grading on device performance. When optimized, base grading leads to substantial improvement in current gain [2-4] and transit time [5].The epitaxial layer structure of the transistor is shown in Figure 1. The electron transport inside the base region of Npn HBTs is modeled with emphasis on the effect of Al mole fraction on carrier lifetime. Figure (2) shows the calculated energy band diagram of the transistor. A new formula to model the reduction of electron lifetime as a function of Al mole fraction is incorporated into the simulation. For the first time, this work models the electron transport across the base of graded $Al_xGa_{1-x}As$ HBTs with the effects of composition dependence, electric field response, and base thickness incorporated [6]. Our simulation results provide better insights into the electron transport across graded base HBTs. The analysis also provides the guidelines for the selection of aluminum mole fraction inside the base region as a function of base thickness. The normalized DC current gains for three transistors with base thicknesses of 500, 1000, and 2000 Å are calculated and plotted in figure 3. Figure (4) shows the optimization curves for the selection of Al mole fraction as a function of base thickness. The trade-off between the current gain and base transit time is clear in this figure.

REFERENCES

[1] D.L. Miller, R.M. Asbeck, R.J. Anderson, F.H. Eisen, Electron. Lett., vol. 19, p. 367, 1983
[2] W. Liu, D. Costa, J.S. Harris, Jr., IEEE Trans. Electron Devices, vol. 39, p. 2422, 1992
[3] H. Ito, T. Ishibashi, T. Sugeta, Jap. J. Appl. Phys., vol. 24, p. L241,1985
[4] J.J. Liou, W.W. Wong, J.S. Yuan, Solid-State Electron., vol. 33, p. 845, 1990
[5] C.M. Maziar, M.S. Lundstrom, IEEE Electron Device Lett., vol. 8, p. 90, 1987
[6] X. Zhou, IEEE Trans. Electron Devices, vol. 41, pp. 484-490, 1994

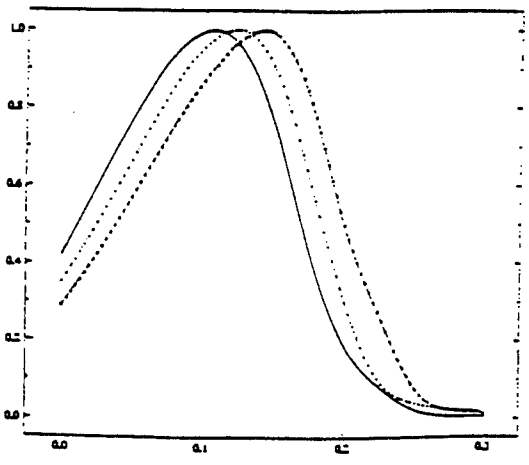
	Thickness (μm)	Material	Doping (cm-3)
Cap	0.05	InGaAs In: 0→0.55 Exponential	9.0E18
Contact	0.15	GaAs	5.0E18
Grade2	0.05	AlGaAs Al: 0.3→0 Exponential	1.0E18
Emitter	0.15	Al0.3GaAs	5.0E17
Grade1	0.03	AlGaAs Al: 0→0.3 Parabolic	5.0E17
Spacer	0.005	AlxGaAs	Undoped
Base	0.05 Group A 0.1 Group B 0.2 Group C	AlGaAs Al: 0→x Linear	2.0E19
Collector	0.6	GaAs	5.0E16
Subcollector	0.8	GaAs	4.0E18

Figure 1. HBT Epitaxial Layer Structure



Distance (μm)

Figure 2. Energy Band Diagram for Graded Al_xGaAs Base HBT ($V_{BE}=V_{CE}=0$ V, $W_B=2000$ Å)



Base Thickness (μm)

Al mole fraction

Figure 3. Normalized DC Current Gains
(a) $W_B=500$ Å, (b) $W_B=1000$ Å,
(c) $W_B=2000$ Å

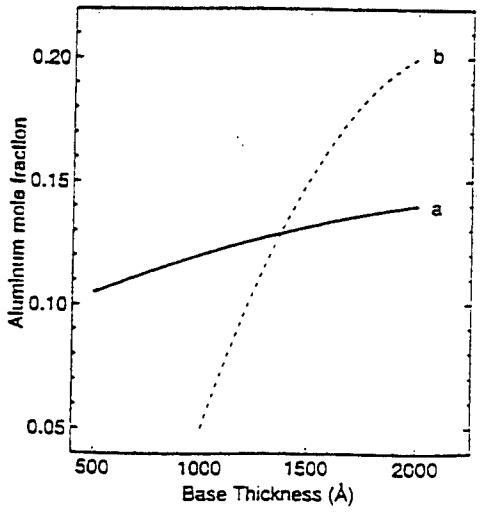


Figure 4. Optimization Curves
(a) Optimized DC Current Gain
(b) Optimized Electron Transit Time [6]

Modeling Bloch Oscillations

James H. Luscombe
Department of Physics, Naval Postgraduate School, Monterey, CA 93943

Marshall Luban
Ames Laboratory and Department of Physics and Astronomy, Iowa State University
Ames, IA 50011

Experimental progress in recent years has made it increasingly likely that Bloch oscillations will someday serve as sources of terahertz (THz) electromagnetic radiation. While first predicted to occur in metals by Zener in 1934, in 1970 Esaki and Tsu suggested that semiconductor superlattices, rather than metals, would provide a realistic class of materials for which Bloch oscillations and the associated THz radiation could be observed. Only in 1992, however, were Bloch oscillations conclusively detected in semiconductor superlattices, while prior to this date the very existence of Bloch oscillations was a matter of controversy among theorists. The primary obstacle in developing a satisfactory theory of Bloch oscillations has been the problem of reliably and systematically including the effects of interband transitions in analytical treatments of the time-dependent Schrödinger equation (TDSE). In this talk, we describe recent work on modeling Bloch oscillations based on high-precision *numerical* solutions of the TDSE for electrons in a semiconductor superlattice. The virtue of a numerical approach is that all interband transitions are explicitly included. Thus, for the first time, one has the ability to reliably *model* Bloch oscillations for a wide class of semiconductor superlattice systems. This work has revealed that the experimental superlattice system must be chosen rather carefully in order to successfully produce Bloch oscillations. We will summarize the major trends for the dynamics of single electrons in semiconductor superlattices, and the conditions under which Bloch oscillations can occur. Our survey will include results for idealized, strictly periodic superlattices, as well as for superlattices including the effects of interfacial roughening and compositional disorder.

Modeling and Simulation of Thin Film Transistors for Active-Matrix Liquid Crystal Displays

M. HACK

Xerox Palo Alto Research Center, 3333 Coyote Hill Road.
Palo Alto, CA 94304, USA

We present good agreement between numerical simulations and experimental data of the steady-state and transient characteristics of both amorhphous and poly-silicon thin film transistors for use in AMLCDs.Transistors made from these materials have characteristics which are strongly influenced by the presence of a continuous distribution of bulk traps throughout their band-gap. We show how these devices are modeled using an effective medium approach which accounts for the energy dependence of the traps, assuming they are distributed in a spatially uniform manner.

INTRODUCTION

Active-Matrix Liquid Crystal technology is now well established as the dominant technology for the production of flat panel displays. The most common choice for the active switch is an amorphous silicon (a-Si) thin film transistor (TFT) for large area displays, and poly-silicon (poly-Si) TFTs for high pixel density small area arrays for projection and viewfinder applications.

a-Si technology is ideally suited for large area applications because of its very low deposition temperature (250 - 300°C), and its consequently low cost production on large area glass substrates. The relatively low field effect mobility (1cm2/Vs) ultimately limits the ability of a-Si TFTs to charge pixels in the short times required for extremely high resolution displays with a high number of scan lines.

Poly-Si technology offers much improved performance on account of higher TFT mobilities, and the ability to fabricate both NMOS and PMOS devices enabling CMOS technology, but at this time it is less mature than its a-Si counterpart. In fact, the reduction of poly-Si TFT leakage current in the "off" state, and the uniform production of high quality poly-Si TFTs over large area low cost substrates, remain the two prerequisites for the wide employment of poly-Si TFTs in numerous commercial applications.

Transistors made from these materials have characteristics which are strongly influenced by the presence of a continuous distribution of bulk traps throughout their band-gap. In a-Si these states are a consequence of defects and the lack of long range order, while for poly-Si they represent the spatial average of all the grain boundaries and intra grain defects. Deep or mid-gap states determine the threshold voltage and subthreshold slopes, while the tail states (near the band edges) control the field effect mobility. On account of these tail states only a fraction of the charge induced into the channel by the gate appears as mobile carriers and therefore the field-effect mobility is lower than the band mobility, and is a function of gate voltage [1].

These devices are modeled using an effective medium approach which accounts for the energy dependence of the traps, but assumes that they are distributed in a spatially uniform manner.

OUTLINE of COMPUTER MODEL

Our two dimensional numerical device simulator has been described elsewhere [2]. To implement a steady-state a-Si or poly-Si device simulator it is important to accurately account for the charged trapped in the states within the band-gap, and for transient simulations it is additionally necessary to realistically describe their emptying and filling kinetics. To achieve convergence and to ensure stability, the distribution of localized states are modeled as a series of discreet levels. We use Shockley-Read-Hall trap kinetics, thereby accounting for both electron and hole capture and emission processes. Smooth simulation results are obtained by placing these traps 50 meV apart. Trap levels in the upper half of the gap are acceptor-like (neutral if empty and negatively charged if occupied by an electron) while the remainder are donor-like (positively charged if empty and neutral if occupied by an electron).

RESULTS

Figures 1 and 2 show the effective density of localized states (DOS) or traps for both a-Si and poly-Si, assuming an effective medium or spatial averaging approach. Both materials have tail state distributions which vary rapidly with energy as well as more shallow distributions of deep or mid-gap states. These DOS spectra are asymmetric with more states in the lower half of the gap, resulting in poly-Si PMOS TFTs having larger threshold voltages and poorer sub-threshold slopes than their NMOS counterparts, as well as no usable p-channel a-Si TFTs. These DOS spectra have enabled us to realistically simulate the device characteristics of both a-Si and p-Si TFTs [3] . The effective DOS for poly-Si was derived by fitting the model to the measured activation energy of the source-drain current as a function of gate bias at low V_{ds}.

Figure 3 shows a direct comparison between the characteristics of a 15 μm channel length a-Si and an NMOS poly-Si TFT, together with

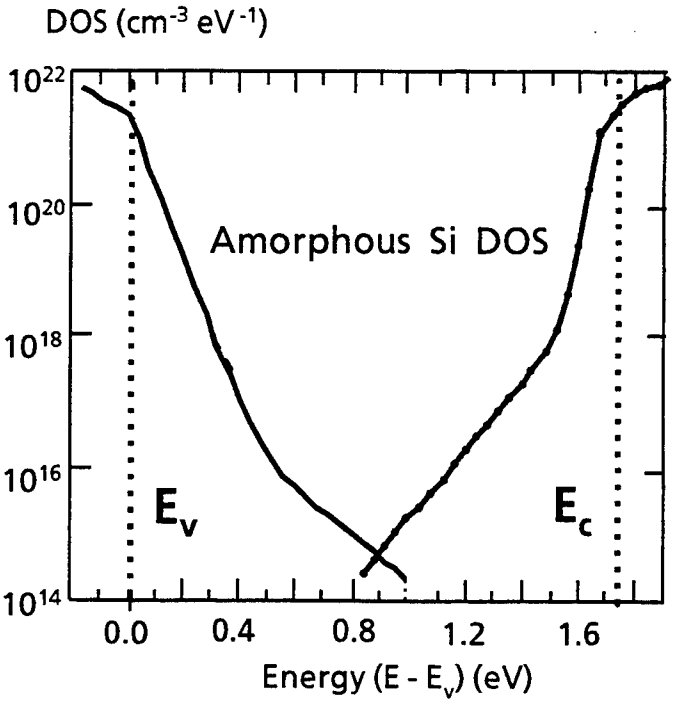


Fig. 1 - Density of states (DOS) for a-Si

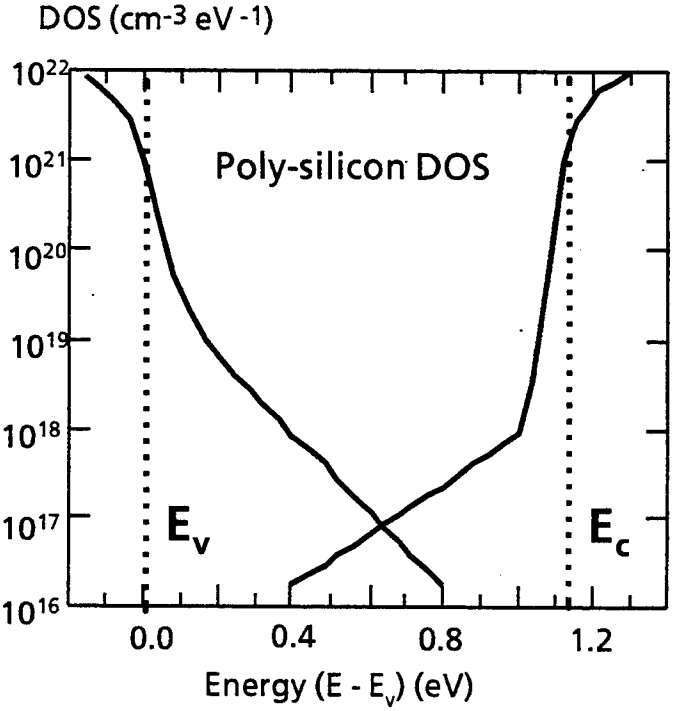


Fig. 2 Effective density of states for poly-Si

the requirements to drive a pixel in a high performance AMLCD. Poly-Si TFTs have ample drive current, while the a-Si devices are almost at their limit. Figure 3 also demonstrates the lower leakage of a-Si TFTs, and the relative lack of latitude in the leakage characteristics of poly-Si TFTs.

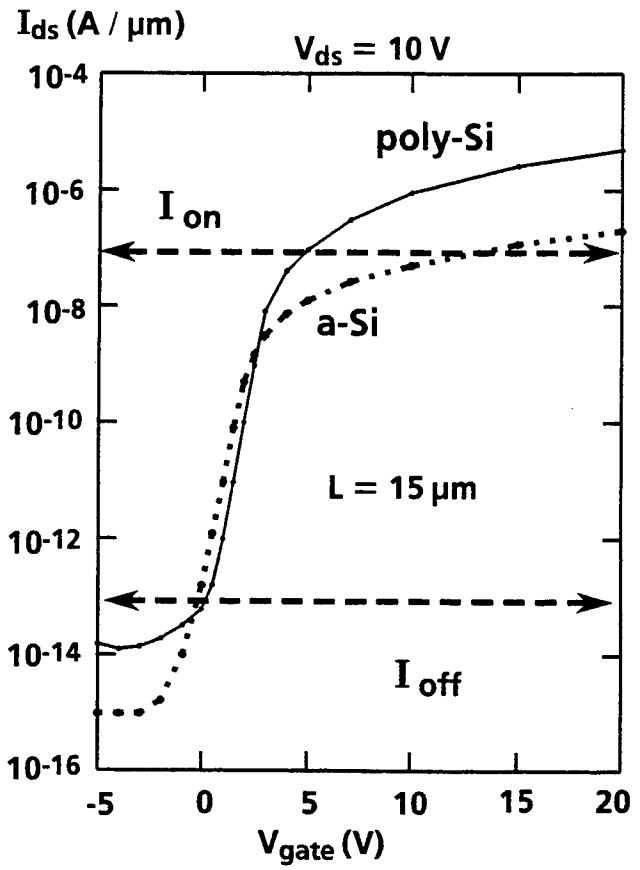


Fig.3 - Poly-Si and a-Si TFT characteristics together with their requirements for a high performance AMLCD .

Figure 4 shows the output data for a typical PMOS poly-Si TFT. At high drain bias (V_{ds}) there is a rapid increase in drain current that arises from avalanche multiplication in the high field region near the TFT drain [4]. Similar results are observed in NMOS devices. This "kink effect" is very strong in poly-Si TFTs as a result of carriers created by the impact ionization disturbing the equilibrium between free and trapped carriers [5]. The kink effect causes poly-Si TFTs to have a low saturated output impedance, and this must be accounted for in circuit designs. The strong channel avalanche effects in poly-Si TFTs also cause short channel effects for gate lengths less than approximately 10μm.

In general, an off-state TFT leakage of less than 1pA is required for a grey scale AMLCD. This leakage is readily achieved for a-Si TFTs, but can only be maintained with poly-Si

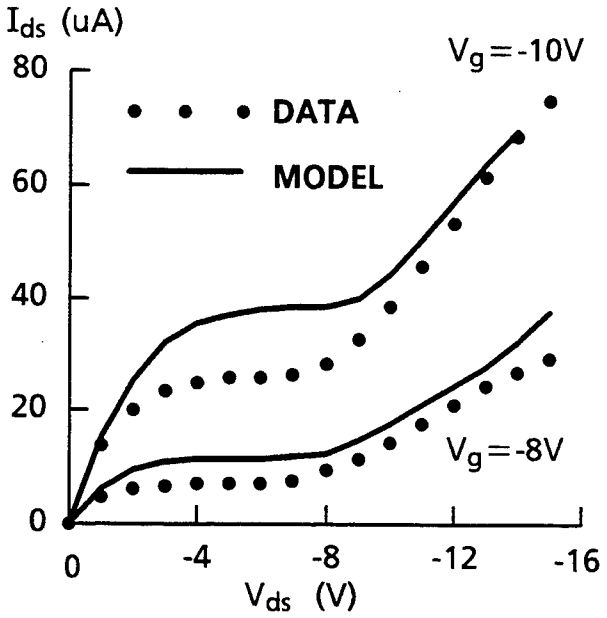


Fig. 4 Output characteristics of a 10 μm PMOS poly-Si TFT. W= 50 μm.

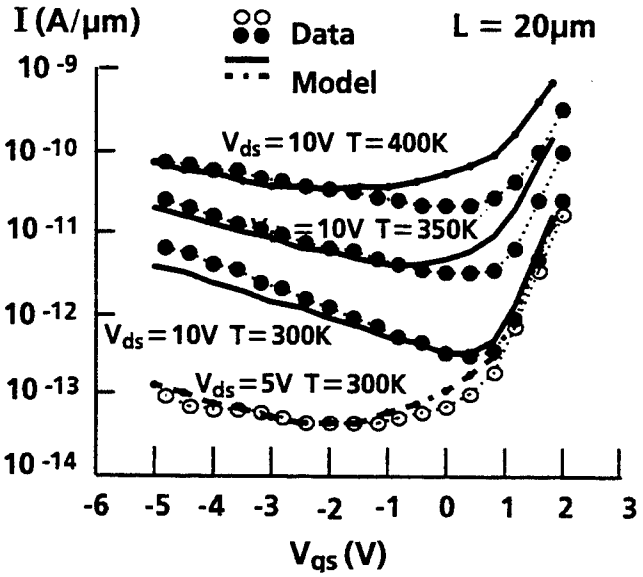


Figure 5. Simulated and experimental dependence of current-gate voltage characteristics for a 20μm NMOS poly-Si TFT

technology if special techniques are used, such as lightly-doped drain structures [6], secondary gate induced drains [7] and multiple gate TFTs [8]. Of these, multiple gates is the simplest as no additional processing is required and no additional pixel bias lines are needed.

An additional feature to an effective medium approach is required to model poly-Si leakage currents. These vary from device

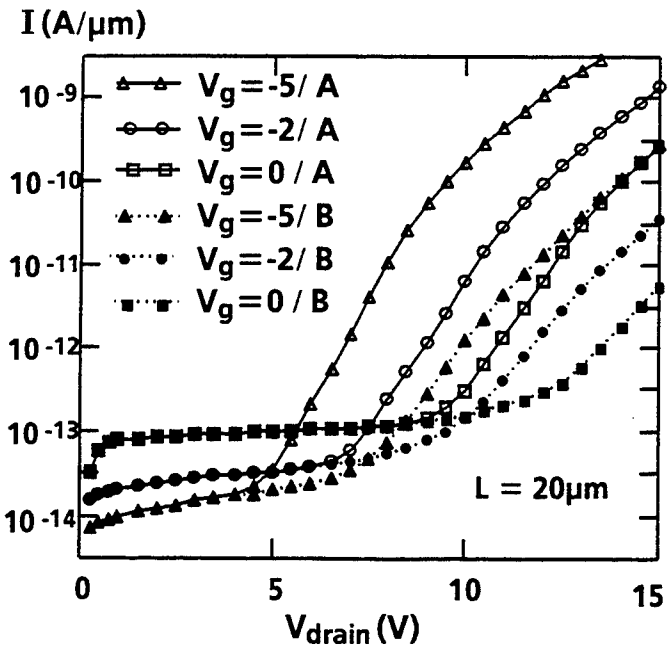


Fig. 6 Simulated leakage current for three gate biasses. The open points, labelled **A**, correspond to a leakage trap 0.17 μm from the gate edge, while solid points (**B**), correspond to the trap 0.27 μm from gate edge.

to device [9] and are generally associated with traps whose spatial position as well as energy in the bandgap varies from TFT to TFT. While both Poole-Frenkel and tunneling mechanisms have been proposed, experimentally leakage is found to depend on shallow and not deep traps, ruling out the P-F mechanism. Figure 5 shows good agreement between simulated leakage current and experimental data at two drain biases, and for three temperatures.

We believe that the variation in leakage current from device to device is caused by the statistical distribution of traps relative to the TFT drain. Leakage currents are modeled by the tunneling of carriers from specific additional traps placed near the TFT drain. Figure 6 shows the simulated V_{ds} dependence of the leakage current, for two different positions of the trap causing leakage currents. These two positions could correspond to two different devices or even the same device with the source and drain reversed [9]. At low V_{ds} the leakage current is independent of the leakage trap position, as it is determined by the TFT channel conductance. Our simulations predict that at low V_{ds} the leakage current is purely a result of drift-diffusion currents in the channel, and is sub-linear with drain bias due to the gate depleting the channel of majority carriers. At high V_{ds} the high field tunneling mechanism becomes dominant, causing device leakage to depend on the position of the traps within the TFT, and the magnitude of the channel electric field in the vicinity of the trap.

CONCLUSIONS

We have outlined details of a computer model for the characteristics of both a-Si and poly-Si TFTs. It is based on an effective medium appoach where defects or traps present in these materials are distributed in a spatially uniform manner.

REFERENCES

1) M. Shur and M. Hack, Journal of Applied Physics 10 (1984) p.3831

2) M. Hack and J.G. Shaw, Mat. Res. Soc. Symp. Proc. vol. 219 (1991) p. 315

3) M. Hack, J.G. Shaw, P.G. LeComber and M. Willums, Jap. J. of Applied Physics 29, (1990) p. L2360

4) A.G. Lewis, M. Hack and I-Wei Wu, Proceedings of 1991 ISDRS, pp. 513-516

5) M. Hack and A.G. Lewis, IEEE Electron Device Letters, 12, 5, pp. 203-205 (1991)

6) S. Seki, O. Kogure and B. Tsujiyama, IEEE Electron Device Lett. EDL-8,9, pp. 434-436 (1987)

7) K. Tanaka, S. Suyama, K. Kato and S. Kohda. Tech. Digest of SID International Symposium, pp. 539-542 (1991)

8) Y. Matsueda, M. Ashizawa, S. Aruga, H. Ohshima and S. Morozumi, Proc. of the Japan Display Conference, pp. 418-422 (1991)

9) I-Wei Wu, A.G. Lewis, T.-Y. Huang, W.B. Jackson and A. Chiang IEDM Tech. Digest pp. 867-870, 1990

High Through-put Processing for Poly-Si TFT

Stephen J. Fonash
Electronic Materials and Processing Research Laboratory
The Pennsylvania State University, University Park, PA 16802

High through-put, low temperature processing for poly-Si TFTs on inexpensive substrates will require a rapid (1) low temperature Si deposition, (2) low temperature crystallization, (3) low temperature dopant activation, (4) low temperature dielectric deposition, and (5) low temperature, grain boundary passivation process. An overview of the possibilities for these steps is presented.

I. Introduction

The high through-put manufacture of poly-Si transistor arrays for active matrix liquid crystal displays (AMLCDs) and active matrix electroluminescent displays (AMELDs) on inexpensive substrates will require a number of demanding processing steps. These will include a rapid (1) low temperature deposition process, (2) low temperature crystallization, (3) low temperature dopant activation, (4) low temperature dielectric deposition, and (5) low temperature grain boundary passivation process [1]. All of these processing steps will have to be done with thermal budgets that are compatible with the display substrate. In this report we will discuss various approaches to these key processing steps.

II. Film Deposition

The first needed critical step in the process flow of Fig. 1 is a low temperature deposition that is compatible with inexpensive substrates and yet has acceptable deposition rates. This means that deposition temperatures that are at least $\leq 600°C$ are required. Candidate processes are low pressure chemical vapor deposition (LPCVD), plasma enhanced chemical vapor deposition (PECVD), and sputtering. Of these, PECVD and sputtering offer lower temperature deposition and are, therefore, very attractive. Both processes can be scaled-up for large areas and offer the potential for acceptable deposition rates. With the advent of high density plasma (HDP) sources such as transformer coupled and inductively coupled sources, PECVD has become particularly scaleable.

If laser exposures are to be used for the crystallization step of Fig. 1, then the film deposited in step one of this figure can be polycrystalline or amorphous, as deposited, since it will be melted [2]. However, if solid phase crystallization (SPC) is to be used and large grain material is the objective, then poly-Si films are inadvisable and amorphous precursor Si films should be used. This is because, in deposited poly-Si films, grain size will be of the order of film thickness. To obtain large grain poly-Si from deposited poly-Si

films of thicknesses ≤ 1000 Å would then require recrystallization and, therefore, temperatures ≥ 950°C.

III. Low Temperature Crystallization

There are two approaches to low temperature crystallization as noted earlier: laser crystallization and solid phase crystallization (SPC). The former melts the deposited film but over times that are short enough that the substrate can be essentially unaffected. The latter does not melt the precursor amorphous silicon that must be used for SPC but, instead, uses furnace or rapid thermal annealing (RTA) for crystallization. For rapid through-put RTA is obviously the preferred SPC approach. Two types of RTA are currently being explored: one using tungsten-halogen sources and the other using xenon sources [3]. The obvious through-put advantage of RTA is seen in Fig. 2.

IV. Dopant Activation

Doping in poly-Si TFT structures is usually accomplished by ion implantation. To achieve the necessary through-put objectives, the emphasis is on ion implantation without mass selection. If laser crystallization is used, then doping must be done after crystallization and an additional dopant activation step must be used in the process flow of Fig. 1. For this path, one needs to try to lower the temperatures needed to activate a dopant in a crystalline Si material and one demonstrated successful approach involves the use of hydrogen [4]. If SPC is used, then the dopant can be implanted before crystallization, since the crystallization temperatures in this approach are so low, significant dopant movement does not occur during annealing. The SPC approach to crystallization has the advantage that crystallization and dopant activation are both done in the same step.

V. Low Temperature Deposited Dielectric

To achieve the thermal budget needed for poly-Si TFTs on inexpensive substrates, it is generally believed a deposited dielectric is needed. The usual "rule-of-thumb" is a deposited Si_3N_4 dielectric for amorphous Si and a deposited SiO_2 dielectric for poly-Si. Hence, for poly-Si silicon dioxide deposition approaches have to be explored and those that have been looked at include sputtered, PECVD, LPCVD, and atmospheric pressure chemical vapor deposition (APCVD).

VI. Low Temperature, High Through-put Passivation

The use of hydrogen for the passivation of poly-Si is a well established procedure. The need for a high through-put process in poly-Si TFT fabrication has spurred the exploration of high density plasma sources for this step [5]. This approach, with [6] or without [7] substrate/plasma biasing, has proved to be very effective.

Acknowledgement

The work in this overview done at Penn State has been supported by the Electric Power Research Institute and by the Advanced Research Projects Agency.

References

1. S.J. Fonash and D. Reber, "Low Thermal Budget High Through-put Processing for Poly-Si TFTs", Proceedings of the ECS Symposium on Thin Film Transistor Technologies II, 186th Electro-chemical Society Meeting, Miami, FL, Oct. 9-14, 1994.

2. T.J. King, "Trends in Poly-Si TFT Technologies for AMLCDs", Proceedings of the 2nd International Workshop on Active Matrix Liquid Crystal Displays, Bethlehem, PA, Sept. 25-26, 1995.

3. G. Liu and S.J. Fonash, "Low thermal budget poly-Si TFTs on glass", Jap. J. Appl. Physics 30, L269 (1991).

4. R. Singh, S.J. Fonash, A. Rohatgi, P. Rai-Choudhury, and J. Gigante, "A low-temperature process for annealing extremely shallow As^+ implanted n^+/p junctions in silicon", J. Appl. Phys. 55, 867 (1984).

5. R.A. Ditizio, S.J. Fonash, and B.-C. Hseih, "Examination of the optimization of TFT passivation with hydrogen electron cyclotron resonance plasmas", J. Vac. Sci. Technol. A10, 59 (1992).

6. J.D. Bernstein et al., to be published in IEEE Electron Device Letters, Oct., 1995.

7. A. Yin and S.J. Fonash, "High Performance p-channel poly-Si TFTs using electron cyclotron resonance hydrogen plasma passivation", IEEE Electron Device Letters 15, 502 (1994).

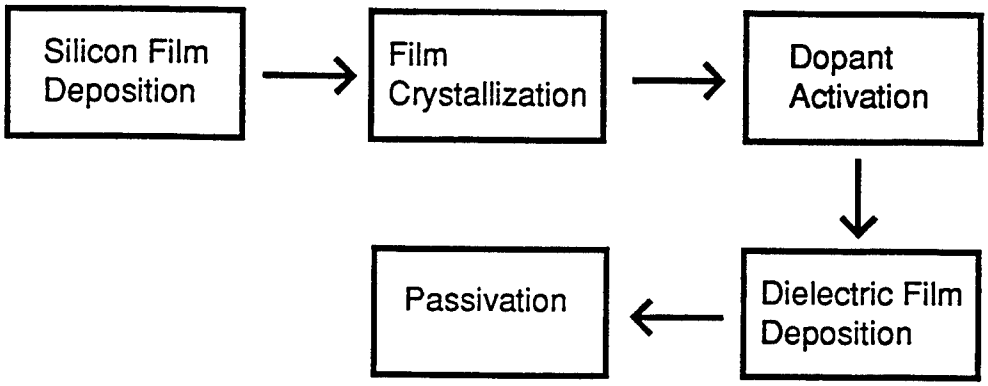


Fig. 1: Critical steps needed to achieve full flow, low thermal budget processing for active matrix TFTs on inexpensive substrates.

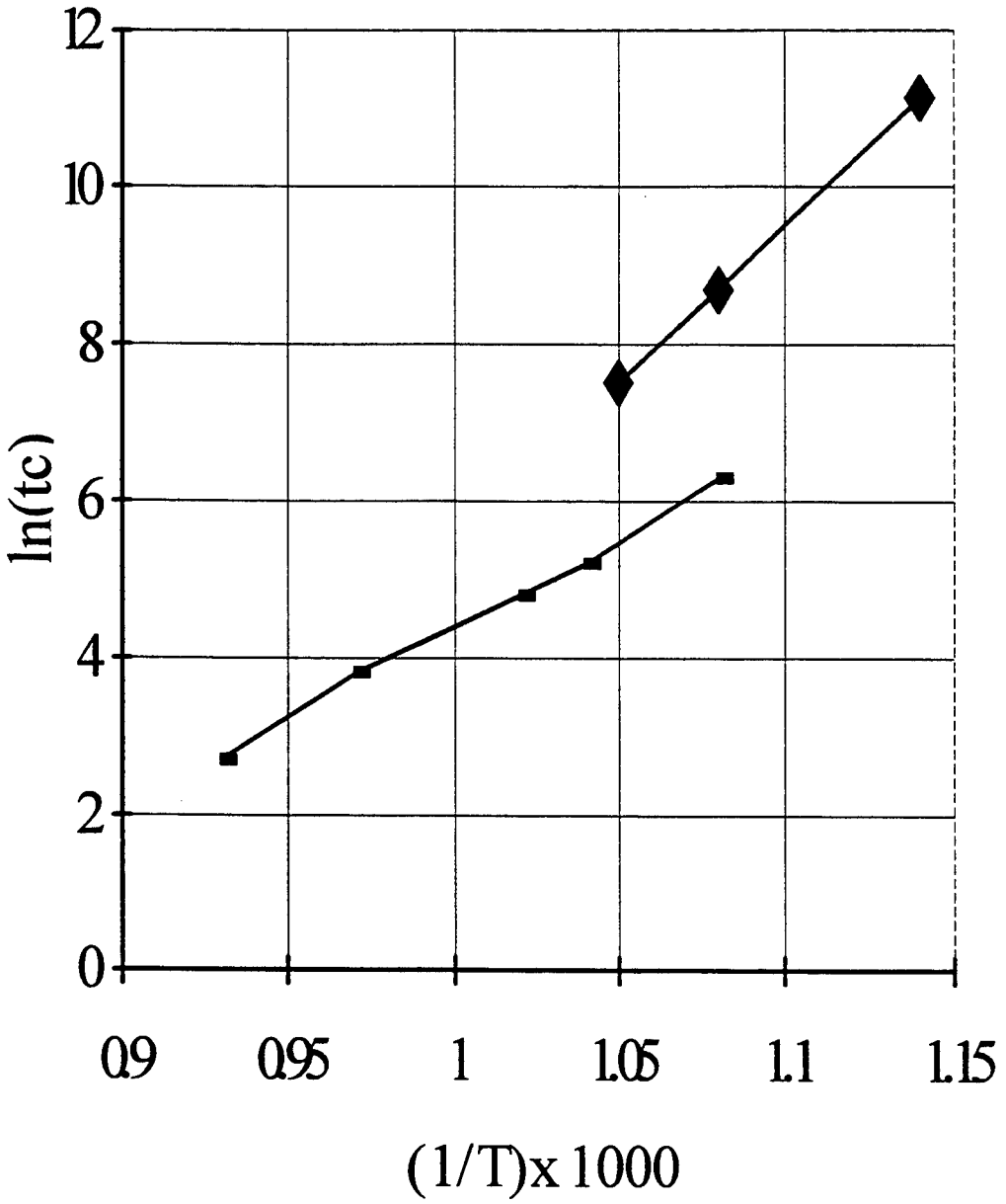


Fig. 2: Diamonds are for furnace annealing; rectangles are for tungsten-halogen rapid thermal annealing.

* Student Paper

Self-Aligned Offset Gated Poly-Si TFTs by Employing a Photo Resist Reflow Process

Cheol-Min Park, Byung-Hyuk Min, and Min-Koo Han

Department of Electrical Engineering, Seoul National University, Seoul , Korea

1. INTRODUCTION

A large leakage current may be one of the critical issues for poly-silicon thin film transistors (poly-Si TFTs) for LCD applications. In order to reduce the leakage current of poly-Si TFTs, several offset gated structures have been reported. [1), 2)] In the most proposed offset structures, an additional photo lithographic step is usually required to fabricate an offset structure. The different offset length is occurred due to misalignment problem. The offset length of the source region is not same as that of the drain region so that those devices exhibit the asymmetric electrical performances such as the threshold voltage shift and the variation of the subthreshold slope. [3), 4)]

In this paper we propose a new fabrication method for poly-Si TFTs with a self-aligned offset gated structure by employing a photo resistor reflow process. The proposed device is designed to employ the gate pattern to define the offset region so that the process does not require any additional mask step and eliminates the misalign problem. In the proposed device, the self-aligned implantation is applicable so that the offset length of the source is identical with that of the drain.

2. DEVICE STRUCTURE

A schematic structure of the proposed device is illustrated in Fig. 1. The gate structure of the proposed device consists of two parts rather one in the conventional device. As shown in Figure 1, we entitle the main gate where the gate bias is applied and the other is the entitled subgate which is separated from both sides of the main gate. The gate oxide of the new device is expanded to the subgate adjacent to the source and drain. We define the expanded part of the gate oxide as the offset oxide. The poly-Si channel layer below the offset oxide is protected from the injected ion impurities for the source/drain implantation. Because the subgate is not connected to any electrode, the gate bias is not applied to the subgate. The poly-Si channel layer below the offset oxide acts as an offset region of the proposed device. The offset length of the device is sum of the subgate length and the space of the subgate and the main gate.

3. FABRICATION PROCESS

The process sequences to form the offset oxide is illustrated in Fig. 2. A 100nm thick poly-Si film was a deposited by LPCVD on a 500nm wet oxidized silicon wafer. A 100nm-thick gate oxide insulator is deposited by APCVD. Then, a 200nm-thick gate poly-Si film is deposited by LPCVD. In order to pattern the poly-Si gate, the poly-Si film is etched out by RIE. The photo resist is reflowed at 160 ^{o}C for 30 minutes (Fig 2(c)) and gate oxide is etched out (Fig. 2(d)), which is followed by the removal of the photo resist (Fig. 2(e)). During the poly-Si gate etch, the oxide between the main gate and the subgate is not etched due to the reflowed photo resist which is filled in the space between the subgate and the main gate. For the source and drain implantation, the ion impurities are not injected into the poly-Si active layer below the offset oxide.

Figure 3 shows a cross-sectional SEM image of the oxide fabricated by photo resist reflow method. The space between the main gate and the subgate is 0.5μm, and subgate length is 0.8μm of offset oxide in SEM image of Fig. 3. In our experiment, the space between the main gate length is varied from 0.2μm to 0.8μm and the subgate length is varied from 0.2μm to 1.2μm respectively. The uniform offset oxide layer is formed at both sides of a poly-Si main gate. We have verified the existence of the offset oxide by SEM. The offset length of 0.4μm to 2.0μm is obtained successfully.

4. SIMULATION RESULTS AND DISCUSSION

We have verified the feasibility of our new fabrication process by SUPREM IV and the SILVACO SPISCES-2B. The simulated transfer characteristics of the proposed poly-Si TFT are shown in Fig.5. The channel length is 10μm and the offset length (L_{off}) is varied from 0.0μm (non-offset) to 1.0μm. The lateral diffusion length which is about 0.2μm is obtained by SUPREM IV. Solid phase crystallized 100nm thick poly-Si film is considered as active layer. Ion impurities injected into the source/drain region are assumed to be activated at 900 ^{o}C for 30 minutes.

In the proposed TFT, the off current on the negative bias is much less than that of a conventional one. As the L_{off} increases, both the on and off current decrease although the reduction of on current is much less than off current reduction. However, a remarkable suppression in the off current is observed in the offset length of 0.5μm. In order to clarify the major factors dictating the off current, we have evaluated the variation of the peak electric field in the drain depletion region as a function of L_{off}.

The peak electric field as shown in Fig.4, decreases with the increase of the offset length. These results imply that the peak electric field is a dominant factor to determine the leakage current. As the offset length increases, the leakage current is reduced from 300 fA to 30 fA. The ON/OFF current ratio with various offset lengths is evaluated as shown in Fig.5. The maximum ON/OFF ratio occurs at L_{off} of 0.5μm and exceeds 10^{8}.

5. CONCLUSION

We propose a new fabrication process for poly-Si TFTs with a self-aligned offset gated structure by employing a photo resist reflow process. The offset region by the photo resist reflow process has been successfully obtained in order to fabricate the offset gated poly-Si TFTs. The symmetrical offset length from 0.5μm to 2.0μm is easily obtained in our experiment. The device simulation shows the maximum ON/OFF ratio of 10^8 at offset length 0.5μm.

REFERENCE

1) S. Nagata, E. Takeda, Y. Nan-no, T. Kawaguchi, Y. Mino, A. Otsuka, and S.I. Ishihara, *SID 89 Digest, (1989)* 242

2) K. Suzuki, *SID 92 Digest*, (1992) 39

3) S. Seki, O. Kogure, and B.tsujiyama, *IEEE Electron Device Lett.*, **8**, (1987) 434

4) K. Tanaka, H. Arai, S. Kohda, *IEEE Electron Device Lett.*, **9**, (1988) 23

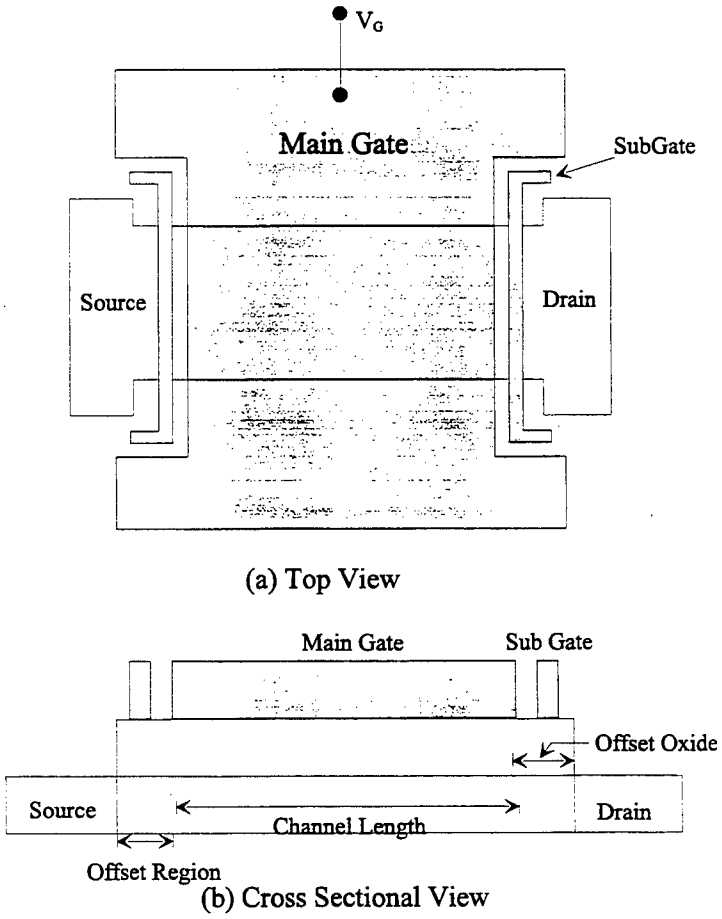


Fig. 1 The schematic view of the proposed TFT
(a) Top view (b) Cross-sectional view

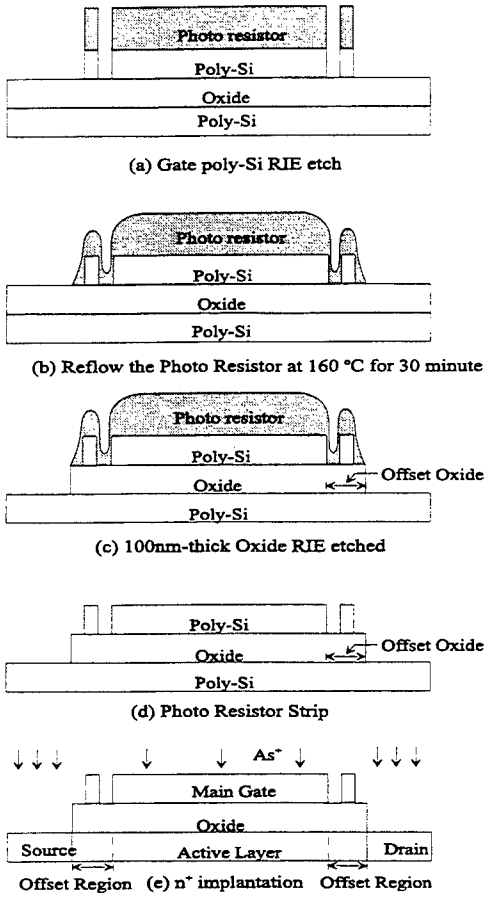


Fig. 2 The key processes for fabricating the offset oxide.

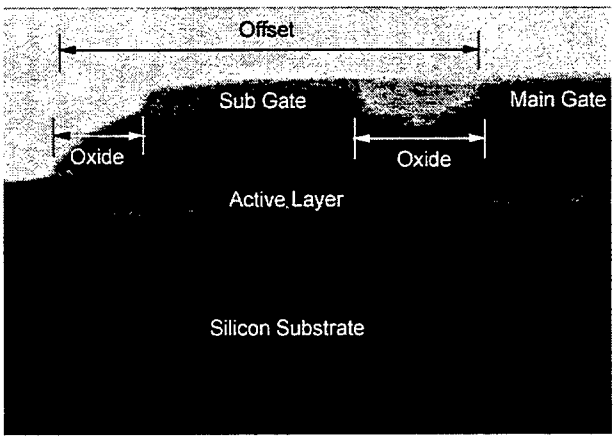


Fig. 3 The SEM image of offset oxide. The space between the main and the subgate is 0.5μm, and subgate length is 0.8μm

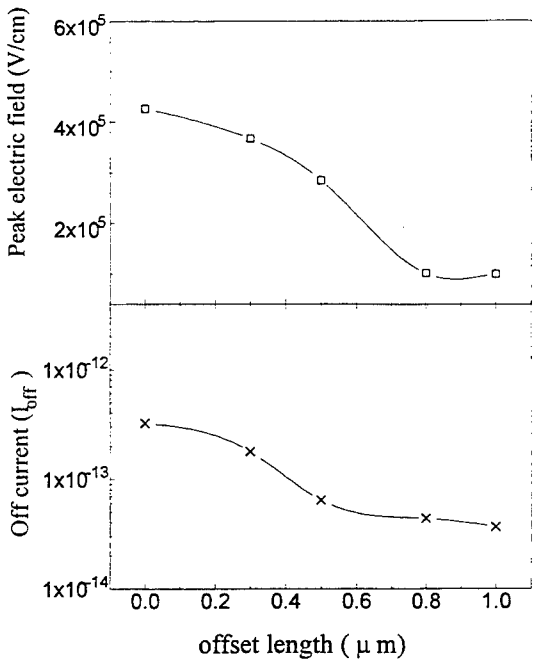


Fig. 4 Peak electric field strength in the drain depletion region and off current as a function of offset length (L_{off}). V_d= 5V, V_g= -20V

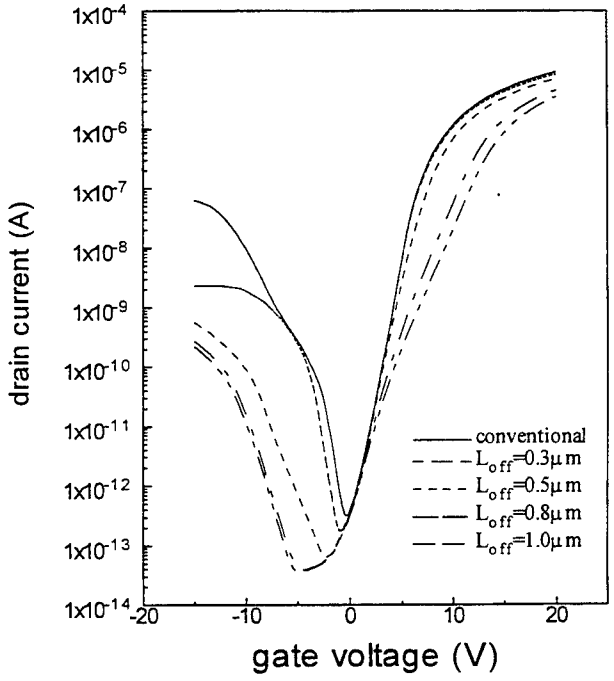


Fig. 5 Transfer characteristics in a conventional and a proposed structure poly-Si TFT. The offset length varies from 0.3μm to 1.0μm. V_d=5V

High Performance Polycrystalline Silicon Thin Film Transistors Fabricated by Ultrahigh Vacuum Chemical Vapor Deposition and Chemical Mechanical Polishing with Plasma Treatment

Chun-Yen Chang, Hsiao-Yi Lin, Tan Fu Lei, Juing-Yi Cheng, Hua-Chou Tseng, Liang-Po Chen*, and Bau-Tong Dai*

Department of Electronics Engineering & Institute of Electronics, National Chiao Tung University and National Nano Device Laboratories, Hsinchu, 300, Taiwan, Republic of China

**National Nano Device Laboratories, Hsinchu, 300, Taiwan, Republic of China*

1 Introduction

To deposit amorphous silicon by conventional low pressure chemical vapor deposition (LPCVD) followed by long-term recrystallization is often used for fabricating poly-Si TFTs. Such process will seriously affect the throughput of fabrication. Recently, it was found that the poly-Si can be obtained at reduced pressures without any recrystallization by ultrahigh vacuum chemical vapor deposition (UHV/CVD) below 550 ℃ [1]. This finding makes poly-Si TFT's fabrication possible at low-temperature, and low thermal budget condition. High throughput is also possible. However, on the other hand, due to the high defect-state density at grain boundaries and in the grains, which degrade the TFT performance, and larger surface roughness of as-deposited poly-Si films grown at reduced pressure, which make these poly-Si films unsuitable for fabricating top-gate devices. In order to overcome these weaknesses, either to enlarge the grain size[2] or to passivate the defect-state by plasma treatment[3] or smooth these films[4] are tried. In this work, as-deposited poly-Si films grown at reduced pressure by UHV/CVD which were used as the channel layer followed by CMP were used.

2 Experimental

A. Film preparation

In this work, we proposed and demonstrated a effective approach for fabricating high performance of poly-Si TFTs without long-term and any post recrystallization. This approach utilizes an UHV/CVD deposited undoped poly-Si film as the channel. The system features an ultraclean growth environment (base pressure ~10^{-8} Torr) which carbon and oxygen concentrations are below the second ion mass spectroscopy (SIMS) detection limit, and a reduced deposition pressures (~ 1 mTorr). The poly film was as-deposited at 550 ℃ using silane as the depositing source and without any post recrystalline. However, the larger surface roughness inheres in these films, which inhibits fabrication of the top-gate self-aligned TFTs. Therefore, the chemical mechanical polishing (CMP) system was used to reduce the surface roughness. KOH and silica slurry were used in polishing process. In our previous works[1], we have shown that using UHV/CVD technique can deposit high quality fine-grain poly-Si films below 550 ℃ without further recrystalline treatment, which is hard to achieve with the conventional LPCVD. Utilizing these techniques and combined with plasma treatment and low temperature grown gate oxide, the fabrication of high performance poly-Si TFTs at low temperature is possible.

B. Device fabrication

A 150-mm silicon wafer coated with a 300 nm-thick thermal oxide was used as the substrate. An 160 nm-thick and 120 nm-thick undoped poly-Si films for CMP polishing and without polishing (unpolished) were deposited, respectively, by UHV/CVD at 550 ℃. The undoped poly-Si was employed as the channel layer with a grain size of 80 nm measured by the transmission electron microscopy (TEM). The 160 nm-thick poly-Si was polished down to 120 nm by CMP. Then these films(unpolished and polished) were patterned and plasma etched to form the remaining active area island, which have a thickness of 120 nm. A 30 nm-thick gate oxide was thermally grown at 850 ℃ at O_2 ambient. After these steps, a 300 nm-thick poly-Si was deposited by UHV/CVD again at 550 ℃ to serve as the gate electrodes also were defined by plasma etching. The gate electrode and

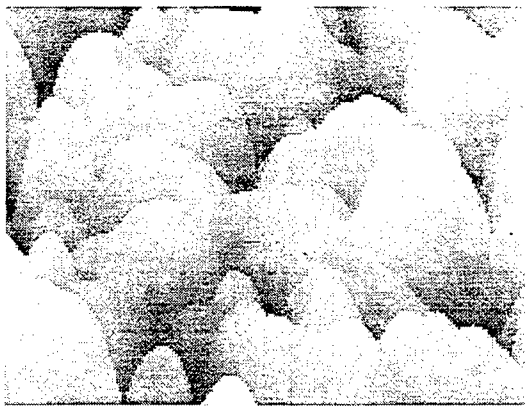


FIG 1(a) The morphology of unpolished films is 9.0 nm.

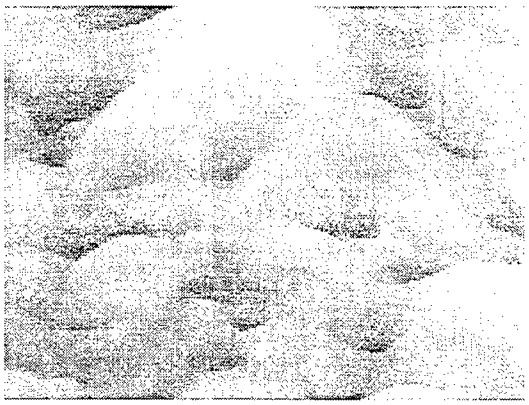


FIG 1(b) The morphology of polished films is 3.7 nm.

source/drain regions were implanted by boron and phosphorus at a dosage of $3X10^{15}$ cm^{-2}, and energies of 20 keV and 60 keV for p+/n+ gates and source/drain contacts, respectively. Then a 550 ℃ post-implant anneal was performed in N_2 ambient for 1 hr and 4 hr for p- and n-channel devices, respectively. The resistivity are 3 mΩ-cm and 7 mΩ-cm for p+ and n+ poly gates, respectively. The 200 nm-thick oxide was formed as the cap layer by plasma enhanced chemical vapor deposition (PECVD) at 300 ℃. Finally, contact hole definition and Al metalization was performed followed by a 400 ℃ sintering in N_2 ambient for 30 min. After these processes, a 2 hr NH_3 plasma treatment was performed for p- and n-channel devices. The plasma power density is 0.67 W/cm^2 and pressure is 300 mTorr.

3 Results and discussion

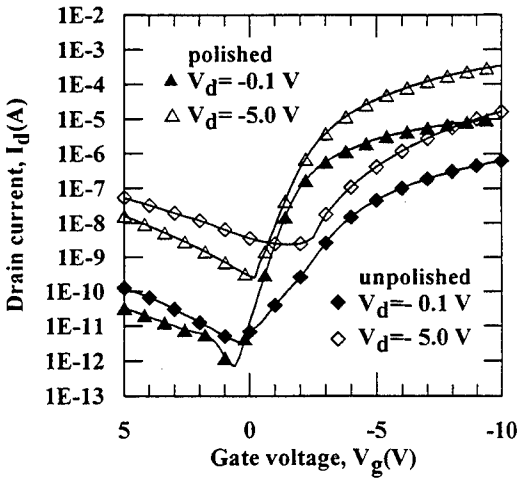


FIG 2(a) The comparison of unpolished and polished characteristics for p-channel devices.

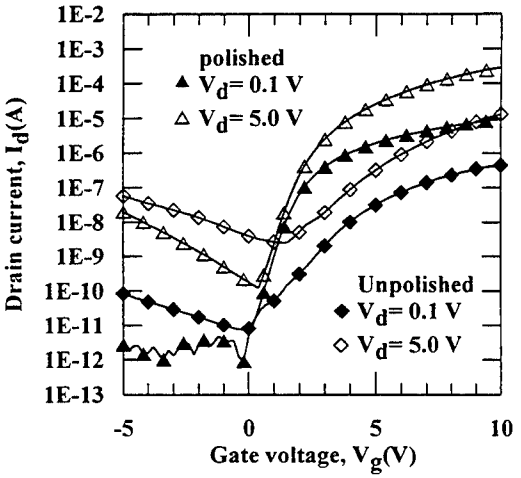


FIG 2(b) The comparison of unpolished and polished characteristics for n-channel devices.

The roughnesses of the poly film are 9.0 nm and 3.7 nm for unpolished and polished, respectively, observed by atomic force microscope (AFM) as in Fig. 1(a) and 1(b). We found that the surface roughness of poly films can be dramatically reduced by CMP technique. And it is believed that the more planar surface could be obtained by furtherly optimizing the polishing technique. Typical transfer curves, drain current, I_d versus gate voltage, V_g at drain bias, 0.1 V and 5 V are shown in Fig. 2(a) and 2(b) for unpolished and polished devices. Due to the CMP to planarize the channel surface, the performance of polished devices were improved by reducing the surface scattering between gate

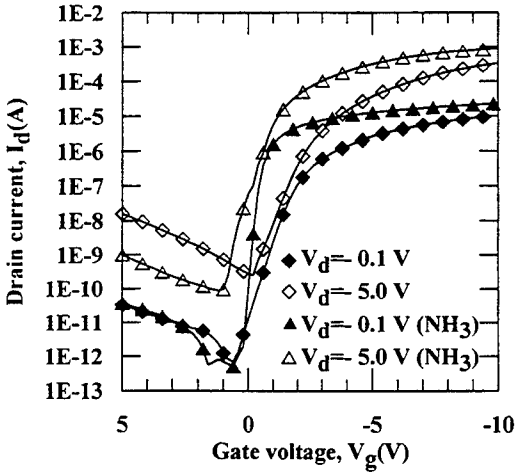


FIG 3(a) The comparison of polished p-channel devices with and without plasma treatment.

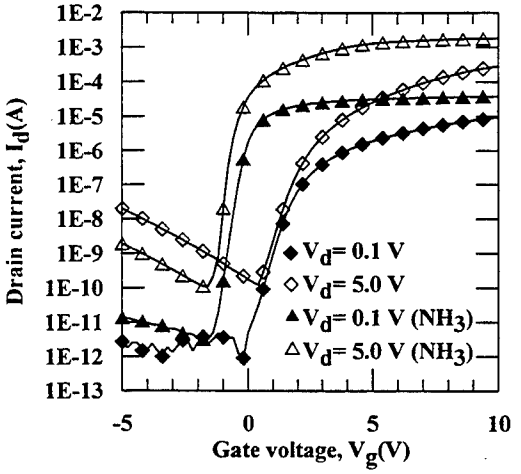


FIG 3(b) The comparison of polished n-channel devices with and without plasma treatment.

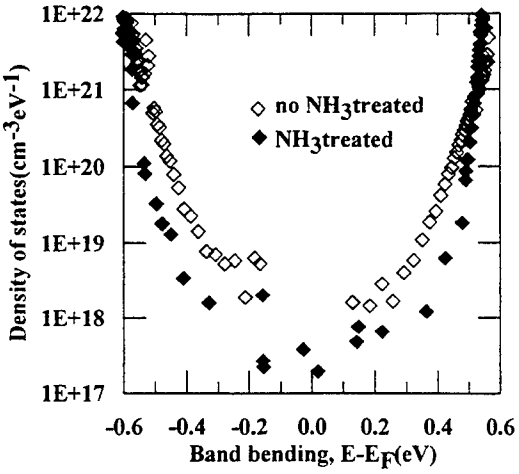


FIG 4 The density of states in band gap of polished films.

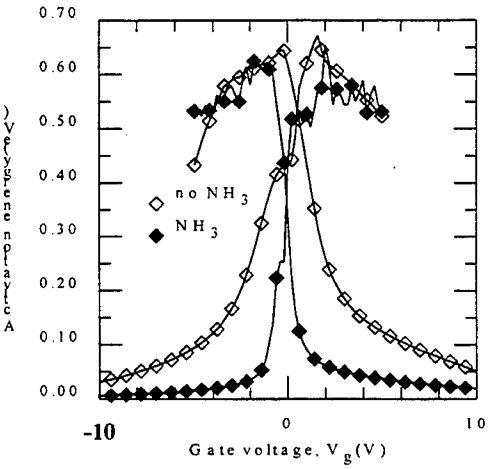


FIG 5 The activation energy curves with and without plasma treatment.

oxide and channel interface. The characteristics of the polished device subjected to NH_3 plasma passivation is shown in Fig. 3(a) and 3(b), and the without NH_3 plasma treated device is also shown for comparison. After NH_3 plasma treatment, the performance is dramatically improved. The I_{ON}/I_{OFF} current ratio is larger than 10^7, subthreshold swing is around 0.2 V/decade, and threshold voltage is smaller than 0.6 V. The greatly improved transistor characteristics were due to the film quality and also due to the post NH_3 annealing. Because the performance of poly-Si TFTs are mainly determined by the grain structure and grain boundary properties of poly-Si films. Although the larger grain size of poly-Si is expected to improve the characteristics, the performance of poly-Si TFTs, such as the mobility is strongly influenced by the grain boundary properties rather than the grain size[5]. Therefore, we can explain why such the smaller grain size (80 nm) of poly-Si can also be used to fabricate high performance TFTs. Fig. 4 shows the density of states in band gap by field-effect conductance method[6] before and after NH_3 treatment. The distribution shows that passivation is effective in tail and midgap states, which accounts for the improvements in mobility, leakage current,

Table I The characteristics of devices: channel width/ length=100 μm/ 10 μm

devices\parameters	field effect mobility (cm^2/V-s)	threshold voltage(V)	subthreshold swing (V/decade)	trap states (cm^{-2})	I_{ON}/I_{OFF}
p-channel(unpolished)	1.9	-6.7	1.2	$6.7X10^{12}$	$7.0X10^3$
p-channel(polished)	14	-4.3	0.45	$4.0X10^{12}$	$6.9X10^5$
p-channel(NH_3 treated)	58	-0.53	0.17	$2.0X10^{12}$	$1.1X10^7$
n-channel(unpolished)	1.6	7.3	1.3	$8.4X10^{12}$	$5.4X10^3$
n-channel(polished)	17	5.1	0.42	$5.0X10^{12}$	$2.5X10^6$
n-channel(NH_3 treated)	98	0.36	0.21	$2.0X10^{12}$	$1.8X10^7$

subthreshold swing, and threshold voltage. Fig. 5 show the gate voltage dependent activation energy before and after NH_3 treatment. The steeper curve also indicates that the low threshold voltage and subthreshold swing. We can found the kink exists in activation energy curves of p-channel devices without and with NH_3 treatment. This phenomenum may be due to the dangling bond exists in lower band gap[7] but the detail is unclear.

In this work, a maximum field effect mobility of 58 cm^2/V-s for p-channel and 98 cm^2/V-s for n-channel were obtained after NH_3 plasma treatment. More detailed device characteristics were summarized in Table I. All characteristics were determined by drain voltage, V_d = 0.1 V except the ON (V_g = 10 V) / OFF (I_d is minimum) current ratio was determined at V_d =5 V. The device performance is dramatically improved by NH_3 plasma is believed to generate positive fixed charges in the gate oxide near the source and drain junction by ionized nitrogen[11], and ionized hydrogen atoms. Finally, there are many matured low temperature gate oxide formation methods but not available in this work[8, 9]. Therefore full low temperature processes on glass is feasible to fabricate poly-Si TFTs.

4 Conclusions

In summary, we have developed very useful techniques to fabricate poly-Si TFTs which use UHV/CVD thchnique to deposit poly-Si films without post recrystallization and CMP technique to planarize these films as the channel layer. Then followed by plasma NH_3 plasma treatment, the performance is dramatically improved which are never achievable before without recrystallization.

5 References

[1] H. C. Lin, H. Y. Lin, C. Y. Chang, T. F. Lei, P. J. Wang, R. C. Deng, J. Lin, and C. Y. Chao, *J. Appl. Phys.* **74**, 9, p. 5395, 1993.

[2] Nobuo Kubo, Naoto Kusumoto, Takashi Inushima, and Shumpei Yamazaki, *IEEE Trans. Electron Devices*, **41**, 10, p. 1876, 1994.

[3] Augio Yin, and Stephen J. Fonash, *IEEE Electron Device Lett.*, **15**, 12, p. 502, 1994.

[4] Hiroshi Takahashi, and Yoshikazu Kojima, *Appl. Phys. Lett.*, **64**, 17, p. 2273, 1994.

[5] K. Ono, T. Aoyama, N. Konishi, and K. Miyata, *IEEE Trans. Electron Devices*, **39**, p. 792, 1992.

[6] G. Fortunato, and P. Migliorato, *Appl. Phys. Lett.*, **49**, 16, pp. 1025-1027, 1986.

[7] M. Cao, T. J. King, and K. C. Saraswat, *Appl. Phys. Lett.*, **61**, 6, pp. 672-674, 1992.

[8] Noriyoshi Yamauchi, Nobuhiko Kakuka, and Tomoko Hisaki, *IEEE Trans. Electron Devices*, **41**, 10, p. 1882, 1994.

[9] Thomas W. Little, Ken-ichi Takahara, Hideki Koike, Takashi Nakazawa, Ichio Yudasaka, and Hiroyuki Ohshima, Jpn. *J. Appl. Phys.*, **30**, 12B, pp. 3724-3728, 1991.

Characteristics of off current in amorphous silicon thin film transistors with SiO_2 gate insulator

Jeong Hyun Kim, Woong Sik Choi and Chan Hee Hong

LCD-SBU R&D Center, LG Electronics Inc., 533 Hogaedong, Anyangshi, 430-080 Korea

Hydrogenated amorphous silicon (a-Si:H) thin film transistors (TFTs) have been used as switching devices of commertial active matrix liquid crystal displays (AMLCDs). The negative gate voltage is applied to the a-Si:H TFTs almost all the time while the LCD is working. The off currents of the TFTs should be sufficiently low so that the data information remains on a pixel until next data signal is applied. Therefore, the off current is one of the most important factors to get a high performance display with no flicker. The flicker can be arised by the degradation of pixel potential. The several mechanisms responsible for the off current of the polysilicon TFTs have been suggested using a junction theory[1][2], i.e., thermal emission and field emission (tunneling) in the drain depletion region. The behavior of the off current for the a-Si:H TFT with SiNx gate insulator has been characterized similar to the polysilicon TFTs [3][4]. However, there is no report on the behavior of off current of a-Si:H TFTs which have atmospheric pressure chemical vapor deposition (APCVD) silicon dioxide (SiO_2) as the gate insulator.

In this work, the off currents for negative gate voltages were compared between the TFTs with the a-Si:H/SiO_2 and with the a-Si:H/SiNx interfaces. The a-Si:H TFT with SiO_2 gate insulator has small off currents and large activation energy (E_a) of the off current compared to the a-Si:H TFT with SiNx gate insulator. The holes induced in the channel by negative gate voltage seem to be trapped in the defect states near the a-Si:H/SiO_2 interface. The interface state density in the lower half of the band gap of a-Si:H/SiO_2 appears to be much higher than that for a-Si:H/SiNx. Figure 1 shows a cross

sectional view of the a-Si:H TFT with the a-Si:H/SiO_2 interface. Figure 2 shows the depth profile of Si, O, H and N for the interface region between a-Si:H and APCVD SiO_2 by SIMS. Figure 3 shows the comparison of a typical transfer characteristics for a-Si:H TFTs. Figure 4 shows the drain-to-source voltage dependence of the currents for a-Si:H TFTs a) with SiNx gate insulator, b) with SiO_2 gate insulator. Figure 5 shows the temperature dependence of the off current characteristics for a-Si:H TFTs a) with SiNx gate insulator, b) with SiO_2 gate insulator at V_d=20V. Figure 6 shows the activation energies of the off current for a-Si:H TFTs

REFERENCES

[1] J. G. Fossum, A. Ortiz-Conde, H. Schijo, and S. K. Banerjee,"Anomalous leakage current in LPCVD polysilicon MOSFET's," IEEE Trans. Electron Devices, vol. 32, No. 9, pp. 1878, 1985.

[2] K. Ono, T. Aoyama, N. Konishi and K. Miyata,"Analysis of current-voltage characteristics of low-temperature-processed polysilicon thin film transistors", IEEE Trans. Electron Devices, vol. 39, No. 4, pp. 792, 1992.

[3] G. E. Possin,"High temperature off current in a-Si TFT's effect of process and structure", Mat. Res. Soc. Symp. Proc., Vol. 219, pp. 327, 1991.

[4] T. Globus, M. Shur and M. Hack,"Studies of the stability of amorphous silicon thin film transistors", Mat. Res. Soc. Symp. Proc., Vol. 258, pp. 1013, 1992.

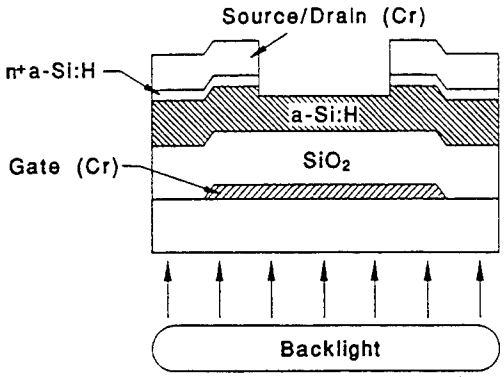
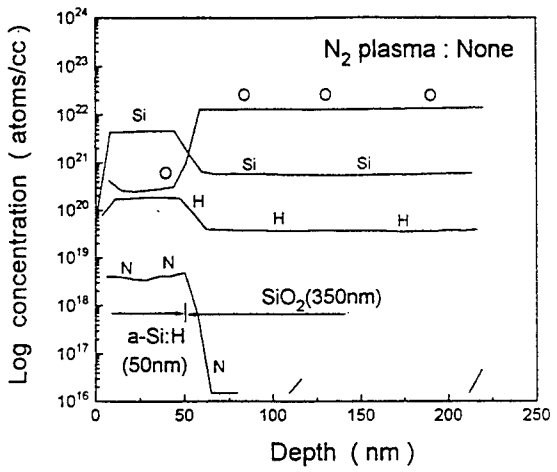


Figure 1



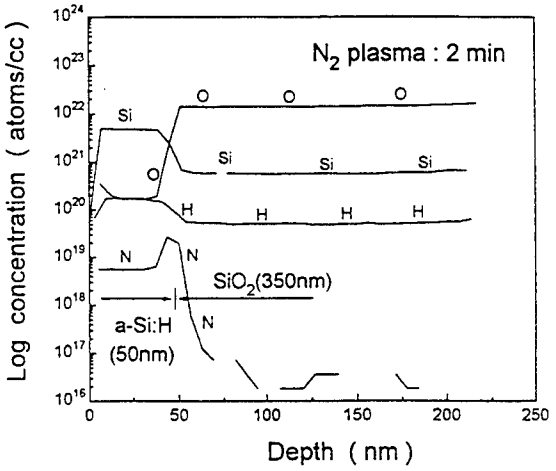
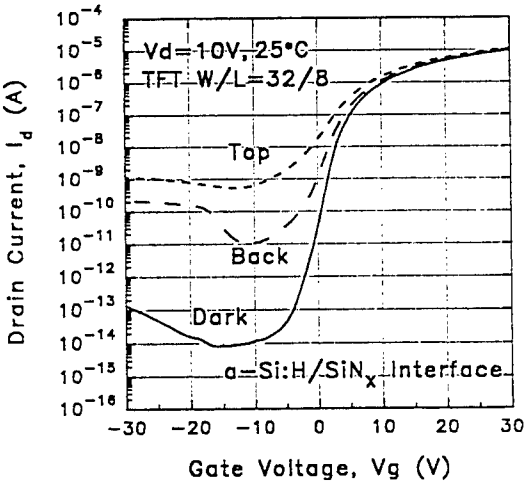


Figure 2 (a) (b)



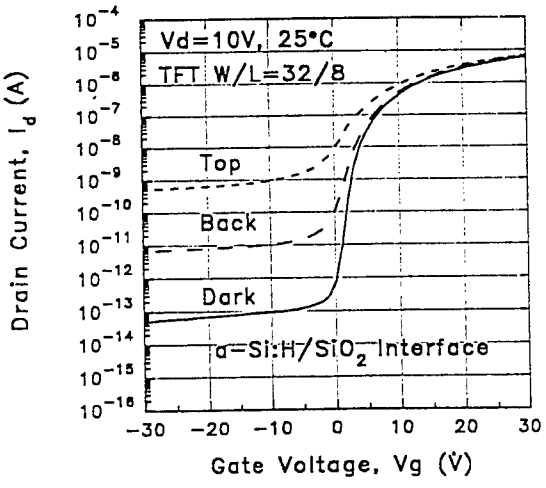
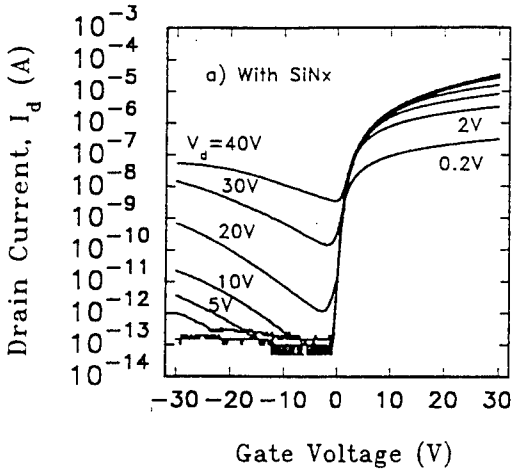


Figure 3 (a) (b)



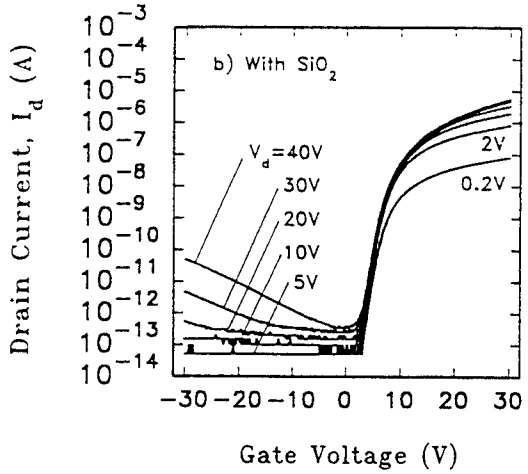
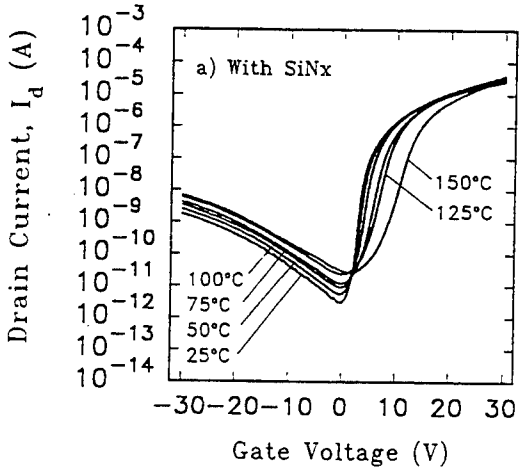


Figure 4 (a) (b)



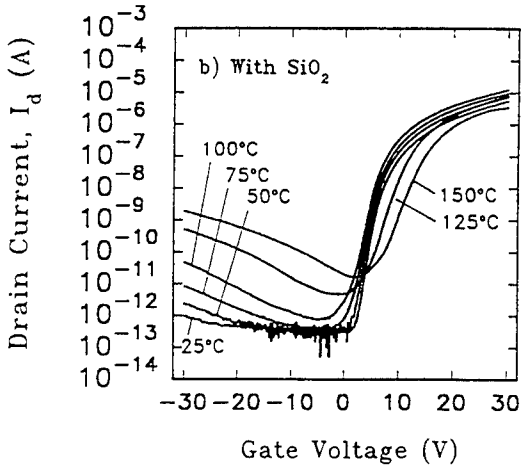


Figure 5 (a) (b)

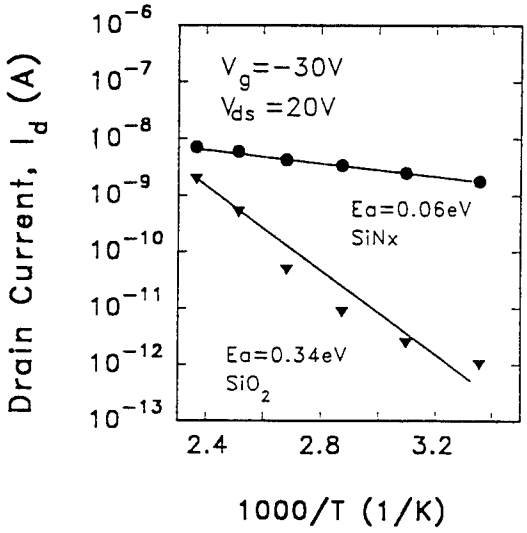


Figure 6

Doping and Geometric Effects on the Transient Drain Current in Amorphous Silicon Thin-film Transistor

M.H. Chu
and
C.H. Wu
Electrical Engineering Department
University of Missouri-Rolla
Rolla, MO 65401

Dynamical characteristic of amorphous silicon thin-film transistor (TFT) has been investigated recently by several authors [1, 2, 3]. In particular, there has been a controversy with regard to the existence of a transient drain current peak as calculated by Hack et al [1] on one hand and the absence of it by Huang and Wu [2] on the other. In this work, we would like to clarify the reason behind its existence or its absence. Doping level near the regions at source and drain contacts can play a very important role in determining the steady-state current levels as well as the transient behavior in which the switching time is determined. Earlier we have shown that switching time of TFT is four to five orders of magnitude greater than that of the transit time in undoped TFT [2]. Additional dopings near source and drain has a great effect in shifting the switching time closer to the transit time. We will show this effect explicitly here for the first time. Static characteristics' changes in TFT due to geometric factors, such as source/drain locations and gate metal length and location, has been investigated by Hack [1]. How those geometric factors can influence the switching time is studied here. The device geometry is shown here in Fig. 1a where the doping level near source and drain is indicated by shaded areas. The bulk trap-state density of the amorphous silicon layer is indicated in Fig. 2. In our numerical computations, continuity equations for electrons and holes, the related Poisson equation as well as the dynamical equation for trap-state occupancy are solved numerically. In our calculations $V_{DS} = 5V, V_G = 10V$, mobility= 20 cm^2/V - s and channel length $L = 10\ \mu m$ are used. In heavily doped cases at the levels of $10^{17}\ cm^{-3}$ *to* $10^{19}\ cm^{-3}$, the values of switch-on time are greatly reduced to 1.5×10^{-8} s from $4 \times 10^{-1}\ s$ in the undoped situation. This switch-on time is determined when the value of drain current is within a few percent to that of the source current since steady-state is actually reached only at infinite time. Because drain current is negative initially (drawing carriers into the channel) and at $t = 4 \times 10^{-9}\ s$, the drain current stops flowing in and begins to flow out. Afterwards the drain current quickly approaches to the value of source current which is decaying with time. Thus between the increasingly upward approaching to the value of source current and the subsequent near equality to the value of drain current, which is decaying, the drain current will exhibit peak, which, for all practical purpose, can be considered as the switch-on time (Fig. 4). However, if the doping level is low at $10^{12}\ cm^{-3}$ to $10^{15}\ cm^{-3}$ range, one will not observe any significant drain current peak because when drain current approaches source current at a much later time the source current is no longer decaying any significantly. The slow approaching of drain current toward source current in this situation is due to the low source and drain current levels at those low dopings. The switch-on time is the time required to fill all trap-states from initial Fermi level to the steady-state quasi-Fermi level, which is fixed regardless of the doping levels near the source and drains. Thus the low current density implies longer time to fill those trap states and thus longer switch-on time. Note

that transit time changes due to doping also. For example, the transit time $t = 10^{-8} s$ in undoped situation and $t = 10^{-10}\ s$ when heavily doped.

At low dopings of $10^{+12} cm^{-3}$ to $10^{15}\ cm^{-3}$, the steady-state source and drain currents increase only slightly (Fig. 3a). At high dopings of $10^{17} cm^{-3}$ to $10^{19}\ cm^{-3}$, the switch-on time (that is: the drain-current peak location) approaches a limiting value of $1.5 \times 10^{-8} s$ which is still two orders of mangitudes longer than that of the transit time (Fig 3b). Furthermore, we also investigate the effect of variation of the thickness of doping regions on static and dynamical characteristics. We find that the thickness has almost no effect on switch-on time or steady-state current level. The dopings at source and drain regions simply provides more uniform carrier initially over the entire contacts. Without such dopings, carrier will increase heavily only at contact regions closest to the gate contact. For example, the carrier concentrations at $t = 10^{-11} s$ and at $t = 10^{-10} s$ for undoped and doped contact regions are shown in Figs. 5a-5b and Figs. 6a-6b respectively.

Different locations for source/drain ohmic contacts are also investigated. As shown in Fig.1(b), we move the contacts from along the sides of the amorphous silicon layer in the x-direction to that in the y-direction. The results are that the switch-on time is longer by a factor of 2.5 and the steady-state drain current is scaled down by a factor of 0.43, if the ohmic contact regions are undoped. However, in the high doping situation, ohmic contact locations, horizontal or vertical, has little effect on the switch-on time or the value of steady-state drain current.

References

1. M. Hack, R. Weisfield, M.F. Williams, G. Masterton, P.G. LeComber, *Proceedings of 1993 MRS meeting;*
   M. Hack and J. Shaw: J. Appl. Phys., 68, 5337 (1990)

2. J.S. Huang and C.H. Wu, J. Appl. Phys., 74, 5231 (1993);
   J.S. Huang and C.H. Wu, J. Appl. Phys., 76, 5981(1994);
   J.S. Huang and C.H. Wu, Proceedings of 1993 *International Semiconductor Device Research Symposium,* Charlottesville, Virginia

3. C. Van Berkel, J.R. Hughes and M.J. Powell, J. Appl. Phys., 66.4488 (1989)

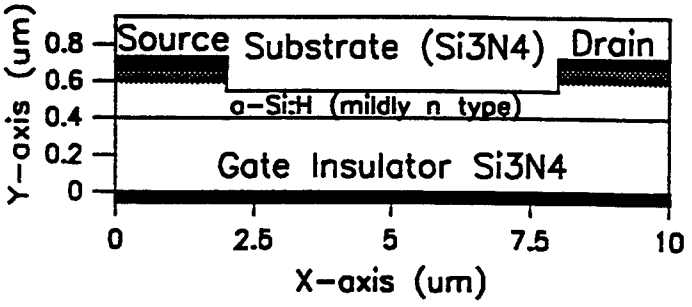


Fig.1 (a) Device geometry of a-Si:H TFTs. The doping regions are indicated by shaded areas.

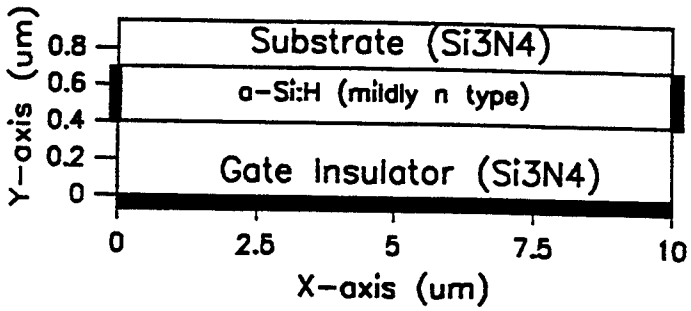


Fig.1 (b) The rectangular geometry of a-Si:H TFTs.

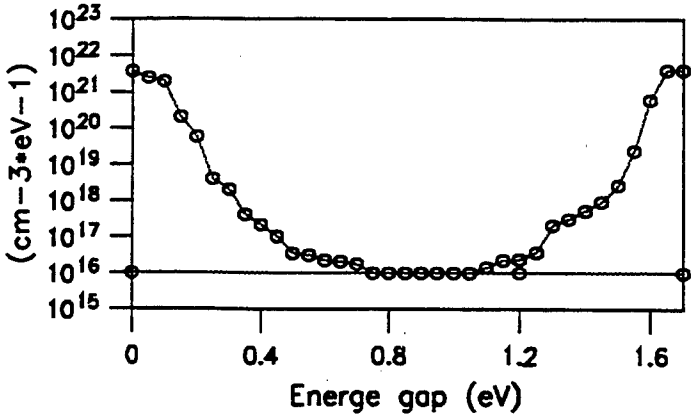


Fig.2 Density of states spectrum for amorphous silicon.

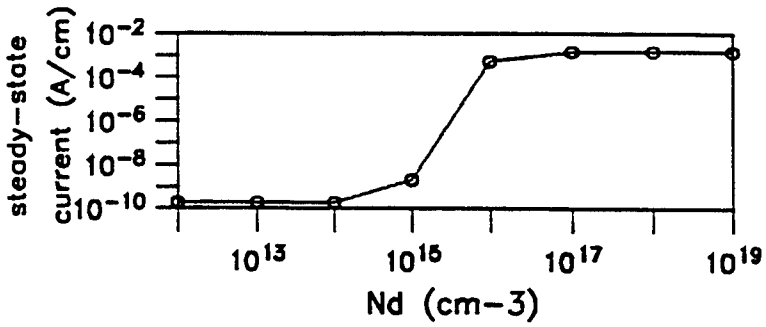


Fig.3 (a) Steady-state current as function of doping level.

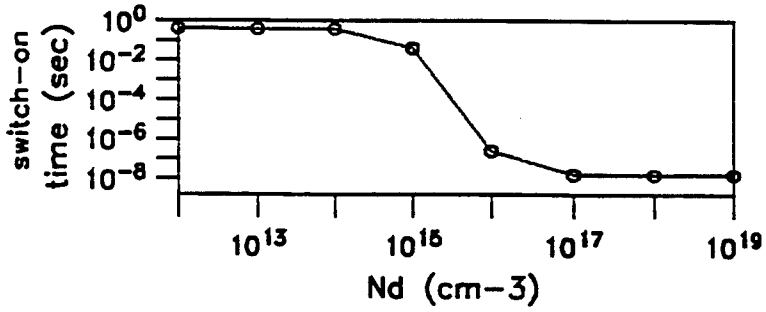


Fig.3 (b) Switch-on time as function of doping level.

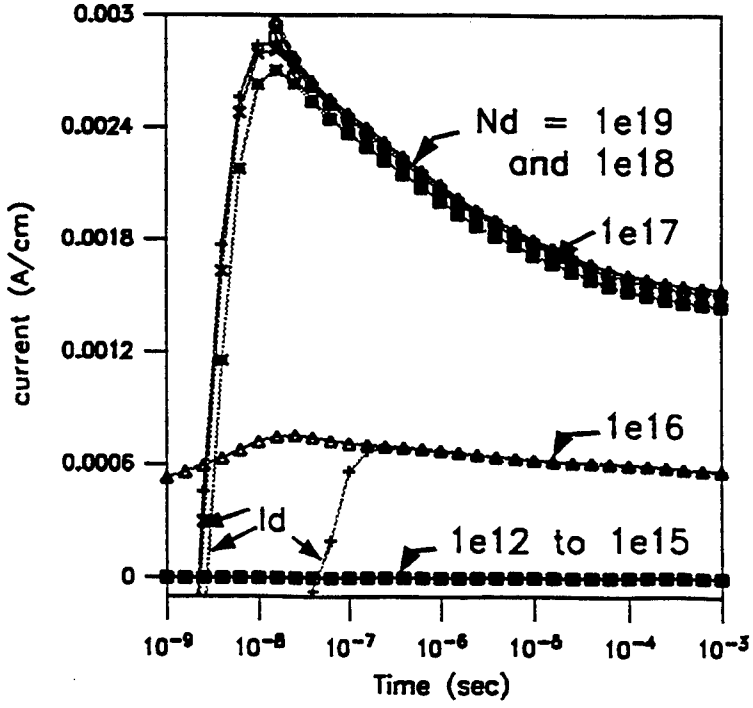


Fig.4 Drain current (Id), and source current (Is) as function of time and doping level (Nd).

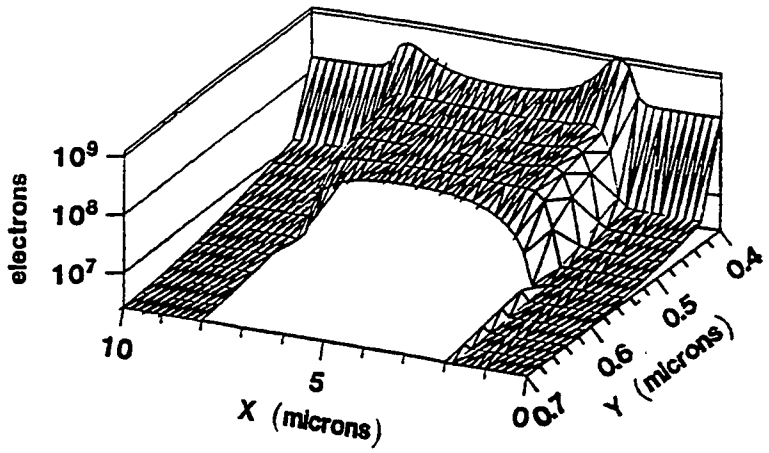
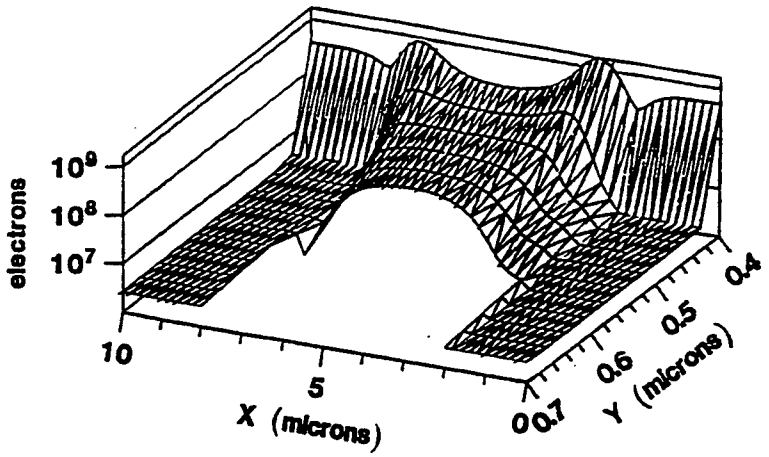


Fig.5 Free carrier density as function of position for undoped.
(a) At time = $10^{-11}s$



(b) At time = $10^{-10}s$

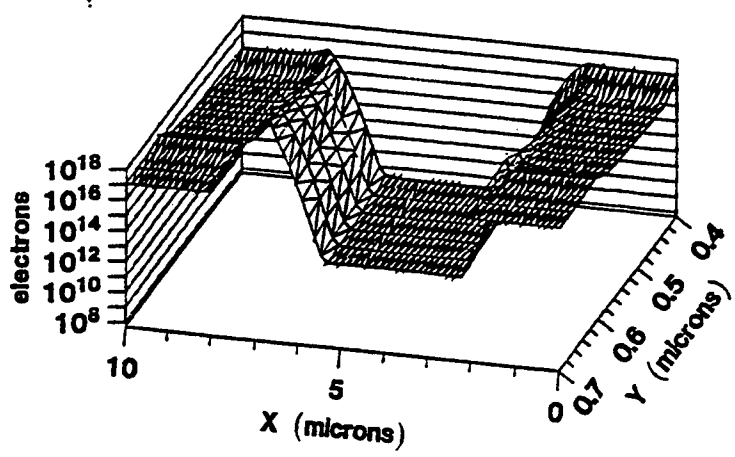
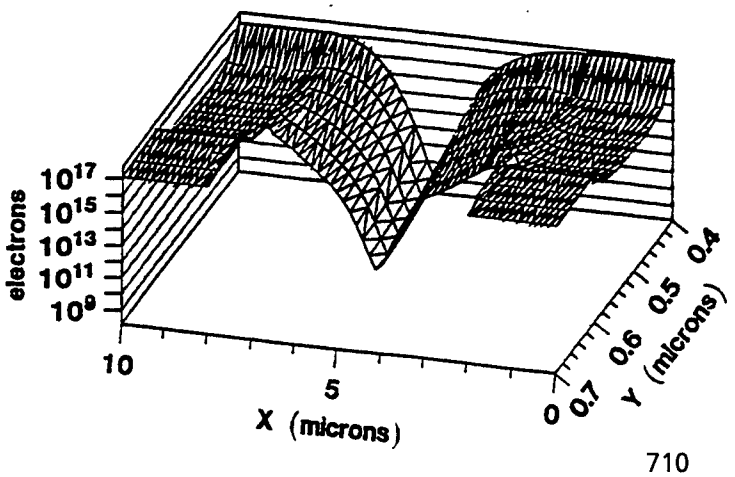


Fig.6 Free carrier density as function of position for heavily doped.
(a) At time = $10^{-11}s$



(b) At time = $10^{-10}s$

DEFECT DENSITY-OF-STATES IN a-Si:H TFTs DETERMINED BY THE FIELD EFFECT METHOD

Tatiana Globus, Boris Gelmont, Liang Quan Sun, Robert J. Mattauch, University of Virginia, Charlottesville, VA 22903

Development of efficient and nondestructive methods for hydrogenated amorphous silicon (a-Si:H) characterization is crucial for the variety of applications of this material for large area microelectronic devices. It is well known that the localized defects and their energy states distribution control the most of a-Si:H properties as well as device performance. Field effect conductance (FEC) methods are among the most commonly used for the density of states (DOS) determination in the bandgap of a-Si:H. Almost all modern modifications of the FEC method are based on the analysis of transfer characteristics of a-Si:H thin film transistors (TFTs). Different approximations have been introduced. It is usually assumed that a-Si:H film is homogeneous and that the flat band voltage, V_{FB}, can be used to account for charge at the film / insulator interface. In most cases, the zero temperature statistics is applied. In spite of all efforts, important questions about the presence of structures in the midgap DOS and the ability of the FEC method to resolve fine-scale features are still controversial issues. The lack of reliable methods to determine the flat band voltage is one of important sources of uncertainties.

Two different approaches for solving the problem have been developed. The first approach have been started from works of Spear, LeComber, and Madan [1, 2] and was further improved in [3-5]. The integral equation can be written which connects the surface sheet conductance, G, or the drain-source current I_{ds} with the effective band bending u_s in the conducting layer, and with the density of states N(E) through the charge density $\rho(u_s)$. Using an iterative process with some initial DOS as a trial characteristic, the actual density of states $N(E)$ can then be obtained that fits the experimental data I_{ds} *vs* V_g. The main disadvantage of this method is that only the broad DOS features can be determined and the uniqueness of solution is questionable. Besides, it requires time-consuming calculations. The second path is the approximate methods of the DOS evaluation [6,7]. In these methods, an incremental form of the same integral equation is used. Suzuki *et al.* [6] obtained the dependence of the surface potential u_s as a function of applied gate voltage by numerical integration of this incremental form for the voltage steps δV_g starting from the flat-band condition. Finally, the density of gap states can be calculated. This method of direct numerical integration of the differential equation has an uncertainty at flat band condition. Grunewald *et al.* [7] demonstrated how to circumvent this difficulty. However, in their approach, the simplified equation for the potential distribution has been used which does not take into account the potential drop inside a-Si:H layer. At the same time, near midgap density of states corresponds to gate voltages interval close to $V_g = 0$, at which condition the band bending in the surface layer is of the same order as the voltage across the insulator.

In this paper, we present our version of the FEC method for the direct DOS determination which represent the further development of the technique proposed in [7]. In our approach to solve the problem we restricted ourselves by an electron contribution in the conductivity and probed only the DOS in the upper half of the gap. The analytical solution of the problem for the low temperature approximation is found in the form of integral equation which relates the surface potential to the gate voltage. We apply the method to the analysis of TFT transfer characteristics. We demonstrate that by using this method, the flat band voltage can be obtained from experimental data. We also demonstrate the ability of this method to resolve fine-scale features in the midgap DOS of a-Si:H. At last, we demonstrate the advantages of this method as a tool for an undestructive, fast, easy, and reliable probe of the DOS in a-Si:H. This technique is used for the analysis of a-Si:H metastabilities and metastable transformations of the DOS.

We consider current- voltage characteristics of a-SI:H TFT in the subthreshold and above threshold regimes (V_g - V_{FB} > 0). The incremental equation which determines a field-induced sheet conductance G as a function of the surface potential u_s caused by the increment in the gate voltageV_g is

$$\frac{dG}{du_s}\frac{d_s F_s}{G_o} = \exp(\frac{qu_s}{kT}) - 1, \qquad (1)$$

where G_O is the conductance at the flat-band condition, d_S is the thickness of an a-Si:H layer, and F_S is the electric field in the a-Si:H film at the interface with the gate insulator. F_S is directly related toV_g by the equation of potential balance:

$$V_g - V_{FB} = \frac{\varepsilon_s F_s}{\varepsilon_i} d_i + u_s, \qquad (2)$$

where d_i is the thickness of an insulator layer, ε_S and ε_i are permitivities of an a-Si:H and an insulator, respectively. At this point, to avoid the uncertainty in equation (2) at the flat band condition, we can integrate the equation (1) over potential u, and after substituting F_S from Eq. (2), the integral equation can be obtained which connects the surface potential with V_g:

$$\frac{kT}{q}[\exp(\frac{qu_s}{kT}) - \frac{qu_s}{kT} - 1] = \frac{\varepsilon_i d_s}{\varepsilon_s d_i G_o}\int_{G_o}^{G} dG(V_g - V_{FB}) - \frac{\varepsilon_i d_s}{\varepsilon_s d_i G_o}\int_{G_o}^{G} dGu\,. \qquad (3)$$

The first integral in this equation is known from experimental data. Solving this integral equation by iterative technique we obtain the surface potential as a function of the gate voltage.

After the dependence u_s vs.V_g is found, we use it for the determination of the charge density $\rho(u_s)$ induced in the amorphous silicon layer by the gate voltage change.

$$\rho(u_s) = \frac{\varepsilon_i G_o}{d_i d_s}[\exp(\frac{qu_s}{kT}) - 1]\frac{d(V_g - u_s)}{dG}. \qquad (4)$$

At last, the density of state $N(E)$ as a function of energy $E = E_{FO} + qu_S$ can be calculated as

$$N(E) = \frac{1}{q}\frac{d\rho(u)}{du_s}. \qquad (5)$$

The detailed structure of a-Si:H TFTs used for FEC measurements was described earlier [8], as well as experimental procedure. Amorphous silicon TFTs with the bottom gate electrode, silicon nitride insulator (3000Å), undoped amorphous silicon (500Å), the top nitride insulator, and n^+ doped contacts has a nominal channel length of 15 μm and a width of 1 mm. In our calculations, we used parabolic approximation of I_{dS} -V_g characteristics for each three neighbor experimental points. This approximation was especially important for analysis of experimental data taken with small steps of gate voltages.

Several parameters are usually used for the FEC analysis. For the estimation of the current I_O at flat band voltage we used the effective density of states in the conduction band of a-Si:H, N_C ≈1.2 x10^{20} cm^{-3} [9], the Fermi level position in the bulk E_{FO} = 0.7 eV from the conduction band and the field effect electron mobility μ = 0.6 cm^2 $V^{-1}s^{-1}$. These parameters give us I_O ≈8x10^{-15} A for our geometry of TFT which is close to measured values of I_{dS} at the offset. The choice of V_{FB} strongly influences the determined density of states in the gap. We can find V_{FB} from the analysis of surface potential u_S as a function of the gate voltage. This dependence is shown in Fig. 1 for the flat band voltage 2.7 eV corresponding to the threshold of the field induced electron current I_O = 10^{-14}A. The extrapolation of this function to zero gives usV_{FB} ≈2.7 eV and this result is almost insensitive to the values of I_O andV_{FB} if we try more

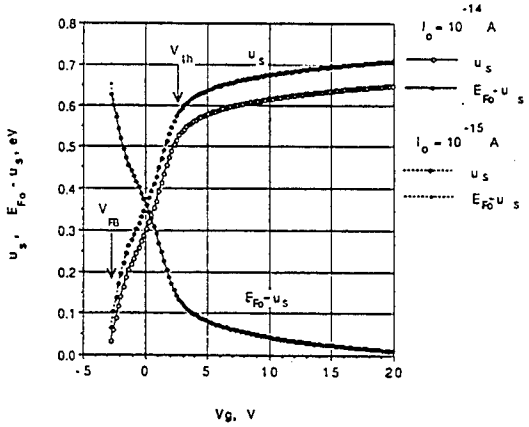


Fig.1. The surface potential u_S and the Fermi level position E_{FO} -u_S as a function of the gate voltage V_g.

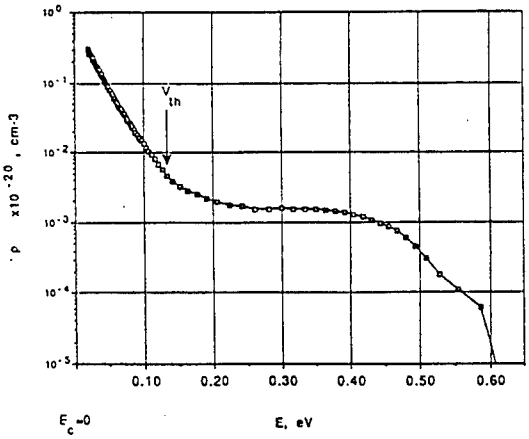


Fig. 2. The dependence of integrated charge density ρ on the energy E.

negative value of V_{FB}. For more positive trial values of the V_{FB}, we obtain only some part of practically the same function.

At large positive gate voltages, the surface potential as a function of gate voltage saturates. The saturation occurs at such a potential for which the Fermi level at the interface becomes very close to the conduction band due to band bending. Thus, from the data in Fig. 1 we can estimate the Fermi level position in the bulk relatively to the conduction band as $E_{FO} \approx 0.67$ eV for $I_O = 10^{-14}$A, and the position of the Fermi level at the interface relatively to the conduction band as E_{FO} -u_S. Although both, the calculated u_S and saturation value of E_{FO}, depend on the choice of I_O, their difference, E_{FO} - u_S, is almost invariant of I_O as it is demonstrated in Fig. 1.

With parameters determined from the dependence u_S vs.V_g, it is easy to calculate the integrated charge $\rho(u_S.)$ and the density of states N (E) as a function of the energy from the conduction band $E=E_{FO}$ -u_S.. The results are shown in Figures 2 and 3. The comparison of data permits us to make the following conclusions. The threshold voltage of the TFT (in our case V_{th} = 2.6 V as determined from linear extrapolation of I_d vs.V_g in the above threshold regime) corresponds to the Fermi energy position approximately 0.13 eV from the conduction band. At this point, all three characteristics u_S vs.V_g, ρ vs. E, and $N(E)$ vs.E change their character. Below the threshold voltage, the band bending u_S is a fast growing function of the gate voltage, but at V_g above the threshold voltage, the band bending changes more slowly as the Fermi level becomes more close to the conduction band (Fig. 1). There are two regions of energies in which the charge is fast growing function of E (Fig. 2). One region with almost exponential change of the charge corresponds to the Fermi level position in the range 0 - 0.13 eV from E_C. We might suggest that this charge change is due to generation of free carriers from the tail states near conduction band. The slope of the curve is very close to the Urbach energy obtained from optical measurements E_O = 0.04-0.06 eV [10] which is usually characterize the width of the tail states band in the device quality a-Si:H. The second region of fast growing ρ is separated from the first by the energy around 0.3 eV in which there is no change in the integrated charge density. This might indicate on the existence of two wide bands of localized states in the upper part of the gap which are separated by the region with lower density of states. One of these bands is the band of tail states and the second is the band of the deep, almost midgap localized states in the range of 0.4- 0.6 eV from E_C. The dependence of the DOS on the energy is close to the exponent in the range 0- 0.15 eV (Fig. 3), while deeper in the gap, the DOS can be described as a series of localized defect bands with amplitude values in the range 10^{17} cm^{-3} eV^{-1} - 2x10^{18} cm^{-3} eV^{-1}.

The results described till now correspond to TFT in unstressed conditions. Fig.4 demonstrates how the density of states varies under bias stress. For stressing, we applied large (30V) positive or negative bias to the gate electrode at the room temperature during 3 hours and

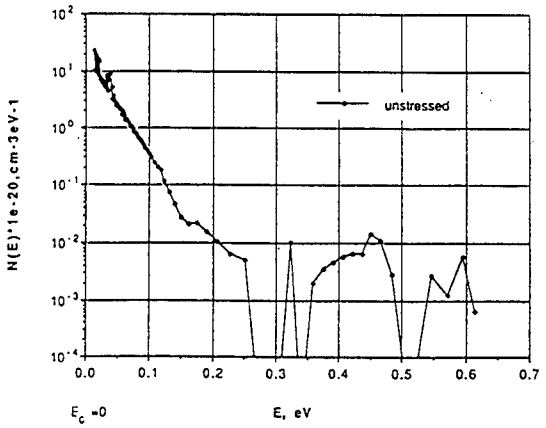


Fig.3. The DOS for unstressed sample.

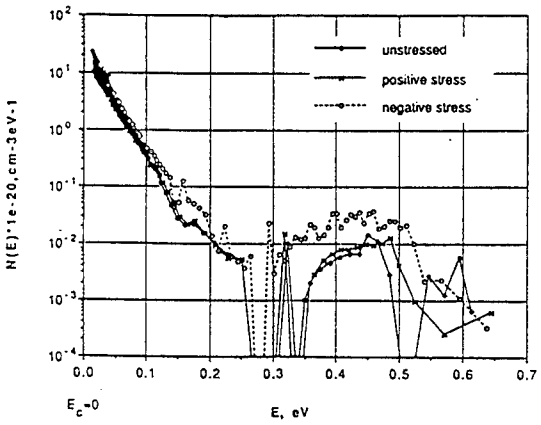


Fig 4. The DOS change after stress.

measured current - voltage characteristics before and after stress. These data show that the positive stress practically does not change the DOS in the upper half of the gap, whereas the negative stress enlarges significantly the density of midgap defects.

More precise analysis indicates that the integrated charge at plateaus in Fig.2 is not a constant, but has an anomaly dependence on u_S with negative slope in the range of the Fermi energy between 0.25 eV and 0.37 eVfrom the conduction band. The effect becomes more pronounced after positive stress. This anomaly is not predicted by our theoretical analysis in which the slope must be positive when the Fermi level moves from the midgap in the direction to the conduction band independent of two possible type of midgap states: acceptor-like or donor-like. One of possible explainations is connected with the 25% of carriers mobility change due to the change of the charge state of midgap defects. This suggestion is supported by the reduction of the field effect mobility determined from the slope of I_{ds} -V_g characteristics in the above threshold region. Against the background of the anomaly section of the curve we can see the peak centered at the energy 0.3 eV from E_C which reproduces quite well at all condition and may be the indicator of the involved defect. The segment of the curve $\rho(u)$ with negative slope results in showing fictitious negative density of states in the corresponding region of energy. This anomaly has to be investigated further.

In conclusion, we note that the developed FEC method resolve fine structure in the DOS which have been previously demonstrated by differential technique [8].

Acknowledgment

The work at the University of Virginia was supported by the National Science Foundation grants # EGER9350110 and ECS-9311033. We are grateful to Dr. M. Hack of Xerox for providing the a-Si:H samples used in this study.

References

1. W. E. Spear and P. G. LeComber, J. Non-crystall. Solids **8/10**, 727 (1972).
2. A. Madan, P. G. LeComber, and W. E. Spear, J. Non-crystall. Solids **20**, 239 (1976).
3. N. B. Goodman, and H. Fritzsche, Phil. Mag. B 42, 149 (1980).
4. M. J. Powell, Phil. Mag. **B 43**, 93 (1981).
5. R. L.Weisfield, and D. A. Anderson, Phil. Mag. **B 44**, 83 (1981).
6. T. Suzuki, Y. Osaka, and M. Hirose, Jpn. J. Appl. Phys. **21**, L159 (1982).
7. M. Grunewald, P. Thomas, and D. Wurtz, Phys. Stat. Sol. **(b) 100**, K139 (1980).
8. T. Globus, H. C. Slade, M. Shur, and M. Hack, MRS Proc. 336, 823 (1994).
9. S. Lee, M. Gunes, C. R. Wronsky, N. Maley and M. Bennet, Appl. Phys. Lett., **V59**, 13, 1579 (1991).
10. G.D. Cody, MRS Proc. **192**, 113 (1990).

Advanced Polysilicon Bipolar Transistors: Noise and Gain Performance Evaluation for Microwave Low-Noise Applications

A. Caddemi, P. Livreri and M. Sannino
Dipartimento di Ingegneria Elettrica - Università di Palermo - Italy

Abstract

Polycristalline silicon BJT's have exhibited highly competitive features for the realization of advanced low-noise receivers at low microwave frequencies.
In this work, the results of an investigation on the noise and gain performance of different series of double polysilicon self-aligned (PSA) bipolar transistors from the point of view of their effectiveness in low-noise amplifiers as compared to GaAs HEMTs are presented.

Introduction

Polysilicon self-aligned (PSA) transistor technology has definitively emerged as the cutting-edge bipolar technology for very high frequency, low-power consumption and low-noise performance applications [1]. The main benefits stemming from the adoption of a double-polysilicon process in comparison with conventional bipolar schemes are, basically: (a) a remarkable increase of the emitter efficiency with less temperature dependence; (b) reduced parasitic resistances and capacitances.
To the aim of exploring the features and performance of a commercially competitive PSA bipolar process, the manufacturer (CoRiMMe, an SGS-Thomson Research Center, Catania, Italy) has supplied us with several devices characterized by different emitter configurations.
The transistor families named Q_2, Q_3 and Q_4 were grouped according to their features:
- Q_2 4 emitters, 5 base contacts, 8 μm emitter length
- Q_3 8 emitters, 9 base contacts, 8 μm emitter length
- Q_4 16 emitters, 17 base contacts, 8 μm emitter length.

By means of noise figure measurements only, we performed the characterization of the above transistor series, in terms of noise, gain and scattering parameters over the 2÷6 GHz frequency range at the bias conditions suggested by the manufacturer which consisted of the fixed low voltage of 2.8 V and two I_C current values proportional to the emitter finger number n_e.
Such measured data was employed to extract an accurate model including noise sources for each measured family. Starting from these noisy models, the noise and gain performance of the transistor families Q_2, Q_3 and Q_4 have been evaluated by means of a graphical tool developed in our Lab. Remarkable differences have been noted between the perfomance of the PSA bipolar transistors and the common trends previously observed for low-noise FETs (such as MESFETs and HEMTs). To evaluate these differences and its relevant implications, a merit figure involving the combined

This work was supported by Italian Space Agency (ASI), National Research Council (CNR) and Ministry of University, Science and Technology Research (MURST).

performance (minimum noise figure- maximum associated operating power gain at a given frequency) has been employed.

Devices characterization and modeling

By means of an automatic system whose measuring procedure has been developed in our Lab, we performed measurements of the noise figure at the system output for either some properly selected values of Γ_S and, at each Γ_S value, for different values of the *receiver* noise figure realized by a high repeatability step attenuator. From these noise data we derived both the noise and the gain parameter sets of the device by an accurate deembedding of the various stage contributions and by applying appropriate data processing techniques [2].
For all device series, we first performed a d.c. characterization and *screening* microwave measurements of the scattering parameters, the available gain G_a and the noise figure F_{50} in input matched conditions (i.e. @ Γ_S =0) as a function of bias voltage and current in the 1-4 GHz frequency range [3].
As a second step, the transistors were completely characterized in the 1-6 GHz range at the following bias conditions:
- **Q_2** @ V_{CE} = 2.8 V, I_C = 2 and 8 mA;
- **Q_3** @ V_{CE} = 2.8 V, I_C = 4 and 16 mA;
- **Q_4** @ V_{CE} = 2.8 V, I_C = 16 and 64 mA;

Since all the measured data for each group exhibited reduced spread, a *Q_i typical* device (bold line in the reported diagrams) has been determined by simple statistic functions for representing each transistor series.
By deembedding the effects of the package (70-mil type) from the measured parameter values, we obtained scattering and noise parameter sets which refer directly to the chip device performance. The optimization procedure was then applied to the chip model network to determine the circuit element values by minimizing the scattering parameter error functions.
The values of the equivalent noise sources were first derived on the basis of the noise theory for bipolar transistors, then optimized by fitting the noise parameters. The adopted noise model is represented by a couple of correlated noise current sources at the input and the output port of the transistor plus the thermal contribution arising from each of the physical resistors. The complete model structure is shown in Fig. 1; the element values, including noise generators, are reported in Tab.1.

Performance evaluation

Starting from the noisy models, fitted to the measured data, the noise and gain performance of the transistor families **Q_2**, **Q_3** and **Q_4** have been evaluated by means of a graphical tool developed in our lab and defined as trade-off chart. As an example, the trade-off chart of the **Q_3** typical device is reported in Fig. 2.
Remarkable differences have been noted between the perfomance of the PSA bipolar transistors and the common trends previously observed for low-noise FETs (such as MESFETs and HEMTs) [4]. To evaluate these differences and its relevant implications, a merit figure involving the combined performance (minimum noise figure F_{min} - maximum associated operating power gain G_P at a given frequency) has been employed, which is defined as follows:

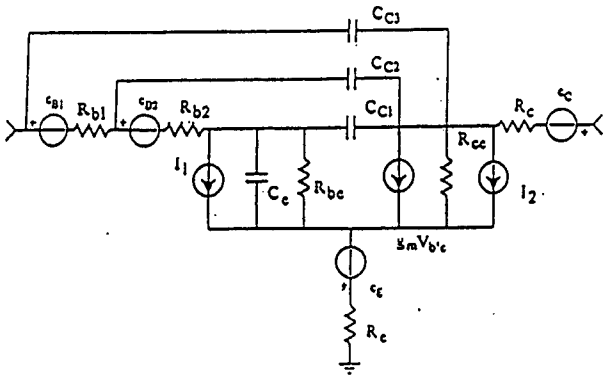


Fig.1. Equivalent circuit model including noise sources

	Q_1 A	Q_1 B	Q_2 A	Q_2 B	Q_3 A	Q_3 B
R_{b1} (Ω)	6	6	10	9	5	6
R_{b2} (Ω)	35	35	16	15	9	7
R_e (Ω)	3.3	3.3	1.5	1.5	0.5	0.5
R_c (Ω)	6	6	6	6	7	10
R_{cc} (Ω)	10000	10000	10000	10000	10000	10000
R_{be} (Ω)	1000	1000	1000	1000	1000	1000
C_e (fF)	0.8	4.4	1.6	9	5	20
C_{c1} (fF)	0.015	0.015	0.017	0.017	0.02	0.02
C_{c2} (fF)	0.09	0.1	0.12	0.13	0.3	0.35
C_{c3} (fF)	0.09	0.1	0.11	0.125	0.35	0.4
$\|I_1\|^2$ (pA²/Hz)	10	35	14	45	20	80
$\|I_2\|^2$ (pA²/Hz)	300	502	450	750	400	4000
$Re(I_1 I_2^*)$	0.8	0.8	0.8	0.8	0.15	0.8
$Im(I_1 I_2^*)$	0.2	026	0.4	0.2	0.85	0.3
T_{RC} (K)	297	297	297	297	1100	1000

Tab.1. Model element values.

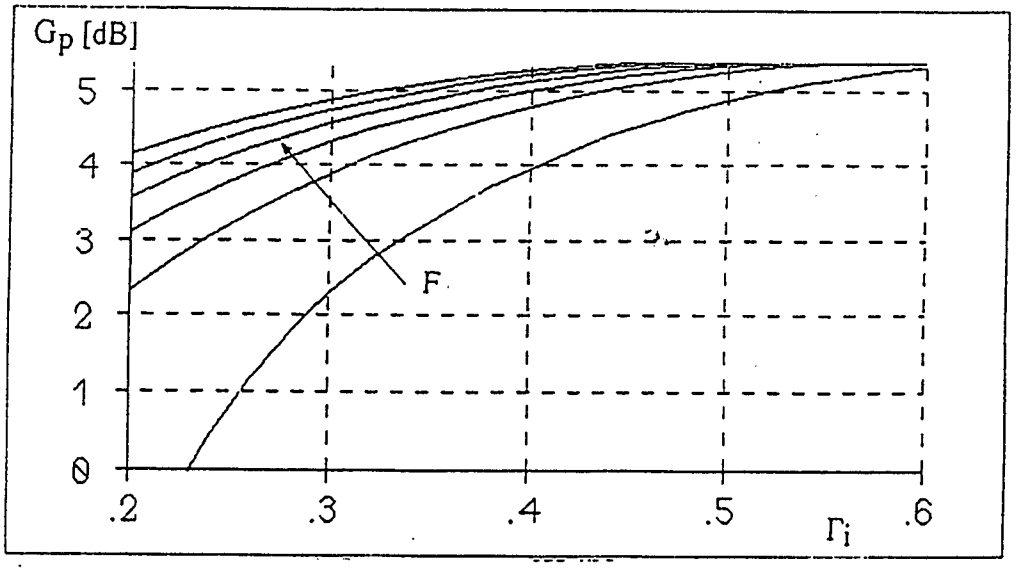


Fig.2. Trade-off chart ot the Q_3 typical device @ 5 Ghz.
The curves are plotted for incresing values of noise figure F
in the range 2-2.2 dB.

On the Performance of the Noise Parameters of Advanced Polysilicon Bipolar Transistors vs Frequency and Bias

A. Caddemi, M. Sannino

Dipartimento di Ingegneria Elettrica - Università di Palermo - Italy

ABSTRACT

It is well known that properly down-scaled silicon bipolar transistors for high performance digital and microwave circuit applications have gained great benefits from the adoption of ion-implanted polysilicon emitter contacts.
In this work, we present the results of an extensive characterization activity carried out on several advanced double polysilicon bipolar transistors. The devices were grouped according to their emitter finger number $\mathbf{n_e}$ and were characterized over the 2-6 GHz frequency range in terms of noise, gain and scattering parameters at different bias conditions.
A comparative analysis has been performed to understand how the transistor noise and gain behavior is affected by operating conditions and $\mathbf{n_e}$. This analysis has evidenced a superior performance of the noise figure of this advanced bipolar process which allows for realizing highly competitive silicon devices for use in telecommunication equipment at microwave frequencies.

INTRODUCTION

In portable communication systems operating over the low microwave range, devices and circuits must be designed to meet their best performance at very low current and voltage levels. The industry's trend is for developing advanced silicon bipolar processes to realize lower cost components, size and performance competitive with solution using GaAs. Among the most advanced bipolar processes for the realization of high speed silicon transistors, double-polysilicon self-aligned (PSA) schemes have definitively emerged as the most effective technique.
The adoption of a ion-implanted polycristalline silicon layer upon the monocristalline emitter allows for the realization of a very shallow junction with peculiar transport characteristics which result in a remarkable increase of the common emitter current gain ß and a smaller dependence of ß itself on temperature than conventional BJT's. In addition, the self-alignment of the extrinsic base and the emitter (double-poly process) drastically reduces parasitic resistances and the capacitances thus allowing for an appreciable improvement in the gain-bandwidth product, maximum oscillation frequency, minimum noise figure, power dissipation and component integration level in VLSI application [1].
To the aim of exploring the features and performance of a commercially competitive PSA bipolar process, the manufacturer (CoRiMMe, an SGS-Thomson Research Center, Catania, Italy) has supplied us with several devices characterized by different emitter configurations. We had previously performed a complete analysis on a preliminary PSA device series from the same manufacturer aimed at the extraction of an accurate circuit model including noise sources [2].
We have characterized a total of 29 PSA transistors supporting 5 different chip topologies to gain a better insight on those effects related to emitter geometry which affect device operation. The features of the measured families (named Q_i) are the following:

This work was supported by Italian Space Agency (ASI), National Research Council (CNR) and Ministry of University, Science and Technology Research (MURST).

- Q_2 4 emitters, 5 base contacts, 8 μm emitter length, with 4.6 μm pitch
- Q_3 8 emitters, 9 base contacts, 8 μm emitter length, with 4.6 μm pitch
- Q_4 16 emitters, 17 base contacts, 8 μm emitter length
- Q_6 same as Q_2, with 3.8 μm pitch
- Q_7 same as Q_3, with 3.8 μm pitch

The emitter finger pitch may be a critical parameter in improving the RF performance of BJT's since the transition frequency f_T can be increased by reducing its size.
We performed the characterization and the model extraction of the transistor series in terms of noise, gain and scattering parameters over the 2÷6 GHz frequency range at the bias conditions suggested by the manufacturer which consisted of the fixed low voltage of 2.8 V and two I_C current values proportional to the emitter finger number $\mathbf{n_e}$.
As a general result, F_O takes on very low values as compared to conventional bipolar transistors: less than 1 dB at 2 GHz for Q_3 and around 2 dB up to 5 GHz for all families. The noise performance at the lowest frequencies improves proportionally to $\mathbf{n_e}$ (which is expected since the base resistance decreases with increasing finger number) and deteriorates with increasing bias current.
The maximum available gain is less affected by either $\mathbf{n_e}$ and the bias current level with tyoical values in the range of 11 to 14 dB @ 2 GHz.
This bipolar process has exhibited an average f_T of 10 GHz and no appreciable differences have been noted in the device performance between the series having different emitter pitch.

NOISE PARAMETER MEASUREMENT PROCEDURE

The PSA devices were packaged in a standard 70-mil microstrip structure which fits measuring text fixture (Maury Microwave, mod. MT950) equipped with proper insert calibration elements (planar package-size devices supporting the *short* and *thru* layouts).
In our measurements, we refer to the representation in terms of the noise parameters which appear in the following relationship

$$F(\Gamma_S) = F_O + 4\, r_n \frac{|\Gamma_S - \Gamma_O|^2}{|1 + \Gamma_O|^2 (1 - |\Gamma_S|^2)}$$

where F and Γ_S are the noise figure and the input termination reflection coefficient of the device under test, respectively, and the four noise parameters are F_O (minimum noise figure), Γ_O (value of the complex variable Γ_S at which the minimum is located) and r_n (equivalent noise resistance normalized with respect to 50 Ω). A similar relationship holds for the reciprocal of the gain parameters which defines the conditions for the maximum value of the available gain (G_{aopt}) vs. Γ_S.
By means of an automatic system whose measuring procedure has been developed in our Lab, we perform measurements of the noise figure at the system output for either some properly selected values of Γ_S and , at each Γ_S value, for different values of the *receiver* noise figure realized by a high repeatability step attenuator. From these noise data we derive both the noise and the gain parameter sets of the DUT by an accurate deembedding of the various stage contributions and by applying appropriate data processing techniques. The scattering parameters are then calculated by use of well-known relationships employing the gain parameters and, therefore, are not measured directly by a network analyzer (see [3] and references therein).
For all device series, we first performed a d.c. characterization and *screening* microwave measurements of the scattering parameters, the available gain G_a and the noise figure F_{50} in input matched conditions (i.e. @ Γ_S =0) as a function of bias voltage and current in the 1-4 GHz frequency range [4].
As a second step, the transistors were completely characterized in the 1-6 GHz range at the following bias conditions:

- Q_2 @ V_{CE} = 2.8 V, I_C = 2 and 8 mA;
- Q_3 @ V_{CE} = 2.8 V, I_C = 4 and 16 mA;
- Q_4 @ V_{CE} = 2.8 V, I_C = 16 and 64 mA;
- Q_6 same as Q_2;
- Q_7 same as Q_3.

Since all the measured data for each group exhibited reduced spread, a *Q_i typical* device (bold line in the reported diagrams) has been determined by simple statistic functions for representing each transistor series. As an example, we report in Fig. 1 the minimum noise figure of all series at the above given bias conditions.
By deembedding the effects of the package from the measured parameter values, we obtained scattering and noise parameter sets which refer directly to the chip device performance. Such parameters have then been employed to extract a bias-dependent circuit model including noise sources for each measured family [5].

EXPERIMENTAL RESULTS AND RELEVANT COMMENTS

Some interesting remarks can be made with reference to the measured noise parameters:

- F_O increases and $|\Gamma_O|$ decreases with increasing bias current (except for an increase of $|\Gamma_O|$ resulting from the characterization of the Q_4 series at the high current level of 4 mA per emitter finger), whereas R_n (Ω) =50 r_n and $/\Gamma_O$ are affected by I_C to a very reduced extent;

- F_O, R_n and $|\Gamma_O|$ decrease markedly with increasing $\mathbf{n_e}$; as a consequence, the Q_2 series exhibit values of the noise figure F_{50} much higher than F_O. Also, the quantity $\Delta F = F_{50} - F_O$ reduces at higher current values;
- the slope of F_O vs. frequency increases proportionally to $\mathbf{n_e}$; therefore, F_O approaches values around 2 dB for all Q_i families @ 5 GHz (lower bias current) ;
- the slope of R_n vs. frequency vanishes with increasing $\mathbf{n_e}$, thus becoming flat for higher $\mathbf{n_e}$.

The performance of R_n for the Q_2, Q_3 and Q_4 series at the lower bias current is reported in Fig. 2. The available gain G_a is less affected by either $\mathbf{n_e}$ and the bias current level than the corresponding noise figure F_{50} as shown in Fig.3 as measured at different bias voltages and currents at the frequency of 2 GHz.
By summarizing the best results, we observed typical values of F_O even lower than 1 dB and available gain values as high as 14 dB @ 2 GHz.
No appreciable variations could be attributable to the different emitter finger pitch between Q_2 and Q_6, as well as between Q_3 and Q_7.

CONCLUSIONS

We have here presented the results of an extensive characterization activity performed on several PSA bipolar transistors.
The devices were characterized by a different emitter finger number $\mathbf{n_e}$ and were tested over the 2-6 GHz frequency range in terms of noise, gain and scattering parameters at different I_C values proportionally to $\mathbf{n_e}$ for each device series. A bias-dependent model extraction including the noise performance has been subsequently accomplished and the effects of the parasitics due to the package have been deembedded from the measured parameters to extract the *chip* performance. A comparative analysis among the measured families has then been carried out and evidenced outstanding performances in terms of minimum noise figure and available gain for this advanced bipolar process suitable for low power applications up to 4-6 GHz.

REFERENCES

[1] C.R. Selvakumar, "Theoretical and experimental aspects of polysilicon emitter bipolar transistors", in *Polysilicon Emitter Bipolar Transistors*, edited by A. Kapoor and D. Roulston, IEEE Press, New York, 1989.

[2] A. Caddemi, M. Sannino, "Small signal and noise model determination for double polysilicon self-aligned bipolar transistor", *Active and Passive Electronic Components*, Vol. 17, pp. 167-175, Dec. 1994.

[3] G. Martines and M. Sannino, "The determination of the noise, gain and scattering parameters of microwave transistors (HEMTs) using only an automatic noise figure test-set", *IEEE Trans. Microwave Theory Tech.*, Vol. MTT-42, pp. 1105-1113, July 1994.

[4] A. Caddemi, M. Sannino, "Advanced PSA bipolar transistors for wireless applications: measurements of scattering parameters and noise figure", *Proceedings of the 44th Conference of the Automatic Radio Frequency Techniques Group (ARFTG)*, Boulder, USA, Dec. 1994.

[5] A. Caddemi, M. Sannino, "Low-power PSA transistors for microwave communication systems: comparison among bias-dependent models extracted from measured noise and scattering parameters", to be presented at the *International Symposium on Signals, Systems and Electronics*, San Francisco, USA, Oct. 1995.

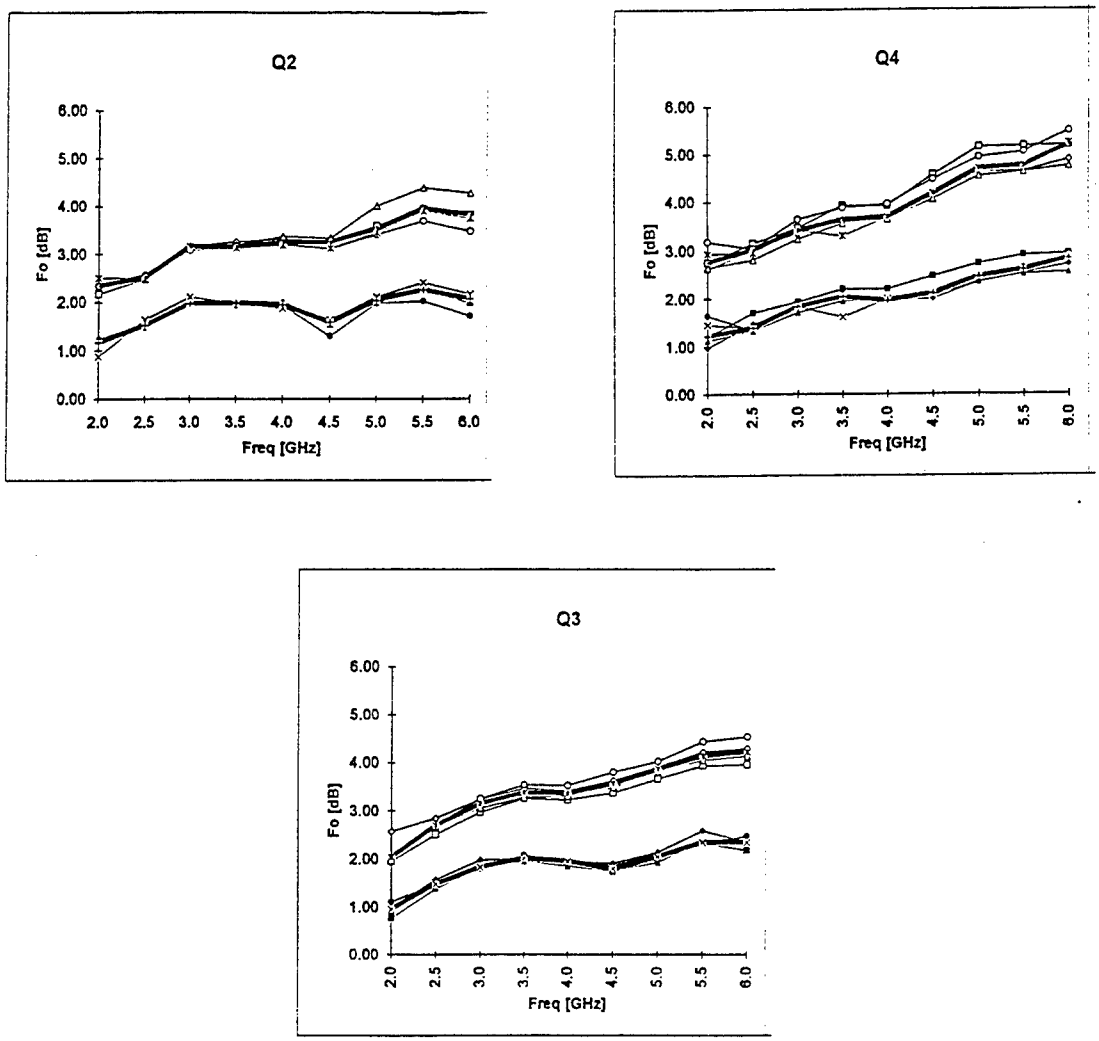


Fig. 1 - Minimum noise figure of the Q_2, Q_3 and Q_4 series at both bias conditions. The bold line refers to the *typical* device.

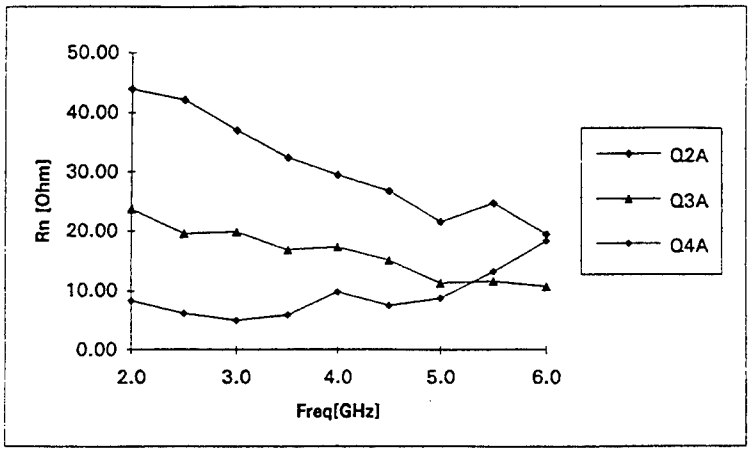


Fig. 2 - Equivalent noise resistance R_n of the Q_2, Q_3 and Q_4 series measured vs. frequency at the lower bias current.

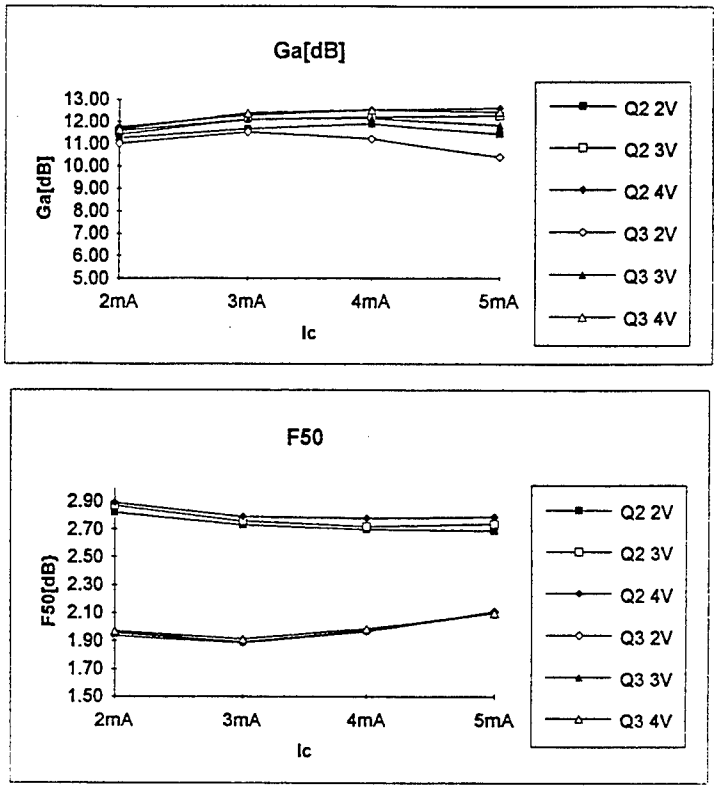


Fig. 3 - Available gain G_a and noise figure F_{50} vs. current measured at different bias voltages at the frequency of 2 GHz.

A Neural Network Based Qualitative Analysis of Semiconductor Device Manufacturing*

Mankuan Vai

Department of Electrical and Computer Engineering
Northeastern University
Boston, MA 02115

ABSTRACT

A neural network model representing the qualitative behaviors of a semiconductor device manufacturing process is presented. This qualitative model extracts qualitative relationships from a set of experiments. One feature of this method is that, in contrast to other neural network techniques, the structure of the neural network directly reflects the qualitative dependency between input and output parameters. The modeling of a plasma etching process is used to explain this technique and the search for a better recipe is demonstrated.

I. Introduction

Computer-integrated manufacturing has become a necessity in the increasingly competitive semiconductor manufacturing industry. Recently, it has been demonstrated that neural networks have a number of advantages over the conventional modeling techniques [1]. The successful applications of neural networks in the modeling and design of semiconductor device manufacturing have also been reported. For example, a large number of references can be found in [2].

Neural networks provide a *black-box* approach to model the complex, nonlinear relationships between sets of input and output parameters. Most significantly, a neural network trained with a limited subset of data has the potential to generalize the overall trends in parameter relationships. A survey of published results indicates that a multi-layer feed-forward neural network trained by the error back propagation learning algorithm is most popular. A good discussion of neural network computing can be found in [3].

While the power of a multi-layer feed-forward neural network in modeling a manufacturing process has been demonstrated, a number of problems remain to be solved. The number of hidden neurons or hidden layers cannot be determined analytically and is commonly obtained by trial and error. The multi-layer feed-forward neural network is unidirectional. In other words, a trained neural network provides a mapping mechanism from input to output parameters and cannot be used in a reverse direction. Furthermore, a neural network does not provide any information on the cause and effect of a behavior being investigated.

An alternative approach for modeling a system with a neural network was described in [4]. This approach used a Hopfield type neural network to model the qualitative behavior of an algebraic relation. A six-neuron network was developed to represent the relationship of three variables. A Hopfield network model for the entire system is represented by iteratively and hierarchically merging these network building blocks together. In addition to the systematic method of constructing a model, the interchangeablity of input and output variables in a Hopfield network allows the designation of certain system parameters as inputs to pursue the other parameters as outputs. The drawback of this approach lies in the fact that since each building block can only represent three parameters, a complex relationship involving more than three parameters has to be modeled by creating intermediate variables. A large number of intermediate variables which have no direct correspondence with the system parameters obscure the readability of the model. Also, as in other types of neural network, the knowledge about the system is encoded by the weights and thresholds together and cannot be readily obtained by studying the structure of the model.

* This research is supported by ARPA under Grant ONR/N00014-94-1-0687.

II. A New Qualitative Approach

Humans are able to understand the behavior of a system and perform a variety of reasoning tasks using a minimal amount of quantitative information. A qualitative approach applies the same principle to solve a problem and take advantage of a computer to overcome the limitation of that a human can only handle a few variables at the same time. A qualitative approach is in contrast with the computationally intensive numerical methods traditionally used. While quantitative methods can provide very accurate solutions, they are difficult to use and modify, expensive in their use of resources, and are not able to explain their solutions.

A designer typically obtains the qualitative relationship between system parameters by performing a number of quantitative measurements or experiments. This qualitative information is typically used to answer the following question:

- Which parameters should be modified to change the system behavior toward a desired goal?

Due to the fact that it is physically impractical to perform experiments with all possible parameter combinations, the qualitative insight is generally only valid in certain ranges of the parameters.

The approach described here applies the same principle to develop a neural network model for the qualitative analysis of a given system. This method will be explained using a plasma etching process as an example. The fact that plasma modeling from a fundamental physical standpoint has had limited success renders it to be an excellent test case for a qualitative approach.

The plasma etching process is taken from [1] which describes the use of a feed-forward neural network to model the etching process of polysilicon. As mentioned, the unidirectional property of a feed-forward neural network restricted its use to predict the outcome of a certain recipe. While the test results of this neural network model are superior to traditional statistical techniques, the neural network structure does not provide any insight to the process and cannot be used to answer the above question directly. Also, although this model provides a *black box* model to try out different recipes, it does not provide a guidance to how such recipes should be generated.

According to [1], six parameters and their ranges have been identified for the definition of a CCl_4 plasma etching recipe. They are the RF power (Rf), the chamber pressure (P), the electrode spacing (G), CCl_4 flow (CCl_4), helium flow (He), and oxygen flow (O_2). Similarly, four parameters were identified to define the quality of a recipe. They are the mean vertical poly etch rate (R_p), the nonuniformity (U), the selectivity of etching poly with respect to oxide (S_{ox}), and the selectivity of etching poly with respect to photoresist (S_{ph}). An artificial recipe is created by selecting the following values for the six parameters: Rf = 350 watts, P = 250 mtorr, G = 1.5 cm, CCl_4 = 125 sccm, He = 70 sccm, O_2 = 15 sccm. In order to reduce the complexity of the example so that it can be more readily understood, only two of the quality parameters, the mean vertical poly etch rate (R_p) and the nonuniformity (U), are used.

The first step in the modeling approach is to perform a quantitative evaluation in the neighborhood of the current recipe. This is done by varying one recipe parameter at a time while keeping the others unchanged. The objective is to obtain the qualitative dependency of each quality parameter on every recipe parameters. The results of this quantitative simulation are shown in Figures 1-6.

Due to the nonmonotonic relationships between the recipe and quality parameters (Figs. 4 and 5), the landmark concept used in qualitative simulation is applied. For example, according to the result shown in Fig. 4, under the current recipe, a landmark value exists at CCl_4 = 131. This implies that if the CCl_4 flow rate is below this landmark, the etch rate increases as the CCl_4 flow rate increases. After the landmark, the etch rate decreases as the CCl_4 flow rate increases. Two other landmarks are also identified according to the results shown in Fig. 5. For further information on the use of landmarks in qualitative simulation, see [5].

Based on the above qualitative analysis, the following qualitative relationships between the quality and recipe parameters are derived, in which the notation X: Y + (-) indicates the positive/increasing (negative/decreasing) effect of Y on X, with the landmarks provided in parentheses:

R_p: Rf +, P +, G -, CCl_4 + (CCl_4 < 131) - (CCl_4 > 131), He + (He < 85) - (He > 85), O_2 +.

U: Rf -, P -, G -, CCl_4 -, He - (He < 67) + (He > 67).

A neural network is created to represent the above qualitative relationships. Two groups of neurons are created for the recipe and quality parameters, respectively. A link is provided between a recipe parameter neuron and a quality parameter neuron. The weight of such a link is assigned according to the

qualitative relationship between its end nodes. A weight of +1 is assigned if the recipe parameter has a positive effect on a quality parameter. A weight of -1 is assigned if the recipe parameter has a negative effect on a quality parameter. A weight of 0 is used when there is no qualitative relationship between a pair of parameters. A neural network created accordingly is shown in Fig. 7.

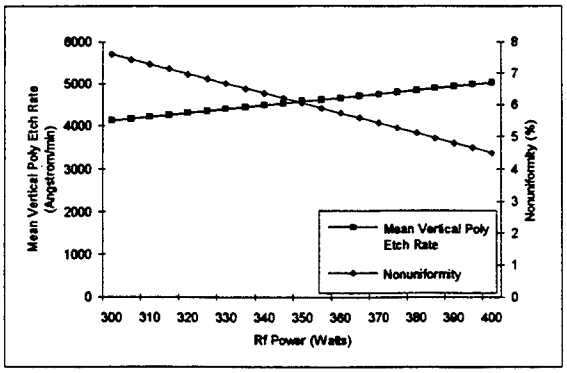


Fig. 1 The poly etch rate and nonuniformity vs. the Rf power.

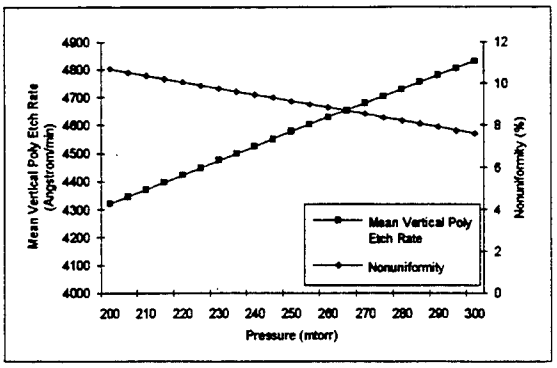


Fig. 2 The poly etch rate and nonuniformity vs. the pressure.

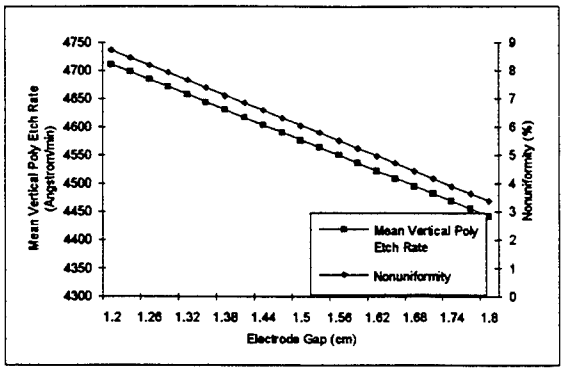


Fig. 3 The poly etch rate and nonuniformity vs. the electrode spacing.

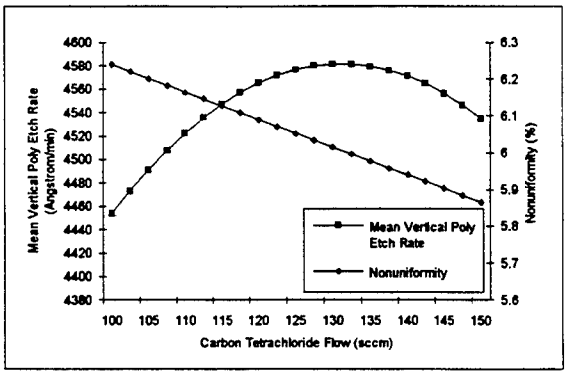


Fig. 4 The poly etch rate and nonuniformity vs. the CCl_4 flow.

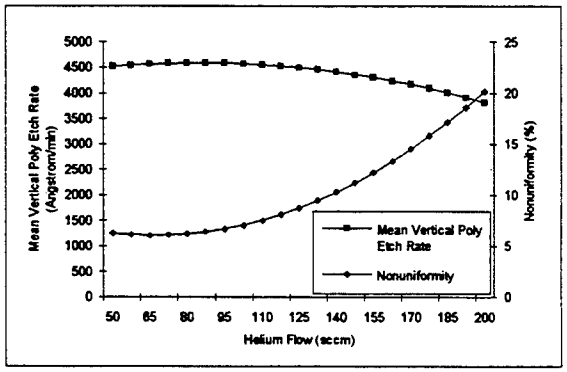


Fig. 5 The poly etch rate and nonuniformity vs. the He flow.

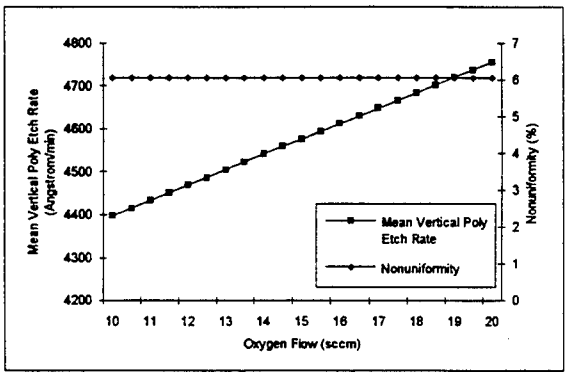


Fig. 6 The poly etch rate and nonuniformity vs. the O_2 flow.

The value of each neuron in the recipe parameter side is updated according to the following rules:

$$X_i = \sum_{j=1}^{n} W_{ij} \times V_j, \quad V_i = \begin{cases} 1 & \text{if } X_i > 0, \\ 0 & \text{if } X_i = 0, \\ -1 & \text{if } X_i < 0, \end{cases}$$

where V_i is the value of a neuron, W_{ij} is the weight of the link connecting neurons i and j, n is the number of neurons on the quality parameter side of the network, and X_i is the overall input of neuron i.

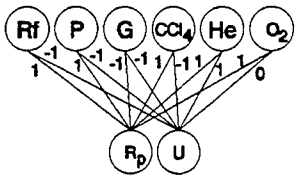


Fig. 7 A neural network representing the qualitative relationships between the recipe and quality parameters.

This neural network can be used to direct the search of a better recipe in the neighborhood of the current one. A common goal of optimizing the plasma etching process is to increase the etch rate and reduce the nonuniformity. This goal can be represented by assigning the quality neurons with the following values: V_{Rp} = 1 and V_U = -1 (1, 0, and -1 indicate increase, unchange, and decrease, respectively). Propagating the values of the quality parameter neurons to the recipe neuron side produces the following results: V_{Rf} = 1, V_P = 1, V_G = 0, V_{CCl4} = 1, V_{He} = 0, and V_{O2} = 1.

A quantitative recipe generated by modifying the parameters using the above qualitative guidance verifies that the quality parameters are improved according to the requirements. The etch rate and nonuniformity are increased and decreased, respectively.

III. Discussion

The above method provides a simple way of generating a neural network to capture the qualitative relationships between the independent and dependent parameters. The structure of the neural network directly reflects the qualitative relationships and can be used to provide the user with insight. While our preliminary experiments show promising results, there are a number of problems remaining to be solved. In general, due to the loss of information in the conversion from quantitative data into qualitative relationships, an exact recipe which produces the best result cannot be guaranteed. However, the size of the solution space is significantly reduced with the guidance provided. The quantitative experiments should be extended beyond the neighborhood of the current recipe. We are currently investigating the use of a variety of techniques such as the fractional factorial design technique to improve the accuracy of the information extracted. Another limitation lies in the inherent ambiguity of qualitative analysis. One obvious ambiguity occurs when two conflicting (increasing and decreasing) factors are controlling a parameter. While the modifications of the factors can be quantitatively controlled to achieve the desired effect, a generic qualitative technique can at best provide three possible cases (increased, unchanged, or decreased). A number of possible solutions to this problem are being studied.

References:

[1] Himmel, C. D. and May, G. S., "Advantages of plasma etch modeling using neural networks over statistical techniques," *IEEE Trans. on Semiconductor Manufacturing*, vol. 6, no. 2, 1993, pp. 103-111.

[2] Huang, S. H. and Zhang, H.-C., "Neural networks in manufacturing: a survey," *Proc. 15th International Electronics Manufacturing Technology Symposium*, Oct. 1993, pp. 177-186.

[3] Lippman, R., "An introduction to computing with neural networks," *IEEE Acoustics, Speech, and Signal Processing Magazine*, April 1987. pp. 4-22.

[4] Vai, M., Xu, Z., and Prasad, S., "Semiconductor device modeling by a neural network guided optimization process," *Proc. 1993 International Semiconductor Device Research Symposium*, pp. 507-510.

[5] Kuipers, B., "Qualitative simulation," *Artificial Intelligence*, vol. 29, 1986, pp. 289-338.

Direct Wafer Bonding Technology for Multi-Material Integration

Takeshi Kamijoh and Hiroshi Wada
Optoelectronics Oki Laboratory, Real World Computing Partnership (RWCP)
c/o Semiconductor Technology Laboratory, Oki Electric Industry Co., Ltd.
Higashiasakawa, Hachioji, Tokyo 193 Japan

Multi-material integration will be very important technology for Optoelectronic Integrated Circuits (OEICs), especially on Si. In this paper, we review recent progress of direct wafer bonding technology for InP-to-GaAs, InP-to-Si, and InP-to-SiO2 using atomic rearrangement by thermal treatment. In the InP-to-Si direct bonding, we demonstrated a low temperature process which is c-MOS compatible. A RT-CW operation of InGaAsP-InP laser diode directly bonded on the Si substrate was achieved at first time. Finally, we point out that the direct wafer bonding is attractive for future integrated optoelectronic devices.

A Novel Method of InAs Dot Array Formation for Nanostructure Devices

Kanji Yoh, Toshiya Saitoh and Arata Tanimura

Research Center for Interface Quantum Electronics, Hokkaido University
North 13, West 8, Sapporo 060, Japan

Self-organized MBE growth of InAs dots on GaAs by Stranski-Krastanow growth mode [1-7] is drawing much attention for possible nanostructure device applications. However, lack of spacial control of InAs dots of this method tend to place the constraints on the possible applications of quantum dots in electronic and optical devices [8]. In this paper, we will show regularly arrayed InAs quantum dots grown on tetrahedral etch-pits and trapezoidal V-grooves patterned on (111)B GaAs substrates by strain effect.

GaAs (111)B substrates were patterned by using conventional optical lithography process and wet-chemical etching. Array of 2 μm square patterns and 2 μm wide line-and-space pattern with 4 μm period were used. Two kinds of V-groove patterns were fabricated: one aligned to [011] and the other to [211] direction. The wet chemical etching were carried out by using solution of NH_4OH: H_2O_2 : H_2O (= 1 : 1 : 20) at 10℃. The etching rate was about 150Å per second on (111)B surface. The thermal cleaning was performed on the etched surface at 600℃ and then 50Å of GaAs layer was grown on the patterned substrate prior to the InAs dot growth at 590℃ with the growth rate of 6000Å per hour and with the arsenic beam equivalent pressure of $4x10^{-5}$ Torr. MBE growth of InAs dots were performed at substrate temperature ranging from 510℃ and 540℃. During the growth of InAs dots, the arsenic beam equivalent pressure of $7.5x10^{-6}$ Torr and the InAs growth rate of 0.05 mono-layer (ML) per second were used. In order to enhance the migration of indium atoms on the surface, growth was interrupted for 4 to 10 seconds after every 2 seconds of InAs growth in each period by shutter control and the total of 20 to 25 periods were deposited for the InAs dot growth of 2.0 ML or 2.5 ML equivalent.

Figure 1 shows a cross sectional SEM image of the etch-pit on GaAs (111)B surface. The base width seems to be much lower than 200Å by the SEM image. InAs dots were found to grow selectively on the bottom of the etch pit by choosing the right growth conditions by the surface migration of indium atoms on surface. Figures 2(a), (b) and (c) show SEM images of inverted tetrahedral shaped surfaces after the InAs growth at substrate temperature of 510℃, 530℃, and 540℃ respectively. The total amount of InAs deposition was 2.5 ML. After every 2 seconds of the InAs growth, 10 seconds of growth interruption was inserted to enhance the indium migration on the surface. Many InAs dots formed on the etched wall at substrate temperature of 510℃ indicate insufficient surface migration of indium atoms on the surfaceas as shown in Fig.2(a). InAs dots were selectively grown on the bottom of the tetrahedral etch-pit when the growth temperature of 530℃ was chosen as shown in Fig.2(b). No InAs dot was observed on the surface of the sample grown at 540℃ as shown in Fig.2(c) indicating re-evaporation of indium atoms from the substrate at this growth temperature. Figure 3 shows SEM image of inverted tetrahedral shaped surface after the InAs growth at temperature of 530℃ using the multiple sequence of 2 seconds of the InAs growth followed by 4 seconds of growth interruption by shutter control. The best yield for dot formation grown at 530℃ was about 70%. Figures 4(a) and (b) shows the blowup SEM image of the InAs dot at the bottom of the etch-pit. The shape of the InAs dot seems to have facets and its shape being close to truncated hexahedron, which is more like a bulky ball as compared with very short dots (disks) grown on a flat surface[1-7].

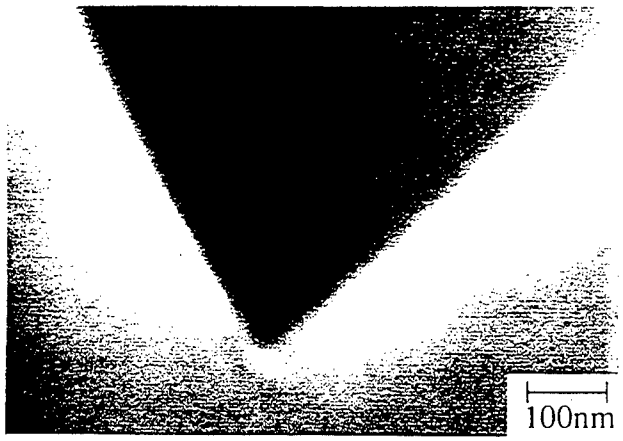


Figure 1 A cross sectional SEM image of inverted tetrahedron formed on GaAs (111)B surface.

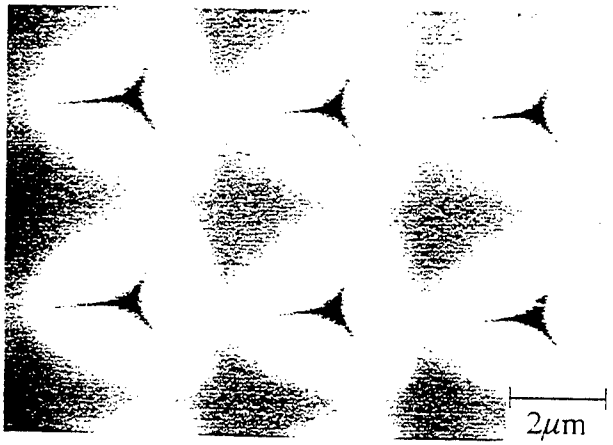


Figure 3 An SEM image of InAs dots grown on the bottom of a group of 6 invertaed tetrahedrons.

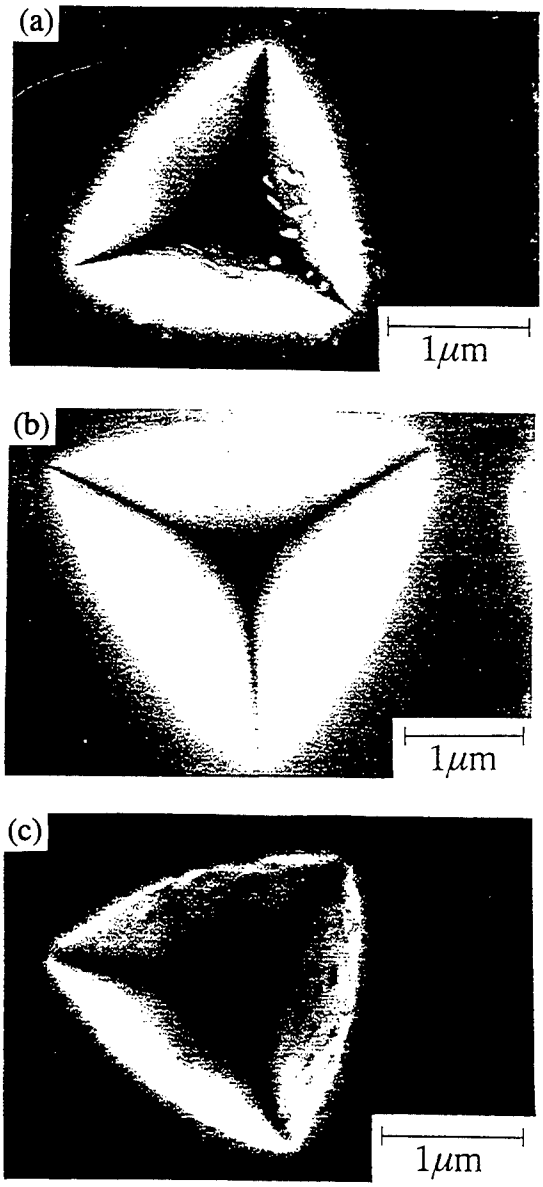


Fig.2 SEM image of inverted tetrahedral shaped surfaces after the InAs growth at temperature of (a)510℃ (b)530℃ and (c)540℃ respectively.

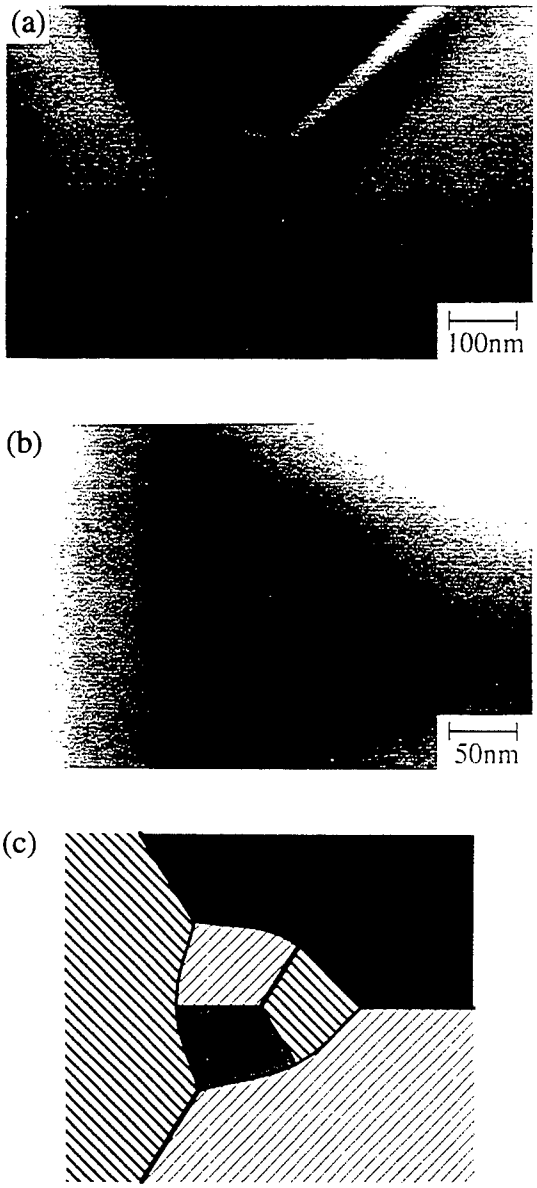


Fig. 4 A blowup SEM image of the InAs dot at the bottom of the etch-pit. (a) side view (b) top view (c) schematic diagram.

InAs growth on trapezoidal grooves was also investigated. Figures 5 (a) and (b) show SEM images of InAs dots grown on trapezoidal grooves. The grooves in Fig.5 (a) and (b) are aligned along the direction of $[2\bar{1}\bar{1}]$ and $[0\bar{1}1]$, respectively. Total amount of InAs growth of 2.5ML and 2.0ML, and the growth interruption of 10 seconds and 4 seconds were used for Fig.5 (a) and (b), respectively. The wafer was rotated during the growth. On the grooves which align to $[2\bar{1}\bar{1}]$ direction, InAs dots were found on the middle of one of the slopes as shown in Fig.5 (a). No indium dots was found on the other side of the slope. Furthermore, the InAs dot were distributed periodically along the line direction. On the other hand, on the grooves aligned to $[0\bar{1}1]$ direction, the InAs dots were formed only on top of the ridge and on bottom of the valley. The InAs dots on the top and bottom of the grooves distributed also periodically along the line direction.

The shape of the InAs dots on the grooved substrates looks hexagonal in its top view, and column shaped in its side view as shown in Fig.6. The bulky shape of the dots on the patterned substrates makes clear contrast with InAs(or InGaAs) dots (or rather disks) on flat substrates. The rather regular dot distribution along the ridge, valley and on the slope are shown in histograms of Figure 7. Figure 7(a) shows the dot distribution along the slope concentrating near mid-point of the slope in trapezoidal grooves aligned to $[2\bar{1}\bar{1}]$ direction with total width of approximately 3.5μm. The average position was 1.53μm measured from the top(ridge) toward the valley and its standard deviation was 0.46μm. Figures 7(b),7(c),7(d) show the histogram of the distance between the nearest neighbor InAs dots on the slope, on the ridge, and on the bottom of the valley, respectively, along the line direction. The solid lines in each diagram show Poisson distributions with the same average distance as the real dot distribution along the line direction. It is clearly seen that the experimentally observed dot distributions have much narrower standard deviation compared with calculated random distributions. The physical origin of these 'regular' distributions of the dots on the patterned substrates is presumably caused by the "periodic" lattice strain expected on the patterned surface in the initial stage of the highly strained layer growth [9-11].

In summary, self-assembled MBE growth of InAs dots on two dimensionally arrayed tetrahedral etch-pits and on trapezoidal groovs fabricated on (111)B GaAs substrates by Stranski-Krastanow growth mode was demonstrated. InAs dots were found to be selectively grown on the bottom of the tetrahedral etch-pit. InAs dots on trapezoidally grooved (111)B GaAs substrates were shown to be selectively formed on the middle of the slope of grooves along the direction of $[2\bar{1}\bar{1}]$ and on the top and the bottom surface of grooves along the direction of $[0\bar{1}1]$. The periodic strain distribution at the initial stage of the highly strained growth of the wetting layer was suggested to account for the periodic nature of the InAs dot distribution.

This work was supported by a Grant-in-Aid for Scientific Research from the Ministry of Education, Science and Culture.

References

1) J.M.Moison, F.Houzay, F.Barthe and L.Leprince, Appl. Phys. Lett., 64, (1993) 196
2) K. Nishi, R.Mirin, D.Leonard, G.Medeiros-Ribeiro, P.M.Petroff and A.C.Gossard, Proc. of 7th Int. Conf. of IPRM, (1995) 759
3) J.M.Gerard et al, J. Crystal Growth, 150 (1995) 351
4) P.M.Petroff and S.P.DenBaars, Superlattices and Microstructures, 15 (1994) 15
5) Y.Nabetani, T.Ishikawa, S.Noda and A.Sasaki, J. Appl. Phys., 76 (1994) 347
6) Y. Sugiyama, Y.Sakuma, S.Muto and N.Yokoyama, Appl.Phys.Lett., 67 (1995) 256
7) D.S.L.Mui, D.Leonard, L.A.Coldren and P.M.Petroff, Appl.Phys.Lett., 66 (1995) 1620
8) A.Takeuchi et al, Proc. 2nd Internatioanl Workshop on Quantum Functional Devices, Matsue, Japan, May 1995, pp. 74-75.
9) K.Yoh, H.Takeuchi, T.Saitoh and H.Hasegawa, presented at EMC, (Virginia, 1995) H4
10) T.Saitoh, H.Takeuchi, J.Konda and K.Yoh, Extended Abstracts of the 1995 International Conference on Solid State Devices and Materials, (Osaka, 1995) 743
11) J.Y.Yao, T.G.Andersson and G.L.Dunlop, Appl.Phys.Lett.,53,(1988) 1420

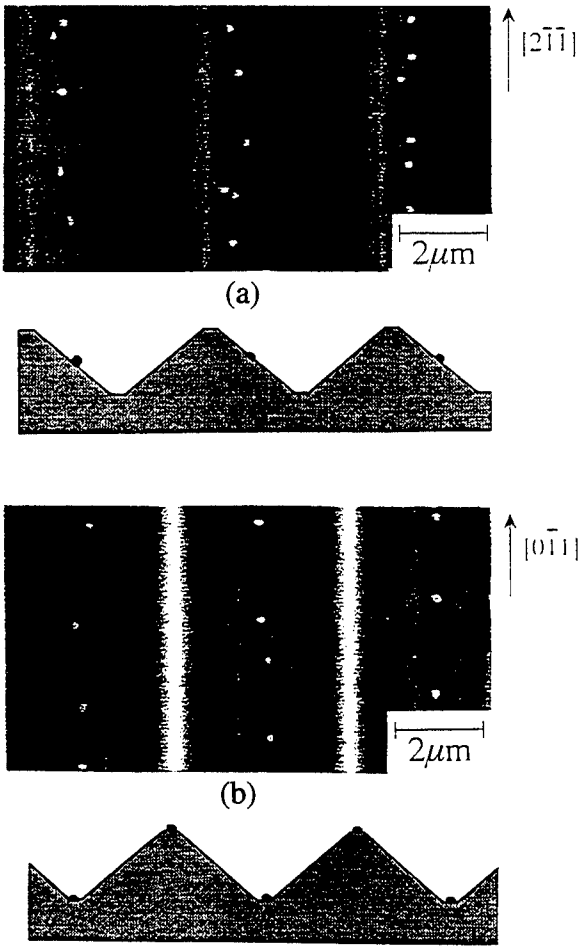


Fig.5 SEM image of InAs dots grown on the groove pattern along the direction of (a) [2$\bar{1}\bar{1}$] and (b) [0$\bar{1}$1].

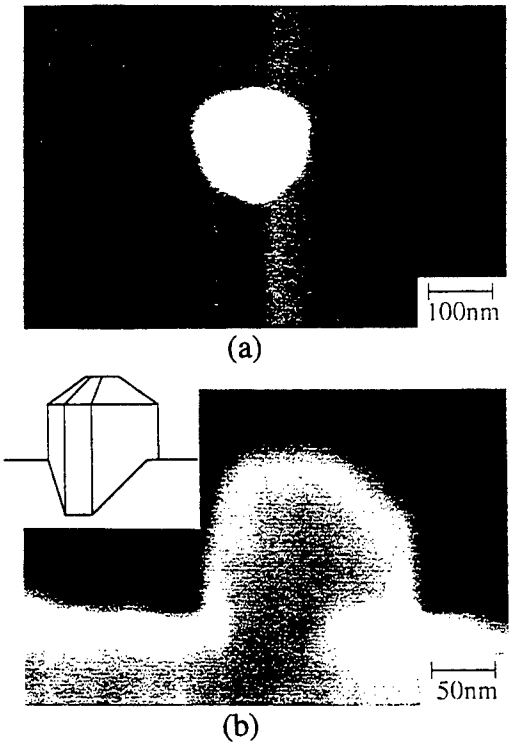


Fig.6 The shape of the InAs dots on the grooved substrates looks hexagonal in its top view (a) and column shaped in its side view(b).

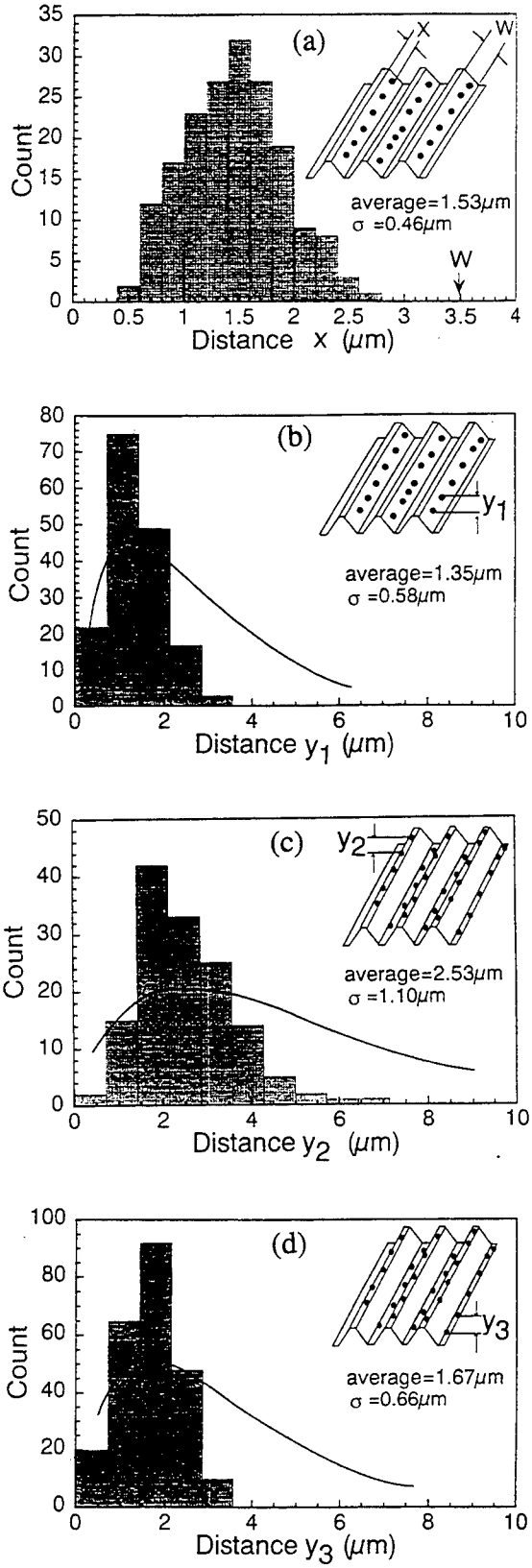


Fig.7 (a) The dot distribution along the slope from ridge to the valley. 7(b),7(c),7(d) show the histogram of the distance between the nearest neighbor dots on the slope along the line, on the ridge, and on the bottom of the valley, respectively. Trapezoidal grooves of (a) and (b) are aligned to [2$\bar{1}\bar{1}$] direction, and (c) and (d) to [0$\bar{1}$1] direction.

NOVEL COMPOUND SEMICONDUCTOR DEVICES BASED ON III-V NITRIDES

S. J. PEARTON, C. R. ABERNATHY and J. W. LEE
University of Florida, Gainesville, FL 32611 USA

F. REN
AT&T Bell Laboratories, Murray Hill, NJ 07974 USA

R. J. SHUL, and J. C. ZOLPER
Sandia National Laboratories, Albuquerque, NM 87185 USA

ABSTRACT

New developments in dry and wet etching, ohmic contacts and epitaxial growth of III-V nitrides are reported. These make possible devices such as microdisk laser structures and GaAs/AlGaAs heterojunction bipolar transistors with improved InN ohmic contacts.

INTRODUCTION

The GaN-AlN-InN materials system offers opportunities to produce electronic and photonic devices with characteristics unobtainable with conventional III-V compound semiconductors. The InGaAlN system allows continuous grading of the bandgap from 1.9 eV to 6.2 eV (InN to AlN) so that green, blue and UV light -emitting diodes and lasers are possible, as well as electronic devices capable of high temperature operation . To date, both blue and green light-emitting diodes are commercially available, UV detectors have been reported and a variety of high electron mobility and field effect transistors have been fabricated. The performance of these devices is currently limited by the relatively low p-type doping levels achievable in GaN, InGaN and AlGaN and the high contact resistances associated with wide bandgap contact layers. There are also limitations related to the excellent chemical stability of the nitrides which make them difficult to etch ,and the lack of an ion implantation technology ,which would lead to high throughput ,inexpensive FET fabrication schemes.

PROCESSING

1. ION IMPLANTATION DOPING

Above 1050°C, implanted Si^+ becomes electrically active with an efficiency of ~90% for a dose of $5x10^{14}$ cm^{-2}. Mg^+ implantation alone did not produce p-type doping, but when co-implanted with P^+ we obtained a sharp n-to-p conversion of the GaN at 1050°C with an activation efficiency of ~60% at a dose of $5x10^{14}$ cm^{-2}. Annealing by itself above 1000°C produced a slight increase in n-type conductivity in GaN ,which may result from creation ,or depassivation of the defects responsible for the as-grown doping(i.e. N-vacancy -related defects or chemical impurities such as O or Si.

2. ION IMPLANTATION ISOLATION

Both n-type and p-type GaN can be efficiently isolated by the type of multiple energy implant schemes used for more conventional III-V materials . We have achieved maximum sheet resistances >$5x10^9$ ohms/square in both conductivity types, after a multiple energy N^+ implant (50-250 keV) at doses of 2-$6x10^{13}$ cm^{-2} and subsequent annealing at ~750°C. Arrhenius plots of conductivity in isolated GaN can be used to determine the energy level of the main defect introduced by this implant /anneal sequence. The activation energy for the p-type material is 0.90 eV and that for the n-type GaN is 0.83 eV. These energy values represent the approximate position of the Fermi level and show why very high resistances can be obtained in implant-isolated GaN. However ,an optimum situation is to produce midgap levels in isolated material, i.e. at ~1.6 eV in GaN. The microstructural nature of the defects responsible for the carrier compensation is not known at this point but is likely to consist of native defect complexes. In both n- and p-type GaN ,these complexes anneal out above ~750°C. Similar experiments have been performed with n-type layers of InAlN and InGaN. Sheet resistances of >10^8 ohm/square were obtained for N^+ implanted InAlN, whereas in InGaN, sheet resistances typically 50-100 times higher than the as-grown values were obtained with N^+, O^+ or F^+ implantation. We studied the evolution of normalized sheet resistance in O^+ implanted $In_{0.75}Al_{0.25}N$ with subsequent annealing. The sheet resistance increases up to ~600°C and then is reduced to the original unimplanted values at ~800°C. This behavior is typical of that seen in other III-V semiconductors, and is caused by the introduction of deep acceptor states related to the implant damage that compensate the shallow native donors.

3. DRY ETCHING

Due to the inert chemical nature of the nitrides, patterning by wet chemical etching has proven difficult. Relatively low etch rates have been reported for GaN(<500Å/min) under reactive ion etching conditions,however significantly higher etch rates (1000-4000 Å/min) have been obtained in high density plasmas under moderate dc-bias conditions. For example, Electron Cyclotron Resonance(ECR) sources provide a high ion density with controllable dc-biasing to minimize plasma-induced damage. Other high density configurations include Inductively Coupled Plasmas(ICP), Helicon, Helical Resonator and magnetron-enhancement. The plasma chemistries attempted for the nitrides include Cl_2/H_2, BCl_3, CCL_2F_2, CH_4/H_2, $SiCl_4$, HBr, HI and $Cl_2/CH_4/H_2/Ar$. The group III elements can be removed as volatile chlorides ,bromides or iodides or as metalorganics while the nitrogen can be removed as NH_3, NF_3 or NCl_3. The bond strengths of the nitrides are quite high relative to other III-V compounds, and therefore a significant physical component is required in addition to the chemistry discussed above.

In the etch chemistries employed to date selectivities for removing one nitride relative to another have not been particularly high(typically less than a factor of 3), so more work is needed on developing higher selectivity. Secondly, there has been little effort on measuring plasma-induced damage in the nitrides . From ion implantation studies it is clear that these materials are very resistant to damage, but some quantification of this phenomenon during ECR or RIE is needed Thirdly, it is also of interest to directly identify the etch products from

the nitrides ,and in particular to see the relative importance of the various N species when both Cl_2 and H_2 or Cl_2 and F_2 are present in the plasma chemistry.

We note finally that ion milling rates for the nitrides are a factor 2-3 slower than for materials like GaAs and InP ,indicating that there must be a chemical component present in order to achieve practical etch rates . In ion milling the removal rate of most mask materials is faster than the etch rates of the nitrides, limiting this technique to formation of shallow features.

4. WET CHEMICAL ETCHING

There were several early reports of wet etching of GaN in NaOH, which progressed by formation of an insoluble gallium hydroxide (GaOH) coating. This film had to be removed by continual jet action. Others have reported that H_3PO_4 will remove GaN. A variety of different etch solutions have been employed for amorphous or polycrystalline AlN, including hot (85 C) H_3PO_4, boiling HF/H_2O, HNO_3/HF or dilute NaOH solutions. However there do not appear to be reliable for single crystal material. For InN, aqueous KOH and NaOH solutions were found to produce etch rates of a few hundred angstroms per minute at 60°C.

We have found that a common photoresist developer solution AZ400K produces controlled, reliable wet etching of single crystal AlN at a rate whose absolute magnitude depends strongly on the crystalline quality of the material. The etching is thermally activated with the same activation energy of 15.5 kCal/mol in all cases . The rate was not sensitive to agitation and was dependent on the etchant concentration. These are characteristics of reaction-limited etching of the form

$$R=R_0 \exp(-E_a/kT)$$

We find that R_0, an attempt frequency for reaction between the (OH-) ions and the AlN surface, is strongly dependent on material quality. A great deal more work needs to be done to develop reliable wet etches for GaN, InN and the ternary alloys in order to accelerate nitride device technology.

InN CONTACT HBTs

Carbon-doped base heterojunction bipolar transistors (HBTs) in the GaAs/AlGaAs system display much better stabilities under bias-stress aging than devices using Be, Mg or Zn for p-type doping. One of the most important parameters for achieving high speed performance in digital applications is the emitter resistance ,and the InGaP or AlGaAs emitter layer is generally capped with highly doped GaAs/InGaAs graded out to InAs to provide a low bandgap layer for subsequent metallization. The InAs can be doped with Sn to achieve high ($n=3x10^{19}$ cm^{-3})conductivity, with typical contact resistivities of $5x10^{-7}$ ohm-cm^2 for TiPtAu nonalloyed metallization. However, the InAs critical layer thickness is generally exceeded in practical HBT structures, leading to rough surface morphologies. This is a potential problem for small emitter dimensions devices since some contacts would potentially be placed in regions of thinner InAs and therefore, poorer contact resistance.

Recently, low contact resistivities have been reported for nonalloyed TiPtAu metallization on unintentional doped InN grown by MOMBE. The polycrystalline InN is

grown at 500°C ,consistent with the growth temperature of high performance GaAs/AlGaAs or GaAs/InGaP HBTs for both digital and power applications ,and the surface morphology of the InN is much smoother than that of InAs-based emitter contact structures. We have demonstrated nonalloyed TiPtAu contacts with excellent contact resistivities($5x10^{-7}$ ohm-cm^2).

The HBT structures were grown by MOMBE on semi-insulating GaAs substrates. The structure was completed in one of two different ways. In the first, 1200Å of InN($n=5x10^{20}$ cm^{-3}) was grown, while in the second the GaAs was graded through InGaAs to InAs (300 Å, $N=1.5x10^{19}$ cm^{-3}) to the 1200Å InN layer. The entire structure was grown at 500°C using all-gaseous sources, as described previously.

Nonalloyed ohmic contacts were formed to the two types of structures using e-beam deposited Ti(500Å)/Pt(750Å)Au(3000Å) patterned by lift-off. HBTs with 2x5 μm^2 emitter dimensions were fabricated using a dry-etched self-aligned process, and this mask set also contained transmission line patterns for determination of contact resistivity.

A contact resistivity of $2\text{-}5x10^{7}$ ohm-cm^2 was obtained for both InN-based contact schemes, but superior performance was displayed by the graded structure . This was ascribed to the formation of GaN at the interface between the abrupt InN/GaAs structure which degraded the contact properties. The maximum dc gain was 35 for 2x5 μm^2 devices. No change in device characteristics was observed during aging at 25°C for 90 h at an emitter current density of $4x10^{4}$ A/cm^2. TEM pictures showed the uniform nature of the InN whereas the more conventional InGaAs/GaAs emitter contacts showed very rough surfaces for the InAs.

While TiPtAu metallization on these structures also yields nonalloyed ohmic contact resistivities of $5\text{-}7x10^{-7}$ ohm-cm^2, there is one significant concern about contact uniformity for submicron dimension devices. Therefore ,the InN-based contact structure is likely to be a superior alternative for small mesa HBTs. The drawback of the InN -based contacts is that they suffer from deterioration in both morphology and contact resistance above 400°C, whereas the InAs -based layers are stable to 500°C. One must therefore reduce the thermal budget during of the former and in particular adjust the implant isolation conditions so that lower annealing temperatures than currently used can be employed.

CONCLUSIONS

The large bandgaps, thermal and chemical stability ,excellent transport properties and good thermal conductivities of the III-V nitrides offer many opportunities for fabrication of novel photonic and electronic devices. Considerable progress has been made in recent times on the growth of these materials and in developing the process modules. Much more effort is required on ohmic contacts, substrate development ,implantation, p-type doping during epitaxial growth and growth of ternary compounds.

Side-Gated Resonant Tunneling Transistors

Venkat Kolagunta, David B. Janes, Guanlong Chen
Kevin J. Webb, and Michael R. Melloch.

School of Electrical and Computer Engineering,
Purdue University, West Lafayette, IN 47907.

Single well resonant tunneling diodes (RTDs) have been shown to be capable of operating in the terahertz regime. Also, physically-based equivalent models and integrable structures have been developed to allow the incorporation of these devices into integrated circuits and microwave applications [1] . In order to achieve higher computing speeds, Capasso et al. proposed the application of multiple quantum well three terminal vertical structures for multi-valued logic [2]. In pursuit of studying such possibilities and to better understand the various characteristics like carrier transport and noise in various three-terminal RT devices, two main device topologies have been used: i) in-plane implanted gates and ii) in-plane Schottky gates [3,4] . Devices using in-plane implanted gates have been reported and applied in the development of logic elements, but the gating that can be achieved in these devices has been quite limited, with the minimum feature of the device being the strongest constraint [4] . The gating topology using an in-plane Schottky gate has shown appreciable gating at 4.2K, but it has non-uniform vertical gating fields for double barrier resonant tunneling quantum structures and hence is not well suited for fabrication of multiple quantum well three terminal devices [4] . More recently, a resonant tunneling transistor (RTT) has been demonstrated with high transconductances at room temperatures for positive gate biases, but these RTTs do not show appreciable gating at negative gate biases (the pinch-off regime) [5] .

We have demonstrated a self-aligned, sidewall gating technique that has been developed to fabricate three terminal RTTs, wherein a uniform gate field can be applied across vertical quantum well structures of up to 1000A° along the direction of current flow in the device [6] . Room-temperature gating of an $Al_{0.3}Ga_{0.7}As/GaAs$ resonant tunneling diode with 45A° barriers and a 50A° well at both positive and negative gate biases has been shown, with maximum transconductances around zero-gate bias. The effective transconductance of the device, when operating in the negative differential resistance (NDR), is expected to be much larger than that in the positive differential resistance region. The cross-sectional view of the device is shown in Fig.1. The Schottky gate is deposited along the sidewall of the mesa using the top contact metallization as the shadow mask. Good isolation between the gate and top-contact is achieved by a controlled two step etching process to give vertical sidewalls. Peak current densities as high as $1.5x10^4$ A/cm^2 at room temperature for these three-terminal RTTs have been measured. To achieve appreciable gating in these new sidewall gated devices, at least one of the minimum features has to be in the sub-micron regime, making them

inherently suitable for high packing densities. It is anticipated that to be able to pinch off the device, the minimum feature of the device needs to be 0.6μm at the maximum.

We have fabricated FET-like structures with minimum feature widths of about 0.8μm and feature lengths of up to 10μm using conventional e-beam lithography. The fabrication of such small area devices has been facilitated by the development of new non-alloyed low-temperature grown GaAs contacts [7]. Preliminary results from these devices indicate a gate bias dependence of the current through these RTTs associated with two mechanisms: i) a change in the active area of the device and ii) variation in the potential of the well region as evidenced by a shift in the voltage at which the negative differential resistance region occurs.

Fabrication of RTT structures with minimum features as small as 0.6μm is in progress and shall be presented. A study on the application of such structures in high-frequency switching/logic circuits shall also be discussed.

[1] D.B.Janes, K.J.Webb, M.S. Carrol, G.E.Starnes, K.C.Huang, J.Shenoy, and M.R.Melloch, "Direct current and microwave characterization of integrated resonant tunneling diodes", to appear in J. Appl. Phys.

[2] F.Capasso, S.Sen, F.Beltram, L.M.Lunardi, A.S.Vengurlekar, P.R.Smith, N.J.Shah, R,J,Malik, A.Y.Cho, "Quantum functional devices: resonant-tunneling transistors, circuits with reduced complexity and multiple-valued logic", IEEE trans. Elect. Dev., vol. 36, no. 10, pp. 2065, 1989.

[3] C.J. Goodings, H. Mizuta, J.R.A. Cleaver, H.Ahmed, "Variable area resonant tunneling diodes using implanted in-plane gate s" J. Appl. Phys. vol. 76, pp. 1276, 1994.

[4] M.W. Dellow, P.H. Beton, M. Henini, P.C. Main, L. Eaves, "Gated resonant tunneling devices", Elect. Lett. vol. 27, 1991.

[5] W.C.B.Peatman, E.R.Brown, M.J. Rooks, P. Maki, W.J. Grimm, M. Shur, "Novel Resonant Tunneling Transistor with high transconducatnce at room temperature", IEEE Elect. Dev. Lett. vol. 15, pp. 236, 1994.

[6] V.R.Kolagunta, G.Chen, D.B.Janes, K.J.Webb, M.R.Melloch, "Self-aligned sidewall gated resonant tunneling devices", submitted to Elect. Lett.

[7] M.P.Patkar, T.P.Chin, J.M.Woodall, M.S.Lundstrom, M.R.Melloch, "Very low resistance nonalloyed ohmic contacts using low-temperature molecular beam epitaxy of GaAs", Appl. Phys. Lett. vol. 66, pp. 1412, 1995.

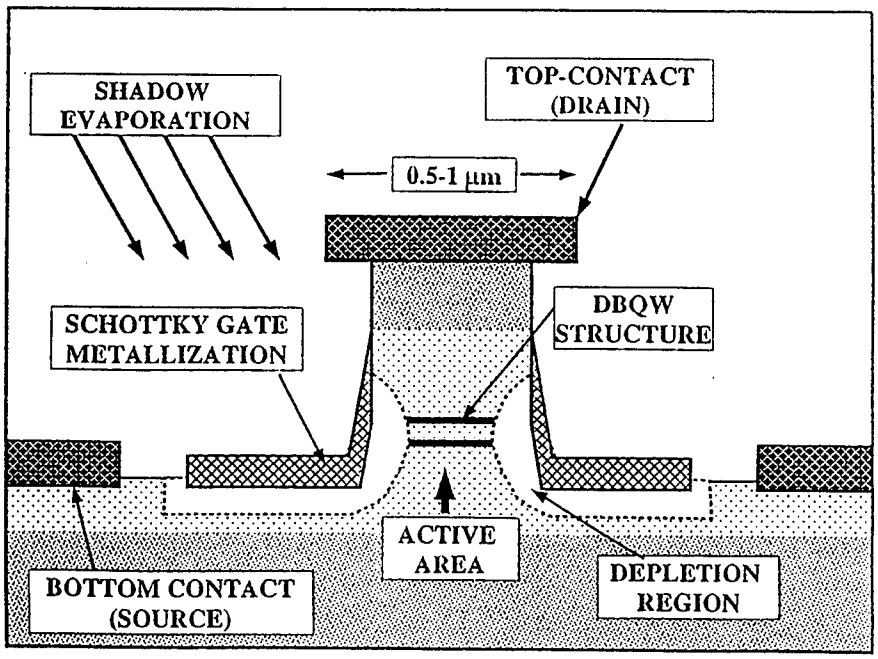


Fig.1 Illustration of the shadow evaporation technique using the top-contact as a self-aligned mask to deposit the Schottky gate on the sidewall of the mesa.

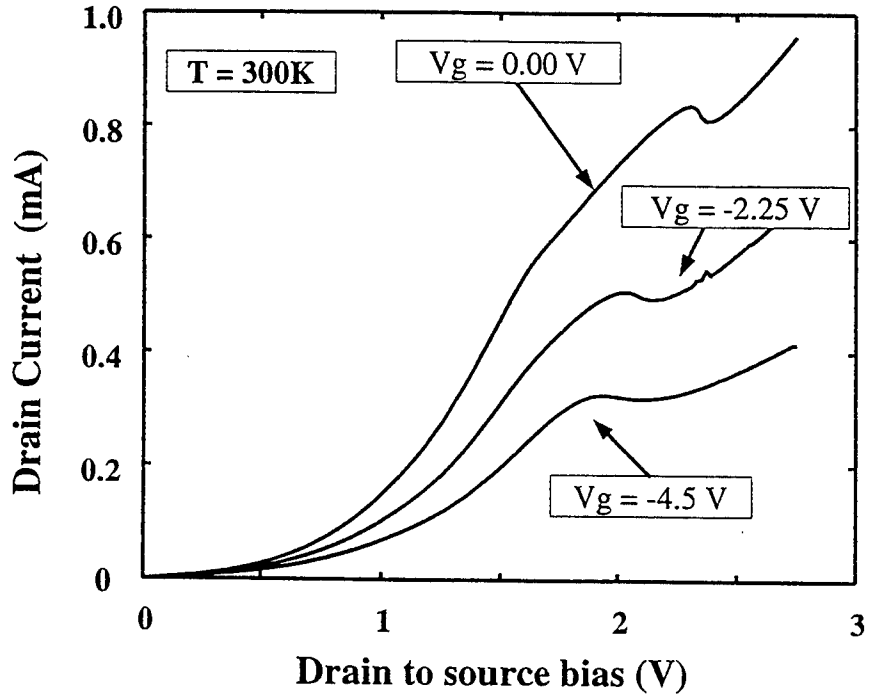


Fig.2 Drain to source currents for a 0.8μm x 10μm device at various gate biases. Gate leakage currents at all biases were below 1μA.

Realization of Silicon Quantum Wires Based on SiGe/Si Heterostructure

Y.Shi, J.L.Liu, F.Wang, Y.Lu, R.Zhang, P.Han, S.L.Gu,
S.M.Zhu, and Y.D.Zheng
Department of Physics and Institute of Solid State Physics,
Nanjing University, Nanjing 210008, P.R.China

Silicon quantum wires(SQWs) would play an important role in ultra large scale integration(ULSI) and high performance quantum effect devices. Hence, much effort has been invested in fabricating SQWs in recent years. Most of SQWs were obtained using metal-oxide-semiconductor(MOS) structures [1-2]. Several authors recently reported the methods of fabricating physical confined SQWs with SiO_2 boundaries by anisotropic chemical etching and thermal oxidation [4-6]. At the present stage, it is still requested urgently to develop advanced fabrication techniques to obtain SQWs of high quality. SiGe/Si heteroepitaxial film has many potential applications in Si technology. It would be very attractive to be applied in fabricating various SQWs and related devices due to its excellent properties such as high-quality epitaxial growth, selective etching and thermal oxidation. In this work, We report on the first successful realization of the physical confined SQWs based on SiGe heterostructure combining SiGe/Si heteroepitaxy, selective chemical wet etching and thermal oxidation. The thermal oxidation characteristic of the Si wires is investigated, it is found that the lateral dimensions of SQWs can be well controlled by selecting the temperature of thermal oxidation process. The observation result of scanning electron microscope(SEM) is demonstrated. The present work provides a very controllable way to fabricate SQWs and is fully compatible with Si microelectronic technology.

The fabrication process of the SWQs is illustrated in Figure 1. Firstly, a $Si_{0.8}Ge_{0.2}$ heteroepitaxal layer was grown on (100) Si substrate by very low pressure chemical vapor deposition. The thickness of the $Si_{0.8}Ge_{0.2}$ layer was 150nm, while a buffer Si layer was grown between the substrate and the SiGe layer. A Si active layer was grown on the top of the $Si_{0.8}Ge_{0.2}$ layer (Fig.1(a)). Using this epitaxial growth, the expected thickness of the Si active layer can be easily achieved. Lithography technique was carried out to generate line-and-space patterns on a mask. Then, trenches were generated in the substrate by using reactive ion etching (Fig.1(b)). Next, the selective chemical etchant consisting of HNO_3:CH_3COOH:HF(49%) at 25°C was used to etch the trench structure to remove the $Si_{0.8}Ge_{0.2}$ layer out and remain the Si wires (Fig.1(c)). After removing the mask, the Si wires were thermally oxidized in wet oxygen atmosphere which smoothes the surface of the Si wires and reduces the lateral dimensions to form expected SQWs. Finally, the thermal oxidation in dry oxygen was carried out to obtain high-quality SiO_2/Si heterointerfaces (Fig.1(d)).

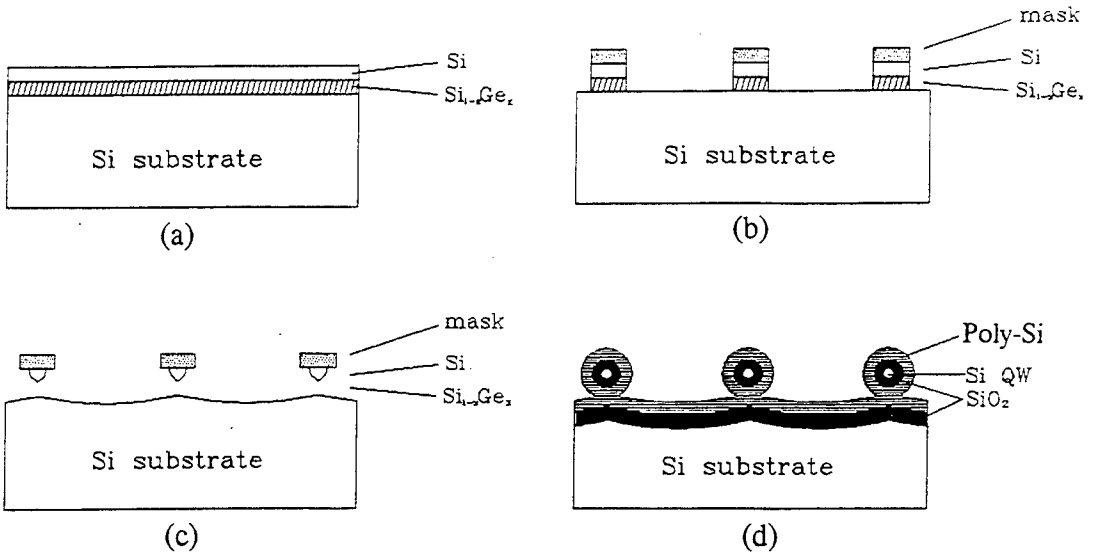


Figure 1. Fabrication process of SQWs. (a) Si/SiGe/Si heteroepitaxy by VLP/CVD, (b) mask pattern and shallow trench formation, (c) selective chemical etching, and (d) thermal oxidation.

In the last several years, the selective chemical etching techniques for SiGe/Si heteroepitaxial films have developed quickly. Among many selective chemical etchant, it has been demonstrated that HNO_3:CH_3COOH:HF was a very good etchant in thinning SiGe nanostructures without any defects and was often used [7]. The optimum etch rate and selectivity are well obtained with altering the composition. The etch selectivity increases with an increase of the mole fraction of Ge. Through the selective chemical etching, the $Si_{0.8}Ge_{0.2}$ layer is removed out and Si active layer is narrowed to form Si wire. Subsequently, the Si wire is smoothed and reduced by thermal oxidation processes. Figure 2 shows the cross section image of SEM of a SQW with circular cross section embedded in the SiO_2 after the thermal oxidation, where the lateral linewidth of the

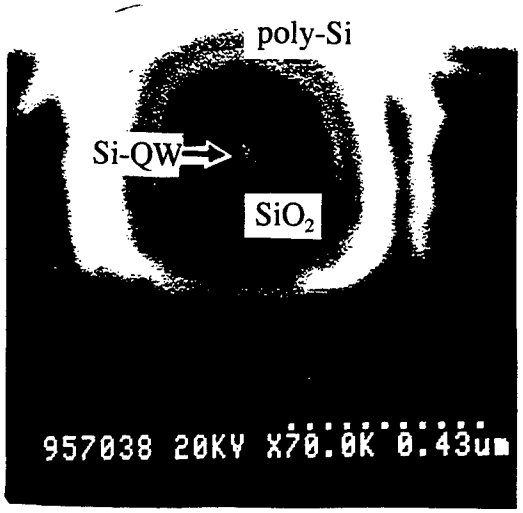


Figure 2. Cross-sectional image of SEM of thinned SQW with the lateral linewidth of ~40nm.

SQW is about 40nm.

The advantage of using dry thermal oxidation to fabricate SQWs has been demonstrated [3,4]. The self-limiting oxidation effect in Si nanostructures was observed. It was seen as an opportunity for producing Si nanostructures with ± 1 nm control in lateral dimensions in the self-limiting regime of oxidation temperatures below 950°C [3]. For the present SiGe/Si heterostructure, however, the high temperature oxidation is forbidden because of SiGe thermal stability, and low temperature dry oxidation is not practical due to taking too long time to thin Si wires to expected lateral dimensions. The wet oxidation at low temperatures offers a suitable opportunity for realizing SQWs. In wet oxidation process, we find that the flat surface oxidizes faster than the Si wires. This retardation of oxidation becomes obviously with decreasing the diameter of the Si wire. In addition, the retardation of oxidation of SQWs depends strongly on the oxidation temperature. In order to clarify the lateral dimension and temperature dependence of the retardation, experiments are performed at three different oxidation temperatures of 850, 800 and 750°C. All the samples used for oxidation are prepared under the same etching conditions to minimize Si wire variations among the samples. Dimensional data are obtained from the micrograph of SEM. These observations are plotted in Figure 3. The vertical axis measures oxide thickness on Si wire surfaces normalized to that on the flat surface, and the horizontal axis denotes the inverse of the radius of the Si wire after oxidation. There is a general trend that the decrease of the lateral dimensions of Si wires shows the retardation of oxidation for three oxidation temperature as the oxidation progresses. However, the retardation of oxidation is more pronounced with decreasing the oxidation temperature. Oxide growth is severely retarded at 750°C. The trend of the data for 750°C indicates that the SQWs seem nonvanishing, moreover, the final radius

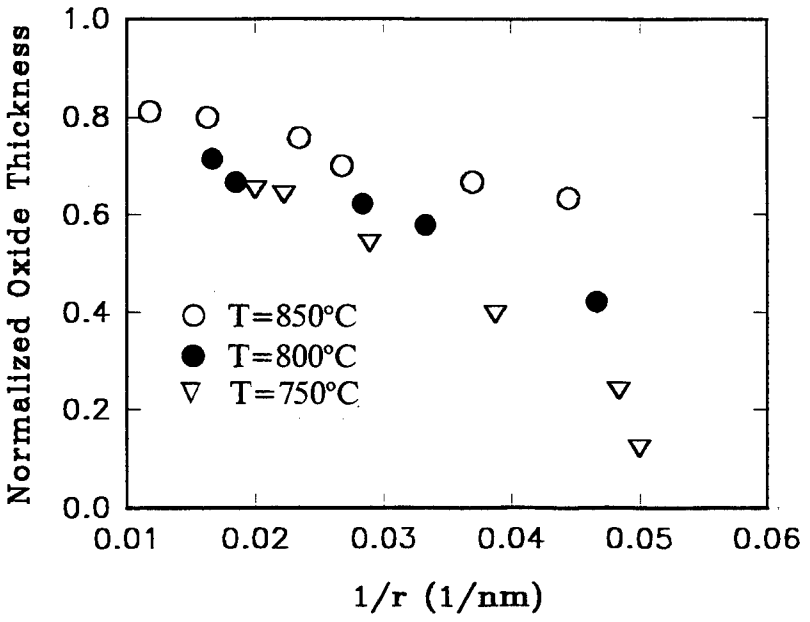


Figure 3. Oxide thickness on SQW surfaces normalized to that on the flat surface as a function of the inverse of the radius of the SQWs for 850, 800 and 750°C wet oxidation, respectively.

seems to self-limit to 20nm. Self-limiting oxidation phenomenon is not observed at 850 and 800°C. It is confirmed that the SQWs disappear after 14 and 20 hour for 850 and 800°C, respectively. The retardation of oxidation is usually contributed to the additional stress from nonplanar viscous deformation of oxide [8]. This viscous stress makes the oxidation reaction at the Si surface more difficulty. Based on the present observations, it is apparent that the extent of retarding oxidation follows the change in the viscous stress with the temperature and the radius of Si wires. It should be noted that self-limiting oxidation phenomenon in wet oxidation is found to occur only for the temperature below 750°C, which is about 200°C lower than that in dry oxidation [3]. This may be due to that the viscous stress of wet oxide is lower than that of dry oxide. There are two likely mechanisms for slowing down the oxidation rate. One is that the surface reaction coefficient K_s is reduced by the normal viscous stress at the Si-SiO_2 interface [8]. Another is that oxidation diffusion is limited in a highly stressed oxide [3]. Further studies are needed to identify the effects of the viscous stress on oxidation kinetic parameters.

This work is supported by the Chinese National Nature Science Foundation and National High Technology Research and Development Foundation.

References

[1] A.C.Warren, D.A.Antoniadis and Henry I. Smith, Phys. Rev. Lett. **56**, 1858(1986).
[2] W.Hansen, M.Horst, J.P.Kotthaus, U.Merkt, Ch.Sikorski, and K.Ploog, Phys. Rev. Lett. **58**, 2586(1987).
[3] H.L.Liu, D.K.Biegelsen, F.A.Ponce, N.M.Johnson, and R.F.W.Pease, Appl. Phys. Lett. **64**, 1383(1994).
[4] Y.Nakajima, Y.Takahashi, S.Horiguchi, K.Iwadate, H.Namatsu, K.Kurihara, and M.Tabe, Appl. Phys. Lett. **65**, 2833(1994).
[5] J.L.Liu, Y.Shi, F.Wang, R.Zhang, P.Han, B.H.Mao, and Y.D.Zheng, J. Vac. Sci. Technol. **B13(5)**, 0000(1995).
[6] K.morimoto, Y.Hirai, K.Yaki, K.Inoue, M.Niwa, and J.Yasui, Extended Abstracts of the 24th Conference on Solid State Devices and Materials, 344(1993).
[7] Y.Shi, F.Wang, J.L.Liu, R.Zhang, Y.D.Zheng, 1995 Spring Mat. Res. Soc. Symp. Proc.
[8] D.B.Kao, J.P.McVittie, W.D.Nix, and K.C.Saraswat, IEEE Trans. Electron Devices, **ED-34**, 1008(1987).

Advanced Contact Technology for a Self Aligned 70GHz Double Mesa Si/SiGe Heterojunction Bipolar Transistor

K. Wieczorek and H.-U. Schreiber
Ruhr-Universität Bochum, Mikroelektronik Zentrum (A), Germany

In view of the significance of future communication networks operating in the multi-Gbit/s range, much effort is focussed on the development of electronic key devices to meet the requirements of high-speed performance as well as of low costs of production. SiGe base layers have emerged as an appropriate means to introduce band-gap engineering into well-established Si-bipolar technology. At present, there are two competing device concepts differing in emitter-design, Ge-profile and processing (Fig.1). The first one is the SiGe base drift transistor, which was derived from the double polysilicon homojunction bipolar transistor. In this device, the Si base layer is replaced by SiGe with a Ge mole fraction increasing from 0% at the emitter- up to 25% at the collector-side, resulting in a speed-enhancing drift field [1]. In order to achieve a sufficient emitter efficiency, and therefore a high current gain, the emitter doping concentration has to be much higher than the base doping concentration, causing a high intrinsic base sheet resistance. The constraints between high current gain and low intrinsic base sheet resistance can be relaxed by the second device concept, the Si/SiGe heterojunction bipolar transistor (HBT), which is marked by an additional emitter base heterojunction. Due to a Ge-content dependent barrier in the valence band, the emitter base doping concentration ratio can be inverted, thus resulting in a drastically reduced base sheet resistance and a high current gain. This device, which will be considered in the following, offers a greater potential concerning high-speed devices and has proven to be suited for IC-realization [2]. Since the base doping concentration exceeds by far the emitter doping concentration, conventional bipolar fabrication processing is not applicable to Si/SiGe HBT fabrication. Particularly due to differences concerning device-structure, the application of novel contact technologies to HBT fabrication is imperative. The main objective of this research is the reduction of device parasitics without degrading the HBT's excellent rf-performance.

For fabrication of the device under investigation, conventional channel-stopper and buried layer formation is followed by the uninterrupted growth of the whole npn vertical layer structure including a highly-doped emitter contact layer using MBE. A schematic cross-section of the complete HBT presented in this study is given in Fig. 2. After emitter mesa RIE and oxide sidewall spacer formation the extrinsic base contact layer is formed by BF_2 ion implantation at 25keV, resulting in an amorphized surface layer of approximately 40nm. After wet-chemical removal of a dummy-emitter layer a short rf sputter-etch process at low bias is required in order to remove Sb-residuals from the emitter surface. Afterwards about 10nm Ti are rf sputter-deposited without breaking the vacuum. Activation of the implanted dopant in the extrinsic base and salicidation of both emitter and extrinsic base are performed simultaneously using a lamp-heated reactor and H_2-atmosphere at 650°C, thus avoiding outdiffusion of the optimized vertical layer sequence. As the base contact salicide is formed directly on the SiGe-layer without any additional polysilicon layer, proper initial Ti-thickness and metal-SiGe interface conditions have to be chosen in order to optimize both emitter- and base-contact resistance and to avoid salicidation-induced degradation of the collector/base-junction resulting in an undesired V_{CE}-offset, as shown in Fig. 3. A cross-sectional TEM micrograph of an extrinsic base layer including BF_2 ion implantation and $Ti(SiGe)_2$ is given in Fig. 4. Although end-of-range defects are still present at high density, specific base-contact resistances as low as $4.5\Omega\cdot\mu m^2$ have been obtained [3]. AFM-studies indicate that simultaneous salicidation and recrystallization of the amorphous extrinsic base layer results in smooth silicide layers required for contacts to nanoscale devices

(Fig. 5). Wet chemical removal of the unreacted Ti is followed by Al/Si/Cu contact metal deposition and subsequent isotropic removal from the poorly covered sidewall spacers, providing full emitter-base self-alignment. As the contact metal is adjacent to the sidewall spacer, the base resistance is optimized compared to devices based on double polysilicon technology by eliminating the polysilicon series resistance.

Base resistance R_B and collector-base capacitance C_{CB} can drastically reduce bipolar circuit speed [4]. Therefore, both parasitics have to be minimized in order to mainly determine the circuit speed by the transistor's switching speed, expressed by the cut-off frequency f_T. A cross section of the HBT along the emitter mesa is given in Fig. 6. Most of the extrinsic C_{CB} is contributed by the base contact area at the head of the emitter mesa, with the first metallization layer located above the collector-base junction. In order to reduce C_{CB}, 40nm SiO_2 were deposited and patterned prior to MBE, resulting in polycrystalline growth of the hetero-stack in the base contact area. Enhanced diffusitivity of the boron in the polysilicon as well as the concentration of the boron rather in the grain boundaries than in the polysilicon grains results in a p^-- polysilicon layer under the base contact area during thermal processing. Measurements of C_{CB} against emitter length (L_E) are given in Fig. 7, indicating that the contribution of the base contact area to C_{CB} is completely eliminated. Furthermore, the insertion of the additional SiO_2 layer drastically reduces undesired leakage currents by avoiding the creation of a parasitic pnp homojunction transistor [2].

As the maximum achievable f_T is strongly dependent on the effective base-width, a hetero-stack design as given in Fig. 8 was chosen for device fabrication. The width of the $Si_{0.72}Ge_{0.28}$ base is 27nm including undoped spacer layers of 15nm and 2nm at the emitter/base- and the collector/base-junction, respectively. The base doping concentration of $3\times10^{19}cm^{-3}$ is exceeding the emitter doping concentration by a factor of 20, resulting in a measured intrinsic base sheet resistance of 3.6kΩ/□. Due to the strict limitaion of the post-epitaxial thermal budget, no outdiffusion of boron from the base into the emitter was observed from reverse output characteristics. Rf-measurements of a completely oxide-passivated and polyimide-planarized HBT with an emitter area of $30\times1.5\mu m^2$ resulted in a maximum cut-off frequency of f_T = 71GHz (V_{CE} = 1V), as shown in Fig. 9. This is an encouraging result considering the minimum feature size of 1.5μm. To date, IC-fabrication is in progress to investigate to what extend the sophisticated contact fabrication processing and the HBT's advanced rf-performance can be translated into digital circuit speed.

Acknowledgements

The authors are indebted to H. Kibbel and U. König from Daimler Benz Research Center in Ulm (Germany) for growing the MBE-layers. They would further like to thank W. Geppert for rf- and capacitance-measurements and K. Höppner and D. Knoll from the Institute for Semiconductor Physics in Frankfurt/Oder (Germany) for performing the AFM- and TEM-micrographs. The HBT-project is supported by the German Ministery for Research and Technology (BMBF).

References

[1] D.L. Harame, J.H. Comfort et al.: *Si/SiGe Epitaxial-Base Transistors-Part I: Materials, Physics and Circuits*, IEEE Trans. El. Dev. 42(3), pp. 455-468, 1995.

[2] H.-U. Schreiber, J.N. Albers, B.G. Bosch: *Self-Aligned Double Mesa Si/SiGe Heterojunction Bipolar Transistor Used for 16Gbit/s IC Realization*, ISDRS Tech. Dig., pp. 457-460, 1993.

[3] K. Wieczorek, H.-U. Schreiber: *Low thermal budget titanium-based salicide contacts and their application to 65GHz f_T Si/SiGe-HBT technology*, El. Lett. 30(18), pp. 1542-1543, 1994.

[4] Z.A. Shafti, P. Ashburn, G.J. Parker: *Predicted Propagation Delay of Si/SiGe Heterojunction Bipolar ECL Circuits*, IEEE J. Sol. States Circuits 25(5), pp. 1268-1276, 1990.

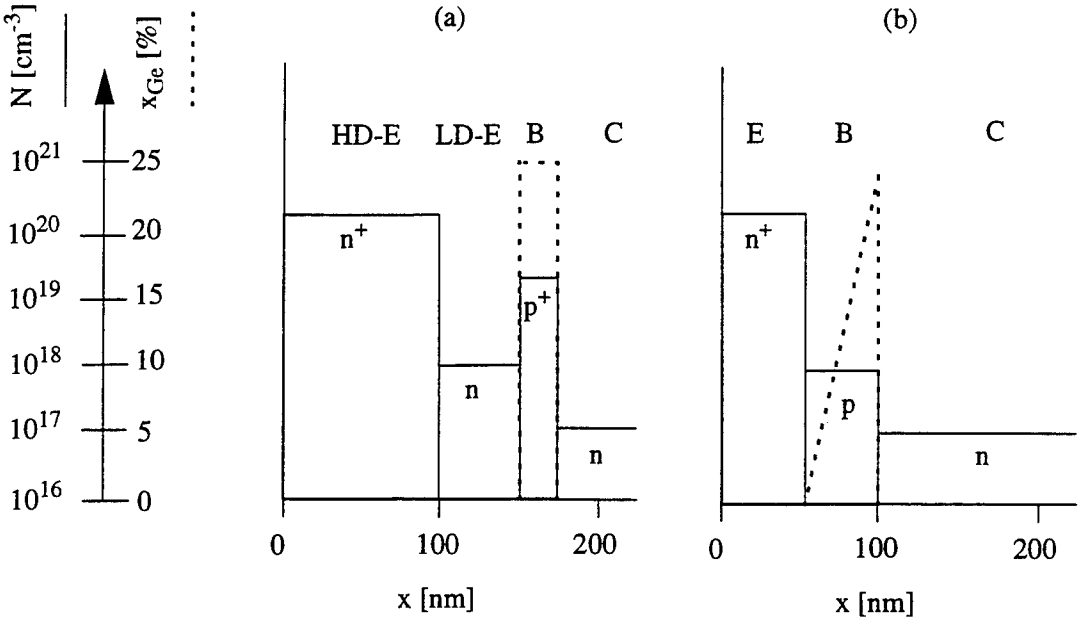


Fig. 1: Schematic differences between a) SiGe heterojunction bipolar transistor and b) SiGe drift transistor

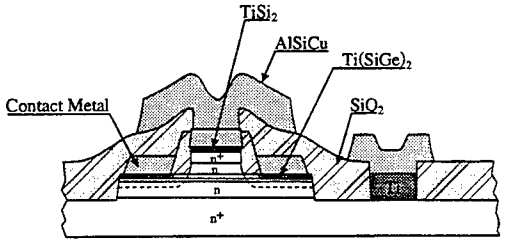


Fig. 2: Schematic cross-section of the Si/SiGe HBT

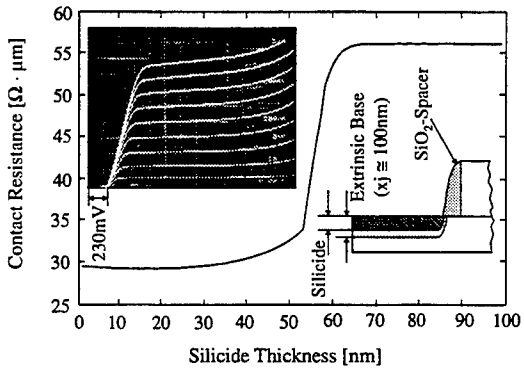


Fig. 3: Calculated contact resistance against silicide thickness taking into account the lateral current-flow into the silicide. The silicidation-induced V_{CE}-offset caused by silicide-layers formed from 30nm Ti is given in the inserted output-characteristics

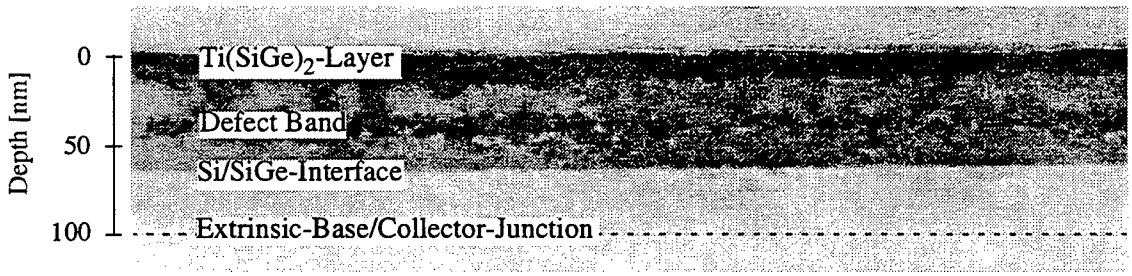
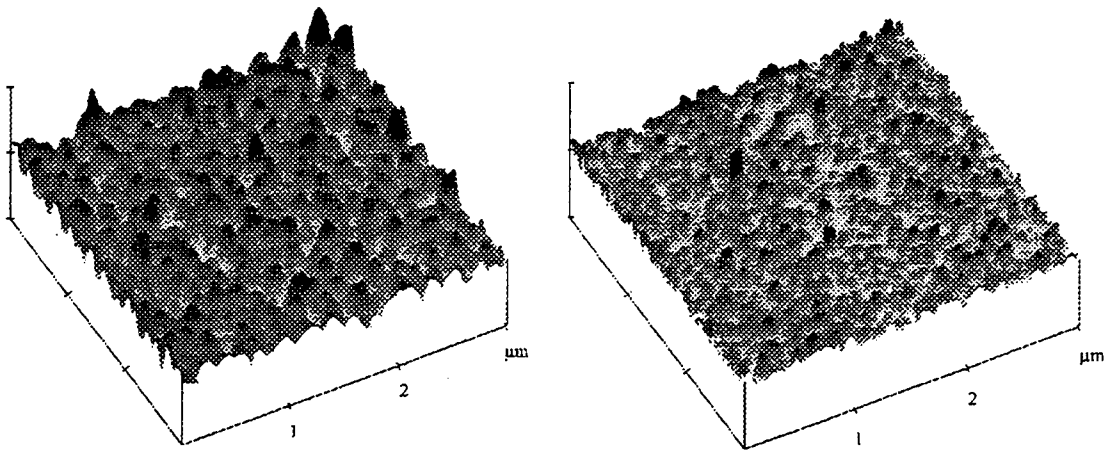


Fig. 4: Cross-sectional TEM micrograph of a BF_2-implanted SiGe base layer. Silicidation of 10nm Ti, recrystallisation and dopant-activation were performed simultaneously at 650°C for 300s.



(a) (b)

Fig. 5: AFM-micrographs of $TiSi_2$ layers grown on single crystalline silicon (a) and on BF_2 pre-amorphized silicon (b), the latter featuring a by far smoother surface morphology. The initial Ti thickness was 10nm. The scale is 1µm/div and 30nm/div for the lateral and the vertical axis, respectively.

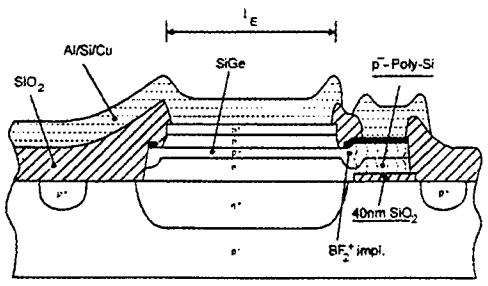


Fig. 6: HBT cross section along the emitter mesa and the base contact area under which a p^--polysilicon layer is formed.

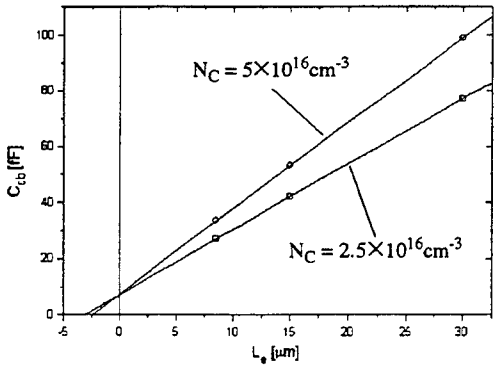


Fig. 7: Measured collector/base capacitance against emitter length. The intercept of the curves with the emitter-length axis is given by the overhang opposite the base contact area (Fig. 6).

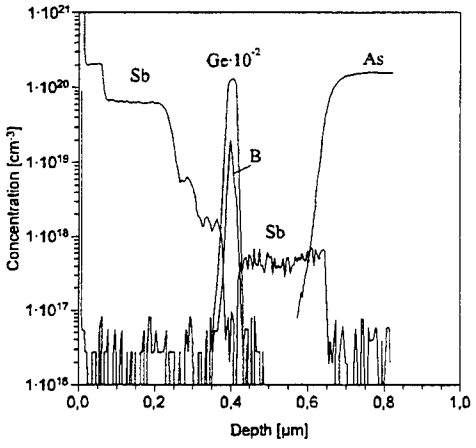


Fig. 8: SIMS-profile of the vertical layer structure.

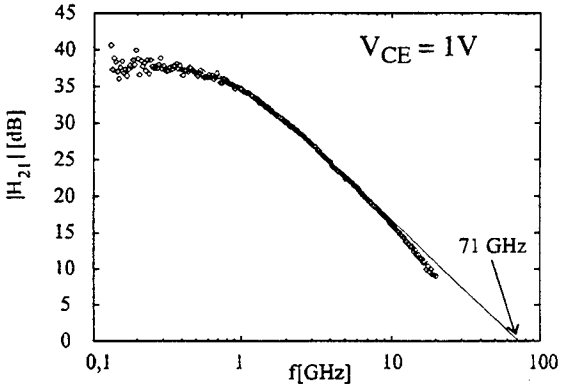


Fig. 9: Measured current gain against frequency featuring a cut-off frequency of 71GHz.

Impact of LDD Structure on Channel-Hot-Electron Programming of Single-Poly EEPROM

Kee-Yeol Na[1], Jae-Chun Han, Sung-Chul Lee[2], Han-Jin Cho[3], and Yeong-Seuk Kim

Dept. of Semiconductor Science, Chungbuk National University,
Gaeshin dong, Cheongju, Chungbuk, 360-763, KOREA
[1]Dept. of Electronics, Chungbuk National Univ., 360-763, KOREA
[2]ULSI Lab., LG semicon Co., Ltd., Cheongju, 360-480, KOREA
[3]Semiconductor Technology Division, ETRI, Daejon, 305-606, KOREA
kimys@cbucc.chungbuk.ac.kr

Introduction

Microprocessors and logic circuits in many cases require embedded EEPROMs. But combining low-voltage standard CMOS logic process with high-voltage double-poly EEPROM process is a big challenge[1]. To overcome this problem, single-poly EEPROM cells have been proposed[2-4]. In this paper we investigated the impact of LDD MOSFET structure on channel-hot-electron (CHE) programming characteristics of the single-poly EEPROM. It was found that, by increasing drain voltage to about 8V, the threshold voltage (V_T) of the cell with the LDD structure can be shifted above the supply voltage (5V) within 10ms programming pulse width. This opens a possibility of designing microprocessors and logic circuits which require low density embedded EEPROMs using pure standard LDD CMOS process without adding any masks or changing any process steps.

Cell Structure

A cross section of single-poly EEPROM with LDD NMOSFET is shown in Fig. 1. The p^+/n^+ diffused layer in the n-well is used for the control gate and the polysilicon layer forms the floating gate. The layout of the single-poly EEPROM memory cell is shown in Fig. 2. Note that the p^+-diffused layer in the n-well increases the coupling ratio during programming. For programming of this cell the CHE method or FN (Fowler-Nordheim) tunneling method can be used. But in case of standard CMOS logic process the n^+-diff./p-sub junction breakdown voltage is about 14V. Hence available high voltage from peripheral circuitry is limited below $14-V_T$, and thus it takes too much programming time if the FN tunneling method is used. To speed up the programming of the cell we use the CHE programming method. For erasing of the cell the source side FN tunneling method is used.

Results and Discussion

Fig. 3 shows the process flow chart of the single-poly EEPROM. The single-poly EEPROM was fabricated using 0.8μm CMOS ASIC process. This process includes twin-tub, self-aligned well structure, LOCOS isolation, 155Å gate oxide, WSi_2 single-polysilicon gate, LDD NMOSFET and PMOSFET, and double metals. To investigate the impact of LDD structure on CHE programming of single-poly EEPROM, the wafer processing was splitted into two groups. One group was processed without any process modifications for LDD formation. For the other group, LDD TEOS deposition, LDD spacer etch, and LDD annealing were skipped to make single drain (SD) structure. Fig. 4 shows one-shot programming characteristics of the single-poly EEPROM with single drain and LDD structures. With increase of drain voltage the horizontal electric field near the drain junction increases and so generates hot electrons (5V for SD, 6V for LDD cell). These

hot electrons can be injected into the floating gate by aided vertical electric field from the gate bias. Hence the threshold voltage of the cell increases and so the drain current drops rapidly. As the drain voltage increases up to about 8.7V for the LDD cell, the drain junction breaks down. The single-poly EEPROM with single drain shows CHE programming at lower drain voltage but at the expense of lower drain junction breakdown voltage. Note that the cell with single drain structure has shorter effective channel length due to elimination of lightly doped region. Fig. 5 shows the I_D-V_G characteristics of the single-poly EEPROM cells with LDD structure : (1) virgin cell, (2) programmed cell, (3) erased cell. The threshold voltage of the virgin cell, programmed cell, and erased cell is 0.8V, 7.5V, and 0.5V, respectively. In Fig. 6, we show CHE programming characteristics of the single-poly EEPROM cell with different control gate structures. The single-poly EEPROM cell with the p^+-diffused control gate (no n^+-diffusion in the n-well) shows about 3 times faster CHE programming characteristics than the cell with the n^+-diffused control gate (no p^+-diffusion in the n-well). This is due to following reasons : the floating gate potential is lower than the control gate during programming, thus the n-well under the floating gate is inverted so that the cell with the p^+-diffused control gate has higher coupling ratio. On the other hand the single-poly EEPROM cell with the n^+-diffused control gate has better coupling ratio during the FN tunneling erase. Fig. 7. shows CHE programming characteristics of the single-poly EEPROM cell with different control gate voltages. The cell with V_{CG}=12V has faster CHE programming characteristics as well as higher V_T shift than the cell with V_{CG}=10V. Higher control gate voltage results in higher floating gate voltage, which enhances the CHE injection efficiency. The CHE programming characteristics of the single-poly EEPROM are compared between two different drain structures as shown in Fig. 8. The single drain cell shows over 100 times faster CHE programming speed than the cell with LDD structure. The threshold voltage of 5V can be achieved with 1ms and 300ms programming pulse for the SD cell and LDD cell, respectively. But as we increase the drain voltage we obtain about same programming speed as shown in Fig. 9. To get V_T of more than 5V with programming pulse of 10ms, V_{DS}=6V for the SD cell and V_{DS}=8V for the LDD cell is required as shown in this figure. The LDD single-poly EEPROM requires more drain voltage due to lower horizontal electric field near the drain junction. But the fabrication of the LDD single-poly EEPROM is more simple than that of the SD single-poly EEPROM. Standard CMOS logic process usually include LDD formation step, so that eliminating this step to make the SD single-poly EEPROM is cumbersome. Note that the SD single-poly EEPROM is fabricated by eliminating n^-/p^- photolithography, ion implantation, TEOS oxide deposition, and LDD spacer etching steps as shown in Fig. 3.

Summary

The single-poly EEPROM with single drain and LDD structures was fabricated using the 0.8μm CMOS ASIC process. We investigated the impact of LDD structure on channel-hot-electron programming of single-poly EEPROM cell. The cell with the single drain was programmed to V_T=6.3V at V_{DS}=6.0V and the cell with LDD structure to V_T=5.7V at V_{DS}=8V with V_{CG}=12V of 10ms programming pulse width. This shows that the single-poly EEPROM with LDD structure can be used for microprocessors and many kinds of logic circuits which require low density embedded EEPROMs at the expense of applying more drain voltage (8V).

References

[1] Yeong-Seuk Kim et. al, IEEE Electron Device Letters, Vol. 14, No.7, p.342, July 1993.
[2] K. Ohsaki et. al, IEEE J. of Solid-State Circuits, Vol.29, No.3, p.311, March 1994.
[3] K. Yoshikawa et. al, IEEE Tran. on Electron Devices, Vol.17, No.3, p.675, March 1990.
[4] P. J. Cacharelis et. al, IEDM, p.60, 1988.

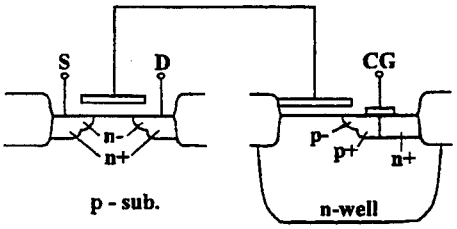


Fig. 1. Cross section of the single-poly EEPROM with LDD.

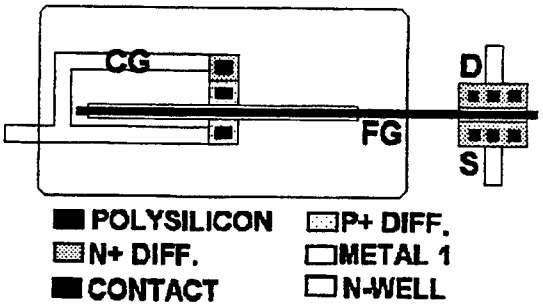


Fig. 2. Layout of the single-poly EEPROM cell (coupling ratio = 0.8).

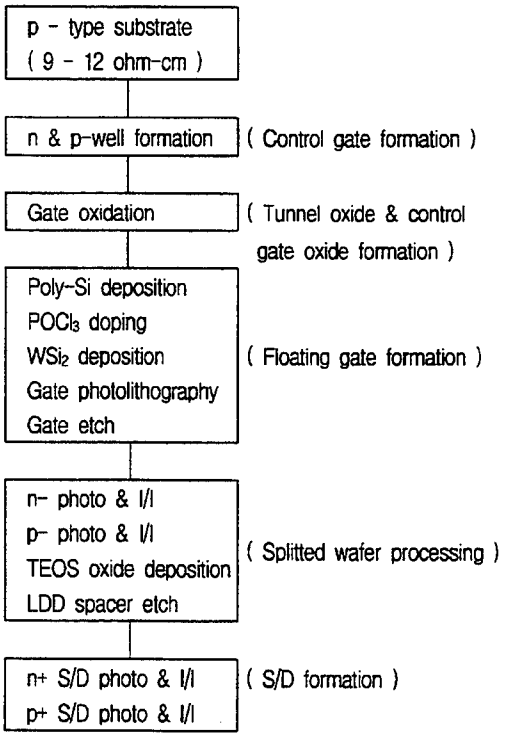


Fig. 3. Process flow of the single-poly EEPROM.

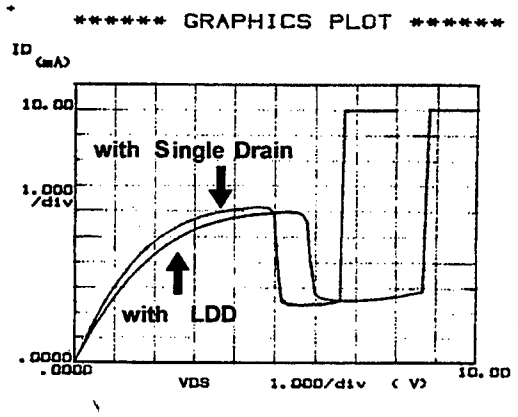


Fig. 4. One-shot programming characteristics of the single-poly EEPROM cells with LDD and single drain structures (V_{CG}=12V, V_S=0).

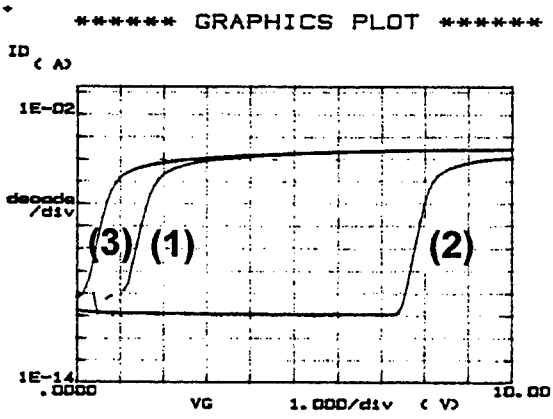


Fig. 5. I_D-V_G characteristics of the single-poly EEPROM cells : (1) virgin cell, (2) programmed cell, (3) erased cell.

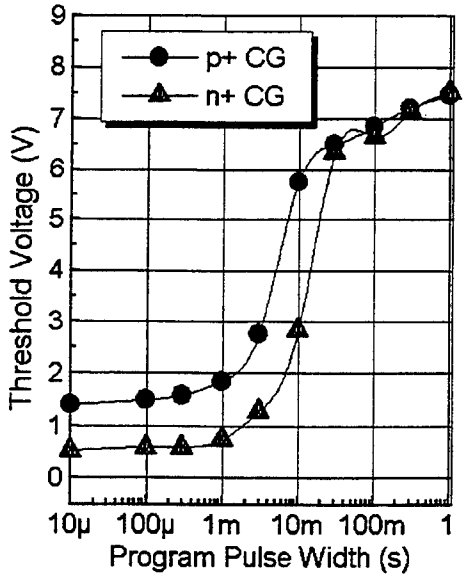


Fig. 6. CHE programming characteristics for p+ control gate and n+ control gate (V_{CG}=12V, V_D=7V, V_S=0V, coupling ratio=0.8 , LDD).

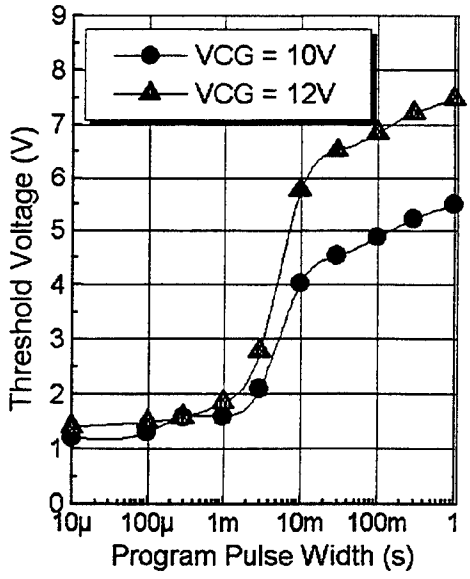


Fig. 7. CHE programming characteristics for different control gate voltage (V_D=7V, V_S=0V, coupling ratio=0.8 , p+ control gate, LDD).

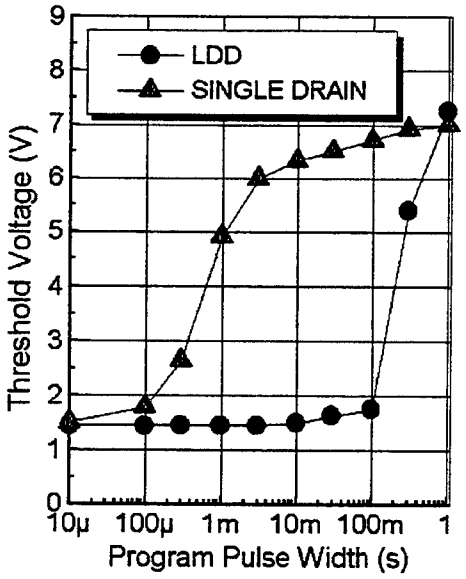


Fig. 8. CHE programming characteristics for the single-poly EEPROM cell with single drain and LDD structures (V_{CG}=12V, V_D=6V, V_S=0V, coupling ratio = 0.8 , p+ control gate).

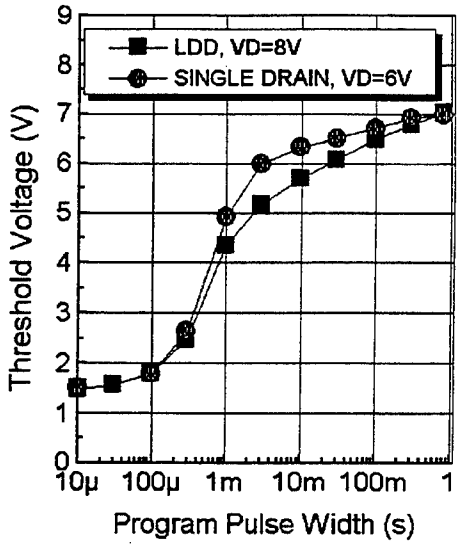


Fig. 9. CHE programming characteristics for the single-poly EEPROM cell with single drain and LDD structure at higher V_D (V_{CG}=12V, V_S=0V, coupling ratio=0.8 , p+ control gate).

Low Work Function Microminiature Thermionic Vacuum (MTV) Diodes

L.P. Sadwick, Y.J. Zhang, B. Baker, R. Petersen,
S. Johnson, D.G. Petelenz and R.J. Hwu
Department of Electrical Engineering
The University of Utah , Salt Lake City, Utah 84112
(801) 581-8282 FAX (801) 581-5281

Abstract

We will report on the fabrication and electrical characteristics of low work microminiature thermionic vacuum (MTV) diodes for use in analog and digital electronic circuit applications. MTV technology is well suited for use in high temperature, high radiation and/or harsh environments, electron beam writing sources and optics, aeronautical control and diagnostics, geothermal and oil exploration, and conventional vacuum tube applications.

Vacuum microelectronics technology [1-18] holds strong promise in areas such as flat panel displays, high speed and high temperature electronics, geothermal and oil exploration, automotive, aeronautical, nuclear, space and satellite applications, and electron beam writing sources. In the last decade, relatively little work has been performed on miniature thermionic emitters [14-18] as compared to field emitters [1-13]. Although it would be expected that miniaturized thermionic emitters would have emission properties similar to those of traditional vacuum tubes that obey Child's law (current proportional to voltage$^{3/2}$), there have been only two published results on microfabricated monolithic thermionic emitters that follow Child's law emission [17,18].

In this work advances in the technology and performance of a novel thermionic analog to field emission vacuum microelectronic emitters that will be referred to by the descriptive name microminiature thermionic vacuum (MTV) emitters will be presented. The salient feature of MTV emitter technology is the use of an air-bridge (suspended) filament that greatly reduces the thermal load and stress on the system. MTV devices can be fabricated using conventional semiconductor and micromachining processing techniques on any thermally stable, vacuum compatible substrate for which a high temperature stable insulating layer can be grown or deposited on. In addition, the small (micron to sub-micron) distances between the cathode and anode allow the possibility of intrinsic operation to high frequencies comparable to that of field emitters since these devices will not suffer from solid-state electron transport effects that limit the upper frequency of operation for all semiconductor devices. Single MTV device element architecture can consist of an uncoated or low work function coated cathode with either a totally vertical structure or a combination of planar and vertical structures.

Figures 1 and 2 show schematic representations of typical planar and vertical MTV diode structures, respectively. Figures 3 and 4 are scanning electron microscope (SEM) pictures of a fully a monolithic planar and vertical MTV diode with an uncoated tungsten (W) air bridge filament/cathode, respectively. Typical filament dimensions ranged from 5 μm x 15 μm to 100 μm x 300 μm with values of W thickness between 0.5 to 1.5 μm. Figure 5 shows a family of anode current (I) vs. anode voltage (V) curves of a fully monolithic planar 15 μm wide 20 μm long 1.5 μm thick W filament low work function coated MTV diode as a function of input filament power level. The low work function coating used in this case was a mixture of barium carbonate, strontium carbonate, and calcium carbonate. Strong rectification was observed; for negative anode potential with respect to the cathode, the current was in the noise level from -3 to -100 volts. Figures 6 through 8 show Child's' law plots of the data presented in Figure 5. From these figures,

it can be seen that Child's law behavior is the dominate emission process for the coated MTV planar diode over a wide range of anode-to-cathode voltages. However, as can be seen from Figure 7, field emission is observed at very low filament input power levels (i.e., 10 mW or less).

The I-V characteristics of a nominally 4 μm spaced cathode-to-anode vertical MTV device are shown in Figures 9 and 10. From Figure 10, it is evident that Child's law emission dominates for V>30 volts. As can be seen in Figure 9, there is an exponential rise in current for 3 volts<V<30 volts. The emission properties of sub-micron vertical MTV diodes are more complicated with both field emission (Fowler-Nordheim tunneling) and Child's law behavior being observed. Although not discussed in this abstract due to space limitations, details of the fabrication and emission properties of sub-micron vertical MTV devices will be presented. Results will also be presented for several low work function MTV cathodes including lanthanum hexaboride (LaB_6) and barium (Ba)-based oxide cathodes. A comparison of the power, performance, and lifetime of these MTV cathodes will also be included.

References

1. K.R. Shoulders, Advances in Computers, Vol 2, Ed. F.L. Alt (New York, Academic, 1961), pp. 135-293.

2. C.A. Spindt, J. Appl. Phys. **39**, 3504 (1968).

3. D. Geppert, US Patent 3,701,919, October 31, 1972.

4. H. F. Gray and G. Haas, NRL Report 7641 (1973).

5. C.A. Spindt, C.E. Holland and R.D. Stowell, J. Phys., **9**, 269 (1984).

6. H.F. Gray and C. Moglestue, 34th International Field Emission Symposium, Osaka, Japan (1987).

7. H.F. Gray, First Conference on High Temperature Electronics, Albuquerque, New Mexico (1988).

8. C.A. Spindt, C.E. Holland, I. Brodie, J.B. Mooney, and E.R. Westerberg, IEEE Trans. Electron Dev., **ED-36**, 225 (1989).

9. I. Brodie, IEEE Trans. Electron Dev., **ED-36**, 2637 (1989) and refs. therein.

10. H.H. Busta, J. Micromech. Microeng. **2**, 43 (1992) and refs. therein.

11. C.A. Spindt, C.E. Holland, A. Rosengreen, and I. Brodie, 1993 IEDM Symposium Proceedings, Paper 31.1, 749 (1993).

12. G. Gammie, R. Kozlowski, R. Mallavarpu, and A. Palevsky, 1993 IEDM Symposium Proceedings, Paper 31.2, 753 (1993).

13. C-M. Tang, Y.Y. Lau, and T.A. Swyden, 1993 IEDM Symposium Proceedings, Paper 31.1, 757 (1993).

14. D.C. Perng, D.A. Crewe and A.D. Feinerman, J. Micromech. Microeng., **2**, 25 (1990).

15. K.R. Williams and R.S. Muller, 1992 IEDM Symposium Proceedings, Paper 14.7, 387 (1992).

16. L.P. Sadwick, Y.J. Zhang, D.J. Schaeffer, S.G. Holmes, D.G. Petelenz, and R.J. Hwu, 1993 IEDM Symposium Proceedings, Paper 31.6, 769 (1993).

17. L.P. Sadwick, Y.J. Zhang, D.J. Schaeffer, S.G. Holmes, D.G. Petelenz, and R.J. Hwu, 1994 IEDM Symposium Proceedings, Paper 31.6, 769 (1994).

18. L.P. Sadwick, Y.J. Zhang, T.H. Zhang, D.J. Schaeffer, D. Petelenz, and R.J. Hwu, Eighth International Vacuum Microelectronics Conference Proceedings, New Approaches and Novel Devices Section, 522 (1995).

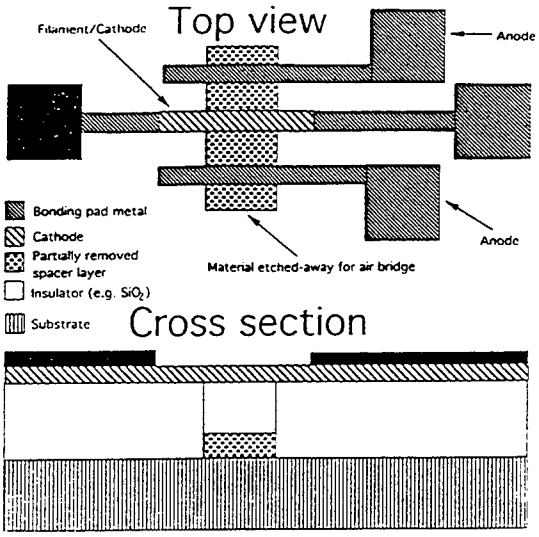


Figure 1. Pictorial schematic drawing of a planar MTV diode.

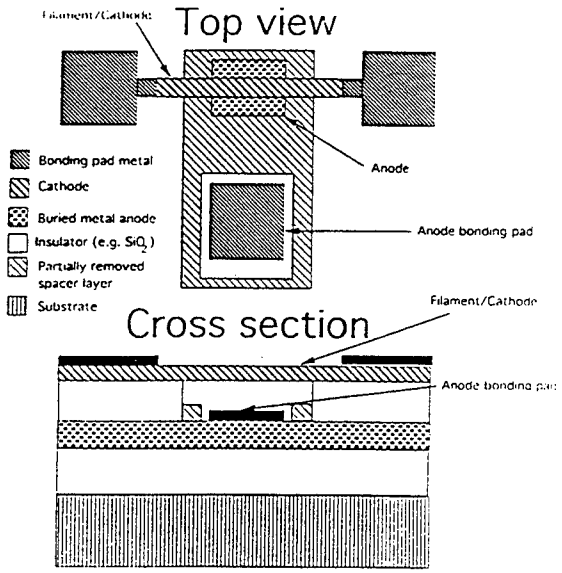
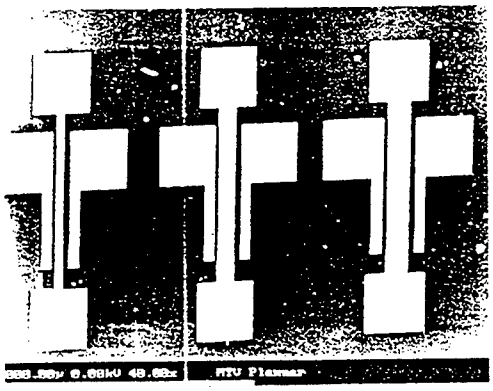


Figure 2. Pictorial schematic drawing of a vertical MTV diode.



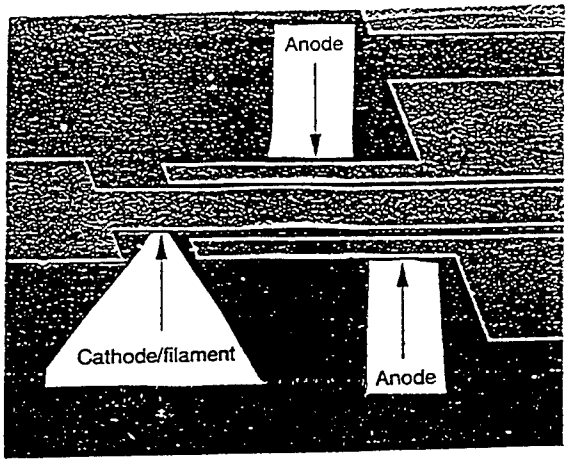


Figure 3. SEM photographs of planar MTV diodes. Note the intentionally raised "air bridge" center region of the filament/cathode for thermal emission.

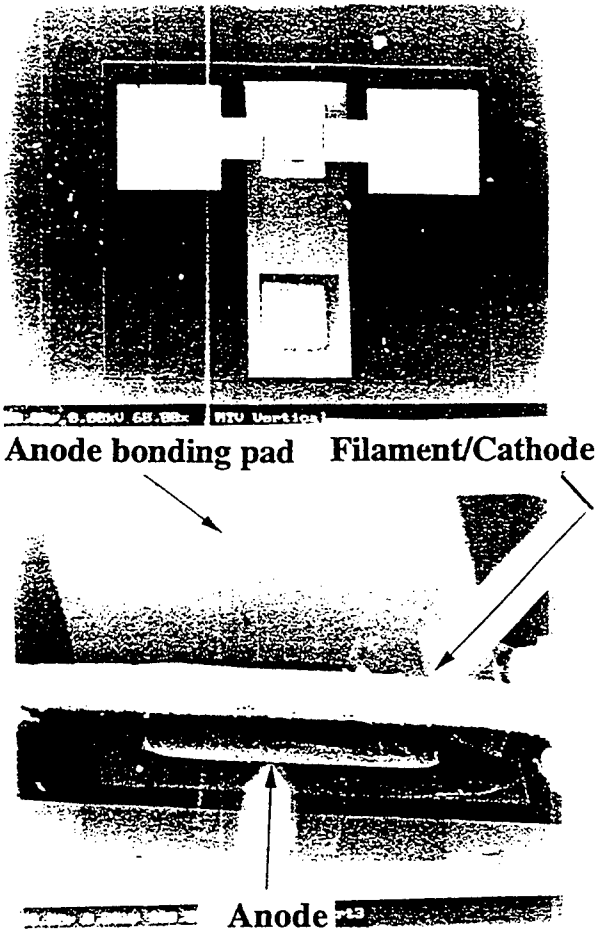


Figure 4. SEM photographs of a vertical MTV diode.

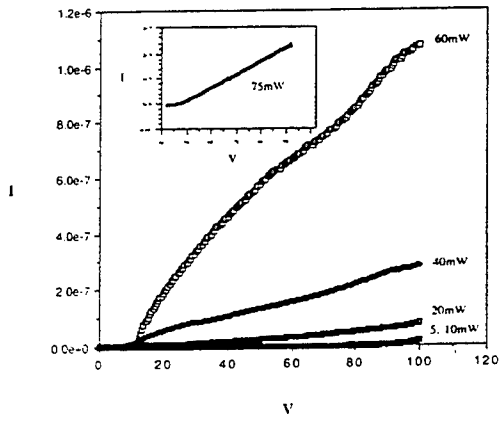


Figure 5. I vs. V characteristics of a tri-oxide planar MTV diode. Insert shows the 75 mW filament input power I-V curve (10^{-5} A range).

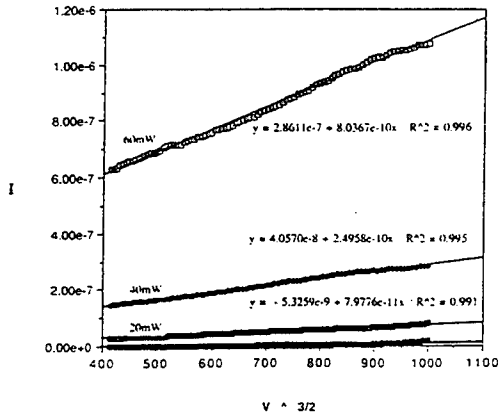


Figure 6. I vs. $V^{3/2}$ plot of the same data as in Figure 5.

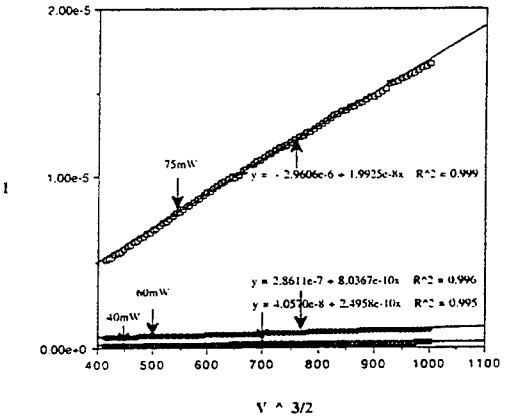


Figure 7. I vs. $V^{3/2}$ plot highlighting the 75 mW input filament power level case.

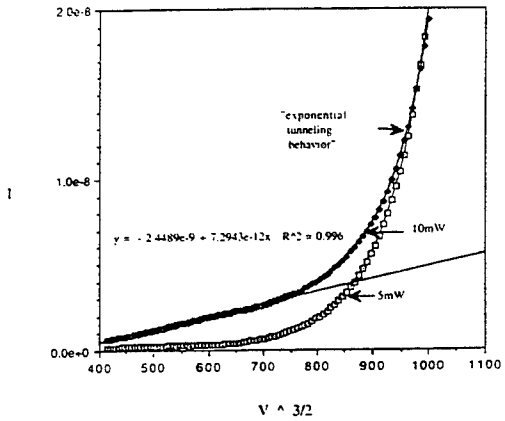


Figure 8. Child's law plot of the 5 and 10 mW input filament power data shown in Figure 5.

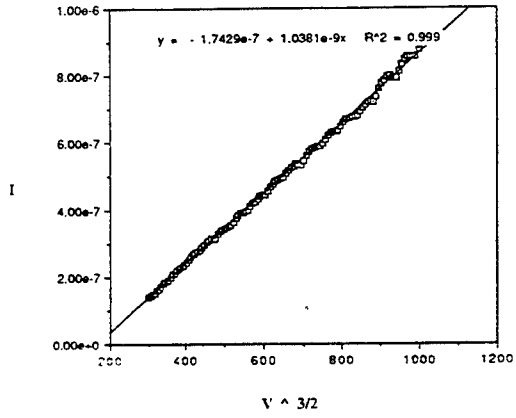


Figure 9. I vs. $V^{3/2}$ plot of an approximately 4 μm cathode-to-anode spaced vertical MTV diode.

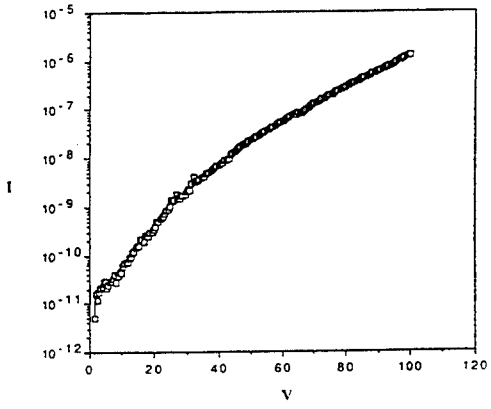


Figure 10. Semi-log I vs. V plot of Figure 9.

Studies and of the Effect of Electron Emission from the Active Region on Performance of InGaAsP/InP Lasers, Experiment and Modeling

G. L. Belenky*#, R. F. Kazarinov*, C. L. Reynolds Jr.+, V. Swaminathan+, S. L. Luryi#
*AT&T Bell Laboratories, Murray Hill, NJ 07974; +AT&T Bell Laboratories, Breinigsville, PA 18031; #State University of New York at Stony Brook, Stony Brook, NY 11794

We utilized a purely electrical technique to measure the leakage of electrons from the active region of InGaAsP/InP MQW laser heterostructures with different profiles of acceptor doping. Comparison of the measured value of threshold currents for devices with different profiles of Zn-doping with measured and calculated value of the leakage current shows that in the case of structure with a low doped p-interface T_0 depends on the profile of p-doping. Calculation shows that the electron leakage current in this type of device can reach 20% of the total injection current at an injection current density of 10kA/cm^2 at 50C.

Modern lasers based on the InGaAsP/InP material system are characterized by high temperature sensitivity of their characteristics. This fact stems from poor electron confinement due to a small conduction band offset in the conventional InGaAsP/InP system and high values of the working injection current density of multi-quantum-well devices. In this work we have measured and calculated the threshold current density and electron leakage current from the active region of InGaAsP/InP multi-quantum-well laser structures with different profiles of acceptor doping near the heterointerface.

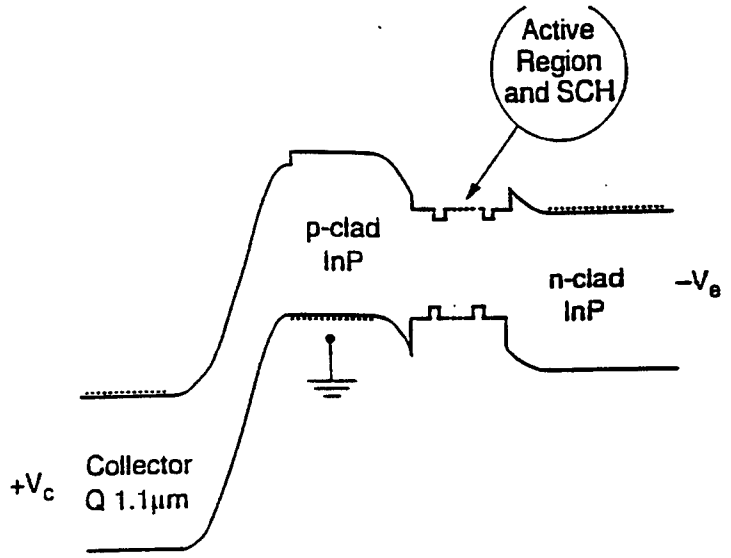


Fig. 1. Band diagram for the device under bias.

Figure 1 shows the band diagram of the device under bias: the p-cladding layer is grounded, negative bias is applied to the n-laser contact and positive voltage is applied to the collector. The diagram illustrates the idea of the experimental method [2]. Electrons emitted from the active region into the p-cladding layer are trapped by the collector. Measurements of the collector reverse current allow us to estimate the value of electron leakage under different conditions. The InGaAsP/InP heterostructures were grown by low pressure (80 mbar) metalorganic chemical vapor deposition (MOCVD) on (100) n^+-InP substrates. The strained MQW region consisted of 70 A wells and 100 A barriers in which the wells were mismatched ~1%. The separate confinement and electron collector layers were lattice matched. We used a secondary ion mass spectrometry (SIMS) to determine the concentration depth profile of the Zn in our structures.

The measured dependencies of the leakage current density, J_L, versus the injection current density, J_E, at two different temperatures are presented in Fig. 2 for structures with the two different acceptor doping. For the undoped heterointerface Fig. 2a J_L reaches ~1% of the total injection current density when J_E is $2kA/cm^2$. By doping the SCH layer, we have reduced the leakage a factor of 10 within measured range of injection Fig. 2b. The threshold current, I_{th}, as measured for devices with cavity length 500 μm and mesa width 20 μm. A typical I_{th} value measured under pulse excitation at 20C for structures with an undoped p-interface was 150 mA and for devices with a doped SCH layer (Fig. 2b) it was 165 mA. At 50C I_{th} reaches 340 mA and 290 mA, correspondingly.

In order to calculate the electron thermionic current from the active region into the p-cladding of strained multi-quantum-well InGaAsP/InP lasers and to estimate how this leakage affects quantum efficiency of the devices with different profiles of Zn doping, we use the modeling procedure "Padre" described in reference [1]. Figure 3 shows the calculated dependencies of the leakage current densities J_L on the injection current densities J_E at two different temperatures for structures with the Zn doping profiles given in Fig. 2. The inset in each figure shows the lowering of the barrier for thermionic emission of electrons from the active region as the injection level increases. In the case of structures with an undoped p-interface the energy of this barrier decreases with a rise in injection level. This reduction explains the measured behavior of J_L versus J_E presented in Fig. 2a. Agreement between theory and experiment is satisfactory within the measured range of injection current. However, in the case of the structures with a doped p-interface (Fig. 1b and Fig. 3b) the reduction of the noted barrier in the range of injection current densities up to $10kA/cm^2$ is very small. The value of this barrier reduction is in the order of several meV in the range of injection current densities $0 \geq J_E \geq 2kA/cm^2$. Within this region, the model [1], based on the effect of barrier reduction with injection, cannot not be sufficient for a quantitative analysis of the dependencies J_L versus J_E presented in Fig. 2b. Other effects which are not included in our calculation can be responsible for the measured J_L value and are discussed below. However, comparison of experimental results with the modeling data presented in Fig. 2a shows that in those conditions when effect of the barrier reduction is dominant, the model [1] is satisfactory for describing the dependence J_L versus J_E. Calculated dependencies of the leakage current density versus injection current density presented in Fig. 3 allow us to understand the difference in temperature dependence of threshold current for structures with different profiles of Zn doping. The estimated T_0 value for structures with an undoped interface is 32K, and for structures with a doped SCH T_0 = 52K. This difference can be explained by the sharp increase (shown in Fig. 3b) of the leakage

current with injection at 50C in the case of the structure with undoped p-interface when J_E reaches 4kA/cm^2, while J_L remains very small for structures with a doped SCH. Electron leakage current in devices with an undoped p-interface can reach 20% of the total injection current at an injection current density of 10kA/cm^2 at 50C and ≈0.03% for a doped SCH. Needless to say, this leakage determines the device internal efficiency and external efficiency.

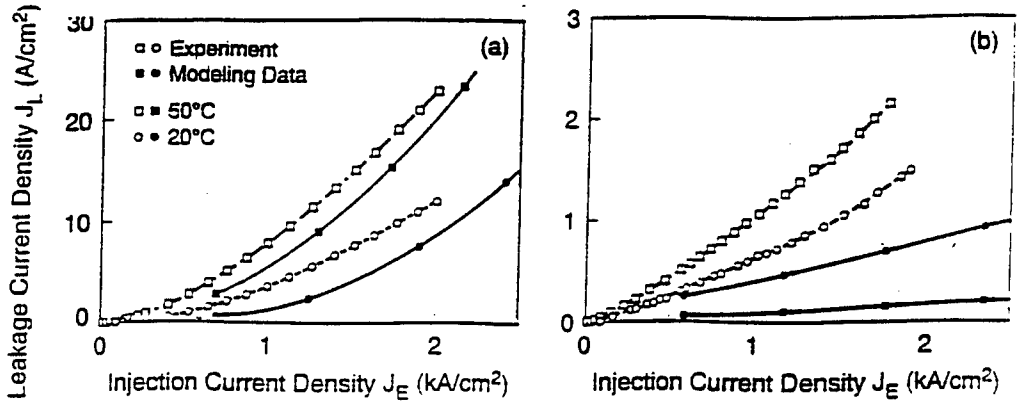


Fig. 2. Dependencies of the measured and calculated (solid lines) leakage current density on injection current density for the structures with two type of Zn doping profile.

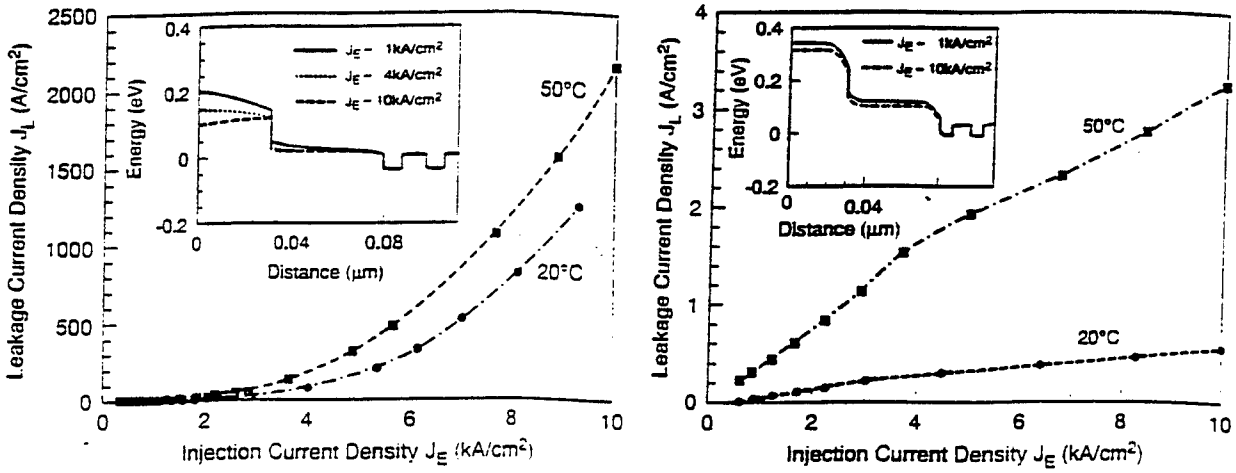


Fig. 3. Calculated dependencies of leakage current density J_L versus injection current density J_E at two different temperatures for structures with an undoped and doped (on the right) p-cladding/SCH interface. The inserted picture shows the barrier for thermionic emission of electrons from active region at different injection levels.

References

[1] R. F. Kazarinov and M. R. Pinto "Carrier Transport in Laser Heterostructures", IEEE, J. Quant. Electr., 30, 49, 1994.

[2] G. L. Belenky, R. F. Kazarinov, J. Lopata, S. Luryi, T. Tanbun-Ek, and P. Garbinski "Direct Measurement of the Carrier Leakage Out of the Active Region in InGaAsP/InP Laser Heterostructure" IEEE Trans. Electron Dev., 42, 215, 1995.

Experiments and Models Probing Carrier Dynamics in Multiquantum Well Lasers

Nir Tessler

Advanced Optoelectronics Center, Electrical Engineering Dept.
Technion, Haifa 32000 ISRAEL

In this talk I will discuss some theoretical and experimental issues related to MQW laser operation. First, some theoretical issues will be discussed and next, two related experiments will be presented. When one attempts to model a multiple quantum well (MQW) laser, one of the first questions to be asked is how detailed should this model be. A formal answer can be found by examining the structure details and by considering the time scales of interest. In [1] rough guidelines are given for silicon based transistors, where the modeling approach is plotted as a function of the characteristic time scale and distance. An examination of some of the experimental results for laser structures [2,3], shows that in MQW lasers the time scales and characteristic distances dictates a modeling approach which is on the boundaries of the drift-diffusion approach and the momentum/energy balance equations or even the full Boltzman transport equations. Namely, by considering the MQW laser structures and the operating conditions of such lasers one can expect that some of these laser properties can be fully understood only through detailed modeling. On the other hand, a laser is often regarded as a system with one input (current) and one output (photons field). This lumped approach calls for a simple, clear, and sometimes phenomenological modeling approach. Indeed, one can find in the current literature a variety of simple and complex models, and sometimes it even seems that there is a certain competition between the two approaches. The reason that not always one can find the two types of models to be complementary to each other, is that the two type of models have evolved side by side without a proper feedback between the two approaches. As I will show, a detailed approach is vital for the understanding of high performance MQW lasers, and that one may gain a lot by linking the detailed understanding to the simple modeling approach.

In order to convince that a detailed modeling is necessary, I will present some of the results obtained by our drift-diffusion-capture model [4]. The results are chosen so that they will demonstrate the importance of a quantity which is often the first to be neglected in simpler approaches. Namely, the effect of the Coulomb attraction between electrons and holes (Poisson eq.) and the accompanying band bending. The structure used in the simulation is an InGaAs/InGaAsP/InP SCH laser with four 8nm wide InGaAs wells separated by 10nm InGaAsP (1.3μm) barriers emitting near 1.5μm, all layers are lattice matched to InP. In the first calculation the waveguide is undoped and the InP cladding layers are doped to $10^{18}cm^{-3}$.

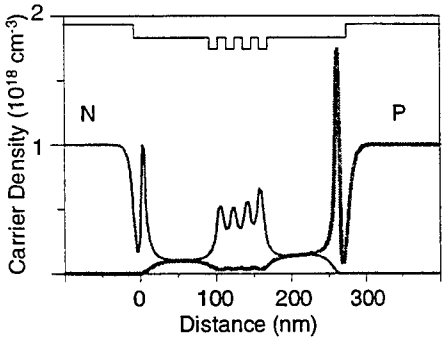


Figure 1. Calculated distribution of 3D (unconfined) electrons and holes at 15mA bias current. The N and P densities in the clading layers are due to doping while the waveguide is undoped.

Figure 1 shows the distribution of high energy carriers which do not reside within the quantized states of the QWs. These carriers are often named "waveguide carriers" or "3D carriers". The 2D carriers which are not shown in this figure are situated within the QWs (at the figure's center). Two issues are pointed out by this figure. First, at the QWs region there is a high density of electrons and a low density of holes. This is caused by the vast mass difference between these two species, which results in a pronounced electron overflow from the wells to the high energy (waveguide) states. Second, the density outside the QWs region is almost equal between electrons and holes and it is set by the **Coulomb** attraction between electrons and holes. Namely, the filing of waveguide states is largely affected by the Coulomb attraction.

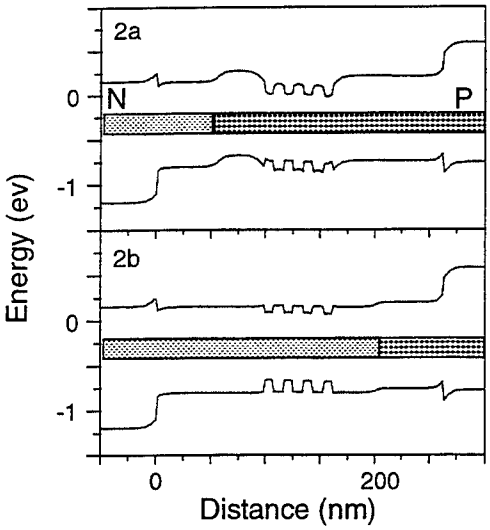


Figure 2. Calculated band profile for two different doping profiles. The doping profile is shown schematically at the center of each graph. The diamonds represents 1e18cm^{-3} P doping and the dashes 1e18cm^{-3} N doping.

Figure 2 is concerned with the band structure itself and its effect on the coupling between the QWs. In the past we have shown that in undoped waveguide MQW lasers the difference between electron and hole confinement results in an altered band diagram at the QWs region [4]. We also showed that this effect shuts off the resonant tunneling between QWs, that would otherwise be a very efficient coupling mechanism. Figure 2 shows the energy band diagram for the structure discussed above, but with the waveguide being doped. The doping profile is shown schematically in the two subfigures of Figure 2. In figure 2a the QWs are P doped to 10^{18}cm^{-3} and in figure 2b the QWs are N doped. When the QWs are P doped the difference in electron and hole densities within the QWs is increased with respect to the undoped case, hence the band structure in the QWs region is farther altered. However, when the QWs region is N doped, the N doping compensates for the difference in electron and hole confinement, thus allowing for a flatter band profile. By properly choosing the density of the N doping in the QWs region it should be possible to achieve a flat band profile and reopen the resonant tunneling coupling channel. Better coupling between the QWs will result in a more uniform distribution between the wells and a better laser performance at high bias currents. The results in figure 2 shows that by taking the Coulomb attraction into account it should be possible to control some of its effects.

As mentioned at the beginning, a lot can be gained by linking the information achieved via the detailed model and improve existing simple models. This will be demonstrated by including the Coulomb enhancement of the state filling effect, shown in figure 1. The simple model used is a 3 level model [5] shown bellow, derived for an undoped waveguide. The three levels are: the gain level (the carriers within the QWs, Ng), the capture level (high energy carriers at the QWs region, Nc), and a transport level (waveguide carriers outside the QWs region, Nd).

$$\frac{dN_d}{dt} = \frac{I}{qV_d} - \frac{N_d - a^{-1}N_c}{\tau_d}$$

$$\frac{dN_c}{dt} = \frac{N_d - N_c}{\tau_d}\frac{V_d}{V_c} - \frac{N_c - \eta_N^{-1}N_g}{\tau_{cn}}$$

$$\frac{dN_g}{dt} = \frac{N_c - \eta_N^{-1}N_g}{\tau_{cn}}\frac{V_c}{V_g} - \frac{N_g}{\tau_n} - GS$$

The equations above represents the 3 level model, written for electrons. The parameter "a" determines the density ratio between the high energy electrons in the QWs region and the carrier density in the SCH region, namely it accounts for the Coulomb enhancement of the state filling. All other parameters has the same meaning as in [5], note that the model is written here for carrier density and hence the volume ratios were added in the appropriate places. Similar equations can be written for holes with all the parameters assuming the appropriate values for holes. Using the detailed model it is possible to show that for holes "a" should be replaced by "a^{-1}". Using this observation along with some simple approximations it is possible to derive an analytic expression for the "a" parameter, which is independent of the detailed model.

$$a^{*2} \cong \frac{\eta_N^{-1}}{\eta_P^{-1}\left(1+\eta_N^{-1}L_c/L_g\right)+\dfrac{I\tau_{cP}}{qV_cN_{gth}}}$$

The simple expression of "a" allows for an easy inclusion of the Coulomb enhancement to the state filling effect. Moreover, it allows to view some of the parameters determining the carrier density in the SCH region. Note the effect of τ_{CP} (not τ_{CN}) which is consistent with the detailed calculations carried out by Hirayama et. al. [6], where the value of τ_{CP} was derived from experimental results. Also, the dependence of the carrier density in the SCH region on the structure parameters, operating temperature, and more; can be easily evaluated using the above expression.

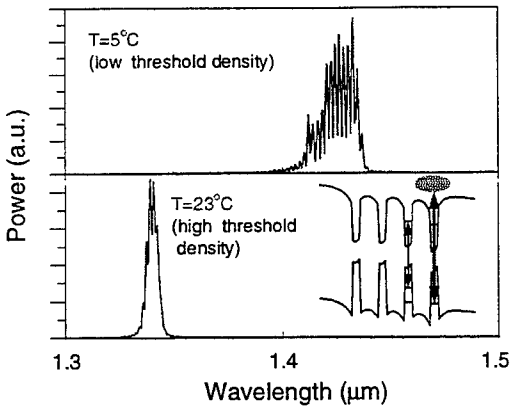


Figure 3. Heat sink temperature dependence of the lasing transition. The inset shows the two relevant transitions, e1-hh1 and high energy electrons to hh2.

The first experimental result to be presented is also directly connected to the Coulomb enhancement of the state filling. As seen in figure 1, there is a localization of electrons above the QWs [4]. This localization results from the internal electric fields which form a wide well above the QWs in the conduction band [4,7]. Fuchs et. al. have shown that the formation of the wide well is accompanied by the formation of a new optical transition between high energy electrons (within the wide well) and the second heavy hole confined level. This new transition was shown to fit well measured gain spectra of an optically pump laser amplifier [7]. We have also examined the formation of this new self induced transition but under laser operating conditions, namely the excitation is via current injection. Figure 3 shows the output power of a short cavity MQW laser with 1.3μm barriers, for two heat sink temperatures. The laser was excited by short low repetition rate current pulses to avoid current heating. At the low temperature (5°c) the laser operates at the "normal" (e1-hh1) transition, where the relatively short wavelength results from the short cavity length. At the higher temperature (23°c) the threshold density increases and the laser wavelength jumps and the laser oscillates at the new self induced optical transition. The nature of the short wavelength lasing as a second level type transition was verified by small signal measurements as well as a systematic study of the length dependence of the lasing wavelength [8]. These results show that the self induced optical transition is formed under forward bias conditions and is strong enough to support lasing in short cavity, as cleaved lasers. The lasing at the self induced transition was observed also in 0.98μm MQW lasers hence, it is a global phenomena. The formation of this new transition is expected also to affect carrier relaxation processes in the QWs region, and to modify the interpretation of experimental results.

The formation of this self induced transition was found to be vital for the better understanding of broad band time resolved pump probe measurements in a MQW laser amplifier with 1.3μm barriers [9]. In that experiment, the laser amplifier was driven at a certain DC bias current and

pumped by a 200fs pulses at the bottom of the well (1.51μm). The transmission of a probe pulse was measured as a function of time delay between pump and probe at two probe wavelengths; 1.51μm and 1.31μm (slightly bellow the barrier energy). This measurement was devised in order to separate the carrier cooling process from the carrier capture process which are of similar nature and of a similar characteristic time constants (~1ps). The 1.31μm probe senses, besides the e1-hh1 transition, the optical transition between high energy (out of well) electrons and the second confined heavy hole level, hence it senses the relaxation (capture) of electrons in the QWs region into the QWs.

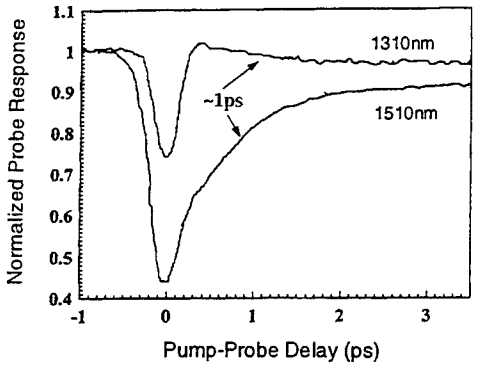


Figure 4. Measured probe transmission as a function of pump probe delay for two probe wavelengths.

Figure 4 shows measured probe transmission traces at 1.51μm and 1.31μm. The probe responses on the 1ps time scale clearly shows that carriers are relaxing from high energy states (1.31μm) to low energy states (1.51μm). In [9] it was pointed out that the opposite slopes of the probe traces may be solely due to the spectral dependence of the carrier cooling. However, when the results are examined taking into account the formation of the self induced optical transition we find that the temperature dependence of the gain spectra can not explain the opposite slopes of the two measured probe traces. Hence, the 1.31μm probe trace is probably an indication for the capture of high energy electrons. This statement is strengthened by measurements of the current dependent probe traces at 1.31μm. At higher bias currents, the results [9] clearly show that the probe transmission is affected by a mixing of two processes. Since there are mainly two processes to be considered (carrier cooling and carrier capture) on this time scale, one may conclude that these measurements show the carrier capture process.

References

1. Fundamentals of carrier transport, by M. Lundstrom, Modular series on solid state devices; Vol. 10, Addison-Wesley, 1990.
2. S. Weiss, J.M. Weisenfeld, D.S. Chemla, G. Raybon, G. Sucha, G. Eisenstein, C.A. Burrus. A.G. Dentai, U. Koren, B.I. Miller, H. Temkin, R.A. Logan, and T. Tanbun-Ek, "Carrier capture times in 1.5μm multiple quantum well optical amplifiers", Appl. Phys. Lett., 60, pp. 9-11, 1992.
3. R. Nagarajan, M. Ishikawa, T. Fukushima, R.S. Geels, and J.E. Bowers, "High speed quantum well lasers and carrier transport effects", IEEE J. Quantum Elect., 28, pp. 1990-2008,1992.
4. N. Tessler and G. Eisenstein, "On carrier injection and gain dynamics in quantum well lasers", IEEE J. Quantum Elect., 29, pp. 1586-1595, 1993.
5. N. Tessler and G. Eisenstein, "Modeling carrier dynamics and small signal modulation response in quantum well lasers", Optical and Quantum Elect., 26, pp. S7676-S787, 1994.
6. H. Hirayama, J. Yoshida, Y. Miyake, and M. Asada, "Estimation of carrier capture time of quantum well lasers by spontaneous emission spectra", Appl. Phys. Lett., 61, pp. 2398-2400, 1992.
7. G. Fuchs, J. Horer, and A. Hangleiter, "Carrier induced localization in InGaAs/InGaAsP separate confinement quantum well structures", Phys. Rev. B., 48, pp. 15175-15181, 1993.
8. N. Tessler, V. Mikhaelashvili, R. Nagar, G. Eisenstein, "Lasing transitions between self localized barrier state electrons and confined state heavy holes in InGaAs/InGaAsP/InP multiple quantum well lasers", IEEE J. Quantum Elect., Nov., 1995.
9. J. Mark, N. Tessler, G.Eisenstein, and J. Mørk, "Broadband femtosecond pump-probe setup operating at 1300 and 1550 nm", Appl. Phys. Lett., 64, pp. 1899-1901, 1994.

Application of Fast Time-Resolved Spectroscopy to Semiconductor Lasers

Jesper Mørk
Tele Danmark Research, Lyngsø Allé 2, DK–2970 Hørsholm, Denmark
E-mail: jm@tdr.dk, Phone +45 4576–6444, Fax +45 4576–6336

Antonio Mecozzi
Fondazione Ugo Bordoni, via B. Castiglione 59, I-00142 Roma, Italy
E-mail: amecozzi@fub.it, Phone +39 (6) 5480–2232, Fax +39 (6) 5480–4402

Abstract: Ultrafast gain and index dynamics in active semiconductor waveguides are modelled using a simple analytical theory derived from semi-classical density matrix equations.

Introduction: Characterization and modelling of the ultrafast carrier dynamic processes in active semiconductor waveguides is the basis for understanding the high-speed properties of semiconductor lasers. In addition, applications of these processes are being pursued in photonic switching devices, such as frequency converters [1] and directional couplers [2]. There has been some dispute as to the main processes governing the ultrafast response of active semiconductor waveguides, but recent time-domain pump-probe [3, 4, 5] as well as frequency domain four-wave mixing studies [6, 7, 8] seem to converge in identifying carrier heating and spectral hole burning as the dominant processes, at least in bulk material. In this paper we outline the general theory for analyzing ultrafast dynamics in semiconductor waveguides and illustrate its application to analysis of pump-probe measurements, short pulse gain saturation and highly non-degenerate four-wave mixing. The important influence of spectral artifacts on pump-probe dynamics is pointed out.

Theory: The evolution of the slowly varying complex envelope of the electric field is governed by

$$\frac{\partial E(z,t)}{\partial z} = \mathcal{L}(t)E(z,t) + R(z,t)\,, \tag{1}$$

where $\mathcal{L}$ is a linear operator describing the linear propagation characteristics and the nonlinear term $R(z,t)$ accounts for the field induced changes of the gain and index

$$R(z,t) = \int_{-\infty}^{\infty} h(t-t')|E(z,t')|^2 dt' E(z,t)\,. \tag{2}$$

Eqs. (1) and (2) are derived from the wave equation coupled with semi-classical density matrix equations for the material dynamics [9]. Relaxation of the carrier distributions by carrier-carrier and carrier-phonon scattering are described within the relaxation time approximation and the material polarization has been eliminated adiabatically. Then, the material dynamics is described by the material response function $h(t)$,

$$h(t) = h_N(t) + h_T(t) + h_{SHB}(t) + h_{TPA}(t), \tag{3}$$

with terms accounting for carrier density changes, carrier heating, spectral holeburning and two-photon absorption. The real parts of these terms account for gain changes and the imaginary parts account for index changes [9].

Pump-and-probe dynamics: In this case the input field to the waveguide is

$$E(0,t) = E_0(0,t+\tau) + E_1(0,t), \tag{4}$$

where E_0 is the strong pump pulse, E_1 is the weak probe, and τ denotes the time delay between them. A perturbation calculation to first order in the pump intensity yields the following expression for the voltage change of the photo detector monitoring the probe

$$\Delta V_R(\tau) + i\Delta V_I(\tau) = K \int_{-\infty}^{\infty} dt' H(t') G^{(2)}(\tau - t') \,. \tag{5}$$

$\Delta V_R(\tau)$ is proportional to the probe intensity change as measured in a standard setup for studying gain dynamics [3, 4] and $\Delta V_I(\tau)$ is the corresponding quadrature component (probe phase) as measured in a set-up for studying refractive index dynamics [5]. $G^{(2)}(\tau)$ is the cross-correlation function of the input pulses, K is a constant and $H(t)$ is the effective waveguide response function [9]

$$H(t) = \frac{e^{\xi_0 L}}{\xi_0} \left[e^{\xi_0 L} - 1 + i\frac{\xi_0'}{2\xi_0} \left(e^{\xi_0 L} - 1 - \xi_0 L \right) \frac{\partial}{\partial t} \right] h(t). \tag{6}$$

Here, L is the waveguide length, ξ_0 the net gain, and ξ_0' the gain slope (derivative of gain with respect to angular frequency). Higher order dispersive effects have been neglected. For simplicity we have considered the common experimental case of orthogonal pump and probe polarizations, but the theory can also be used to calculate coherent artifacts present for parallel polarizations [10].

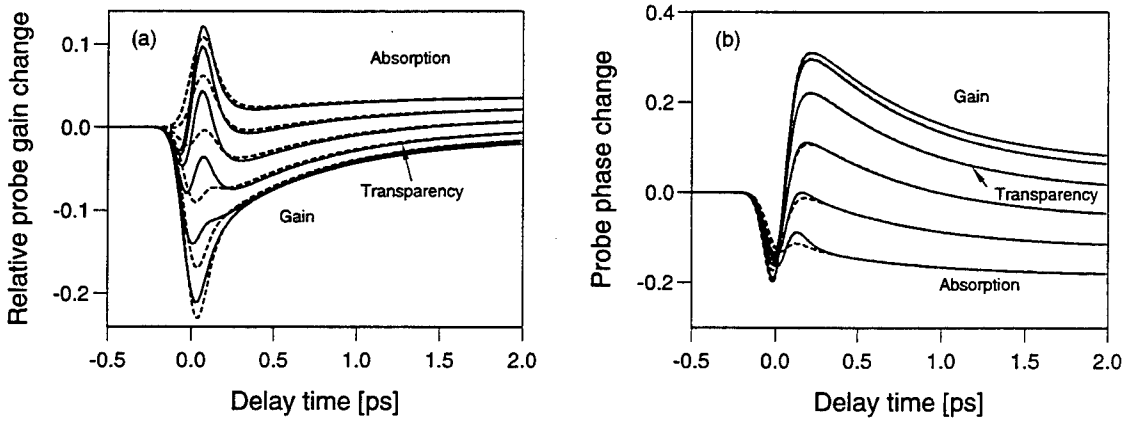


Fig. 1 Normalized pump-probe response for (a) gain dynamics $\Delta V_R(\tau)$ and (b) index dynamics $\Delta V_I(\tau)$. Dashed curves: without spectral effects ($\xi_0' = 0$). Solid curves: including spectral effects. The traces correspond to different photon energies for the pump and the probe pulses. Parameters as in [9], except the pulsewidth is 100 fs.

Fig. 1 shows the calculated responses for a range of photon energies. The dashed curves correspond to neglecting spectral effects ($\xi_0' = 0$) and the solid curves include spectral effects.

For a detailed interpretation of the probe traces in the absence of spectral effects see [3, 9]. For the probe gain change, the appearance of a time derivative in the term proportional to ξ_0' in Eq. (6) should be clear: The refractive index change induced by the pump corresponds to a probe phase change $\varphi(t)$ (cf. Fig. 1(b)), i.e., a change of the instantaneous frequency $\delta\omega(t) = \partial\varphi(t)/\partial t$ and therefore a gain change $\delta g(t) = (\partial g/\partial\omega)\delta\omega(t) = \xi_0'\partial\varphi(t)/\partial t$. We see that that the inclusion of spectral effects leads to a much more pronounced undulation of the probe gain change near zero delay time. Such strong undulations have been experimentally observed, but were ascribed to a delay in carrier heating [4, 5]. We should emphasize, that our theory does predict a delay given by the carrier-carrier scattering time (70 fs in the present case) of the gain change due to carrier heating. However, this delay only gives rise to the very small undulation seen in the dashed curve in Fig. 1(a) at the transparency point.

Further support for the influence of spectral artifacts on short pulse pump-probe dynamics can be found in experimental data taken by Hultgren [11]. Since the gain slope at the transparency point increases with carrier density, the influence of spectral artifacts on the probe gain dynamics at the transparency point increases with density. The experimental data do show a pronounced increase with carrier density of probe gain undulations near zero time delay [11] and is in good agreement with theoretical predictions. The effect of a delay in carrier heating does not explain this dependence.

Short pulse gain saturation: The model can also be used to calculate the saturation characteristics, when a semiconductor laser amplifier is being used for amplification of short optical pulses. In this case, the perturbation calculation is carried out for the self-induced gain change of a single input pulse. We find the following expression for the 3-dB input saturation energy U_{in}^{sat}, i.e., the input energy at which the amplifier gain is half of the small-signal value ($\exp(\xi_0 L)$):

$$U_{in}^{sat} = \frac{\xi_0}{2(e^{\xi_0 L}-1)} \frac{1}{\mathrm{Re}\{-h_s(t=0) - 2\eta_2 h_f(\Omega=0)/\tau_p\}}. \tag{7}$$

Here, τ_p is the FWHM pulsewidth, $h_s(t)$ denotes the components of the material response $h(t)$ whose decay time is slow compared to τ_p, and $h_f(\Omega)$ is the Fourier transform of the fast components. η_2 is a constant (near unity) depending on the pulse shape. Eq. (7) shows that the saturation energy depends on the pulsewidth: shorter pulses receive less gain due to the fast processes which lead to a saturation that depends on peak power rather than pulse energy. For pulses which are shorter than a few ps, the saturation by spectral holeburning and carrier heating are found to be as important as the usually considered effect of carrier density depletion (described by $h_N(t)$). The result derived here is in agreement with the numerical findings in [12] and the experimental results of [4].

Non-degenerate four-wave mixing: In the last few years it has been shown that wave-mixing in semiconductor laser amplifiers, besides offering a spectroscopic technique for investigating ultrafast carrier dynamic processes, can be utilized for photonic switching, i.e., frequency conversion and optical de-multiplexing. The efficiency of the four-wave mixing process can be easily calculated within the present framework. Taking the input field to the waveguide as the sum of a pump pulse A_0, and a probe pulse A_1 with a

frequency detuning Ω:

$$E(0,t) = A_0(0,t) + A_1(0,t)e^{-i\Omega t}, \tag{8}$$

we get the output energy U_2 of the conjugate pulse generated at a frequency detuning $-\Omega$:

$$U_2 = \frac{1}{\xi_0^2} e^{\xi_0 L}[e^{\xi_0 L} - 1]^2 |h(-\Omega)|^2 \int_{-\infty}^{\infty} |A_1(0,t)|^2 |A_0(0,t)|^4 dt. \tag{9}$$

We assumed the spectra of the pump, probe and conjugate fields to be non-overlapping and dispersion of the gain was neglected. Eq. (9 displays the well-known result, that the magnitude of the conjugate signal is determined by the Fourier transform of the material response function [8]. For pulses, the conjugate signal also depends on the overlap of the pump and probe pulses, see also [13], showing the potential for ultrafast switching applications.

Eq. (9) is the result of a first-order perturbation calculation. Taking the calculations to second-order in the pump, one also gets the saturation behaviour of the conjugate signal for strong pump pulses. In agreement with [8, 13] we find an optimum conversion efficiency. However, due to the inclusion of saturation by the ultrafast carrier dynamic processes, which was not considered in [8, 13], the optimum conversion efficiency, and the pump energy at which it is attained, depend on the pulsewidth.

Conclusion: We have developed a simple theory for analyzing ultrafast dynamic processes in active semiconductor waveguides. Its application to pump-probe dynamics, short pulse gain saturation and non-degenerate four-wave mixing has been demonstrated.

References

[1] R. Schnabel, W. Pieper, M. Ehrhardt, M. Eiselt, and H. G. Weber, Electron. Lett., **29**, 2047 (1993).

[2] D.A.O. Davies, M. A. Fisher, D. J. Elton, S. D. Perrin, M. J. Adams, G. T. Kennedy, R. S. Grant, P. D. Roberts, and W. Sibbett, Electron. Lett. **29**, 1710 (1993).

[3] J. Mark and J. Mørk, Appl. Phys. Lett. **61**, 2281 (1992).

[4] K. L. Hall, G. Lenz, A. M. Darwish, and E. P. Ippen, Opt. Commun., **111**, 589 (1994).

[5] C. T. Hultgren and E. P. Ippen, Appl. Phys. Lett. **61**, 2767 (1992).

[6] J. Zhou, N. Park, J. W. Dawson, K. J. Vahala, M. A. Newkirk, and B. I. Miller, Appl. Phys. Lett. **63**, 1179 (1993).

[7] A. Uskov, J. Mørk, and J. Mark, IEEE J. Quantum Electron. **30**, 1769 (1994).

[8] A. Mecozzi, S. Scotti, A. D'Ottavi, E. Iannone, and P. Spano, IEEE J. Quantum Electron. **31**, 689 (1995). A. Mecozzi, Opt. Lett. **19**, 892 (1994).

[9] J. Mørk and A. Mecozzi, Appl. Phys. Lett. **65**, 1736 (1994). J. Mørk and A. Mecozzi, submitted to J. Opt. Soc. Am. B, June 1995.

[10] A. Mecozzi and J. Mørk, unpublished.

[11] C. T. Hultgren, Ph.D. Thesis, Massachusetts Institute of Technology, July 1994.

[12] A. Uskov, J. Mørk, and J. Mark, IEEE Photon. Technol. Lett. **4**, 443 (1992).

[13] M. Shtaif and G. Eisenstein, Appl. Phys. Lett. **66**, pp. 1458–1460 (March 1995).

Gain in InGaAsP Based Lasers: Comparison of Models to Experiment

M. S. Hybertsen, D.A. Ackerman, G.E. Shtengel, P.A. Morton,
R.F. Kazarinov, G.A. Baraff, T. Tanbun-Ek and R.A. Logan

AT&T Bell Laboratories, Murray Hill, New Jersey, 07974

Gain in bulk and multiquantum well (MQW) active layer 1.3 μm InGaAsP based lasers has been measured along with spontaneous emission, loss, transparency energy and carrier density in the subthreshold regime at room and elevated temperatures. The electronic states and optical properties have been calculated using an eight band $\mathbf{k}\cdot\mathbf{p}$ model. The results of the models have been carefully compared to experiment showing several points of good agreement. The measurements show that the temperature sensitivity of the gain is crucial for understanding the well known low values of T_0 in InGaAsP based lasers. The calculated results demonstrate that the temperature sensitivity of the gain depends on the structure e.g. bulk versus multiquantum well. However, the model does not show as strong a temperature sensitivity as found experimentally. Possible physical mechanisms are discussed.

Modeling of laser performance has become increasingly important as the performance requirements for lasers in telecommunications applications have become more demanding. This is driving a move from qualitative modeling for guidance or intuition to quantitative analysis of the performance implications of specific design changes. The importance of direct modeling of crucial material properties such as optical gain is tied to the continued effort to exploit artificial structures, e.g. multiquantum well structures, to improve laser performance. A multidimensional design space must be mapped out including well width, material strain and barrier composition. At the same time, development of low cost, uncooled laser modules has brought renewed emphasis on the temperature dependence of laser performance. The T_0 parameter empirically describes the temperature sensitivity through $I_{th} = I_0 \exp(T/T_0)$. For InGaAsP based lasers, T_0 is typically 60-80 K near room temperature, indicating substantial degradation of laser performance at elevated operating temperatures. A fundamental explanation for the low value of T_0 in this material system remains a long standing puzzle at a time when the practical implications underscore its importance.

Here we review our experimental and theoretical results for 1.3 μm InGaAsP based lasers, both bulk active and multiquantum well devices [1-6]. We systematically compare the models with the data in order to provide an assessment of conventional gain models for these systems. This is a crucial part of developing quantitative, predictive models for material gain. We also address the temperature sensitivity of laser performance. Many explanations for the relatively low T_0 (i.e. in comparison to GaAs based lasers) have been proposed, the most prevalent being the relatively larger contribution of Auger processes in InGaAsP based devices. We find that the temperature dependence of material gain is important in determining the low value of T_0. This presents an important challenge for the model.

Devices used in this study consisted of MQW and bulk active 1.3μm capped mesa buried heterostructure Fabry-Perot lasers containing either multi-quantum well (7 to 10 compressively strained quaternary wells) or bulk quaternary active regions. Laser cavities of ~1 μm width and ~300 μm length were surrounded by conventional InP current blocking layers. Lasers exhibit low current leakage with internal efficiency remaining high (~80%) over the measured temperature range (25-85 C). For each device, the modal gain and loss, as well as the spontaneous emission, were measured as a function of current below threshold. A direct determination of the transparency energy yields the average quasifermi level separation in the active region. The average carrier density in the active region was determined by integrating the measured differential lifetime over current, taking account of the internal efficiency and correcting for the effect of the finite load impedance. This was done for the temperature range 25-85 C. Details of the experimental techniques and relevant citations appear in Refs. [2,4-6].

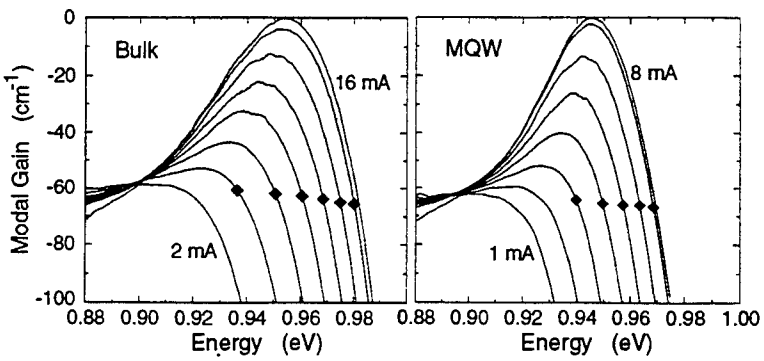


Figure 1. Families of measured gain spectra as a function of photon energy for the indicated ranges of device current for a bulk active and a MQW active laser at 25 C.

The electronic states for each constituent material are represented by an eight band $\mathbf{k}\cdot\mathbf{p}$ model. The needed input parameters are: (1) the Luttinger parameters which describe the light and heavy hole masses, (2) the momentum matrix element connecting the s-like and p-like bulk states at the zone center, (3) the conduction band effective mass, (4) the fundamental band gap, and (5) the spin-orbit splitting of the zone center valence band states. In addition, incorporation of epitaxial strain requires knowledge of several deformation potentials and the elastic compliance coefficients. The electronic states for heterostructures are calculated using the envelope function approximation. Details of the Hamiltonian, the parameters and the computational technique appear in Refs. [2,3]. This Hamiltonian naturally accounts for the non-parabolicity of the bands, including the light hole to heavy hole mixing and the anisotropy of the hole states. The widely used axial approximation has been tested as a special case and found to be sufficiently accurate in the present context. The quasifermi levels are determined for each pumping level from the calculated density of states for electrons and holes. The optical absorption and spontaneous emission are then computed following the usual density matrix formulation. Broadening is included phenomenologically with a constant dephasing time of 0.1 ps, incorporated in such a way as to preserve the transparency energy as the quasifermi level separation. The many-body contribution to the quasifermi level separation is included as an overall shift.

Figure 1 summarizes some of the basic experimental gain data. Modal gain, including mirror and distributed losses, is shown as a function of photon energy for a set of subthreshold currents. The direct measurement of the transparency energy for each current yields the diamonds. At these energies, the material gain is zero, so the modal gain corresponds to the other modal losses. For each current, the peak gain achieved by pumping the active material is obtained as the difference between the peak and the point indicated by the diamond.

Bulk active lasers are modeled by quaternary composition $(In_{0.53}Ga_{0.47}As)_{0.6}(InP)_{0.4}$. The MQW region of the laser diode is modeled by an extended superlattice, expected to well represent the present situation with 7 to 10 wells. An example of the energy bands and density of states for such a superlattice is shown in Fig. 2. A single electron band is bound in the wells; the three dimensional density of states starts above the energy of the barrier. The first two hole subbands are of heavy-hole character while the third is the first light-hole derived subband. The density of states is far from the step function associated with a simple one-band model. Since the structure is within a few times kT of the band edges, this has an important influence on the degree of inversion achieved for a given amount of pumping. The structure in the hole density of states depends critically on the choice of well width and strain. A simple parameterization is the effective density of states parameter

$$N_v = \int_{-\infty}^{E_{VBM}} dE\ D(E)\exp[(E-E_{VBM})/kT]$$

which reduces to the familiar parameter in the limit of a single parabolic band. Figure 2 illustrates that this parameter is sensitive to the structure of the quantum well.

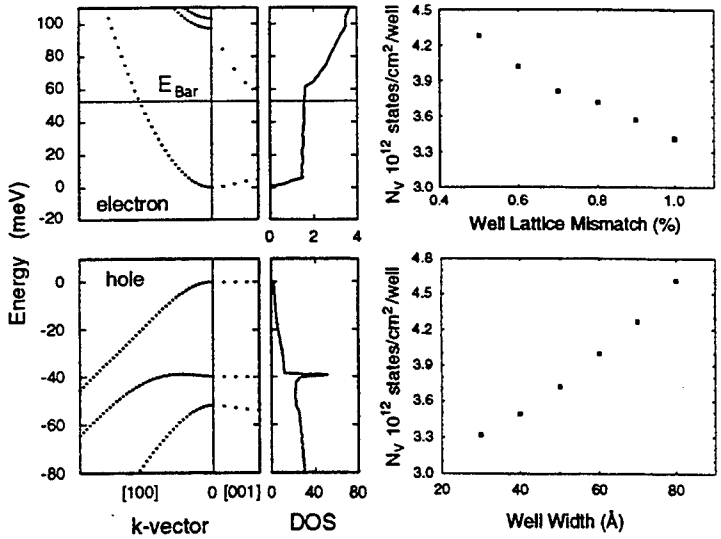


Figure 2. The calculated energy bands and corresponding density of states (DOS, in units of 10^{19} states/eV$-$cm^3) for the case of a superlattice with 70 Å compressively strained wells and 100 Å lattice matched barriers chosen to give a 0.94 eV band gap. The right hand panels survey the hole density of states parameter defined in the text as a function of well lattice mismatch (50 Å well, top) and as a function of well width (0.8% lattice mismatch, bottom).

Examples of calculated gain spectra are shown in Fig. 3. The range of density roughly covers the region from transparency to threshold. Qualitatively, the results agree well with the experimental curves. In particular, the MQW gain spectra are systematically narrower. However, quantitative comparison shows that the calculated spectra are too narrow. This can not be trivially resolved by a faster dephasing time (larger Lorentzian broadening) because the low energy tail has the wrong shape.

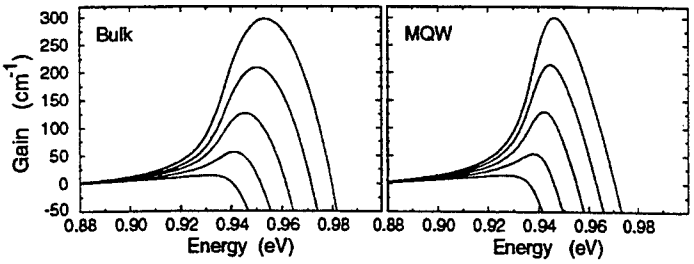


Figure 3. Calculated gain spectra for bulk active and MQW (bands in Fig. 2) active layer materials. Carrier densities: n = p = 1.2, 1.4, 1.6, 1.8 and 2.0×10^{18} cm^{-3} for the bulk case; n = p = 0.7, 0.8, 0.9, 1.0 and 1.1×10^{18} cm^{-3} for the superlattice case.

For the bulk active case, the measured chemical potential (quasifermi level separation) and the peak modal gain are shown as a function of density in Fig. 4. The calculated results are shown for comparison. The calculated quasifermi level separation, including a many-body correction, agrees well with the measured transparency energy as a function of density and temperature. This suggests that the calculated density of states is accurate for the bulk material. The calculated peak modal gain at room temperature yields a differential gain which is larger than experiment and a transparency density which is also too large. The gain observed in the data at lower density is not reproduced. This may largely be due to the discrepancy between theory and experiment for the width and shape of the gain spectra noted above. The measured gain as a function of density at 85 C indicates a substantial temperature sensitivity which the model underestimates. The differential gain is measured to drop noticeably with a corresponding increase

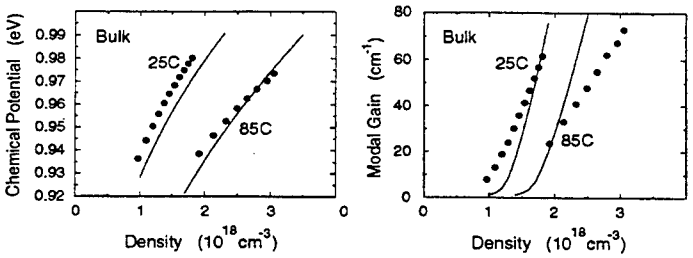


Figure 4. Comparison of the model (lines) to experiment (solid circles) for the chemical potential and peak modal gain as a function of density for the bulk active 1.3 μm device at room temperature and 85 C.

in the threshold carrier density. The measurements for the MQW active layer devices show similar trends. The comparison with the model calculations is complicated by the carrier spill-over into the separate confinement layers surrounding the MQW region.

The temperature sensitivity of the gain can be parameterized empirically by a "$T_{0,g}$" parameter assigned either to the threshold density or to the differential gain near threshold. These are measured to be in the range of 100 K, showing that the changes in the gain with temperature are a crucial factor in determining the overall low value of T_0 for these devices. As Fig. 4 illustrates, the model overestimates $T_{0,g}$, giving values in the range of 200 K. However, the calculations show that the band structure of the active layer does play a role. The $T_{0,g}$ for MQW material is systematically lower. Also, simplified models which only account for a single parabolic band for electrons and holes yield values of $T_{0,g}$ which are substantially too large.

It remains a challenge to quantitatively model all the processes which contribute to the gain spectrum and its dependence on temperature and carrier density. The present work highlights the importance of the broadening of the gain. A theory beyond the simple dephasing time approximation is clearly required. In addition, inhomogeneous broadening may be important, including the role of p-type dopants (Zn) and the possibility of spinodal decomposition of quaternary alloys. Despite these shortcomings, the present gain model provides semiquantitative guidance for design decisions in the multidimensional parameter space of MQW laser active layers.

[1] D.A. Ackerman, P.A. Morton, G.E. Shtengel, M.S. Hybertsen, R.F. Kazarinov, T. Tanbun-Ek and R.A. Logan, "Analysis of T_0 in 1.3 μm multi-quantum-well and bulk active lasers," *Appl. Phys. Lett.*, vol. 66, pp. 2613-2615, 1995.

[2] D.A. Ackerman, G.E. Shtengel, M.S. Hybertsen, P.A. Morton, R.F. Kazarinov, T. Tanbun-Ek and R.A. Logan, "Analysis of gain in determining T_0 in 1.3μm semiconductor lasers," *IEEE J. of Selected Topics in Quantum Electronics,* vol. 1, pp. 250-263, 1995.

[3] M.S. Hybertsen, R.F. Kazarinov, G.A. Baraff, D.A. Ackerman, G.E. Shtengel, P.A. Morton, T. Tanbun-Ek and R.A. Logan, "Modeling of gain for InGaAsP based lasers," *SPIE Proceedings Series,* vol. 2399, pp. 132-145, 1995.

[4] G.E. Shtengel and D.A. Ackerman, "Internal optical loss measurements in 1.3 μm InGaAsP lasers," *Electron. Lett.*, vol. 31, pp. 1157-1159, 1995.

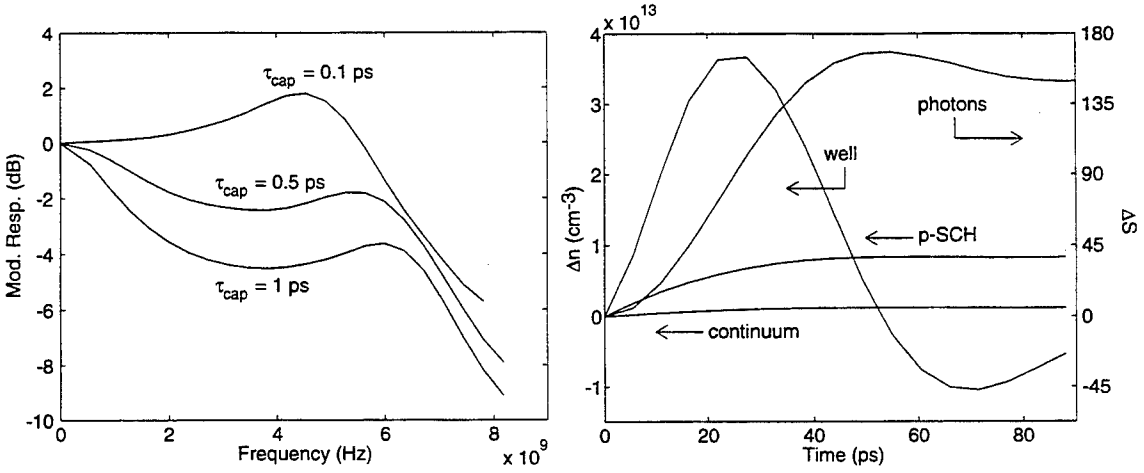
[5] G.E. Shtengel, D.A. Ackerman, P.A. Morton, E.J. Flynn, and M.S. Hybertsen, "Impedence-corrected carrier lifetime measurements in semiconductor lasers," to be published, *Appl. Phys. Lett.*, vol. 67, no. 11, 1995.

[6] G.E. Shtengel, D.A. Ackerman, and P.A. Morton, "True Carrier Lifetime Measurements of Semiconductor lasers," accepted for publication, *Electron. Lett.*

Role of Carrier Transport and Spectral Hole Burning in the Modulation Response of Semiconductor Quantum-Well Lasers

Karl Hess and Matt Grupen
Beckman Institute
University of Illinois

Much research has been devoted to gain nonlinearities in quantum-well (QW) laser diodes due to their influence on the dynamic response [1]-[6]. Although the nonlinearities may manifest themselves in a variety of ways, they are all associated with some form of carrier transport. For example, frequency chirp is due to variations in the index of refraction that result from the modulation of carrier densities in the QW and the separate confinement heterostructure (SCH) [7]. The low frequency rolloff in the intensity modulation (IM) response results from carrier leakage over the QW [8]. Also, the height of the resonant peak in the IM response depends on carrier transport in energy space, i.e. intrasubband scattering [9]. This paper will discuss the modeling of carrier transport using the Minilase-II laser simulator. Results will also be presented to illustrate transport effects and the effects of violations of local charge neutrality on the IM responses of single (SQW) and multiple quantum-well (MQW) lasers.

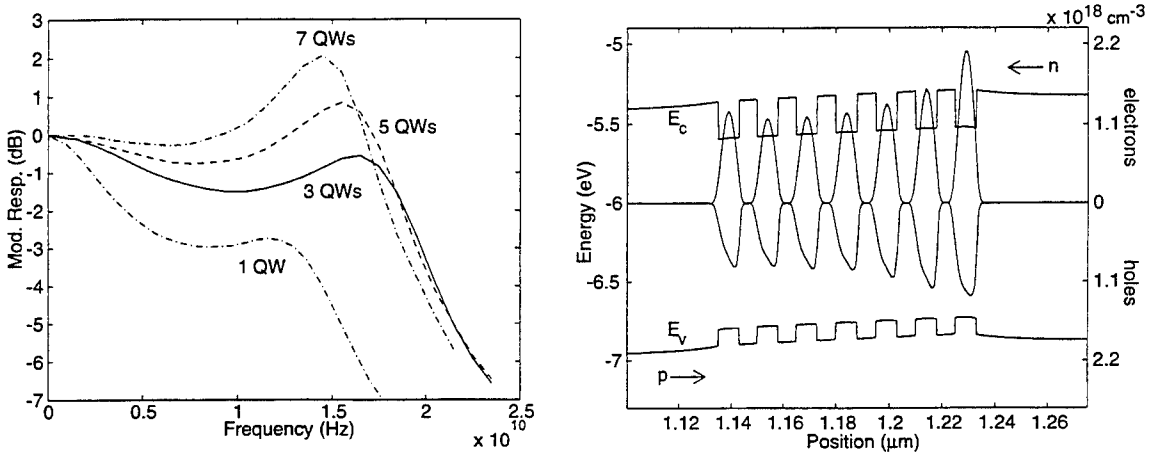


(a) (b)

Figure 1: (a) Simulated small signal IM responses for different capture rates. (b) The change in the electron densities and photon population as functions of time after a small change in external bias. The densities are plotted at certain key locations within the laser for $\tau_{cap} = 1$ ps.

Leakage current in a QW laser leads to additional diffusion capacitance which causes a low frequency rolloff that degrades the IM response [8]. As a result, explicitly treating the capture of injected carriers into the QW is very important for predicting the IM characteristics. Minilase-II models the capture process by treating quantum carriers that occupy the quasi-continuum states above the well separately from quantum carriers that occupy bound states inside the well. Continuum carriers can scatter into the bound states, resulting in

a net capture rate, or they can thermionically emit back into the bulk SCH. Carriers that are not captured contribute to the diffusion capacitance that degrades the IM response. Figure 1(a) shows a set of modulation responses calculated for a given SQW laser and a given bias using different capture rates. Figure 1(b) shows the time evolution of the photon population and electron densities resulting from a small change in bias current as calculated for $\tau_{cap} = 1$ ps. The curve labeled "continuum" refers to electrons in the quasi-continuum states above the well. The small increase in this density corresponds to a small amount of gain saturation that slightly decreases the height of the resonant peak. The curve labeled "p-SCH" shows a significant increase in minority electrons on the p-side of the bulk SCH. This increase in minority electrons corresponds to the charging of a diffusion capacitance that causes the significant low frequency rolloff observed in Figure 1(a).



(a) (b)

Figure 2: (a) IM responses for a set of lasers with different numbers of QW's. (b) The nonuniform distribution of bound electrons and holes in the seven QW's.

An obvious way to reduce the leakage current is to use multiple quantum wells. Figure 2(a) shows IM responses for a set of lasers that differ only in the number of QW's. Each laser is biased at 50 mA, corresponding to single facet output powers of about 26 mW. The low frequency range shows that the leakage current decreases with each additional QW. However, Figure 2(a) also shows that the resonant frequency, ω_{res}, first increases when the number of wells is increased from one to three but then decreases when the number of wells is increased further. This anomalous decrease in ω_{res} can be explained with Figure 2(b), which shows the densities of bound electrons and holes in the seven QW laser. The positions of the QW's are revealed by the variations in the conduction and valence band edges. The electrons are plotted such that their densities increase towards the conduction band, while the holes increase towards the valence band. The figure shows that the distributions of bound carriers are highly nonuniform. This nonuniformity becomes more severe with additional QW's and increased forward bias. Consequently, a small increase in the bias causes the occupation probability of the lasing states in the two wells closest to the p-side to actually decrease. The result is a decrease in the total differential gain and a decrease in ω_{res}.

In addition to real space transport, Minilase-II also treats carrier transport in energy space, i.e. spectral hole burning. It does this by dividing each QW into several real space cross sections. The bound energy range of each cross section is then discretized, and the net capture rate into each energy point is balanced with the recombination at that point

and the net scattering rate from all other energy points in the cross section. The simulator iterates between this spectral problem and the real space problem until both are satisfied self-consistently. Figure 3(a) shows three simulated IM responses calculated for the same laser under the same bias conditions. The simulations use different intrasubband scattering rates, as indicated by the labels on the responses. The figure shows that the low frequency rolloff is similar for each response. This indicates that spectral hole burning does not significantly affect the coupling of the bound states with the surrounding bulk states. However, the figure also shows that an intrasubband scattering rate of 10^{13} s^{-1} results in a significant decrease in the differential gain and the height of the resonant peak.

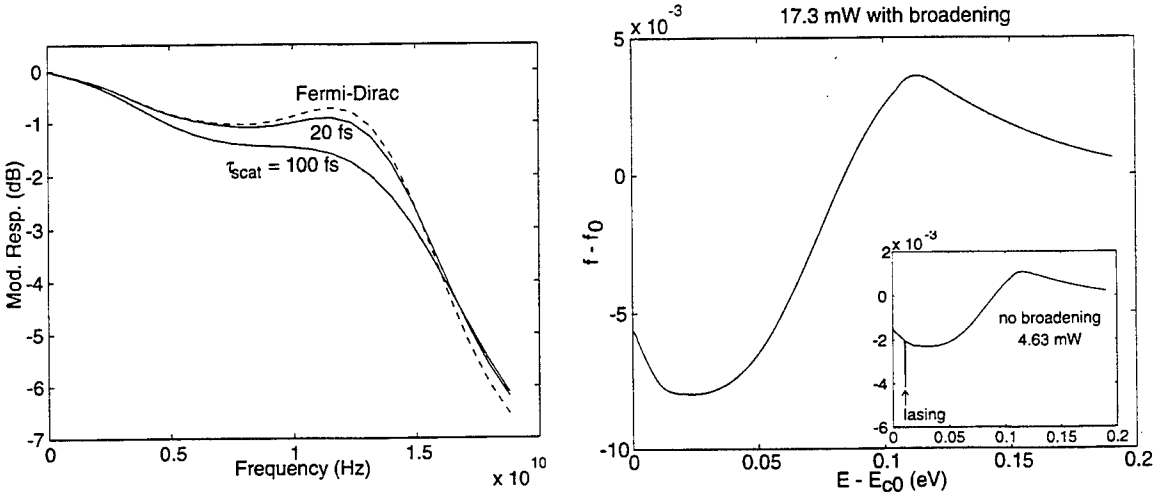


Figure 3: (a) IM responses calculated for the same laser and the same bias using different intrasubband scattering rates. (b) The difference between the bound electron distribution calculated for the τ_{scat} = 0.1 ps case and a quasi-Fermi distribution corresponding to the same electron density.

The decrease in differential gain due to spectral hole burning is also apparent from Figure 3(b), which shows the difference between the calculated electron distribution, f, and a quasi-Fermi distribution, f_0, corresponding to the same electron density. The rapid depletion of the lasing state by stimulated emission and the capture of higher energy carriers from the continuum states causes an increase in the average energy of the carriers when compared to the quasi-Fermi distribution. Note from Figure 3(b) that a very small perturbation of the distribution function, $< 1\%$, results in significant gain saturation. The figure also shows the effect of collision broadening on spectral hole burning. The inset of Figure 3(b) shows that an unbroadened optical transition produces a sharp and deep spectral hole at relatively low output powers when compared to a broadened transition. This result implies that collision broadening prevents the IM response from becoming overdamped by spectral hole burning.

We have presented here some of the salient features of Minilase-II, which, to our knowledge, is the first self-consistent laser simulator to explicitly treat carrier capture and spectral hole burning. The simulator shows that the carrier capture efficiency has very significant effects on the IM responses of both SQW and MQW lasers. Minilase-II also shows that stimulated emission can produce depletion and "heating" of the bound carriers which, although small in magnitude, can lead to sizeable gain saturation.

Acknowledgment

This work was supported by the Office of Naval Research and the Illinois NSF-ERC.

References

[1] A.A. Bernuusi, H. Temkin, D.L. Coblentz, and R.A. Logan, "Gain nonlinearity and its temperature dependence in bulk and quantum-well quaternary lasers", *IEEE Photon. Technol. Lett.*, vol. 7, pp. 348-350, 1995.

[2] C.H. Henry, R.A. Logan, H. Temkin, and F.R. Merritt, "Absorption, emission, and gain spectra of 1.3 μm InGaAsP quaternary lasers," *IEEE J. Quantum Electron.*, vol. 19, pp. 941-946, 1983.

[3] F. Girardin, G.H. Duan, C. Chabran, P. Gallion, M. Blez, and M. Allovon, "Determination of nonlinear gain coefficient of semiconductor lasers from above threshold spontaneous emission measurement," *IEEE Photon. Technol. Lett.*, vol. 6, pp. 894-896, 1994.

[4] H. Hirayama, J. Yoshida, Y. Miyade, and M. Asada, "Carrier capture time and its effect on the efficiency of quantum-well lasers," *IEEE J. Quantum Electron.*, vol. 30, pp. 54-61, 1994.

[5] T. Fukushima, R. Nagarajan, M. Ishikawa, and J.E. Bowers, "High speed dynamics in InP based multiple quantum well lasers," *Jpn. J. Appl. Phys.*, vol. 32, pp. 70-83, 1993.

[6] J. Huang and L.W. Casperson, "Gain and saturation in semiconductor laseres," *Optical and Quantum Electron.*, vol. 25, pp. 369-390, 1993.

[7] R.F.S. Ribeiro, J.R.F. da Rocha, A.V.T. Cartaxo, H.J.A. da Silva, B. Franz, and B. Wedding, "FM response of quantum-well lasers taking into account carrier transport effects," *IEEE Photon. Technol. Lett.*, vol. 7, pp. 857-859, 1995.

[8] M. Grupen, G. Kosinovsky, and K. Hess, "The effect of carrier capture on the modulation bandwidth of quantum well lasers," *Proc. of the Int. Electron Device Meeting*, ed. by IEEE, Washington DC, pp. 609-612, 1993.

[9] M. Grupen, K. Hess, and L. Rota, "Simulating spatial and spectral hole burning and the modulation response of quantum well laser diodes," in *Proc. of the SPIE Int. Conf. on Physics and Simulation of Optoelectronic Devices III*, vol. 2399, ed. by M. Osiński and W.W. Chow, San Jose, pp. 468-479.

Comprehensive Model of Vertical Cavity Surface Emitting Laser Performance

G. R. Hadley, K. D. Choquette
Sandia National laboratories, MS0603
Albuquerque, New Mexico 87185-5800

Vertical-cavity surface-emitting lasers (vcsels) are presently the subject of intense research due to their potential as compact, efficient, astigmatic laser sources for a number of important applications. Of special interest are the index-guided vcsels fabricated by selective oxidation, which have recently resulted in devices with record low thresholds[1] and record high wallplug efficiencies[2]. At present these devices are poorly understood at best, and their ultimate potential has yet to be realized. Unfortunately, their complexity precludes optimization based solely upon empirical methods, and points instead to the need for a comprehensive model.

In order to better understand the operation of these lasers and to allow accurate design optimization, we have constructed a highly-sophisticated and complete numerical model that simulates virtually all major device processes. This is the first vcsel simulation to include self-consistently the effects of thermal and carrier transport with a multimode optical model, so as to explore the onset of higher-order lateral modes. In particular, we include the following physical processes modeled in 3D (assuming cylindrical symmetry): (1) The Ohmic transport of carriers through the cladding layers to an active region, including anisotropic conductivities, (2) The transport of heat towards a heat sink beneath the substrate, including source terms from Ohmic dissipation, non-radiative recombination and reabsorbed laser radiation, (3) The diffusion of carriers inside the quantum well, and their recombination via spontaneous emission, stimulated emission, and non-radiative processes (both through traps and Auger transitions), (4) The cw behavior of five different optical cavity modes, denoted by their assumed azimuthal dependences of the form $\exp[\pm im\varphi]$, with $m = 0-4$, and (5) The interaction of each of these modes with carriers in the quantum well through a comprehensive gain model that includes effects arising from the strained band structure of our InGaAs quantum well.

Our optical model is based on a modified effective index method derived specifically for use in optical cavities[3]. This model simplifies the computation of the optical field by removing the spatial dependence normal to the mirror layers by integration, resulting in an effective index that depends (for cylindrically symmetric devices) only upon the radial coordinate. The resulting time-dependent Maxwell equation for the scalar field then has the form of a beam propagation equation and is solved using the familiar Thomas algorithm. When applied to the selectively oxidized vcsel structure shown in Fig. 1, this technique predicts an effective index step induced by the oxide layers that is different from that calculated from simple integral averaging methods, but in agreement with a value inferred from measurements of lateral mode spacing below threshold[4].

We have applied our comprehensive model to the simulation of selectively-oxidized lasers shown schematically in Fig. 1 with varying oxide apertures. Although the lasers were fabricated with square apertures, we performed the simulation assuming cylindrical symmetry with radii determined by equating areas. A typical result for a 3-μm diameter device is shown in Fig. 2. As can be seen, overall agreement is good, but the predicted performance is systematically better than the measured performance, with regard to threshold, output power, and quantum efficiency. We understand this discrepancy in terms of an extra "scattering" loss caused by the low-index oxide layer. This loss is not accounted for by the effective-index model, which averages the change in index over the wave profile, thus effectively washing out any large index variations. This procedure accurately predicts lateral confinement but cannot account for the excess scattering. The latter is studied by solving for the mode using a 2D finite-difference code that treats field variations in both the vertical and later directions. Modal losses calculated using this technique may then be inserted into the vcsel code for each lateral mode of interest.

1. G. M. Yang, M. H. MacDougal, and P. D. Dapkus, "Ultralow threshold VCSELs fabricated by selective oxidation from all epitaxial structure", Conference on Lasers and Electrooptics, paper CPD4-1, Baltimore, MA, May 21-26, 1995.

2. K. L. Lear, K. D. Choquette, R. P. Schneider, Jr., S. P. Kilcoyne, and K. M. Geib, "Selectively Oxidized Vertical Cavity Surface Emitting Lasers with 50% Power Conversion Efficiency", Electron. Lett. Vol. 31, No. 3, p208-209(1995).

3. G. R. Hadley, "Effective index model for vertical-cavity surface-emitting lasers", Optics Lett. Vol. 20, No. 13, p1483-1485(1995).

4. K. L. Lear, K. D. Choquette, R. P. Schneider, Jr., S. P. Kilcoyne, "Modal analysis of a small surface-emitting laser with a selectively-oxidized waveguide", App. Phys. Lett. 66, p2616-2618(1995).

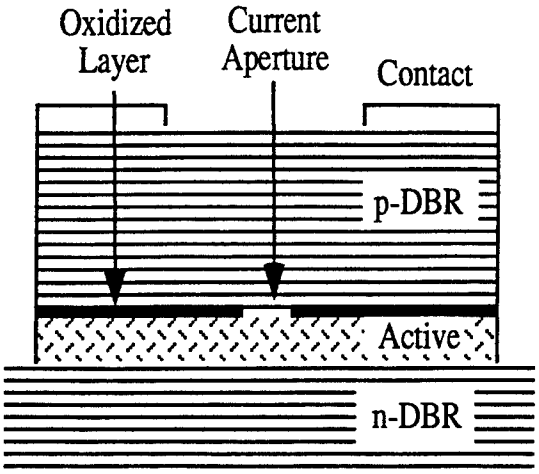


Figure 1.

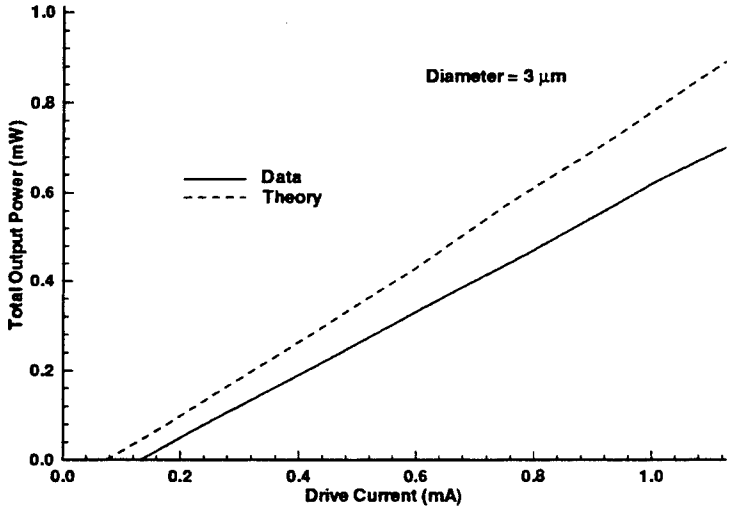


Figure 2.

Propagation of Defects in Hot-Carrier Degradation of LDD NMOSFETs - from the Early Mode to the Late Mode

A. Raychaudhuri[#], W.S. Kwan[#], M.J. Deen[#], and M.I.H. King*
[#]School of Engineering Science, Simon Fraser University, Burnaby, B.C., Canada V5A 1S6
***Northern Telecom Limited, 185 Corkstown Road, Nepean, Ontario, Canada K2H 8V4**

The purpose of this work is to model the propagation of defects from the spacer region of an LDD NMOSFET into the region under the gate using measurements and 2-D device simulation (MEDICI [1]). The reason for the two-stage degradation (see figs. 1 & 2) [2-7] is shown to be the saturating nature of the length of the degraded region that expands with stress, as opposed to defects accumulating at one place with increasing barrier height to defect creation (ϕ_{it}) [4], or decreasing lateral electric field (E_m) [6]. All MOSFETs tested/simulated had mask L=0.8 μm, T_{ox}=175 Å, spacer length of 0.2 μm, LDD P-dose of $2x10^{13}$ /cm^2 at 40 keV.

Based on the gate currents (I_G) (see fig. 3) obtained from a floating gate (FG) measurement [8,9], we use the Lucky-Electron Model (LEM) [10] to calculate the evolution of the barrier height to electron injection (ϕ_b) (see fig. 4) in the early mode of the degradation. The corresponding evolution of the parasitic drain resistance (R_D), extracted from reverse saturation transconductances ($g_{m,sat}$) using a new method [11] is superimposed on the ϕ_b evolution. Remarkable correlation between these two evolutions point to a region with negative trapped charges in the oxide near the interface over the gate edge region, indicated by Region 1 in fig. 9. From extensive simulations, we found that using $2.5x10^{18}$ /cm^3 trapped electrons over 100Å above the interface matches with our calculated ϕ_b (~0.6eV) and simulates an equivalent potential barrier (see fig. 5). The simulations based on this damage also agree well with the drop and flattening of I_G (see fig. 3), drop in I_B (see fig. 6), linear I_D degradation with gate bias (fig. 7), and the voltage shifts in the reverse saturation I_D-V_G characteristics (fig. 8), measured before and after the FG cycles. Thus, the location and quantity of the defects corresponds to the early mode of the degradation where R_D increase is the main phenomenon [12]. On the other hand, placing the damage region before the electron temperature peaks, marked as Region 2 in fig. 9, does not produce matching simulation results as indicated in figs. 6-8. However, the simulated trend of the degradation with defects placed in Region 2 matches the late mode of degradation, where I_B increases, linear I_D degradation falls with gate bias [2], and V_T shifts occur. These observations coupled with the simulated lateral electron temperature (T_e) profiles (figs. 9-11) indicate the following points. 1. The defects attract the T_e peaks outwards and the damage profile moves inwards with stress. 2. The negatively charged defects, whatever their position, always increase the interfacial peak T_e (see fig. 10); however, their location influences the pushing of the electron currents below the interface (see fig.11), thus affecting I_B (see figs 2 and 6), and possibly determining the physics of the degradation - R_D increase versus mobility degradation/V_T shift.

Based on the above picture, we assume a saturated damage region of a fixed number of interfacial defects moves with stressing time t, and that N_{it} is given by a function of $(t\cdot(I_D/W)\cdot\exp[-\phi_{it}/(q\lambda E_m)])$ [3], where λ is electron mean free path, W is device width, q is electronic charge, and E_m is the maxima of lateral electric field (E) profile. We can show that the damage region length x increases with time t as

$$x = \frac{\frac{E_m}{s}\cdot ln\left(\frac{t}{t_0}\right)}{\frac{\phi_{it}}{q\lambda E_m} + ln\left(\frac{t}{t_0}\right)}, \qquad (1)$$

where E_m corresponds to the T_e maxima under damage for a particular stress V_{GS} in fig. 9, and s is the magnitude of the slope of E versus x into the channel as obtained by converting the slope of linearly falling T_e's into that of E's. Using expressions for E_m and E versus T_e from [13], and using a value of 7.3 nm [13] for λ, we plot x vs. t for V_{GS}=5V and V_{DS}=7.5V in fig. 12. The two-stage saturating nature of growth of the degradation length is evident from this qualitative picture, for which t_0 was taken to be 100s, to roughly match the degradation length after the early mode degradation. This figure suggests that it will take about 10 years to reach a degradation length of just above .1 μm. Further work needs to be done to correlate the current degradation to x, and to consider non-uniform density of defect sites along the length. But, the eqn. (1) tells us that for fixed density of defect sites along the interface, the growth of the degraded region is indepenent of the number of defect sites.

REFERENCES:

[1] TMA MEDICI Two-Dimensional Device Simulation Program, Version 2.0, Technology Modeling Associates, Inc., Palo Alto, California, 1994.

[2] V.-H. Chan and J. E. Chung, IEEE Trans. Electron Devices, vol. 42, p. 957, 1995.

[3] J.-S. Goo, H. Shin, H. Hwang, D.-G. Kang, and D.-H. Ju, Jap. J. Appl. Phys., vol. 33, p. 606, 1994.

[4] C. Liang, H. Gaw, and P. Cheng, IEEE Electron Device Lett., vol. 13, p. 569, 1992.

[5] Q. Wang, W.H. Krautschneider, M. Brox, and W. Weber, Microelectronic Eng., vol. 15, p. 441, 1991.

[6] K.M. Cham, J. Hui, P.V. Voorde, and H.S. Fu, Proc. 25th Int. Conf. Reliab. Phys., 1987, p.191.

[7] A. Raychaudhuri, W.S. Kwan, and M.J. Deen, in 7th Canadian Semicond. Tech. Conf., 1995, p. 94.

[8] A. Raychaudhuri, M.J. Deen, M.I.H. King, and W.S. Kwan, IEEE Trans. Electron Devices, accepted for publication, 1995.

[9] M.J. Deen and A. Raychaudhuri, Proc. of the third symposium on silicon nitride and silicon dioxide thin insulating films, Eds. V.J. Kapoor and W.D. Brown, The Eletrochemical Society, Inc., 1994, p. 375.

[10] S. Tam, P.K. Ko, and C. Hu, IEEE Trans. Electron Devices, vol. 31, p. 1116, 1984.

[11] A. Raychaudhuri, J. Kolk, J. Deen, and M.I.H. King, IEEE Trans. Electron Devices, vol. ED-42, p. 1388, Jul. 1995.

[12] Y. Pan, K.K. Ng, and C.C. Wei, IEEE Electron Device Lett., vol. 15, p. 499.

[13] C. Hu, 'Hot-carrier effects', in Advanced MOS Device Physics, VLSI Electronics Microstructure Science, vol. 18, Eds. N.G. Einspruch and G.Sh. Gildenblat, Academic Press, Inc, 1989.

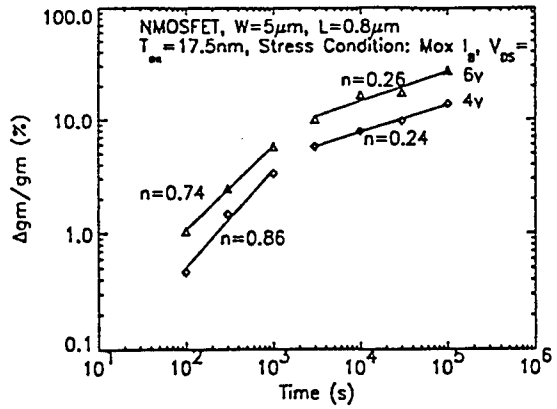


Figure 1. Evidence of two-stage hot-carrier degradation in oxide-spacer LDD NMOSFET characterized by a sharp rate (high n) of initial degradation, and a much slower rate (low n) afterwards.

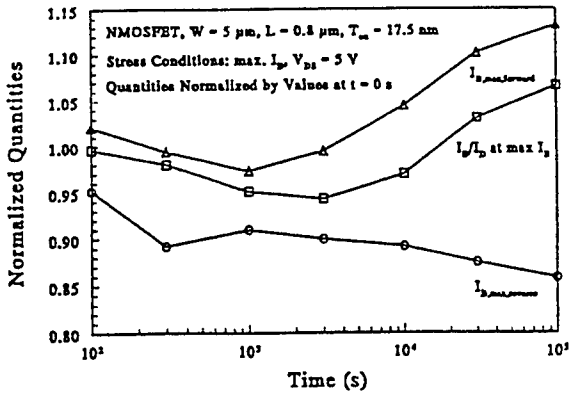


Figure 2. Both $I_{B,max}$ and I_B/I_D at max. I_B measured in the forward mode drop in the initial phase. As we show later, this does not mean that the electron temperature is falling. In the reverse mode $I_{B,max}$ falls all the way as in conventional degradation.

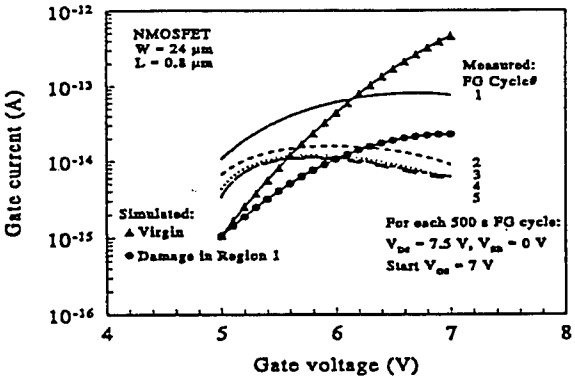


Figure 3. Gate currents extracted from five 500s-floating gate (FG) cycles. Progressive decrease and shift in peak are notable. Simulated gate currents for virgin and damaged device (for Region 1 see fig. 10) are superimposed.

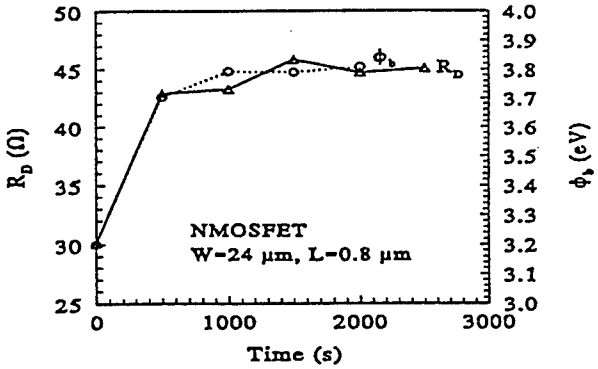


Figure 4. Evolution of drain parasitic resistance R_D and the barrier height to electron injection ϕ_b, extracted from reverse saturation transconductances and the measured gate currents of fig. 3 respectively. The remarkable correlation is notable.

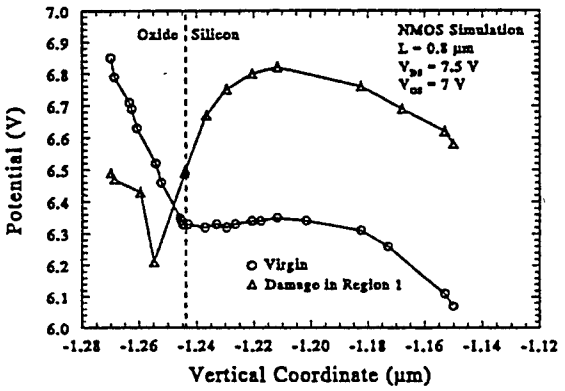


Figure 5. Simulation of the vertical potential profiles at the peak of lateral electron temperature profiles (see fig. 10). ϕ_b of ~0.6eV as observed in fig. 4 is obtained in simulation here with the damage located in Region 1 of fig.10.

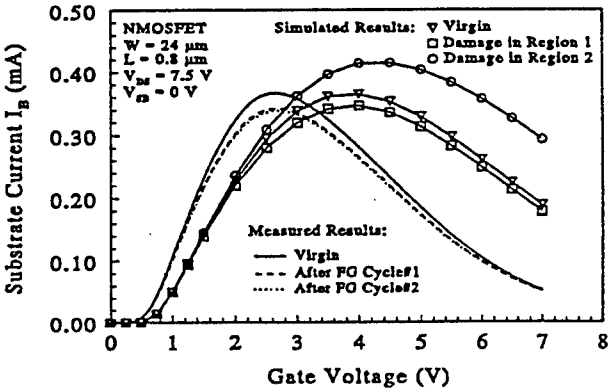


Figure 6. Decrease of measured I_B with the FG cycles. The current does not change much after the FG cycle #2. Simulated I_B for virgin and damaged (both Regions 1 & 2 of fig. 10) devices suggests that the probable location of damage is Region 1 (gate edge).

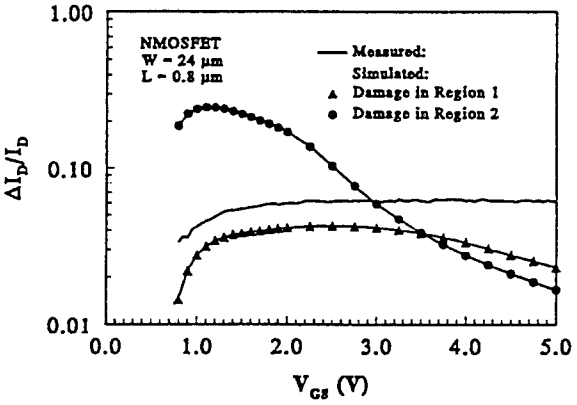


Figure 7. Measured linear current degradation vs. gate bias over the 5 FG cycles matches better with the simulated values for damage in Region 1 (see fig. 10).

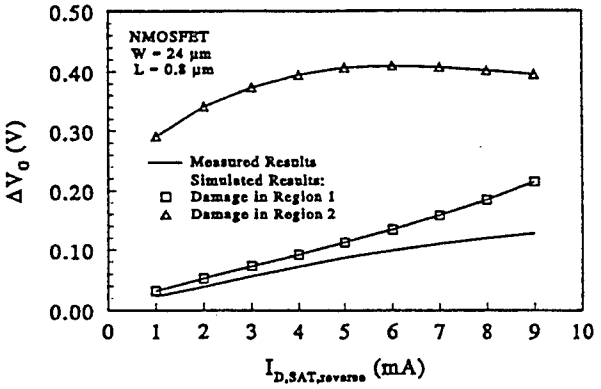


Figure 8. Measured voltage shift in the reverse $I_{D,sat}$ vs. V_G curve with V_D=5 V over the 5 FG cycles matches better with the simulated values for damage in Region 1 (see fig. 10).

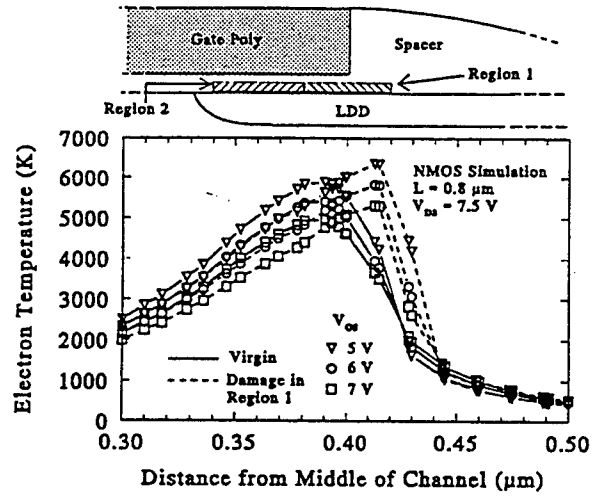


Figure 9. Lateral electron temperature (T_e) profiles for virgin and damaged device (damage in Region 1). The damage attracts T_e peaks outwards, and, damage profile moves in with time.

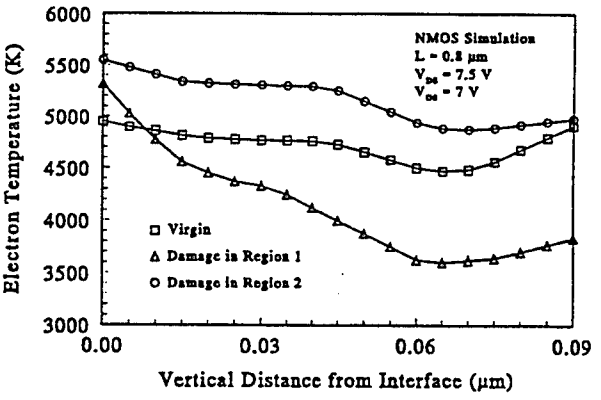


Figure 10. Simulated vertical electron temperature profiles into silicon from the interface through the lateral electron temperature peaks (as in fig. 10). Sharp fall for damage in Region 1 is notable.

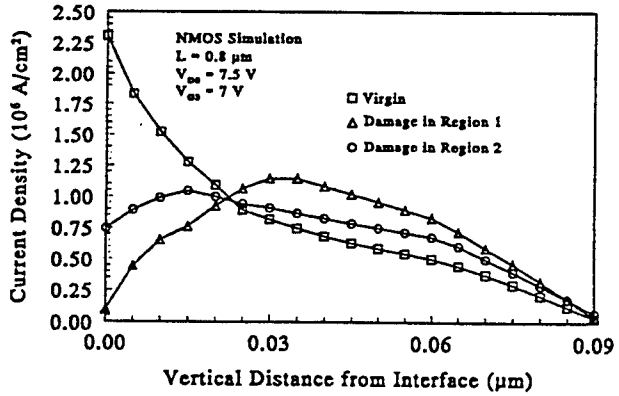


Figure 11. Simulated current density profiles into silicon from the interface through the lateral electron temperature peaks (as in fig. 10). The profile gets pushed inwards for damage in Region 1.

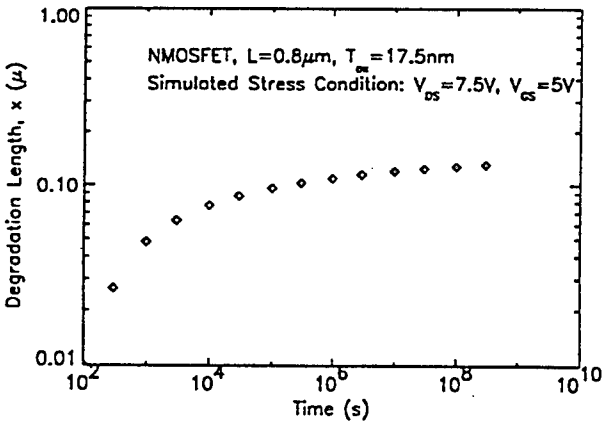


Figure 12. Growth of the degradation length with time for the case with V_{GS}=5V and V_{DS}=7.5V of fig. 9. The two-stage nature of the process is evident. The model for this growth is given by eqn. (1).

Technology-CAD applied to the development of DMOS devices

D. Wojciechowski, A. Van Calster
University of Gent, ELIS-TFCG/IMEC, Sint-Pietersnieuwstraat 41, 9000 Gent, Belgium

J. S. Witters
Alcatel-Mietec, Westerring 15, 9700 Oudenaarde, Belgium

Introduction

The performance of MOS-transistors has progressed significantly over the recent years. This is due to experience built-up and much better process and device simulations. This has lead to the development of Technology-CAD (TCAD). TCAD enables one to achieve optimum performance within a given technology without having to build costly test lots [1]. The TCAD tools used in this paper are from Silvaco Data Systems [2]. Among the most important ones are Athena (process simulation) and Atlas (device simulation).

Inside a BiCMOS technology [3] and thanks to TCAD, new MOS-devices have been developed. First, a Vertical-double Diffused MOSFET with a Terraced-Gate (TG-VDMOS) is studied. The unique gate structure of the TG-VDMOS reduces the on-state resistance, without increasing the device's area, resulting in improved power performance. Secondly, Symmetrical-DMOSs (SDMOS) are shown to be well suited as a switch for x-Si Active Matrix Liquid-Crystal Displays (AMLCD) where high driving voltages are required.

TG-VDMOS

Terraced-gate VDMOS is made by forming a thick oxide layer on the gate-drain overlapping region. Such Terraced-gate [4] is the result of a controlled LOCOS [5] process. The cross section of the TG-VDMOS is shown in Fig. 1.

Process simulation: The input syntax of TCAD simulators permits the development of 2D-physical structures by means of a baseline process flow that results from real processing steps. The process flow is modular: starting from a core CMOS process, a TG-VDMOS is added as a module. The n-type silicon surface is subjected to a dry thermal oxidation in a manner to grow a basic pad-oxide where the field oxide and the gate oxide will be defined, following a LOCOS process. The field oxide is grown at 1000 C under wet oxidation conditions. Onto this, some 0.4 μm of polycrystalline silicon, heavily doped with phosphorous, is deposited. This forms finally the Terraced-gate. Then, the core CMOS subsequent process steps complete the structure. For process simulation, we make use of fact that the TG-VDMOS structure is symmetrical; a mirror and a stretching (control of the TG-length) operations give the final device structures. Fig. 1 shows the simulated structure. The drain is located at the backside of the substrate. The gate oxide film and the field oxide thickness' are respectively 410 Å and 6700 Å. The resulting lateral channel length is 4 μm. The distance between the two p-bodies is 10 μm for a constant device length and width of 21.5 μm and 1 μm, respectively.

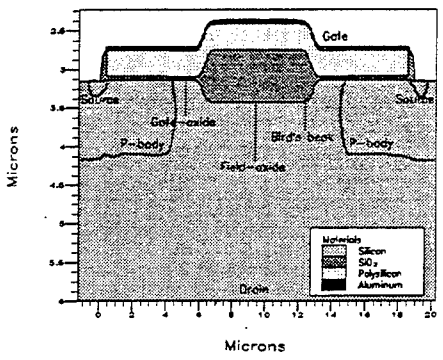


Fig. 1: Cross section of a simulated 6 µm Terraced-gate length VDMOS; the p/n junctions are drawn.

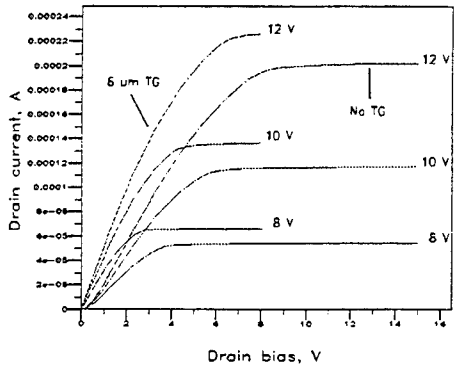


Fig. 2: Simulated output characteristics of TG-VDMOS normalised on 1 µm channel length width.

Device simulation: The device simulation consists of a 2D-computation of the potential, electron, hole, and energy distributions inside the structure as a function of the applied bias. This computation is done by using finite element approximations to Poisson's and electron and hole continuity equations. Fig. 2 shows the simulated I-V output characteristics for 3 gate to source voltages and 2 devices configurations having a 6 µm TG and no TG. The current-voltage characteristics are normalised on 1 µm channel width. The output characteristics are modified in the linear and saturation region owing to the TG existence leading to a better Ron. The explanation of this phenomenon is given by the simulation results: the improvement in Ron is due to an improved separation of the current flows thanks to the TG presence.

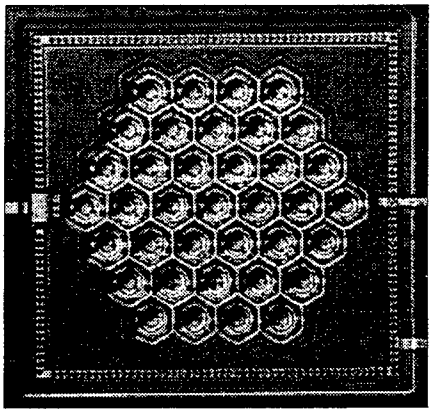


Fig. 3: Photograph of a Hexagonal Terraced-gate VDMOS chip with 37 cells.

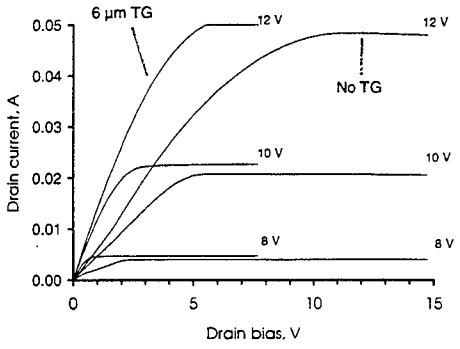


Fig. 4: Experimental I-V characteristics of 37 paralleled Hexagonal TG-VDMOS.

Device fabrication and measurement: In order to obtain a dense stacking, the TG-VDMOS are made hexagonal and paralleled. Experimental devices were fabricated following the BiCMOS technology briefly described above [3]. A photograph of the chip is shown in Fig. 3. The hexagonal white shape contrast is due to the 6 µm TG thicker oxide presence between the devices. The gate oxide and the field oxide thickness' are respectively 800 Å and 12500 Å. The I-V characteristics of 37 paralleled HEX-TG-VDMOS are shown in fig. 4. It is an overlay plot of output characteristics for 3 gate to source bias conditions for 2 devices comparable with ones used for building fig. 2. The main conclusion extracted from these curves, as expected from simulations, is that the Ron is greatly improved for the structure with a TG. A TG leads also to slightly higher source to drain current saturation.

S-DMOS

Transmissive single-crystal silicon Active Matrix Liquid Crystal Displays (x-Si AMLCDs) are rapidly moving from development to production [6]. These displays are formed by a unique process in which the active matrix circuits are fabricated as integrated circuits (ICs) on silicon wafers and subsequently transferred to glass for LCD assembly. The active matrix circuit is formed using standard CMOS design rules and processing instead of thin-film technologies. This means that the AM circuits can be fabricated in an existing IC facility (BiCMOS technology [3]) using NMOS (or PMOS) that is typically designed to operate at less than 18 V [7]. However, a higher operating voltage is needed for some liquid crystals. At this point, the supported working voltage can be increased by implementing the AM circuit with high voltage DMOS transistors (100 V) of the BiCMOS technology. But DMOSs are not ideal because they are not symmetric. So, based on DMOSs, new devices have been developed: Symmetrical-DMOSs (SDMOSs) which still support high voltages.

Experimental n-MOS: For display applications, the important criteria are a high drive voltage and a low off-current characteristics of the pixel transistor. Fig. 5 shows such experimental current-voltage characteristic of a n-MOS transistor which sustains a breakdown voltage of 18 V. Note that the off-current is lower than 1 pA while the drive current approaches 1 mA for this single gate transistor having a 15 µm channel width and 15 µm channel length. This is representative of what can be achieved in the CMOS circuitry for a pixel switch.

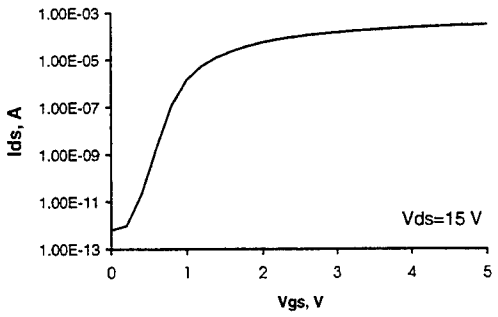


Fig. 5: Experimental current-voltage characteristic for a 15 µm width x-Si n-MOS transistor (to compare with the SDMOS).

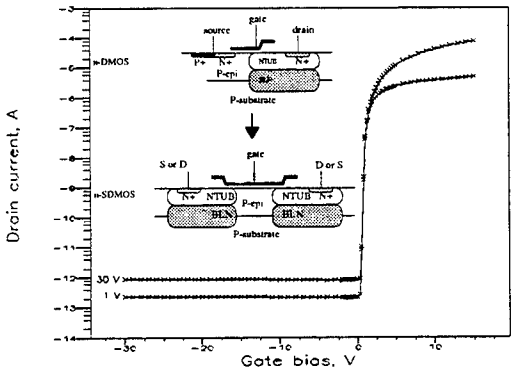


Fig. 6: Simulated current-voltage characteristics for a n-SDMOS described in insert.

Process simulation: The electrical performance of the x-Si devices are equivalent before and after transfer to glass substrates. Here, non-transferred n-type SDMOS devices are depicted. The process is similar to the TG-VDMOS, only a buried layer and n-type TUB is added. The schematic cross section of a normal n-DMOS and the derived n-SDMOS are given as an insert in fig. 6. The channel is located in a p-epi layer.

Device simulation: Fig. 6 shows the simulated current-voltage characteristics of a n-channel SDMOS for two drain to source voltages (0 and 30 V). In the off-state (Vgs<0), the current is limited by the p-n junction between the channel and the NTUB and by the intrinsic resistivity of Silicon. For Vgs larger than the threshold voltage Vt, a n-type channel is formed. From the device simulation, we found that the output characteristics are similar to the classical n-MOS transistor with linear and saturation regions. As a result, the off and on current are comparable to conventional n-MOS but with a much higher avalanche breakdown. Consequently, SDMOS can be used in AMLCD as a pixel switch replacing a low voltage n-MOS switch.

Conclusions

The use of simulation tools has proven to be a valuable aid in the development and characterisation of new type of structures while reducing the cost. Based on a BiCMOS technology, process and device simulation tools have been used to study new devices: Terraced-gate VDMOS and Symmetrical-DMOS transistors.

The terraced-gate technique gives the possibility to decrease the total resistance without increasing the device's area and to avoid technological limitations and parasitic phenomena related to small dimensions. Nevertheless, there are some requirements: the optimum TG-VDMOS, in point of view of the minimum Ron achievement, depends mainly on device layout considerations. TCAD simulations is really suited for such considerations.

N-type SDMOS as a pixel switch allows to use higher voltage liquid-crystal materials in silicon active matrix displays. Its output characteristics are comparable to classical n-MOS ones but with driving voltages up to 100 V. Moreover, storage and parasitic or overlapping capacitances, leakage currents in x-Si AMLCD using SDMOS can be evaluated with TCAD.

References

[1] M. E. Law, 'The virtual IC factory...can it be achieved ?', *IEEE circuits & Devices*, 1995, pp. 25-31

[2] Silvaco International, 'The Silvaco solution for Technology CAD', *Simulation Standard*, 1994, **5**, pp. 4-7

[3] J. S. Witters, 'A modular BICMOS technology including 85V DMOS devices for analogue/digital ASIC applications', *Microelectronic Engineering*, 1992, **19**, pp. 555-560

[4] D. Ueda, H. Takagi, G. Kano, 'A new vertical double diffused MOSFET-The self-aligned Terraced-gate MOSFET', *IEEE Trans. on Electron Devices*, 1984, **ED-31**, pp. 416-420

[5] J. A. Appels, E. Kooi, M. M. Paffen, J. J. H. Schatorjé, W. H. C. G. Verkuylen, 'Local oxidation of silicon and its application in semiconductor-device technology', *Philips Res. Repts*, 1970, **25**, pp. 118-132

[6] J. P. Salerno, 'Single crystal silicon AMLCD's', *Proceeding of the International Display Research Conference*, 1994, pp. 39-44

[7] J. De Baets, A. Van Calster, H. De Smet, J. Van Den Steen, G. Van Doorselaer, D. Wojciechowski, G. Schols, J. Witters, 'Design of an x-Si active matrix for high resolution reflective displays', to be published in the *Proceedings of the Asia Displays'95*, october 16-18, 1995

β-MOS FET: a Novel High Performance Transistor

Kanji Yoh[a], Ryouji Koizumi[a]
(a) Research Center for Interface Quantum Electronics, Hokkaido University,
North 13, West 8, Kita-ku, Sapporo 060 Japan (phone)+81-11-706-6872

Naotaka Hashimoto[b] and Shuji Ikeda[b]
(b) Semiconductor & Integrated Circuits Division, Hitachi Ltd.,
5-20-1 Josuihoncho, Kodaira-shi, Tokyo 187, Japan

We have fabricated a β (Bipolar Enhanced Transistor Action) MOS FET device which operates in combined FET and bipolar modes *with extended operational voltage* up to -4 volts due to gate-voltage-controlled base resistance of the parasitic lateral bipolar transistor. The p-channel β-MOS FET showed dramatic improvements in transconductance by a factor of 4 while maintaining the same threshould voltage(≈-1V) compared with conventional MOS structures.

There have been attempts to incorporate bipolar action in MOSFET structure[1-2]. However, the reported devices operate basically in bipolar mode although the structure appears to be a MOSFET. As a result, the device operates only when the gate (base) voltage is below V_F(≈0.7V) of the base-emitter diode. On the other hand, high performance MOSFET is reported using ultrathin tunneling gate oxide[3]. Here we propose a new approach which is different from above approaches but has somewhat common features with both of them: a MOSFET with small gate-to substrate contact (some samples with ultrathin tunnel barrier) which operates in mixed bipolar-FET mode,while perfectly maintaining the MOSFET circuit configuration.

The β-MOS device has a generic MOS structure with single Boron diffusion source/drain except that there is small (0.3 - 0.5 μm$^{\square}$ in the present case) contact hole between the gate n^+-poly and the n^--substrate as shown in Fig.1. The structure can be regarded as a MOSFET with parasitic bipolar transistor *whose emitter/collecor is 2 dimensional hole gas*. The nominal gate oxide thickness was nominally 90Å. Basically, we have investigated 3 types of structures plus one control structure (conventional MOSFET) as shown in Fig.2. Sample A has direct contact hole between gate and substrate, sample B and C have 15Å and 30Å of oxide inserted at the pinhole contact between poly and the substrate, respectively, in order to further reduce the gate leakage current. The gate electric field helps to control the gate-to-substrate resistance, which helps to soften the rapid increase of the gate leakage current at high gate biases as depicted in Fig.1(b).

Maximum transconductance of 325mS/mm and the saturation current of 100 mA/mm (with Vg set to -1.8 volt) were obtained with 1.3μm-gate-length device with no control-oxide at the interface of the pinhole contact as shown in Fig.3 and 4. The effect of inserted tunnel barrier is shown in Fig.5 and 6. Sample A (0Å oxide) operates with gate voltage up until -2V with quadrupled maximum transconductance. Sample B (15Å oxide) operates with extended gate voltage with only 50% increase in maximum transconductance. Sample C showed only 30% increase in maximaum gm. Gate-to-substrate contact size dependence on gm and Ig shows that the critical contact(gate-to sub.) size falls in 0.35μm below which parasitic BJT becomes depleted base mode as shown in Fig.7. Transconductance and Ig turn-on voltage dependence on gate length shows clearly that the β-MOS superiority to conventional MOSFET develops rapidly in the short channel limit as shown in Fig.8. The present result demonstrates that the β-MOS could be a candidate of a new type of high speed device in the era of deep submicron.

[1] S.Verdonckt-Vanderbroek et al, IEEE Trans.Electron.Devices, Vol.38, pp.2487-2495(1991)
[2] S.Verdonckt-Vanderbroek et al, IEEE Electron. Device Lett., Vol.13, pp.312-313 (1992)
[3] H.Momose et al, IEDM Tech.Dig. pp.593-596, 1994

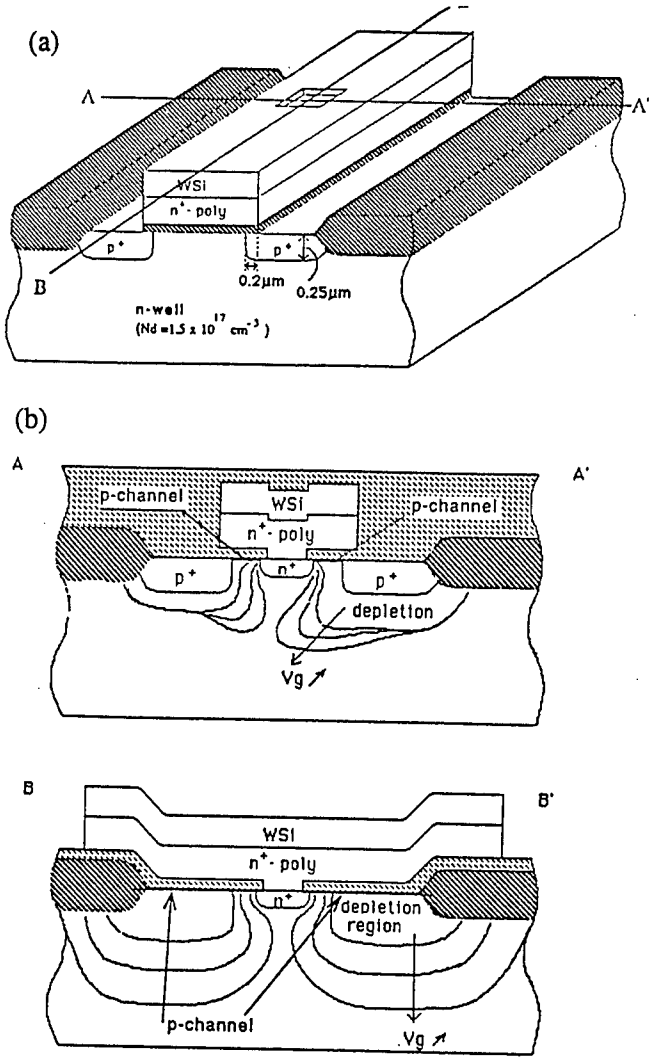


Fig.1 (a) Schematic diagram of β-MOS structure. (b) Schematic cross sectional diagram of β-MOS FET (Sample A).

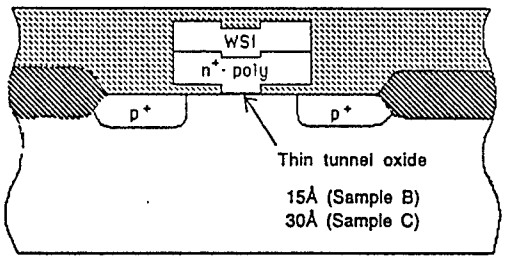


Fig.2 Schematic diagram of SampleB (15Å of tunnel barrier.) and Sample C (30Å of tunnel barrier.)

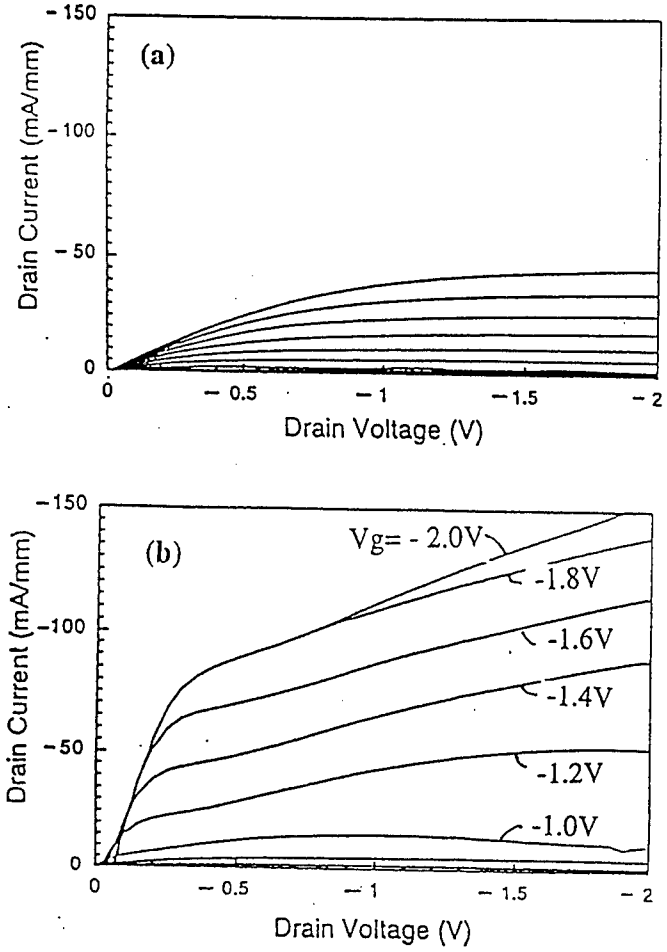


Fig.3 Drain current versus drain voltage characteristics of (a) the conventional and (b) β-MOS FET(Sample A).

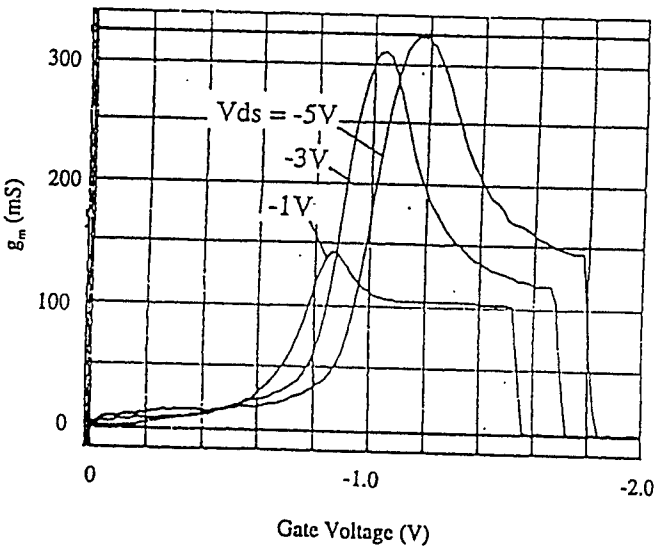


Fig.4 Transconductance vs gate voltage characteristics of β-MOS FET (Sample A).

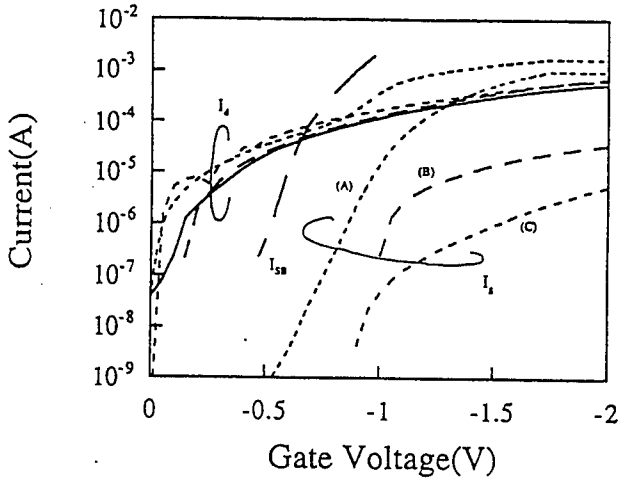


Fig.5 Id,Ig dependence on Vg.
Reduced gate voltage can be seen in the order of ISB(Lateral BJT), Sample A, Sample B, SampleC.

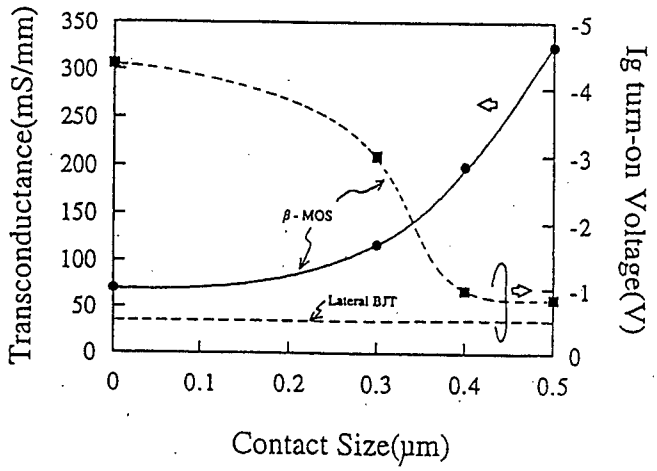


Fig.7 Gate-to-substrate contact size dependence on gm and Ig

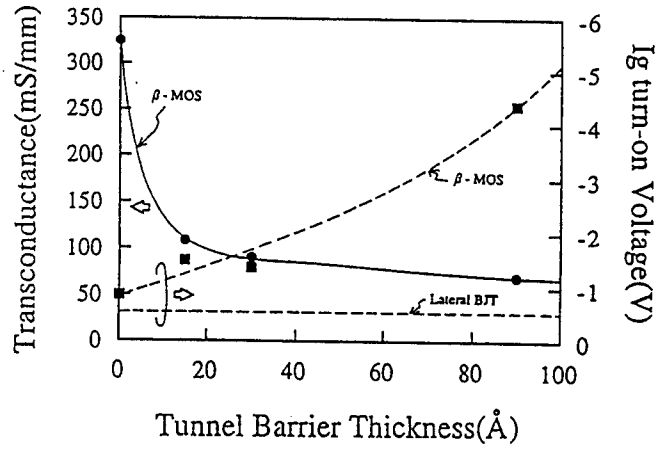


Fig.6. Transconductance and Ig turn-on voltage dependence on tunnel barrier thickness.

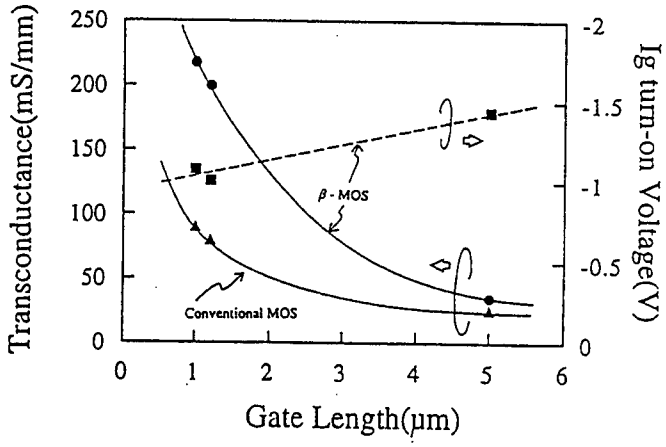


Fig.8. Transconductance and Ig turn-on voltage dependence on gate length

Self-Consistent Model for Fully Depleted SOI/MOSFETs Including Self-Heating

Yuhua Cheng*# and Tor A. Fjeldly*
*Dept. of Physical Electronics, Norwegian Inst. of Technology, N-7034 Trondheim, Norway
Institute of Microelectronics, Peking University, Beijing 100871, China

Abstract– We present a new, physically based *I–V* model including self-heating for fully depleted SOI MOSFETs. The model is intended for use in circuit simulation and accounts for drain induced conductivity enhancement (DICE) and barrier lowering (DIBL) as well as channel length modulation (CLM), and describes the subthreshold, near threshold and above threshold regimes of operation using one single expression. It also ensures a continuous transition of current and conductance from the linear to the saturation regime. The model shows good agreement with measured data for devices with a wide range of channel lengths (down to 0.28 μm) and film thicknesses (94 nm – 162 nm).

Introduction Thin film SOI/MOSFETs are becoming increasingly competitive with bulk MOSFETs in submicrometer CMOS applications, creating a need for accurate and efficient SOI/MOSFET models for use in circuit simulators. But it is well known that fully depleted SOI devices are particularly susceptible to self-heating effects (SHE) [1,2], which cause reduced drain current and negative differential conductance [3,4]. Up to now, the influence of SHE on the electrical characteristics of SOI devices has been simulated with two-dimensional device simulators (TDDS) incorporating heat flow [5], or by combining a temperature (T) rise model with an intrinsic *I-V* expression through an iteration procedure [6]. However, both the heavy calculations involved in TDDS and additional iterations are time consuming and inconvenient in circuit simulations. Instead, efficient analytical models with fully closed expressions are preferred for circuit CAD.

A SPICE *I–V* model for fully-depleted SOI devices was recently suggested by Su et al. [7]. This model which is based on a bulk MOSFET model differs in principle from that of SOI devices in several repects, owing to fundamental differences in device structure. Moreover, the influnce of SHE on the temperature-dependent parameters in the model cannot be determined self-consistently through the *I–V* model itself, and an extra optimization step is needed in order to obtain suitable parameters to fit the measured data. Hence, this model also tends to be inconvenient for use in SOI/MOSFET circuit simulation.

Here, we present for the first time a unified, physically based *I–V* model including SHE for fully depleted SOI/MOSFETs with channel lengths down to the deep submicrometer range. The *I–V* expressions describe characteristics in the subthreshold, near-threshold and above-threshold regimes of operation using one single expression with a fully closed analytical form suitable for circuit simulators such as SPICE, but including SHE self-consistently. The model is in good agreement with measured data for devices of various channel lengths (down to 0.28 μm) and film thicknesses.

I-V model The present model is based on a previously developed unified SOI/MOSFET *I–V* model [8,9], but containing the temperature dependencies of key physical parameters, such as mobility μ_n, threshold voltage V_T, saturation velocity v_s, and the impact ionization parameter β_i. The following set of well know empirical relationships summarized from experiments were used to describe the temperature dependencies of these parameters [10,11]: $\mu_n = \mu_{no}(T/T_o)^{-n}$, $V_T = V_{To}[1 - (T_c - T_o)/T_V]$, $v_s = 2.4\text{x}10^7/[1 + 0.8\exp(T/600)]$, and $\beta_i = \beta_{io}[1 + (T_c - T_o)/T_\beta]$. To obtain an analytical model in a fully-closed form, the relationships for μ_n and v_s are linearized as follows: $\mu_n = \mu_{no}[1 - (T_c - T_o)/T_\mu]$, $v_s^{-1} = v_{so}^{-1}[1 - (T_c - T_o)/T_v]$. Here T_c and T_o are the absolute temperatures of the silicon film and of the substrate, respectively, μ_{no}, V_{to}, v_{so} and β_{io} are parameter values at temperature T_o without self-heating, and T_μ, T_V, T_β,

and T_V are appropriate temperature coefficients for these parameters, all extractable from experiments.

The temperature rise in the active silicon layer can be described by the expression [2]:

$$T_c = T_o + R_{th} I_d V_{ds} \tag{1}$$

where I_d and V_{ds} are drain current and the drain-source voltage, respectively, $R_{th} = \kappa t_{ob}/(\lambda WL)$ is the thermal resistance of the buried oxide layer, t_{ob} is the thickness and λ is the thermal conductivity of this layer, W and L are channel width and length, and κ is a fitting parameter to account for the effects ignored by the simple model.

An analytical SOI/MOSFET I–V expression that includes SHE self-consistently can be found by combining (1) with the basic I–V model for the below-saturation regime [8,9], using the above temperature dependencies of the parameters:

$$I_{DL} = \frac{I_{DLo}}{1 + X R_{th} I_{DLo} V_{DS}} \tag{2a}$$

where

$$X = \frac{1}{T_\mu} - \frac{V_{To}}{\alpha V_{bo} T_V} - \frac{a n_{so} V_{To} / \left(\alpha^2 V_{bo} T_V\right) + 2\eta k_B/(q\alpha)}{1 - V_{DS}/(2V_{bo})} \tag{2b}$$

Here I_{DLo} is the current in the linear regime and n_{so} is the electron sheet charge density at the source side of the channel, both at the ambient temperature ($T_c = T_o$) [8,9]. Furthermore, V_{DS} is the intrinsic drain-source voltage and $V_{bo} = (a n_{so} + 2\eta k_B T_o/q)/\alpha$, where α (body factor), η (ideality factor) and $a \approx q/c_{of}$ (c_{of}: front oxide capacitance per unit area) are parameters of the unified charge control model [12].

The expression for the intrinsic saturation voltage (including SHE) becomes:

$$V_{SAT} = \frac{2V_{SATo}}{\chi + \sqrt{\chi^2 - 4X R_{th} I_{SATo} V_{SATo}}} \tag{3a}$$

where

$$\chi = 1 - R_{th} I_{SATo} V_{SATo} \left[\frac{1}{T_\mu} - \frac{V_{To}}{\alpha V_{bo} T_V} - \frac{a n_{so} V_{To} / \left(\alpha^2 V_{bo}^2 T_V\right) + 2\eta k_B/(q\alpha)}{2V_{bo}/V_{SATo} - 1} \right] \tag{3b}$$

Here V_{SATo} and I_{SATo} are the saturation voltage and current at the room temperature [8,9].

The corresponding expression for the current in the saturation regime was derived using the requirement that the drain conductivity be continuous at the onset of saturation. Adding the series resistances, we also succeed in obtaining analytical expressions for the extrinsic I–V characteristics. A full account of these results will be reported elsewhere [13].

Results and Discussion The present I–V model is in good agreement with measured data for various channel lengths and film thicknesses in all regimes of device operation, as indicated in Figs. 1-4. Note that only one additional fitting factor (κ in the thermal resistance) was used to include SHE. The results predicted by the model without SHE (letting $R_{th} = 0$) show significant deviation from the measured data at large current and bias levels where SHE is important [4]. Emipirical thermal parameters used for the computations are: $T_\mu = 170$ K, $T_V = 1000 \times V_{To}$ K $T_\beta = 4760 \times \beta_{io}$ K, and $T_v = 1650$ K.

In Fig.1, the influence of SHE on the floating body effect is emphasized for a 1 μm device, indicating an increase in the breakdown voltage with SHE. In Figs. 2 and 3, we see that our model reproduces the measured I–V characteristics very well for devices of different geometries. In particular, we have found that the behavior in the saturation regime is well

described by the present model in whole range of drain and gate biases used. For devices with serious SHE, our model predicts a clear negative differential resistance, with reduced drain current and increased breakdown voltage (not shown here). In Fig.4, modeled and measured transfer characteristics at different back gate biases V_{subs} are shown for a device with a 1.5 μm channel length. Again, the agreement is excellent, demonstrating that our model can describe the current characteristic both above and below threshold using a single closed-form expression.

With the present model, the influence of SHE on physical parameters such as the saturation voltage, the CLM factor, and the impact ionization factor, were also analyzed. From this investigation, we find that (i) the saturation voltage increases with SHE; (ii) the voltage at the saturation point inside the channel is different from the saturation voltage and decreases strongly with increasing drain bias; (iii) the channel potential and electric field distributions are significantly influenced by SHE at large gate bias; causing a reduction in CLM and in the impact ionization rate.

Summary A physically based unified *I–V* model for fully depleted SOI/MOSFETs including the effects of self-heating has been presented. The model offers improved accuracy, efficiency and convergence for use in circuit simulation. The model incorporates a wide range of important physical mechanisms related to short channel and thin film phenomena, to parasitic resistances, and to drain breakdown, ensuring a precise description of device operation in all regimes of operation. Comparing the model with measured data has demonstrated that the model can accurately reproduce measured *I–V* characteristics of devices with a wide range of geometric and process parameters.

Acknowledgment: This work was supported by the Research Council of Norway.

References

[1] K. E. Goodson and M. I. Flik, "Effects of microscale thermal conduction on packing limit of silicon-on-insulator electronic devices", *IEEE Trans. Comp. Hybrids and Manufacturing Tech.*,Vol.15, pp. 715-722, 1992.
[2] L. J. McDaid, S. Hall, P. H. Mellor and W. Eccleston, "Physical orign of negative differential resistance in SOI transistors", *Electron. Lett., Vol.25*, pp. 827-828, 1989.
[3] D. Yachou, J. Gautier and C. Raynaud, "Self-heating effects on SOI devices and implication to parameter extraction", *IEEE SOI Conf. Proc.*, pp. 148-149, 1993.
[4] T. C. Hsiao, N. A. Kistler and J. C. S. Woo, "Modeling the I-V characteristics of fully depleted submicrometer SOI MOSFET's", *IEEE Electron Device Letters*, EDL-15, pp. 45-47, 1994.
[5] M. Koyanagi, H. Kiba, H, Kurino, T. Hashimoto, H. Mori and K. Yamaguchi, "Coupled Monto Carlo Energy transport simulation with quasi-three-dimensional temperature analysis for SOI MOSFET", *IEEE Trans. Electron Devices*, TED 39, p. 2640 ,1992.
[6] N. Yasuda, S. Ueno, K. Taniguchi, C. Hamaguchi, Y. Yamaguchi and T. Nishimura, "Analytical device model of SOI MOSFET's including self-heating", *Japan. J. Appl. Phys.*, Vol. 30, pp. 3677-3684, 1991.
[7] L. T. Su, D. A. Antoniadis, N. D. Arora, B. S. Doyel, and D. B. Krakauer, "SPICE model and parameters for fully-depleted SOI MOSFET's including self-heating", *IEEE Electron Devices Letters*, EDL-15, pp. 374-376, 1994.
[8] Y. H. Cheng and T. A. Fjeldly, "Unified submicrometer SOI/MOSFET model for circuit simulation," *Proceeding of 1994 IEEE SOI International Conference,* pp. 11-12, Oct. 1994.
[9] Y. H. Cheng and T. A. Fjeldly, "Unified physical I-V model of fully depleted SOI/MOSFETs for analog/digital circuit simulation", accepted for publication in *Solid-State Electronics.*
[10] D. S. Jeon and D. E. Burk, "MOSFET electron inversion layer mobilities-A physically based semi-empirical model for a wide temperature range," *IEEE Trans. Electron Devices*, TED-36, pp. 1456-1463, 1989.
[11] D. S. Jeon and D. E. Burk, "A temperature -dependent SOI MOSFET model for high-temperature application (27-300°C)", *IEEE Trans. Electron Devices*, TED-36, pp. 2101-2111, 1991.
[12] K. Lee, M. Shur, T. A. Fjeldly and T. Ytterdal, *Semiconductor Device Modeling for VLSI*, Prentice Hall, New Jersey (1993).
[13] Y. H. Cheng and T. A. Fjeldly, "Unified physical I-V model including self-heating effect for fully depleted SOI/MOSFETs", unpublished.
[14] J. R. Davis, G. A. Armstrong, N. J. Thomas and A. Doyel, "Thin-film SOI MOSFET transistors with p+-polysilicon gates," *IEEE Trans. Electron Devices*, TED-38, pp. 32-38, 1991.

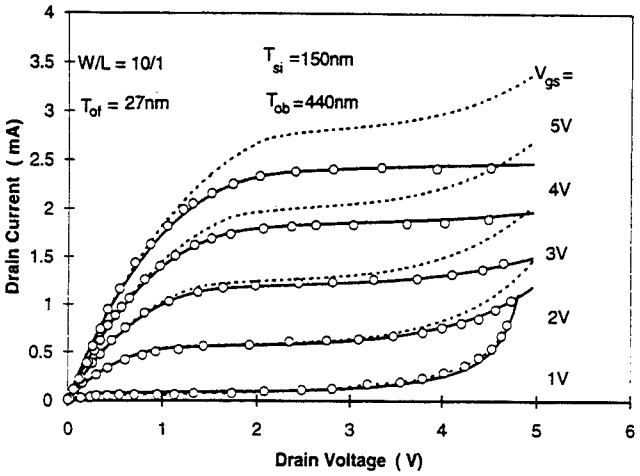


Fig.1. Measured (open circles) and modeled (solid and dashed lines: with and without SHE) *I-V* characteristics of a 1 μm *n*-SOI/MOSFET (data from J. R. Davis et al. [14]). Major model parameters are: R_{ds} = 40Ω, μ_{no} = 706 cm²/Vs, θ = 0.09, v_{so} = 8.8x10⁶cm/s, η = 1.46, N_{ch} = 3.2x10¹⁶cm⁻³. Threshold voltage parameters: σ_o = 0.015, V_σ = 0.2 V, $V_{\sigma o}$ = 1.2 V [12].

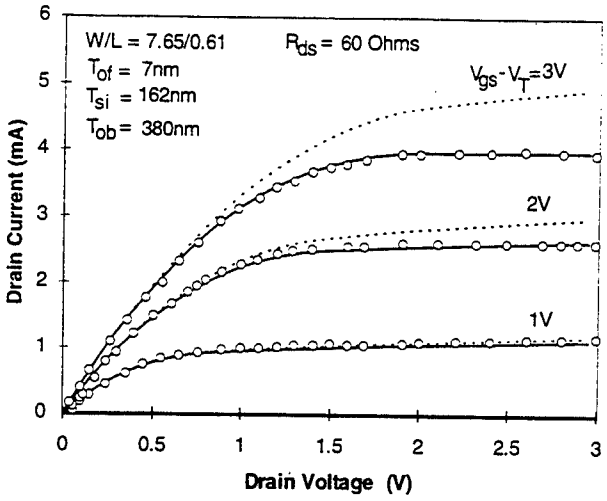


Fig.2. Measured (open circles) and modeled (solid and dashed lines: with and without SHE) *I-V* characteristics of a 0.61 μm *n*-SOI/MOSFET (data from T. C. Hsiao et al. [4]). Major model parameters are: R_{ds} = 60Ω, μ_{no} = 462 cm²/Vs, θ = 0.19, v_{so} = 9.6x10⁶cm/s, η = 1.016, N_{ch} = 1x10¹⁵cm⁻³. Threshold voltage parameters: σ_o = 0.03, V_σ = 0.2 V, $V_{\sigma o}$ = 1.2 V [12].

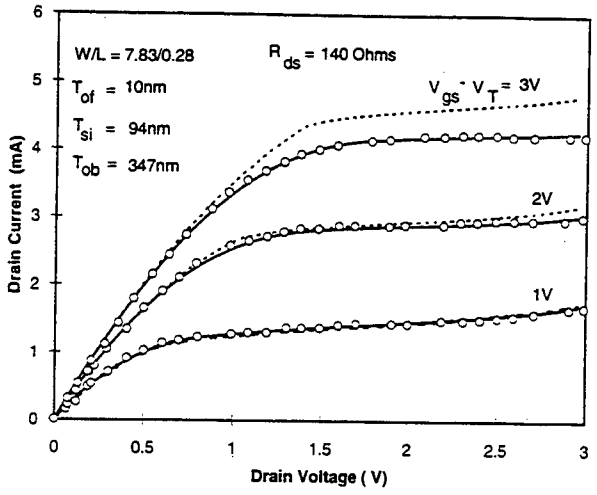


Fig.3. Measured (open circles) and modeled (solid and dashed lines: with and without SHE) *I-V* characteristics of a 0.28 μm *n*-SOI/MOSFET (data from T. C. Hsiao et al. [4]). Major model parameters are: R_{ds} = 140Ω, μ_{no} = 612 cm²/Vs, θ = 0.14, v_{so} = 8.3x10⁶cm/s, η = 1.026, N_{ch} = 1x10¹⁶cm⁻³. Threshold voltage parameters: σ_o = 0.06, V_σ = 0.2 V, $V_{\sigma o}$ = 1.2 V [12].

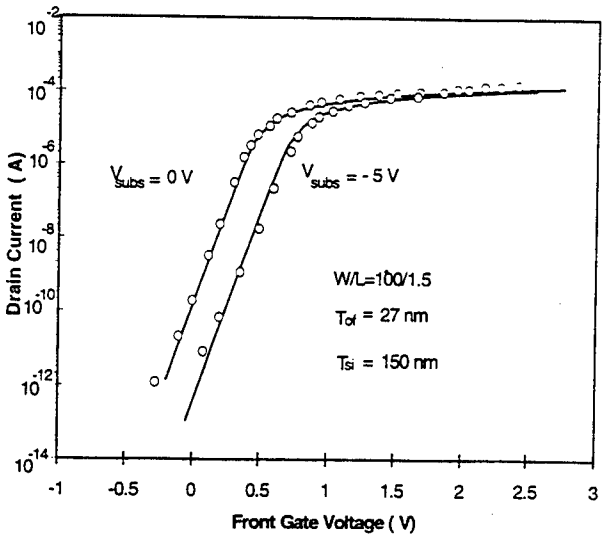


Fig.4. Measured (open circles) and modeled transfer characteristics of a 1.5 μm *n*-SOI/MOSFET (Data from J. R. Davis et al. [14]). Major model parameters are: R_{ds} = 20Ω, μ_{no} = 706 cm²/Vs, θ = 0.09, v_{so} = 8.8x10⁶cm/s, η = 1.46, N_{ch} = 3.2x10¹⁶cm⁻³, T_{ob} = 440 nm. Threshold voltage parameters: σ_o = 0.015, V_σ = 0.2 V, $V_{\sigma o}$ = 1.2 V [12]. V_{ds} = 0.1 V.

Top-Gate Threshold Voltage Shifts Using an Individually Isolated Back Gate Bias in Dual-Gated P&N Channel Thin-Film SOI MOSFETs

John P. Denton and Gerold W. Neudeck
School of Electrical Engineering, Purdue University, West Lafayette, IN 47907-1285 USA

Fully Depleted P and N-channel Dual-Gated Thin-Film Silicon-on-Insulator (DG-TFSOI) MOSFETs have been fabricated with an individually isolated buried polysilicon backgate. Present technologies such as SIMOX and Wafer Bonding & Etch Back use the entire substrate as the bottom back gate. The structure in Figure 1 allows **individual backgate operation** for each device and is fabricated using Epitaxial Lateral Overgrowth(ELO) to form SOI Islands. This fabrication method allows the buried polysilicon gate to act as an subterranean interconnect to any number of devices or to the surface. It also used a thin thermal high quality low leakage and low interface state buried oxide, which has been a problem for the other technologies. The SOI Islands have a reported defect density of less than SIMOX or Bonded wafers[1]. A voltage controlled V_T shift of the top gate by a second gate is important for low power circuits where the shift will boost drive currents and increase switching speeds, or turn the FET even more off by shifting the subthreshold characteristics. Our fabricated devices show a 1 volt shift in top gate V_T for a 3.75 volt change in V_{BG}. For high-dose SIMOX, a 14 volt substrate swing was necessary and for low-dose SIMOX, a 5 volt substrate change was is required for a 1 volt shift of the top gate V_T. [2].

Process: Fabrication of the buried backgate P or N Channel DG-TFSOI MOSFET started with a N(100), 10-20 Ω-cm, phosphorus doped silicon wafer. An RIE trench 450 nm deep was followed by a 180 nm oxidation. The oxidized trench was then filled with amorphous silicon (a-Si) deposited by LPCVD, then was heavily doped. The a-Si not needed on the surface of the wafer was removed via Chemical-Mechanical Polishing (CMP) (Fig. 1a). The wafer was oxidized to 230 nm and the SOI active area was defined by lithography and a wet oxide etched. The exposed polysilicon backgate was thermally oxidized to 106 nm for the backgate buried oxide. Hence the SiO_2 recess was 162 nm deep and this defined the initial SOI thickness (Fig.1b). A seed window for the selective epitaxial growth of silicon (SEG) was defined next to the SOI recess. SEG (phosphorus doped at $8x10^{15}/cm^3$) was grown out of the seed window and into the recess by ELO (Fig. 1c) [3]. The SEG growth above the SiO_2 field was removed with CMP using the SiO_2 as a local area etchstop for excellent thickness control (Fig. 1d). The result is a SOI island isolated from all other islands, and its thickness is primarily defined by a double oxidation step. Subsequent top-gate processing consisted of a normal self-aligned S/D polysilicon gate MOSFET (Fig.1e). For N-MOSFETs, the SEG was implanted with boron to convert to P-type material. After metallization the resulting DG-TFSOI MOSFETs were then annealed in hydrogen at 450°C to minimize interface trap density. Table 1 shows the comparison of the physical dimensions between the P- and N-channel devices. The thin buried oxide is a great improvement over SIMOX in leakage, uniformity, low interface states and can be make at least 5-8 times thinner than high dose. **Results:** A DG-TFSOI MOSFET has operation in: topgate active and backgate as a bias (TG); topgate as a bias and backgate active (BG); topgate and backgate both active (DG). The devices were tested in all three modes and the normalized device parameters extracted are presented in Table 2. Note the low values of D_{it} and the small values of S for the thicknesses of the oxides used. Top-gate V_T operation versus backgate bias for P-devices is shown in Fig. 2 and V_T shift versus backgate bias in Fig. 3 which shows a nice linear region. The N-channel devices are shown in Fig. 4 while Fig. 5 shows the P-device S change in slope and value with backgate bias. Hence the device can be turned-off more by several orders of magnitude. The V_T shift sensitivity can be engineered by the thickness of the thermally grown backgate oxide which can be 20nm using nitrided oxides.

[1]J. Kessler, J. Glenn Jr., G. Neudeck, "Microlectronic Engr., V.28, No. 1-4, p 435-438, 1995.
[2] Shoichi Masui, etal, 1994 IEEE Inter. SOI Conf. Proceedings, pp83, Oct 1994.
[3] J. L. Glenn, G. Neudeck, et al., Applied Physics Letters, Vol. 60, No. 4, pp 483, 1992.
[4] P. C. Yang and S. S. Li, Solid-State Electr., Vol. 36, No. 5, pp 801, 1993.
[5] H. K. Lim and J. G. Fossum, IEEE Trans. Electron Devices, ED-30, pp 1244, 1983.

*Supported by the SRC 95-SJ-108

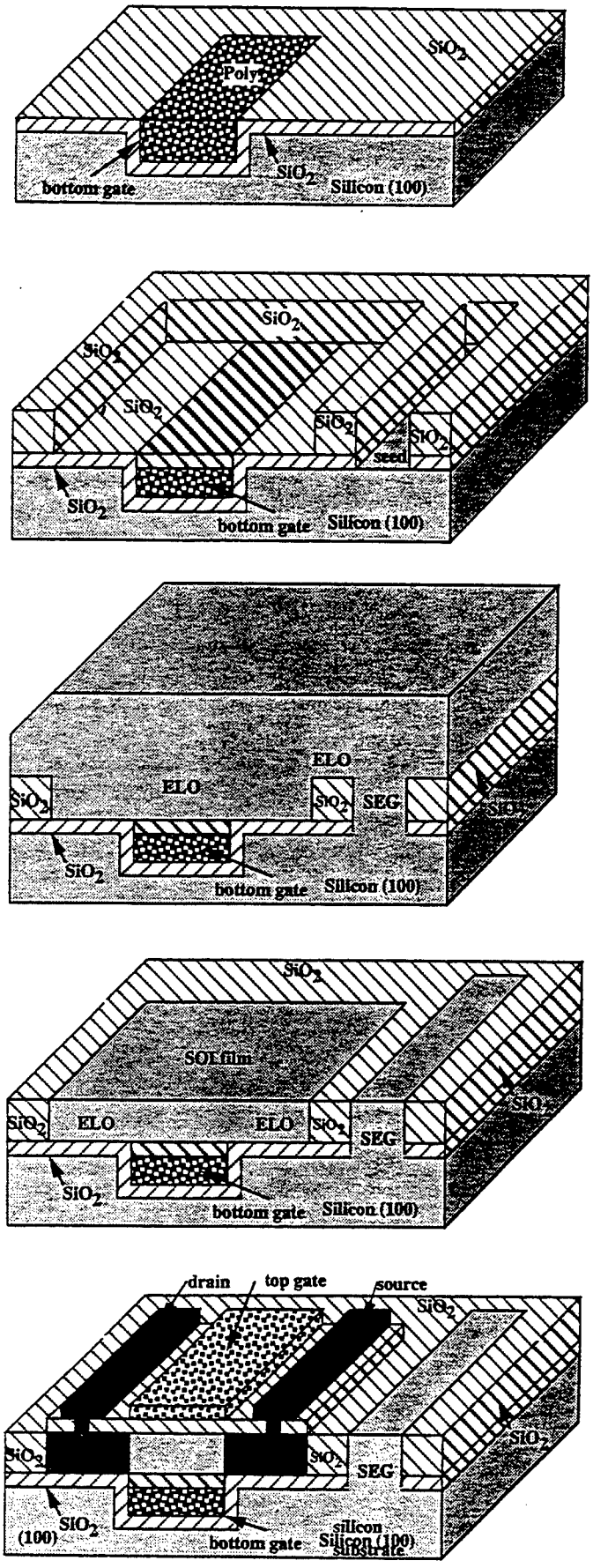


Figure 1 P or N Channel Fully Depleted Dual Gated SOI MOSFET with an Individually Isolated Buried Bottom Gate with a Thin Thermal Oxide That Also Serves as an Interconnection Level

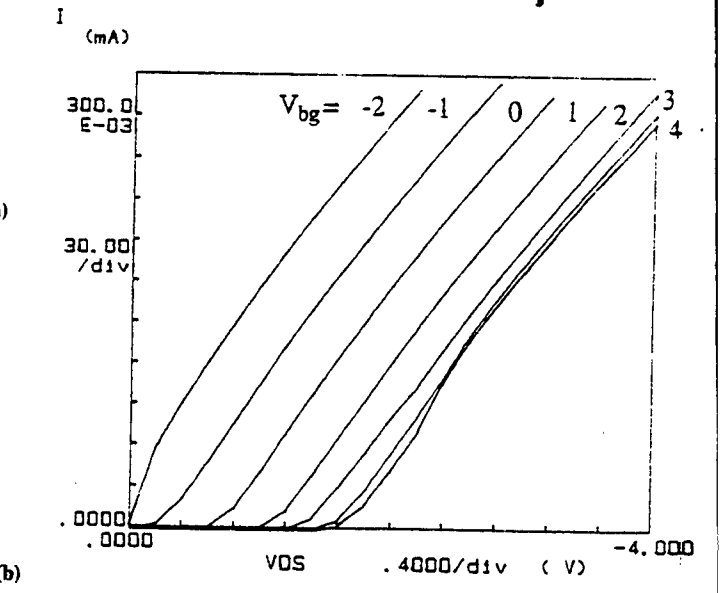


Figure 2. Threshold voltage operation of P-channel DG-TFSOI MOSFET versus applied backgate voltage (V_{b}

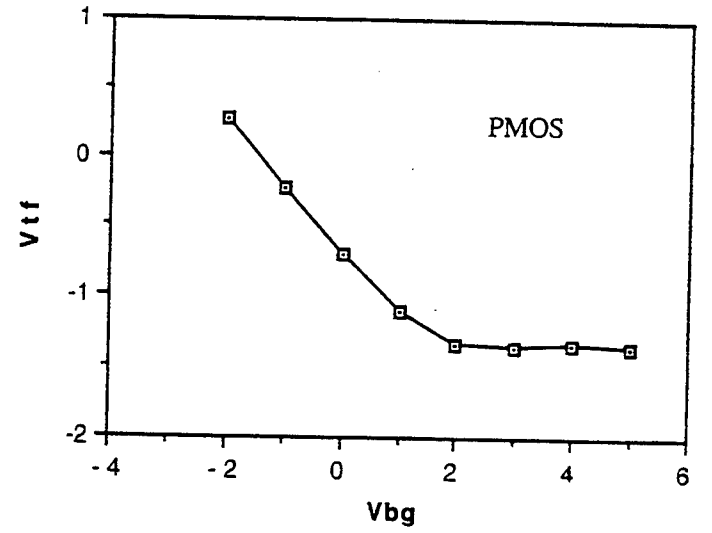


Figure 3. Threshold voltage shift for P-channel DG-TFSOI MOSFET versus applied backgate voltage (V_{bg}

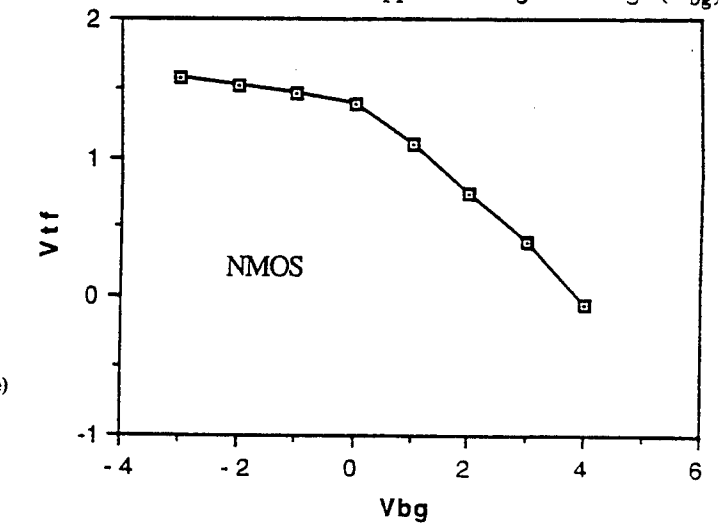


Figure 4. Threshold voltage shift for N-channel DG-TFSOI MOSFET versus applied backgate voltage (V_{bg}).

Table 1 Summary of physical dimensions for N-channel and P-channel DG TFSOI MOSFETs

Device Dimensions		
parameter	N-channel	P-channel
SOI thickness	965Å	1450Å
topgate oxide	575Å	550Å
backgate oxide	1060Å	1060Å
drawn L	2.0μm	2.0μm

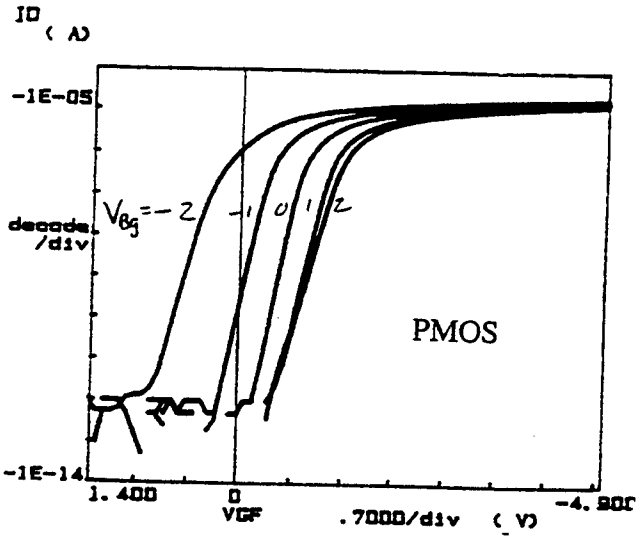


Figure 5. Topgate subthreshold characteristics versus backgate voltage (V_{bg}) for P-channel DG-TFSOI MOSFET.

Table 2 Summary of normalized electrical parameters extracted from N-channel and P-channel DG-TFSOI MOSFETs. The bias conditions were $I_{D,sat}$ at V_G-V_T= 5V, V_{ds}=5V, the transconductance at V_{ds}=100mV, D_{it} were extracted by the threshold shift method [4,5]. P-Channel devices were negatively biased. In TG and BG cases, the opposite gate was biased to 0 volts.

	N-channel			P-channel		
Parameter	TG	BG	DG	TG	BG	DG
$I_{D,sat}$ (μA)	295	84.8	470	-122	-128	-234
S (mV/dec)	108	449	83	97	188	70
Leakage (pA)	<1	<1	<1	<1	<1	<1
V_t (v)	1.14	1.72	0.82	-0.66	-1.39	-0.46
g_m (μS)	6.5	1.48	8.76	2.16	1.09	3.4
D_{it} ($x10^{11}$, $cm^{-2}eV^{-1}$)	2.6	4.6	-	5.7	7.5	-

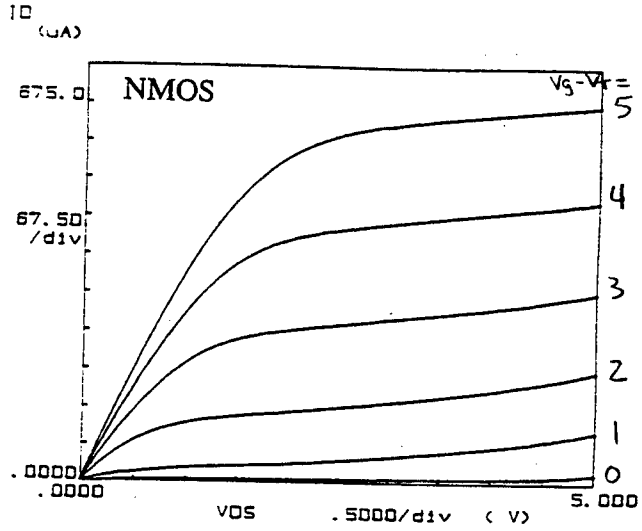
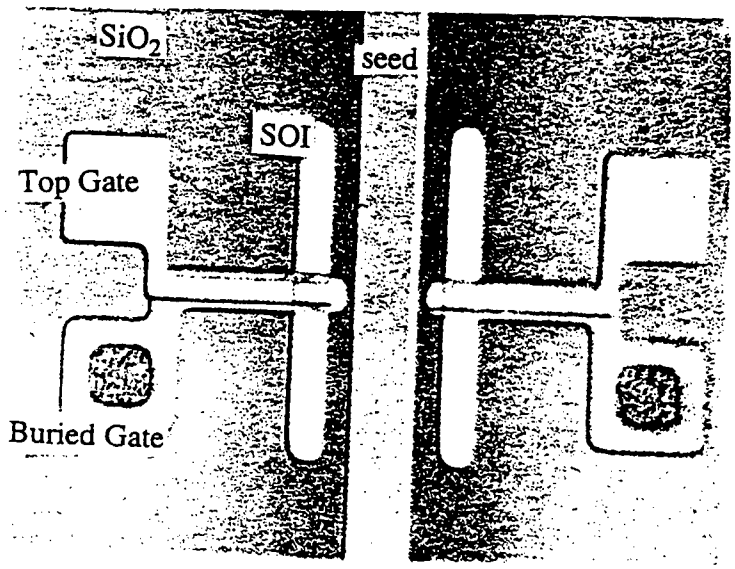


Figure 6. I_{DS} versus V_g-V_t for the topgate N-channel DG-TFSOI MOSFET.



Future Trend of Scaled LSI Devices and Single Electronics

Toshiro Hiramoto
University of Tokyo
Institute of Industrial Science
7-22-1 Roppongi, Minato-ku, Tokyo 106, Japan

The feature size of LSI devices has been reduced drastically in the past 30 years. This technology trend is believed to continue for at least next ten years. However, the number of electrons associated with one bit storage or one gate transition had remained almost unchanged until recently. This fact indicates that the trend of the LSI devices was not toward the single electron devices.

In this talk, technology trend of LSI devices toward single electronics is addressed. It is shown that the design concept of the LSI devices will split into two directions: high speed and low power, and that the extremely low power design will lead to the idea of single electronics. Our recent experimental data on Coulomb oscillations and giant random telegraph signals (RTS) in very narrow Si MOSFETs will also be shown.

SUITABILITY OF SUB 0.10 μm NMOSFET FOR LOW & HIGH INTEGRATION CIRCUITS

F.BENISTANT, G.GUEGAN, S.TEDESCO, F.MARTIN, M.HEITZMANN
LETI (CEA) 17, rue des Martyrs38054 Grenoble cedex 9 FRANCE
Phone : (33) 76 88 97 95 - Fax : (33) 76 88 94 57 - email : benistan@dmel.ceng.cea.fr

Abstract :

In this paper, four different sub-0.10 μm NMOSFET architectures are compared for suitability for ULSI circuits. Conventional architectures are used, with 45Å gate oxide, Boron channel and pocket doping, with Arsenic S/D and extensions. The influence of the extension doping on the short channel effects (SCE) is shown. Moreover, combined pocket implantation with low doping extension dramatically reduces SCE. The trade off for these reduced SCE is low current drive capability. Therefore, for sub - 0.10 μm generations, specific devices should be realized for specific applications.

1- Introduction :

Future ULSI circuits will incorporate nearly one billion transistors per chip (ref.1). With such high integration, power consumption at room temperature, is the critical parameter. Therefore, devices with low leakage current will be necessary. On the other hand, some specific applications will not necessitate such high integration but high speed, and devices with higher leakage current can be tolerated. Therefore, in this article, we study four different architectures (table1). The first, designed for high integration, is made with ultra-shallow low doped extensions, and the second, designed for lower integration, is fabricated with shallow higher doped extensions. In addition, a pocket implantation is used as another design parameter to minimize SCE, as described in rows 3 and 4 of table1.

2- Device design :

Devices have been fabricated with Boron channel doping and Arsenic extension doping. A Boron pocket implantation has been used with higher concentration than that of the channel. A conventional well is used, and the well concentration is maintained approximately at $1x10^{16}$ cm^{-3}. For this process, the gate stack consists of 45 Å gate oxide and 150 nm αPoly-Si (Fig.1). The gate level is patterned by a hybrid e-beam and DUV process which fully integrates e-beam lithography with optical process and equipment (ref.2). The thermal budget has been optimized to reduce, as much as possible, the dopant diffusion. For example, no gate reoxidation occurs after the gate etch ; instead a thin oxide has been deposited at low temperature (750°C). This deposition suppresses the bird's beak at the poly gate edge, and in addition preserves the as-implanted channel profile. Moreover, before the source/drain implantation, a thermal annealing (850°C) in a nitrogen ambient is performed to provide good gate extension overlap. After the gate etch, 0.10 μm length oxide spacer is deposited, and source/drain are implanted and activated with a rapid thermal anneal. The shallow extensions are about 350 and 400 Å deep, and the source/drain 800 Å. These depths are estimated both by SIMS measurements and simulations (SUPREMIV).

3- Results and Discussion:

This section compares the influence of the extension and pocket doping levels on SCE and current drive capability for deep submicron devices. We compare two different extension dopings, which are both degenerate, with maximum concentration of about $2.5x10^{19}$ cm^{-3} for samples P04 & P21, and $1x10^{20}$ cm^{-3} for samples P13 and P23. Fig.2 shows the Vt roll-off for the four architectures. As previously published (ref.3), the Boron pocket implantation increases the Vt, due to lateral Boron spreading, i.e.samples P23 and P21 present a higher long channel threshold voltage than samples P13 and P04. The higher the extension doping level , the higher the Vt roll-off. In addition, when the extension doping is high, the Boron

pocket has a smaller effect on the Vt roll-off. The subthreshold slope is dramatically reduced with a combination of low extension doping and pocket implantation (Figs.3-4), and substantial improvement in leakage current is achieved (Fig.5). This improvement is confirmed by the 0.10 µm off-state leakage current, which is about three orders of magnitude lower with sample P21. Because of higher Vt and and better DIBL control the saturation current is lower for sample P21 than P23, and sample P04 than P13 (Fig.6). The same trend is observed for the Saturation Transconductance (Fig.7). It is worth noting that sample P04, with low extension doping and no pocket, has approximatly the same saturation current as sample P23, with higher extension doping and with pockets. Fig.8 to Fig.12 show Id-Vd curves vs. Vg. Because of high extension doping and no pocket sample P13 (Fig.8) presents poor saturation and works in punch-through mode, while sample P04 shows good gate control because of lower extension doping (Fig.9). In an other hand, samples P21 and P23 presents good Id-Vd characteristics (Fig.10-11), and combined with low extension doping permits the fabrication of 0.075 µm NMOSFET for sample P21 with a 0.38 V threshold voltage (Fig.12). With low extension doping and pocket, deeper sub-micron devices can been fabricated with good saturation characteristics and low leakage current, but the trade off is lower saturation current. In summary, it is difficult to satisfy both requirements of low SCE and high device drive capability (ref.4). Therefore, the fabrication of specific devices for specifics applications appears as a solution to maintain both the above requirements.

4-Conclusion:

In this paper, sub-0.10 µm gate length MOSFET have been fabricated. It clearly appears that, for future ULSI generations with low consumption, pocket architectures with low doping extensions are good candidates. On the other hand, devices with higher extension doping could be useful for lower density circuits with higher consumption. Therefore, the concept of specific devices made for specific consumption/integration circuits emerges for deep submicron technologies.

[1] : Güchi Inoue et al.
in 1995 Symposium on VLSI Tech.Digest of Tech.Process ; p.1

[2] : F.Bénistant et al.
Micro and Nano Engineering' 95

[3] : F.Bénistant et al.
ESSDERC'95

[4] : M. Koyanagi
Extended Abstract of the 1993 International Conference on Solid State Devices and Materials, Makuhari ; p.20

* Well definition
* Channel Doping
* Gate Oxide (45 Å)
* a-Poly Si deposition (in situ doped)
* Hybrid lithography (e-beam/DUV)
* Gate etch (Dry)
* Thin side wall deposition(45 Å)
* Extension implantation
* Pocket implantation
*Spacer (0.10 μm)
* S/D implantation
* RTA 950°C - 15 sec
* Metalllization

Fig.1 : Process Steps

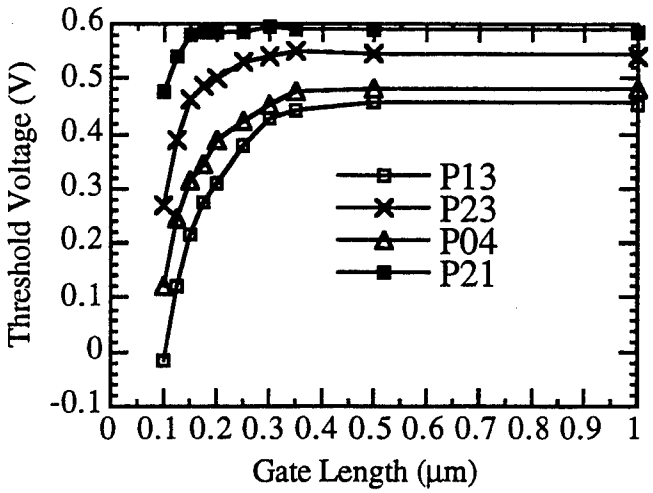


Fig.2: Vt (Vds=0.1V) vs. gate length

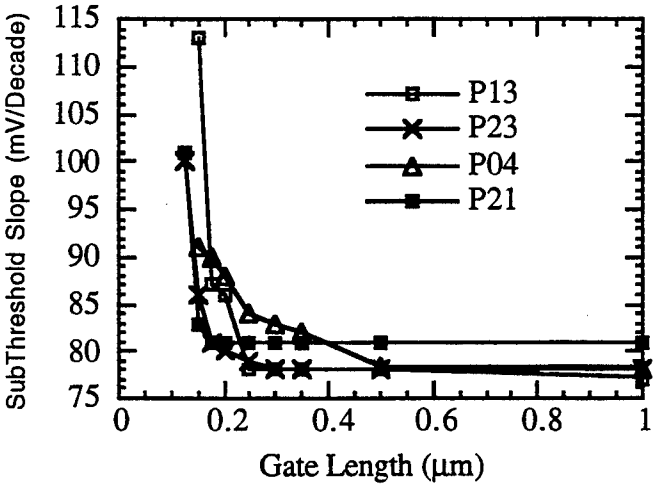


Fig.3: Subthreshold slope vs. gate length

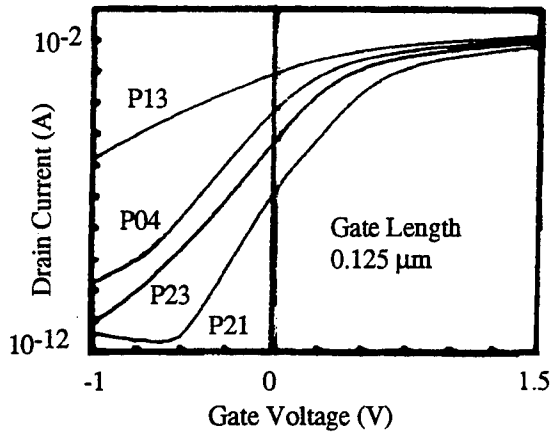


Fig.4: Log(Id) vs. gate length at Vds = 1.5 V

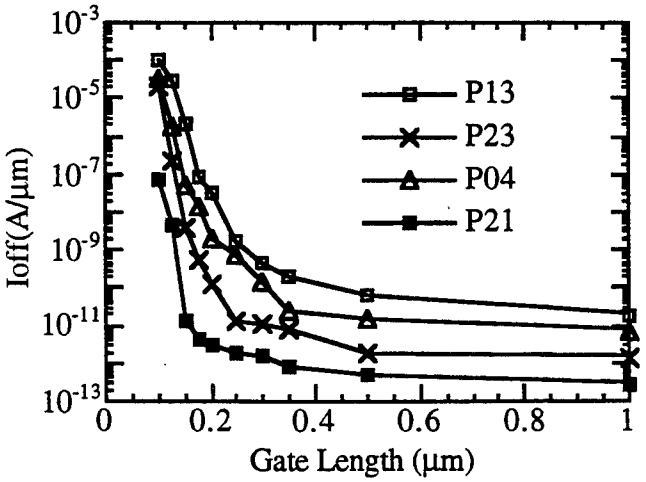


Fig.5: Leakage current vs. gate length

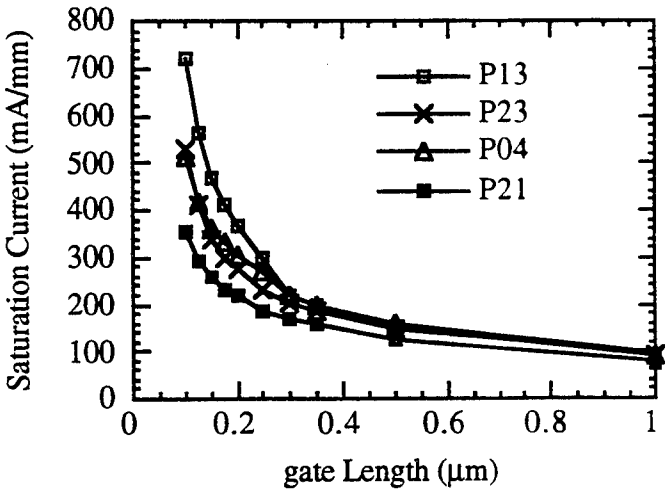


Fig.6: Idsat vs. gate length

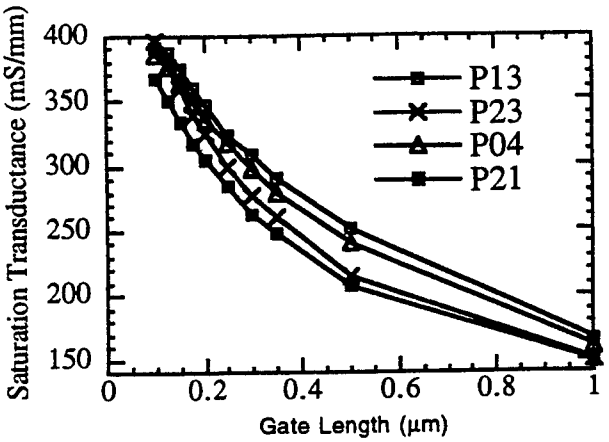


Fig.7 : I-V Characteristics of 0.10 μm NMOSFET

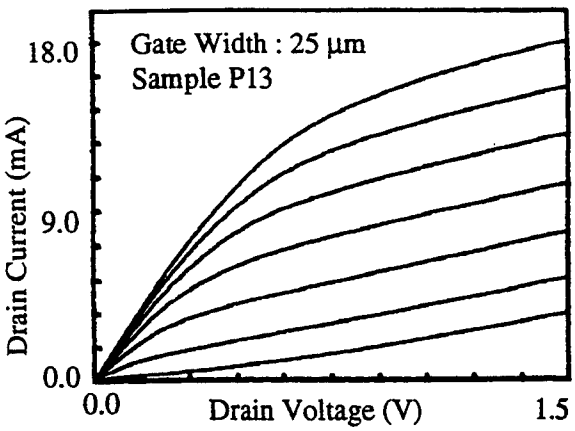


Fig.8 : I-V Characteristics of 0.10 μm NMOSFET

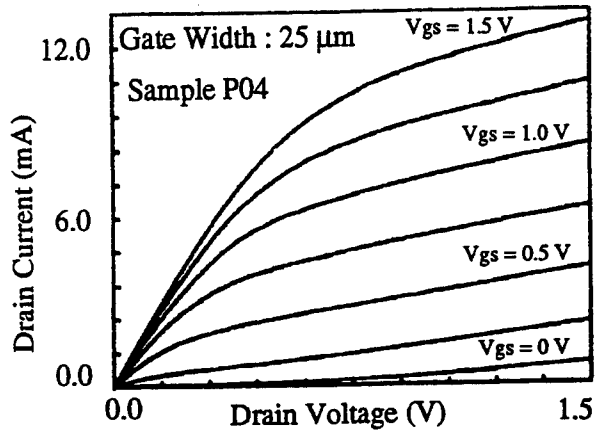


Fig.9 : I-V Characteristics of 0.10 μm NMOSFET

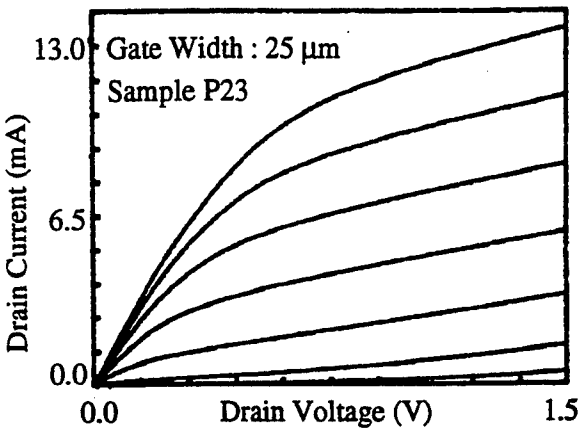


Fig.10 : I-V Characteristics of 0.10 μm NMOSFET

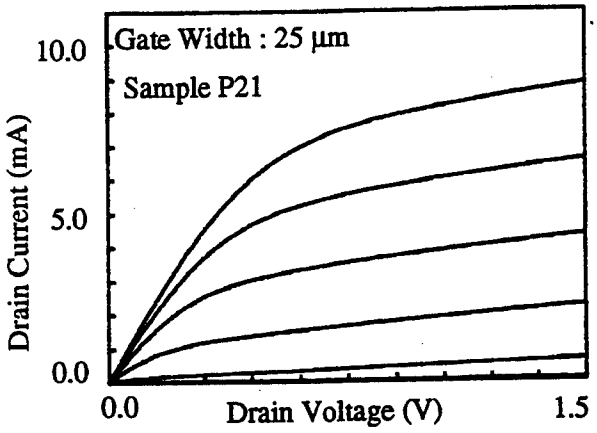


Fig.11 : I-V Characteristics of 0.10 μm NMOSFET

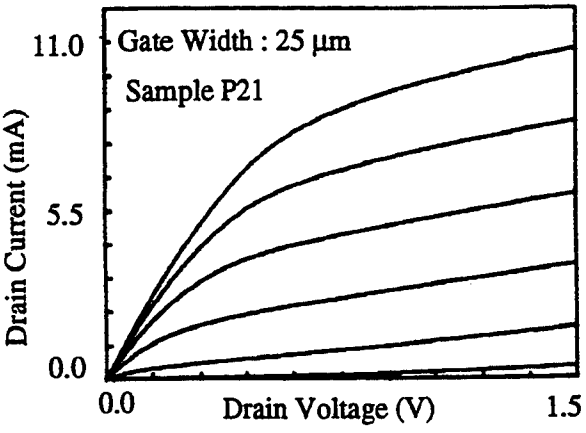


Fig.12 : I-V Characteristics of 0.075 μm NMOSFET

	Channel	Extensions	Source/Drain	Pockets
Sample P04	25 keV $5x10^{12}$ cm^{-2}	15 keV $1x10^{14}$ cm^{-2}	40 keV $1x10^{15}$ cm^{-2}	
Sample P13	20 keV $4x10^{12}$ cm^{-2}	15 keV $3.6x10^{14}$$cm^{-2}$	40 keV $1x10^{15}$ cm^{-2}	
Sample P21	25 keV $5x10^{12}$ cm^{-2}	15 keV $1x10^{14}$ cm^{-2}	40 keV $1x10^{15}$ cm^{-2}	20 keV $1x10^{13}$ cm^{-2}
Sample P23	20 keV $4x10^{12}$ cm^{-2}	15 keV $3.6x10^{14}$$cm^{-2}$	40 keV $1x10^{15}$ cm^{-2}	20 keV $1x10^{13}$ cm^{-2}

Table 1 : Implantation Conditions

Reliable Gate-Voltage-Dependent Channel-Length and Series Resistance Extraction Technique taking into account Threshold Voltage Reduction in MOSFETs

Serge Biesemans, Stefan Kubicek, Kristin De Meyer
IMEC, Kapeldreef 75, B-3001 Leuven, Belgium

Abstract

A measurement algorithm to extract the effective channel length (L_{eff}) and source-drain series resistance (R_S) of MOSFETs is presented. The method is based on an existing algorithm known as 'shift & ratio'. We extended the method to extract physical meaningful values for L_{eff} and R_S. We applied the method to our 0.1 μm nMOS technology and are able to extract electrically the metallurgical channel length L_{met} as well.

Introduction

The effective channel length of a MOSFET is a critical parameter. Process engineers use it to monitor lithography and etching during process development and manufacturing. Device designers who model I-V characteristics need to know the effective channel length of the device they are modeling. As gate lengths in research labs have entered the 0.1 μm era [1,2,3], reliable methods to extract L_{eff} and R_S have become indispensable. An excellent review of existing extracting methods is given in [4]. The parameters which most directly measure how much current a particular MOSFET delivers are the effective channel length, the series resistance and the effective mobility (μ_{eff}). In order to optimise the performance-short channel effect trade-off, these three parameters have to be quantified reliably.

Channel length can be described in four ways : mask length, poly length, metallurgical length (L_{met}) and effective channel length. The last quantity is the only parameter that allows for a large quantity of automated measurements since it is extracted from electrically measured terminal currents and is suitable for circuit models. In contrast, measuring the poly length is very time consuming, and the metallurgical channel length is a technological parameter which is believed not to be practically measurable. However, we believe that with the 'shift & ratio' algorithm [5], it is possible to find L_{met} as well as the gate voltage dependent L_{eff}. As gate lengths become smaller and current levels increase, the series resistance and the voltage drop across it has to be extracted as well. Since deep submicron transistors can suffer from a reduced V_T due to the short channel effect, a proper V_T has to be found as well.

We apply the method on experimental devices. The details of the 0.1 μm process are reported elsewhere [3].

Extraction algorithm

The shift & ratio algorithm is a recent [5] method proposed to extract L_{eff} from terminal currents. However, two assumptions are made which are of consequence. First, it is assumed that L_{eff} is independent of gate voltage which is not necessarily valid in extension or LDD devices [8]. Second, it is assumed that the external gate potential equals the internal one ($V'_{gs}=V_{gs}$ in Fig.1). In this report, we try to remove both assumptions.

The algorithm itself starts from the expression for MOSFET current in the linear (low drain bias) regime

$$I_{ds} = \frac{W}{L_{eff}} \mu_{eff} C_{ox} (V'_{gs} - V_T - V'_{ds}/2) V'_{ds} \qquad (1)$$

where μ_{eff} is the effective channel mobility, C_{ox} the gate oxide capacitance per unit area, V'_{gs} and V'_{ds} the internal gate and drain voltages. Because experimental data are based on external terminal voltages, one has to rework (1) by substituting

$$V_{gs} = V'_{gs} - I_{ds}\frac{R_s}{2}$$
$$V_{ds} = V'_{ds} - I_{ds}R_s \quad (2)$$

Combining (1) and (2), one can find an expression for I_{ds}. However, the expression is rather complicated [9] and unpractical to work with.
However, it is possible to rework the expression in terms of external voltages without simplification

$$I_{ds} = \frac{W}{L^*}\mu_{eff}C_{ox}(V_{gs} - V_T^* - V_{ds}/2)V_{ds} \quad (3)$$

with

$$L^* = L_{eff} + W C_{ox}\mu_{eff} R_s (V_{gs} - V_T^* - V_{ds}/2)$$
$$V_T^* = V_T - \frac{W C_{ox}\mu_{eff} R_s V_{ds}^2}{4 L_{eff}}\left(\frac{1}{1+\frac{W C_{ox}\mu_{eff} R_s V_{ds}}{2L}}\right) \cong V_T - 1mV \cong V_T \quad (4)$$

Expression (3) which is referenced to the external terminal voltages has the same form as the expression referenced to the internal voltages (1) except for the values of V^*_T and L^*. Fortunately, if one plugs real numbers into the expression for V^*_T (4), the second term turns out to be negligible if V_{ds} is small enough (<100 mV) because of the square dependence. The reason we write the current in this manner (3) is to be able to apply the shift & ratio algorithm without suffering from the simplifications otherwise needed.
The actual S&R algorithm works as follows. First, the total resistance is written as

$$R_{tot} = \frac{V_{ds}}{I_{ds}} = \frac{L^*}{W\mu_{eff}C_{ox}(V_{gs} - V_T^* - V_{ds}/2)} = L^* f(V_{gs} - V_T) \quad (5)$$

By writing R_{tot} as done in (5), one does not have to use $R_{tot}=R_s+R_{ch}$. This is advantageous because the questionable assumption that R_s is a weak function of V_{gs} can be removed in what follows. Next, one defines S as

$$S(V_{gs}) = \frac{dR_{tot}}{dV_{gs}} = L^* f' + f L^{*'} \cong L^* f' + f W\mu_{eff}C_{ox}R_s \quad (6)$$

where the primes mean derivative with respect to V_{gs} and f is defined in (5). It is further assumed that f' reduces to

$$f' = \frac{-f}{(V_{gs} - V_T^* - V_{ds}/2)} \quad (7)$$

In order to find L_{eff} and V_T for a particular device, one curve S is shifted horizontally to the right by a varying amount, δ, and the ratio r

$$r(\delta) = \frac{S_o(V_{gs})}{S_i(V_g - \delta)} \quad (8)$$

between two devices is computed as a function of V_{gs}. Here, S_o is a curve from a reference device (L_o=10 μm) while S_i is the curve from the device under investigation. The key is then to find out the δ value for which the ratio is a constant. A typical result of r is shown in Fig.2 with V_{gs} as a parameter. It is easily shown that the value of δ^*, for low V_{gs} values, yields $\delta^*=V_{To}-V_{Ti}$. As such, the threshold voltage V_{Ti} can be determined. It can be shown as well that

$$r(\delta^*) = \frac{S_o(V_{gs})}{S_i(V_{gs} - \delta^*)} = \frac{R_s - L_o^* f}{R_s - L_i^* f} = \frac{L_o}{L_i} \quad (9)$$

and L_i (=L_{eff} of device number i) can also be determined.
One problem the original S&R method has is explained in Fig.3. It can be seen that when the parameter V_{gs} spans an interval which is of practical interest (e.g..

[0V,2.5V]), there is no single point of intersection. This is due to the series resistances. However, this problem is solved by taking (6) instead of $S=L^*f'$ as in [5].
If one performs the same analysis in the sub-threshold region ($V_{gs}<V_T$) instead of the linear region ($V_{gs}>V_T$) following expression is obtained

$$r(\delta) = \frac{L_o}{L_i} exp(\delta / V_{th}) \tag{10}$$

which is, in contrast with (8), independent of V_{gs}. Indeed, making a similar plot as Fig.2 using experimental data, one ends up with a single curve of exponential type as calculated theoretically in (10).

The extraction algorithm then has to be applied as follows. One calculates $r(\delta)$ for V_{gs} ranging from 0 to V_T+0.5 V in steps of 100 mV. The curves with $V_{gs}<V_T$ fall on top of each other while the curves with $V_{gs}>V_T$ deviate from them producing a single intersection point. Indeed, the current levels are still small enough so that the voltage drop across R_s can be neglected. From this intersection point (δ^*,$r(\delta^*)$), the V_T and L_i can be determined. Then, one calculates $r(\delta)$ for V_{gs} from V_T+0.5 V up to 2.5 V for instance. For each V_{gs} the intersection of $r(\delta)$ with the vertical line $\delta=\delta^*$ is found as shown in Fig.4. As such, a curve L_i versus V_{gs} can be set up as done in Fig.5.
The easiest way to proceed then in order to find R_s is by using (3) and (4), resulting in

$$R_s = \frac{W \mu_{eff} C_{ox} V_{ds} (V_{gs} - V_T - V_{ds}/2) - I_{ds} L_i}{I_{ds} W \mu_{eff} C_{ox} (V_{gs} - V_T - V_{ds}/2)} \tag{11}$$

R_s can then easily be calculated using the experimental data for I_{ds} and the Li values obtained previously, as is done in Fig.6.

Discussion

We left μ_{eff} unspecified so far because it cancels out in the extraction of L_i. However, it plays a major role in the determination of R_s. Some authors take it to be a constant while others use some analytical expression for its degradation with V_{gs} [9]. Our approach is such that we identify μ_{eff} with the universal mobility [10] and extract it from the reference (L_o=10 µm) device. In the calculations above we used this experimentally determined μ_{eff}.
Hu [8] argued that in LDD and extension devices L_i as well as R_s can be dependent on V_{gs}. This is because the inversion layer extends into the LDD as V_{gs} increases. As a result L_i increases and R_s decreases. This allows one to find the metallurgical channel length because at the condition that the inversion channel layer has diminished, i.e. $V_{gs}<V_T$, L_i equals the constant quantity L_{met} as shown in Fig.7. This is consistent with the present method where $r(\delta)$ is independent of the gate voltage. As a result the extracted L_i in the low bias regime is possibly equal to L_{met}.

Most extraction techniques, except the S&R algorithm, use an L-array and extract ΔL and R_s from it which are averages over the devices of the L-array. The method often depends on the linearity of some measured quantity. However, for very small gate lengths severe deviations from linearity are observed. An extra problem might be that the L-array is not equidistant because of process variations in poly definition (e-beam writing, poly etching). On the contrary, the S&R method is capable of scanning each particular device for its L_{eff}, L_{met} and R_s which is of major importance for devices near the 0.1 µm region. A benchmark for the reliability of the S&R method could be that, as shown in Fig.5 and 6, the extracted R_s and L_i should have the same behaviour.

Conclusion

A measurement algorithm to extract the effective channel length (L_{eff}) and source-drain series resistance (R_s) of MOSFETs was presented. The method is based on an existing algorithm known as 'shift & ratio'. We applied the method to our 0.1 µm nMOS technology and are able to extract electrically the L_{met} as well as L_{eff} and R_s.

References

[1] G.G. Shahdi. et al., Symp. VLSI Techno., p.93 (1993)
[2] H. Hu, et al., Symp. VLSI Techno., p.17 (1994)
[3] S. Kubicek, et al., Symp VLSI Techno., p.105 (1995)
[4] K.K. NG, J. R. Brews, Circuits & Devices, p.33 (Nov. 1990)
[5] Y. Taur, et al., IEEE EDL, p267 (1992)
[6] R.H. Yan, et al., IEEE TED., p.1704 (1992)
[7] S Biesemans, Solid State Electronics, To be published (1995)
[8] G. J. Hu, et al., IEEE TED, p.2469, (1987)
[9] P. I. Suciu, R. L. Johnston, IEEE TED, p.1846 (1980)
[10] A.G. Sabnis, et al., IEDM Techn. Digest ,p.18 (1979)

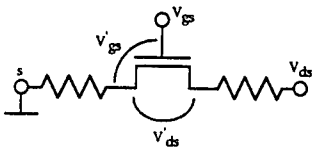


Fig.1 MOS transistor with series resistances

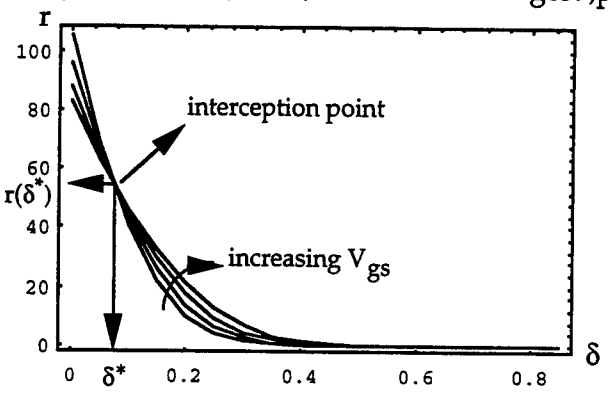


Fig.2 r as a function of δ, V_{gs} is a parameter.

The intersection point is (δ^*,$r(\delta^*)$)

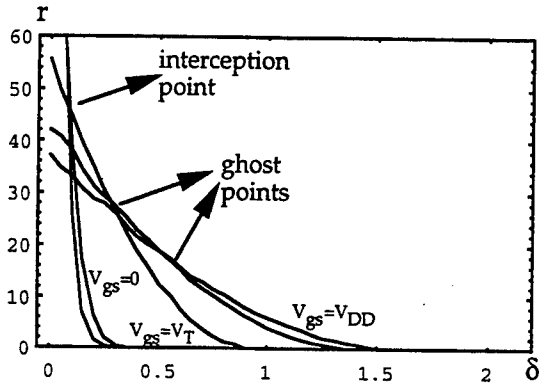


Fig.3 as Vgs increases, more intersection points appear

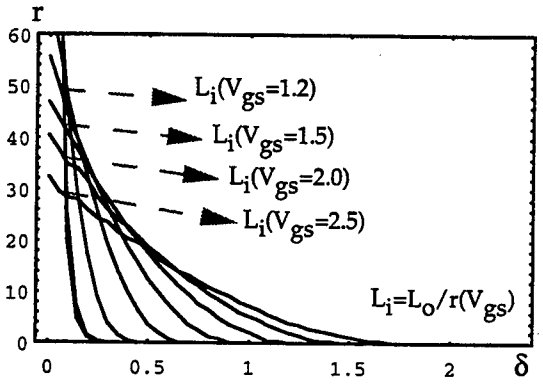


Fig.4 Leff as a function of Vgs can be found as shown

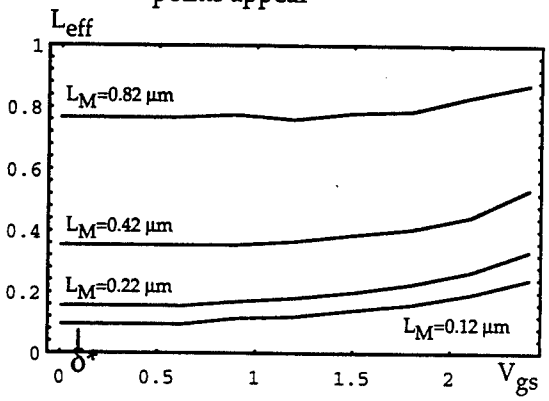


Fig.5 Leff as a function of Vgs for four different mask lengths

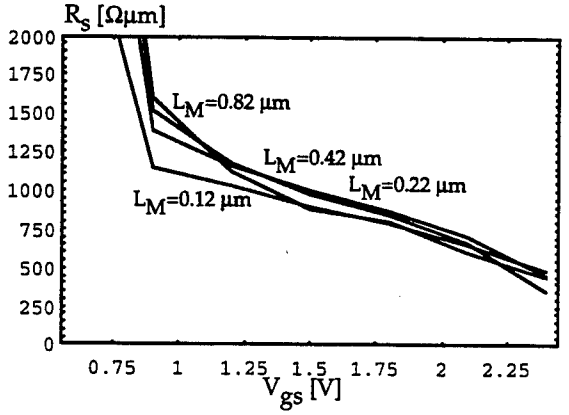


Fig.6 Rs as a function of Vgs for the same masks lengths as in Fig.5

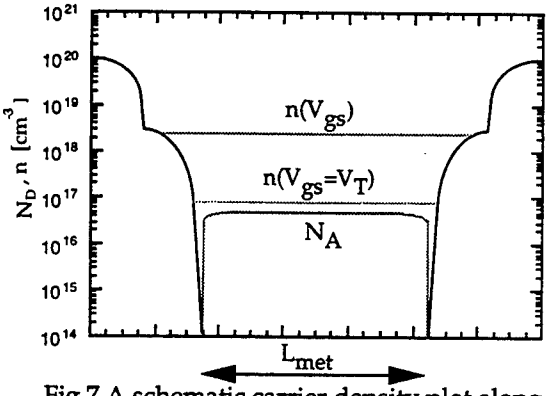


Fig.7 A schematic carrier density plot along the Si/SiO2 interface.The free electron density, and consequently Leff and Rs, change with Vgs.

Thermionic Emission Model for Electron Gate Current in Submicron NMOSFETs

K. Hasnat, C.-F. Yeap, S. Jallepalli, W.-K. Shih, S.A. Hareland, V. M. Agostinelli, Jr., A. F. Tasch, and C. M. Maziar*
Microelectronics Research Center, Department of Electrical and Computer Engineering
The University of Texas at Austin, Austin, Texas 78712, (512) 471-1640
* now with Intel Corporation, Aloha, Oregon

ABSTRACT

A thermionic emission model based on a non-Maxwellian electron-energy distribution function for the electron gate current in NMOSFETs is described. A generalized analytical function is used to describe the high energy tail of the electron energy distribution function. Coefficients of this generalized function are determined by comparing the simulated gate currents with the experimental data. Good agreement with gate currents over a wide range of bias conditions for three different sets of devices is demonstrated with a single set of coefficients. The model also calculates the tunneling component of the gate current self-consistently by using the WKB approximation and by using a more accurate representation of the oxide barrier by including the image potential.

I. INTRODUCTION

Conventionally, the problem of modeling gate current in MOSFETs has been treated in one of two different ways: the lucky electron model [1], or Richardson's thermionic emission model [2]. The lucky electron model is essentially a local-field model, in which it is assumed that the carriers instantaneously attain the steady-state energy associated with the electric field at each point in the device. However, in submicron devices the electric field changes rapidly such that the electrons do not have sufficient time to acquire the steady-state energy associated with the local electric field. Richardson's thermionic emission model is based on the assumption of a Maxwellian hot-electron energy distribution, which does not hold for the high energies associated with gate injection.

Recently, a number of improved approaches for modeling gate current [3-6] have been proposed in the literature. However, some of these approaches [3,5,6] are based on carrier distribution functions obtained from Monte Carlo (MC) simulators employing band structures that are not valid for the high energies involved with gate current. In addition, the tunneling component of the gate current was found to be estimated either as a barrier lowering phenomena [3,6], or calculated by assuming a triangular barrier configuration in the oxide [4,5]. Both of these approaches may result in an incorrect estimation of the tunneling current.

The proposed thermionic emission model for the gate current is based on a generalized function for the electron energy distribution function. It also calculates the tunneling current self-consistently by using the WKB approximation, and considers a more accurate description of the oxide barrier by including the image potential. In order to retain CPU efficiency, the proposed model uses the hydrodynamic post-processor described in [7] for obtaining the average carrier energy in the device.

II. PROPOSED MODEL

A generalized equation for gate current based on the thermionic emission of a heated electron population over the $Si - SiO_2$ interface barrier can be written as:

$$I_g = q \int_0^L dx \int_0^\infty d\varepsilon \, n(x) P(x, E_{ox}) v_\perp(\varepsilon) T(\varepsilon) f(\varepsilon), \tag{1}$$

where ε is electron energy, $v_\perp(\varepsilon)$ is the electron microscopic velocity in the direction normal to the interface, and $T(\varepsilon)$ is the tunneling probability. $\phi_B(x)$, $n(x)$, and $f(\varepsilon, x)$ are the barrier height, electron concentration, and electron energy distribution function, respectively, at an interface location x. $P(x, E_{ox})$ is the probability that an electron will not suffer any collision in the image potential well in the oxide, and is modeled as in [8]. The perpendicular velocity used in the proposed model is extracted from the SLAPSHOT-2B MC simulator [9].

A generalized form for the high energy tail of the energy distribution function based on carrier temperature is used in equation 1 for calculating the gate current.

$$f(\varepsilon) = A \exp\left(-\frac{\varepsilon^\xi}{\eta (kT)^\nu}\right), \tag{2}$$

where A is a normalizing constant, and ξ, ν, and η are coefficients that are to be determined by comparing simulation results with the experimental data. kT is the thermal kinetic energy of the electrons.

Estimation of tunneling current as a barrier lowering phenomena introduces an additional uncertainty in the model, as the amount of barrier lowering depends on the form of the distribution used in the model [5]. In order to eliminate this uncertainty, the tunneling probability is calculated in a self-consistent manner. However, the self-consistent calculation of the tunneling probability used in [4,5] is based on the tunneling probabilities that are derived by neglecting the image potential. But, for the energies involved with the hot-carrier injection in MOSFETs, the image potential must be included when evaluating the tunneling probability. Our proposed model calculates the tunneling probability based on a tunneling barrier in the oxide that includes the image potential. It should be noted that in [4,5] the authors used a triangular barrier with the peak of the barrier reduced by Schottky barrier barrier lowering. Such an approach results in a reduction of the tunneling barrier width as shown in Figure 1, and consequently, an overestimation of the tunneling probability, as shown in Figure 2.

An important point to note is that the energy associated with the calculation of the tunneling probability depends on the condition for momentum conservation at the $Si - SiO_2$ interface. However, if the conservation of parallel momentum held true, both the $< 111 >$ and $< 110 >$ orientations are expected to give much higher effective barrier heights compared to the $< 100 >$ orientation, because of the much larger parallel momentum mismatch. However, this effect is not observed experimentally [10]. This may be due to the disorder in the interfacial region and the amorphous nature of SiO_2. Therefore, the gate current model proposed in this paper, does not invoke momentum conservation at the $Si - SiO_2$ interface.

III. COMPARISON WITH EXPERIMENTAL DATA

The gate current model based on a generalized non-Maxwellian distribution function proposed in this paper has been compared with the experimental data for LDD MOSFETs for three different technologies obtained from two different sources. The 1-D doping profiles obtained for these devices are transformed into 2-D doping profiles by using a complimentary-error function in the lateral direction. The value of the external series resistance to be added to the simulated device is determined by using the method described in [11]. This approach considers the V_G dependence of both ΔL and the series resistance, and therefore, provides a more accurate estimation of the series resistance that is to be added in simulations. The effect of quantization of electrons in the inversion layer is considered by using the model developed in [12]. The inversion layer mobility model of reference [13] was used to obtain the best agreement with experimental $I_D - V_G$ and $I_D - V_D$ characteristics. Figures 3-6 show the comparison of the simulated gate currents (using the thermionic emission model) with the experimental data. Our analysis indicates that for obtaining overall good agreement with the experimental gate current data over a wide range of bias conditions for the three sets of devices, the following values for these coefficients must be used: $\xi = 1.3$, $\eta = 0.265$, and $\nu = 0.75$. It can be seen that the thermionic emission model with this single set of coefficients used for the distribution function predicts the experimental gate current data very well for large variations in the bias conditions for the three sets of devices.

IV. CONCLUSIONS

In this paper we have proposed a gate current model for NMOSFETs based on a generalized function for the high-energy tail of the carrier energy distribution function. The coefficients for this generalized function have been determined by comparing simulated gate currents with the available experimental data. We have demonstrated that with a single set of coefficients for this functional form for the distribution function, good agreement can be obtained for a wide range of bias conditions, and for three sets of devices. The model also calculates the tunneling component of the gate current self-consistently by considering a more complete description of the oxide potential.

REFERENCES

[1] S. Tam et al. *IEEE Trans. on ED*, vol. ED-31, no. 9, p. 1116, 1984.
[2] E. Takeda et al. *IEEE Trans. on ED*, vol. ED-29, no. 4, p. 611, 1982.
[3] C. Fiegna et al. *IEEE Trans. on ED*, vol. ED-38, no. 3, p. 603, 1991.
[4] C. Huang et al. *IEEE Trans. on ED*, vol. 39, no. 11, p. 2562, 1992.
[5] C. Fiegna et al. *IEEE Trans. on ED*, vol. 40, no. 11, p. 2018, 1993.
[6] J.Z. Peng et al. *IRPS*, p. 154, 1994.
[7] V.M. Agostinelli et al. *IEEE Trans. on ED*, vol. 41, no. 10, p. 1784, 1994.
[8] T.H. Ning et al. *J. Appl. Phys.*, vol. 48, p. 286, 1977.
[9] X.L. Wang et al. *J. Appl. Phys.*, vol. 73, no. 7, p. 3339, 1993.
[10] Z.A. Weinberg, *J. Appl. Phys.*, vol. 53, no. 7, p. 5052, 1982.
[11] A. Azuma et al. *Symp. VLSI Tech.*, p. 129, 1994.
[12] M.J. Van Dort et al. *Solid-State Electronics*, vol. 37, no. 3, p. 435, 1994.
[13] H. Shin et al. *IEEE Trans. on ED*, vol. 36, no. 6, p. 1117, 1989.

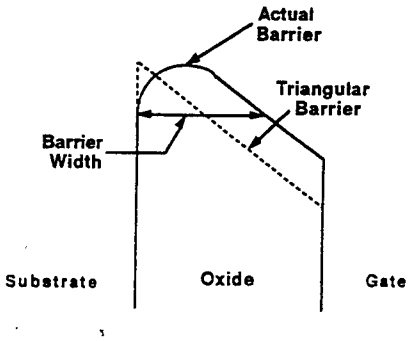


Figure 1: A comparison of the tunneling barrier in the oxide by including the image potential (solid line), and by using a triangular barrier but with a Schottky lowered barrier peak (dashed line).

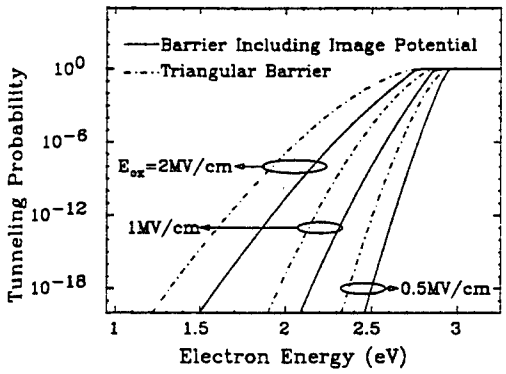


Figure 2: Tunneling probabilities as a function of energy for several oxide fields. Solid lines: including barrier potential; dashed lines: based on triangular oxide potential barrier.

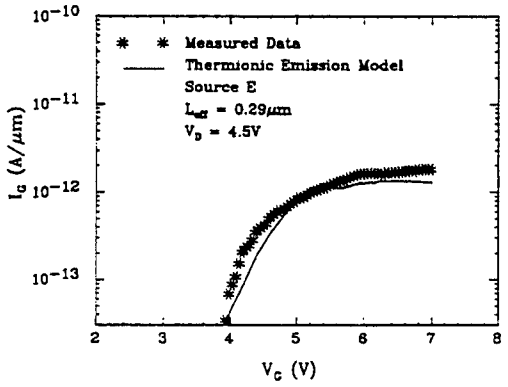


Figure 3: Comparisons of simulated and experimentally measured $I_G - V_G$ curves for the Source E LDD device with L_{eff}=0.29μm.

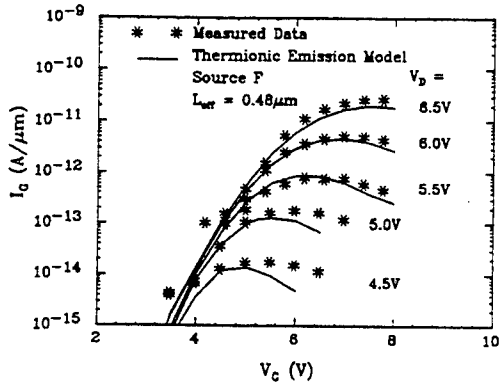


Figure 4: Comparisons of simulated and experimentally measured $I_G - V_G$ curves for the Source F LDD device with L_{eff}=0.48μm.

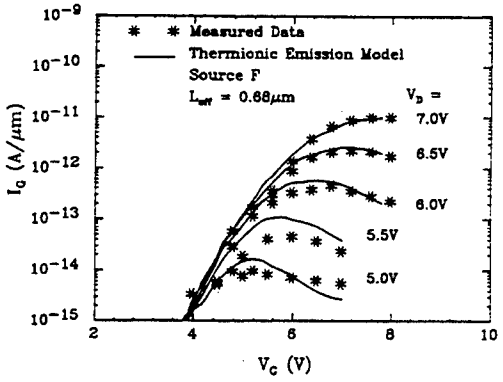


Figure 5: Comparisons of simulated and experimentally measured $I_G - V_G$ curves for the Source F LDD device with L_{eff}=0.68μm.

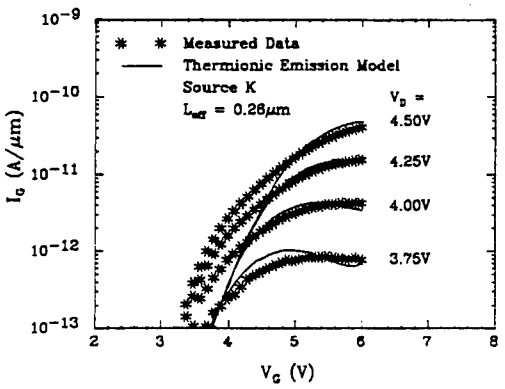


Figure 6: Comparisons of simulated and experimentally measured $I_G - V_G$ curves for the Source K LDD device with L_{eff}=0.26μm.

Better Understanding of the Hydrodynamic and Energy Transport Models for the Terminal Current and Reliability Predictions of deep Submicron MOSFETs

Woo-Sung Choi, Young-June Park, and Hong-Shick Min

Department of Electronics Engineering and Inter-University Semiconductor Research Center
Seoul National University, San 56-1 Shinlim-Dong, Kwanak-Ku, Seoul 151-742, Korea
Phone: +82-2-880-7274, Fax: +82-2-885-4459

The prediction of two important MOSFET characteristics, the drain current enhancement due to the velocity overshoot and the substrate current, by the advanced transport models, the hydrodynamic(HD) and energy transport(ET) models [1] [2], have been studied by means of the device simulator SNU-2D [3] and experimental devices having the channel length in the range of $0.1 \sim 0.2\mu m$. It will be shown that the most important parameters in determining the device characteristics are the heat flow coefficient c in the HD model and the energy flow factor C_e in the ET model(refer to Table 1 for the expression of energy flux vector, $\vec{S}$). Both models give reasonable drain currents if the energy flow parameters are chosen properly. However, these parameters do not necessarily produce identical peak temperature and the substrate current, accordingly.

In the energy balance equation, the spatial variation of energy flow, $\nabla \cdot S$, is the source of non-local effect where the carrier energy (or temperature) is different from the local energy. To see the effect of c and C_e, we performed a sensitivity analysis in which the drain current and the peak temperature(substrate current) are observed with respect to the variation of the energy parameters. For experimental devices, a $0.12\mu m$ SOI N-MOSFET [4], a bulk $0.09\mu m$ N-MOSFET [5], and $0.19\mu m$ and $0.23\mu m$ bulk LDD N-MOSFETs, have been simulated using both models. We plot the simulated and measured drain currents in Fig. 1 and the peak electron temperature in Fig. 2 as functions of $(5/2 + c)$ in the HD model and C_e in the ET model. The ET current/temperature shows relatively larger dependence on C_e than the HD current/temperature on c. It can be easily understood since the whole S is influenced by C_e in the ET model, while only the heat flow term is influenced in the HD model. For devices with the channel length of $0.1\mu m$, both models predict a reasonable drain current compared with the measurement if C_e and $(5/2+c)$ are chosen to be between $1.5 \sim 2.0$. However, for the C_e values in that range, ET model tends to give higher peak temperature than the HD model in the drain region. This trend becomes more prominent for the device with shorter channel length. This trend can be understood from the internal physics of the two models; the mobility and carrier temperature distributions. Figs. 3 and 4 show the velocity components from the HD and ET simulations of a $0.12\ \mu m$ SOI N-MOSFET [4], respectively. Even though the average velocities (v_{total} in the figures) in the channel are identical for the two models, the temperature profiles, so that the mobilities, are different as shown in Figs. 5 and 6. The ET model has additional velocity term (caused by the mobility non-uniformity, $\nabla\mu$) which is + at the source end and − at the drain end of the channel. For the same velocity profiles(so is the drain current), the ET temperature is expected to be higher near the source region (so μ is lower) and lower near the drain region (so μ is higher). From the Fig. 5 and 6, it can be seen that the mobility and the temperature are distributed as expected.

Now the prediction of the substrate current by the HD/ET models will be presented and compared with the measurements. For the impact ionization(I/I) model, the depth-dependent I/I model with the α as a functions of carrier temperature suggested in [6] is used. In Fig. 7,

the I_B/I_D dependence on C_e and $(5/2+c)$ are shown from the ET and HD simulations for the LDDs ($L_{eff} = 0.19\mu m$ and $0.23\mu m$) at $V_G = 2V$ and $V_D = 4V$ together with the measurement data. It is important to notice that the energy flow parameters for best substrate current prediction is larger than that for the drain current prediction. Moreover, the simulation tends to overestimate in the lower drain bias as shown in Fig. 8.

In summary, we have shown that both the HD and ET models predict the drain current enhancement due to velocity overshoot and the peak carrier temperature(so the substrate current) well if the energy flow parameters are chosen properly. However, both models give overestimation of I/I rate at the low drain bias. This suggests that the energy balance equation needs more improvement for the I/I modeling at the low voltage operation.

This work was supported by the Samsung Electronics corporation and the ETRI of Korea.

References

[1] K. Bløtekjær, *IEEE Trans. on Electron Devices,* vol. 17, No.1, p. 38, 1970.
[2] D. Chen et al., *IEEE Electron Device Letters,* vol. 13, p. 26, Jan 1992.
[3] W.-S. Choi et al., *IEEE trans. on CAD/ICAS,* vol. 13, p. 899, July 1995.
[4] W.-S. Choi et al., *IEEE Electron Device Letters*, vol. 16, p. 333, July 1995.
[5] Y. Taur et al., *IEDM Tech. Dig.*, p. 127, 1993.
[6] M. J. van Dort et al., *SISDEP Tech. Dig.*, p. 469, Wien : Springer-Verlag, 1993.

Table 1: Energy flow vectors of the HD and ET models

HD	$-\left(\frac{5}{2}+c\right)\frac{k_B^2}{q}T\mu n\nabla T+(W+k_BT)\vec{v}$
ET	$-C_e\left[\mu nk_BT\vec{E}+\frac{k_B^2}{q}\nabla(n\mu T^2)\right]$

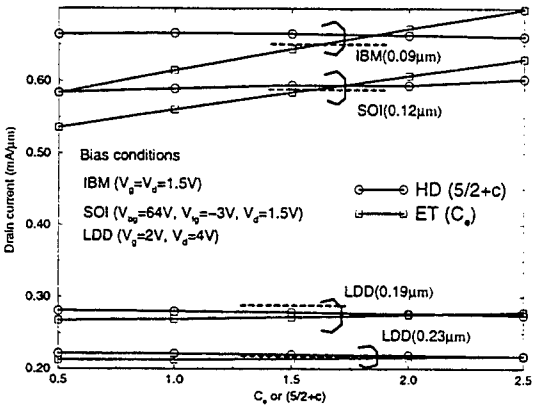


Figure 1: The drain currents as a function of $5/2+c$ in the HD model and as a function of C_e in the ET model for four device structures. Measured current levels are denoted by dashed lines.

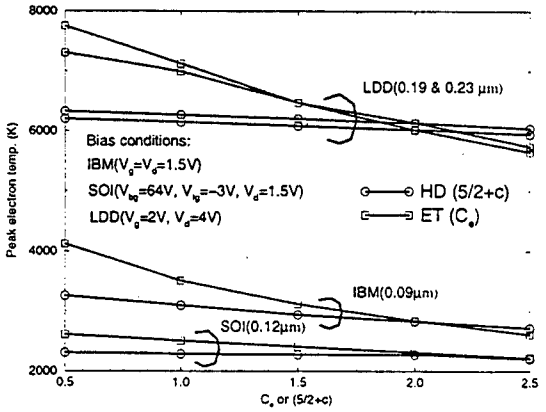


Figure 2: The dependence of the peak temperatures on $5/2+c$ and C_e, in the HD model and in the ET model, respectively for four device structures.

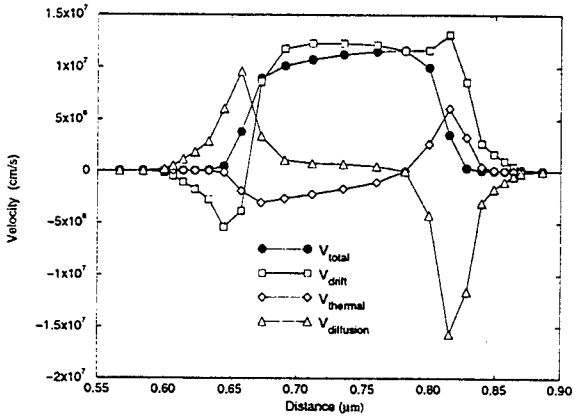


Figure 3: The channel velocity and its components obtained from the HD model in the SOI N-MOSFET using $c=-0.5$. The drain bias, the back-gate bias, and the front-gate bias are 1.5V, 64V, and -3V, respectively.

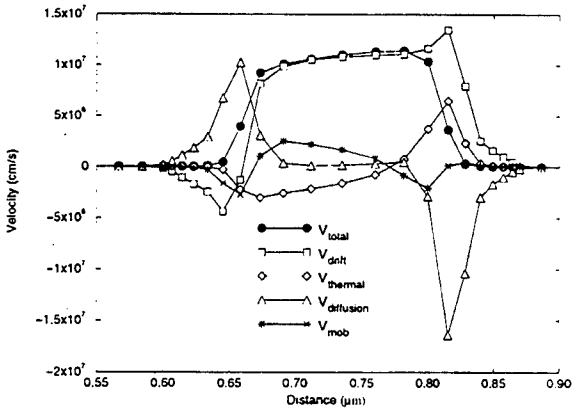


Figure 4: The channel velocity and its components obtained from the ET model in the SOI N-MOSFET using $C_e=1.5$. The drain bias, the back-gate bias, and the front-gate bias are 1.5V, 64V, and -3V, respectively.

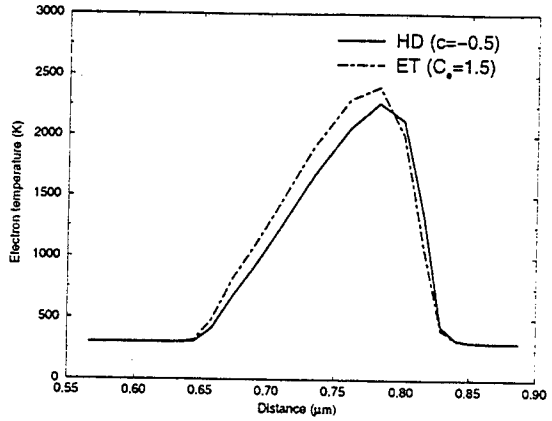


Figure 5: The profiles of channel electron temperature from the HD and ET simulations for the same bias conditions and parameter values used in Fig. 3.

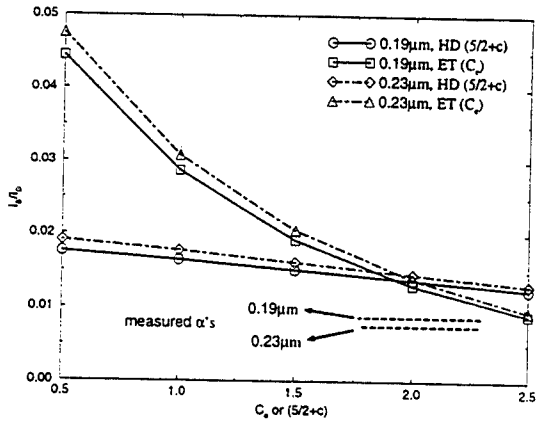


Figure 7: The dependence of I_B/I_D on $5/2+c$ and C_e, in the HD model and in the ET model, respectively for the LDD MOSFETs with channel lengths of $0.19\mu m$ and $0.23\mu m$. The measured α is denoted by the dashed line.

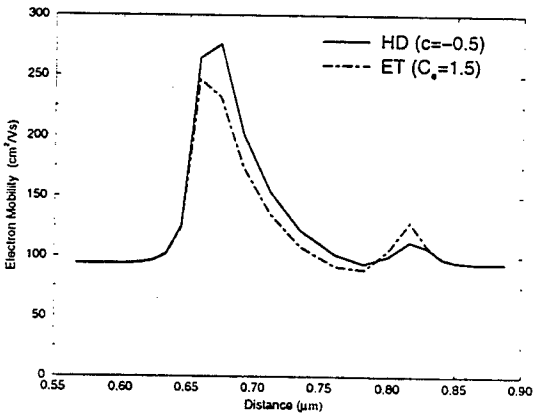


Figure 6: The profiles of channel mobility from the HD and ET simulations for the same bias conditions and parameter values used in Fig. 3.

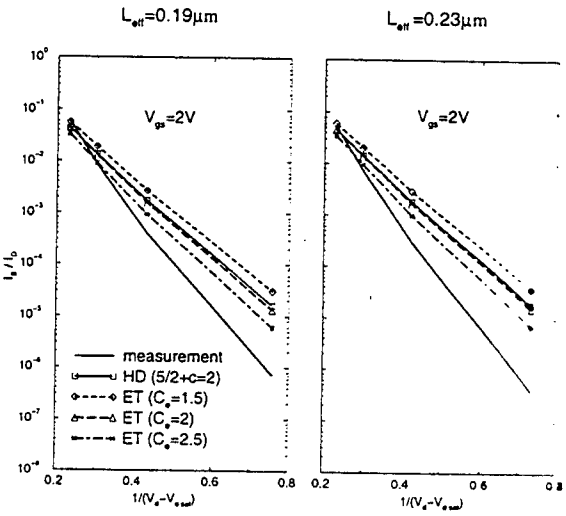


Figure 8: The measured and simulated (I_B/I_D)'s as functions of $1/(V_d - V_{d,sat})$ for the LDD devices with two different channel lengths

Author Index

Abbott, T. 589
Abbott, T. 589
Abdel-Aty-Zohdy, H.S. 313
Abernathy, C.R. 735
Abou-Elnour, A. 549
Ackerman, D.A. 771
Adesida, I. 535
Agostinelli, Jr., V.M. 811
Ahn, H. 239
Aktas, Ö. 531
Aktas, Ö. 575
Alekseev, E. 467
Allen, S.J. 19
Andrukhiv, A. 183
Aninkevicius, V. 193
Appel, C.S. 595
Apte, R.B. 405
Bachem, K. 247
Baker, B. 127
Baker, B. 755
Ballato, A. 359
Bambha, N. 275
Bannov, N. 359
Bannov, N. 39
Banoo, K. 123
Baraff, G.A. 771
Barbieri, S. 459
Bareikis, V. 193
Bark, J.O. 163
Belenky, G.L. 759
Beltram, F. 459
Benistant, F. 351
Benistant, F. 803
Bergendahl, J. 619
Bhapkar, U.V. 263
Bierlein, J.D. 425
Biesemans, S. 807
Bilenko, D. 545
Bimberg, D. 581
Bochkariova, L.V. 183
Boric-Lubecke, O. 251
Botchkarev, A.E. 531
Botchkarev, A.E. 575
Bourel, P. 159
Bradley, R.F. 271
Bradley, R.F. 585
Braunstein, J. 247
Brehmer, D. 19
Brock, T. 589
Brock, T. 589
Bronevoi, I.L. 157
Brown, E. 365
Brown, E.R. 433
Bründermann, E. 307
Bründermann, E. 347
Bründermann, E. 503
Bykhovski, A.D. 541
Caddemi, A. 715
Caddemi, A. 719
Calcatera, M. 61
Cantraine, G. 373
Carleson, P.D. 147
Cavus, A. 275
Cerny, C. 31
Chalyi, V.P. 643
Chan, M. 603
Chang, C.-Y. 699
Chao, I.-N. 505
Chao, K.A. 59
Char, K. 635
Chen, C.J. 87
Chen, G. 739
Chen, H. 139
Chen, J.C. 525
Chen, K. 603
Chen, K. 607
Chen, L. 95
Chen, L.-P. 699
Chen, Q. 535
Chen, W.L. 237
Cheng, J.-Y. 699
Cheng, M.-C. 657
Cheng, Y. 417
Cheng, Y. 603
Cheng, Y. 793
Cho, H.-J. 751
Cho, K. 111
Choi, H.K. 491
Choi, J.H. 677
Choi, K.K. 87
Choi, W.J. 111
Choi, W.-S. 661
Choi, W.S. 703
Choi, W.-S. 815
Choquette, K.D. 779
Chou, A. 13
Christenson, T.R. 397
Chu, M.H. 707
Chung, H. 111
Coldobanova, O. 545
Cooper, Jr., J.A. 517
Cowen, A. 409
Crowe, T.W. 267
Crowe, T.W. 271
Crowe, T.W. 585
Cui, H.L. 103
Currie, M. 631
Dagys, M. 471
Dahan, F. 281
Daher, N. 327
Dai, B.-T. 699
Dai, N. 275
Daneman, M.J. 381
Daniels-Race, T. 123
Danilov, S.N. 273
Dapkus, P.D. 417
Das, M.B. 287
de Boer, W.B. 91
de Lange, G. 463
De Los Santos, H.J. 669
De Meyer, K. 807
Deboy, G. 51
Deen, M.J. 781
Dekker, R. 91
del Alamo, J. 337
DeMain, C.S. 155
Dengler, R.J. 481
Denisov, D.V. 643
Denton, J.P. 797
Dessenne, F. 159
Destine, J. 373
Dhuler, V.R. 409
Dmitriev, V.A. 529
Donetsky, D.V. 273
Drugova, A.A. 197
Dubois, E. 563
Dubois, E. 71
Dubon, O.D. 503
Duster, J. 607
Dutta, M. 119
Dutta, M. 359
Dyakonov, M.I. 455
East, J. 589
East, J. 589
East, J.R. 237
Eastman, L.F. 247
Ekström, H. 611
El Nokali, M. 239
Eppers, C. 61
Erickson, N.R. 267
Ershov, O.G. 421
Faist, J. 489
Fan, Z. 575
Fan, Z.F. 531
Fauquembergue, R. 159
Feldman, M.J. 631
Feng, S. 337
Feofanov, G.N. 291
Firsov, D.A. 273
Fitzgerald, E.A. 35
Fjeldly, T.A. 591
Fjeldly, T.A. 793
Fonash, S.J. 689
Forrest, S.R. 5
Förster, A. 337
Förster, A. 433
Fouks, B.I. 295
Fradkov, A.L. 221
Frantsuzov, A.A. 291
Fu, T.L. 167
Fulford, J. 13
Gaevski, M.E. 643
Gaidukov, M. 627
Galishnikova, Y. 545
Ganichev, S.D. 99
Gardner, M. 13
Gausepohl, S.C. 635
Gedridge, Jr., R.W. 19
Gelmont, B. 171
Gelmont, B. 559
Gelmont, B. 711
Gelmont, B.L. 277
Gelmont, B.L. 541
Gerecht, E. 619
Gershenzon, E.M. 619
Geva, M. 147
Gildenblat, G. 163
Gildenblat, G. 171
Globus, T. 155
Globus, T. 27
Globus, T. 567
Globus, T. 711
Gol'tsman, G.N. 619
Gol'tsman, G.N. 639
Gornik, E. 495
Govindan, T.R. 649
Gribnikov, Z.S. 451
Grisé, W.R. 553
Grisé, W.R. 653
Groves, J.F. 567
Grubin, H.L. 649
Grupen, M. 775
Gu, S.L. 525
Gu, S.L. 743
Guegan, G. 351
Guegan, G. 803
Guo, L. 657
Hack, M. 685
Haddad, G. 589
Haddad, G. 589
Haddad, G.I. 237
Haddad, G.I. 335
Hadley, G.R. 779
Haller, E.E. 503
Han, I.K. 111
Han, J.-C. 751

Han, J.-H. 673
Han, M.-K. 695
Han, P. 135
Han, P. 139
Han, P. 743
Hangleiter, A. 107
Hansen, W.L. 503
Hareland, S.A. 811
Härle, V. 107
Hartnagel, H.L. 299
Haruyama, J. 303
Harvey, J. 243
Hashimoto, N. 789
Hasnat, K. 811
Heiss, W. 495
Heitzmann, M. 351
Heitzmann, M. 803
Henderson, R. 429
Hergenrother, J.M. 615
Hesler, J.L. 271
Hesler, J.L. 585
Hess, K. 775
Hiramoto, T. 801
Hobart, K.D. 115
Hong, C.H. 703
Hong, K. 467
Horing, N.J.M. 103
Horton, T.U. 437
Horvath, L.F. 259
Hsiang, T.Y. 631
Hsu, C.C. 151
Hsu, J.W.P. 35
Hu, C. 603
Hu, C. 607
Hu, L.Q. 135
Hu, L.Q. 139
Hu, Q. 337
Hu, Q. 433
Hu, Q. 463
Hu, Q. 623
Huang, J. 603
Huang, W. 521
Huang, X.D. 135
Huang, Z.C. 525
Hübers, H.-W. 307
Hübers, H.-W. 347
Hull, R. 147
Hurkx, G.A.M. 91
Hurt, M.J. 79
Hwang, H. 243
Hwu, R.J. 143
Hwu, R.J. 19
Hwu, R.J. 201
Hwu, R.J. 755
Hybertsen, M.S. 771
Iafrate, G.J. 359
Iafrate, G.J. 39
Ieong, M.-K. 47
Ikeda, S. 789
Ikossi-Anastasiou, K. 55
Iliadis, A.A. 571
Iliadis, A.A. 681
Iñíguez, B. 591
Ipatova, I.P. 323
Itoh, T. 251
Jacobs-Perkins, D. 631
Jain, F. 521
Jalali, B. 179
Jallepalli, S. 811
Janes, D.B. 739
Jarkova, A. 545
Jeng, M.-C. 603
Jo, N.H. 677
Johnson, S. 755
Jones, J.R. 259
Jones, S.H. 155
Jones, S.H. 259
Jones, S.H. 567
Jordan, S. 595
Juciene, V. 187
Kaiser, W.J. 389
Kamijoh, T. 729
Kanaley, J. 445
Kancleris, Z. 471
Kang, K.N. 111
Karasik, B. 611
Karlicek, Jr., R.F. 147
Kasahara, K. 441
Katilius, R. 193
Kazarinov, R.F. 759
Kazarinov, R.F. 771
Keilitz, W. 51
Kenny, T.W. 389
Khan, M.A. 535
Khasina, E. 545
Kholodnov, V.A. 197
Khvalkovskii, N.A. 225
Khylap, G. 183
Khylap, G. 209
Kiang, M.-H. 381
Kim, D.J. 111
Kim, D.-K. 287
Kim, H.J. 111
Kim, H.R. 677
Kim, J.H. 703
Kim, J.-K. 577
Kim, J.-S. 377
Kim, K.W. 359
Kim, M.-J. 287
Kim, S.H. 111
Kim, S.J. 111
Kim, S.-J. 287
Kim, W. 531
Kim, W. 575
Kim, Y.-S. 205
Kim, Y.-S. 751
King, M.I.H. 781
Kirchoefer, S.W. 83
Klaassen, E.H. 385
Klaassen, F.M. 131
Klimenko, A.G. 291
Klimov, A.E. 291
Knorr, C. 107
Ko, P.K. 603
Ko, P.K. 607
Kochegarov, Y.V. 273
Koester, D.A. 409
Koh, P.J. 267
Koizumi, R. 789
Kolagunta, V. 739
Kollberg, E. 611
Kop'ev, P.S. 581
Korman, C.E. 43
Kornegay, K.T. 517
Korobov, V. 283
Korotkov, A.N. 355
Korshak, A.N. 451
Kotel'nikov, I.N. 99
Kougianos, E. 55
Kovacich, J.A. 389
Kovacs, G.T.A. 385
Krowne, C.M. 55
Kruglick, E. 389
Krystek, W. 23
Kub, F.J. 115
Kubicek, S. 807
Kumar, K. 13
Kuramochi, E. 413
Kuznetsov, N.I. 529
Kwack, K.D. 677
Kwan, W.S. 781
Kwok, H.L. 95
Lai, K. 13
Lam, M.P. 517
Lau, K.M. 445
Lau, K.Y. 381
Lazzarino, M. 459
Leburton, J.P. 319
Leburton, J.P. 373
Ledentsov, N.N. 581
Lee, J.C. 13
Lee, J.-H. 377
Lee, J.-H. 377
Lee, J.I. 111
Lee, J.W. 735
Lee, K. 673
Lee, M. 189
Lee, M. 635
Lee, P.P. 19
Lee, S.-C. 751
Lee, S.-H. 377
Lee, T.H. 481
Lei, T.F. 699
Lei, X.L. 103
Leibovitch, M. 23
Lent, C.S. 309
Lerme, M. 351
Levinshtein, M. 343
Levinshtein, M.E. 513
Li, B. 167
Li, R.-G. 67
Liang, J.-B. 67
Liberis, J. 193
Likharev, K.K. 355
Lin, H.-Y. 699
Lin, L.-Y. 67
Linhart, A.M. 503
Lippens, D. 645
Liu, C.-P. 127
Liu, J.L. 743
Liu, L.-T. 393
Liu, Z. 603
Livreri, P. 715
Lo, T.-C. 393
Loehr, J.P. 31
Logan, R.A. 771
Lu, J.G. 615
Lu, X.J. 485
Lu, Y. 743
Lubecke, V.M. 477
Lujan, R. 405
Luryi, S.L. 759
Luscombe, J. 683
Lutz, C.R. 445
Lutz, Jr., C.R. 619
Lyubomirsky, Il 623
MacDougal, M.H. 417
Mahadevan, R. 409
Malikova, L. 23
Markus, K.W. 409
Martin, F. 351
Martin, F. 803
Martynov, J.B. 175
Maslov, A.Y. 323
Masselink, W.T. 571
Massey, J.G. 189
Matagne, P. 319
Matagne, P. 373
Mattauch, R.J. 263
Mattauch, R.J. 277
Mattauch, R.J. 711
Matulioniene, I. 193
Matulionis, A. 193
Mayergoyz, I.D. 43

Mayerhofer, B. 99
Maziar, C.M. 811
McAlister, S.P. 599
McCann, P.J. 505
McCormick, K. 19
McGrath, W.R. 477
McKinnon, W.R. 599
Mecozzi, A. 767
Medvedev, B.K. 585
Mehdi, I. 481
Mei, P. 405
Melloch, M.R. 337
Melloch, M.R. 739
Metze, G. 61
Micheel, L.J. 299
Mickevicius, V. 359
Mikhailov, S.A. 665
Mikhailova, M.P. 421
Miller, L.M 389
Min, B.-H. 695
Min, H.-S. 661
Min, H.-S. 815
Minarsky, A.M. 213
Mink, J.W. 243
Mitin, V. 283
Mitin, V. 359
Mitin, V. 39
Mitin, V. 451
Mohammad, S.N. 531
Mohammad, S.N. 575
Mohammad, S.N. 75
Moiseev, K.D. 421
Moon, B.J. 79
Moore, M.V. 147
Mordovets, N.A. 99
Mørk, J. 767
Morkoç, H. 531
Morkoç, H. 575
Morkoç, H. 75
Morton, P.A. 771
Moskovits, M. 303
Mueller, E.R. 619
Müller, G. 91
Muller, R.S. 381
Müller, U. 51
Munns, G.O. 237
Musante, C.F. 619
Na, K.-Y. 205
Na, K.-Y. 751
Nagaraja, S. 373
Nagaraja, S.H. 319
Najafi, K. 401
Narasimhan, R. 201
Neidhard, B. 61
Neil, T. 571
Neudeck, G.W. 797
Nguyen, L.D. 1
Nikols, M. 19
Nishiya, T. 413
Nötzel, R. 413
Nurmikko, A.V. 7
Nuteson, T.W. 243
Nylen, P. 405
Oakley, B.A. 313
Onat, B. 429
Orsevskij, V. 471
Osadchiy, V. 627
Otten, J.A.M 131
Palmour, J.W. 513
Pan, D.-S. 251
Pan, S.-K. 271
Pan, S.-K. 585
Paolella, A. 243
Papanicolaou, N. 115
Papanicolaou, N.A. 143
Park, C.-M. 695
Park, H. 281
Park, H. 343
Park, Y.-J. 661
Park, Y.-J. 815
Patel, M. 19
Paulavicius, G. 39
Pavlidis, D. 467
Pearton, S.J. 735
Pease, A. 481
Peatman, W.C.B. 267
Peatman, W.C.B 343
Peatman, W.C.B. 365
Peatman, W.C.B. 79
Pedersen, F. 591
Pereiaslavets, B. 247
Peskov, N.V. 585
Petelenz, D.G. 755
Petersen, R. 755
Peterson, R. 127
Petikov, N.I. 291
Petrou, A. 119
Petrov, V.A. 585
Phillips Jr., A. 595
Ping, A.T. 535
Podosek, J.A. 389
Pokrovskii, Y.E. 225
Pollak, F.H. 23
Pomrenke, G. 333
Posse, V. 179
Posvyanskii, D.V. 665
Pozela, J. 187
Pozela, K. 187
Prasad, S. 167
Prettl, W. 99
Proshina, O.V. 323
Pudikov, V. 417
Qin, L.H. 525
Rahman, A. 463
Ratnaparkhi, P.L. 567
Raychaudhuri, A. 781
Ready, S.E. 405
Reay, R.J. 385
Ren, F. 735
Reynolds, Jr., C.L. 759
Rhodes, D.L. 485
Rishton, S. 571
Roberson, D. 409
Robertson, J. 365
Robilliart, E. 563
Robilliart, E. 71
Rodin, P.B. 213
Rooks, M.J. 337
Röser, H.P. 307
Röser, H.P. 347
Röser, H.P. 503
Routkevitch, D. 303
Rozario, R.P. 201
Ruden, P.P. 369
Rumyantsev, S.L. 343
Rumyantsev, S.L. 513
Russell, E. 143
Rutledge, D.B. 477
Ryoo, J.-H. 577
Sadwick, L. 127
Sadwick, L.P. 143
Sadwick, L.P. 19
Sadwick, L.P. 201
Sadwick, L.P. 755
Saitoh, T. 731
Sakalas, P. 193
Saltis, R. 193
Samelis, A. 467
Sannino, M. 715
Sannno, M. 719
Sawdai, D. 467
Schacham, S.E. 281
Schäpers, T. 337
Scholz, F. 107
Schreiber, H.-U. 747
Schuermeyer, F. 31
Schulman, J.N. 669
Schünemann, K. 549
Semendy, F. 275
Shadchin, S.A. 221
Shaffner, T.J. 9
Shafirova, T.U. 291
Shalapaev, S.N. 291
Shalygin, V.A. 273
Shchukin, V.A. 581
Shen, B. 525
Sherman, V. 627
Sherriff, R.E. 31
Shi, Y. 139
Shi, Y. 525
Shi, Y. 743
Shield, J.E. 19
Shih, W.-K. 811
Shtengel, G.E. 771
Shul, R.J. 735
Shul'man, A.Y. 229
Shul'man, A.Y. 99
Shumsky, V.N. 291
Shur, M. 365
Shur, M. 79
Shur, M.S. 277
Shur, M.S. 343
Shur, M.S. 455
Shur, M.S. 535
Shur, M.S. 541
Siegel, P.H. 481
Silverman, P.J. 35
Sim, J.-H. 377
Simin, G.S. 221
Simin, G.S. 343
Simin, G.S. 513
Simniskis, R. 471
Sinkevitch, V.F. 175
Sinkevitch, V.F. 233
Sirenko, Y. 359
Sleiman, A. 159
Smirnova, O.I. 225
Smith, L. 409
Smolski, O.V. 643
Sobolewski, R. 631
Soh, S.-H. 127
Soldatenkova, V.V. 291
Solgaard, O. 381
Song, B.G. 677
Song, J.-H. 661
Sorba, L. 459
Steer, M.B. 243
Stengel, F. 75
Stillman, G.E. 437
Stone, D.R. 681
Street, R.A. 405
Streit, D.C. 19
Strel'chuk, A.M. 509
Stroscio, M.A. 359
Stroscio, M.A. 39
Subashiev, A. 217
Sugimoto, Y. 441
Sugo, M. 413
Sun, C.J. 535
Sun, L.Q. 711
Sung, Y.-K. 577
Suzue, K. 531
Swaminathan, V. 759
Swishchev, A. 627

Tabatabaei, S.A. 681
Tager, A.A. 303
Tager, A.S. 175
Tait, G.B. 259
Tamamura, T. 413
Tamargo, M. 275
Tan, G.L. 303
Tanaka, T. 607
Tanbun-Ek, T. 771
Tang, T.-W. 47
Tanimura, A. 731
Tasch, A.F. 811
Tedesco, S. 351
Tedesco, S. 803
Temmyo, J. 413
Tessler, N. 763
Thalhammer, R. 51
Thean, V.Y. 373
Thean, V.Y.A. 319
Theunissen, M.J.J. 91
Thobel, J.L. 159
Thompson, P.E. 115
Thornber, K.K. 103
Tidrow, M.Z. 87
Tien, N.C. 381
Tinkham, M. 615
Tishinin, D. 417
Tougaw, P.D. 309
Towe, E. 281
Towe, E. 429
Tsai, R. 365
Tsai, R. 79
Tsien, P.-H. 393
Tsui, D.C. 87
Turner, G.W. 491
Ünlü, M.S. 429
Unterrainer, K. 495
Vagidov, N.Z. 451
Vai, M. 725
Van Calster, A. 785
van den Einden, W.T.A. 91
van der Weide, D.W. 255
Varakorn, K. 239
Varvanin, N.A. 99
Vaschenko, V.A. 175
Vaschenko, V.A. 233
Vatannia, S. 171
Vendik, I. 627
Verghese, S. 337
Verghese, S. 433
Volkov, V.A. 665
Vorobjev, L.E. 273
Voronov, B.M. 619
Wachutka, G. 51
Wada, H. 729
Wadley, H.N.G 567
Waldman, J. 619
Walker, J.F. 147
Walker, J.F. 17
Wang, C.-C. 631
Wang, F. 743
Wang, R.H. 135
Wang, X. 237
Wang, Z. 619
Wann, H.C. 607
Webb, K.J. 739
Weikle, R.M. 271
Weikle, R.M. 585
Weiser, K. 281
Weisfield, R. 405
Whalen, J. 61
Whittaker, E.A. 499
Wieczorek, K. 747
Wilhelm, U. 107
Witters, J.S. 785
Wojciechowski, D. 785
Wong, Z.-G. 67
Woo, D.H. 111
Wood, C.E.C. 681
Woolard, D.L. 485
Wu, C.H. 707
Wu, D.-X 67
Wu, X.D. 405
Wyss, R.A. 337
Xie, Y.H. 35
Xu, B. 623
Xu, J.M. 303
Yakovlev, Y.P. 421
Yakubo, K. 337
Yang, E.S. 151
Yang, G.M. 417
Yang, J.W. 535
Yang, K. 525
Yang, R. 369
Yang, Y.F. 151
Yeap, C.-F. 811
Yngvesson, K.S. 619
Yoh, K. 731
Yoh, K. 789
Yoo, S.D. 677
Yoshida, M. 607
Ytterdal, T. 365
Ytterdal, T. 79
Yu, S.G. 359
Yuan, S. 505
Zahurak, J.K. 571
Zamdmer, N. 433
Zavada, J. 359
Zegrya, G.G. 421
Zeng, L. 275
Zengingönül, H.P. 429
Zhan, C.-Q. 393
Zhang, R. 525
Zhang, R. 743
Zhang, Y.J. 755
Zheng, Y.D. 135
Zheng, Y.D. 139
Zheng, Y.D. 525
Zheng, Y.D. 743
Zhu, S.M. 135
Zhu, S.M. 743
Ziaie, B. 401
Zirath, H. 475
Zolper, J.C. 735